# Mathematical modeling in the environment: from tsunamis to powder-snow avalanches

Denys Dutykh

Université de Savoie

---

**Demande d'habilitation à diriger des recherches**

*Spécialité : Mathématiques appliquées*

---


Présentée par

**Denys DUTYKH**


# Modélisation mathématique pour l'environnement

Présentée et soutenue le 3 décembre 2010 devant le jury composé de :

| | |
|---|---|
| M. Didier BRESCH | Examinateur |
| M. Thierry COLIN | Examinateur |
| M. Benoît DESJARDINS | Rapporteur |
| M. Florian DE VUYST | Rapporteur |
| M. Frédéric DIAS | Examinateur |
| M. Christian KHARIF | Rapporteur |
| M. David LANNES | Examinateur |
| M. Paul MILEWSKI | Rapporteur |

*To my parents, my sister.*

# Remerciements

*Physics is, hopefully, simple. Physicists are not.*

Edward Teller

*En tout premier lieu je tiens à remercier Frédéric Dias qui m'a formé pendant ma thèse. Sans lui ce travail n'aurait pas été possible. Il m'a beaucoup soutenu et conseillé tout au long de ces dernières années de recherche. Frédéric, je t'en suis très reconnaissant.*

*Je dois également beaucoup à Didier Bresch qui m'a proposé de venir travailler au LAMA et qui m'a constamment soutenu dans mes aventures savoisiennes. Ses oeuvres scientifiques et nos discussions informelles ont été une source inépuisable de mon ispiration. Didier, merci beaucoup pour la confiance que tu m'as accordée ainsi que pour tes encouragements qui m'ont aidés à mener à bien mes projets.*

*Je voudrais ici remercier Didier Clamond qui m'a beaucoup appris sur la théorie des vagues. J'espère continuer à collaborer avec lui. En plus de notre collaboration fructueuse, il m'a toujours passionné par sa façon de procéder: franche, droite et honnête. Il est pour moi un exemple à suivre.*

*J'adresse mes remerciements les plus vifs aux membres de mon jury : Benoît Desjardins, Christian Kharif et Paul Milewski qui ont accepté la lourde tâche d'être rapporteurs, ainsi que Thierry Colin, Florian De Vuyst et David Lannes que je remercie pour l'intérêt qu'ils portent à mes travaux en acceptant de faire partie du jury.*

*Je dois énormement à mes collaborateurs sans qui une grande partie de ces travaux n'auraient sans doute pas pu voir le jour.*

*Ces années de recherche au sein du LAMA se sont déroulées dans un environnement scientifique exceptionnel. Ce laboratoire de mathématiques est un lieu où il fait bon faire de la science. Je remercie chaleureusement les membres de l'équipe EDPs$^2$ ainsi que les autres*

*membres du laboratoire pour leur accueille et soutien permanent. Plus personnellement je voudrais remercier ici Céline Acary-Robert, Claudia Billat, Marguerite Gisclon et Édouard Oudet pour leur amitié tout à fait réciproque. Je remercie également les étudiants qui ont accepté de faire leurs premiers pas dans la recherche sous mon (co-)encadrement.*

*J'exprime ma gratitude aux personnes qui m'ont soutenu parfois indirectement dans les démarches administratives dès mon installation à l'Université de Savoie : Luc Frappat (VPCS de l'Université de Savoie), Pierre Baras (directeur de l'UFR SFA), Laurent Vuillon et Didier Bresch (directeurs du LAMA). J'ai également une pensée particulière pour notre sécretaire Nadine Mari qui a toujours fait de son mieux pour accompagner les chercheurs du LAMA au quotidien.*

*Je dis un grand merci à mes amies Alexandra Pradeau, Alexandra Vasylchenko, Kristina Lelyukh et Olga Nikolaeva pour tous les moments agréables partagés ensemble.*

*Finalement, je remercie ma famille et leur dédie ce manuscrit pour leur soutien sans limites et toutes les autres raisons qui s'imposent.*

# Abstract

*Scientific discovery may not be better than sex, but the satisfaction lasts longer.*

Stephen Hawking

The present manuscript is devoted to the mathematical modeling of several environmental problems ranging from water waves to powder-snow avalanches. This Habilitation is organized globally in three parts. The first part is essentially introductive and contains also the complete description of my scientific activities.

Scientific works dealing with water waves are regrouped in Part II. The spectrum of covered topics is large. We start by proposing in Chapter 3 a generalized Lagrangian for the water wave problem. This generalization allows for easy and flexible derivation of approximate models in shallow, deep and intermediate waters. Some questions of viscous wave damping are also investigated in the same chapter. Chapter 4 is entirely devoted to various aspects of tsunami wave modeling. We investigate the complete range of physical processes from the generation, through energy transformations and propagation up to the run-up onto coasts. The next Chapter 5 is devoted specifically to the numerical simulation and mathematical modeling of the inundation phenomena. This question is studied by various approaches: Nonlinear Shallow Water Equations (NSWE) solved analytically and numerically, Boussinesq-type systems and two-fluid Navier-Stokes equations.

In Part III we investigate two important questions belonging to the field of multi-fluid flows. Chapter 6 is essentially devoted to the formal justification of the single-velocity two-phase model proposed earlier for aerated flows modeling. Several numerical results are presented as well. Moreover, similar analytical computations performed in a simpler barotropic setting are provided in Appendix A. These results could apply, for example, to the simulation of violent wave breaking.

Finally, in Chapter 7 we propose a novel model for powder-snow avalanche flows. This system is derived from classical bi-fluid Navier-Stokes equations and has several nice properties. Numerical simulations of the avalanche interaction with obstacle are also presented.

# Résumé

*It is by logic that we prove, but by intuition we discover.*

Henri Poincaré

Ce mémoire est consacré à la modélisation mathématique de quelques problèmes environnementaux. Ces travaux couvrent des thématiques allant des vagues jusqu'aux avalanches de neige poudreuse. Cette habilitation se compose de trois parties. La première partie est essentiellement introductive et contient également la description complète des mes activités de recherche.

Les travaux scientifiques en lien avec la théorie des vagues sont regroupés dans la partie II. Le spectre des sujets abordés est large. Dans le chapitre 3 nous proposons un Lagrangien généralisé pour le problème des vagues. Cette généralisation permet d'obtenir de nouveaux modèles approchés des vagues dans l'eau profonde, peu profonde ou en profondeur intermédiaire. Dans le même chapitre nous étudions également quelques questions liées à la dissipation visqueuse de l'intumescence. Le chapitre 4 traite de différents aspects de la modélisation des tsunamis. Nous étudions toute la gamme des processus physiques de la génération, transformations d'énergie, propagation jusqu'à l'inondation des côtes. Le chapitre 5 est spécialement dédié aux différents aspects de la simulation numérique et de la modélisation d'inondation. Ces questions sont traitées par différentes approches: les équations de Saint-Venant, les équations de type de Boussinesq et le système de Navier-Stokes bi-fluide.

Dans la partie III nous nous intéressons à deux problèmes relevant principalement des écoulements multi-fluides. Le chapitre 6 contient la justification formelle du modèle bifluide à quatre équations proposé avant pour la modélisation des écoulements aérés. Quelques résultats numériques sont également présentés. Les calculs similaires effectués dans le cas barotrope sont donnés dans l'appendice A. Ces résultats peuvent s'appliquer, par exemple, à la simulation numérique du déferlement. Finalement, dans le chapitre 7 nous proposons un nouveau modèle pour les avalanches de neige poudreuse. Ce système est dérivé du Navier-Stokes bifluide classique et possède de bonnes propriétés qualitatives. Les simulations numériques d'interaction d'une avalanche avec obstacle sont présentées.

# Contents

# List of Figures

# List of Tables

# Part I

# Preface

# Chapter 1

# Introduction

*Science is like sex. Sure, it may give some practical results, but that's not why we do it.*

Richard Phillips Feynman

Scientific works presented in this Habilitation have been essentially performed during the last three years (2008 — 2010). After defending my PhD thesis in December 2007, I spent the third year of my PhD grant at LRC Méso CEA/CMLA, ENS de Cachan, where I continued my research work and prepared various competitions for permanent positions.

Fortunately, in May 2008 I was admitted to CNRS as a « Chargé de Recherche » and appointed in October 2008 to the Laboratory of Mathematics (LAMA UMR # 5127, University of Savoie) which has become my new working place. I have been always enjoying the exceptional environment and beneficial conditions of this laboratory.

The new breath in my research activities can be ascribed to fruitful interactions with my new colleagues — Didier Bresch, Marguerite Gisclon and Céline Acary-Robert. In August 2008 I had a chance to meet Didier Clamond in Adelaide, Australia. I learned a lot from him about the water wave problem. Finally, a productive collaboration with Dimitrios Mitsotakis and Theodoros Katsaounis was also initiated.

The present Habilitation contains three parts. The first one is introductive and contains additionally a detailed description of my professional activities, while the two others are devoted to the description of my scientific works.

In this introductive chapter we make a general review of the manuscript and point out, whenever possible, the context and motivations for various studies described below. Introductions specific to considered research fields are systematically given in the beginning of each chapter.

## 1.1 Water waves

The Part II includes scientific works on various aspects of the water wave theory. It is also the largest part in my Habilitation. This fact reflects my deep and old interest in this subject.

Chapter 3 contains two studies devoted to completely different questions of the water wave theory. Section 3.1 is based on our recent collaborative research work with Didier Clamond [CD10]. More precisely, we propose a generalized Lagrangian variational formulation which is exploited further to derive several known and several novel approximate models for water waves in shallow, intermediate and deep waters.

During my PhD thesis in collaboration with Frédéric Dias we initiated a research on the inclusion of weak dissipative effects into the water wave problem [DD07b, DD07c, Dut09b]. A little sequel to these studies is given in Section 3.2 where we investigate the transient behaviour of the viscopotential flow group velocity.

The next Chapter 4 is devoted to my preferred topic in water waves theory — a tsunami wave modeling. Recent events, especially the Tsunami Boxing Day 2004 [SB06], attracted a lot of attention to this problem. The destructive potential of these waves (see Figure 1.1 for illustration) represents a primary hazard for a large number of coastal communities in Indian and Pacific Oceans. Many studies in this chapter were initiated during my PhD but finalized much later.

Section 4.1 discusses the notion of tsunami wave energy and approaches to its estimation. Energy transformations are studied from the generation and during the wave propagation [DD09a]. The next study described in Section 4.2 was initiated by a question of Costas Synolakis during my PhD thesis defense. He wondered if we can predict the effect of mud layers on tsunami generation process. A complete answer on this question required some time and resulted in this publication [DD10] which greatly relies on methods developed in our previous work [DD09b]. Section 4.3 is entirely devoted to the operational and efficient numerical simulation of tsunami waves from the generation and to the run-up onto coasts. This work was done in collaboration with Raphaël Poncet and Frédéric Dias [DPD10]. Finally, Chapter 4 ends with Section 4.4 which contains our very recent study of tsunami generation process using the latest advances in seismology (finite fault inversion algorithm) [DMG10].

Continuously we move to Chapter 5 devoted to the simulation of inundation processes. In Section 5.1 we present several finite volume schemes to discretize Boussinesq-type equations [DKM10]. These schemes were developed in collaboration with Theodoros Katsaounis and Dimitrios Mitsotakis. One of the main novelties in this study is the simulation of run-up using a dispersive wave model. Our scheme is validated by comparisons with


**Figure 1.1:** Picture of Banda Aceh before and after Tsunami Boxing Day 2004.

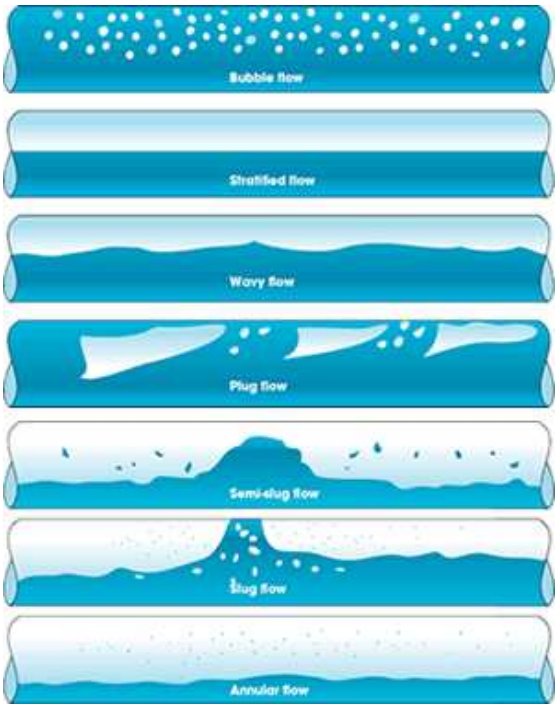


**Figure 1.2:** Various types of two-phase flows.

experimental data of C. Synolakis [Syn87]. Section 5.2 contains a comparison of three different approaches to solve the well-known dam-break problem: an analytical approach, a numerical one with Nonlinear Shallow Water Equations (NSWE) and expensive two-fluid simulations. The limits of each approach are then discussed.

Consequently, in this part of the manuscript we investigate a wide spectrum of problems ranging from a tsunami wave generation to wave run-up onto coasts. A generalized variational structure and weak dissipative effects are also discussed.

## 1.2 Multi-fluid flows

Part III deals with my second big interest in Fluid Mechanics — multi-fluid and two-phase flows. Various types of two-phase flows are illustrated on Figure 1.2.

When the number of interfaces is so big that it is impossible to follow them individually, the usual modeling procedure consists in applying an average operator to governing equations written separately for each phase [Ish75, IH06]. Traditionally, the averaging of nonlinear terms and interface boundary conditions requires some very strong assumptions and semi-empiric modeling. Consequently, there is no consensus in this field at the present time.

My interest in two-phase flows is initially due to informal discussions with Jean-Michel Ghidaglia, Gérard Le Coq, Fayssal Benkhaldoun and other members of CMLA. Later, these discussions resulted in a series of works with Frédéric Dias and Jean-Michel Ghidaglia [DDG08b, DDG08c, DDG10] where we proposed in an ad hoc manner a simple single velocity model for aerated flows. Only later, in collaboration with Yannick Meyapin (our Master degree student) and Marguerite Gisclon, we provided a formal justification of the proposed four-equations model [MDG10]. This scientific work is given in Chapter 6.

In LAMA we are developing a new research axis on the mathematical modeling of powder-snow avalanches. This research work is joint with Didier Bresch and Céline Acary-Robert. Recently we proposed a novel two-fluid model for powder-snow avalanches [DARB10]. The model derivation and several numerical results are presented in Chapter 7.

Finally, in Appendix A we provide the derivation of a single velocity model but in a simpler barotropic setting. Mathematical approach is inspired by the derivation given above in Chapter 6. This is a joint work with Yannick Meyapin and Marguerite Gisclon [MDG09].

# Chapter 2

# Curriculum vitæ

*One of the major ingredients for professional success in science is luck. Without this, forget it.*

Leon Lederman

*If you want to succeed in the world, you don't have to be much cleverer than other people. You just have to be one day earlier.*

Leo Szilard

## Contents

# 2.1 Vitæ

## 2.1.1 Renseignements personnels


| | |
|---|---|
| Nom | DUTYKH |
| Prénom | Denys |
| Date de naissance | le 17 Août 1982 |
| Lieu de naissance | Pologui, Ukraine |
| Nationalité | ukrainienne |
| Situation familiale | célibataire |
| Permis de conduire | catégorie B |
| Adresse professionnelle | Université de Savoie,<br>LAMA UMR CNRS 5127,<br>Campus Scientifique,<br>73376 Le Bourget-du-Lac |
| Adresse personnelle | 723 Avenue de Lyon,<br>73000 Chambéry |
| Tél | +33 04 79 75 86 52 |
| Fax | +33 04 79 75 81 42 |
| Portable | +33 06 66 06 97 58 |
| E-mail | Denys.Dutykh@univ-savoie.fr |
| Page web | http://www.lama.univ-savoie.fr/~dutykh |


# 2.2 Prix scientifiques

- Le Prix La Recherche 2007, mention « Environnement » parrainée par Veolia Environnement, recherche: « *Vagues extrêmes: de la physique à la prévision effective* » . La remise des prix a eu lieu le 27 Novembre 2007 au Sénat, Palais du Luxembourg, Paris

- Best Student Paper Award at « *The Fifth IMACS International Conference on Nonlinear Evolution Equations and Wave Phenomena: Computation and Theory* » , Athens, GA, USA, April 16 – 19, 2007

## 2.3 Qualifications

| *Section* | *Corps* | *Intitulé* |
|---|---|---|
| 26 | Maître de conférences (2008) | Mathématiques appliquées et applications des mathématiques |
| 60 | Maître de conférences (2008) | Mécanique, génie mécanique, génie civil |

## 2.4 Formation et diplômes

**Octobre 2005 – Décembre 2007:** Thèse de Doctorat en Mathématiques Appliquées au CMLA, ENS de Cachan.

Directeur de thèse: Professeur Frédéric DIAS.

Titre: « *Modélisation mathématique des tsunamis* » , Mention « Très honorable »

**Octobre 2004 – Juillet 2005:** Master Recherche 2 « *Méthodes Numériques pour les Modèles des Milieux Continus* » (ex DEA MN2MC) au CMLA, ENS de Cachan. Mention « Très bien » , classement 1/10,

spcialité « Mathématiques appliquées »

**Septembre 2003 – Juin 2004:** Master à l'Université Nationale de Dnepropetrovsk, Faculté des Mathématiques Appliquées, Département de Modélisation Mathématique

**Septembre 1999 – Juin 2003:** Equivalent de Licence et Maîtrise à la Faculté des Mathématiques Appliquées, l'Université Nationale de Dnepropetrovsk, Ukraine

**Septembre 1997 – Mai 1999:** Ecole N° 23, classe spcialisée en physique, Dnepropetrovsk, Ukraine

**Septembre 1989 – Mai 1997:** Ecole N° 83, Dnepropetrovsk, Ukraine

### 2.4.1 Expérience professionnelle

**Octobre 2008 – présent:** Chargé de recherche C.N.R.S. de 2me classe (CR2) affecté au LAMA - UMR 5127, Université de Savoie

**Décembre 2007 – Septembre 2008:** Post-doctorat au LRC Méso CEA DAM/CMLA sous la direction de Frédéric Dias et de Jean-Michel Ghidaglia

### 2.4.2 Séjours à l'étranger

**21 – 28 Mars 2010 :** School of Mathematics, University College Dublin

### 2.4.3 Stages de recherche

**Mars 2004 – Juillet 2005:** Stage de M2 MN2MC, CMLA, ENS de Cachan, sous la direction de Frédéric DIAS.

Titre: « *Moving load on a layered floating ice sheet* »

**Février 2004 – Juin 2004:** Travail de fin d'études l'Université Nationale de Dnepropetrovsk, Ukraine, sous la direction de Vladimir Lamzyuk.

Titre: « *Harmonic oscillations of an inhomogeneous elastic layer* »

### 2.4.4 Compétences informatiques

| | |
|---|---|
| Langages de programmation | C/C++, Fortran, Pascal |
| Langages de script | python |
| Systmes d'exploitation | Linux/Unix, Windows, Dos |
| Logiciels math. | Maple, MatLab, Mathematica, Scilab, Octave |
| FEM | FreeFem++, FreeFEM3D |
| Librairies de calcul | OpenFOAM, Deal.II, libMesh, gmm++, blitz++, gsl, FFTW |
| Mailleurs | GiD, GMSH |
| Visualisation | ParaView, OpenDX, MatLab, gnuplot |
| Bureautique | LaTeX, OpenOffice, AbiWord |

### 2.4.5 Langues vivantes

| | |
|---|---|
| Ukrainien | langue maternelle |
| Russe | langue maternelle |
| Français | excellent |
| Anglais | excellent (TOEIC score 885/990) |
| Italien | notions de base |

## 2.5 Activités de recherche

### 2.5.1 Intérêts scientifiques

- Mécanique des fluides
  - écoulements à surface libre
  - modèles des ondes longues
  - simulation numériques des vagues
  - écoulements compressibles et diphasiques
- Mécanique des solides
  - théorie et dynamique des dislocations
  - sources et propagation des ondes sismiques
- Méthodes numériques et calcul scientifique
  - volumes finis
  - éléments finis
  - méthodes spectrales et pseudo-spectrales

### 2.5.2 Thèse

**Thèse de Doctorat de l'École Normale Supérieure de Cachan en Mathématiques Appliquées**

TITRE « *Modélisation mathématique des tsunamis* »
DIRECTEUR Frédéric Dias (Professeur, ENS de Cachan)

**Thse soutenue le 3 décembre 2007 l'École Normale Supérieure de Cachan, après avis de**:

- Jean-Claude Saut (Professeur, Université Paris-Sud),
- Didier Bresch (DR CNRS, Université de Savoie),

**devant le jury formé de**:

| | | |
|---|---|---|
| Jean-Michel Ghidaglia | Professeur, ENS de Cachan | Examinateur |
| Jean-Claude Saut | Professeur, Paris-Sud | Rapporteur et Président |
| Didier Bresch | DR CNRS, Université de Savoie | Rapporteur |
| Costas Synolakis | Professeur, USC | Examinateur |
| Vassilios Dougalis | Professeur, University of Athens | Examinateur |
| Daniel Bouche | HDR, CEA/DAM IdF | Membre invit |
| Frédéric Dias | Professeur, ENS de Cachan | Directeur de thèse |

USC = University of Southern California

**Résumé.** Cette thèse est consacrée à la modélisation des tsunamis. La vie de ces vagues peut être conditionnellement divisée en trois parties: génération, propagation et inondation. Dans un premier temps, nous nous intéressons à la génération de ces vagues extrêmes. Dans cette partie du mémoire, nous examinons les différentes approches existantes pour la modélisation, puis nous en proposons d'autres. La conclusion principale à laquelle nous sommes arrivés est que le couplage entre la sismologie et l'hydrodynamique est actuellement assez mal compris.

Le deuxième chapitre est dédié essentiellement aux équations de Boussinesq qui sont souvent utilisées pour modéliser la propagation d'un tsunami. Certains auteurs les utilisent même pour modéliser le processus d'inondation (le run-up). Plus précisement, nous discutons de l'importance, de la nature et de l'inclusion des effets dissipatifs dans les modèles d'ondes longues.

Dans le troisième chapitre, nous changeons de sujet et nous nous tournons vers les écoulements diphasiques. Le but de ce chapitre est de proposer un modèle simple et opérationnel pour la modélisation de l'impact d'une vague sur les structures côtières. Ensuite, nous discutons de la discrétisation numérique de ces équations avec un schèma de type volumes finis sur des maillages non structurés.

Finalement, le mémoire se termine par un sujet qui devrait être présent dans tous les manuels classiques d'hydrodynamique mais qui ne l'est pas. Nous parlons des écoulements viscopotentiels. Nous proposons une nouvelle approche simplifiée pour les écoulements faiblement visqueux. Nous conservons la simplicité des écoulements potentiels tout en ajoutant la dissipation. Dans le cas de la profondeur finie nous incluons un terme correcteur dû à la présence de la couche limite au fond. Cette correction s'avère être non locale en temps. Donc, la couche limite au fond apporte un certain effet de mémoire à l'écoulement.

**Mots clés**: Ondes de surface, génération des tsunamis, équations de Boussinesq, écoulements diphasiques, écoulements viscopotentiels, volumes finis

## 2.5.3 Publications

### 2.5.3.1 Revues internationales

- **D. Dutykh**, D. Mitsotakis, L. Chubarov, Yu. Shokin. *Horizontal displacements contribution to tsunami wave energy balance*. Submitted, 2010
  http://hal.archives-ouvertes.fr/hal-00530999/

- **D. Dutykh**, D. Mitsotakis, X. Gardeil. *On the use of finite fault solution for tsunami generation problems*. Submitted, 2010
  http://hal.archives-ouvertes.fr/hal-00509384/

- D. Clamond, **D. Dutykh**. *Practical use of variational principles for modeling water waves*. Submitted, 2010
  http://hal.archives-ouvertes.fr/hal-00456891/

- **D. Dutykh**, C. Acary-Robert, D. Bresch. *Mathematical modeling of powder-snow avalanche flows*. Accepted to Studies in Applied Mathematics, 2010
  http://hal.archives-ouvertes.fr/hal-00354000/

- **D. Dutykh**, Th. Katsaounis, D. Mitsotakis. *Finite volume schemes for dispersive wave propagation and runup*. Submitted, 2010
  http://hal.archives-ouvertes.fr/hal-00472431/

- **D. Dutykh**, R. Poncet, F. Dias. *The VOLNA code for the numerical modelling of tsunami waves: generation, propagation and inundation*. Submitted, 2010
  http://hal.archives-ouvertes.fr/hal-00454591/

- Y. Meyapin, **D. Dutykh**, M. Gisclon. *Velocity and energy relaxation in two-phase flows*. Studies in Applied Mathematics, **125(2)**, 179 – 212, 2010
  http://hal.archives-ouvertes.fr/hal-00440852/

- **D. Dutykh**, D. Mitsotakis. *On the relevance of the dam break problem in the context of nonlinear shallow water equations*. Discrete and Continuous Dynamical Systems, **3**(2), 2010
  http://hal.archives-ouvertes.fr/hal-00369795/

- **D. Dutykh**. *Group and phase velocities in the free-surface visco-potential flow: new kind of boundary layer induced instability*. Physics Letters A, **373**, 3212 - 3216, 2009
  http://hal.archives-ouvertes.fr/hal-00334440/

- **D. Dutykh**. *Visco-potential free-surface flows and long wave modelling*. European Journal of Mechanics B/Fluids, **28**(3), 430-443, 2009
  http://hal.archives-ouvertes.fr/hal-00270926/

- **D. Dutykh**, F. Dias. *Energy of tsunami waves generated by bottom motion*. Proc. R. Soc. A (2009) **465**, 725-744
  http://hal.archives-ouvertes.fr/hal-00311752/

- **D. Dutykh**, F. Dias. *Influence of sedimentary layering on tsunami generation*, Computer Methods in Applied Mechanics and Engineering, **199**, 1268 - 1275, 2010
  http://hal.archives-ouvertes.fr/hal-00288696/

- F. Dias, **D. Dutykh**, J.-M. Ghidaglia. *A two-fluid model for violent aerated flows*, Computers and Fluids, 39(2), 283-293, 2010
  http://hal.archives-ouvertes.fr/hal-00285037/

- **D. Dutykh**, F. Dias. *Tsunami generation by dynamic displacement of sea bed due to dip-slip faulting*. Math. Comp. Sim., **80**(4), 837-848, 2009
  http://hal.archives-ouvertes.fr/hal-00174439/

- **D. Dutykh**, F. Dias. *Viscous potential free-surface flows in a fluid layer of finite depth*, C. R. Acad. Sci. Paris, Ser. I, **345** (2007), 113–118
  http://hal.archives-ouvertes.fr/hal-00145315/

- **D. Dutykh**, F. Dias. *Dissipative Boussinesq equations*, C. R. Mcanique, **335** (2007), 559–583. Special issue dedicated to J. V. Boussinesq
  http://hal.archives-ouvertes.fr/hal-00137633/

- Y. Kervella, **D. Dutykh**, F. Dias. *Comparison between three-dimensional linear and nonlinear tsunami generation models*, Theor. Comput. Fluid Dyn. (2007) **21**:245–269
  http://hal.archives-ouvertes.fr/hal-00113909/

- **D. Dutykh**, F. Dias, Y. Kervella. *Linear theory of wave generation by a moving bottom*, C. R. Acad. Sci. Paris, Ser. I **343** (2006) 499–504
  http://hal.archives-ouvertes.fr/hal-00114954/

#### 2.5.3.2 Chapitres dans livres

- **D. Dutykh**, F. Dias, *Water waves generated by a moving bottom*. In book: "Tsunami and Nonlinear Waves", Kundu, Anjan (Editor), Springer Verlag 2007, Approx. 325

p., 170 illus., Hardcover, ISBN: 978-3-540-71255-8
http://hal.archives-ouvertes.fr/hal-00115875/

#### 2.5.3.3 Actes de conférences avec comité de lecture

- Y. Meyapin, **D. Dutykh**, M. Gisclon. *Two-fluid barotropic models for powder-snow avalanche flows*, Proceedings of "The Fourth Russian-German Advanced Research Workshop on Computational Science and High Performance Computing" in Springer series "Notes on Numerical Fluid Mechanics and Multidisciplinary Design", 2009
http://hal.archives-ouvertes.fr/hal-00394437/

- **D. Dutykh**, F. Dias. *How does sedimentary layering affect the generation of tsunamis?* Proceedings of OMAE 2009, 28th International Conference on Ocean, Offshore and Arctic Engineering, May 31-June 5, 2009, Honolulu, USA

- **D. Dutykh**. *Visco potential free-surface flows*, XXII ICTAM, 25 - 29 August 2008, Adelaide, Australia

- F. Dias, **D. Dutykh** and J.-M. Ghidaglia. *Simulation of Free Surface Compressible Flows Via a Two Fluid Model*, OMAE 2008, Nick Newman Symposium on Marine Hydrodynamics. Estoril, Portugal, 15-20 June 2008
http://hal.archives-ouvertes.fr/hal-00258161/

- F. Dias, **D. Dutykh**. *Dynamics of tsunami waves*. In Book: "Extreme Man-Made and Natural Hazards in Dynamics of Structures", NATO Advanced Research Workshop, Opatija, Croatia, May 28 - June 1, pp. 35–60, 2006
http://hal.archives-ouvertes.fr/hal-00113612/

### 2.5.4 Actes de conférences

- D. Clamond, **D. Dutykh**. *Dispersive wave equation derivation from a relaxed variational formulation*, $3^r d$ International Scientific Conference « Applied problems of hydro- and aerodynamics » , Dnepropetrovsk National University, Ukraine, October 2010

- **D. Dutykh**, F. Dias. *Tsunami wave energy*, 4th Canadian Conference on Geohazards, Université Laval, May 20-24, 7 p., 2008

- **D. Dutykh**, F. Dias, *Fault dynamics and tsunami generation*, ECCOMAS Thematic Conference on Multi-scale Computational Methods for Solids and Fluids. A. Ibrahimbegovic, F. Dias, H. Matthies, P.Wriggers (eds.), 79–81, 2007

- C. Kassiotis, F. Dias, A. Ibrahimbegovic and **D. Dutykh**, *A partitioned approach to model tsunami impact on coastal protections*, ECCOMAS Thematic Conference on Multi-scale Computational Methods for Solids and Fluids. A. Ibrahimbegovic, F. Dias, H. Matthies, P.Wriggers (eds.), 134–139, 2007

#### 2.5.4.1 Revue de livres

- M. S. Howe, *Hydrodynamics and Sound*, Cambridge University Press, Cambridge (2007). European Journal of Mechanics - B/Fluids, In Press, 2007 doi:10.1016/j.euromechflu.2007.06.002

#### 2.5.4.2 Mémoires

- **D. Dutykh**. « *Modélisation mathématique des tsunamis* » , Mémoire de thèse, CMLA, ENS de Cachan, 2007 http://tel.archives-ouvertes.fr/tel-00194763/
- **D. Dutykh**. « *Moving load on a layered floating ice sheet* » , Mmoire de Master 2 MN2MC, CMLA, ENS de Cachan, 2005
- **D. Dutykh**. « *Harmonic oscillations of an inhomogeneous elastic layer* » , Mémoire de Master, Faculté des mathématiques appliquées, Université Nationale de Dnepropetrovsk (en ukrainien), 2004

#### 2.5.4.3 Rapports de recherche

- **D. Dutykh**. *Visco-potential free-surface flows*. Research report of CMLA, 2008
- F. Dias, **D. Dutykh** and J.-M. Ghidaglia. *A compressible two-fluid model for the finite volume simulation of violent aerated flows. Analytical properties and numerical results*. Research report of CMLA, 2008 http://hal.archives-ouvertes.fr/hal-00279671/

#### 2.5.4.4 Articles grand public

- Simuler une avalanche. La Recherche N428 - Avril 2009
- Springy sediments may amplify tsunamis. Issue 2662 of New Scientist magazine, 25 June 2008, page 20
- D. Dutykh. *Comment naît un tsunami?*, Le Mensuel de l'Université, N° 23, Février 2008

### 2.5.5 Activités de rapporteur

#### 2.5.5.1 Revues internationales

- Journal of Computational Physics
- Communications on Pure and Applied Analysis
- Comptes Rendus Mécanique
- European Journal of Mechanics - B/Fluids
- Mathematics and Computers in Simulation
- Numerische Mathematik
- Ocean Modelling
- SIAM Journal on Applied Mathematics (SIAP)
- Wave Motion
- Natural Hazards and Earth System Sciences

#### 2.5.5.2 Actes de conférences

- FVCA6
- ISOPE 2010
- ICTAM 2008
- ISOPE 2007
- FVCA5

#### 2.5.5.3 Appels à projets

- Cluster Environnement Rhône-Alpes (Projet 2: Risques gravitaires, séismes)
- Coopération universitaire et scientifique, Ambassade de France en Ukraine

### 2.5.6 Communications scientifiques

- **Numerical simulation of dispersive waves**, 29 Octobre 2010, Colloque EDP Normandie, University of Caen, France
- **Modeling of tsunami wave generation**, 21st September 2010, Summer school and workshop on "Numerical Methods for interactions between sediments and water", Paris 13 University, France
- **Modeling and simulation of compressible two-phase flows**, 17th September 2010, NumAn 2010 Conference in Numerical Analysis , Crete, Greece
- **Tsunami wave modeling**, 6 April 2010, « Exploring structural controls on great earthquake rupture and architecture of the Sunda/Sumatran convergent margin: international collaboration, links to tsunami modeling and planning of future research activities » , Fondation des Treilles, France
- **A generalized variational principle for water wave modeling**, 11 December 2009, Hydrodynamique des lacs et approximation de Saint-Venant, Institut Jean le Rond d'Alembert, Université Pierre et Marie Curie (Paris 6), Paris, France
- **Mathematical modelling of tsunami wave generation**, 12 November 2009, Institut Jean le Rond d'Alembert, Université Pierre et Marie Curie (Paris 6), Paris, France
- **Powder-snow avalanche flow modelling**, 12 - 16 October 2009, 4th Russian-German Advanced Research Workshop, Freiburg, Germany
- **Tsunami wave energy**, 22 September 2009, Session "Numerical methods for complex fluid flows", Wolfgang Pauli Institute, Vienna, Austria
- **Numerical simulation of powder snow avalanches**. 26 March 2009, Atelier VOR, Laboratoire 3S-R, Grenoble, France
- **Numerical simulation of tsunami waves. Presentation of VOLNA code**. 27 January 2009, Ocanographie et Mathmatiques, Ecole Normale Suprieure, Paris, France
- **Simulation of free surface compressible flows via a two fluid model**, 27 October 2008, Séminaire et Groupe de travail de Modélisation Mathématique, Mécanique et Numérique (M3N), Laboratoire de Mathématiques Nicolas Oresme, Université de Caen, Caen, France

- **Mathematical modelling of tsunami waves**, 23 October 2008, Sminaire EDP-MOISE, Laboratoire Jean Kuntzmann, Grenoble, France

- **Simulation of free surface compressible flows via a two fluid model**, 20 October 2008, Rencontres Niçoises de la Mécanique des Fluides, Laboratoire J.A. Dieudonné, Nice, France

- **Mathematical modelling of tsunami generation**, LAMA, Université de Savoie, 10 October 2008, Le Bourget-du-Lac, France

- **Visco potential free-surface flows**, XXII International Congress of Theoretical and Applied Mechanics, Adelaide, Australia, 24–30 August 2008

- **Tsunami wave energy**, SIAM Conference on Nonlinear Waves and Coherent Structures (NW08), Universit di Roma "La Sapienza", Rome, Italy, July 21–24, 2008

- **Numerical modelling of tsunami waves. VOLNA code presentation**, LAMA, Université de Savoie, 4th July 2008, Le Bourget-du-Lac, France

- **Simulation of Free Surface Compressible Flows Via a Two Fluid Model**, The 27th International Conference on OFFSHORE MECHANICS AND ARCTIC ENGINEERING Estoril, Portugal, 15–20 June, 2008

- **Numerical modelling of tsunami generation and runup**, Groupe de Travail Mécanique des Fluides Réels, 18 February 2008, CMLA, ENS de Cachan, France

- **Influence of the mud layer on sea-bed deformations**, 2nd FORTH Workshop on Tsunami generation, 12 & 13 February, 2008, Heraklion, Crete (Greece)

- **Simulation d'écoulements compressibles avec surface libre par un modèle bifluide**, CLAROM - Séminaire hydrodynamique et océano-météo, 29 novembre 2007, Institut Français du Pétrole

- **Simulation of free surface motions via a two fluid model**, International conference « Trends in Numerical and Physical Modeling for Industrial Multiphase Flows » , September 17-21, 2007 Cargèse, Corsica, France

- **On the dynamic generation of tsunamis by a moving bottom**, TRANSFER Workshop « Numerical Models, Inundation Maps and Test Sites » , June 12 - 14, 2007, Fethiye, Turkey

- **Derivation and numerical resolution of long wave equations**, Wolfgang Pauli Institute, Vienna, Working session « Dispersive nonlinear longwave PDE's and applications in physics » organis par Jean-Claude Saut, 21 – 25 mai 2007
- **On the generation of tsunamis by earthquakes**, The Fifth IMACS International Conference on Nonlinear Evolution Equations and Wave Phenomena: Computation and Theory, Athens, GA, USA, April 16 – 19, 2007
- **Viscous shallow water equations: potential approach and numerical methods**, 13 mars 2007, Institut de Mathématiques de Bordeaux, Groupe de travail Océanographie
- **Unstructured Finite Volume solver for dissipative shallow-water equations**, 12 février 2007, CMLA, ENS de Cachan, Groupe de travail mécanique des fluides réels
- **Tsunami generation**, SIAM Conference on Nonlinear Waves and Coherent Structures, September 9 – 12, 2006, University of Washington, Seattle, Washington
- **Génération des tsunamis**, Inauguration de LRC CMLA/CEA, 19 juin 2006
- Conférence « **Results of the Sumatra Earthquake and Tsunami Offshore Survey 2005** » , October 19 – 24, 2005, Fondation des Treilles

#### 2.5.6.1 Conférences grand public

- *Tsunamis: du terrain au modèle numérique.* Conférence grand public donnée avec **C. Beck** au Cinéma Curial lors de la Fête de la Science 2009 à Chambéry
- *What is applied mathematics?* Talk given for general audience at Ecole Normale Supérieure de Cachan, 27 April 2007
- *Tsunami waves.* Talk given for general audience at Ecole Normale Supérieure de Cachan, 5 December 2006

### 2.5.7 Développement des logiciels

- **VOLNA** : code des volumes finis sur des maillages triangulaires non-structurs pour la simulation de la gnration, de la propagation et de l'inondation des tsunamis (en collaboration avec **R. Poncet** et **F. Dias**). Actuellement ce code est hbrg Irish Centre for High-End Computing (ICHEC) et maintenu par School of Mathematics, University College Dublin

### 2.5.8 Animation de la vie scientifique

- Membre du Comité Scientifique de la conférence « *Finite Volumes for Complex Applications VI* » qui aura lieu du 6 au 10 juin 2011
  http://fvca6.fs.cvut.cz/

- Organisation (avec **D. Bresch** et **M. Gisclon**) d'une session sur le thème « *Numerical models and methods for compressible and two-phase flows* » à Wolfgang Pauli Institute (Vienne) qui a eu lieu du 17 au 21 mai 2010
  http://www.lama.univ-savoie.fr/~dutykh/wpi10/

- Organisation (avec **D. Bresch** et **C. Acary-Robert**) d'une session « *Numerical methods for complex fluid flows* » Wolfgang Pauli Institute (Vienne) qui a eu lieu du 21 au 25 septembre 2009
  http://www.lama.univ-savoie.fr/~dutykh/wpi09/

- Atelier Cargèse: « *Modélisation physico–numérique pour les fluides, les particules et le rayonnement. Confrontation modèles physiques et modèles numériques* » . Institut d'Etudes Scientifique de Cargèse, Corse, 24 – 30 Septembre 2006

### 2.5.9 Financement de la recherche

#### 2.5.9.1 Projets ANR

- Projet **ANR MathOcéan** (2009 – 2012) : « *Analyse mathématique en océanographie et applications* » . Porteur du projet: **D. Lannes** (ENS Paris)

- Projet **ANR HEXECO** (2007 – 2010) : « *Hydrodynamique extrême du large à la côte* » . Porteur du projet: **O. Kimmoun** (Ecole Centrale Marseille)

#### 2.5.9.2 Autres projets

- Projet **PEPS CNRS** (2010 – 2011) « *Simulation numérique des vagues nonlinéaires dans les milieux variables* » . Porteur: **D. Dutykh** (LAMA, Université de Savoie)

- Projet **PEPS CNRS** (2009 – 2010) « *PML, l'arithmétique et le calcul : vers l'arithmétique et le calcul numérique efficace et élégamment certifié* » . Porteur: **C. Raffalli** (LAMA, Université de Savoie)

- Projet « *Simulation numérique des avalanches de neige* » . Porteur: **D. Dutykh**, **Appel d'offre Cluster Environnement** (2009 – 2010), région Rhône-Alpes

#### 2.5.9.3 Mobilité internationale

- **Partenariat Hubert Curien – ULYSSES 2010** (coopération franco-irlandaise). Titre: « *Numerical Models for Compressible and Incompressible Flows and Applications* » . Partenaires: School of Mathematical Sciences (University College Dublin), CMLA (ENS de Cachan). Porteur français: **D. Dutykh** (LAMA, Université de Savoie), porteur irlandais: **T. Cox** (School of Mathematical Sciences, University College Dublin)

- Projet **PICS CNRS** (2010 – 2012) « *Numerical simulation of higly nonlinear water waves* » . Partenaire russe: Institute of Computational Technologies, Siberian Branch of Russian Academy of Sciences and Novosibirsk State University. Porteur français: **D. Dutykh** (LAMA, Université de Savoie), porteur russe: **Yu. Shokin** (academician, director of Institute of Computational Technologies)

- **Coopération franco-russe** dans le cadre de l'accord CNRS/ASR 2010. Titre du projet « *Solutions analytiques et numériques pour les modèles des avalanches de neige poudreuse* » . Porteur français: **D. Dutykh** (LAMA, Université de Savoie), partenaire russe: **V. Trushkov** (System Ananlysis Research Center, Russian Academy of Sciences)

## 2.6 Activités d'enseignement

**2005 – 2006:** Première année de monitorat à l'ENS de Cachan rattaché au Département de mathématiques et au Centre d'Initiation à l'Enseignement Supérieur (CIES) de Versailles

- TDs sur ordinateur de **Calcul Scientifique** sous MatLab, Option « *Modélisation, Calcul Scientifique* » , Préparation à l'agrégation de Mathématiques, Département de Mathématiques, ENS de Cachan (**39h**)
- TDs sur ordinateur d'**Optimisation** sous MatLab, option « *Modélisation, Calcul Scientifique* » , Préparation à l'agrégation de Mathématiques, Département de Mathématiques, ENS de Cachan (**9h**)
- Les **oraux blancs**, Préparation à l'agrégation de Mathématiques, Département de Mathématiques, ENS de Cachan (**16h**)

**2006 – 2007:** Deuxième année de monitorat à l'ENS de Cachan rattaché au Département de mathématiques et au Centre d'Initiation à l'Enseignement Supérieur (CIES) de Versailles

- TDs sur ordinateur de **Calcul Scientifique** sous MatLab, Option « *Modélisation, Calcul Scientifique* » , Préparation à l'agrgation de Mathématiques, Département de Mathématiques, ENS de Cachan (**64h**)

**2007 – 2008:** Troisième année de monitorat à l'ENS de Cachan rattaché au Département de mathématiques et au Centre d'Initiation à l'Enseignement Suprieur (CIES) de Versailles

- TDs sur ordinateur de **Calcul Scientifique** sous MatLab, Option « *Modélisation, Calcul Scientifique* » , Préparation à l'agrégation de Mathématiques, Département de Mathématiques, ENS de Cachan (**64h**)

**2009 – 2010:** Vacations à l'Université de Savoie

- TDs sur ordinateur pour les étudiants de L3 MATH (8h) et L3 MASS (8h) sur la résolution numérique des **Equations Différentielles Ordinaires**

## 2.6.1 Encadrement d'étudiants

### 2.6.1.1 Étudiants en thèses

- **Louis Stephan**: participation à l'encadrement avec E. Wurtz (INES-LOCIE, Université de Savoie). Sujet de thèse: « *Modélisation de la ventilation naturelle pour l'optimisation du rafraîchissement passif des bâtiments* »

### 2.6.1.2 Stages M2

- **Yannick Meyapin** (Mars – Juillet 2010): Co-encadrement avec M. Gisclon (LAMA, Université de Savoie). Sujet: « *Numerical simulation of single-velocity two-phase flows* »

- **Ahmed Ossama Ghanem** (Mars – Juillet 2010): Co-encadrement avec M. Gisclon (LAMA, Université de Savoie) et J. Rajchenbach (LPMC, Université de Nice Sophia-Antipolis). Sujet: « *Numerical simulation of Faraday instability* »

- **Xavier Gardeil** (Mars – Septembre 2010): Co-encadrement avec C. Beck (LGCA, Université de Savoie). Sujet: « *Tsunami wave modeling at the North of Venezuela* »

- **Yannick Meyapin** (Mars – Juin 2009): Co-encadrement avec M. Gisclon (LAMA, Université de Savoie). Sujet: « *Velocity and energy relaxation in two-phase flows* »

- **Youen Kervella** (Mars – Juillet 2006): Co-encadrement avec F. Dias du stage de Master 2 Recherche Physique Océan-Atmosphère, Université de Brest. Sujet: « *Comparaison entre les modèles linéaires et nonlinéaires de génération des tsunamis* »

#### 2.6.1.3 Stages M1

- **Mahmut Tuz** (Mai – Juin 2010): Sujet de stage « *Numerical computation of the Dirichlet-to-Neumann map* »

#### 2.6.1.4 Autres encadrements

- **Ianis Bernard** (Mars – Juin 2009): participation à l'encadrement d'un TIPE. Sujet: « *Modélisation d'un soliton hydraulique* »

### 2.6.2 Participation dans les jurys de thèse

- **Louis Stephan**: *Modélisation de la ventilation naturelle pour l'optimisation du rafraîchissement passif des bâtiments*, le 16 avril 2010, INES-LOCIE, Université de Savoie. Directeur de thèse: E. Wurtz

- **Marx Chhay**: *Intégrateurs géométriques: Application à la Mécanique des Fluides*, le 16 décembre 2008, LEPTIAB, Université de La Rochelle. Directeurs de thèse: A. Hamdouni & P. Sagaut

## 2.7 Activités collectives

### 2.7.1 Responsabilités administratives

- Membre du **Conseil de l'UFR** SFA (2009 - présent)

- Membre du **Conseil Recherche** du LAMA (2009 - présent)

- **Correspondant valorisation** du LAMA (2008 - présent)

- Reprsentant du LAMA dans la **Fédération de recherche Vulnérabilité des Ouvrages aux Risques** (VOR) (2008 - présent)

- Correspondant du LAMA pour **International Center for Applied Computational Mechanics** (ICACM) (2008 - présent)

### 2.7.2 Affiliations professionnelles

- Société de Mathématiques Appliquées et Industrielles (SMAI)
- Société Mathématique de France (SMF)
- The European Mathematical Society (EMS)
- GDR CNRS 2948: Groupement de Recherche MOAD (2005 – 2009) : *MOdélisation, Asymptotique, Dynamique non-linéaire*

### 2.7.3 Séminaires

**2008 – prsent:** Séminaire de l'équipe EDP, LAMA, Université de Savoie. Participation, invitation des orateurs.

**2004 – 2008:** Groupe de travail: « Mécanique des Fluides Réels » .

Ce groupe de travail mensuel, organisé par le CMLA, permet de réunir des chercheurs de l'Ecole Centrale de Paris, du CEA, d'EDF et du CMLA dont les thèmes de recherche sont en relation avec la mécanique des fluides.

### 2.7.4 Événements grand public

- Stand sur les tsunamis en partenariat avec LGCA (Université de Savoie) à la **Fête de la Science 2009** à la Galérie Eureka à Chambéry
- Participation régulière aux **Journées Portes Ouvertes** de l'Université de Savoie avec des exposés sur les tsunamis

## 2.8 Divers

| | |
|---|---|
| Sport | musculation, badminton, cyclisme, randonnée, tennis de table |
| Passe-temps | lecture, photographie |

# Part II

# Water waves

# Chapter 3

# Water wave modeling

*παντα ρει, ουδεν μενει*
*(Everything flows, nothing is stationary)*

Heraclitus

## Contents

## 3.1 Practical use of variational principles for modeling water waves

*One should always generalize (Man muss immer generalisieren).*

Carl Jacobi

*You do not really understand something unless you can explain it to your grandmother.*

Albert Einstein

ABSTRACT. This Section describes a method for deriving approximate equations for irrotational water waves. The method is based on a 'relaxed' variational principle, i.e., on a Lagrangian involving as many variables as possible. This formulation is particularly suitable for the construction of approximate water wave models, since it allows more freedom while preserving the variational structure. The advantages of this relaxed formulation are illustrated with various examples in shallow and deep waters, as well as arbitrary depths. Using subordinate constraints (e.g., irrotationality or free surface impermeability) in various combinations, several model equations are derived, some being well-known, other being new. The models obtained are studied analytically and exact travelling wave solutions are constructed when possible.

### 3.1.1 Introduction

The water wave problem in fluid mechanics has been known since more than two hundreds years [Cra04]. The classical mathematical formulation of surface gravity waves involves five equations: the irrotationality of the fluid flow, the fluid incompressibility, the bottom and the surface impermeabilities, and the surface isobarity [Mei89]. This system of equations cannot be generally solved exactly and, historically, the water wave theory has been developed by constructing various approximations. In shallow water, we have the equations of Korteweg and de Vries (1895) [KdV95], Boussinesq (1871) [Bou71a], Benjamin *et al.* (1972) [BBM72], Serre (1953) [Ser53], Green and Naghdi (1976) [GN76], Camassa and Holm (1993) [CH93], Degasperis–Procesi (1999) [DP99], and many other model equations. For more mathematical derivations and justifications we refer to [BCS02, BCS04, BCL05]. On finite depth and deep water, there is the celebrated nonlinear Schrödinger equation Mei (1989) [Mei89] and the equations of Dysthe (1979) [Dys79], Trulsen *et al.* (2000) [TKDV00], Kraenkel *et al.* (2005) [KLM05], among others. These equations are most often derived via some perturbation techniques and are thus valid for waves of small amplitude. Moreover, these equations are generally valid for a very limited range of the ratio *wavelength/water depth* and for narrow-banded spectra. However, for many applications

it is necessary to use models uniformly valid for all depths and which are accurate for large amplitudes. It is well-known in theoretical physics that variational formulations are tools of choice to derive such approximations when small parameter expansions are inefficient. Variational principles have also the big advantage of ensuring that one can build approximations with optimal 'fit' among all the equations defining the problem at hand.

There are mainly two variational formulations for irrotational surface waves that are commonly used, namely the Lagrangian of Luke (1967) [Luk67] and the Hamiltonian of Zakharov (1968) [Zak68]. Details on the variational formulations for surface waves can be found in review papers, e.g., Radder (1999) [Rad99], Salmon (1988) [Sal88], Zakharov and Kuznetsov (1997) [ZK97]. The water wave problem is also known to have the multi-symplectic structure [Bri96]. These variational principles have been exploited, in different variants, to build analytical and numerical approximations, e.g., [Bal96, KBEW01] just to mention a few references.

Luke's Lagrangian assumes that the flow is exactly irrotational, i.e., the Lagrangian involves a velocity potential but not explicitly the velocity components. If in addition the fluid incompressibility and the bottom impermeability are satisfied identically, the equations at the surface can be derived from Zakharov's Hamiltonian [Zak68]. Thus, both principles naturally assume that the flow is exactly irrotational, as it is the case of the water wave problem formulation, but Zakharov's Hamiltonian is more constrained than Luke's Lagrangian. Luke's and Zakharov's variational formulations require that part or all of the equations in the bulk of the fluid and at the bottom are satisfied identically, while the remaining relations must be approximated [CS93]. It is because the irrotationality and incompressibility are mathematically easy to fulfill, that they are chosen to be satisfied identically. Beside simplicity, there are generally no reasons to fulfill irrotationality and/or incompressibility instead of the impermeability or the isobarity of the free surface, for example. In this study, we illustrate the benefit of releasing the constraints of exact irrotationality and incompressibility, since approximations of these relations are sufficient in most practical cases.

Variational formulations involving as few dependent variables as possible are often regarded as simpler [YLB08]. It is understandably tempting to solve exactly (i.e., analytically) as many equations as possible in order to 'improve' the solution accuracy. This is not always a good idea, however. Indeed, numerical analysis and scientific computing know many examples when efficient and most used algorithms do exactly the opposite. These so-called *relaxation methods* — e.g., pseudo-compressibility for incompressible fluid flows [KKS05] — have proven to be very efficient for stiff problems. The same idea may also apply to analytical approximations. When solving a system of equations, the exact resolution of a few equations does not necessarily ensure that the overall error is reduced:

what really matters is that the global error is minimized. Since for irrotational water waves it is possible to use a variational formulation, approximations derived from the latter are guaranteed to be optima.

In this study we would like to elucidate the benefit of using relaxed variational methods for the water wave problem. In other words, we illustrate the advantage of using a variational principle involving as many dependent variables as possible. We emphasize that our primary purpose here is to provide a generalized framework for deriving model equations for water waves. This methodology is explained on various examples, some of them being new to our knowledge. However, the potential of the present approach is far from being fully exploited.

The Chapter is organized as follows. In Section 3.1.2, Luke's Lagrangian is *relaxed* to incorporate explicitly more degrees of freedom. This modification yields the Hamilton principle in its most general form. The advantage of this formulation is subsequently illustrated with examples over a fixed horizontal bottom, for the sake of simplicity. We begin in Section 3.1.3 with shallow water models, where some well-known and a few novel models are derived from the same Lagrangian, but with different subordinate constraints. In Section 3.1.4, similar model equations are derived in the deep water limit. In particular, a generalization of the Klein–Gordon equation and a remarkably simple accurate approximation for traveling waves are derived. A generalized ansatz, including the shallow and deep waters as limiting particular cases is presented in Section 3.1.5. Further generalizations are discussed in Section 3.1.6 and their advantage is illustrated with a variant of Serre's equations. Finally, conclusions and perspectives for future studies are outlined in Section 3.1.7.

### 3.1.2 Generalized variational formulation

Water wave problem possesses several variational structures [Whi65, Luk67, Zak68]. In the present study we will extensively exploit the Lagrangian variational formalism. Surface gravity wave equations, for a potential flow with an impermeable bottom and an impermeable free surface where the pressure is constant (taken to be zero), can be derived minimizing the following functional [Luk67]:

$$\mathcal{L} = \int_{t_1}^{t_2} \int_{\Omega} \mathscr{L}\, \rho \, \mathrm{d}^2\boldsymbol{x} \, \mathrm{d}t, \quad \mathscr{L} = -\int_{-d}^{\eta} \left[ gy + \phi_t + \tfrac{1}{2}(\boldsymbol{\nabla}\phi)^2 + \tfrac{1}{2}\phi_y^2 \right] \mathrm{d}y, \tag{3.1}$$

with $\boldsymbol{x} = (x_1, x_2)$ the horizontal Cartesian coordinates, $y$ the upward vertical coordinate, $t$ the time, $\boldsymbol{\nabla}$ the horizontal gradient, $\Omega$ the horizontal domain, $\phi$ the velocity potential and $g > 0$ the acceleration due to gravity; $y = \eta(\boldsymbol{x}, t)$, $y = 0$ and $y = -d(\boldsymbol{x}, t)$ being, respectively, the equations of the free surface, of the still water level and of the bottom.

For the sake of simplicity, the surface tension effect is neglected and the fluid density $\rho$ is constant (and can thus be set to unity without any loss of generality), but this is not a limitation for the purpose of this study.

Integrating by parts, then neglecting the terms at the horizontal and temporal boundaries because they do not contribute to the minimization (this will be done repeatedly below without explicit mention), Luke's variational formulation (3.1) can be rewritten with the following Lagrangian density:

$$\mathscr{L} \;=\; \tilde{\phi}\,\eta_t \;+\; \check{\phi}\,d_t \;-\; \tfrac{1}{2}g\eta^2 \;+\; \tfrac{1}{2}gd^2 \;-\; \int_{-d}^{\eta} \big[\, \tfrac{1}{2}(\boldsymbol{\nabla}\,\phi)^2 \;+\; \tfrac{1}{2}\phi_y^{\,2} \,\big]\,\mathrm{d}y, \tag{3.2}$$

where the over 'tildes' and 'wedges' denote, respectively, the quantities written at the free surface $y = \eta$ and at the bottom $y = -d$. We shall also denote with 'bars' the quantities averaged over the water depth, e.g.

$$\bar{\boldsymbol{u}}(\boldsymbol{x},t) \;\equiv\; \frac{1}{\eta(\boldsymbol{x},t) + d(\boldsymbol{x},t)} \int_{-d(\boldsymbol{x},t)}^{\eta(\boldsymbol{x},t)} \boldsymbol{u}(\boldsymbol{x},y,t)\,\mathrm{d}y.$$

The variational formulations (3.1) and (3.2) impose that any approximation is exactly irrotational, i.e., the choice of an ansatz for $\phi$ necessarily implies an irrotational motion. Note that the term $\frac{1}{2}gd^2$ in (3.2) can be omitted because, $d$ being prescribed, it does not contribute to the minimization process. Note also that Luke's Lagrangian (3.1) can been extended to the case where the bottom function $d(\boldsymbol{x},t)$ is unknown if a condition at $y = -d$ is added to the problem [TC88].

To give us more freedom while keeping an exact formulation, the variational principle is modified (relaxed) by introducing explicitly the horizontal velocity $\boldsymbol{u} = \boldsymbol{\nabla}\phi$ and the vertical one $v = \phi_y$. The variational formulation can thus be reformulated with the Lagrangian density

$$\mathscr{L} = \tilde{\phi}\eta_t + \check{\phi}d_t - \tfrac{1}{2}g\eta^2 - \int_{-d}^{\eta} \big[\tfrac{1}{2}(\boldsymbol{u}^2 + v^2) + \boldsymbol{\mu}\cdot(\boldsymbol{\nabla}\phi - \boldsymbol{u}) + \nu(\phi_y - v)\big]\,\mathrm{d}y, \tag{3.3}$$

where the Lagrange multipliers $\boldsymbol{\mu}$ and $\nu$ have to be determined. By variations with respect of $\boldsymbol{u}$ and $v$, one finds at once the definition of the Lagrange multipliers:

$$\boldsymbol{\mu} \;=\; \boldsymbol{u}, \qquad \nu \;=\; v. \tag{3.4}$$

Using these definitions, (3.3) becomes

$$\mathscr{L} \;=\; \tilde{\phi}\,\eta_t \;+\; \check{\phi}\,d_t \;-\; \tfrac{1}{2}\,g\,\eta^2 \;+\; \int_{-d}^{\eta} \big[\, \tfrac{1}{2}\,\boldsymbol{u}^2 \;+\; \tfrac{1}{2}\,v^2 \;-\; \boldsymbol{u}\cdot\boldsymbol{\nabla}\phi \;-\; v\,\phi_y \,\big]\,\mathrm{d}y. \tag{3.5}$$

However, it is advantageous to keep the most general form of the Lagrangian (3.3), because it allows to choose ansatz for Lagrange multipliers $\boldsymbol{\mu}$ and $\nu$ that are different

from the velocity field $\boldsymbol{u}$ and $v$. Indeed, the Lagrangian density (3.3) involves six variables $\{\eta, \phi, \boldsymbol{u}, v, \boldsymbol{\mu}, \nu\}$, while the simplified Lagrangian (3.5) involves only four variables $\{\eta, \phi, \boldsymbol{u}, v\}$ and the original Lagrangian (3.2) only two ($\eta$ and $\phi$). These additional variables introduce additional freedom in the construction of approximations, thus allowing more subordinate relations to be fulfilled. The Lagrangian density (3.5) was used by Kim *et al.* (2001) [KBEW01] to derive the 'irrotational' Green–Naghdi equations for long waves in shallow water. The more general Lagrangian density (3.3) provides more flexibility to derive model equations, as illustrated below.

The connection of (3.3) with the variational formulation of the classical mechanics can be seen applying Green's theorem to (3.3) that yields another equivalent variational formulation involving the Lagrangian density

$$\begin{aligned}\mathscr{L} \;&= (\eta_t + \tilde{\boldsymbol{\mu}} \cdot \boldsymbol{\nabla}\eta - \tilde{\nu})\,\tilde{\phi} \;+\; (d_t + \check{\boldsymbol{\mu}} \cdot \boldsymbol{\nabla} d + \check{\nu})\,\check{\phi} \;-\; \tfrac{1}{2}\, g\, \eta^2 \\ &\quad + \int_{-d}^{\eta} \big[\, \boldsymbol{\mu} \cdot \boldsymbol{u} - \tfrac{1}{2}\boldsymbol{u}^2 \;+\; \nu v - \tfrac{1}{2} v^2 \;+\; (\boldsymbol{\nabla} \cdot \boldsymbol{\mu} + \nu_y)\,\phi \,\big]\, \mathrm{d}y, \end{aligned} \tag{3.6}$$

which in deep water limit ($d \to \infty$) becomes (if $\phi$ decay faster than $y^{-1}$ as $y \to -\infty$)

$$\begin{aligned}\mathscr{L} \;&= (\eta_t + \tilde{\boldsymbol{\mu}} \cdot \boldsymbol{\nabla}\eta - \tilde{\nu})\,\tilde{\phi} \;-\; \tfrac{1}{2}\, g\, \eta^2 \\ &\quad + \int_{-\infty}^{\eta} \big[\, \boldsymbol{\mu} \cdot \boldsymbol{u} - \tfrac{1}{2}\boldsymbol{u}^2 \;+\; \nu v - \tfrac{1}{2} v^2 \;+\; (\boldsymbol{\nabla} \cdot \boldsymbol{\mu} + \nu_y)\,\phi \,\big]\, \mathrm{d}y. \end{aligned}$$

Thus, in the special case $\boldsymbol{\mu} = \boldsymbol{u}$ and $\nu = v$, the Hamilton principle of classical mechanics is recovered in Eulerian description of motion, i.e., the variational principle involves the kinetic energy minus the potential energy plus some constraints for the fluid incompressibility, for the flow irrotationality and for the bottom and surface impermeabilities, as already pointed out by Miles [Mil77]. In other words, the Lagrangian density (3.6) is the Hamilton principle in its most general form for irrotational surface gravity waves.

Note that, via the integration by parts, the term $\eta_t\tilde{\phi}$, for example, can be replaced by $-\eta\tilde{\phi}_t$ in all the Lagrangian densities given above, without loss (nor gain) of generality. Note also that the relaxed variational formulations involving (3.3) and (3.6) being strictly equivalent, one should use the more convenient one depending on the problem under consideration. Note finally that extensions of (3.3) and (3.6) including, e.g., obstacles, surface tensions and stratifications in several homogeneous layers are straightforward generalizations. For instance, to include the surface tension it is sufficient to add the term $-\sigma(\sqrt{1+(\boldsymbol{\nabla}\eta)^2}-1)$ into the definition of the Lagrangian density (3.6), $\sigma$ being the surface tension coefficient.

The goal in this study is to illustrate the power of the relaxed variational principle via some simple examples. We shall thus consider, for simplicity, a fixed horizontal bottom and

we shall derive various approximate equations for shallow and deep waters. Possibilities for arbitrary depths and some other generalizations will also be discussed.

### 3.1.3 Examples in shallow water

Let consider first the shallow water case, with constant depth for the clarity of exposition. We introduce a realistic ansatz for these waves and then apply several constraints to derive various approximations, some of them being well-known, others being new.

#### 3.1.3.1 Choice of a simple ansatz

For a long wave in shallow water, in potential motion on a horizontal impermeable sea bed at $y = -d$, it has long been noticed that the velocity field can be well approximated truncating the following expansion by Lagrange (1781) [Lag81]:

$$\boldsymbol{u} \;=\; \check{\boldsymbol{u}} \;-\; \tfrac{1}{2}(y+d)^2\,\boldsymbol{\nabla}^2\check{\boldsymbol{u}} \;+\; \tfrac{1}{24}(y+d)^4\,\boldsymbol{\nabla}^4\check{\boldsymbol{u}} \;+\; \cdots . \tag{3.7}$$

All Lagrange's followers (e.g., Airy, Boussinesq, Rayleigh and many others) used this type of expansions to derive their respective approximations [Cra04]. Reviews on shallow water approximations can be found in Bona *et al.* (2002, 2004) [BCS02, BCS04], Kirby (1997) [Kir97], Madsen and Schäffer (1999) [MS99], Wu (2001) [Wu01], Dougalis & Mitsotakis (2008) [DM08], among others.

We consider here a simple ansatz of polynomial type, that is a zeroth-order polynomial in $y$ for $\phi$ and for $\boldsymbol{u}$, and a first-order one for $v$, i.e., we approximate flows that are nearly uniform along the vertical direction. Our ansatz thus reads

$$\phi \;\approx\; \bar{\phi}(\boldsymbol{x},t), \qquad \boldsymbol{u} \;\approx\; \bar{\boldsymbol{u}}(\boldsymbol{x},t), \qquad v \;\approx\; (y+d)\,(\eta+d)^{-1}\,\tilde{v}(\boldsymbol{x},t). \tag{3.8}$$

Such ansatz are the basis of most shallow water approximations. We have also to introduce suitable ansatz for the Lagrange multiplier $\boldsymbol{\mu}$ and $\nu$. Since $\boldsymbol{\mu} = \boldsymbol{u}$ and $\nu = v$ for the exact solution, the natural ansatz for the multipliers are

$$\boldsymbol{\mu} \;\approx\; \bar{\boldsymbol{\mu}}(\boldsymbol{x},t), \qquad \nu \;\approx\; (y+d)\,(\eta+d)^{-1}\,\tilde{\nu}(\boldsymbol{x},t). \tag{3.9}$$

With the ansatz (3.8) and (3.9), the Lagrangian density (3.6) becomes

$$\begin{aligned}\mathscr{L} \;=\;& (\eta_t + \bar{\boldsymbol{\mu}}\cdot\boldsymbol{\nabla}\eta)\,\bar{\phi} \;-\; \tfrac{1}{2}\,g\,\eta^2 \\ &+ (\eta+d)\left[\,\bar{\boldsymbol{\mu}}\cdot\bar{\boldsymbol{u}} \;-\; \tfrac{1}{2}\,\bar{\boldsymbol{u}}^2 \;+\; \tfrac{1}{3}\,\tilde{\nu}\,\tilde{v} \;-\; \tfrac{1}{6}\,\tilde{v}^2 \;+\; \bar{\phi}\,\boldsymbol{\nabla}\cdot\bar{\boldsymbol{\mu}}\,\right].\end{aligned} \tag{3.10}$$

Using the Green formula, the variational problem can also be written such that the Lagrangian density is in the following simpler form

$$\mathscr{L} = \bar{\phi}\eta_t - \tfrac{1}{2}\,g\eta^2 + (\eta+d)\left[\bar{\boldsymbol{\mu}}\cdot\bar{\boldsymbol{u}} - \tfrac{1}{2}\bar{\boldsymbol{u}}^2 + \tfrac{1}{3}\,\tilde{\nu}\tilde{v} - \tfrac{1}{6}\tilde{v}^2 - \bar{\boldsymbol{\mu}}\cdot\boldsymbol{\nabla}\bar{\phi}\right]. \tag{3.11}$$

The two Lagrangian densities (3.10) and (3.11) differing by a divergence term, they yield exactly the same equations. Thus, depending on the constraints, we use the Lagrangian density leading to the simpler expression. We now investigate equations led by this shallow water model under various subordinate relations.

#### 3.1.3.2 Unconstrained approximation

Without further constraints, the minimization of (3.11) yields

$$\delta\,\bar{\boldsymbol{u}}: \quad 0 = \bar{\boldsymbol{\mu}} - \bar{\boldsymbol{u}}, \tag{3.12}$$

$$\delta\,\tilde{v}: \quad 0 = \tilde{\nu} - \tilde{v}, \tag{3.13}$$

$$\delta\,\bar{\boldsymbol{\mu}}: \quad 0 = \bar{\boldsymbol{u}} - \boldsymbol{\nabla}\bar{\phi}, \tag{3.14}$$

$$\delta\,\tilde{\nu}: \quad 0 = \tilde{v}, \tag{3.15}$$

$$\delta\,\bar{\phi}: \quad 0 = \eta_t + \boldsymbol{\nabla}\cdot[\,(\eta+d)\,\bar{\boldsymbol{\mu}}\,], \tag{3.16}$$

$$\delta\,\eta: \quad 0 = \bar{\boldsymbol{\mu}}\cdot\bar{\boldsymbol{u}} - \tfrac{1}{2}\,\bar{\boldsymbol{u}}^2 + \tfrac{1}{3}\,\tilde{\nu}\,\tilde{v} - \tfrac{1}{6}\,\tilde{v}^2 - \bar{\boldsymbol{\mu}}\cdot\boldsymbol{\nabla}\bar{\phi} - \bar{\phi}_t - g\,\eta. \tag{3.17}$$

The relations (3.12)–(3.15) imply that the motion is exactly irrotational, but the fluid incompressibility is not satisfied identically. With these four relations, the last two equations can be rewritten in the form:

$$h_t + \boldsymbol{\nabla}\cdot[\,h\,\bar{\boldsymbol{u}}\,] = 0, \tag{3.18}$$

$$\bar{\boldsymbol{u}}_t + (\bar{\boldsymbol{u}}\cdot\boldsymbol{\nabla})\,\bar{\boldsymbol{u}} + g\,\boldsymbol{\nabla}\,h = 0, \tag{3.19}$$

where $h = \eta + d$ is the total water depth. Equations (3.18)–(3.19) are the very well-known nonlinear shallow water equations, also known as Airy or Saint-Venant equations (Wehausen & Laitone 1960 [WL60], §28). They are sometimes called *non-dispersive fully-nonlinear approximation* because their classical derivation assumes long waves without the extra hypothesis of small amplitudes.

The Saint-Venant equations do not admit smooth progressive wave solutions. They are nevertheless widely used because they can be solved analytically by the method of characteristics [Sto57]. Moreover, numerous efficient finite volumes type schemes have been proposed [ZCIM02]. These equations have also been validated by comparisons with experimental data even for the wave runup case [Syn87]. Below we present several more elaborated models.

#### 3.1.3.3 Constraining with free surface impermeability

We now constrain the ansatz (3.8) imposing that the impermeability of the free surface is satisfied identically. Since the surface impermeability is expressed through the velocity

$(\boldsymbol{\mu}, \nu)$ in (3.6), we substitute

$$\tilde{\nu} \;=\; \eta_t \;+\; \bar{\boldsymbol{\mu}} \cdot \boldsymbol{\nabla}\eta, \tag{3.20}$$

into the Lagrangian density (3.10), and the minimization procedure gives

$$\begin{aligned}
\delta\,\bar{\boldsymbol{u}}: \quad & 0 \;=\; \bar{\boldsymbol{\mu}} \;-\; \bar{\boldsymbol{u}}, && (3.21)\\
\delta\,\tilde{v}: \quad & 0 \;=\; \eta_t \;+\; \bar{\boldsymbol{\mu}} \cdot \boldsymbol{\nabla}\eta \;-\; \tilde{v}, && (3.22)\\
\delta\,\bar{\boldsymbol{\mu}}: \quad & 0 \;=\; \bar{\boldsymbol{u}} \;+\; \tfrac{1}{3}\,\tilde{v}\,\boldsymbol{\nabla}\eta \;-\; \boldsymbol{\nabla}\bar{\phi}, && (3.23)\\
\delta\,\bar{\phi}: \quad & 0 \;=\; \eta_t \;+\; \boldsymbol{\nabla}\cdot\left[\,(\eta + d)\,\bar{\boldsymbol{\mu}}\,\right], && (3.24)\\
\delta\,\eta: \quad & 0 \;=\; \bar{\boldsymbol{\mu}}\cdot\bar{\boldsymbol{u}} \;-\; \tfrac{1}{2}\,\bar{\boldsymbol{u}}^2 \;-\; \tfrac{1}{6}\,\tilde{v}^2 \;-\; \bar{\boldsymbol{\mu}}\cdot\boldsymbol{\nabla}\bar{\phi} \;-\; \bar{\phi}_t \;-\; g\,\eta \\
& \qquad -\; \tfrac{1}{3}\,(\eta + d)\left[\,\tilde{v}_t \;+\; \bar{\boldsymbol{\mu}}\cdot\boldsymbol{\nabla}\tilde{v} \;+\; \tilde{v}\,\boldsymbol{\nabla}\cdot\bar{\boldsymbol{\mu}}\,\right]. && (3.25)
\end{aligned}$$

The relations (3.21) and (3.23) link the velocity potential and the horizontal velocity as $\boldsymbol{\nabla}\bar{\phi} \neq \bar{\boldsymbol{u}} = \bar{\boldsymbol{\mu}}$ and, therefore, equations (3.21)–(3.25) cannot be derived from Luke's variational principle. Nevertheless, the relaxed variational principle ensures that the vorticity induced by the ansatz choice is minimum. Relations (3.21) and (3.24) provide the mass conservation and hence, with (3.20), the approximation (3.21)–(3.25) implies that the fluid incompressibility is fulfilled identically.

Eliminating $\bar{\phi}$, $\bar{\boldsymbol{\mu}}$ and $\tilde{v}$ from the horizontal gradient of (3.25), the system (3.21)–(3.25) becomes

$$\begin{aligned}
h_t + \boldsymbol{\nabla}\cdot[h\bar{\boldsymbol{u}}] \;&=\; 0, && (3.26)\\
\bar{\boldsymbol{u}}_t + \bar{\boldsymbol{u}}\cdot\boldsymbol{\nabla}\bar{\boldsymbol{u}} + g\boldsymbol{\nabla}h + \tfrac{1}{3}h^{-1}\boldsymbol{\nabla}[h^2\tilde{\gamma}] \;&=\; (\bar{\boldsymbol{u}}\cdot\boldsymbol{\nabla}h)\,\boldsymbol{\nabla}(h\boldsymbol{\nabla}\cdot\bar{\boldsymbol{u}}) \\
& \qquad -\; [\,\bar{\boldsymbol{u}}\cdot\boldsymbol{\nabla}(h\boldsymbol{\nabla}\cdot\bar{\boldsymbol{u}})\,]\,\boldsymbol{\nabla}h, && (3.27)
\end{aligned}$$

with $h = \eta + d$ and where

$$\tilde{\gamma} \;=\; \tilde{v}_t \;+\; \bar{\boldsymbol{u}}\cdot\boldsymbol{\nabla}\tilde{v} \;=\; h\,\left\{\,(\boldsymbol{\nabla}\cdot\bar{\boldsymbol{u}})^2 \;-\; \boldsymbol{\nabla}\cdot\bar{\boldsymbol{u}}_t \;-\; \bar{\boldsymbol{u}}\cdot\boldsymbol{\nabla}\left[\,\boldsymbol{\nabla}\cdot\bar{\boldsymbol{u}}\,\right]\,\right\}, \tag{3.28}$$

is the fluid vertical acceleration at the free surface.

In the two-dimensional case (one horizontal dimension) the right-hand side of (3.27) vanishes and the system (3.26), (3.27) reduces to the equations first derived by Serre (1953) [Ser53], independently rediscovered by Su and Gardner (1969) [SG69] and again by Green, Laws and Naghdi (1974) [GLN74]. It is sometimes called *weakly-dispersive fully-nonlinear approximation* [Wu01]. These equations admit a traveling solitary wave solution

$$\eta \;=\; a\,\mathrm{sech}^2\,\tfrac{1}{2}\varkappa(x_1 - ct), \qquad c^2 \;=\; g\,(d + a), \qquad (\varkappa d)^2 \;=\; 3\,a\,(d + a)^{-1},$$

which is linearly stable [Li02]. Note that this solution does not impose any limitation on the wave amplitude, meaning that Serre's equations are inconsistent for the highest waves. Note also that the Serre equations have a *non-canonical* Hamiltonian structure [Li02].

In three dimensions, equations (3.26)–(3.27) were called by Kim *et al.* (2001) [KBEW01] 'irrotational' Green–Naghdi equations. If the right-hand side of (3.27) is neglected, we recover the classical Green–Naghdi equations [GN76].

Craig and Grooves (1994) [CG94], and many others, also derived various shallow water models starting from a variational principle. The main difference with our approach is that we do not introduce any small parameter but we make assumptions on the vertical structure of the flow.

#### 3.1.3.4 Constraining with incompressibility and partial potential flow I

Here, we restrict the freedom imposing that the velocity potential is related to the horizontal velocity as $\boldsymbol{u} = \boldsymbol{\nabla}\phi$, and that the fluid incompressibility $\boldsymbol{\nabla}\cdot\boldsymbol{u} + v_y = 0$ is fulfilled, together with the relations $\boldsymbol{\mu} = \boldsymbol{u}$ and $\nu = v$, i.e., we take the subordinate conditions

$$\bar{\boldsymbol{\mu}} \;=\; \bar{\boldsymbol{u}}, \qquad \tilde{\nu} \;=\; \tilde{v}, \qquad \bar{\boldsymbol{u}} \;=\; \boldsymbol{\nabla}\bar{\phi}, \qquad \tilde{v} \;=\; -(\eta+d)\,\boldsymbol{\nabla}^2\bar{\phi}.$$

These constraints do not impose exact irrotationality because $v \neq \phi_y$. Obviously, we shall derive an approximation which lies "between" the Saint-Venant and Serre equations.

Thus, the Lagrangian density (3.11) becomes

$$\mathscr{L} \;=\; \bar{\phi}\,\eta_t \;-\; \tfrac{1}{2}\,g\,\eta^2 \;-\; \tfrac{1}{2}\,(\eta+d)\,\big(\boldsymbol{\nabla}\bar{\phi}\big)^2 \;+\; \tfrac{1}{6}\,(\eta+d)^3\,\big(\boldsymbol{\nabla}^2\bar{\phi}\big)^2,$$

and its minimization yields

$$\begin{aligned}
\delta\,\bar{\phi}: \qquad 0 \;&=\; \eta_t \;+\; \boldsymbol{\nabla}\cdot\big[\,(\eta+d)\,\boldsymbol{\nabla}\bar{\phi}\,\big] \;+\; \tfrac{1}{3}\,\boldsymbol{\nabla}^2\big[\,(\eta+d)^3\,\big(\boldsymbol{\nabla}^2\bar{\phi}\big)\,\big],\\
\delta\,\eta: \qquad 0 \;&=\; \bar{\phi}_t \;+\; g\,\eta \;+\; \tfrac{1}{2}\,\big(\boldsymbol{\nabla}\bar{\phi}\big)^2 \;-\; \tfrac{1}{2}\,(\eta+d)^2\,\big(\boldsymbol{\nabla}^2\bar{\phi}\big)^2.
\end{aligned}$$

It seems that these equations have never appeared before in the literature. They are a generalization of the so-called Kaup–Boussinesq (or canonical Boussinesq) equations [Kau75, Kup85] and are thus referred to as the gKB equations. This can be seen noticing that the gKB equations can be derived from the canonical Hamiltonian

$$\int_\Omega \Big\{\, \tfrac{1}{2}\,g\,\eta^2 \;+\; \tfrac{1}{2}\,(\eta+d)\,\big(\boldsymbol{\nabla}\bar{\phi}\big)^2 \;-\; \tfrac{1}{6}\,(\eta+d)^3\,\big(\boldsymbol{\nabla}^2\bar{\phi}\big)^2 \,\Big\}\;\mathrm{d}^2\boldsymbol{x}, \tag{3.29}$$

while the classical Kaup–Boussinesq (cKB) equations are obtained replacing $(\eta+d)^3$ by $d^3$ in (3.29) and restricting the resulting Hamiltonian to one horizontal dimension.

The linearized gKB and cKB systems admit the special traveling wave solution

$$\eta \;=\; a\cos k(x_1 - ct), \qquad c^2 \;=\; gd\,(1-\tfrac{1}{3}k^2d^2), \tag{3.30}$$

implying that these equations are linearly ill-conditioned ($c^2 < 0$ for $kd > \sqrt{3}$). However, if, like the cKB, the gKB equations are integrable, they may be a somewhat interesting model for gravity waves in shallow water.

#### 3.1.3.5 Constraining with incompressibility and partial potential flow II

So far, all the approximations derived turned out to be such that $\boldsymbol{\mu} = \boldsymbol{u}$ and $\nu = v$. We propose here a novel approximation that does not satisfies one of these identities and that is an interesting variant of the previous model.

We impose a partially potential flow such that $\boldsymbol{\mu} = \boldsymbol{\nabla}\phi$ and $\nu = \phi_y$, together with the incompressibility condition $\boldsymbol{\nabla}\cdot\boldsymbol{u} + v_y = 0$ and the condition $\boldsymbol{u} = \boldsymbol{\mu}$. Thus, substituting the constraints

$$\bar{\boldsymbol{\mu}} \;=\; \bar{\boldsymbol{u}} \;=\; \boldsymbol{\nabla}\bar{\phi}, \qquad \tilde{\nu} \;=\; 0, \qquad \tilde{v} \;=\; -(\eta+d)\,\boldsymbol{\nabla}^2\bar{\phi},$$

into the Lagrangian density (3.11) yields

$$\mathscr{L} \;=\; \bar{\phi}\,\eta_t \;-\; \tfrac{1}{2}\,g\,\eta^2 \;-\; \tfrac{1}{2}\,(\eta+d)\,\big(\boldsymbol{\nabla}\bar{\phi}\big)^2 \;-\; \tfrac{1}{6}\,(\eta+d)^3\,\big(\boldsymbol{\nabla}^2\bar{\phi}\big)^2,$$

and the minimization procedure gives the equations

$$\delta\,\bar{\phi}: \qquad 0 \;=\; \eta_t \;+\; \boldsymbol{\nabla}\cdot\big[\,(\eta+d)\,\boldsymbol{\nabla}\bar{\phi}\,\big] \;-\; \tfrac{1}{3}\,\boldsymbol{\nabla}^2\big[\,(\eta+d)^3\,\big(\boldsymbol{\nabla}^2\bar{\phi}\big)\,\big], \tag{3.31}$$

$$\delta\,\eta: \qquad 0 \;=\; \bar{\phi}_t \;+\; g\,\eta \;+\; \tfrac{1}{2}\,\big(\boldsymbol{\nabla}\bar{\phi}\big)^2 \;+\; \tfrac{1}{2}\,(\eta+d)^2\,\big(\boldsymbol{\nabla}^2\bar{\phi}\big)^2. \tag{3.32}$$

These equations can be derived from the canonical Hamiltonian

$$\int_\Omega \Big\{\, \tfrac{1}{2}\,g\,\eta^2 \;+\; \tfrac{1}{2}\,(\eta+d)\,\big(\boldsymbol{\nabla}\bar{\phi}\big)^2 \;+\; \tfrac{1}{6}\,(\eta+d)^3\,\big(\boldsymbol{\nabla}^2\bar{\phi}\big)^2 \,\Big\}\;\mathrm{d}^2\boldsymbol{x},$$

which is always positive (an interesting feature for modeling water waves). To the linear approximation, equations (3.31), (3.32) have the progressive wave solution

$$\eta \;=\; a\cos k(x_1 - ct), \qquad c^2 \;=\; gd\,(1+\tfrac{1}{3}k^2d^2), \tag{3.33}$$

which is well-behaved (i.e., $c^2$ is never negative). Comparisons with the gKB equations suggest to refer to equations (3.31)–(3.32) as *regularized general Kaup-Boussinesq* (rgKB). However, the linear dispersion relation (3.33) approximates the dispersion relation of linear waves — i.e., $c^2 = g\tanh(kd)/k$ — only to the order $\mathrm{O}(k^2)$, while (3.30) is $\mathrm{O}(k^4)$. Therefore, the rgKB equations are not very interesting for modeling water waves, but these equations may be of interest to model other physical processes.

#### 3.1.3.6 Other constraints and generalizations

We briefly discuss now some other possible generalizations.

**3.1.3.6.1 Constraining with incompressibility and potential flow I** In the previous example, we have constructed an approximation such that $\boldsymbol{\mu} = \boldsymbol{u}$ but $\nu \neq v$. Now, we release the constraint $\boldsymbol{\mu} = \boldsymbol{u}$ and keep the other constraints. Thus, we impose

$$\bar{\boldsymbol{\mu}} \;=\; \boldsymbol{\nabla}\bar{\phi}, \qquad \tilde{\nu} \;=\; 0, \qquad \tilde{v} \;=\; -(\eta + d)\,\boldsymbol{\nabla}\cdot\bar{\boldsymbol{u}},$$

so that the pseudo velocity field $(\boldsymbol{\mu}, \nu)$ is irrotational while the velocity field $(\boldsymbol{u}, v)$ is incompressible. After same elementary algebra, the Lagrangian density becomes

$$\mathscr{L} \;=\; \bar{\phi}\,h_t \;-\; \tfrac{1}{2}\,g\,\eta^2 \;+\; h\,\bar{\boldsymbol{u}}\cdot\boldsymbol{\nabla}\bar{\phi} \;-\; \tfrac{1}{2}\,h\,\bar{\boldsymbol{u}}^2 \;-\; \tfrac{1}{6}\,h^3\,(\boldsymbol{\nabla}\cdot\bar{\boldsymbol{u}})^2 \;-\; h\left(\boldsymbol{\nabla}\bar{\phi}\right)^2,$$

where $h = \eta + d$. The minimization procedure yields

$$\begin{aligned}
\delta\,\bar{\boldsymbol{u}}: \quad & 0 \;=\; h\,\boldsymbol{\nabla}\bar{\phi} \;-\; h\,\bar{\boldsymbol{u}} \;+\; \tfrac{1}{3}\,\boldsymbol{\nabla}\left[\,h^3\,\boldsymbol{\nabla}\cdot\bar{\boldsymbol{u}}\,\right],\\
\delta\,\bar{\phi}: \quad & 0 \;=\; h_t \;-\; \boldsymbol{\nabla}\cdot\left[\,h\,\bar{\boldsymbol{u}}\,\right] \;+\; 2\,\boldsymbol{\nabla}\cdot\left[\,h\,\boldsymbol{\nabla}\bar{\phi}\,\right],\\
\delta\,\eta: \quad & 0 \;=\; \bar{\phi}_t \;+\; g\,\eta \;+\; \tfrac{1}{2}\,\bar{\boldsymbol{u}}^2 \;+\; \left(\boldsymbol{\nabla}\bar{\phi}\right)^2 \;-\; \bar{\boldsymbol{u}}\cdot\boldsymbol{\nabla}\bar{\phi} \;+\; \tfrac{1}{2}\,h^2\,(\boldsymbol{\nabla}\cdot\bar{\boldsymbol{u}})^2.
\end{aligned}$$

The linearization of this system of equations have a $(2\pi/k)$-periodic sinusoidal traveling wave solution with the dispersion relation

$$c^2 \;=\; gd\,(1 + \tfrac{2}{3}k^2d^2)\,(1 + \tfrac{1}{3}k^2d^2)^{-1} \;=\; gd\,(1 + \tfrac{1}{3}k^2d^2) \;+\; \mathrm{O}(k^4),$$

which, like the previous example, is not satisfactory for water waves. However, these equations may be of interest in other contexts than water waves.

**3.1.3.6.2 Constraining with incompressibility and potential flow II** We now assume that the pseudo velocity field $(\boldsymbol{\mu}, \nu)$ is divergence free, while the velocity field $(\boldsymbol{u}, v)$ is irrotational, i.e., we impose the constraints

$$\bar{\boldsymbol{u}} \;=\; \boldsymbol{\nabla}\bar{\phi}, \qquad \tilde{v} \;=\; 0, \qquad \tilde{\nu} \;=\; -(\eta + d)\,\boldsymbol{\nabla}\cdot\bar{\boldsymbol{\mu}}.$$

The Lagrangian density becomes

$$\mathscr{L} \;=\; \bar{\phi}\,\eta_t \;-\; \tfrac{1}{2}\,g\,\eta^2 \;-\; \tfrac{1}{2}\,(\eta + d)\left(\boldsymbol{\nabla}\bar{\phi}\right)^2,$$

which, after minimization, yields the Saint-Venant equations. Thus, these constraints do not bring anything new. It should be emphasized that this is the case for the special shallow water ansatz we are considering here, but this is not necessarily the case for other ansatz.

**3.1.3.6.3 Further possibilities** The constraints of Sections (3.1.3.4) to (3.1.3.6.2) can be unified into a single formalism considering combinations. Indeed, the velocity field $(\boldsymbol{u}, v)$ being not more (nor less) physical than the pseudo-velocity field $(\boldsymbol{\mu}, \nu)$ and the potential velocity field $(\boldsymbol{\nabla}\phi, \phi_y)$, the constraints can be imposed by combinations of these three fields. For instance, we could impose the irrotationality for the field

$$( c_1\boldsymbol{u} + c_2\boldsymbol{\mu} + (1-c_1-c_2)\boldsymbol{\nabla}\phi \ , \ c_1 v + c_2\nu + (1-c_1-c_2)\phi_y \ ),$$

the fluid incompressibility for the field

$$( c_3\boldsymbol{u} + c_4\boldsymbol{\mu} + (1-c_3-c_4)\boldsymbol{\nabla}\phi \ , \ c_3 v + c_4\nu + (1-c_3-c_4)\phi_y \ ),$$

and so on for any constraint we may think of. The $c_n$ are parameters at our disposal. We can choose them in a convenient way based on some mathematical and physical considerations. For example, imposing that the approximate equations derived must be linearly well-posed and/or have better dispersion relation properties.

In the examples above, only some kinematic constraints (irrotationality, incompressibility, impermeability) were used. We could have also considered dynamical constraints based on, e.g., the Bernoulli equation, or other relevant dynamical equations.

The relaxed variational principle provided a common platform for deriving several shallow water equations from the same ansatz in changing only the constraints. Beside the ansatz, no further approximation were made and the derivations required only some elementary algebra. Using more general ansatz — i.e., involving more free functions and parameters — one can introduce more constraints, if desired, and derives more accurate approximations. A simple example is given in Section 3.1.6 below.

## 3.1.4 Examples in deep water

We illustrate here the advantages of the relaxed variational principle in the opposite limiting case of deep water.

### 3.1.4.1 Choice of an ansatz

For progressive waves in deep water, the Stokes expansion shows that the velocity field varies nearly exponentially along the vertical (Appendix 3.1.8). Even for very large unsteady waves (including breaking waves), accurate numerical simulations and experiments have shown that the vertical variation of the velocity field is indeed very close to an exponential [GCHJ03, JCHG07]. Thus, this property is exploited here to derive simple approximations for waves in deep water.

Let $\kappa > 0$ be a characteristic wavenumber corresponding, for example, to the carrier wave of a modulated wave group or to the peak frequency of a JONSWAP spectrum. Following the discussion above, it is natural to seek approximations in the form

$$\{\,\phi\,;\,\boldsymbol{u}\,;\,v\,;\,\boldsymbol{\mu}\,;\,\nu\,\}\;\approx\;\{\,\tilde{\phi}\,;\,\tilde{\boldsymbol{u}}\,;\,\tilde{v}\,;\,\tilde{\boldsymbol{\mu}}\,;\,\tilde{\nu}\,\}\,\mathrm{e}^{\kappa(y-\eta)}, \tag{3.34}$$

where $\tilde{\phi}$, $\tilde{\boldsymbol{u}}$, $\tilde{v}$, $\tilde{\mu}$ and $\tilde{\nu}$ are functions of $\boldsymbol{x}$ and $t$ that will be determined using the variational principle. The ansatz (3.34) is certainly the simplest possible that is consistent with experimental evidences. This ansatz has already been used by Kraenkel *et al.* (2005) [KLM05] for building their approximation. Possible generalizations are discussed in Section 3.1.6.

For the sake of simplicity, we introduce the constraints $\tilde{\boldsymbol{\mu}} = \tilde{\boldsymbol{u}}$ and $\tilde{\nu} = \tilde{v}$. Thus, the ansatz (3.34) substituted into the Lagrangian density (3.5) yields

$$2\kappa\,\mathscr{L} \;=\; 2\kappa\,\tilde{\phi}\,\eta_t \;-\; g\kappa\,\eta^2 \;+\; \tfrac{1}{2}\tilde{\boldsymbol{u}}^2 \;+\; \tfrac{1}{2}\tilde{v}^2 \;-\; \tilde{\boldsymbol{u}}\cdot(\boldsymbol{\nabla}\tilde{\phi} - \kappa\tilde{\phi}\boldsymbol{\nabla}\eta) \;-\; \kappa\,\tilde{v}\,\tilde{\phi}. \tag{3.35}$$

With (or without) subordinate relations, this Lagrangian gives various equations. We investigate two cases here.

### 3.1.4.2 Unconstrained approximation

Without further constraints, the minimization procedure yields

$$\begin{aligned}
\delta\,\tilde{\boldsymbol{u}}: &\quad 0 \;=\; \tilde{\boldsymbol{u}} \;-\; \boldsymbol{\nabla}\tilde{\phi} \;+\; \kappa\,\tilde{\phi}\,\boldsymbol{\nabla}\eta,\\
\delta\,\tilde{v}: &\quad 0 \;=\; \tilde{v} \;-\; \kappa\,\tilde{\phi},\\
\delta\,\tilde{\phi}: &\quad 0 \;=\; 2\kappa\,\eta_t \;+\; \boldsymbol{\nabla}\cdot\tilde{\boldsymbol{u}} \;-\; \kappa\,\tilde{v} \;+\; \kappa\,\tilde{\boldsymbol{u}}\cdot\boldsymbol{\nabla}\eta,\\
\delta\,\eta: &\quad 0 \;=\; 2g\kappa\,\eta \;+\; 2\kappa\,\tilde{\phi}_t \;+\; \kappa\,\boldsymbol{\nabla}\cdot(\,\tilde{\phi}\,\tilde{\boldsymbol{u}}\,).
\end{aligned}$$

The two first relations imply that this approximation is exactly irrotational and their use in the last two equations gives

$$\eta_t \;+\; \tfrac{1}{2}\kappa^{-1}\boldsymbol{\nabla}^2\tilde{\phi} \;-\; \tfrac{1}{2}\kappa\tilde{\phi} \;=\; \tfrac{1}{2}\,\tilde{\phi}\left[\,\boldsymbol{\nabla}^2\eta \;+\; \kappa\,(\boldsymbol{\nabla}\eta)^2\,\right], \tag{3.36}$$

$$\tilde{\phi}_t \;+\; g\,\eta \;=\; -\tfrac{1}{2}\,\boldsymbol{\nabla}\cdot\left[\,\tilde{\phi}\,\boldsymbol{\nabla}\tilde{\phi} \;-\; \kappa\,\tilde{\phi}^2\,\boldsymbol{\nabla}\eta\,\right]. \tag{3.37}$$

Since equations (3.36)–(3.37) derive from an irrotational motion, they can also be obtained from Luke's Lagrangian (3.2) under ansatz (3.34). Equations (3.36)–(3.37) are a deep water counterpart of Saint-Venant equations for shallow water waves; this claim will appear clearer in Section 3.1.5. They can also be derived from the canonical Hamiltonian

$$\int_\Omega \left\{\,\tfrac{1}{2}\,g\,\eta^2 \;+\; \tfrac{1}{4}\,\kappa^{-1}\left[\,\boldsymbol{\nabla}\tilde{\phi} \;-\; \kappa\,\tilde{\phi}\,\boldsymbol{\nabla}\eta\,\right]^2 \;+\; \tfrac{1}{4}\,\kappa\,\tilde{\phi}^2\,\right\}\mathrm{d}^2\boldsymbol{x}. \tag{3.38}$$

This 'simple' Hamiltonian is quartic in nonlinearities and involves only first-order derivatives. It has to be compared with Zakharov's quartic Hamiltonian (3.58) which involves second-order derivatives and pseudo-differential operators. However, Zakharov's quartic Hamiltonian is valid for broad spectra. Note that the Hamiltonian (3.38) cannot be derived from the exact one (3.57), since the latter assumes that irrotationality and incompressibility are both satisfied identically in the bulk, while the incompressibility is not fulfilled by equations (3.36)–(3.37).

To the linear approximation, after elimination of $\tilde{\phi}$, equations (3.36)–(3.37) yield

$$\eta_{tt} \;-\; \tfrac{1}{2}\,(g/\kappa)\,\boldsymbol{\nabla}^2\eta \;+\; \tfrac{1}{2}\,g\,\kappa\,\eta \;=\; 0, \tag{3.39}$$

that is a Klein–Gordon equation. For this reason, equations (3.36)–(3.37) will be referred here as *generalized Klein–Gordon* (gKG). The Klein–Gordon equation is prominent in mathematical physics and appears, e.g., as a relativistic generalization of the Schrödinger equation. The Klein–Gordon equation (3.39) admits a special $(2\pi/k)$-periodic traveling wave solution

$$\eta \;=\; a\,\cos k(x_1 - ct), \qquad c^2 \;=\; \tfrac{1}{2}\,g\,(k^2+\kappa^2)\,(\kappa\,k^2)^{-1}.$$

Therefore, if $k=\kappa$ the exact dispersion relation of linear waves (i.e., $c^2 = g/k$) is recovered, as it should be. This means, in particular, that the gKG model is valid for spectra narrow-banded around the wavenumber $\kappa$.

We focus now on $(2\pi/\kappa)$-periodic progressive waves solution of the gKG equations, i.e., we seek for solutions depending only on the variable $\theta = \kappa(x_1 - ct)$. We were not able to find an exact analytic solution but a Stokes-like expansion gives some interesting insights. To the seventh-order, we have

$$\begin{aligned}
\kappa\,\eta \;&=\; \alpha\cos\theta \;+\; \tfrac{1}{2}\alpha^2\big(1+\tfrac{\mathbf{25}}{12}\alpha^2+\tfrac{\mathbf{1675}}{\mathbf{192}}\alpha^4\big)\cos 2\theta \\
&\quad+\tfrac{3}{8}\alpha^3\big(1+\tfrac{\mathbf{99}}{16}\alpha^2+\tfrac{\mathbf{11807}}{320}\alpha^4\big)\cos 3\theta \;+\; \tfrac{1}{3}\alpha^4\big(1+\tfrac{\mathbf{64}}{\mathbf{5}}\alpha^2\big)\cos 4\theta \\
&\quad+\tfrac{125}{384}\alpha^5\big(1+\tfrac{\mathbf{6797}}{\mathbf{300}}\alpha^2\big)\cos 5\theta \;+\; \tfrac{27}{80}\alpha^6\cos 6\theta \;+\; \tfrac{16807}{46080}\alpha^7\cos 7\theta \;+\; \mathrm{O}(\alpha^8), \\
g^{-\frac{1}{2}}\kappa^{\frac{3}{2}}\,\tilde{\phi} \;&=\; \alpha\,\big(1-\tfrac{1}{4}\alpha^2-\tfrac{\mathbf{59}}{96}\alpha^4-\tfrac{\mathbf{4741}}{1536}\alpha^6\big)\sin\theta \;+\; \tfrac{1}{2}\alpha^2\big(1+\tfrac{\mathbf{11}}{12}\alpha^2+\tfrac{\mathbf{547}}{\mathbf{192}}\alpha^4\big)\sin 2\theta \\
&\quad+\tfrac{3}{8}\alpha^3\big(1+\tfrac{\mathbf{163}}{\mathbf{48}}\alpha^2+\tfrac{\mathbf{221}}{\mathbf{15}}\alpha^4\big)\sin 3\theta \;+\; \tfrac{1}{3}\alpha^4\big(1+\tfrac{\mathbf{149}}{\mathbf{20}}\alpha^2\big)\sin 4\theta \\
&\quad+\tfrac{125}{384}\alpha^5\big(1+\tfrac{\mathbf{5057}}{\mathbf{375}}\alpha^2\big)\sin 5\theta \;+\; \tfrac{27}{80}\alpha^6\sin 6\theta \;+\; \tfrac{16807}{46080}\alpha^7\sin 7\theta \;+\; \mathrm{O}(\alpha^8), \\
g^{-\frac{1}{2}}\kappa^{\frac{1}{2}}\,c \;&=\; 1 + \tfrac{1}{2}\alpha^2 + \tfrac{1}{2}\alpha^4 + \tfrac{\mathbf{899}}{384}\alpha^6 + \mathrm{O}(\alpha^8).
\end{aligned}$$

The expansions of $\eta$ and $\tilde{\phi}$ match the exact Stokes wave (c.f. Appendix 3.1.8) up to the third-order (non-matching coefficients are displayed bold). This is not surprising since the gKG equations are cubic in nonlinearities. A bit more surprising is that the phase velocity

$c$ is correct up to the fifth-order. But the most interesting is that, to the leading order, the $n$-th Fourier coefficient is (for all $n$ up to infinity)

$$\frac{n^{n-2}\ \alpha^n}{2^{n-1}\,(n-1)!}, \tag{3.40}$$

which is also the case for the exact Stokes wave (Appendix 3.1.8).

In comparison, for the cubic Zakharov equations (3.59)–(3.60), the phase velocity is correct only up to the third-order and the Fourier coefficients do not verify the asymptotic behavior (3.40) (see Appendix 3.1.9). Truncating Zakharov's Hamiltonian at the order $N+1$ in nonlinearities, the corresponding Stokes double series is correct up to the order $N$ in the expansion parameter. But none of these higher approximations have the exact asymptotic behavior (3.40) for their Fourier coefficients because they involve expansions around $\eta = 0$, while the gKG does not.

#### 3.1.4.3 Constraining with the free surface impermeability

In order to satisfy the free surface impermeability identically, we take

$$\tilde{v} \ = \ \eta_t \ + \ \tilde{\boldsymbol{u}} \cdot \boldsymbol{\nabla}\eta,$$

and the Lagrangian density (3.35) becomes

$$2\kappa\,\mathscr{L} \ = \ \tilde{\phi}\,(\kappa\,\eta_t + \boldsymbol{\nabla}\cdot\tilde{\boldsymbol{u}}) \ - \ g\kappa\,\eta^2 \ + \ \tfrac{1}{2}\tilde{\boldsymbol{u}}^2 \ + \ \tfrac{1}{2}(\eta_t + \tilde{\boldsymbol{u}}\cdot\boldsymbol{\nabla}\eta)^2, \tag{3.41}$$

while the minimization procedure yields the equations

$$\delta\,\tilde{\boldsymbol{u}}: \qquad 0 \ = \tilde{\boldsymbol{u}} + (\eta_t + \tilde{\boldsymbol{u}}\cdot\boldsymbol{\nabla}\eta)\boldsymbol{\nabla}\eta - \boldsymbol{\nabla}\tilde{\phi}, \tag{3.42}$$

$$\delta\,\tilde{\phi}: \qquad 0 \ = \kappa\eta_t + \boldsymbol{\nabla}\cdot\tilde{\boldsymbol{u}}, \tag{3.43}$$

$$\delta\,\eta: \qquad 0 \ = 2g\kappa\eta + \kappa\tilde{\phi}_t + \eta_{tt} + (\tilde{\boldsymbol{u}}\cdot\boldsymbol{\nabla}\eta)_t + \boldsymbol{\nabla}\cdot(\tilde{\boldsymbol{u}}\eta_t) + \boldsymbol{\nabla}\cdot[(\tilde{\boldsymbol{u}}\cdot\boldsymbol{\nabla}\eta)\tilde{\boldsymbol{u}}]. \tag{3.44}$$

The relation (3.43) implying that $\boldsymbol{\nabla}\cdot\boldsymbol{u} + v_y = 0$, the solution satisfies the incompressibility identically. On the other hand, the irrotationality being not verified identically, equations (3.42)–(3.44) cannot be derived from Luke's variational formulation. Note that (3.42) yields $\boldsymbol{\nabla}\tilde{\phi} = \tilde{\boldsymbol{u}} + \tilde{v}\boldsymbol{\nabla}\eta$ that is exact for potential flows [CS93, FCKG05].

As for the shallow water case, the potential $\tilde{\phi}$ can be eliminated from equations (3.42), thus yielding a deep water analog of Serre's and the Green–Naghdi equations.

To the linear approximation, relations (3.42)–(3.44) can be combined into a single equation for the elevation of the free surface:

$$(\boldsymbol{\nabla}^2 - \kappa^2)\,\eta_{tt} \ + \ 2\,g\,\kappa\,\boldsymbol{\nabla}^2\eta \ = \ 0,$$

which admits the special $(2\pi/k)$-periodic solution

$$\eta \;=\; a\,\cos k(x_1 - ct), \qquad c^2 \;=\; 2\,g\,\kappa\,(k^2+\kappa^2)^{-1}.$$

Therefore, if $k=\kappa$ the exact linear approximation is recovered, as it should be. Again, this means that this model is valid for narrow-banded spectra. How narrow will be investigated now.

**3.1.4.3.1 Two-dimensional progressive waves** We seek now exact solutions depending only on $\xi \equiv x_1 - ct$ (two-dimensional progressive waves). Equations (3.42)–(3.43) yield respectively

$$\tilde{\phi}_\xi \;=\; \tilde{u} \;+\; (\tilde{u}-c)\,\eta_\xi^2, \qquad \tilde{u} \;=\; c\,\kappa\,\eta \;+\; c\,K_1,$$

where $K_1$ is an integration constant. Substituting these relations into (3.44) and multiplying the result by $\eta_\xi$, after one integration and some algebra, we obtain

$$\left(\frac{\mathrm{d}\,\eta}{\mathrm{d}\xi}\right)^2 \;=\; \frac{K_0^2 \;-\; \left(\,\kappa\,\eta \;-\; K_1\,\hat{\varepsilon}^{-2}\,\right)^2}{\hat{\varepsilon}^{-2}\,\left(\,\kappa\,\eta \;+\; K_1 \;-\; 1\,\right)^2}, \tag{3.45}$$

where

$$\hat{\varepsilon}^2 \;\equiv\; 2\,g\,\kappa^{-1}\,c^{-2} \;-\; 1,$$

and where $K_0$ is another integration constant. Assuming that $\eta_\xi = 0$ at the wave crest where $\eta = a$ and at the trough where $\eta = -b$ (hence $a+b$ is the total wave height), we find

$$K_0 \;=\; \tfrac{1}{2}\,\kappa\,(a+b), \qquad K_1 \;=\; \tfrac{1}{2}\,\kappa\,(a-b)\,\hat{\varepsilon}^2.$$

Solving equation (3.45), together with the condition of zero mean free surface elevation, we obtain an exact $(2\pi/k)$-periodic solution in the parametric form [Gen03]:

$$k\,\xi(\tau) = \tau \;-\; \varepsilon\,\hat{\varepsilon}^{-1}\,\sin\tau, \qquad k\,\eta(\tau) = \tfrac{1}{2}\,\varepsilon^2\,\hat{\varepsilon}^{-1} \;+\; \varepsilon\,\cos\tau, \tag{3.46}$$

with

$$\varepsilon \;=\; \tfrac{1}{2}\,k\,(a+b), \qquad k\,\kappa^{-1} \;=\; \hat{\varepsilon} \;+\; \tfrac{1}{2}\,(\,\hat{\varepsilon}^{-1} + \hat{\varepsilon}\,)\,\varepsilon^2,$$

$\varepsilon$ being a wave steepness and $\tau$ being a parametric variable such that a crest is at $\tau = 0$ and the closest troughs at $\tau = \pm\pi$. This remarkably simple solution describes surface waves as trochoids. Smooth surface profiles are obtained for $0 \leqslant \varepsilon < \hat{\varepsilon}$, $\varepsilon \ll \hat{\varepsilon}$ corresponding to quasi-sinusoidal solutions (infinitesimal waves). For the limiting case $\varepsilon = \hat{\varepsilon}$, in the vicinity of the crest $k(a-\eta) \sim \frac{1}{2}\varepsilon(6k\xi)^{\frac{2}{3}}$ so the solution involves a sharp angle forming a $0^\circ$ inner angle (i.e., a cusp), while the exact angle should be $120^\circ$ for irrotational traveling waves.

So far, $\kappa$ is a free parameter at our disposal. We shall now investigate various choices.

**3.1.4.3.2 Simple approximation** A 'natural' choice is to take $\kappa = k$, yielding the steepness $\hat{\varepsilon} \approx 0.596$ for the limiting wave. With this peculiar choice of $\kappa$, a Stokes-like expansion of the solution of (3.46) is

$$\begin{aligned} k\,\eta &= \alpha\cos k\xi \,+\, \tfrac{1}{2}\alpha^2\big(1+\tfrac{\mathbf{13}}{12}\alpha^2+\tfrac{\mathbf{395}}{\mathbf{192}}\alpha^4\big)\cos 2k\xi \\ &\quad + \tfrac{3}{8}\alpha^3\big(1+\tfrac{\mathbf{35}}{16}\alpha^2+\tfrac{\mathbf{1727}}{320}\alpha^4\big)\cos 3k\xi \,+\, \tfrac{1}{3}\alpha^4\big(1+\tfrac{\mathbf{33}}{\mathbf{10}}\alpha^2\big)\cos 4k\xi \\ &\quad + \tfrac{125}{384}\alpha^5\big(1+\tfrac{\mathbf{53}}{\mathbf{12}}\alpha^2\big)\cos 5k\xi \,+\, \tfrac{27}{80}\alpha^6\cos 6k\xi \,+\, \tfrac{16807}{46080}\alpha^7\cos 7k\xi \,+\, \mathrm{O}(\alpha^8), \\ \sqrt{k/g}\,c &= 1+\tfrac{1}{2}\alpha^2+\tfrac{1}{2}\alpha^4+\tfrac{\mathbf{611}}{384}\alpha^6+\mathrm{O}(\alpha^8). \end{aligned}$$

As for the gKB approximation, the Fourier coefficients of this Stokes-like expansion satisfy the asymptotic expression (3.40) and the expansion of $c$ is exact up to the fifth-order. Therefore, taking $\kappa = k$ leads to a quite accurate approximation. However, the optimum value of $\kappa$ leads to an even more interesting approximation.

**3.1.4.3.3 Optimum parameter** With the trochoidal solution and the relation between the parameters obtained above, the Lagrangian density (3.41) integrated over one wavelength yields the Lagrangian

$$\mathcal{L} \;=\; \frac{\pi\, g\, \varepsilon^4}{4\,k^3} \;=\; \frac{\pi\, g}{k^3}\left[-1\,+\,\frac{\kappa\, c^2}{2\, g}\,+\,\sqrt{\frac{k^2\, c^2}{2\, g\,\kappa}\,-\,\frac{k^2\, c^4}{4\, g^2}}\right]^2 .$$

Thus, the Lagrangian is minimum when the steepness is minimum or, equivalently, the wavelength is maximum if the wave height is kept constant. The variational principle being defined with fixed horizontal and temporal boundaries, the optimum parameter $\kappa$ is obtained minimizing $\mathcal{L}$ keeping $k$ and $c$ constant. After some algebra, the equation $\mathrm{d}\mathcal{L}/\mathrm{d}\kappa = 0$ gives two possible solutions for $\kappa$:

$$\kappa_\pm \;=\; \sqrt{2}\,k\left[1\,+\,2\varepsilon^2\,\pm\,\sqrt{1-4\varepsilon^2}\right]^{-\frac{1}{2}},$$

provided that $\varepsilon \leqslant 1/2$. Both solutions correspond to an extremum of $\mathcal{L}$. However, a solution is stable only if the optimal $\kappa$ is a minimum of $\mathcal{L}$, i.e., if

$$\left.\frac{\mathrm{d}^2\,\mathcal{L}}{\mathrm{d}\kappa^2}\right|_{\kappa=\kappa_\pm} \;>\; 0,$$

which, after some algebra, yields the condition

$$\sqrt{3}\;\varepsilon\;\kappa_\pm \;<\; k. \tag{3.47}$$

The first solution

$$\kappa_+ \,/\, k \;=\; \sqrt{2}\left[1\,+\,2\varepsilon^2\,+\,\sqrt{1-4\varepsilon^2}\right]^{-\frac{1}{2}} \;=\; 1\;+\;\tfrac{1}{2}\,\varepsilon^4\;+\;\mathrm{O}\big(\varepsilon^6\big)\,,$$

is very close to the wavenumber $k$ when the steepness $\varepsilon$ is small. When the steepness increases form 0 to 1/2, the dimensionless parameters $\kappa/k$, $kc^2/g$ and $\sqrt{3}\varepsilon\kappa/k$ increase monotonically. The highest wave is obtained for $\varepsilon = 1/2$, where $\kappa/k = 2/\sqrt{3} \approx 1.15$, $kc^2/g = 3\sqrt{3}/4 \approx 1.3$ and $\sqrt{3}\varepsilon\kappa/k = 1$. All these waves are smooth and stable because condition (3.47) is fulfilled.

The second solution

$$\kappa_- / k \;=\; \sqrt{2}\left[1 \,+\, 2\varepsilon^2 \,-\, \sqrt{1-4\varepsilon^2}\right]^{-\frac{1}{2}},$$

is admissible (i.e., real) if $1/2 \geqslant \varepsilon \geqslant \sqrt{\sqrt{5}-2} \approx 0.486$. As the steepness decays form 1/2 to $\sqrt{\sqrt{5}-2}$, the crest sharpens, the limiting value $\varepsilon = \hat{\varepsilon} = \sqrt{\sqrt{5}-2}$ corresponding to a cusp at the crest. Thus the sharp-crested wave is not the highest one. All these waves are unstable because condition (3.47) is violated, i.e., the solution $\kappa_-$ is a maximum of the Lagrangian and not a minimum.

**Remark 1.** *Taking the optimum parameter $\kappa$ has improved the accuracy of the approximation. The main gain is qualitative, however. Indeed, we found that waves are unstable before a sharp crest is formed. Such behavior is not predicted by low-order perturbation expansions. This simple example is a remarkable illustration of the power of the variational method. The trochoidal wave described here is probably the approximation with the highest ratio* accuracy/complexity *ever derived for a traveling wave in deep water. This approximation has first been derived by Geniet (2003) [Gen03] via a different approach.*

### 3.1.5 Arbitrary depth

A general ansatz, for waves in finite constant depth and satisfying identically the bottom impermeability, is suggested by the linear theory of water waves:

$$\begin{aligned} \phi \approx \frac{\cosh \kappa Y}{\cosh \kappa h}\tilde{\phi}(\boldsymbol{x},t), \quad \boldsymbol{u} \approx \frac{\cosh \kappa Y}{\cosh \kappa h}\tilde{\boldsymbol{u}}(\boldsymbol{x},t), \quad v \approx \frac{\sinh \kappa Y}{\sinh \kappa h}\tilde{v}(\boldsymbol{x},t), \\ \boldsymbol{\mu} \approx \frac{\cosh \kappa Y}{\cosh \kappa h}\tilde{\boldsymbol{\mu}}(\boldsymbol{x},t), \quad \nu \approx \frac{\sinh \kappa Y}{\sinh \kappa h}\tilde{\nu}(\boldsymbol{x},t), \end{aligned} \tag{3.48}$$

where $Y = y + d$ and $h = \eta + d$. The parameter $\kappa$ is a characteristic wave number to be made precise *a posteriori*. This ansatz is uniformly valid for all depths because it yields the shallow water one (3.8) as $\kappa \to 0$, and the deep water one (3.34) as $d \to \infty$. Obviously, the ansatz (3.48) is valid for wave fields with wavenumber spectra that are narrow-banded around $\kappa$. Substituting the ansatz (3.48) into the relaxed variational principle (3.6), we

obtain

$$\begin{aligned}\mathscr{L} &= [\,\eta_t + \tilde{\boldsymbol{\mu}}\cdot\boldsymbol{\nabla}\eta\,]\,\tilde{\phi} - \tfrac{1}{2}\,g\,\eta^2 + [\,\tilde{\nu}\,\tilde{v} - \tfrac{1}{2}\,\tilde{v}^2\,]\,\frac{\sinh(2\kappa h)-2\kappa h}{2\kappa\cosh(2\kappa h)-2\kappa}\\ &+ [\tilde{\boldsymbol{\mu}}\cdot\tilde{\boldsymbol{u}} - \tfrac{1}{2}\tilde{\boldsymbol{u}}^2 + \tilde{\phi}\boldsymbol{\nabla}\cdot\tilde{\boldsymbol{\mu}} - \kappa\tanh(\kappa h)\tilde{\phi}\,\tilde{\boldsymbol{\mu}}\cdot\boldsymbol{\nabla}\eta]\,\frac{\sinh(2\kappa h)+2\kappa h}{2\kappa\cosh(2\kappa h)+2\kappa}\\ &+ \tfrac{1}{2}\,\tilde{\phi}\,\tilde{\nu}\left[\frac{2\kappa h}{\sinh(2\kappa h)} - 1\right].\end{aligned}$$

Applying various constraints, one obtains generalized equations including the ones derived in Sections 3.1.3 and 3.1.4 as limiting cases. In particular, we can derive arbitrary depth generalizations of the Saint-Venant and 'irrotational' Green–Naghdi equations. Thus, the relaxed variational principle leads simple derivations of model equations for finite amplitude waves in arbitrary depth, which is not the case with the classical perturbations techniques. These developments are left to future investigations.

### 3.1.6 Generalizations

The ansatz (3.48) can be generalized in many relevant ways, depending on the problem under consideration. Natural generalizations can be based on the velocity vertical variations given by, e.g., higher-order deep and shallow water theories, or obtained fitting some experimental data. In this section we propose a possible generalization based on an ansatz of the form

$$\phi \approx \left[\frac{\cosh\kappa Y}{\cosh\kappa h}\right]^{\lambda}\tilde{\phi}(\boldsymbol{x},t),\ \ \boldsymbol{u} \approx \left[\frac{\cosh\kappa Y}{\cosh\kappa h}\right]^{\lambda}\tilde{\boldsymbol{u}}(\boldsymbol{x},t),\ \ v \approx \left[\frac{\sinh\kappa Y}{\sinh\kappa h}\right]^{\lambda}\tilde{v}(\boldsymbol{x},t), \tag{3.49}$$

where $\lambda$ is a parameter at our disposal. If $\lambda = 1$, the ansatz (3.48) is recovered, but the case $\lambda \neq 1$ does not correspond to the vertical profile predicted by any theory based on perturbation expansions. Still, this type of ansatz is of some interest, as we shall see below.

Note first that in the deep water limit $d \to \infty$, the ansatz (3.49) becomes

$$\phi \approx \mathrm{e}^{\lambda\kappa(y-\eta)}\tilde{\phi}(\boldsymbol{x},t),\quad \boldsymbol{u} \approx \mathrm{e}^{\lambda\kappa(y-\eta)}\,\tilde{\boldsymbol{u}}(\boldsymbol{x},t),\quad v \approx \mathrm{e}^{\lambda\kappa(y-\eta)}\,\tilde{v}(\boldsymbol{x},t),$$

and thus, via the change of parameter $\lambda\kappa \mapsto \kappa$, the ansatz (3.34) is recovered. This means that (3.49) is not more general than (3.48) in deep water. On the contrary, these two ansatz are very different in finite depth. We illustrate this claim in the simple case of shallow water ($\kappa h \to 0$) when (3.49) becomes

$$\phi \approx \bar{\phi}(\boldsymbol{x},t),\qquad \boldsymbol{u} \approx \bar{\boldsymbol{u}}(\boldsymbol{x},t),\qquad v \approx \left[\frac{y+d}{\eta+d}\right]^{\lambda}\tilde{v}(\boldsymbol{x},t),$$

where we have replaced $\tilde{\phi}$ and $\tilde{\boldsymbol{u}}$ by $\bar{\phi}$ and $\bar{\boldsymbol{u}}$, respectively, since they are equal in this limiting case.

#### 3.1.6.1 Modified Serre's equations

For the sake of simplicity, we consider here only one horizontal dimension, say $x_1$, and we set $x_1 = x$ and $u_1 = u$, for brevity. We also consider the special case $\mu = u$ and $\nu = v$ together with the constraint $\tilde{v} = \eta_t + \tilde{u}\eta_x$ (free surface's impermeability). Thus, the Lagrangian density (3.6) yields

$$\mathscr{L} \;=\; (\eta_t + [(\eta+d)\bar{u}]_x)\,\tilde{\phi} - \tfrac{1}{2}g\eta^2 \;+\; \tfrac{1}{2}(\eta+d)\bar{u}^2 \;+\; \tfrac{1}{2}\beta(\eta+d)\,[\eta_t + \bar{u}\eta_x]^2\,, \tag{3.50}$$

where $\beta = (2\lambda+1)^{-1}$. After some algebra, the minimization procedure leads to the following equations

$$h_t \;+\; [\,h\,\bar{u}\,]_x \;=\; 0, \tag{3.51}$$

$$\bar{u}_t \;+\; \bar{u}\,\bar{u}_x \;+\; g\,h_x \;+\; \beta\,h^{-1}\,[\,h^2\,\tilde{\gamma}\,]_x \;=\; 0, \tag{3.52}$$

where $\tilde{\gamma}$ is defined in (3.28). If $\beta = \frac{1}{3}$ the classical Serre equations are recovered.

Equations (3.51)–(3.52) admit a $(2\pi/k)$-periodic cnoidal traveling wave solution:

$$\bar{u} \;=\; \frac{c\,\eta}{d+\eta}, \tag{3.53}$$

$$\eta \;=\; a\,\frac{\mathrm{dn}^2\big(\frac{1}{2}\varkappa(x-ct)|m\big) - E/K}{1-E/K} \;=\; a \;-\; H\;\mathrm{sn}^2\big(\tfrac{1}{2}\varkappa(x-ct)|m\big)\,, \tag{3.54}$$

dn and sn being elliptic functions of Jacobi of parameter $m$ ($0 \leqslant m \leqslant 1$), and where $K = \mathrm{K}(m)$ and $E = \mathrm{E}(m)$ are the complete ellipic integrals of the first and second kinds, respectively (Abramowitz & Stegun 1965, #17.3, [AS65]). The parameter $\varkappa$ is a sort of wavenumber, $a$ is the wave amplitude (mean level to crest elevation), $H$ is the total wave height (trough to crest elevation) and $c$ is the wave phase velocity observed in the frame of reference without mean flow. The wave parameters are related via the relations

$$k \;=\; \frac{\pi\,\varkappa}{2\,K}, \qquad H \;=\; \frac{m\,a\,K}{K-E}, \qquad (\varkappa d)^2 \;=\; \frac{g\,H}{m\,\beta\,c^2}, \tag{3.55}$$

$$m \;=\; \frac{g\,H\,(d+a)\,(d+a-H)}{g\,(d+a)^2\,(d+a-H) \;-\; d^2\,c^2}. \tag{3.56}$$

In the limiting case $m \to 1$, we have $K \to \infty$,$E/K \to 0$, $k \to 0$, $H \to a$ and hence, the classical solitary wave solution is recovered

$$\eta \;=\; a\,\mathrm{sech}^2\tfrac{1}{2}\varkappa(x-ct), \qquad c^2 \;=\; g\,(d+a), \qquad \frac{a}{d} \;=\; \frac{\beta\,(\varkappa d)^2}{1 \;-\; \beta\,(\varkappa d)^2}.$$

At this stage, $\beta$ is still a free parameter. An optimum expression for this parameter can be obtained substituting the solution (3.53), (3.54) into the Lagrangian density (3.50),

integrating $\mathscr{L}$ over one wavelength, then solving $\mathrm{d}\mathcal{L}/\mathrm{d}\beta = 0$ keeping $k$ and $c$ constant (as well as $g$ and $d$), the other parameters varying according to relations (3.55), (3.56). Thus, after some cumbersome algebra, we found that $\beta = 0$ is the optimum value for this parameter, which is not very interesting for practical applications. A possible alternative here is to choose $\beta$ such that the exact relation $c^2 = g\tanh(\kappa d)/\kappa$ is satisfied identically or up to some asymptotic order.

The main objective of this section is to show that one can derive sensible equations from ansatz not deriving from some classical approximation procedure. This is another illustration of the power of the variational procedure.

### 3.1.7 Discussion

In this study, we have illustrated the advantage of using a variational principle with as many variables as possible. We call it the *relaxed* variational principle, since the Lagrangian density (3.6) involves more degrees of freedom (i.e., the variables $\eta$, $\phi$, $\boldsymbol{u}$, $v$, $\boldsymbol{\mu}$ and $\nu$) compared to the two degrees of freedom ($\eta$ and $\phi$) in the classical case. In particular, these extra variables can be used to impose various constraints such as incompressibility, irrotationality, impermeability, etc. The practical use of the relaxed formulation was illustrated on numerous examples in shallow, deep and intermediate waters. Thus, we obtained several approximations, some well-known, some new to our knowledge.

In the shallow water regime, we have first obtained the classical nonlinear shallow water (or Saint-Venant) equations (3.18)–(3.19). Then, with the same ansatz (3.8) but imposing the constraint of the free surface impermeability, we have derived the irrotational Green–Naghdi equations (3.26)–(3.27). Applying the incompressibility constraint and choosing differently the pseudo-velocity field, we have obtained two kinds of *generalized Kaup-Boussinesq* equations. Several ways of further generalizations were also outlined.

In deep water, two models were considered. Namely, we derived deep water counterparts of the celebrated Saint-Venant and Serre equations. The former has a canonical Hamiltonian formulation and degenerates to the Klein–Gordon equation in the linear approximation; we thus called the new system (3.36)–(3.37) *generalized Klein–Gordon* equations. The latter could be solved analytically for a two-dimensional traveling wave. This solution is a striking illustration of the power of the variational formulation compared to asymptotic expansion methods, especially for large amplitudes when the small expansion parameter is no longer small. In addition, both equations were shown to possess excellent asymptotic properties with respect to Stokes-like expansions.

The case of arbitrary depth has also been briefly considered. In particular, it has been shown how easily one can introduce an ansatz valid for all depths. Indeed, the vertical

variation of the velocity field suggested by the linear theory provides at once such a general ansatz which degenerates to previous cases when the water is shallow ($\kappa d \to 0$) or deep ($d \to \infty$). This simplicity and flexibility of the variational principle is quite remarkable.

Finally, we considered a generalized ansatz and we illustrated its consequence in the limiting case of shallow water. In this way, we derived the *modified Serre equations* and subsequently obtained exact cnoidal and solitary wave solutions. The main purpose of this example was to illustrate the fact that one can introduce an ansatz which is not inspired by any asymptotic expansion and nevertheless lead to good approximations.

In the present study, some further possibilities for generalizations are also mentioned. However, we have to emphasize that not all ansatz and constraints will necessarily lead to physically relevant and tractable approximations; the same is true for models derived from asymptotic expansions. Nonetheless, the relaxed variational formulation is sufficiently versatile to allow easy derivations of physically sound models. We have illustrated this claim, in particular, by showing how it is simple to obtain approximate equations valid for all depths.

Sometimes, the choice of the constraints may seem to be rather *ad hoc*, but that should not be surprising. Indeed, the water wave theory already knows several *ad hoc* 'tricks' intended to improve the approximation quality. For instance, it was proposed in [MBS03] to replace the polynomial shallow water expansion (3.7) by a $(m, n)$-Padé approximation, the orders $m$ and $n$ being chosen to improve the linear dispersion relation of progressive waves. Another example is the use of the velocity potential defined at some depth $y_0$ [Nwo93] and, as before, the free parameter $y_0$ is chosen to improve linear dispersion characteristics. The approach proposed here is not more *ad hoc* that any example mentioned above. Moreover, the variational principle automatically minimizes the approximation error while allowing for greater flexibility in the choice of ansatz and constraints.

In the several examples presented here, the ansatz involve free parameters that we have chosen constant for simplicity. One can also consider these parameters as functions and find their optimum value minimizing the functional. Doing so will lead to more complicated equations, but this is not a major issue if these equations are intended to be treated numerically.

In order to derive approximate models, variational formulations are more efficient than asymptotic expansions. However, both approaches can be also combined. Indeed, once the variational principle has been applied to an ansatz, asymptotic expansions can be further applied to obtain simpler models. For instance, one could consider 'unidirectionalized' approximations [Olv84, Olv88] to derive variants of Korteweg and de Vries (1895) [KdV95], Dysthe (1979) [Dys79], Camassa and Holm (1993) [CH93], Degasperis and Procesi (1999) [DP99], Kraenkel *et al.* (2005) [KLM05], and other equations. This possibility will be

investigated in future works.

For the sake of simplicity, we have considered only gravity waves propagating at the surface of a single layer of a homogeneous fluid with a horizontal bottom. It is trivial to introduce a relaxed variational formulation including, e.g., surface tension, stratifications in several homogeneous layers and obstacles. Such general variational formulations, together with relevant ansatz and well chosen constraints, will easily lead to interesting models. For perfect fluids, variational formulations can also be obtained for rotational motions [Eck60, Luk67, LMMR86, Sal88, Mor98, CSS06]. A relaxed version of such variational principles will facilitate the derivation of approximate models.

The numerical models for simulating water waves are undergoing constant improvements. The state of the art can be found in recent reviews (e.g., [Fen99, DB06, Ma10]). Certainly, the variational principle is the tool of choice to derive efficient approximations. By efficient, we mean models that capture most of the relevant physics and which, in the same time, can be easily and rapidly solved numerically. One interesting direction for future researches is the development of numerical schemes preserving hamiltonian structure at the discrete level. Another interesting application is the derivation of new improved models with uneven bathymetry for coastal hydrodynamics and tsunami wave modeling (Synolakis & Bernard 2006, [SB06]).

The use of a variational principle for modeling surface waves is by no mean new. However, its power has not yet been fully exploited. The present study is a further contribution in this direction. Obviously, advantages of relaxed variational principles may as well be exploited in physical contexts other than water waves, such as plasma physics, nonlinear optics, etc.

### 3.1.8 Appendix A. Exact Stokes wave

In deep water, a seventh-order Stokes expansion (for the exact equations) is

$$\begin{aligned}
\kappa\,\eta &= \alpha\cos\theta \;+\; \tfrac{1}{2}\alpha^2\big(1+\tfrac{17}{12}\alpha^2+\tfrac{233}{64}\alpha^4\big)\cos 2\theta \\
&\quad + \tfrac{3}{8}\alpha^3\big(1+\tfrac{51}{16}\alpha^2+\tfrac{3463}{320}\alpha^4\big)\cos 3\theta \;+\; \tfrac{1}{3}\alpha^4\big(1+\tfrac{307}{60}\alpha^2\big)\cos 4\theta \\
&\quad + \tfrac{125}{384}\alpha^5\big(1+\tfrac{10697}{1500}\alpha^2\big)\cos 5\theta \;+\; \tfrac{27}{80}\alpha^6\cos 6\theta \;+\; \tfrac{16807}{46080}\alpha^7\cos 7\theta \;+\; \mathrm{O}(\alpha^8), \\
g^{-\frac{1}{2}}\kappa^{\frac{3}{2}}\,\tilde{\phi} &= \alpha\,\big(1-\tfrac{1}{4}\alpha^2-\tfrac{43}{96}\alpha^4-\tfrac{2261}{1536}\alpha^6\big)\sin\theta \;+\; \tfrac{1}{2}\alpha^2\big(1+\tfrac{7}{12}\alpha^2+\tfrac{81}{64}\alpha^4\big)\sin 2\theta \\
&\quad + \tfrac{3}{8}\alpha^3\big(1+\tfrac{281}{144}\alpha^2+\tfrac{5813}{1080}\alpha^4\big)\sin 3\theta \;+\; \tfrac{1}{3}\alpha^4\big(1+\tfrac{431}{120}\alpha^2\big)\sin 4\theta \\
&\quad + \tfrac{125}{384}\alpha^5\big(1+\tfrac{3369}{625}\alpha^2\big)\sin 5\theta \;+\; \tfrac{27}{80}\alpha^6\sin 6\theta \;+\; \tfrac{16807}{46080}\alpha^7\sin 7\theta \;+\; \mathrm{O}(\alpha^8), \\
g^{-\frac{1}{2}}\kappa^{\frac{1}{2}}\,c &= 1+\tfrac{1}{2}\alpha^2+\tfrac{1}{2}\alpha^4+\tfrac{707}{384}\alpha^6+\mathrm{O}(\alpha^8),
\end{aligned}$$

where $\theta = x - ct$. Note that, to the leading order, the $n$-th Fourier coefficient is $2^{1-n} n^{n-2} \alpha^n / (n-1)!$ (this is also true for all $n > 7$). In the bulk of the fluid, the velocity potential is

$$\begin{aligned} g^{-\frac{1}{2}} \kappa^{\frac{3}{2}} \phi \;&=\; \alpha \left(1 - \tfrac{1}{8}\alpha^2 - \tfrac{7}{12}\alpha^4 - \tfrac{14761}{9216}\alpha^6\right) \mathrm{e}^{\kappa y} \sin\theta \;+\; \tfrac{1}{2}\alpha^4 \left(1 + \tfrac{11}{6}\alpha^2\right) \mathrm{e}^{2\kappa y} \sin 2\theta \\ &\quad + \tfrac{1}{12}\alpha^5 \left(1 + \tfrac{191}{24}\alpha^2\right) \mathrm{e}^{3\kappa y} \sin 3\theta \;+\; \tfrac{1}{72}\alpha^6 \, \mathrm{e}^{4\kappa y} \sin 4\theta \\ &\quad + \tfrac{1}{480}\alpha^7 \, \mathrm{e}^{5\kappa y} \sin 5\theta \;+\; \mathrm{O}(\alpha^8), \end{aligned}$$

meaning that harmonics appear at the fourth-order only, thus justifying the ansatz (3.34). Note that, to the leading order, the $n$-th Fourier coefficient is $\alpha^{n+2}/n!(n-1)$ for all $n > 1$.

### 3.1.9 Appendix B. Cubic Zakharov's equations

Satisfying exactly the Laplace equation and the bottom impermeability, the gravity waves variational formulation [Luk67] yields the Hamiltonian [Zak68]:

$$\mathcal{H} \;=\; \tfrac{1}{2} \int \Big\{ g\,\eta^2 \;+\; \tilde{\phi}\, V \Big\} \, \mathrm{d}^2\boldsymbol{x}, \qquad V = \left[\, \phi_y - \boldsymbol{\nabla}\eta \cdot \boldsymbol{\nabla}\phi \,\right]_{y=\eta}. \tag{3.57}$$

Introducing a Dirichlet–Neumann operator $G$, such that $V = G(\eta)\tilde{\phi}$ (Craig & Sulem 1993, [CS93]), expanding $G$ around $\eta = 0$ and neglecting the terms beyond the quartic nonlinearities, the Hamiltonian (3.57) becomes

$$\begin{aligned} \mathcal{H} \;&=\; \tfrac{1}{2} \int \Big\{ g\eta^2 + \tilde{\phi} \Big[ \mathfrak{d}\tilde{\phi} - \mathfrak{d}(\eta \mathfrak{d}\tilde{\phi}) - \boldsymbol{\nabla} \cdot (\eta \boldsymbol{\nabla}\tilde{\phi}) \\ &\qquad + \tfrac{1}{2}\mathfrak{d}(\eta^2 \boldsymbol{\nabla}^2 \tilde{\phi}) + \mathfrak{d}(\eta\, \mathfrak{d}(\eta\, \mathfrak{d}\tilde{\phi})) + \tfrac{1}{2}\boldsymbol{\nabla}^2(\eta^2\, \mathfrak{d}\tilde{\phi}) \Big] \Big\} \, \mathrm{d}^2\boldsymbol{x}, \end{aligned} \tag{3.58}$$

with the pseudo-differential operator $\mathfrak{d} = (-\boldsymbol{\nabla}^2)^{\frac{1}{2}} \tanh[(-\boldsymbol{\nabla}^2)^{\frac{1}{2}} d\,]$. (For one horizontal dimension in infinite depth $\mathfrak{d} f = -\mathfrak{H}(f_x)$, $\mathfrak{H}$ the Hilbert transform.) Thus, the cubic Zakharov's equations (CZE) are

$$\begin{aligned} \eta_t - \mathfrak{d}\tilde{\phi} \;&=\; -\boldsymbol{\nabla} \cdot (\eta \boldsymbol{\nabla}\tilde{\phi}) - \mathfrak{d}(\eta \mathfrak{d}\tilde{\phi}) + \\ &\quad \tfrac{1}{2}\boldsymbol{\nabla}^2(\eta^2 \mathfrak{d}\tilde{\phi}) + \mathfrak{d}(\eta \mathfrak{d}(\eta \mathfrak{d}\tilde{\phi})) + \tfrac{1}{2}\mathfrak{d}(\eta^2 \boldsymbol{\nabla}^2 \tilde{\phi}), \qquad (3.59) \\ \tilde{\phi}_t + g\eta \;&=\; \tfrac{1}{2}(\mathfrak{d}\tilde{\phi})^2 - \tfrac{1}{2}(\boldsymbol{\nabla}\tilde{\phi})^2 - (\eta \mathfrak{d}\tilde{\phi})\boldsymbol{\nabla}^2\tilde{\phi} - (\mathfrak{d}\tilde{\phi})\mathfrak{d}(\eta \mathfrak{d}\tilde{\phi}). \qquad (3.60) \end{aligned}$$

For progressive $(2\pi/\kappa)$-periodic solutions in infinite depth, a seventh-order Stokes ex-

pansion is

$$
\begin{aligned}
\kappa\,\eta &= \alpha\cos\theta + \tfrac{1}{2}\alpha^2\big(1+\boldsymbol{\tfrac{3}{2}}\alpha^2+\boldsymbol{\tfrac{445}{96}}\alpha^4\big)\cos 2\theta \\
&\quad + \tfrac{3}{8}\alpha^3\big(1+\boldsymbol{\tfrac{41}{12}}\alpha^2+\boldsymbol{\tfrac{5213}{384}}\alpha^4\big)\cos 3\theta + \boldsymbol{\tfrac{7}{24}}\alpha^4\big(1+\boldsymbol{\tfrac{263}{42}}\alpha^2\big)\cos 4\theta \\
&\quad + \boldsymbol{\tfrac{67}{384}}\alpha^5\big(1+\boldsymbol{\tfrac{2569}{201}}\alpha^2\big)\cos 5\theta - \boldsymbol{\tfrac{9}{320}}\alpha^6\cos 6\theta - \boldsymbol{\tfrac{16751}{46080}}\alpha^7\cos 7\theta + \mathrm{O}(\alpha^8), \\
g^{-\frac{1}{2}}\kappa^{\frac{3}{2}}\,\tilde{\phi} &= \alpha\big(1-\tfrac{1}{4}\alpha^2-\boldsymbol{\tfrac{31}{64}}\alpha^4-\boldsymbol{\tfrac{465}{256}}\alpha^6\big)\sin\theta + \tfrac{1}{2}\alpha^2\big(1+\boldsymbol{\tfrac{3}{4}}\alpha^2+\boldsymbol{\tfrac{123}{64}}\alpha^4\big)\sin 2\theta \\
&\quad + \tfrac{3}{8}\alpha^3\big(1+\boldsymbol{\tfrac{89}{36}}\alpha^2+\boldsymbol{\tfrac{27271}{3456}}\alpha^4\big)\sin 3\theta + \boldsymbol{\tfrac{7}{24}}\alpha^4\big(1+\boldsymbol{\tfrac{1795}{336}}\alpha^2\big)\sin 4\theta \\
&\quad + \boldsymbol{\tfrac{67}{384}}\alpha^5\big(1+\boldsymbol{\tfrac{24769}{2010}}\alpha^2\big)\sin 5\theta - \boldsymbol{\tfrac{9}{320}}\alpha^6\sin 6\theta - \boldsymbol{\tfrac{16751}{46080}}\alpha^7\sin 7\theta + \mathrm{O}(\alpha^8), \\
g^{-\frac{1}{2}}\kappa^{\frac{1}{2}}\,c &= 1 + \tfrac{1}{2}\alpha^2 + \boldsymbol{\tfrac{41}{64}}\alpha^4 + \boldsymbol{\tfrac{913}{384}}\alpha^6 + \mathrm{O}(\alpha^8),
\end{aligned}
$$

where the incorrect (compared to the exact expansion) coefficients and signs are displayed in bold face. Thus, the CZE match the exact Stokes wave up to the third-order only. Truncating the Hamiltonian at the order $N+1$ in nonlinearities, the corresponding Stokes double series is correct up to the order $N$ in the expansion parameter. None of these approximations have the exact asymptotic behavior (3.40) for their Fourier coefficients.

## 3.2 Group and phase velocities in the free-surface visco-potential flow: new kind of boundary layer induced instability

*Should I refuse a good dinner simply because I do not understand the process of digestion?*

Oliver Heaviside

*Sir, I have found you an argument. I am not obliged to find you an understanding.*

Samuel Johnson

ABSTRACT. Water wave propagation can be attenuated by various physical mechanisms. One of the main sources of wave energy dissipation lies in boundary layers. The present work is entirely devoted to thorough analysis of the dispersion relation of the novel visco-potential formulation. Namely, in this study we relax all assumptions of the weak dependence of the wave frequency on time. As a result, we have to deal with complex integro-differential equations that describe transient behaviour of the phase and group velocities. Using numerical computations, we show several snapshots of these important quantities at different times as functions of the wave number. Good qualitative agreement with previous study [Dut09b] is obtained. Thus, we validate in some sense approximations made anteriorly. There is an unexpected conclusion of this study. According to our computations, the bottom boundary layer creates disintegrating modes in the group velocity. In the same time, the imaginary part of the phase velocity remains negative for all times. This result can be interpreted as a new kind of instability which is induced by the bottom boundary layer effect.

### 3.2.1 Introduction

The classical potential free-surface flow theory is known to be a good and relatively inexpensive model of water waves (especially in comparison with free-surface Navier-Stokes equations formulation [HW65, SZ99, WY07]). However, there are some physical situations where viscous effects cannot be neglected. The necessity of including some dissipation into various water waves models was pointed out explicitly in a number of experimental studies [ZG71, Wu81, BPS81]. For example, in the "Rsum" section of [BPS81] one finds:

> ...it was found that the inclusion of a dissipative term was much more important than the inclusion of the nonlinear term, although the inclusion of the nonlinear term was undoubtedly beneficial in describing the observations...

Obviously this conclusion is related to dissipation description only and does not have the general character. One can find many other evidences in the literature which point out the importance of viscous effects.

Historically, the researchers tried first to include the dissipative effects into various long wave models such as Burgers, Korteweg-de Vries and Boussinesq equations. There is a vast literature on this subject [Keu48, OS70, KM75, Mil76, Mat76, Kha87, Lun89, Sug91, SKP96, Kha97, DD07b, Dut07].

In order to include some dissipation into the framework of free-surface potential flows, we developed the so-called visco-potential formulation [LO04, DDZ08, DD07c, Dut07, Dut09b]. The kinematic viscosity (or eddy viscosity more precisely) appears through local dissipative terms in kinematic and dynamic free-surface boundary conditions. The main peculiarity consists in modifying the bottom kinematic condition due to the presence of the boundary layer which is assumed to be laminar. Mathematically, this correction procedure leads to a nonlocal in time term. Note, that from fractional calculus point of view this nonlocal term is also a half-order integral. The physical relevance of the visco-potential formulation was shown in [LSVO06]. They compared model predictions with experiments on the damping and shoaling of solitary waves. It was shown that the viscous damping due to the bottom boundary layer is well represented by this theory.

To complete our literature review, recall that there is also an alternative approach to potential flows of viscous fluids developed by Daniel Joseph and his collaborators [JL94, FJ02, JW04, Jos06].

The main goal of the present study is twofold. On one hand, we refine our previous dispersion relation analysis. In particular, we do not neglect the evolution terms $it\frac{\partial \omega}{\partial t}$, where $\omega(t;\mathbf{k})$ is the wave frequency (3.65). Consequently, we have to deal with complex integro-differential equations. On the other hand, we show that bottom boundary layer can induce a disintegrating instability of the wave packets. This result is new to author's knowledge.

The present study is organized as follows. In Section 3.2.2 we describe the governing equations and perform classical dispersion relation analysis. Then, we derive an equation for the group velocity in Section 3.2.2.1. Section 3.2.3 contains several numerical results and their discussion. Finally, this Letter is ended by outlining main conclusions of the study in Section 3.2.4.

### 3.2.2 Mathematical formulation and dispersion relation analysis

Consider the 3D fluid domain bounded above by the free-surface $z = \eta(\mathbf{x}, t)$, $\mathbf{x} = (x, y)$ and below by the rigid boundary $z = -h(\mathbf{x})$. A Cartesian coordinate system with the

$z$-axis pointing vertically upwards and the $xOy$-plane coinciding with the still-water level. The flow is assumed incompressible and the fluid viscous with the kinematic viscosity $\nu$. The governing equations of the free-surface visco-potential flow have the following form [DD07c, Dut07, Dut09b]:

$$\Delta\phi = 0, \qquad (\mathbf{x}, z) \in \Omega = \mathbb{R}^2 \times [-h, \eta], \tag{3.61}$$

$$\eta_t + \nabla\eta \cdot \nabla\phi = \phi_z + 2\nu\Delta\eta, \qquad z = \eta, \tag{3.62}$$

$$\phi_t + \frac{1}{2}\left|\nabla\phi\right|^2 + g\eta + 2\nu\phi_{zz} = 0, \qquad z = \eta, \tag{3.63}$$

$$\phi_z = -\sqrt{\frac{\nu}{\pi}} \int\limits_0^t \frac{\phi_{zz}(\mathbf{x}, z = -h, \tau)}{\sqrt{t-\tau}}\, d\tau, \qquad z = -h. \tag{3.64}$$

We can derive corresponding long wave models from the visco-potential formulation (3.61) – (3.64). The derivation can be found in [LO04, DD07c, Dut07].

In order to perform the dispersion relation analysis, we have to linearize equations (3.61) – (3.64) over the flat bottom $z = -h$. This procedure is classical [Sto57, Whi99] and we do not detail it here. Then, we look for the following periodic plane wave solutions:

$$\phi(\mathbf{x}, z, t) = \varphi(z) e^{i(\mathbf{k}\cdot\mathbf{x} - \omega(t;\mathbf{k})t)}, \qquad \eta(\mathbf{x}, t) = \eta_0 e^{i(\mathbf{k}\cdot\mathbf{x} - \omega(t;\mathbf{k})t)}, \tag{3.65}$$

where $\mathbf{k}$ is the wavenumber and $\omega(t;\mathbf{k})$ is the wave frequency.

**Remark 2.** *It is important to assume from the beginning of the derivation that the wave frequency $\omega$ explicitly depends on the time $t$. Consequently, we get some additional important terms of the form $it\frac{\partial\omega(t;\mathbf{k})}{\partial t}$ (see equation (3.66)) which were neglected in our previous study [Dut09b].*

We plug the special form of solutions (3.65) into the linearized version of the governing equations (3.61) – (3.64). After performing some simple computations (details can be found in [Dut07, Dut09b]), we come to the following necessary condition of periodic solution (3.65) existence:

$$\Omega^2 + gk\tanh(kh) - kF(\omega, t)(\Omega^2\tanh(kh) + gk) = 0, \tag{3.66}$$

where we introduced several notations $k := |\mathbf{k}|$, $\Omega := it\partial_t\omega + i\omega - 2\nu k^2$ and $F(\omega)$ is inherited from the nonlocal term:

$$F(\omega, t) := \sqrt{\frac{\nu}{\pi}} \int\limits_0^t \frac{e^{i\omega(\tau)(t-\tau)}}{\sqrt{t-\tau}}\, d\tau.$$

Once the wave frequency $\omega$ is computed from equation (3.66), the phase speed can be immediately deduced by its definition:

$$c_p(t;k) := \frac{\omega(t;k)}{k}.$$

**Remark 3.** *The classical dispersion relation for water waves* $\omega^2 = gk\tanh(kh)$ *can be immediately recovered from (3.66) if we replace* $\Omega$ *by* $i\omega$ *and* $F(\omega)$ *by* $0$.

#### 3.2.2.1 Group velocity

The group velocity is defined as follows:

$$c_g(t;k) := \frac{\partial\omega(t;k)}{\partial k}.$$

There are several physical interpretations of this quantity. One can see it as the wave energy propagation speed. Another interpretation consists in viewing it as the wavetrain amplitude variation speed. Anyhow, the group speed $c_g$ plays an important role in the description of the wavetrains and wavepackets. The evolution equation of this quantity can be obtained by simple differentiation of (3.66) with respect to the wavenumber modulus $k$:

$$2\Omega\Gamma + g\tanh(kh) + gkh(1-\tanh^2(kh)) - (F + k\partial_k F)(\Omega^2\tanh(kh) + gk) \\ - kF\big(2\Omega\Gamma\tanh(kh) + \Omega^2(1-\tanh^2(kh))h + g\big) = 0, \quad (3.67)$$

where $\Omega$ was defined above and $\Gamma := it\partial_t c_g + ic_g - 4\nu k$.

Integro-differential equations (3.66) and (3.67) are too complex for any mathematical analysis so far. Therefore, we use numerical methods in order to explore some properties of the solutions.

### 3.2.3 Numerical results and discussion

In order to have an insight into the transient behaviour of the phase and group velocities, we have to solve numerically equations (3.66) and (3.67) correspondingly. Hence, in this study we discretize all local terms with a first order implicit scheme, while the integral term $F(\omega,t)$ is computed in explicit way for the sake of computational efficiency. Resulting algebraic equations are solved analytically. Initial conditions were chosen according to [DDZ08]:

$$c_p|_{t=0} = \sqrt{\frac{g}{k}\tanh(kh)} - 2i\nu k, \quad c_g|_{t=0} = \Big(\frac{1}{2} + \frac{kh}{\sinh(2kh)}\Big)\mathrm{Re}\, c_p|_{t=0} - 4i\nu k.$$

The values of all parameters used in numerical computations can be found in Table 3.1. The time step $\Delta t$ is chosen to achieve the convergence up to graphical resolution.

In this section upper and lower images always refer to the real and imaginary parts respectively unless special indications are given. Presented here results are normalized by $\sqrt{gh}$. Thus, all real parts at the infinitely long wave limit $kh \to 0$ take the unitary value.

| *parameter* | *definition* | *value* |
|---|---|---|
| $\nu$ | eddy viscosity | $10^{-3}\ \frac{m^2}{s}$ |
| $g$ | gravity acceleration | $9.8\ \frac{m}{s^2}$ |
| $h$ | water depth | $1\ m$ |
| $\Delta t$ | time step | 0.05 s |

**Table 3.1:** Values of the parameters used in the phase and group velocities numerical computations.

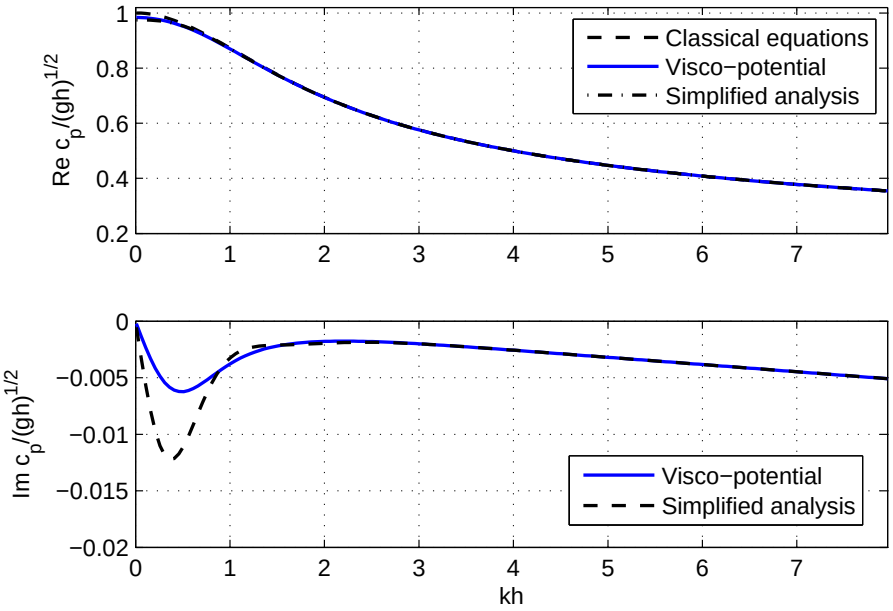


**Figure 3.1:** Real and imaginary parts of the phase velocity at $t = 2$ s.

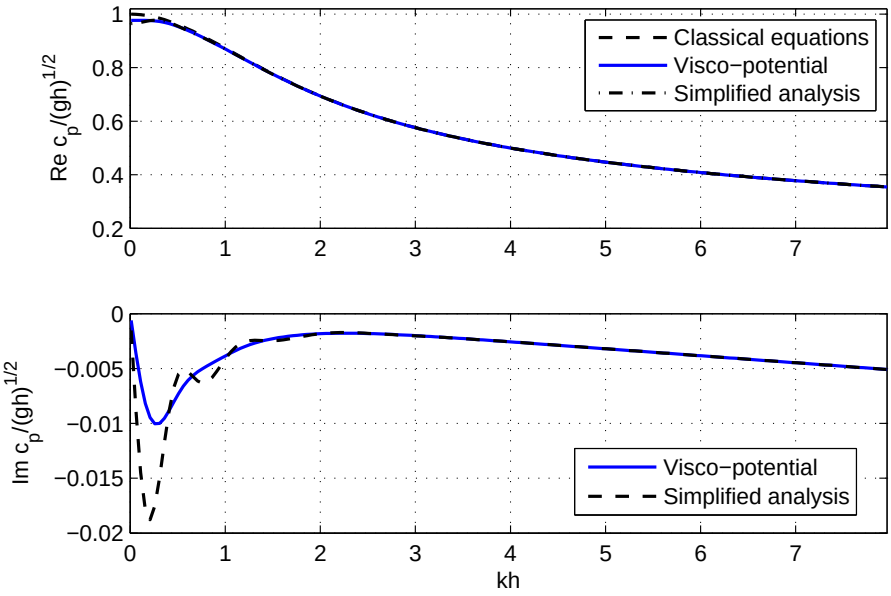


**Figure 3.2:** Real and imaginary parts of the phase velocity at $t = 4$ s.

First of all, on Figures 3.1 and 3.2 we show two snapshots of the phase velocity at different times. In these figures we plot also computational results of our previous *weakly dynamic* analysis [Dut09b], which consists in neglecting differential evolution terms $it\frac{\partial\omega}{\partial t}$ in equation (3.66). We can state an excellent agreement for the real part of the phase velocity. However, with the simplified approach we get only the qualitative behaviour of the imaginary part. This discrepancy is located in the region of long waves where the boundary layer damping is predominant. The dissipation of short waves is perfectly described again. From quantitative point of view, our previous analysis overestimates the dissipation rate for long wavelengths. We refer to [Dut09b] for the discussion and physical interpretation of the phase velocity behaviour.

Group velocity snapshots are presented on Figures 3.3 – 3.7. The real part of the group velocity $c_g$ is shown only on Figure 3.7 since its evolution is slow as in the phase velocity case. The whole animation of the group velocity can be downloaded at [GRP].

The imaginary part of the group velocity remains negative until about 1 s (see Figure 3.4). Then, it was very unexpected for the author to observe the formation of modes with positive imaginary part (see Figure 3.5). These destabilizing modes may be responsible of wavepackets disintegration. We refer to the next section for the discussion of this interesting result.

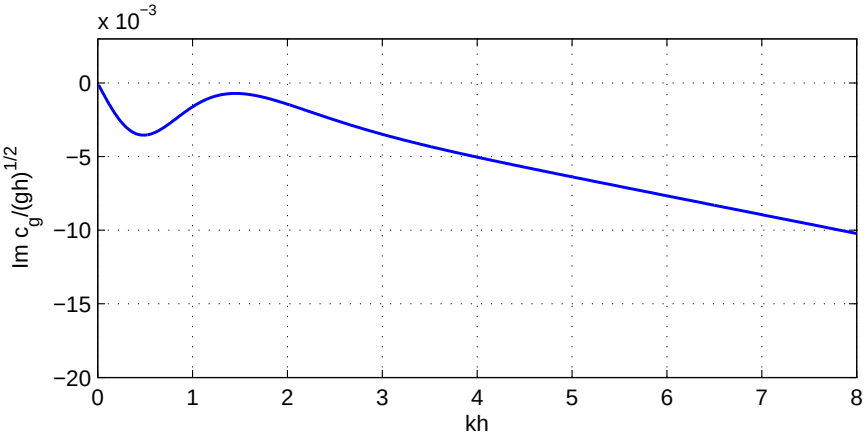


**Figure 3.3:** Imaginary part of the group velocity at $t = 0.8$ s.

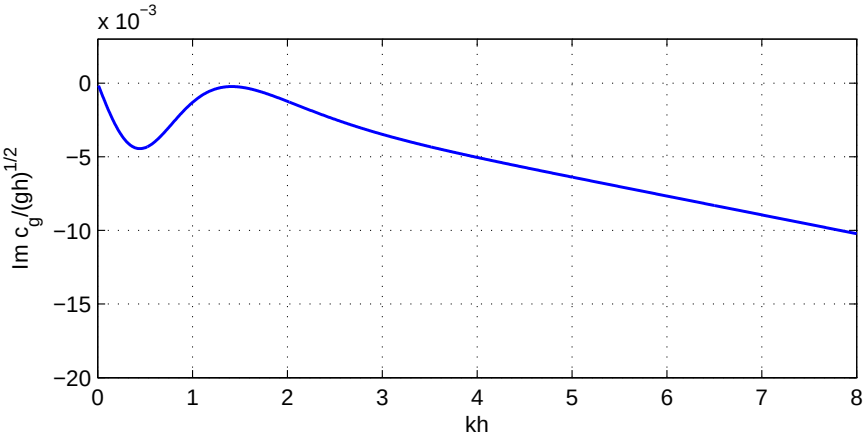


**Figure 3.4:** Imaginary part of the group velocity at $t = 1$ s.

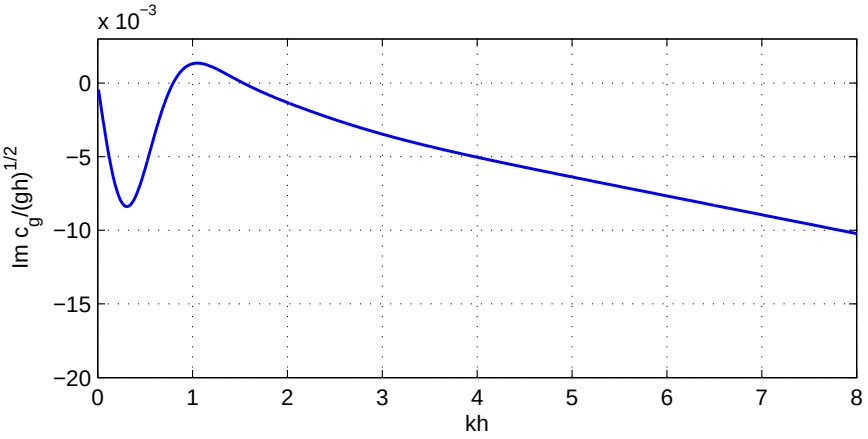


**Figure 3.5:** Imaginary part of the group velocity at $t = 2$ s.

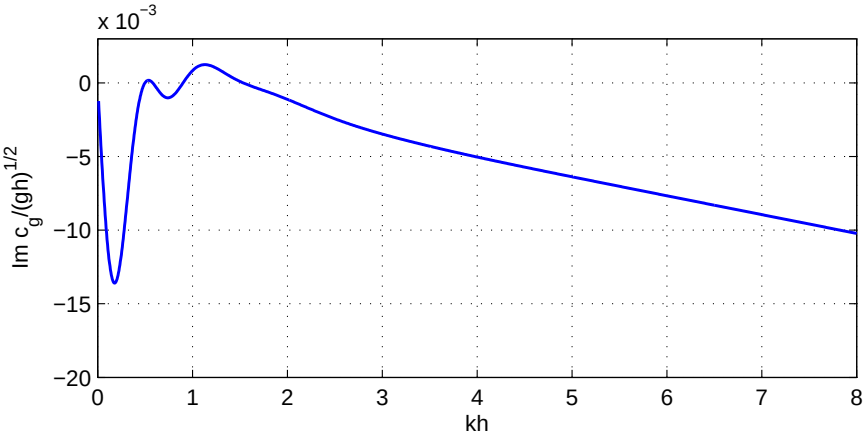


**Figure 3.6:** Imaginary part of the group velocity at $t = 4$ s.

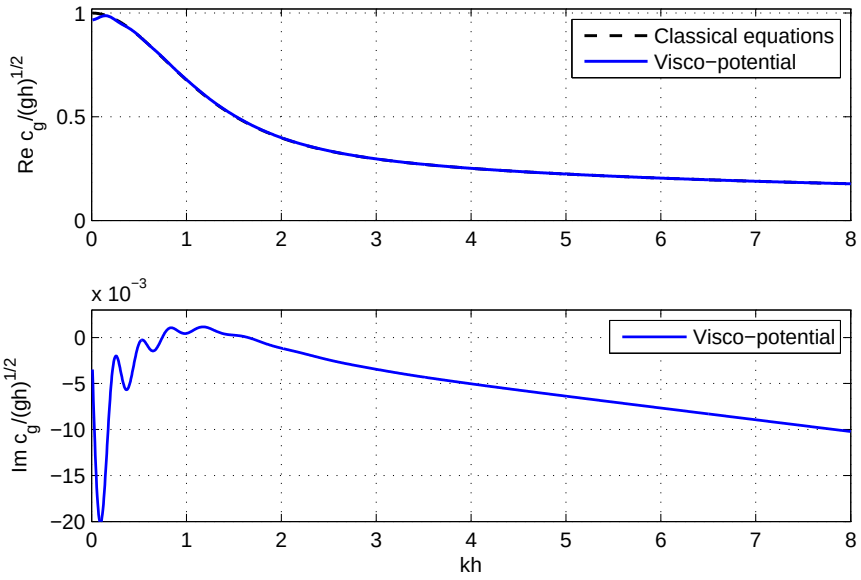


**Figure 3.7:** Real and imaginary parts of the group velocity at $t = 8$ s.

### 3.2.4 Conclusions

In this work we performed an analysis of linear dispersion relation for visco-potential flow formulation. Several numerical snapshots of the phase and group velocities were presented. The main particularity in this study is that we make no assumption of the weak dependence on time. Therefore, we come up with additional terms of the form $it\omega'(t;k)$ which complicate analysis and numerical computations. We can conclude that we obtain a good qualitative agreement with preceding results [Dut09b]. Thus, we validate in some sense approximations made anteriorly. However, our computations reveal less oscillatory behaviour in the imaginary part of the phase velocity for intermediate wavelengths.

Furthermore, we studied the evolution of the group velocity with time for the visco-potential formulation. Physically, this quantity represents the energy propagation speed. There exists also another interpretation. The group velocity $c_g(t;k)$ can be seen as the wavetrain amplitude variation speed. Numerical simulations show the appearance of modes with positive imaginary part for $\frac{1}{2} < kh < \frac{3}{2}$ in the group velocity. These modes may destabilize wave packets. Physically, this effect comes from the bottom boundary layer. Previous numerical study [WLY06] did not reveal this instability since the authors did not take into account for the boundary layer effect. Hence, they included only a local dissipative term which has a stabilizing effect.

It is well known that Stokes wavepacket can be disintegrated by the Benjamin-Feir instability [Ben67, BF67]. This instability comes from the resonant quartet wave interaction. The classical result of T. Brooke Benjamin [Ben67], refined later by R.S. Johnson [Joh77], states that no instability is present if $kh < \sigma_0$ and the modes inside a certain band-width grow without bound if $kh \geq \sigma_0$. The critical value of $\sigma_0$ is estimated about 1.363. There is a certain surprising interplay with our results that we would like to point out here. Our theory gives less sharper results. That is why we prefer to speak about the instability zone defined as $\mathbb{U}(t) = \{kh \in \mathbb{R}^+ : \operatorname{Im} c_g(t;k) > 0\}$ in $kh$-space. According to our computations, the topological structure of the set $\mathbb{U}(t)$ is a union of finite number of intervals (see the animation [GRP]). It is curious that the critical value $\sigma_0$ lies inside this zone (see Figure 3.5).

The wave turbulence can be perfectly described in the framework of potential flows. It gives direct cascade of energy from the waves spectral maximum to the dissipative region [ZLF92]. However, in the present study we did not investigate the effect of viscous interaction with bottom onto the wave turbulence. Presumably, it will modify the dissipation region. This question deserves a thorough consideration.

Recently it was shown that the Benjamin-Feir instability can be enhanced by dissipation [BD07]. The peculiarity lies in the form of dissipative terms that we put into the model. Our computations show the stabilizing effect of local dissipative terms [SHC+05, WETG01,

WLY06] and the destabilizing effect of our nonlocal dissipation.

The experiments should confirm our theoretical result, provided that a generated wave-train have sufficiently big wavelength to interact with the bottom boundary layer.

# Chapter 4

# Tsunami wave modeling

*Tandis que des séismes se produisaient, la mer recula loin de ce qui était alors la terre, puis se souleva et envahit un secteur du territoire de la cité, dont elle submergea une partie, alors qu'elle se retira du reste, si bien qu'est actuellement mer ce qui auparavant était terre; et la mer fit prir tous les gens qui n'avaient pas pu la devancer en courant sur les hauteurs. La cause d'un tel phénomène est, à mon avis, qu'au point où le séisme est le plus fort, à cet endroit la mer se rétracte, puis soudain s'étirant en sens inverse produit une vague plus violente; tandis que sans séisme il ne me semble pas qu'un tel phénomène puisse se produire.*

Thucydide (411 av. J.-C.)

## Contents

# 4.1 Energy of tsunami waves generated by bottom motion

*The fundamental concept in social science is Power, in the same sense in which Energy is the fundamental concept in physics.*

Bertrand Russell

*For those who want some proof that physicists are human, the proof is in the idiocy of all the different units which they use for measuring energy.*

Richard P. Feynman

ABSTRACT. In the vast literature on tsunami research, few articles have been devoted to energy issues. A theoretical investigation on the energy of waves generated by bottom motion is performed here. We start with the full incompressible Euler equations in the presence of a free surface and derive both dispersive and non-dispersive shallow-water equations with an energy equation. It is shown that dispersive effects only appear at higher order in the energy budget. Then we solve the Cauchy–Poisson problem of tsunami generation for the linearized water wave equations. Exchanges between potential and kinetic energies are clearly revealed.

## 4.1.1 Introduction

Oceanic waves can be devastating as shown by recent events. Whilst some areas are more vulnerable than others, the recent history shows that catastrophic waves can hit even where they are not expected. The tsunami waves generated by the huge undersea earthquake in Indonesia on 26 December 2004 caused devastation across most of the coasts of the Bay of Bengal. The tsunami waves generated by the massive submarine landslide in Papua-New Guinea on 17 July 1998 as well as the 17 July 2006 Java tsunami and the 2 April 2007 Solomon Islands tsunami also caused devastation, but on a smaller scale. Unfortunately, such cataclysmic tsunamis are likely to be generated again by earthquakes, massive landslides or volcano eruptions [SB06].

Information on tsunami energy can be obtained by applying the normal mode representation of tsunami waves, as introduced by [War80]. For example, [Oka03] considers the total energy released into tsunami waves. He obtains expressions for the energy of tsunamis (see his expressions (31) for a tsunami generated by an earthquake and (36) for a tsunami generated by a landslide). In the case of a landslide, he computes the ratio between tsunami energy and total change in energy due to the slide. In the present study, we use the incompressible fluid dynamics equations. Tsunamis have traditionally been considered as non-dispersive long waves. However various types of data (bottom pressure records [RWG95]; satellite data [KML05]; hydrophone records [OTR07]) indicate that tsunamis

are made up of a very long dispersive wave train, especially when they have enough time to propagate. These waves travel across the ocean surface in all directions away from the generation region. Recent numerical computations using dispersive wave models such as the Boussinesq equations show as much as 20% reduction of tsunami amplitude in certain locations due to dispersion [DT07]. But one has to be careful with the interpretation of satellite data: as indicated by [KS06], the mid-ocean steepness of the 2004 Sumatra tsunami measured from satellite altimeter data was less than $10^{-5}$. Nonlinear dispersive theory is necessary only when examining steep gravity waves, which is not the case in deep water.

The wavelength of tsunamis and, consequently, their period depend essentially on the source mechanism. If the tsunami is generated by a large and shallow earthquake, its initial wavelength and period will be greater. On the other hand, if the tsunami is caused by a landslide (which happens less commonly but can be devastating as well), both its initial wavelength and period will be shorter as indicated for example by [KRTB96]. From these empirical considerations one can conclude that dispersive effects are a priori more important for submarine landslide and slump scenarios than for tsunamigenic earthquakes.

Once a tsunami has been generated, its energy is distributed throughout the water column. Clearly, the more water is displaced, the more energetic is the tsunami (compare for example the December 2004 and March 2005 Sumatra tsunamis). Due to the large scale of this natural phenomenon and limited power of computers, tsunami wave modellers have to adopt simplified models which reduce a fully three-dimensional (3D) problem to a two-dimensional (2D) one. This approach is natural, since in the case of very long waves the water column moves as a whole. Consequently the flow is almost 2D. Among these models one can mention the nonlinear shallow water equations (SWE), Boussinesq type models, the Green-Naghdi and Serre equations. There is a wide variety of models, depending on whether or not the effects of run-up/run-down, bottom friction, turbulence, Coriolis effects, tidal effects, etc, are included.

Today scientists can easily predict when a tsunami will arrive at various places by knowing source characteristics and bathymetry data along the paths to those places. Unfortunately one does not know as much about the energy propagation of such waves. Obviously tsunami amplitude is enhanced over the major oceanic ridges. [TRM+05] clearly describe the waveguide type effect from mid-ocean ridges that has funnelled the 2004 megatsunami away from the tip of Africa. As emphasized by [KKLW07], travel-time computation based on the first arrival time may lead to errors in the prediction of tsunami arrival time as higher energy waves propagate slower along ridges. At the beginning, the energy is essentially potential, although it depends on the generation mechanism. Then it redistributes itself into half kinetic and half potential energies. Finally, it converts its potential compo-

nent into kinetic energy. How do these conversions take place? The purpose of this study is to shed some light on this topic and to see if the importance of dispersion in tsunamis can be studied by looking at the energy rather than at wave profiles.

Previous researchers have considered the topic of tsunami wave energy. [Kaj70, DK97, VDP02] studied the energy exchange between the solid bottom and the overlying water associated with the bottom deformation. There were recent attempts to obtain equations for tsunami energy propagation. We can mention here the work of [TB00] devoted to idealized theoretical cases and the work of [KKLW07] using the energy flux point of view to study the changes in the 2004 tsunami signal as it travelled from Indonesia to the Pacific Ocean. We believe that these models can be improved, given the present state of the art in wave modelling.

A point of interest is that some of the equations used for wave modelling have an infinite number of conserved quantities. There has been some confusion in the literature on which quantities can be called energy. Indeed there is here an interesting question. In incompressible fluid mechanics, the internal energy equation is decoupled from the equation of continuity and from the fundamental law of dynamics. It is used only when one is interested in computing the temperature field once the velocity distribution is known. In addition to the internal energy equation, one can write a total energy (internal energy + kinetic energy) equation, or a total enthalpy equation. The confusing part is that for perfect fluids one usually defines the total energy differently: it is the sum of internal energy, kinetic energy, and potential energies associated to body forces such as gravitational forces and to the pressure field. If in addition the fluid is incompressible, then the internal energy remains constant. In the classical textbooks on water waves [Sto58, Joh97], one usually introduces the energy $E$ as the sum of kinetic and potential energies and then looks for a partial differential equation giving the time derivative $dE/dt$. In any case, when one uses a depth-integrated model such as the nonlinear SWE, one can compute the energy a posteriori (the potential energy is based on the free-surface elevation and the kinetic energy on the horizontal velocity). But one can also apply the nonlinear shallow water assumptions to the full energy equation to begin with. Then one obtains a nonlinear shallow water approximation of the energy equation. Are these two approaches equivalent? We show that the answer is no.

First we present the energy equation in three different forms: full water wave equations, dispersive SWE and non-dispersive SWE. Surprisingly, the energy equation is the same for dispersive and non-dispersive SWE at leading order. Then we present some numerical computations over a flat bottom. It allows us to concentrate on the generation process and the energy transfer through the moving seabed. We refer to [DPD10] for simulations of some real world events including energy pumping and its transformation over uneven

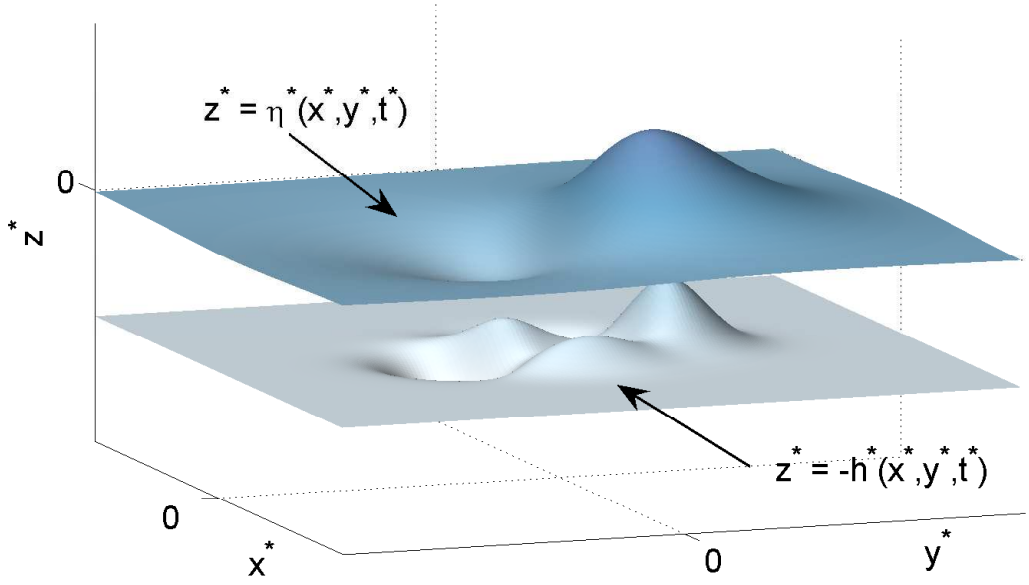


**Figure 4.1:** Sketch of the 3D fluid domain for wave generation by a moving bottom.

bathymetry, using the SWE with energy. Finally we present the energy equation in a fourth form: the linearized dispersive water wave equations. We solve the Cauchy–Poisson problem of tsunami generation. Exchanges between potential and kinetic energies are clearly revealed.

### 4.1.2 Derivation of the energy equation

Consider the 3D fluid domain shown in Figure 4.1. It is bounded above by the free surface $z^* = \eta^*(x^*, y^*, t^*)$ and below by the solid boundary with prescribed motion $z^* = -h^*(x^*, y^*, t^*)$. A Cartesian coordinate system with the $z^*-$axis pointing vertically upwards and the $x^*Oy^*-$plane coinciding with the still-water level is chosen.

The fluid is assumed to be inviscid. Its motion is governed by the 3D Euler equations, written here in their incompressible form (see for example [Gis08] for the compressible counterpart, after replacing $\rho$ by $p$ in the pressure term of his Eq. 3):

$$\nabla \cdot \vec{u}^* = 0, \tag{4.1}$$

$$\frac{\partial \vec{u}^*}{\partial t^*} + \nabla \cdot \left( \vec{u}^* \otimes \vec{u}^* + \frac{p^*}{\rho^*} \mathrm{Id} \right) = \vec{g}, \tag{4.2}$$

$$\frac{\partial e^*}{\partial t^*} + \nabla \cdot \left[ \left( e^* + \frac{p^*}{\rho^*} \right) \vec{u}^* \right] = 0, \tag{4.3}$$

where $\rho^*$ is the fluid density, $\vec{u}^* = (u^*, v^*, w^*)$ the velocity vector, $e^*$ the sum of kinetic energy density $e_K^* = \frac{1}{2}|\vec{u}^*|^2$ and potential energy density $e_P^* = gz^*$, $p^*$ the pressure and $\vec{g}$ the acceleration due to gravity. In the present study $\vec{g} = (0, 0, -g)$. For incompressible flows, the energy equation (4.3) is redundant. Indeed it can be obtained from Eq. (4.2). However we keep it since it is not equivalent to derive shallow water equations with or without the energy equation.

Equations (4.1)–(4.3) have to be completed by the kinematic and dynamic boundary conditions. Since surface tension effects are not important for long waves, the dynamic boundary condition on the free surface reads

$$p^* = p_s^*, \quad \text{at} \quad z^* = \eta^*. \tag{4.4}$$

Later we will replace the surface pressure $p_s^*$ by 0 but we keep it arbitrary for now.

The kinematic boundary conditions on the free surface and at the seabed are, respectively,

$$w^* = \frac{\partial \eta^*}{\partial t^*} + u^* \frac{\partial \eta^*}{\partial x^*} + v^* \frac{\partial \eta^*}{\partial y^*}, \qquad z^* = \eta^*, \tag{4.5}$$

$$w^* = -\frac{\partial h^*}{\partial t^*} - u^* \frac{\partial h^*}{\partial x^*} - v^* \frac{\partial h^*}{\partial y^*}, \qquad z^* = -h^*. \tag{4.6}$$

Below we denote the horizontal gradient by $\nabla_\perp$ and the horizontal velocity by $\vec{u}_\perp^*$. After a few manipulations and integration across the water column from bottom to top, one can write the following global energy equation:

$$\frac{\partial E^*}{\partial t^*} + \nabla_\perp \cdot \Phi^* + P^* = 0, \tag{4.7}$$

where $E^*$ is the sum of kinetic and potential energies in the flow, per unit horizontal area, $\Phi^*$ the horizontal energy flux vector, and $P^*$ the net energy input due to the pressure forces doing work on the upper and lower boundaries of the fluid. They are given by the following expressions:

$$E^* = \int_{-h^*}^{\eta^*} \left( \frac{1}{2} \rho^* |\vec{u}^*|^2 + \rho^* g z^* \right) dz^*, \tag{4.8}$$

$$\Phi^* = \int_{-h^*}^{\eta^*} \vec{u}_\perp^* \left( \frac{1}{2} \rho^* |\vec{u}^*|^2 + p^* + \rho^* g z^* \right) dz^*, \tag{4.9}$$

$$P^* = p_s^* \eta_{t^*}^* + p_b^* h_{t^*}^*, \tag{4.10}$$

where $p_s^*$ is the pressure exerted on the free surface and $p_b^*$ the bottom pressure. In the case of a stationary bottom boundary and of a free surface on which the pressure vanishes, then as expected the net energy input $P^*$ is identically zero. Energy can be brought to the system by a moving bottom or by a pressure disturbance on the free surface. From now on, we take $p_s^* = 0$.

#### 4.1.2.1 Dimensionless equations

The problem of tsunami propagation possesses two characteristic length scales: the average water depth $h_0$ for the vertical dimension and a typical wavelength $l$ for the horizontal dimensions. It is classical to introduce the following dimensionless variables. The scaling for the independent variables is

$$x = \frac{x^*}{l}, \quad y = \frac{y^*}{l}, \quad z = \frac{z^*}{h_0}, \quad t = \frac{\sqrt{gh_0}}{l}t^*.$$

In order to introduce the dimensionless dependent variables we need one more parameter, the typical wave amplitude $a$:

$$u = \frac{h_0}{a\sqrt{gh_0}}u^*, \quad v = \frac{h_0}{a\sqrt{gh_0}}v^*, \quad w = \frac{h_0}{l}\frac{h_0}{a\sqrt{gh_0}}w^*, \quad \eta = \frac{\eta^*}{a}, \quad h = \frac{h^*}{h_0},$$
$$\pi = \frac{p^* + \rho^* g z^*}{\rho^* g a}, \quad p = \frac{p^*}{\rho^* g h_0}, \quad e = \frac{e^*}{gh_0}.$$

The hydrostatic pressure $-\rho^* g z^*$ has been incorporated into $\pi$.

The following dimensionless parameters, which are assumed to be small, are introduced:

$$\varepsilon := a/h_0, \quad \mu := h_0/l.$$

The parameter $\varepsilon$ represents the relative importance of nonlinear terms and $\mu$ measures dispersive effects. Note that

$$e = \frac{1}{2}\varepsilon^2(u^2 + v^2) + \frac{1}{2}\frac{\varepsilon^2}{\mu^2}w^2 + z.$$

The Euler equations of motion (4.1)–(4.3) become in dimensionless form

$$\mu^2(u_x + v_y) + w_z = 0, \tag{4.11}$$
$$\mu^2 u_t + \varepsilon\mu^2(u^2)_x + \varepsilon\mu^2(uv)_y + \varepsilon(uw)_z + \mu^2\pi_x = 0, \tag{4.12}$$
$$\mu^2 v_t + \varepsilon\mu^2(uv)_x + \varepsilon\mu^2(v^2)_y + \varepsilon(vw)_z + \mu^2\pi_y = 0, \tag{4.13}$$
$$\mu^2 w_t + \varepsilon\mu^2(uw)_x + \varepsilon\mu^2(vw)_y + \varepsilon(w^2)_z + \mu^2\pi_z = 0, \tag{4.14}$$
$$\mu^2 e_t + \varepsilon\mu^2\left((e+p)u\right)_x + \varepsilon\mu^2\left((e+p)v\right)_y + \varepsilon\left((e+p)w\right)_z = 0. \tag{4.15}$$

In dimensionless form the boundary conditions (4.4)–(4.6) become

$$\pi = \eta, \qquad z = \varepsilon\eta, \tag{4.16}$$
$$w = \mu^2\eta_t + \varepsilon\mu^2 u\eta_x + \varepsilon\mu^2 v\eta_y, \qquad z = \varepsilon\eta, \tag{4.17}$$
$$\varepsilon w = -\mu^2 h_t - \varepsilon\mu^2 u h_x - \varepsilon\mu^2 v h_y, \qquad z = -h. \tag{4.18}$$

In the case of a static bottom $h = h(x, y)$, the order of magnitude of the vertical velocity $w$ at the bottom is $\mathcal{O}(\mu^2)$. With a moving bathymetry the behaviour is different:

$$w|_{z=-h} = -\frac{\mu^2}{\varepsilon}h_t + \mathcal{O}(\mu^2).$$

#### 4.1.2.2 Integration over the depth

Next we reduce the above 3D problem (4.11)–(4.18) into a 2D one by integrating all the equations over the water column. We begin with the continuity equation (4.11) which we integrate with respect to $z$ from $-h$ to $\varepsilon\eta$. Taking into account the boundary conditions (4.17) and (4.18), one obtains

$$\eta_t + \frac{\partial}{\partial x}\int_{-h}^{\varepsilon\eta} u\, dz + \frac{\partial}{\partial y}\int_{-h}^{\varepsilon\eta} v\, dz = -\frac{1}{\varepsilon}h_t. \tag{4.19}$$

A source term appears in equation (4.19) due to the moving bathymetry. For tsunami generation, the function $h^*$ can be represented as follows:

$$h^*(x^*, y^*, t^*) = h_0^*(x^*, y^*) - \zeta^*(x^*, y^*, t^*),$$

where $h_0^*(x^*, y^*)$ is the static sea bed profile and $\zeta^*(x^*, y^*, t^*)$ the bottom displacement due for example to coseismic displacements or landslides. In nondimensional form this representation takes the form:

$$h(x, y, t) = h_0(x, y) - \varepsilon\zeta(x, y, t),$$

since the bottom variation must be of the same order of magnitude as the typical wave amplitude $a$: $\zeta^*(x^*, y^*, t^*) = a\zeta(x, y, t)$. Differentiating with respect to time yields

$$\frac{1}{\varepsilon}\frac{\partial h}{\partial t} = -\frac{\partial \zeta}{\partial t} = \mathcal{O}(1).$$

Below we will replace $\frac{1}{\varepsilon}h_t$ by $-\zeta_t$.

Integrating the vertical momentum conservation equation (4.14) yields

$$\pi|_{z=-h} = \eta + \frac{\partial}{\partial t}\int_{-h}^{\varepsilon\eta} w\, dz + \varepsilon\frac{\partial}{\partial x}\int_{-h}^{\varepsilon\eta} uw\, dz + \varepsilon\frac{\partial}{\partial y}\int_{-h}^{\varepsilon\eta} vw\, dz. \tag{4.20}$$

A more general expression for the pressure can be obtained if we integrate equation (4.14) from $z$ to $\varepsilon\eta$ and use the boundary conditions (4.16) and (4.17):

$$\pi = \eta + \frac{\partial}{\partial t}\int_{z}^{\varepsilon\eta} w\, dz + \varepsilon\frac{\partial}{\partial x}\int_{z}^{\varepsilon\eta} uw\, dz + \varepsilon\frac{\partial}{\partial y}\int_{z}^{\varepsilon\eta} vw\, dz - \frac{\varepsilon}{\mu^2}w^2. \tag{4.21}$$

The vertical velocity $w$ is obtained by integrating the continuity equation (4.11) from $-h$ to $z$ and applying the seabed kinematic condition (4.18):

$$w = \mu^2\zeta_t - \mu^2\left(\frac{\partial}{\partial x}\int_{-h}^{z} u\, dz + \frac{\partial}{\partial y}\int_{-h}^{z} v\, dz\right). \tag{4.22}$$

Finally, the integration of the equation of energy conservation (4.15) yields

$$\frac{\partial}{\partial t}\int_{-h}^{\varepsilon\eta} e\,dz + \varepsilon\frac{\partial}{\partial x}\int_{-h}^{\varepsilon\eta}(e+p)u\,dz + \varepsilon\frac{\partial}{\partial y}\int_{-h}^{\varepsilon\eta}(e+p)v\,dz - \varepsilon\, p|_{z=-h}\,\zeta_t = 0, \tag{4.23}$$

which is nothing else than the dimensionless counterpart of Eq. (4.7).

All the equations derived above are exact and no assumption has been made about the orders of magnitude of $\varepsilon$ and $\mu$.

#### 4.1.2.3 The nonlinear shallow-water equations with energy equation

In Appendix A, we briefly summarize the derivation of various systems of shallow-water wave equations. The non-dispersive SWE are obtained by taking the limit $\mu \to 0$. Here we provide the dispersive and non-dispersive SWE in their conservative forms [ES05] with dimensions, based on the depth-averaged horizontal velocity $\bar{\vec{u}}^*$. The total water depth $h^* + \eta^*$ is denoted by $H^*(x^*, y^*, t^*)$. The definition of $E^*$ is given by Eq. (4.8).

##### 4.1.2.3.1 SWE with dispersion and energy equation

$$\frac{\partial H^*}{\partial t^*} + \nabla\cdot(H^*\bar{\vec{u}}^*) = 0, \tag{4.24}$$

$$\begin{aligned}\frac{\partial(H^*\bar{\vec{u}}^*)}{\partial t^*} + \nabla\cdot\left(H^*\bar{\vec{u}}^*\otimes\bar{\vec{u}}^* + \frac{1}{2}gH^{*2}\right) + \\ \left(\frac{h^{*3}}{6}\nabla\left(\nabla\cdot\left(\frac{H^*\bar{\vec{u}}^*}{h^*}\right)\right) - \frac{h^{*2}}{2}\nabla\left(\nabla\cdot\left(H^*\bar{\vec{u}}^*\right)\right)\right)_{t^*} = gH^*\nabla h^*,\end{aligned} \tag{4.25}$$

$$\frac{\partial E^*}{\partial t^*} + \nabla\cdot\left(\bar{\vec{u}}^*\left(E^* + \frac{1}{2}\rho^* gH^{*2}\right)\right) = \rho^* gH^*\frac{\partial\zeta^*}{\partial t^*}. \tag{4.26}$$

##### 4.1.2.3.2 SWE without dispersion and with energy equation

$$\frac{\partial H^*}{\partial t^*} + \nabla\cdot(H^*\bar{\vec{u}}^*) = 0, \tag{4.27}$$

$$\frac{\partial(H^*\bar{\vec{u}}^*)}{\partial t^*} + \nabla\cdot\left(H^*\bar{\vec{u}}^*\otimes\bar{\vec{u}}^* + \frac{1}{2}gH^{*2}\right) = gH^*\nabla h^*, \tag{4.28}$$

$$\frac{\partial E^*}{\partial t^*} + \nabla\cdot\left(\bar{\vec{u}}^*\left(E^* + \frac{1}{2}\rho^* gH^{*2}\right)\right) = \rho^* gH^*\frac{\partial\zeta^*}{\partial t^*}. \tag{4.29}$$

Between (i) and (ii), only the equation for the evolution of the horizontal velocity (4.28) differs. In particular, it is interesting to note (this is the first main result of the present study) that the energy equations are the same in the dispersive and non-dispersive cases.

Differences appear only at higher order (terms of order $\mathcal{O}(\varepsilon\mu^2)$). The physical meaning is that the vertical velocity as well as the non-uniform structure of the horizontal velocity appear only at the next order. An additional remark can be made about the hyperbolic structure of the system (4.27)–(4.29). We restrict our observations to one space dimension. Let us assume that a shock wave propagates from left to right at velocity $s > 0$. The states before and after the discontinuity are denoted by $(H^*_{l,r}, \bar{u}^*_{l,r}, E^*_{l,r})$ correspondingly. From entropy considerations one can conclude that for an admissible state $H^*_l > H^*_r$. For a general system of conservation laws $v_t + \partial_x f(v) = 0$, the Rankine-Hugoniot relations have the simple form $f(v_r) - f(v_l) = s(v_r - v_l)$.

Some simple algebraic calculations yield the following relations:

$$s = \frac{H^*_l \bar{u}^*_l - H^*_r \bar{u}^*_r}{H^*_l - H^*_r}, \quad \bar{u}^*_r = \bar{u}^*_l \pm \sqrt{\frac{1}{2} g (H^{*2}_l - H^{*2}_r)\Big(\frac{1}{H^*_r} - \frac{1}{H^*_l}\Big)},$$

$$\frac{E^*_r}{H^*_r} = \frac{E^*_l}{H^*_l} - \frac{1}{2}\rho^* g \Big(\frac{1}{H^*_r} - \frac{1}{H^*_l}\Big) \frac{H^{*2}_r \bar{u}^*_r - H^{*2}_l \bar{u}^*_l}{\bar{u}^*_r - \bar{u}^*_l}. \tag{4.30}$$

These formulas relate left and right states connected in the $(H^*, \bar{u}^*, E^*)$ space by a shock wave. The first two relations are well known. What is new to our knowledge is the formula (4.30) which gives an insight into the energy states in a shock wave. In practice, they can be used for the theoretical analysis of bores and as a validation test for nonlinear SWE codes (with energy equation).

### 4.1.3 Simulations of energy

Next we illustrate the main features of energy evolution in tsunami generation. The importance of dispersive effects strongly depends on the extent of the source area (the smaller the source the stronger the dispersive effects) and the ocean depth in the source area [KDD07]. We restrict our study to the non-dispersive SWE (4.27)–(4.29). We solve these equations numerically with a finite volume method [DPD10].

While the common practice in modeling tsunami generation consists in translating the initial sea bottom deformation to the water surface, thus neglecting all dynamical effects, we prefer to include some dynamics in the process in an effort to be closer to what happens in reality [DDK06]. We construct the bottom motion by multiplying Okada's static solution $\zeta^*_{OK}(x^*, y^*)$[1] by a function of time [Ham73]:

$$h^*(x^*, y^*, t^*) = h^*_0(x^*, y^*) - (1 - e^{-\alpha^* t^*})\zeta^*_{OK}(x^*, y^*).$$

[1]Okada's solution is a steady analytical solution for the seafloor displacement following an underwater earthquake, based on dislocation theory in an elastic half-space [Oka85].

| *Parameter* | *Value* |
|---|---|
| Dip angle, $\delta$ | 13° |
| Slip angle, $\theta$ | 90° |
| Fault length, $L^*$ | 18 km |
| Fault width, $W^*$ | 14 km |
| Fault depth | 5 km |
| Slip along the fault | 10 m |
| Poisson ratio | 0.27 |
| Young modulus | $9.5 \times 10^9$ Pa |
| Acceleration due to gravity, $g$ | 9.81 m/$s^2$ |
| Water depth, $h_0$ | 1 km |
| Characteristic rise time, $t_0^*$ | 8 s |
| $\alpha^* = \log(3)/t_0^*$ | 0.1373 $s^{-1}$ |

**Table 4.1:** Values of physical parameters used for the energy density computations.

The parameter $\alpha^*$ is related to the characteristic time $t_0^*$ under consideration. We chose

$$1 - e^{-\alpha^* t_0^*} = \frac{2}{3} \Leftrightarrow \alpha^* = \frac{\log 3}{t_0^*}.$$

The various parameters used in the computations are given in Table 4.1.

Other time laws are possible and we refer to [DD07d] for more details. In the present numerical computations we chose $h_0^*(x^*, y^*) = h_0 = \text{const}$. This choice is not only made for the sake of simplicity. Another reason is that Okada's solution is derived within the assumption of an elastic half-space which does not take into account the bathymetry. In order to be coherent with this solution we assume the bottom to be flat before deformation.

With our definition of potential energy, the total energy is nonzero both at time $t^* = 0$ and at time $t^* \to \infty$. For practical applications it is important to isolate the energy available to the tsunami wave. One possibility is to define the wave energy as follows:

$$E^*_{\text{wave}} = E^* + \frac{1}{2}\rho^* g h^{*2}. \tag{4.31}$$

Clearly $E^*_{\text{wave}} = 0$ both at time $t^* = 0$ and at time $t^* \to \infty$ when the wave has left the generation region. From Eq. (4.29), one finds that the energy equation satisfied by $E^*_{\text{wave}}$ is

$$\frac{\partial E^*_{\text{wave}}}{\partial t^*} + \nabla \cdot \left( \vec{\bar{u}}^* \left( E^*_{\text{wave}} + \frac{1}{2}\rho^* g H^{*2} - \frac{1}{2}\rho^* g h^{*2} \right) \right) = \rho^* g (H^* - h^*) \frac{\partial \zeta^*}{\partial t^*}. \tag{4.32}$$

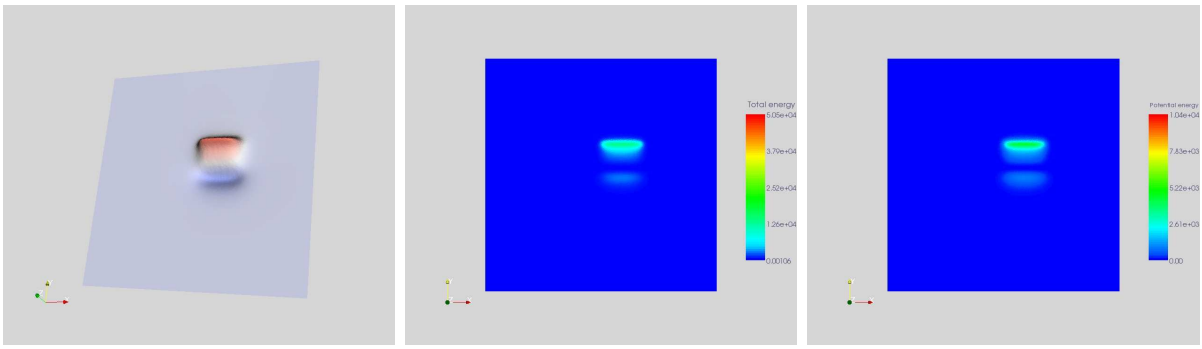

(a) Free surface (b) Total energy (c) Potential energy

**Figure 4.2:** Tsunami generation leading to a dipolar wave form; $t^* = 4$ s. The same scales are used in Figures 4.2–4.9: for the free surface, red denotes a rise of sea level; for the total energy, the scale goes from 0 (blue) to $5 \times 10^4$ (red); for the potential energy, the scale goes from 0 (blue) to $10^4$ (red).

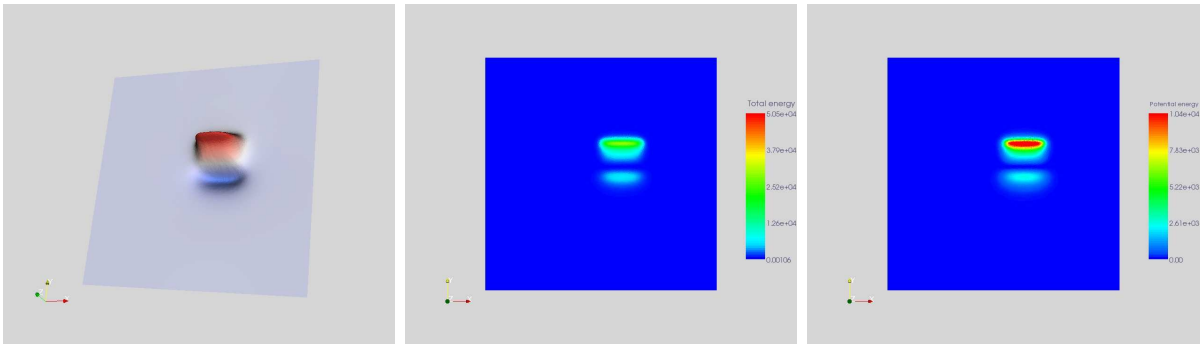

(a) Free surface (b) Total energy (c) Potential energy

**Figure 4.3:** $t^* = 6$ s

Figures 4.2–4.9 show the distributions of free-surface elevation $\eta^*(x^*, y^*)$, total wave energy $E^*_{\text{wave}}(x^*, y^*)$ and potential wave energy $\frac{1}{2}\rho^* g \eta^{*2}$ at various times. One clearly sees the generation process. The formation of the leading elevation and depression waves takes a few seconds. Then the propagation begins. As shown by [BMR72], tsunami energy radiates primarily at right angles to a rupturing fault (see also [Kaj70]). The distribution of potential energy makes sense when one compares the potential energy plots with the free-surface plots. The total energy spreads in a more uniform manner across the area affected by the waves.

It is also of interest to see how the wave energy $E^*_{\text{wave}}$, integrated over the whole fluid domain, varies during the generation process. This evolution is shown in figure 4.10. Three curves are plotted in figure 4.10(a). The solid curve simply is the energy (4.8) integrated

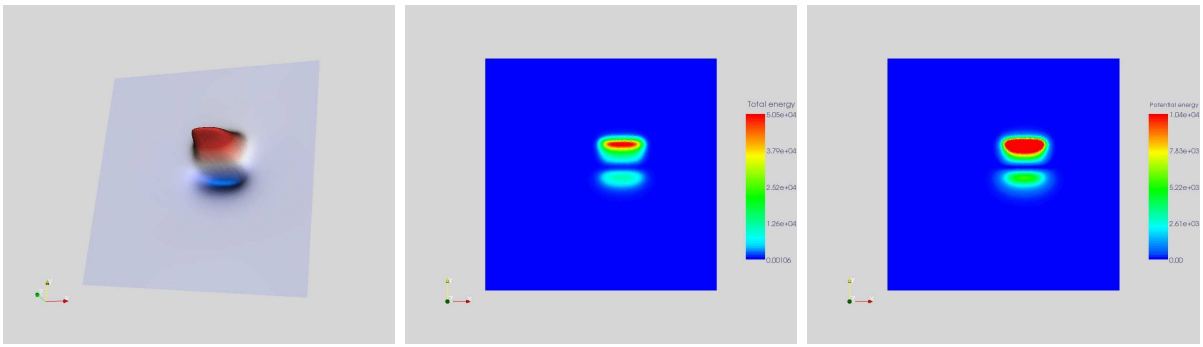

(a) Free surface (b) Total energy (c) Potential energy

**Figure 4.4:** $t^* = 10$ s

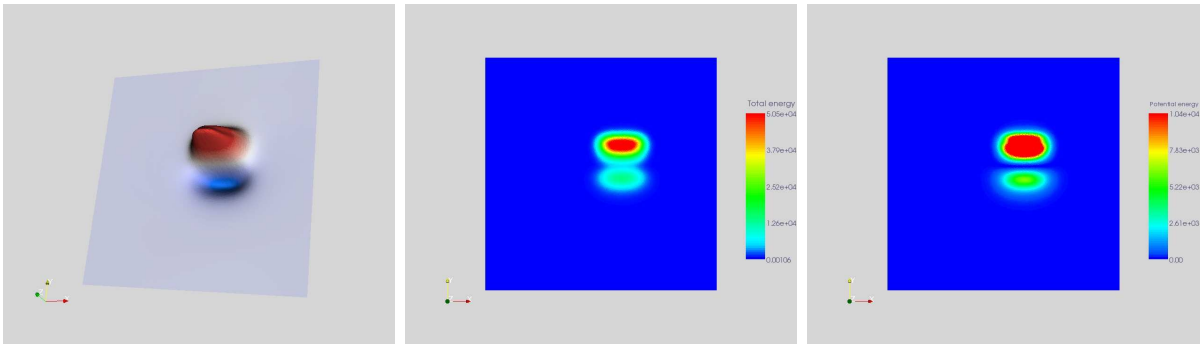

(a) Free surface (b) Total energy (c) Potential energy

**Figure 4.5:** $t^* = 20$ s

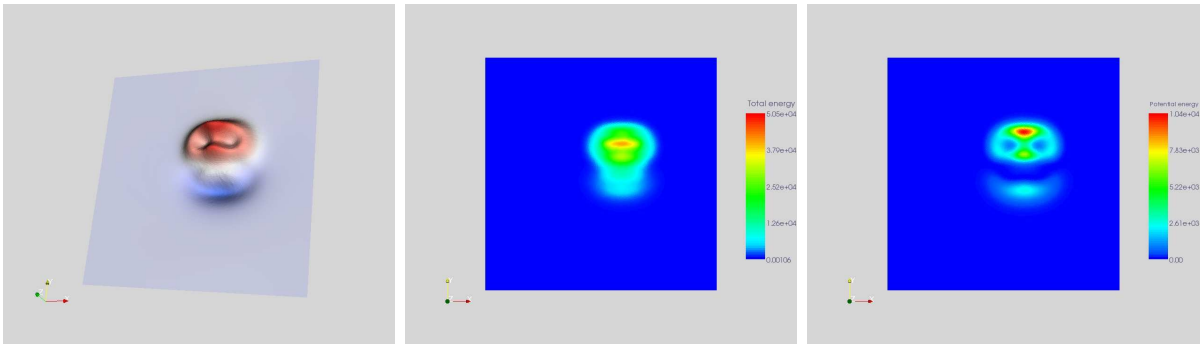

(a) Free surface (b) Total energy (c) Potential energy

**Figure 4.6:** $t^* = 40$ s

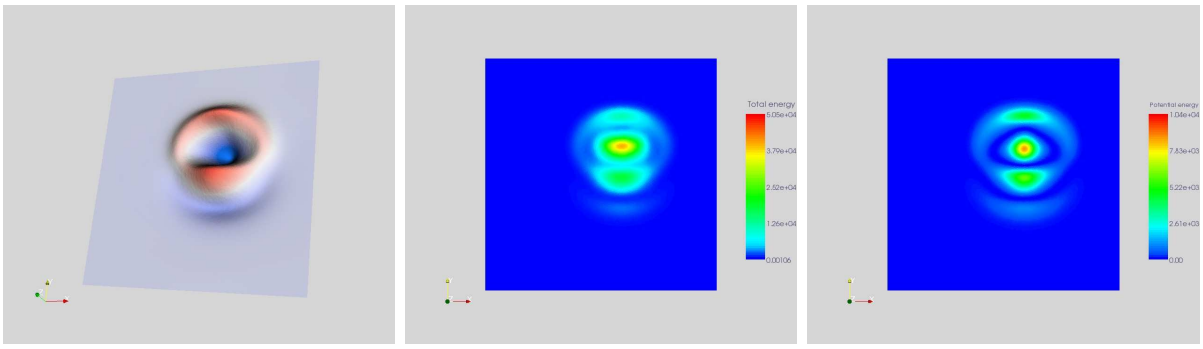

(a) Free surface (b) Total energy (c) Potential energy

**Figure 4.7:** $t^* = 80$ s

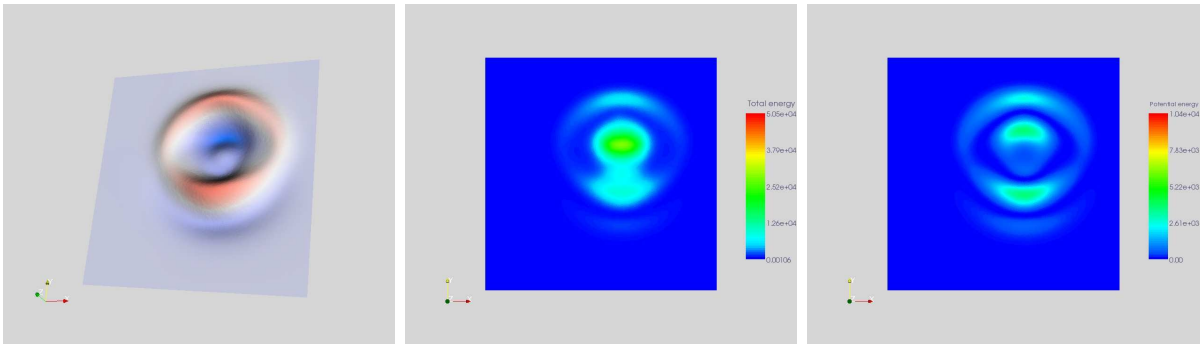

(a) Free surface (b) Total energy (c) Potential energy

**Figure 4.8:** $t^* = 120$ s

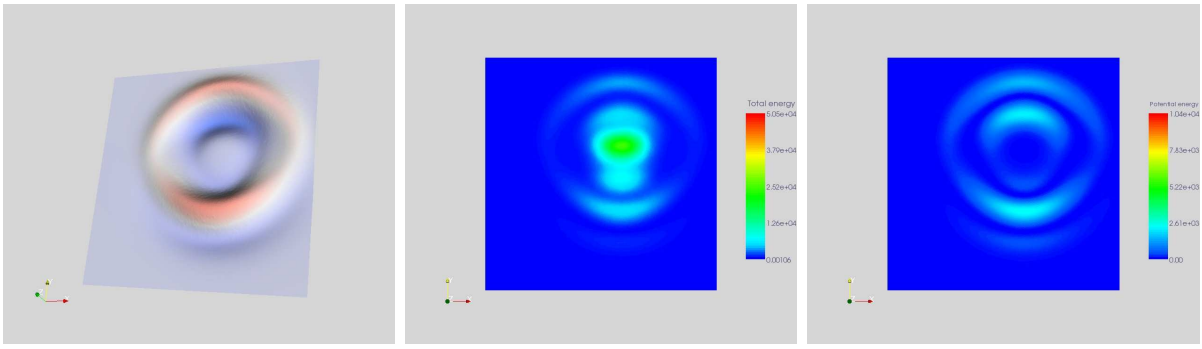

(a) Free surface (b) Total energy (c) Potential energy

**Figure 4.9:** $t^* = 160$ s

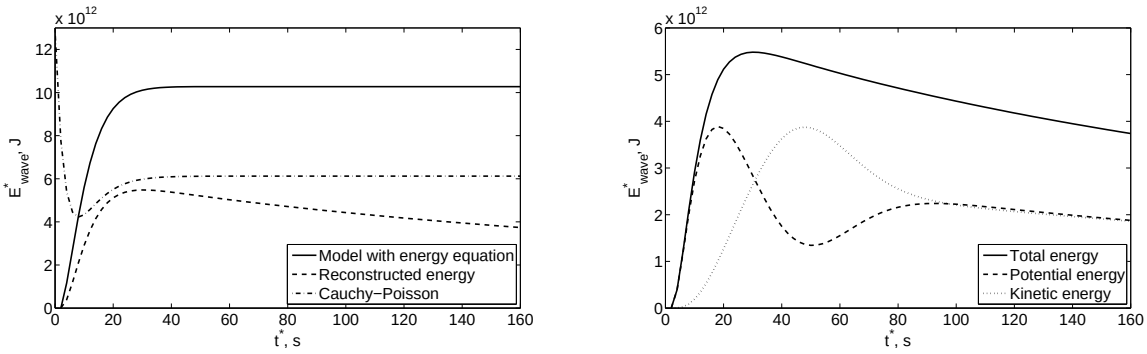


(a) Total energy

(b) Total, potential and kinetic energies

**Figure 4.10:** (a) Total energy $\iint E^*_{\text{wave}} d\mathbf{x}^*$ as a function of time computed with the SWE with energy (4.27) – (4.29) (top curve), the linearized water wave equations (middle curve) and reconstructed from the flow variables $\bar{\vec{u}}^*$ and $\eta^*$ when no energy equation is used (bottom curve). (b) Partition between potential and kinetic energies as a function of time for the reconstructed energy. The top curve of (b) is the same as the bottom curve of (a).

over the water surface. The middle curve will be explained in Section 4 (linearized theory). The bottom curve is obtained as follows. Imagine that one is solving the SWE without the energy equation. In order to look at the energy, a natural way to do it is to approximate the wave energy $E^*_{\text{wave}}$ as

$$E^*_{\text{wave}} \approx \frac{1}{2}\rho^* H^* |\bar{\vec{u}}^*|^2 + \frac{1}{2}\rho^* g \eta^{*2},$$

and then to integrate over the whole fluid domain. The second main result of the present study is that the difference between the proper way to compute the energy and the approximate way can be large. It is probably due to the vertical velocity, which is completely neglected in the second approach. Once the motion of the sea bottom has stopped, the total energy remains constant. However the reconstructed energy decreases with time. This indicates that computing the wave energy directly from the conservative energy equation (4.32) is much better, especially with the type of numerical method we use. In figure 4.10(b), one clearly sees the exchange between potential and kinetic energies until equipartition is reached.

### 4.1.4 Energy in the framework of the dispersive linearized equations

In the case of tsunamis generated by earthquakes, nonlinear effects are not important during the process of generation and propagation. This is why it is valid to use the linearized water-wave equations. [DDK06] and others showed that taking an instantaneous

seabed deformation is not equivalent to instantaneously transferring the seabed deformation to the ocean surface, except in the framework of the linearized shallow water equations (very long waves). The difference comes from the vertical velocities and dispersion. In this case we must go back to the initial set of equations (4.1)–(4.3). Since the motion starts from the state of rest, it can be considered as irrotational (potential flow) and one can introduce the velocity potential $\vec{u}^* = \nabla\phi^*$.

We perform the linearization of the equations (4.1) and (4.2), and of the boundary conditions (4.4) – (4.6). It is equivalent to taking the limit of the equations as $\varepsilon \to 0$. For the sake of convenience, we switch back to the physical variables. The linearized problem in dimensional variables reads [DD07d]

$$\Delta_\perp \phi^* + \partial^2\phi^*/\partial z^{*2} = 0, \qquad (x^*, y^*, z^*) \in \mathbb{R}^2 \times [-h^*, 0], \tag{4.33}$$

$$\frac{\partial \phi^*}{\partial z^*} = \frac{\partial \eta^*}{\partial t^*}, \quad z^* = 0, \quad \text{kinematic condition}, \tag{4.34}$$

$$\frac{\partial \phi^*}{\partial t^*} + g\eta^* = 0, \quad z^* = 0, \quad \text{dynamic condition}. \tag{4.35}$$

Within linear theory the forces that cause perturbations are so weak that the boundary condition at the bottom (4.6) is also simplified:

$$\frac{\partial \phi^*}{\partial z^*} = \frac{\partial \zeta^*}{\partial t^*}, \quad z^* = -h^*. \tag{4.36}$$

The bottom motion appears in the right-hand side of Eq. (4.36).

The Laplace equation (4.33) together with the boundary conditions (4.34), (4.35) and (4.36) determine the boundary-value problem for the velocity potential $\phi^*$ within the linear theory. In order to solve the equations for a prescribed bottom motion, one can use Fourier and Laplace transforms (this approach is followed here) or Green's functions. Three scenarios are considered for the bottom motion [DDK06]: the passive generation in which the deformation of the sea bottom is simply translated to the free surface (one is then solving an initial value problem) and two dynamical processes $\zeta^*(x^*, y^*, t^*) = T(t^*)\zeta^*_{OK}(x^*, y^*)$, where $\zeta^*_{OK}(x^*, y^*)$ is given by Okada's solution. The two choices for $T$ are the instantaneous deformation with $T(t^*) = T_i(t^*) = \mathcal{H}(t^*)$, where $\mathcal{H}(t^*)$ denotes the Heaviside step function, and the exponential law used above in Section 3:

$$T(t^*) = T_e(t^*) = \begin{cases} 0, & t^* < 0, \\ 1 - e^{-\alpha^* t^*}, & t^* \geq 0, \end{cases} \qquad \text{with } \alpha^* > 0.$$

Let $\widehat{\zeta^*_{OK}}$ be the Fourier transform of $\zeta^*_{OK}$, $\omega^2 = g|\mathbf{k}^*| \tanh(|\mathbf{k}^*|h^*)$ the dispersion relation and $\mathbf{x}^* = (x^*, y^*)$. We provide the general integral solution for the free surface elevation in

the three cases,

$$\eta_o^*(\mathbf{x}^*, t^*) = \frac{1}{(2\pi)^2} \iint_{\mathbb{R}^2} \widehat{\zeta}_{OK}^* e^{i\mathbf{k}^*\cdot\mathbf{x}^*} \cos(\omega t^*)\, d\mathbf{k}^*, \quad \text{(passive)} \tag{4.37}$$

$$\eta_i^*(\mathbf{x}^*, t^*) = \frac{1}{(2\pi)^2} \iint_{\mathbb{R}^2} \frac{\widehat{\zeta}_{OK}^* e^{i\mathbf{k}^*\cdot\mathbf{x}^*}}{\cosh(|\mathbf{k}^*|h^*)} \cos(\omega t^*)\, d\mathbf{k}^*, \quad \text{(instantaneous)} \tag{4.38}$$

$$\eta_e^*(\mathbf{x}^*, t^*) = \frac{-\alpha^{*2}}{(2\pi)^2} \iint_{\mathbb{R}^2} \frac{\widehat{\zeta}_{OK}^* e^{i\mathbf{k}^*\cdot\mathbf{x}^*}}{\cosh(|\mathbf{k}^*|h^*)} \frac{e^{-\alpha^* t^*} - \cos(\omega t^*) - \omega/\alpha^* \sin(\omega t^*)}{\alpha^{*2} + \omega^2}\, d\mathbf{k}^*, \tag{4.39}$$

and the velocity potential in the passive case (the expressions for the other two active cases are a bit cumbersome) [DDK06],

$$\phi_o^*(\mathbf{x}^*, t^*) = \frac{1}{4\pi^2} \iint_{\mathbb{R}^2} \frac{-g}{\omega} \widehat{\zeta}_{OK}^* e^{i\mathbf{k}^*\cdot\mathbf{x}^*} (\cosh|\mathbf{k}^*|z^* + \tanh|\mathbf{k}^*|h^* \sinh|\mathbf{k}^*|z^*)\, d\mathbf{k}^*. \tag{4.40}$$

Then one can easily compute the kinetic and potential energies:

$$E_K^* = \frac{1}{2}\rho^* \iint_{\mathbb{R}^2} \int_{-h^*}^{\eta^*} |\nabla\phi^*|^2\, d\mathbf{x}^* dz^*, \quad E_P^* = \frac{1}{2}\rho^* g \iint_{\mathbb{R}^2} \eta^{*2}\, d\mathbf{x}^*. \tag{4.41}$$

Results are shown in figures 4.11 and 4.12. Even though there are differences during the first few seconds, the three mecanisms lead to the same almost exact equipartition between kinetic and potential energy once the dipolar waves start to propagate. The simplest estimate proposed for the energy of tsunamis generated by a dislocation source is that given by [OS03]. They compute the increase in potential energy of the ocean by displacing a volume of water $S \times \delta h^*$ from the bottom to the surface of the ocean. This also represents the work of the pressure forces displacing the ocean bottom. Then they explain that the center of mass of the displaced water, initially at height $\delta h^*/2$ above the ocean floor, is transferred to the ocean surface, so that the change in potential energy is not as much. The difference between the two is the energy available to the tsunami wave:

$$\iint E_{\text{wave}}^* d\mathbf{x}^* = \frac{1}{2}\rho^* g S (\delta h^*)^2. \tag{4.42}$$

Incidentally, this expression does not depend on the sign of $\delta h^*$ and is also valid for a sudden subsidence of a section of the ocean floor. It can be extended to a more realistic sea floor deformation, such as the one used in this study, $\zeta_{OK}^*(x^*, y^*)$:

$$\iint E_{\text{wave}}^* d\mathbf{x}^* = \frac{1}{2}\rho^* g \iint (\zeta_{OK}^*)^2 d\mathbf{x}^*. \tag{4.43}$$

This quantity corresponds to the square in figure 4.11(b).

| *Parameter* | *Value* |
|---|---|
| Dip angle, $\delta$ | 13° |
| Slip angle, $\theta$ | 90° |
| Fault length, $L^*$ | 150 km |
| Fault width, $W^*$ | 50 km |
| Fault depth | 35 km |
| Slip along the fault | 15 m |
| Poisson ratio | 0.27 |
| Young modulus | $9.5 \times 10^9$ Pa |
| Acceleration due to gravity, $g$ | 9.81 m/$s^2$ |
| Water depth, $h^*$ | 4 km |
| Characteristic rise time, $t_0^*$ | 50 s |
| $\alpha^* = \log(3)/t_0^*$ | 0.0220 $s^{-1}$ |

**Table 4.2:** Values of physical parameters used for the Cauchy-Poisson analysis of tsunami generation.

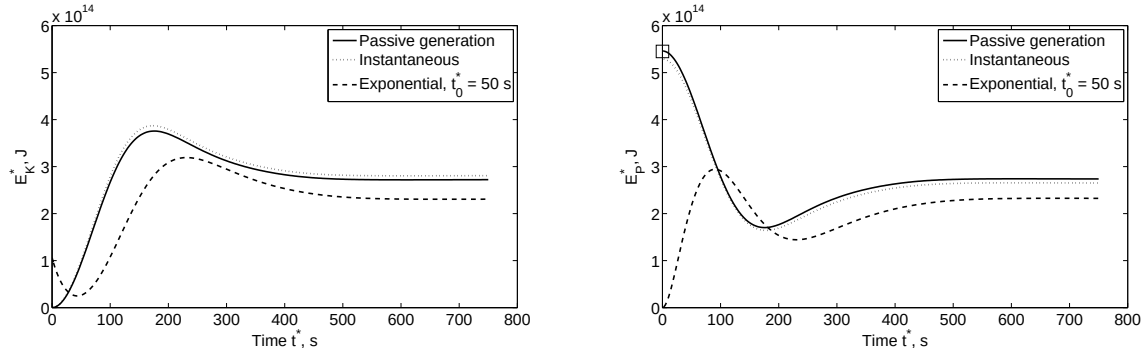


(a) Kinetic energy

(b) Potential energy

**Figure 4.11:** Time evolution of kinetic and potential energies (4.41) for three mechanisms of tsunami generation: passive generation, instantaneous bottom motion and exponential bottom motion. The square in plot (b) indicates the estimate (4.43).

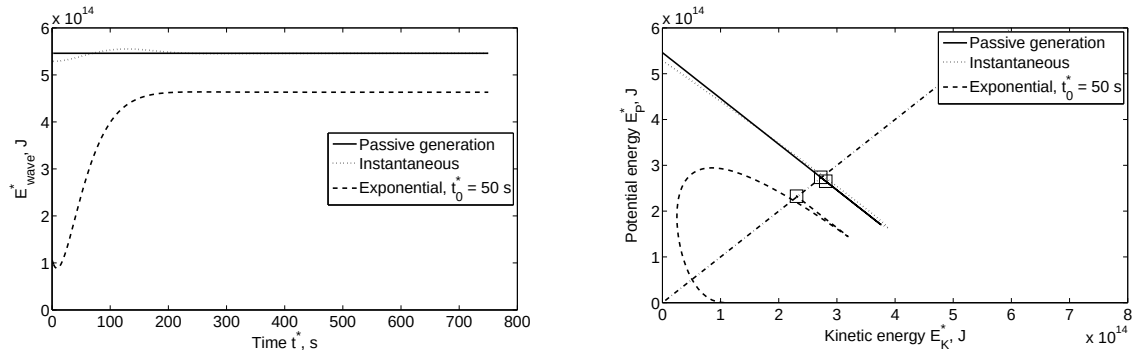


(a) Total energy

(b) Trajectory in energy space

**Figure 4.12:** Same as figure 4.11. Time evolution of total energy $E^*_{\text{wave}} = E^*_K + E^*_P$ (a) and trajectory in energy space (b). The straight dashed-dotted line represents equipartition of kinetic and potential energies. The squares represent the last computed points.

### 4.1.5 Concluding remarks

In this article we provided a formal derivation of the total energy equation in the framework of the nonlinear SWE, both for dispersive and non-dispersive waves. We also made an attempt to better understand the energy transfer from a moving bottom to the water above. The importance of this topic is clear, given the serious hazard that tsunamis represent for coastal regions.

Tsunami energy can be studied at several levels. A simple formula was given by [OS03]. In the present work, we extended it to more spatially realistic sea floor deformations. But this formula does not involve any dynamics, which can play an important role in tsunami generation. A somewhat counterintuitive consequence of this simple estimate is that the energy carried by the full tsunami wave is practically independent of depth [OS04]. One would think that the energy involved in lifting a 4 km column of water above a rupture is different from lifting only 100 m of water (whether instantaneously or in a few seconds). But no difference can be found in wave height. The assumption of incompressibility may in fact no longer be valid, especially for a very deep ocean.

The emphasis of this paper has been on tsunami generation. At the runup or inundation stage, energy is also quite important. Potential energy is being transferred into kinetic energy and the study of these exchanges is left for future work. Our approach can also be used to analyze the structure of the wave field in caustics more accurately than with ray theory [Ber07]. The present studyr can be considered as a first step towards a better understanding of tsunami wave energy, in order to provide scales for tsunami magnitudes for example. More profound mathematical and physical analysis is needed.

Another extension is the study of other mechanisms. For example [Oka03] showed that

the combination of a lesser absolute level of excitation and a more pronounced shift of the spectral energy towards higher frequencies characterized by strong dispersion makes landslide sources significantly deficient far-field tsunami generators, as compared to classical dislocations.

### 4.1.6 Appendix. Derivation of dispersive shallow-water equations with variable bathymetry

We derive the Boussinesq equations following the method used, for example, by [YL89, VS93, Nwo93]. A moving bathymetry was considered in the framework of the Boussinesq equations by [VS93], but they dealt with a 2D problem leading to a 1D system of equations.

We need to know the depth dependence of the horizontal velocity $\vec{u}_\perp$ in order to reduce the problem to a 2D one. We expand $\vec{u}_\perp$ in a Taylor series in the vertical coordinate $z$ about the seabed $z = -h$:

$$\vec{u}(x,y,z,t) = \vec{u}|_{z=-h} + (z+h)\,\vec{u}_z|_{z=-h} + \frac{(z+h)^2}{2!}\,\vec{u}_{zz}|_{z=-h} + \dots . \tag{4.44}$$

From now on, the horizontal velocity at the bottom is denoted by

$$\vec{u}_b := \vec{u}_\perp(x,y,-h,t).$$

If the flow is assumed to be irrotational, there is an additional relation which closes the system:

$$(\vec{u}_\perp)_z = \nabla w. \tag{4.45}$$

Substituting (4.22) into (4.45) clearly shows that $(\vec{u}_\perp)_z(x,y,-h,t) = \mathcal{O}(\mu^2)$. Substituting (4.44) into (4.22) and integrating then yields

$$w = \mu^2\zeta_t - \mu^2\nabla\cdot\big((z+h)\vec{u}_b\big) + \mathcal{O}(\mu^4). \tag{4.46}$$

The vertical velocity varies linearly with respect to $z$ over the depth at leading order $\mathcal{O}(\mu^2)$.

The horizontal velocities can be found by integrating the irrotationality condition (4.45) from $-h$ to $z$:

$$\vec{u}_\perp = \vec{u}_b + \int_{-h}^{z} \nabla w\, dz. \tag{4.47}$$

Substituting (4.46) for $w$ and integrating gives

$$\vec{u}_\perp \;=\; \vec{u}_b \;+\; \mu^2(z\;+\;h)\left[\nabla\zeta_t - \frac{1}{2}(z-h)\nabla(\nabla\cdot\vec{u}_b) - \nabla\big(\nabla\cdot(h\vec{u}_b)\big)\right] \;+\; \mathcal{O}(\mu^4). \tag{4.48}$$

We see that the horizontal velocities vary quadratically with respect to $z$ over the depth at leading order $\mathcal{O}(\mu^2)$.

Following [Urs53], we introduce a number which measures the relative importance of nonlinear and dispersive effects in long waves:

$$S := \varepsilon/\mu^2.$$

In order to simplify the computations we now assume that $S = \mathcal{O}(1)$. Dispersive terms can be neglected if $S \gg 1$.

An expression for the pressure can be obtained by substituting (4.48) and (4.46) into (4.21), integrating and retaining leading order terms:

$$\pi = \eta + \frac{\mu^2}{2} z^2 \nabla \cdot \vec{u}_{bt} + \mu^2 z\big(\nabla \cdot (h\vec{u}_{bt}) - \zeta_{tt}\big) + \mathcal{O}(\mu^4). \tag{4.49}$$

The equation for the free-surface evolution is derived by substituting (4.48) into the depth-integrated continuity equation (4.19) and integrating:

$$\eta_t + \nabla \cdot \big((h+\varepsilon\eta)\vec{u}_b\big) - \mu^2 \nabla \cdot \Big[\frac{h^2}{2}\nabla\big(\nabla \cdot (h\vec{u}_b) - \zeta_t\big) - \frac{h^3}{3}\nabla\big(\nabla \cdot \vec{u}_b\big)\Big] - \zeta_t = 0. \tag{4.50}$$

The equation for the evolution of the horizontal velocity is obtained by substituting (4.48) and (4.49) into (4.12) and (4.13):

$$\vec{u}_{bt} + \varepsilon(\vec{u}_b \cdot \nabla)\vec{u}_b + \nabla\eta + \mu^2\Big[\frac{h^2}{2}\nabla(\nabla \cdot \vec{u}_b) - h\nabla\big(\nabla \cdot (h\vec{u}_b) - \zeta_t\big)\Big]_t = 0.$$

Using the irrotationality condition this equation can be rewritten as

$$\vec{u}_{bt} + \frac{\varepsilon}{2}\nabla|\vec{u}_b|^2 + \nabla\eta + \mu^2\Big[\frac{h^2}{2}\nabla(\nabla \cdot \vec{u}_b) - h\nabla\big(\nabla \cdot (h\vec{u}_b) - \zeta_t\big)\Big]_t = 0. \tag{4.51}$$

Finally we write the energy equation by substituting (4.48) and (4.49) into (4.23):

$$\frac{\partial}{\partial t}\int_{-h}^{\varepsilon\eta} e\, dz + \varepsilon\nabla \cdot \left[\left(\int_{-h}^{\varepsilon\eta} e\, dz + \frac{1}{2}(h+\varepsilon\eta)^2\right)\vec{u}_b\right] - \varepsilon(h+\varepsilon\eta)\zeta_t = 0. \tag{4.52}$$

The higher-order terms are of order $\mathcal{O}(\varepsilon\mu^2)$.

Another possibility for the choice of variables is to introduce the depth averaged velocity. The corresponding standard Boussinesq-type equations were obtained by [Per67] in the case of a fixed seabed. We extend the results to a moving bathymetry and add the energy equation. The main advantage of the depth averaged velocity consists in the fact that the continuity equation (or equivalently the equation for the free-surface elevation) is very simple and exact in this variable.

Let us rewrite all equations in terms of the depth-averaged velocity defined by

$$\bar{\vec{u}} = \frac{1}{h+\varepsilon\eta}\int_{-h}^{\varepsilon\eta} \vec{u}_\perp \, dz. \tag{4.53}$$

The depth-integrated continuity equation (4.19) yields immediately

$$\eta_t + \nabla\cdot\big((h+\varepsilon\eta)\bar{\vec{u}}\big) - \zeta_t = 0. \tag{4.54}$$

In order to derive equations for the horizontal velocity and the energy we need a relation between $\vec{u}_b$ and $\bar{\vec{u}}$. The desired relation is deduced directly from the definition (4.53) by substituting (4.48) in it:

$$\bar{\vec{u}} = \vec{u}_b - \frac{\mu^2}{2}h\nabla\big(\nabla\cdot(h\vec{u}_b) - \zeta_t\big) + \frac{\mu^2}{3}h^2\nabla(\nabla\cdot\vec{u}_b) + \mathcal{O}(\varepsilon^2+\varepsilon\mu^2+\mu^4).$$

Inverting the last equation yields

$$\vec{u}_b = \bar{\vec{u}} + \mu^2\Big[\frac{h}{2}\nabla\big(\nabla\cdot(h\vec{u}_b) - \zeta_t\big) - \frac{h^2}{3}\nabla(\nabla\cdot\vec{u}_b)\Big] + \mathcal{O}(\varepsilon^2+\varepsilon\mu^2+\mu^4). \tag{4.55}$$

Substituting the relation (4.55) into equation (4.51) gives the standard Boussinesq equations for a moving bottom:

$$\bar{\vec{u}}_t + \frac{\varepsilon}{2}\nabla\left|\bar{\vec{u}}\right|^2 + \nabla\eta + \mu^2\Big[\frac{h^2}{6}\nabla(\nabla\cdot\bar{\vec{u}}) - \frac{h}{2}\nabla(\nabla\cdot(h\bar{\vec{u}}) - \zeta_t)\Big]_t = 0. \tag{4.56}$$

The energy equation is obtained by substituting the relation (4.55) into equation (4.52):

$$\frac{\partial}{\partial t}\int_{-h}^{\varepsilon\eta} e\, dz + \varepsilon\nabla\cdot\left[\left(\int_{-h}^{\varepsilon\eta} e\, dz + \frac{1}{2}(h+\varepsilon\eta)^2\right)\bar{\vec{u}}\right] - \varepsilon(h+\varepsilon\eta)\zeta_t = 0. \tag{4.57}$$

Since the energy equation is redundant for incompressible flows, the linear dispersion relation is unaffected by the inclusion of the energy equation. As is well-known, it can be improved by defining the horizontal velocity at an arbitrary level.

## 4.2 Influence of sedimentary layering on tsunami generation

*The most incomprehensible thing about the world is that it is comprehensible.*

Albert Einstein

ABSTRACT. The present Section is devoted to the influence of sediment layers on the process of tsunami generation. The main scope here is to demonstrate and especially quantify the effect of sedimentation on vertical displacements of the seabed due to an underwater earthquake. The fault is modelled as a Volterra-type dislocation in an elastic half-space. The elastodynamics equations are integrated with a finite element method. A comparison between two cases is performed. The first one corresponds to the classical situation of an elastic homogeneous and isotropic half-space, which is traditionally used for the generation of tsunamis. The second test case takes into account the presence of a sediment layer separating the oceanic column from the hard rock. Some important differences are revealed. We conjecture that deformations in the generation region may be amplified by sedimentary deposits, at least for some parameter values. The mechanism of amplification is studied through careful numerical simulations.

### 4.2.1 Introduction

The primary application of this study is that of tsunami generation by the deformation of the sea bottom following an underwater earthquake. We do not explicitly compute the tsunami waves induced above the generation region. The coupling between solid and water motions was already performed in our previous work [DD09b] and can be done again if necessary. Here we are mainly interested in the extreme amplitudes of the seabed displacements during the first minutes of a tsunamigenic earthquake. Recall that the free surface motion roughly follows these displacements. There are two fundamental reasons for this. The first one is that the rupture velocity of the seismic source, $V$, is much larger than the phase velocity of the tsunami, $c$. In practice, for seismic sources, $V$ is of the order of 3 km/s, whereas $c$ is typically less than 250 m/s, even for the deepest ocean basins [OS03]. It means that the gravitational forces do not have enough time to change the shape of the free surface during the characteristic time of the seabed motion [BMR72]. The second reason is that water is assumed to be incompressible and shallow. Altogether it means that for our purpose we can restrict our attention to the motion of the ocean bottom. Profiles of the ocean free surface are not computed in this study.

The two fundamental reasons mentioned above are often used to justify the passive approach for tsunami generation where the static sea-bed displacement is simply translated

to the free surface to generate the initial condition. Our previous investigations [DDK06, DD07d, DD09b] showed important differences between passive and active generations when the resulting wave is generated by a moving bottom.

We would like to underline that the present study is a theoretical one at this stage and must be followed by a thorough study of the influence of the various parameters such as rupture velocity, focal depth, dip angle, slip angle, fault size (only one-dimensional – 1D – faults are considered in this paper), sedimentary structure (the sedimentary layer is taken as a Poisson solid in this study). Moreover, the far-field effect might be different from the near-field effect. We simply explore some aspects of the influence of the sedimentary layering on tsunami generation. We do not consider historical examples, even though it should be done in the future. Our goal is to present a framework for studying the process of tsunami generation. Recall that ten years ago, Synolakis et al. [SLCY97] were writing: "There is a lack of quantitative information on sediment layers overlying tsunamigenic faults and about how these layers affect directly the generation of tsunamis." Our study is a small step toward a better understanding of the rôle of sediments.

The influence of sedimentary layering was already mentioned in some studies [Fuk79, Oka88, FWB06]. Let us comment on the various results obtained so far. Both studies [Fuk79] and [Oka88] point out that fracturing through thick sediments produces large displacements in the source region but relatively small displacements in the far field. In the work by Okal [Oka88], the influence of the sediment layer was studied in the framework of normal modes and interesting results were obtained for sources inside as well as outside the layer of sediments. In the present study we perform direct numerical simulations by solving the elastodynamics equations with a finite element method (FEM).

To our knowledge, the most recent numerical study concerning the rôle of sedimentation in subduction-zone thrust faults is [FWB06]. The scope of that paper was the long-term evolution of a typical subduction wedge. A quite sophisticated thermo-mechanical modelling of the plate movement with realistic rheology was used. As in our study, the governing equations were solved with a two-dimensional FEM. The authors came to some important conclusions (see also [SB06] for interesting remarks on sediment layers). We would like to quote some of them since there is a connection with our results:

> "Our numerical simulations demonstrate that sedimentation stabilizes the underlying wedge, preventing internal deformation beneath the basin. Maximum slip during great-thrust earthquakes tends to occur where sedimentary basins stabilize the overlaying wedge. The lack of deformation in these stable regions increases the likelihood of thermal pressurization of the subduction thrust, allows the fault to load faster, and allows greater healing of the fault between rupture events."

In view of the above results, it is interesting to compare the distribution of sediment thickness in the world oceans (see Figure 4.13) with the seismic hazard map (see Figure 4.14). As one can see on Figure 4.13, the sediment thickness varies from 0 to 20 km. Important deposits can be found along the Eastern coasts of America and the Western coasts of Africa. Fortunately there is no substantial seismic activity in these regions. But in the Bay of Bengal, and in particular in the Andaman sea, the situation is different. In this part of the world two factors are present simultaneously: an important seismic hazard and thick sediment layers. Unfortunately, we do not have reliable information on sediment thickness in the Mediterranean region. One can find different information in the literature. The estimates go from 25 m [HRR+04] to 1500 m or even more [EOS+05]. So, it is difficult to draw any conclusions. In this study we try to understand what kind of implications this may have for tsunami generation processes.

The present study is organised as follows. In Section 4.2.2 we briefly describe the simplified mathematical model which represents the Earth crust. In the same section we also give some ideas about the discretisation procedure of the governing equations. Section 4.2.3 contains the description of two idealised test cases. Then, some results on the profile of the seafloor are presented. Finally, important conclusions and practical recommendations to tsunami wave modelers are given in Section 4.2.4. Some directions for future research are also outlined.

### 4.2.2 Mathematical model and numerical method

In this paper we use the same mathematical model as in our previous study [DD09b]. Nevertheless, we give here a brief description of the model and refer to [Dut07, DD09b, KDID07] for more details. We emphasize again that we consider a 1D fault. In other words the fault has only one dimension, its length $L$.

The fault is assumed to lie inside a linear elastic isotropic material. In the next section both homogeneous and inhomogeneous distributions of the Earth crust properties will be considered.

We provide the 3D version of the governing equations. Let $\underline{\underline{\sigma}}$ represent the stress tensor. The displacement field $\vec{u} = (u, v, w)(x, y, z, t)$ satisfies the classical elastodynamic equations issued from continuum mechanics [AR02]:

$$\nabla \cdot \underline{\underline{\sigma}} = \rho \frac{\partial^2 \vec{u}}{\partial t^2}, \tag{4.58}$$

where $\rho$ the material density. It is common in seismology to assume that the stress tensor is determined by Hooke's law through the strain tensor $\underline{\underline{\varepsilon}} = \frac{1}{2}(\nabla \vec{u} + \nabla^t \vec{u})$. Therefore

$$\underline{\underline{\sigma}} = \lambda (\nabla \cdot \vec{u}) \underline{\underline{I}} + 2\mu \underline{\underline{\varepsilon}}, \tag{4.59}$$

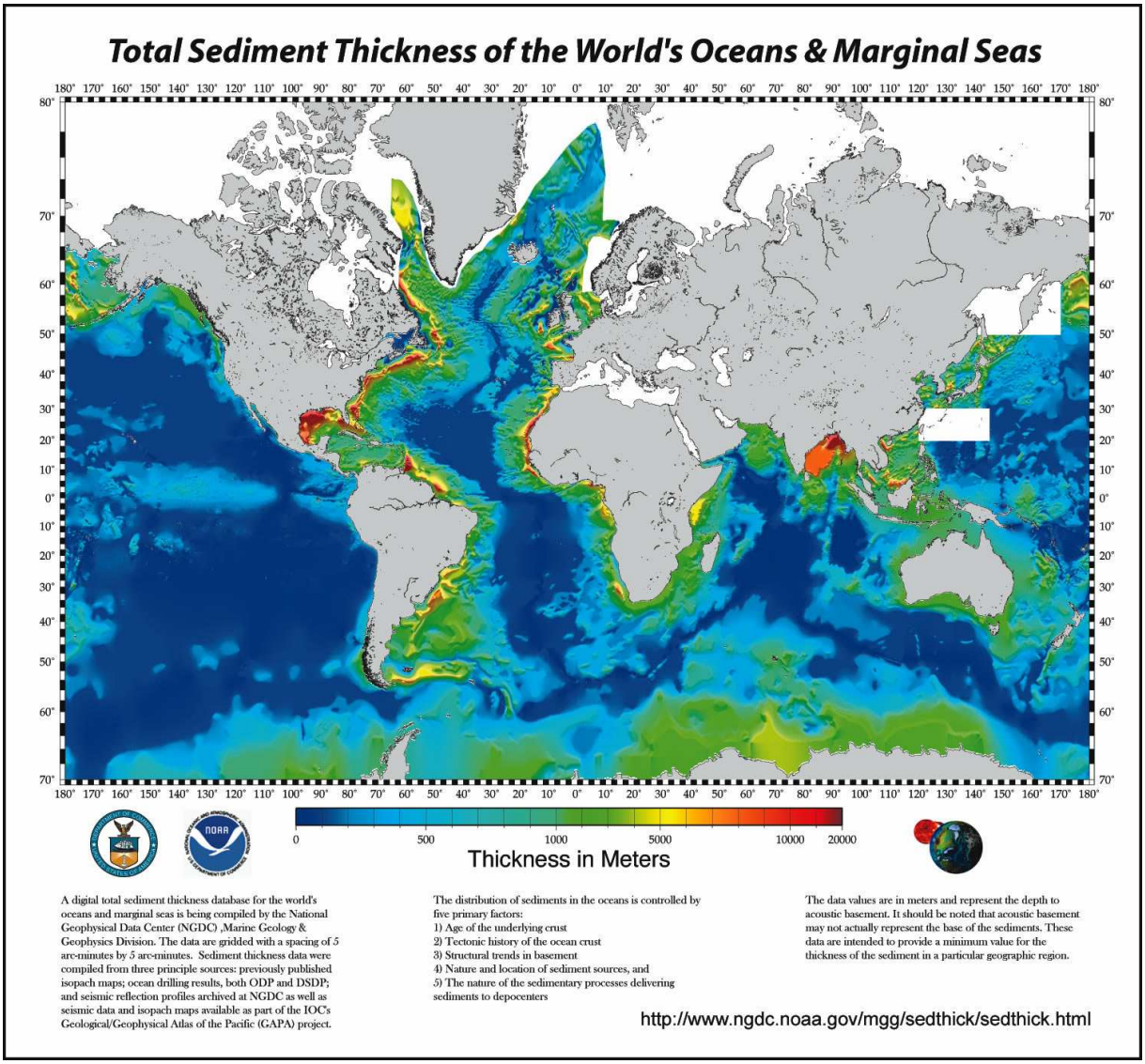


**Figure 4.13:** Total sediment thickness of the world's ocean and marginal seas (source: NOAA).

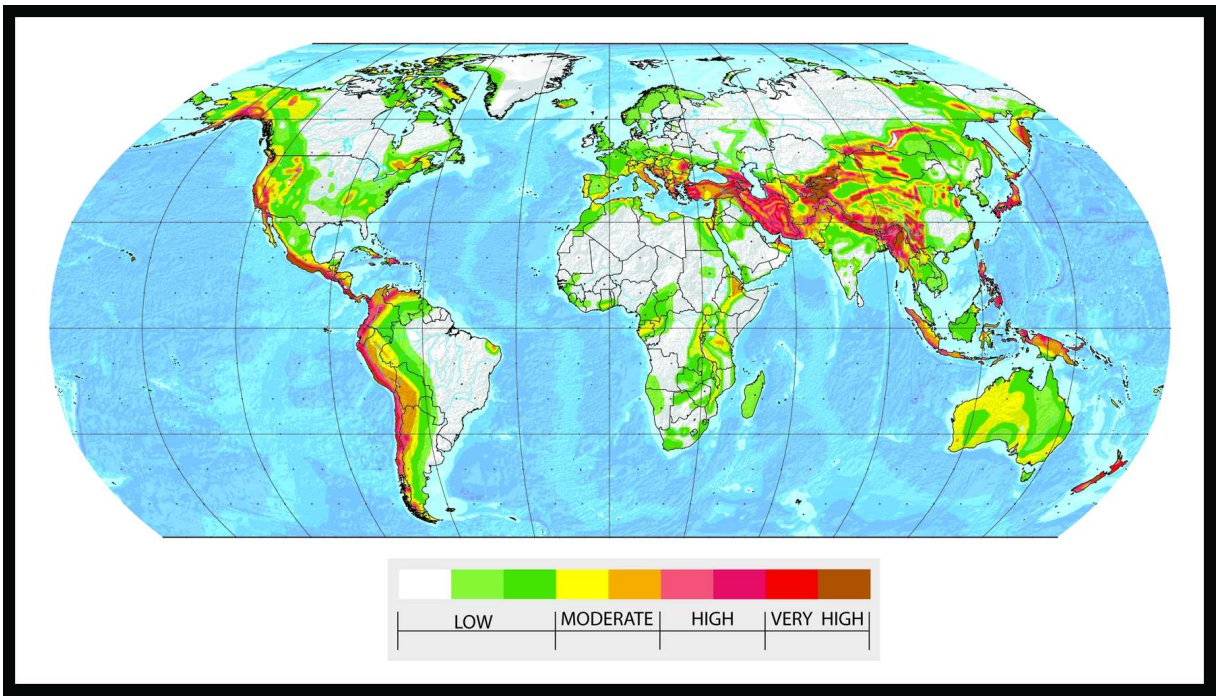


**Figure 4.14:** Global seismic hazard map (source: Swiss Seismological Service).

where $\lambda$ and $\mu$ are the Lamé coefficients. The coefficient $\mu$ is the shear modulus. Thus, we come to the following linear elastodynamic problem:

$$\nabla \cdot \left(\lambda(\nabla \cdot \vec{u})\underline{\underline{I}} + \mu(\nabla\vec{u} + \nabla^t\vec{u})\right) = \rho\frac{\partial^2\vec{u}}{\partial t^2}. \tag{4.60}$$

As already pointed out, these coefficients can possibly depend on the spatial coordinates $(x, y, z)$ ($x, y$: horizontal, $z$: vertical). The Lamé coefficients can be expressed in terms of Poisson's ratio $\nu$ and Young's modulus $E$ as follows:

$$\lambda = \frac{2\mu\nu}{1-2\nu} = \frac{E\nu}{(1+\nu)(1-2\nu)}, \quad \mu = \frac{E}{2(1+\nu)}.$$

This remark immediately leads to the following property of solutions to the steady version of Equation (4.60): such solutions do not depend on Young's modulus but only on Poisson's ratio.

The fault is modeled as a dislocation inside an elastic material. This type of model is widely used for the interpretation of seismic motion. A dislocation is considered as a surface (in three-dimensional problems) or a line (in two-dimensional problems) in a continuous medium where the displacement field is discontinuous. The displacement vector is increased by the amount of the Burgers vector $\vec{b}$ along any contour $C$ enclosing the dislocation surface

(or line), i.e.

$$\oint_C d\vec{u} = \vec{b}. \tag{4.61}$$

We let a dislocation run at speed $V$ along a fault inclined at an angle $\delta$ with respect to the horizontal. The rupture starts at the point $x = 0$ and $z = -d$ (it is supposed to be infinitely long in the transverse $y-$direction), propagates at constant rupture speed $V$ for a finite time $L/V$ in the direction $\delta$ and stops at a distance $L$. Let $\zeta$ be a coordinate along the dislocation line. On the fault located in the interval $0 < \zeta < L$, the slip is assumed to be constant. The rise time is assumed to be 0. We insist here that in real situations, the fault is two-dimensional and the rupture velocity usually refers to the velocity at which the fault ruptures in the transverse $y-$direction (see for example [Oka88]).

#### 4.2.2.1 Discretization of the elastodynamics equations

In order to apply the FEM we rewrite the governing equation (4.60) in the domain $\Omega$ in variational form. One has

$$\int_\Omega \rho \frac{\partial^2 \vec{u}}{\partial t^2} \cdot \vec{v} \; d\Omega + \int_\Omega \underline{\underline{\sigma}}(\vec{u}) : \nabla \vec{v} \; d\Omega = \int_{\Gamma_N} \vec{f} \cdot \vec{v} \; dS, \quad \forall \vec{v} \in \mathcal{V},$$

where $\mathcal{V}$ is the linear closed subspace of $\left(H^1(\Omega)\right)^2$ and $\vec{f}$ is the loading applied to the Neumann boundary $\Gamma_N$. This term is equal to zero in our computations, since the seabed is considered to be a free boundary in geophysics.

In order to discretize the time derivative operator we apply a classical second order finite-difference scheme. We underline that the resulting method is fully implicit and has the advantage of being free of any CFL-type condition. In such problems implicit schemes become advantageous since the velocity of propagation of seismic waves is of the order of $3 - 4$ km/s. After discretizing in time, one obtains the following variational form:

$$\int_\Omega \rho \frac{\vec{u}^{(n+1)} - 2\vec{u}^{(n)} + \vec{u}^{(n-1)}}{\Delta t^2} \cdot \vec{v} \quad d\Omega + \int_\Omega \underline{\underline{\sigma}}(\vec{u}^{(n+1)}) \; : \; \nabla \vec{v} \quad d\Omega \; = \; \int_{\Gamma_N} \vec{f} \cdot \vec{v} \quad dS,$$

where the superscript denotes the time step number, e.g. $\vec{u}^{(n)} = \vec{u}(\mathbf{x}, t_n)$. Then, we apply the usual $\mathbb{P}2$ finite-element discretization procedure. For the numerical computations, we used the freely available code FreeFem++ [HPHO].

Let us say a few words about the boundary conditions and the treatment of the dislocation in the program. As already stated, the seabed is assumed to be a free surface:

$$\underline{\underline{\sigma}} \cdot \vec{n} = \vec{f} = \vec{0}, \quad z = 0.$$

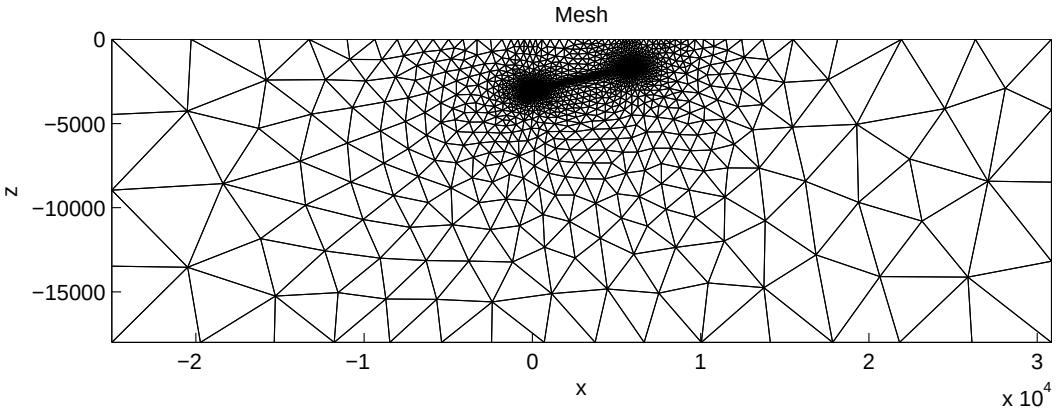


**Figure 4.15:** Typical mesh used in the numerical computations. The length scale is in meters.

The other boundaries are assumed to be fixed or in other words, we apply Dirichlet type boundary conditions $\vec{u} = \vec{0}$. The authors are aware of the reflective properties of this type of boundary conditions. But we take a computational domain which is sufficiently large, so that the seismic waves do not reach the boundaries during the simulation time. This approach is not computationally expensive since we use adaptive mesh algorithms [HPHO] and in the regions far from the fault, element sizes are considerably bigger than in the fault vicinity. A typical mesh used in simulations is plotted on Figure 4.15.

Now, let us discuss the implementation of the dislocation. Across the fault, the displacement field is discontinuous and satisfies the following relation:

$$\vec{u}^{+}(\mathbf{x}, t) - \vec{u}^{-}(\mathbf{x}, t) = \vec{b}(\mathbf{x}, t), \tag{4.62}$$

where the signs $\pm$ denote the upper and lower boundary of the dislocation surface, respectively. In order to satisfy the condition (4.62) we apply the following boundary conditions on the fault surface:

$$\vec{u}|_{\mathbf{x}\in\Gamma^{+}} = \frac{\vec{b}}{2}, \qquad \vec{u}|_{\mathbf{x}\in\Gamma^{-}} = -\frac{\vec{b}}{2}.$$

**Remark 4.** *Due to the presence of huge hydrostatic pressures in the crust, the two sides of the fault cannot detach physically. In any case this situation does not occur in nature. Mathematically it means that the Burgers vector $\vec{b}$ is tangent to the dislocation surface at each point.*

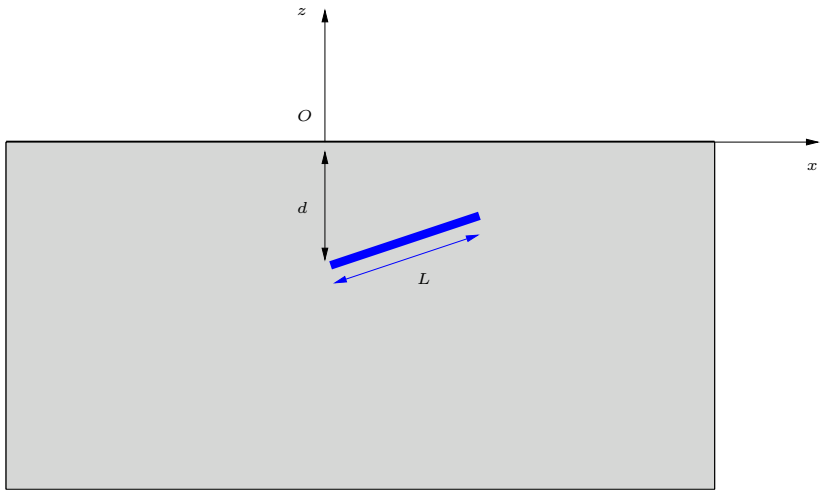


**Figure 4.16:** Test case with a homogeneous medium.

### 4.2.3 Numerical results

The numerical method described in the previous section was validated in our previous study [DD09b] by comparing numerical results with analytical results. In the present work we compare vertical displacements at the ocean bottom in two different situations. The first test case corresponds to the traditional modelling procedure where the Earth crust is assumed to be a homogeneous elastic material. It is schematically depicted on Figure 4.16. For example, the well known Okada solution[2] [Oka85], which is still widely used to construct initial conditions for various tsunami propagation codes, is based on these assumptions.

In the second test case, we add a sediment layer of thickness $h_s$ on top of the previous configuration. This situation is depicted on Figure 4.17. Let us provide some comments on the model for sediments chosen in this study. In fact, what we call sediments here is an elastic layer which has the mechanical properties of sand according to [Mei94]. It means that porosity and the two-phase nature of this medium are neglected. These effects should be investigated in the future. As stated by Okal [Oka88], detailed oceanic models of sedimentary structure have evidenced strong gradients of seismic velocities. The chosen sedimentary model is not extreme; much looser and weaker structures are encountered in nature.

Let us now discuss the results. First we present static solutions corresponding to the test cases described above. Two solutions are plotted on Figure 4.18. In this case we take a

[2]The original paper by Okada was published in 1985. In the Russian literature this solution was already known in 1978, after the publication of results by Gusiakov [Gus78]. Some particular cases of Okada solution were known even earlier [MS71, FB76].

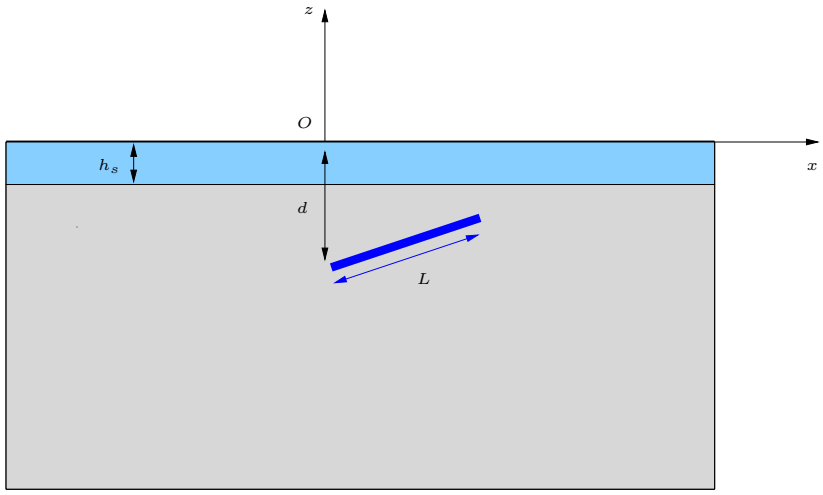


**Figure 4.17:** Test case with a sediment layer in between the oceanic column and the hard rock.

| **parameter** | **value** |
|---|---|
| Fault depth, $d$ | 4000 m |
| Dip angle, $\delta$ | 13° |
| Fault length, $L$ | 2000 m |
| Slip along the fault, $b$ | 10 m |
| Fault propagation velocity, $V$ | 2500 m/s |

**Table 4.3:** Values of fault parameters used in this study.

| **parameter** | **sand** | **granite** |
|---|---|---|
| Shear modulus $\mu$, Pa | $2 \times 10^8$ | $30 \times 10^9$ |
| Poisson's ratio | 0.3 | 0.27 |
| Shear wave velocity $\sqrt{\mu/\rho}$, m/s | 330 | 3230 |

**Table 4.4:** Values of mechanical parameters for sand and granite.

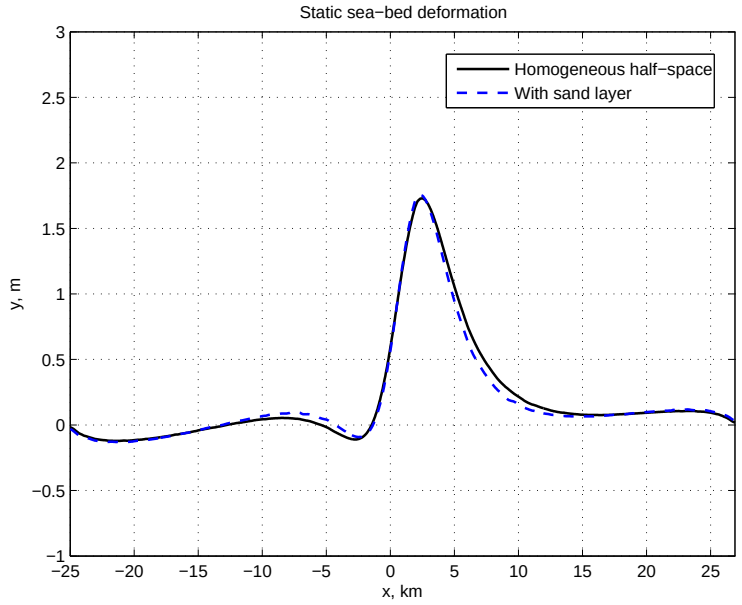


**Figure 4.18:** Volterra dislocation source. Static solutions with (dashed line) and without (solid line) sediments. The thickness of the sediment layer is $h_s = 600$ m.

sediment layer thickness $h_s$ equal to 600 m. In all figures of this section we plot the vertical displacement at the free surface of the Earth crust (or at the seabed, in other words). The values of the other parameters used in the computations are given in Tables 4.3 and 4.4. As the reader can see, there is no significant difference between the two solutions. In other words, sediments do not influence the static deformations due to a dislocation source. Physically, we can understand this situation, since in the static case the sand layer is just raised up by the deformed granite. Note that the parameters used here are not realistic. Indeed the length of the fault $L$ is quite small and we repeat that the fault is 1D. The slip $b$ is extremely large but since at this stage the problem is linear, the absolute value of the slip is not that important.

There is another rather mathematical explanation. In fact, as mentioned above, the steady Lamé equations[3] do not depend on Young's modulus but only on Poisson's ratio. Not surprisingly the Okada solution has the same property since the analytical expressions contain the Lamé coefficients in the combination $\lambda/(\lambda+\mu)$, which depends only on Poisson's ratio $\nu$. One can see in Table 4.4 that Poisson's ratio $\nu$ is almost the same for sand and granite. This is why the sediment layer does not have a strong effect on the steady solution.

Now, let us consider the dynamical effects. The results are presented on Figures 4.19–

[3]We assume that we neglect volume forces as well. So, the system of governing equations is homogeneous.

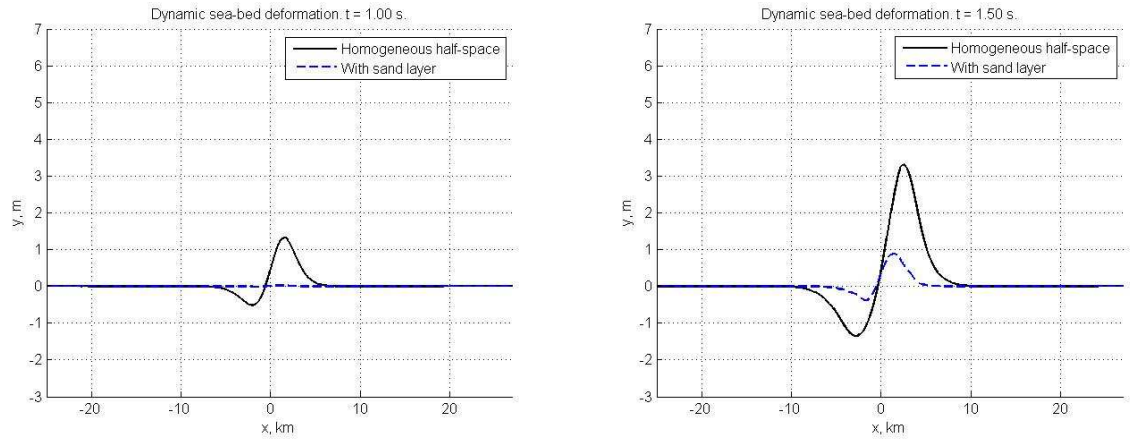


(a) $t = 1.0s$ (b) $t = 1.5s$

**Figure 4.19:** Dynamic sea-bed displacements at the beginning of the rupture process. The thickness of the sediment layer is $h_s = 600$ m.

4.21. In these computations we take the same thickness of the sand layer as in the static case ($h_s = 600$ m). It can be seen on Figure 4.19 that the deformation in the homogeneous case is initiated earlier. This is to be expected since the shear wave velocity in the sand is almost ten times slower than in the granite. Later, the deformation in the inhomogeneous case starts to evolve. It is surprising that it produces much bigger displacements – see Figure 4.20. In other words, taking into account the sediments increases considerably the seabed deformations. When time evolves, both solutions eventually reach comparable amplitudes (see Figure 4.21).

We performed other computations where the sediment layer thickness was reduced to 150 m. Results are presented on Figures 4.22–4.23. In this case, both solutions (homogeneous and inhomogeneous) evolve together and are almost indistinguishable within graphical accuracy. These results suggest to study the dependence of the vertical displacement amplitude on the sediment layer thickness.

#### 4.2.3.1 Sediment amplification factor

In order to quantify the influence of sediments on the vertical seabed displacements, we introduce a new quantity $\mathbf{S}_a$ that is called the *sediment amplification factor*. We give first the formula for $\mathbf{S}_a$ and then explain our definition.

**Definition 1.** *Let us denote by $v_0(x,t)$ and $v_s(x,t)$ the vertical displacements at the free surface in a homogeneous half-space and at the top of the sediment layer respectively*[4].

[4]In the idealized situation of our test cases, it means that we evaluate the vertical displacements at

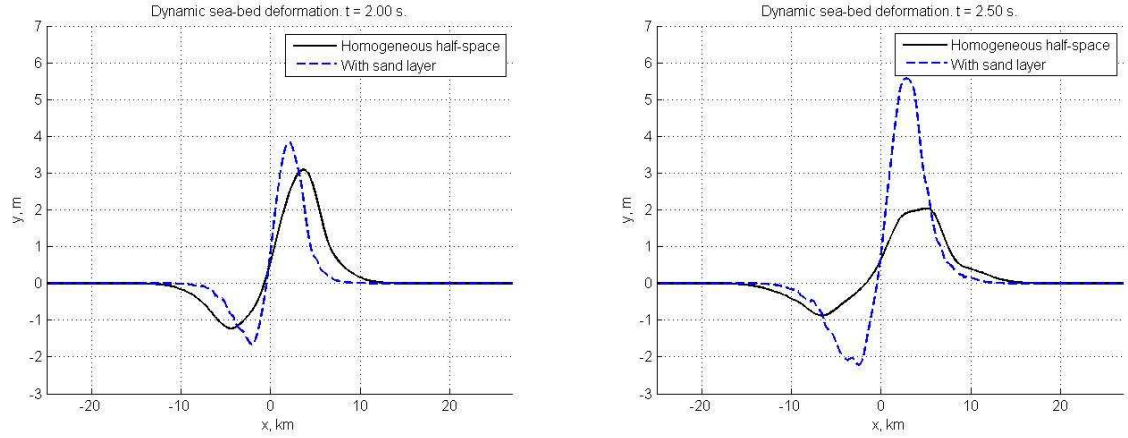


(a) $t = 2.0s$ (b) $t = 2.5s$

**Figure 4.20:** Dynamic sea-bed displacements. The solution, which takes into account the presence of the sediments, produces much bigger vertical displacements. The thickness of the sediment layer is $h_s = 600$ m.

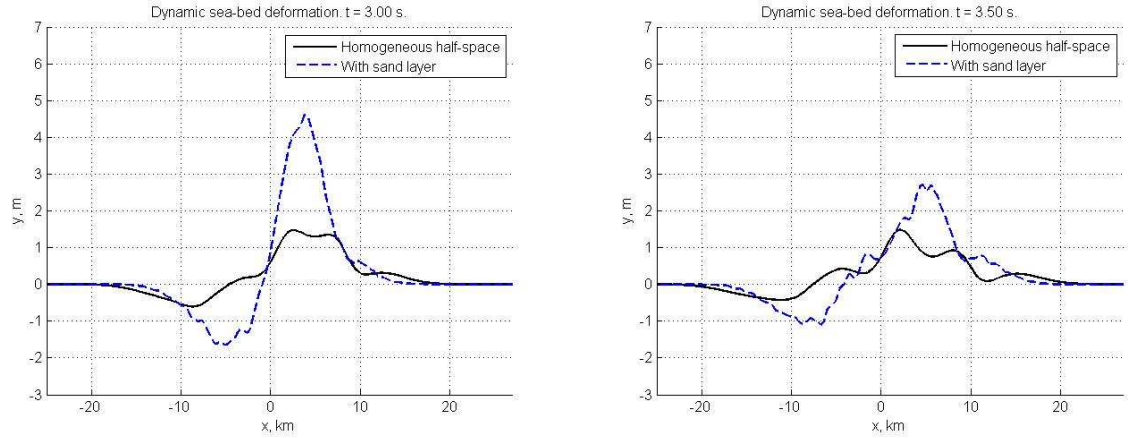


(a) $t = 3.0s$ (b) $t = 3.5s$

**Figure 4.21:** Dynamic sea-bed displacements at the end of the simulation. The thickness of the sediment layer is $h_s = 600$ m.

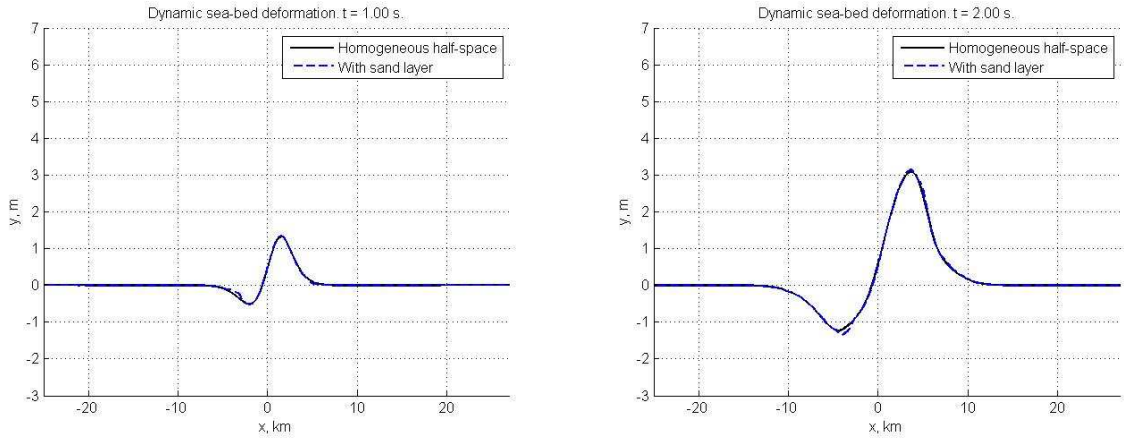


(a) $t = 1.0s$ (b) $t = 2.0s$

**Figure 4.22:** Dynamic sea-bed displacements at the beginning. The thickness of the sediment layer is $h_s = 150$ m.

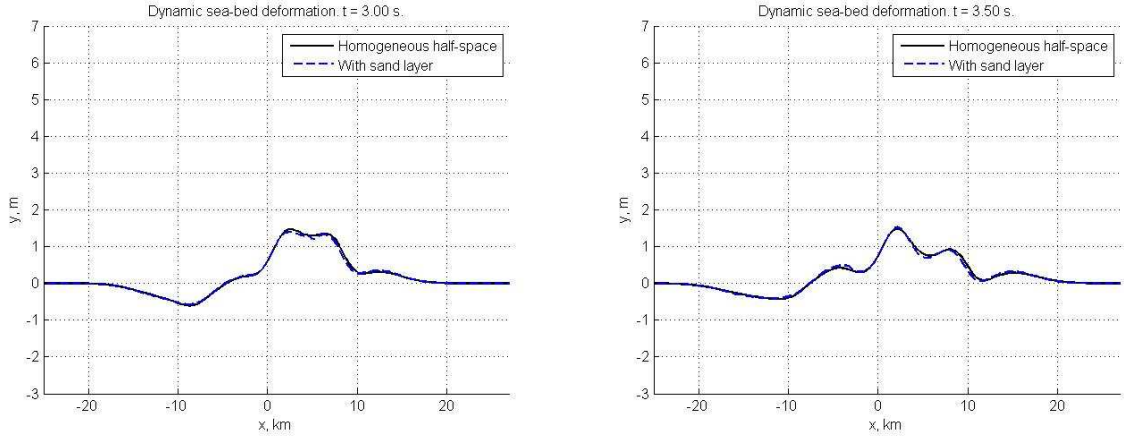


(a) $t = 3.0s$ (b) $t = 3.5s$

**Figure 4.23:** Dynamic sea-bed displacements. End of the process. The thickness of the sediment layer is $h_s = 150$ m.

*Then, the sediment amplification factor is defined as follows:*

$$\mathbf{S}_a = \frac{\max\limits_{(x,t)} |v_s(x,t)|}{\max\limits_{(x,t)} |v_0(x,t)|} - 1.$$

Let us provide some explanations. First of all, it is clear that we compare the values of two extreme amplitudes. The maximum is taken in both space and time, since both processes are not synchronised in time[5]. Finally, we substract one because we want the amplification factor to be equal to zero when sediments are absent.

Once this quantity $\mathbf{S}_a$ is defined, a parametric study must be performed. Here we are mainly interested in the dependence on the sediment layer thickness. But it is better to choose a dimensionless quantity. In this problem there are three lengths: the fault length $L$, the fault depth $d$ and the sediment layer thickness $h_s$. It is natural to choose the ratio $h_s/d$ as dimensionless parameter.

We performed a lot of computations for different values of $h_s/d$ and obtained the curve shown on Figure 4.24. It leads to several comments. On the left, the curve starts from zero and it is expected since the sediment layer disappears at this extremity. Thus, its amplification is equal to zero as well. It is interesting that the amplification factor has a maximum in the vicinity of $h_s/d = 0.12$. It means that there exists an optimal configuration when the sediment layer has its strongest effect. When we gradually increase the dimensionless parameter $h_s/d$ past the maximum, the amplification decreases. In the limit, one has to be careful as $h_s/d \to \infty$. Indeed one approaches an elastic half-space completely filled with sediment and dislocation theory may no longer be appropriate, especially if the material is loose.

### 4.2.4 Conclusions and perspectives

In the present study we investigated the influence of sedimentary layering on displacements due to an earthquake. We showed that there is practically no effect in the case of static deformation. This is to be expected in the framework of our model. Both curves can be superimposed up to graphical accuracy. On the other hand, dynamics makes a big difference. Our computations show that the vertical displacement amplitude can be amplified by a factor up to 1.7. We point out that there exists some kind of "optimal" sediment layer thickness, which provides the biggest amplification factor. Of course, this

$z = 0$.

[5] We saw on Figures 4.19 – 4.21 that the homogeneous solution evolves faster since sediments slow down the properties of elastic wave propagation.

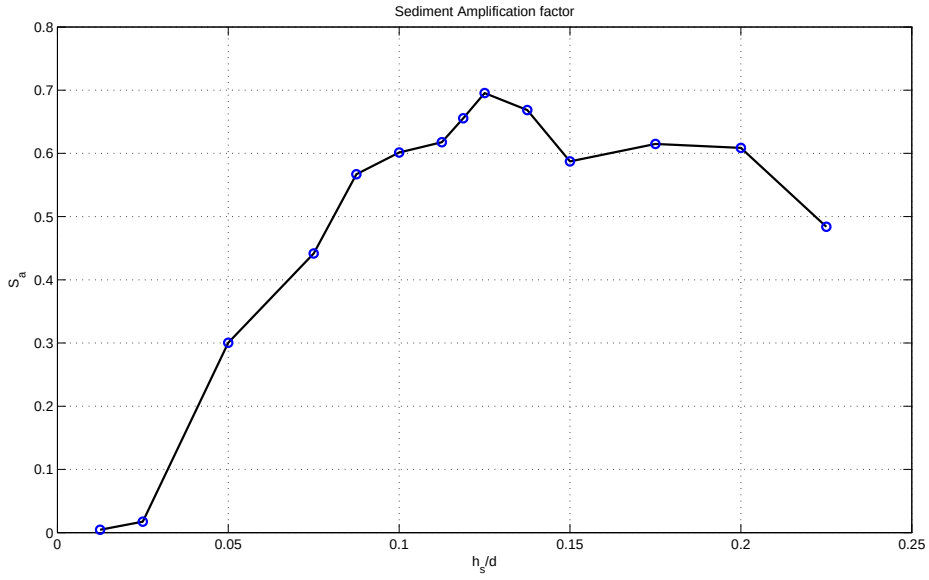


**Figure 4.24:** Dependence of the sediment amplification factor $S_a$ on the sand layer relative depth $h_s/d$.

optimal value depends on various mechanical parameters. It can be estimated in each specific situation by similar numerical techniques.

There is another predictible effect of the sediment layer. It slows down considerably the velocity of propagation of elastic and Rayleigh waves. In our simulations it is reflected by the fact that the maximum amplitude is reached much later than in the homogeneous case.

We introduced a new quantity $\mathbf{S}_a$, that we called *sediment amplification factor*. This dimensionless quantity measures the relative increase of the vertical displacement amplitude with respect to the homogeneous half-space solution. The dependence of this quantity $\mathbf{S}_a$ on the dimensionless thickness of the sediment layer was studied. We showed that there exists an optimal ratio $h_s/d \approx 0.125$ between sediment thickness and depth of the event which provides the biggest amplification factor $\mathbf{S}_a \approx 0.7$.

It is of interest to see how these results apply to the 2004 Indian Ocean Earthquake, which produced a megatsunami with local runup greater than 30 m at some locations [SK06]. According to Figure 4.13, we can estimate the sediment thickness $h_s$ in the generation region to be about 3 km. In [LKA+05, NSS+05], the centroid depth $d$ was set to 25 km for all fault subdivisions. If we compute the ratio of these parameters, we obtain $h_s/d = 0.12$. This value approximatively corresponds to the value (see Figure 4.24) which provides the maximal sediment amplification factor. The natural question is: is it a coin-

cidence? It is not possible to answer at this stage. Indeed the values we have used for the fault size are not realistic. Most likely there can be an amplification in real situations but not as large.

The overall conclusion of this study is that one may have to revise the initial conditions used in some tsunami simulations. More precisely one has to take care of situations where the generation region contains sediment deposits. Most likely it was the case of the Boxing Day Tsunami of 2004 [SB06]. Several researchers had to take unphysically large values of the slip along the fault[6] in order to generate a significant tsunami wave (see for example [IAK+07]). If one takes sediments into account, this value can be reduced while producing the same wave amplitude.

We finally outline some directions for future research in this field. First of all, the application of these techniques to real world events requires, of course, 3D computations, even if we do not think that it will change qualitatively our results. On the other hand, the fracturing through the sediments should be further investigated since it was conjectured to provide a much bigger amplification factor [Fuk79, Oka88]. At the same time, the question of the influence of sediment porosity has not been addressed in the present study and is left for future investigations. We have the feeling that porosity may enhance sea-bed deformations in the near field but it should be checked by thorough computations.

Finally it should be emphasized that the present study has focused on the deformation of the sea-bed. The question of the amplification of tsunami waves is a different one. Even if there is an effect in the near-field, it is not obvious that there is an effect in the far-field. The normal mode theory used by Okal [Oka88] provides an ideal framework to study both near-field and far-field effects. Moreover it is relatively easy to vary as many parameters as possible (focal depth, rupture velocity, dip angle, slip angle, thickness of sediment layer, fault size, sedimentary structure, etc).

[6] In terms of dislocations, it means the absolute value of the Burgers vector.

## 4.3 The VOLNA code for the numerical modeling of tsunami waves: generation, propagation and inundation

*I seem to have been only like a boy playing on the seashore, and diverting myself in now and then finding a smoother pebble or a prettier shell than ordinary, whilst the great ocean of truth lay all undiscovered before me.*

Sir Isaac Newton

ABSTRACT. A novel tool for tsunami wave modelling is presented. This tool has the potential of being used for operational purposes: indeed, the numerical VOLNA code is able to handle the complete life-cycle of a tsunami (generation, propagation and run-up along the coast). The algorithm works on unstructured triangular meshes and, thus, can be run in arbitrary complex domains. It is often the case since natural coasts tend to be of fractal shape [SBG04]. This paper contains the detailed description of the finite volume scheme implemented in the code. We explain the numerical treatment of the wet/dry transition. This point is crucial for accurate run-up computation. Most existing tsunami codes use semi-empirical techniques at this stage, which are not always sufficient. The main reason is that people evacuation is decided on the base of inundation maps which are produced with this type of numerical tools. Finally we present several realistic test cases that partially validate our algorithm. Comparisons with analytical solutions and experimental data are performed. Finally the main conclusions are outlined and the perspectives for future research presented.

### 4.3.1 Introduction

After the Boxing Day tsunami [SB06] there is no need to explain the importance of research on tsunami waves. One of the primary objectives in this field consists in establishing and developing Tsunami Warning Systems (TWS) [Tat97, TGB+05]. This task is non trivial as explained by Synolakis [Syn05]:

> For reference, the United States and Japan took more than 20 years to develop *validated numerical models* to predict tsunami evolution. And it took the US National Oceanic and Atmospheric Administration 30 years to fully develop its bottom-pressure recorders, which have been reliably detecting tsunamis for the past ten years.

After the Boxing Day tsunami, while developing their own national and regional capabilities, countries in the Indian Ocean and the Caribbean Sea have asked the PTWC (Pacific

Tsunami Warning Center) to act as their interim warning center. India and Australia now have fully working national centers, while the National Oceanic and Atmospheric Administration of the U.S. has assisted both with instrumentation and the sophisticated forecast technology used in the Pacific. Europe however is trying to reinvent the early warning wheel. As a result, the Mediterranean remains the only world ocean or sea unprotected by any warning system.

The mathematical modelling and computation of propagating tsunami waves play an important rôle in TWS. Precision and robustness of the algorithm will affect performance and reliability of the whole system.

The importance of tsunami generation modelling is often underestimated by the scientific community. During several years the research of our group was focused on this topic and many interesting results were obtained [DD07d, Dut07, DDK06, KDD07, DD09b, DD10]. We tried to incorporate some recent developments [DD07d] from this field into the VOLNA code.

It is difficult to find a topic in numerical analysis of hyperbolic PDEs which has been studied more than the numerical solution to the Nonlinear Shallow Water Equations (NSWE). The numerical scheme presented in this paper is not completely novel. The discretization methods used in VOLNA can be found in the modern literature on finite volumes methods [Kro97, BO04]. The main purpose here is to present a tool for tsunami wave modelling which covers the whole spectrum from generation to inundation. The emphasis is on the technical work which is typical of a numerical analyst and software developer. Tsunami practicioners can then concentrate on the physical aspects of tsunami propagation.

Nowadays, one is facing a somewhat strange situation. On one hand, there are only a few truly operational codes for tsunami wave modelling: MOST, NAMI, ComCot [Ima96, TG97, GOSI97, LWC98]. The numerical schemes used in these codes essentially correspond to the state of the art of the eighties. On the other hand, there is a plethora of NSWE codes developed in academic environments [Gla88, Cas90, Tor92, BDDV98, AC99, VC99, AGN05, BQ06, GNVC00, GHS03, ABB$^+$04, KCY07, Geo06, GL06, ZCIM02, CIM$^+$00, NPPN06, CFGR$^+$05, WMC06, Geo08, DKK08]. These codes use modern numerical methods but most of them run have been developed for rectangular domains and Cartesian meshes. They can be successfully used to test new numerical ideas, but these tools have little interest for tsunami operational research. This is why we had the idea to develop VOLNA . We tried to combine modern numerical techniques for hyperbolic systems with real world application-oriented design. The VOLNA code can be run efficiently in realistic environments. It was shown that natural coasts tend to have fractal forms [SBG04]. Hence, unstructured meshes are a natural choice in this type of situations.

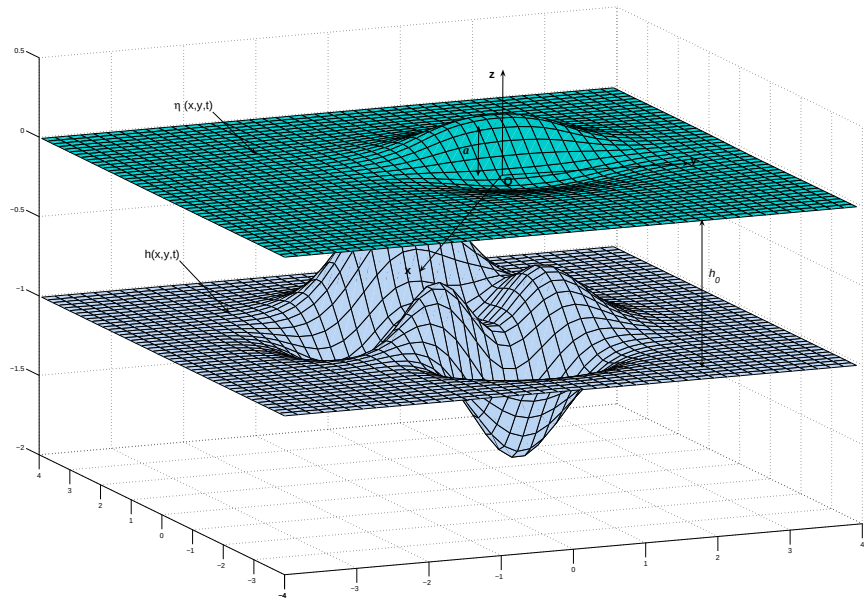


**Figure 4.25:** Sketch of the fluid domain.

The present study is organised as follows. In Section 4.3.2 the physical context of the study and some motivation for the choice of the mathematical model are presented. Section 4.3.3 contains a detailed description of the numerical method implemented in the VOLNA code. Then, we show in Section 4.3.4 some computations, which validate and illustrate the capabilities of VOLNA . Finally the main conclusions are outlined and the perspectives for future research presented in Section 4.3.5.

### 4.3.2 Physical context and mathematical model

In this study we focus on long wave propagation over realistic bathymetry. A sketch of the physical problem under investigation is given on Figure 4.25. Let us explain the main assumptions and the domain of applicability of the VOLNA code.

Introduce some characteristic lengths. We denote by $a_0$ the typical wave amplitude, by $h_0$ the average depth and by $\ell$ the characteristic wave length. Several dimensionless numbers can be built from these three quantities, but traditionally one introduces the following two:

$$\varepsilon = \frac{a_0}{h_0}, \quad \mu^2 = \left(\frac{h_0}{\ell}\right)^2.$$

The first parameter $\varepsilon$ measures the wave nonlinearity ($\varepsilon \ll 1$ means than nonlinearity is weak) while the second parameter $\mu^2$ quantifies the importance of dispersive effects ($\mu \ll 1$

means than dispersion is weak). Taking a typical megatsunami offshore with roughly

$$a_0 \simeq 0.5\ m, \quad h_0 \simeq 4\ km, \quad \ell \simeq 100\ km$$

yields $\varepsilon = 1.25 \times 10^{-4}$ for the nonlinearity parameter and $\mu^2 = 1.6 \times 10^{-3}$ for the dispersion parameter. Both are weak. Using asymptotic expansions in the small parameters $\varepsilon \ll 1$ and $\mu^2 \ll 1$, one can derive Serre-type equations [Ser53, Per67, MBS03, DD07b, DM10]. Note that no operational codes based on the Serre equations exist. For example FUNWAVE is not a truly operational code. Neglecting the dispersive effects yields the classical Nonlinear Shallow Water Equations (NSWE):

$$H_t + \nabla \cdot (H\vec{u}) = 0, \tag{4.63}$$

$$(H\vec{u})_t + \nabla \cdot \left( H\vec{u} \otimes \vec{u} + \frac{g}{2} H^2 \right) = gH\nabla h, \tag{4.64}$$

where $H = h + \eta$ is the total water depth and $\vec{u} = (u, v)(\mathbf{x}, t)$ is the depth-averaged horizontal velocity. Traditionally, $g$ denotes the acceleration due to the gravity and $h(\mathbf{x}, t)$ describes the bathymetry.

**Remark 5.** *The bathymetry $h(\mathbf{x}, t)$ is allowed to be time-dependent. It is important for the problem of tsunami generation by underwater earthquakes, submarine landslides, etc. The coupling with seismology is done through this function. Namely, various simplified earthquake models [DD07d, KDD07, DD09b, DD10] provide the seabed displacements which are then transmitted to the ocean layer.*

In this study, the NSWE (4.63) and (4.64) are chosen to model tsunami generation, propagation and run-up. It is computationally advantageous to have a uniform model for all stages of tsunami life since many technical problems are thus avoided. The validity of the NSWE for tsunami generation was already examined in our previous study [KDD07], where an excellent performance of this model was shown for nondispersive long waves. In the present paper we show in Section 4.3.4 the ability of the NSWE to model the run-up process. For this purpose, comparisons with a laboratory experiment are performed. Thus, the chosen *complete* approach to tsunami wave modelling is very attractive from both the operational and research viewpoints.

The governing equations (4.63) and (4.64) have several nice mathematical properties. In particular, this system is strictly hyperbolic provided that $H > 0$. This property will be used extensively in the construction of the numerical scheme (see Section 4.3.3).

Let us discuss the eigensystem of the advective flux. First, we introduce conservative variables and rewrite the governing equations as a system of conservation laws:

$$\frac{\partial \mathbf{w}}{\partial t} + \nabla \cdot \mathcal{F}(\mathbf{w}) = \mathbf{S}(\mathbf{w}), \tag{4.65}$$

where the following notation was introduced:

$$\mathbf{w}(x,t) : \mathbb{R}^2 \times \mathbb{R}^+ \mapsto \mathbb{R}^3, \qquad \mathbf{w} = (w_1, w_2, w_3) = (H, Hu, Hv),$$

$$\mathcal{F}(\mathbf{w}) = \begin{pmatrix} Hu & Hv \\ Hu^2 + \frac{g}{2}H^2 & Huv \\ Huv & Hv^2 + \frac{g}{2}H^2 \end{pmatrix} = \begin{pmatrix} w_2 & w_3 \\ \frac{w_2^2}{w_1} + \frac{g}{2}w_1^2 & \frac{w_2 w_3}{w_1} \\ \frac{w_2 w_3}{w_1} & \frac{w_3^2}{w_1} + \frac{g}{2}w_1^2 \end{pmatrix}, \mathbf{S}(\mathbf{w}) = \begin{pmatrix} 0 \\ gH\frac{\partial h}{\partial x} \\ gH\frac{\partial h}{\partial y} \end{pmatrix}.$$

After projecting the flux $\mathcal{F}(\mathbf{w})$ on a normal direction[7] $\vec{n} = (n_x, n_y)$, one can compute the Jacobian matrix $\mathbb{A}_n$. Its expression in physical variables has the following form:

$$\mathbb{A}_n = \frac{\partial(\mathcal{F}(\mathbf{w}) \cdot \vec{n})}{\partial \mathbf{w}} = \begin{pmatrix} 0 & n_x & n_y \\ -uu_n + gHn_x & u_n + un_x & un_y \\ -vu_n + gHn_y & vn_x & u_n + vn_y \end{pmatrix},$$

where $u_n = un_x + vn_y$ is the velocity vector projected on $\vec{n}$. The Jacobian matrix $\mathbb{A}_n$ has three distinct eigenvalues:

$$\lambda_1 = u_n - c, \quad \lambda_2 = u_n, \quad \lambda_3 = u_n + c, \tag{4.66}$$

where $c = \sqrt{gH}$ is the speed of gravity waves in the limit of infinite wavelength. This quantity plays the same rôle as the sound speed in compressible fluid mechanics. It is now obvious that the system (4.63), (4.64) is strictly hyperbolic provided that $H > 0$. The eigenstructure of the Jacobian matrix $\mathbb{A}_n$ is fundamental for constructing the numerical flux function (see Section 4.3.3.1) and thus, upwinding the discrete solution.

### 4.3.3 Discretization procedure

In this study we selected the most natural numerical method for this type of equations. Finite volume methods are a class of discretization schemes that have proven highly successful in solving numerically of a wide class of systems of conservation laws. These systems often come from compressible fluid dynamics. In electromagnetism, for example, Discontinuous Galerkin methods have proven to be more efficient [CLS04]. When compared to other discretization methods such as finite elements or finite differences, the primary advantages of finite volume methods are robustness, applicability on very general unstructured meshes, and the intrinsic local conservation properties. Hence, with this type of discretization, mass, momentum and total energy are conserved exactly[8].

[7] In the finite volume method one often projects onto the face normal.

[8] This statement is true in the absence of source terms and appropriate boundary conditions.

In order to solve numerically the system of balance laws (4.63), (4.64) one uses again the conservative form of governing equations (4.65). System (4.65) should be provided with an initial condition

$$\mathbf{w}(\mathbf{x}, 0) = \mathbf{w}_0(\mathbf{x}), \quad \mathbf{x} = (x, y) \in \Omega \tag{4.67}$$

and appropriate boundary conditions. The implementation of different boundary conditions will be discussed below (see Section 4.3.3.7).

#### 4.3.3.1 First order scheme

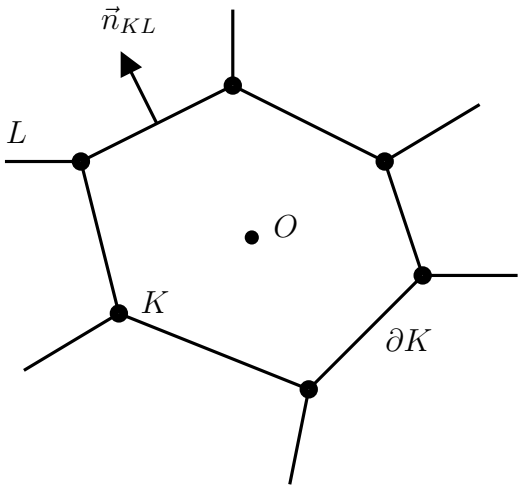


**Figure 4.26:** An example of control volume $K$ with barycenter $O$. The normal pointing from $K$ to $L$ is denoted by $\vec{n}_{KL}$.

The computational domain $\Omega \subset \mathbb{R}^2$ is triangulated into a set of non overlapping control volumes that completely cover the domain. Let $\mathbf{T}$ denote a tesselation of the domain $\Omega$ with control volume $K$ such that

$$\cup_{K \in \mathbf{T}} \bar{K} = \bar{\Omega}, \quad \bar{K} := K \cup \partial K.$$

For two distinct control volumes $K$ and $L$ in $\mathbf{T}$, the intersection is an edge with oriented normal $\vec{n}_{KL}$ or else a vertex. We need to introduce the following notation for the neighbourhood of $K$:

$$\mathcal{N}(K) := \{L \in \mathbf{T} : \text{area}(K \cap L) \neq 0\},$$

a set of all control volumes $L$ which share an edge in 2D or a face in 3D with the given volume $K$. In this study, we denote by $\text{vol}(\cdot)$ and $\text{area}(\cdot)$ the area and length respectively.

The choice of control volume tesselation is flexible in the finite volume method. In the present study we selected the cell-centered approach (see Figure 4.27), which means that degrees of freedom are associated to cell barycenters. There exists an alternative vertex-centered method [BJ89, BO04] (see Figure 4.28) which requires the construction of dual mesh even for first-order schemes. In the *cell-centered* finite volume scheme, the triangles themselves serve as control volumes with solution unknowns attributed to triangles barycenters. In the *vertex-centered* finite volume scheme, control volumes are formed as a geometric dual to the triangle complex and solution unknowns stored on vertex basis.

**Remark 6.** *Except for the construction of dual mesh in the vertex-centered approach, these two methods are almost equivalent in the interior of the computational domain $\Omega$. However, the boundary conditions treatment is different and it is harder (or less natural in the authors' opinion) when data is stored at vertices. This is one more reason why we selected cell centers to store the solution's information.*

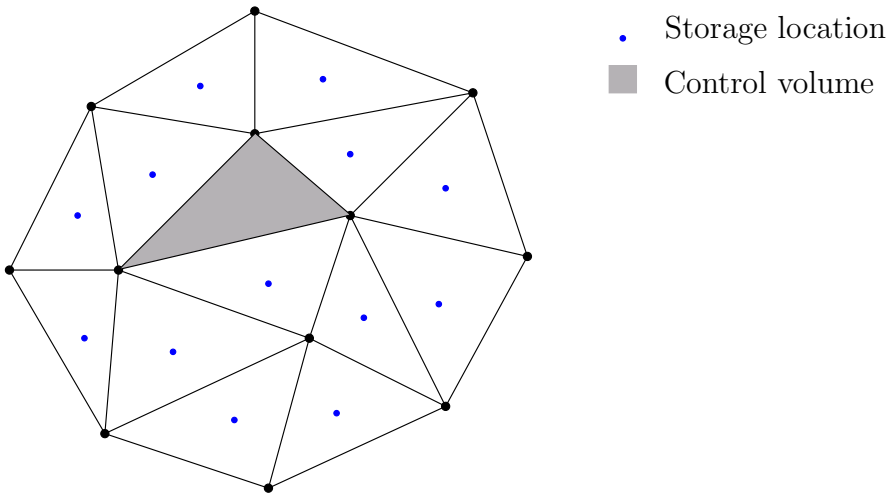


**Figure 4.27:** Illustration for cell-centered finite volume method

The first steps in Finite Volume (FV) methods are classical. One starts by integrating equation (4.65) on the control volume $K$ (see Figure 4.26 for illustration) and one applies Gauss-Ostrogradsky theorem for advective and diffusive fluxes. Then, in each control volume, an integral conservation law statement is imposed:

$$\frac{d}{dt}\int_K \mathbf{w}\, d\Omega + \int_{\partial K} \mathcal{F}(\mathbf{w})\cdot \vec{n}_{KL}\, d\sigma = \int_K \mathbf{S}(\mathbf{w})\, d\Omega \tag{4.68}$$

Physically an integral conservation law states that the rate of change of the total amount of a quantity (for example: mass, momentum, total energy) with density $\mathbf{w}$ in a fixed control

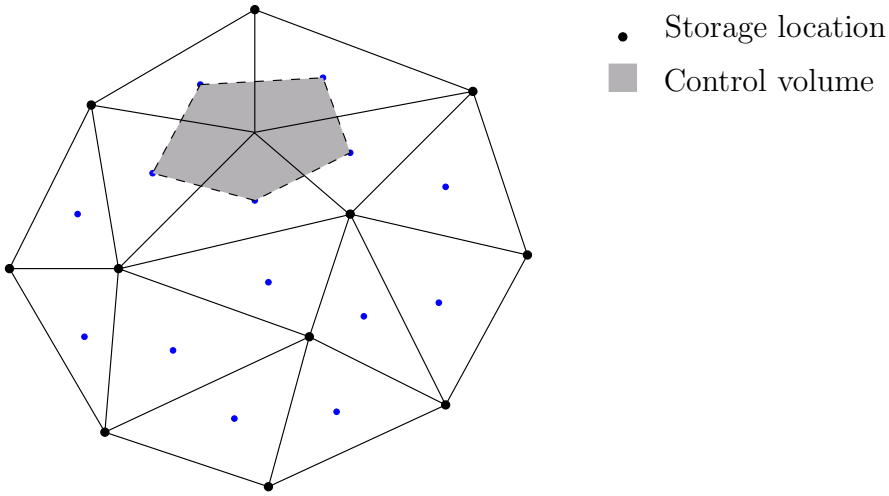


**Figure 4.28:** Illustration for vertex-centered finite volume method

volume $K$ is balanced by the flux $\mathcal{F}$ of the quantity through the boundary $\partial K$ and the production of this quantity $\mathbf{S}$ inside the control volume.

The next step consists in introducing the control volume cell average for each $K \in \mathbf{T}$

$$\mathbf{w}_K(t) := \frac{1}{\mathrm{vol}(K)} \int_K \mathbf{w}(\mathbf{x}, t)\, d\Omega \,.$$

After the averaging step, the finite volume method can be interpreted as producing a system of evolution equations for cell averages, since

$$\frac{d}{dt} \int_K \mathbf{w}(\mathbf{x}, t)\, d\Omega = \mathrm{vol}(K) \frac{d\mathbf{w}_K}{dt} \,.$$

Godunov was first [God59] to pursue and apply these ideas to the discretization of the gas dynamics equations.

However, the averaging process implies piecewise constant solution representation in each control volume with value equal to the cell average. The use of such a representation makes the numerical solution multivalued at control volume interfaces. Thereby the calculation of the fluxes $\int_{\partial K} (\mathcal{F}(\mathbf{w}) \cdot \vec{n}_{KL})\, d\sigma$ at these interfaces is ambiguous. A fundamental aspect of finite volume methods is the idea of substituting the true flux at interfaces by a numerical flux function

$$\left(\mathcal{F}(\mathbf{w}) \cdot \vec{n}\right)\big|_{\partial K \cap \partial L} \longleftarrow \Phi(\mathbf{w}_K, \mathbf{w}_L; \vec{n}_{KL}) : \mathbb{R}^3 \times \mathbb{R}^3 \mapsto \mathbb{R}^3 \,,$$

a Lipschitz continuous function of the two interface states $\mathbf{w}_K$ and $\mathbf{w}_L$. The key ingredient is the choice of the numerical flux function $\Phi$. In general this function is calculated as an exact or even better approximate local solution of the Riemann problem posed at these

interfaces. In the present study we implemented several numerical fluxes (HLL, HLLC, FVCF) described below.

Any numerical flux is assumed to satisfy the following properties:

**Conservation.** This property ensures that fluxes from adjacent control volumes sharing an interface exactly cancel when summed. This is achieved if the numerical flux function satisfies the identity

$$\Phi(\mathbf{w}_K, \mathbf{w}_L; \vec{n}_{KL}) = -\Phi(\mathbf{w}_L, \mathbf{w}_K; \vec{n}_{LK}).$$

**Consistency.** Consistency is obtained when the numerical flux with identical state arguments (in other words it means that the solution is continuous through an interface) reduces to the true flux of the same state, i.e.

$$\Phi(\mathbf{w}, \mathbf{w}; \vec{n}) = (\mathcal{F}(\mathbf{w}) \cdot \vec{n})(\mathbf{w}).$$

In the following paragraphs 4.3.3.1.1 – 4.3.3.1.3 we give several examples of numerical flux functions $\Phi(\mathbf{v}, \mathbf{w}; \vec{n})$ which were implemented in the VOLNA code. These choices are justified by efficiency, clarity and personal preferences of the authors. However, we do not impose them and a final user can easily implement his favourite numerical flux function.

**4.3.3.1.1 FVCF approach** First we describe the scheme called Finite Volumes with Characteristic Flux (FVCF) and proposed by Ghidaglia et al. in [Ghi95, GKC96, GKC01].

Consider a general system of conservation laws in 1D that can be written as follows:

$$\frac{\partial w}{\partial t} + \frac{\partial f(w)}{\partial x} = 0\,, \tag{4.69}$$

where $w \in \mathbb{R}^m$ and $f : \mathbb{R}^m \mapsto \mathbb{R}^m$. We denote by $A(w)$ the Jacobian matrix $\frac{\partial f(w)}{\partial w}$ and we deal with the case where (4.69) is *smoothly hyperbolic*, that is to say: for every $w$ there exists a smooth basis $(r_1(w), \ldots, r_m(w))$ of $\mathbb{R}^m$ consisting of eigenvectors of $A(w)$. That is $\exists \lambda_k(w) \in \mathbb{R}$ such that $A(w)r_k(w) = \lambda_k(w)r_k(w)$. It is then possible to construct $(l_1(w), \ldots, l_m(w))$ such that ${}^tA(w)l_k(w) = \lambda_k(w)l_k(w)$ and $l_k(w) \cdot r_p(w) = \delta_{k,p}$.

Let $\mathbb{R} = \cup_{j\in\mathbb{Z}}[x_{j-1/2}, x_{j+1/2}]$ be a one dimensional mesh. The goal is to discretize (4.69) by a finite volume method. We set $\Delta x_j \equiv x_{j+1/2} - x_{j-1/2}$, $\Delta t_n \equiv t_{n+1} - t_n$ (we also have $\mathbb{R}_+ = \cup_{n\in\mathbb{N}}[t_n, t_{n+1}]$) and

$$\tilde{w}_j^n \equiv \frac{1}{\Delta x_j}\int_{x_{j-1/2}}^{x_{j+1/2}} w(x, t_n)\, dx\,, \quad \tilde{f}_{j+1/2}^n \equiv \frac{1}{\Delta t_n}\int_{t_n}^{t_{n+1}} f(w(x_{j+1/2}, t))\, dt\,.$$

With these notations, we deduce from (4.69) the *exact* relation:

$$\tilde{w}_j^{n+1} = \tilde{w}_j^n - \frac{\Delta t_n}{\Delta x_j}\left(\tilde{f}_{j+1/2}^n - \tilde{f}_{j-1/2}^n\right) . \tag{4.70}$$

Since the $(\tilde{f}_{j+1/2}^n)_{j\in\mathbb{Z}}$ cannot be expressed in terms of the $(\tilde{w}_j^n)_{j\in\mathbb{Z}}$, one has to make an approximation. In order to keep a compact stencil, it is more efficient to use a three point scheme: the physical flux $\tilde{f}_{j+1/2}^n$ is approximated by a numerical flux $g_j^n(w_j^n, w_{j+1}^n)$. Let us show how this flux is constructed here. Since $A(w)\frac{\partial w}{\partial t} = \frac{\partial f(w)}{\partial t}$ we observe that according to (4.69)

$$\frac{\partial f(w)}{\partial t} + A(w)\frac{\partial f(w)}{\partial x} = 0 . \tag{4.71}$$

This shows that the flux $f(w)$ is advected by $A(w)$ like $w$. The numerical flux $g_j^n(w_j^n, w_{j+1}^n)$ represents the flux at an interface. Using a mean value $\mu_{j+1/2}^n$ of $w$ at this interface, we replace (4.71) by the linearization:

$$\frac{\partial f(w)}{\partial t} + A(\mu_{j+1/2}^n)\frac{\partial f(w)}{\partial x} = 0 . \tag{4.72}$$

It follows that, defining the $k$-th characteristic flux component to be $f_k(w) \equiv l_k(\mu_{j+1/2}^n)\cdot f(w)$, one has

$$\frac{\partial f_k(w)}{\partial t} + \lambda_k(\mu_{j+1/2}^n)\frac{\partial f_k(w)}{\partial x} = 0 . \tag{4.73}$$

This linear equation can be solved explicitly now:

$$f_k(w)(x,t) = f_k(w)(x - \lambda_k(\mu_{j+1/2}^n)(t-t_n), t_n) . \tag{4.74}$$

From this equation it is then natural to introduce the following definition.

**Definition 2.** *For the conservative system (4.69), at the interface between the two cells* $[x_{j-1/2}, x_{j+1/2}]$ *and* $[x_{j+1/2}, x_{j+3/2}]$*, the characteristic flux* $g^{CF}$ *is defined by the following formula for* $k \in \{1, \dots, m\}$ *:*
$\Big($*we take* $\mu_{j+1/2}^n \equiv \big(\Delta x_j w_j^n + \Delta x_{j+1} w_{j+1}^n\big)/\big(\Delta x_j + \Delta x_{j+1}\big)\Big)$

$$\begin{aligned}
l_k(\mu_{j+1/2}^n)\cdot g_j^{CF,n}(w_j^n, w_{j+1}^n) &= l_k(\mu_{j+1/2}^n)\cdot f(w_j^n) , \ \textit{when } \lambda_k(\mu_{j+1/2}^n) > 0 , \\
l_k(\mu_{j+1/2}^n)\cdot g_j^{CF,n}(w_j^n, w_{j+1}^n) &= l_k(\mu_{j+1/2}^n)\cdot f(w_{j+1}^n) , \ \textit{when } \lambda_k(\mu_{j+1/2}^n) < 0 , \\
l_k(\mu_{j+1/2}^n)\cdot g_j^{CF,n}(w_j^n, w_{j+1}^n) &= l_k(\mu_{j+1/2}^n)\cdot \left(\frac{f(w_{j+1}^n) + f(w_j^n)}{2}\right) ,
\end{aligned} \tag{4.75}$$

*when* $\lambda_k(\mu_{j+1/2}^n) = 0$.

**Remark 7.** *At first glance, the derivation of (4.71) from (4.69) is only valid for continuous solutions since* $A(w)\frac{\partial f(w)}{\partial x}$ *is a non conservative product. In fact, equation (4.71) can be justified even in the case of shocks as proved in [Ghi98]. Let us briefly recall here the key point. Assuming that the solution undergoes a discontinuity along a family of disjoint curves, we can focus on one of these curves that we parameterize by the time variable* $t$*. Hence, locally, on each side of this curve,* $w(x,t)$ *is smooth and jumps across the curve* $x = \Sigma(t)$*. The Rankine-Hugoniot condition implies that* $f(w(x,t)) - \sigma(t)w(x,t)$*, where* $\sigma(t) \equiv \frac{d\Sigma(t)}{dt}$*, is smooth across the discontinuity curve and therefore* $A(w)\frac{\partial f(w)}{\partial x}$ *can be defined as* $A(w)\frac{\partial f(w)}{\partial x} \equiv A(w)\frac{\partial (f(w)-\sigma w)}{\partial x} + \sigma\frac{\partial f(w)}{\partial x}$ *.*

**Lemma 1.** *Formula (4.75) can be written as follows:* $g_j^{CF,n}(w_j^n, w_{j+1}^n) = g^{CF}(\mu_j^n; w_j^n, w_{j+1}^n)$ *where*

$$g^{CF}(\mu; v, w) \equiv \sum_{\lambda_k(\mu)<0} (l_k(\mu)\cdot f(w))r_k(\mu) + \sum_{\lambda_k(\mu)=0} \left(l_k(\mu)\cdot \frac{f(v)+f(w)}{2}\right) r_k(\mu) + \\ + \sum_{\lambda_k(\mu)>0} (l_k(\mu)\cdot f(v))r_k(\mu)\,. \quad (4.76)$$

*Proof.* This comes from the useful identity valid for all vectors $\Phi$ and $\mu$ in $\mathbb{R}^m$: $\Phi = \sum_{k=1}^{k=m}(l_k(\mu)\cdot\Phi)r_k(\mu)$. We also observe that (4.76) can be written under the following condensed form:

$$g^{CF}(\mu; v, w) = \frac{f(v)+f(w)}{2} - U(\mu; v, w)\frac{f(w)-f(v)}{2}\,, \quad (4.77)$$

where $U(\mu; v, w)$ is the sign of the matrix $A(\mu)$ which is defined by

$$\mathrm{sign}(A(\mu))\Phi = \sum_{k=1}^{m} \mathrm{sign}(\lambda_k)(l_k(\mu)\cdot\Phi)r_k(\mu).$$

The form (4.77) refers to what we have called a numerical flux leading to a flux scheme [Ghi98]. ∎

**Remark 8.** *Let us discuss the relation, in the conservative case, between the characteristic numerical flux* $g^{CF}$ *and the numerical flux leading to Roe's scheme [Roe81]. The latter scheme relies on an algebraic property of the continuous flux* $f(w)$ *which is as follows. It is assumed that for all admissible states* $v$ *and* $w$*, there exists a* $m \times m$ *matrix* $A^{ROE}(v,w)$ *such that* $f(v) - f(w) = A^{ROE}(v,w)(v-w)$ *(Roe's identity). Then the numerical flux leading to Roe's scheme is given by:*

$$g^{ROE}(v,w) = \frac{f(v)+f(w)}{2} - |A^{ROE}(v,w)|\frac{w-v}{2}\,. \quad (4.78)$$

*But using Roe's identity, we obtain that*

$$g^{ROE}(v,w) = \frac{f(v)+f(w)}{2} - \text{sign}(A^{ROE}(v,w))\frac{f(w)-f(v)}{2}, \tag{4.79}$$

*which is of the form (4.77): Roe's scheme is also a flux scheme. The characteristic flux proposed in this paper is more versatile than Roe's scheme in the sense that it does not rely on an algebraic property of the flux. Hence for complex systems (like those encountered in the context of two phase flows) this scheme appears like an efficient generalization of Roe's scheme. Moreover, as we shall see below, this scheme has a natural generalization to arbitrary non conservative systems. Finally, the fact that the numerical flux is a linear combination of the two fluxes induces a quite weak dependence on the state $\mu$ which appears in formula (4.76), see [CG00].*

**4.3.3.1.2 HLL numerical flux** Now we present another approximate Riemann solver which was proposed by Harten, Lax and van Leer [HLvL83]. Nowadays this method is known as the HLL scheme. While the exact solution to the Riemann problem contains a large amount of detail, the HLL solver assumes fewer intermediate waves. The simplified Riemann fan is illustrated on Figure 4.29. It consists of two waves separating three constant states.

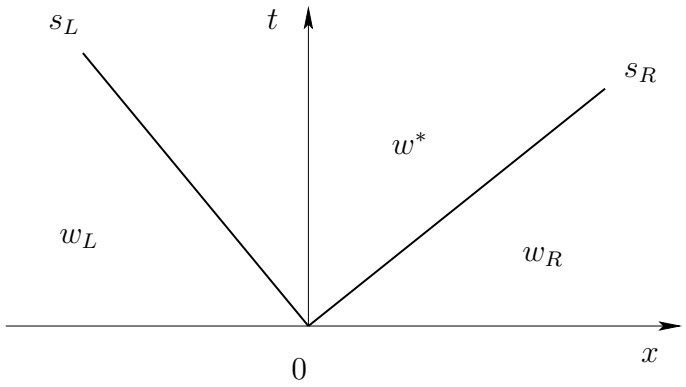


**Figure 4.29:** Approximate Riemann fan corresponding to the HLL scheme.

Consider the following Riemann problem:

$$\mathcal{R}(w_L,w_R): \begin{cases} \frac{\partial w}{\partial t} + \frac{\partial F(w)}{\partial x} = 0, \\ w(x,0) = \begin{cases} w_L, & x<0, \\ w_R, & x>0. \end{cases} \end{cases} \tag{4.80}$$

The intermediate state in the approximate Riemann fan will be denoted by $w^*$ and two shock wave speeds are denoted by $s_L$ and $s_R$ respectively (see Figures 4.29 and 4.30

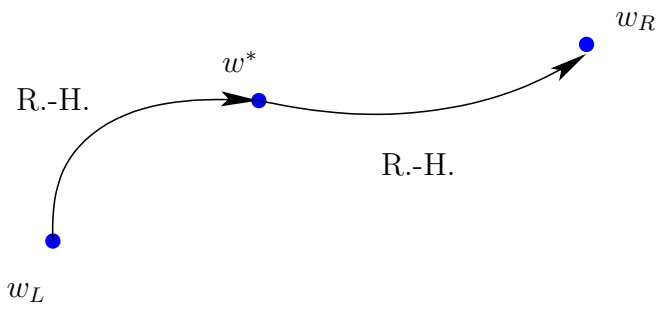


**Figure 4.30:** Two states $w_L$ and $w_R$ connected by Rankine-Hugoniot curves represented in the phase space.

for illustration). In order to determine the unknown intermediate state, we write the Rankine-Hugoniot conditions twice:

$$\begin{cases} s_L(w^* - w_L) &= F^* - F_L, \\ s_R(w_R - w^*) &= F_R - F^*, \end{cases}$$

where $F_{L,R} := F(w_{L,R})$. It is straightforward to find the solution to this system:

$$w^* = \frac{s_R w_R - s_L w_L - (F_R - F_L)}{s_R - s_L},$$

$$F^* = F_L + s_L(w^* - w_L) = \frac{s_R F_L - s_L F_R + s_L s_R (w_R - w_L)}{s_R - s_L}. \tag{4.81}$$

Now we have all the elements to define the numerical flux of the HLL scheme:

$$\Phi_{HLL}(w_L, w_R) := \begin{cases} F_L, & s_L \geq 0, \\ F^*, & s_L < 0 \leq s_R, \\ F_R, & s_R < 0. \end{cases}$$

During the presentation of the HLL scheme we missed one important point: how to estimate the wave speeds $s_L$ and $s_R$? The answer is crucial for the overall performance of the scheme. With appropriate choices for the wave speeds $s_L$ and $s_R$, the HLL scheme possesses very nice numerical properties. Namely, it satisfies an entropy inequality [Dav88], resolves isolated shocks exactly [HLvL83] and preserves positivity [EMRS91]. In our code we implemented the following choice for $s_L$ and $s_R$ which is motivated by analytical expressions for the Jacobian eigenvalues (4.66):

$$s_L = \min(u_L - c_L, u^* - c^*), \quad s_R = \min(u^* + c^*, u_R + c_R),$$

where $c_{L,R} := \sqrt{g H_{L,R}}$ is the gravity wave speed for the left and right states and

$$u^* = \frac{1}{2}(u_L + u_R) + c_L - c_R, \quad c^* = \frac{1}{2}(c_L + c_R) - \frac{1}{4}(u_R - u_L).$$

Numerical experiments show that this approximate Riemann solver is very robust with the above choice for the wave speeds [CIM+00, ZCIM02].

However, the HLL scheme has one important shortcoming: it cannot resolve isolated contact discontinuities. In the next section 4.3.3.1.3 we present another scheme which was designed to remedy this problem.

**Remark 9.** *Does the HLL scheme belong to the class of flux schemes or not? Recall that a finite volume scheme is called a flux scheme if its numerical flux can be written in the following form:*

$$\Phi = \frac{F(w_L) + F(w_R)}{2} - U(w_L, w_R)\frac{F(w_R) - F(w_L)}{2},$$

*where $U(w_L, w_R)$ is some matrix. From the formula (4.81) for the flux $F^*$ it follows that the answer depends on the existence of a matrix $M$ such that*

$$w_R - w_L = M(F_R - F_L) \quad \text{or} \quad F_R - F_L = M^{-1}(w_R - w_L).$$

*Fortunately, the answer is positive for NSWE and the matrix $M$ can be effectively constructed. It allows us to rewrite the HLL numerical flux in the shorthand form $\Phi_{HLL} = U_R F_R + U_L F_L$, where*

$$U_R = \begin{cases} 0, & s_L \geq 0, \\ \frac{s_L s_R}{s_R - s_L} M - \frac{s_L}{s_R - s_L}\underline{\underline{I}}, & s_L < 0 \leq s_R, \\ \underline{\underline{I}}, & s_R < 0, \end{cases} \qquad U_L = \begin{cases} \underline{\underline{I}}, & s_L \geq 0, \\ -\frac{s_L s_R}{s_R - s_L} M + \frac{s_R}{s_R - s_L}\underline{\underline{I}}, & s_L < 0 \leq s_R, \\ 0, & s_R < 0, \end{cases}$$

*with $\underline{\underline{I}} := (\delta_{ij})$. In part, the robustness of the HLL scheme can be explained by this nice property.*

#### 4.3.3.1.3 HLLC flux

The HLL scheme presented briefly in the previous section was later improved by Toro, Spruce and Speares [TSS94]. Their modification concerns essentially the structure of the Riemann fan which is depicted on Figure 4.31. Namely, they introduced a contact discontinuity between two shock waves of the HLL scheme. That is why the novel scheme was called the HLLC scheme [FT95].

Here we do not provide details on the derivation of the HLLC scheme and refer to the original articles and others which can feel this gap [BCCC97, KCY07].

We consider the same Riemann problem (4.80). In the HLLC approximation, the solution to this Riemann problem consists of three waves with speeds $s_L$, $s^*$ and $s_R$ separating four constant states $w_L$, $w_L^*$, $w_R^*$ and $w_R$. Wave speeds $s_{L,R}$ are estimated as in previous section 4.3.3.1.2, while $s^*$ is given by this formula:

$$s^* = \frac{s_L H_R(u_R - s_R) - s_R H_L(u_L - s_L)}{H_R(u_R - s_R) - H_L(u_L - s_L)}.$$

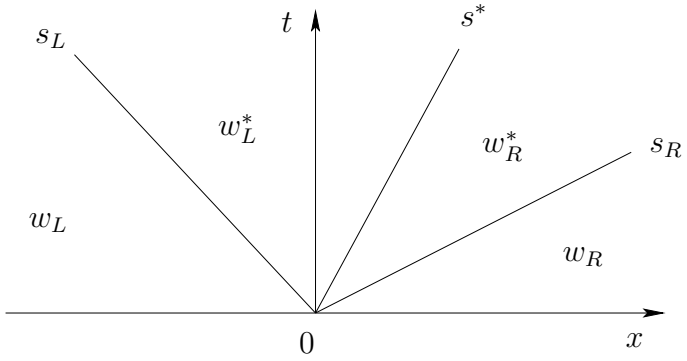


**Figure 4.31:** Approximate Riemann fan corresponding to the HLLC scheme.

The intermediate states $w^*_{L,R} = (H^*_{L,R}, (Hu)^*_{L,R}, (Hv)^*_{L,R})$ are computed in this way:

$$\begin{aligned}
H^*_{L,R} &= \tfrac{s_{L,R}-u_{L,R}}{s_{L,R}-s^*} H_{L,R},\\
(Hu)^*_{L,R} &= \tfrac{s_{L,R}-u_{L,R}}{s_{L,R}-s^*}(Hu)_{L,R} + \tfrac{g}{2}H^2_{L,R}\tfrac{(2s_{L,R}-s^*-u_{L,R})(s^*-u_{L,R})}{(s_{L,R}-s^*)^3},\\
(Hv)^*_{L,R} &= \tfrac{s_{L,R}-u_{L,R}}{s_{L,R}-s^*}(Hv)_{L,R} + \tfrac{g}{2}H^2_{L,R}\tfrac{(2s_{L,R}-s^*-u_{L,R})(s^*-u_{L,R})}{(s_{L,R}-s^*)^3}.
\end{aligned}$$

Finally, the numerical flux of the HLLC scheme is defined as

$$\Phi_{HLLC}(w_L, w_R) := \begin{cases} F_L, & s_L \geq 0,\\ F^*_L := F_L + s_L(w^*_L - w_L), & s_L < 0 \leq s^*,\\ F^*_R := F_R + s_R(w^*_R - w_R), & s^* < 0 \leq s_R,\\ F_R, & s_R < 0. \end{cases}$$

**Remark 10.** *As in the previous scheme, one can check whether the HLLC scheme is a flux scheme or not. It turns out that it is.*

#### 4.3.3.2 Semidiscrete scheme

After introducing the cell averages $\mathbf{w}_K$ and numerical fluxes into (4.68), the integral conservation law statement becomes

$$\frac{d\mathbf{w}_K}{dt} + \sum_{L\in\mathcal{N}(K)} \frac{\text{area}(L\cap K)}{\text{vol}(K)}\Phi(\mathbf{w}_K, \mathbf{w}_L; \vec{n}_{KL}) = \frac{1}{\text{vol}(K)}\int_K \mathbf{S}(\mathbf{w})\, d\Omega\,.$$

We denote by $\mathbf{S}_K$ the approximation of the quantity $\frac{1}{\text{vol}(K)}\int_K \mathbf{S}(\mathbf{w})\, d\Omega$. The source term discretization is discussed in Section 4.3.3.4. Thus, the following system of ordinary differential equations (ODE) is called a semi-discrete finite volume method:

$$\frac{d\mathbf{w}_K}{dt} + \sum_{L\in\mathcal{N}(K)} \frac{\text{area}(L\cap K)}{\text{vol}(K)}\Phi(\mathbf{w}_K, \mathbf{w}_L; \vec{n}_{KL}) = \mathbf{S}_K, \quad \forall K \in \mathbf{T}\,. \tag{4.82}$$

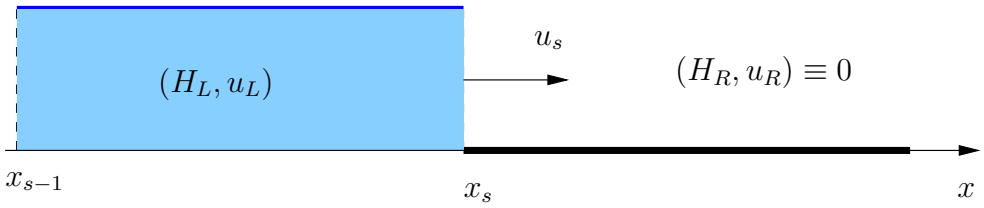


**Figure 4.32:** Shoreline left Riemann problem.

The initial condition for this system is given by projecting (4.67) onto the space of piecewise constant functions

$$\mathbf{w}_K(0) = \frac{1}{\text{vol}\, K} \int_K \mathbf{w}_0(x)\, d\Omega\ .$$

This system of ODE should also be discretized. There is a variety of explicit and implicit time integration methods. Let $\mathbf{w}_K^n$ denote a numerical approximation of the cell average solution in the control volume $K$ at time $t^n = n\Delta t$. The simplest time integration method is the forward Euler scheme

$$\frac{d\mathbf{w}_K}{dt} \cong \frac{\mathbf{w}_K^{n+1} - \mathbf{w}_K^n}{\Delta t}\ .$$

When applied to (4.82) it produces the fully-discrete finite volume scheme:

$$\frac{\mathbf{w}_K^{n+1} - \mathbf{w}_K^n}{\Delta t} + \sum_{L \in \mathcal{N}(K)} \frac{\text{area}(L \cap K)}{\text{vol}(K)} \Phi(\mathbf{w}_K^n, \mathbf{w}_L^n; \vec{n}_{KL}) = \mathbf{S}_K^n, \quad \forall K \in \mathbf{T}\ . \tag{4.83}$$

The time discretization used in this study is detailed in Section 4.3.3.5.

#### 4.3.3.3 Run-up algorithm

As already pointed out above, the NSWE are strictly hyperbolic if $H > 0$, i.e. when some water is present. The shoreline position is given by the following implicit relation $H(\mathbf{x}, t) = 0$. In these locations the system loses its strict hyperbolicity. Finally, in dry regions, $H < 0$, the system is non-hyperbolic, i.e. ill-posed. All these facts mean that there are some major theoretical difficulties in considering the inundation problem.

Very often some ad-hoc artificial techniques are implemented to circumvent run-up and run-down problems ("slot technique" of Madsen et al. [MSS97], algorithm of Hibberd-Peregrine [HP79], use of coordinate transformations [OHK97] and so on).

Analytically, shoreline boundary conditions have a very simple form:

$$H(\mathbf{x}_s(t), t) = 0, \qquad \frac{d\mathbf{x}_s}{dt} = \vec{u}(\mathbf{x}_s(t), t),$$

where $\mathbf{x}_s(t)$ is the shoreline position.

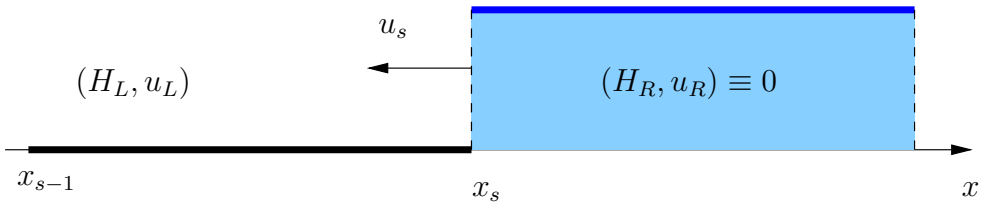


**Figure 4.33:** Shoreline right Riemann problem.

The algorithm proposed by Brocchini et al. [BBMA01] was chosen for the VOLNA code. It is based on the shoreline Riemann problem (see Figures 4.32 and 4.33 for illustration) [Sto57]:

$$\mathcal{R}_{\text{left}}(\mathbf{w}_L): \begin{cases} \frac{\partial \mathbf{w}}{\partial t} + \frac{\partial F(\mathbf{w})}{\partial x} = 0, \\ \mathbf{w}(x,0) = \begin{cases} \mathbf{w}_L, & x < 0, \\ 0, & x > 0. \end{cases} \end{cases} \quad \mathcal{R}_{\text{right}}(\mathbf{w}_R): \begin{cases} \frac{\partial \mathbf{w}}{\partial t} + \frac{\partial F(\mathbf{w})}{\partial x} = 0, \\ \mathbf{w}(x,0) = \begin{cases} 0, & x < 0, \\ \mathbf{w}_R, & x > 0. \end{cases} \end{cases}$$

The main idea to solve the shoreline Riemann problem is to pass to the limit $\mathbf{w}_L \to 0$ or $\mathbf{w}_R \to 0$ in the solution to the classical Riemann problem (4.80). Technical details can be found in [BBMA01]. However, we do not need to know the complete solution. It is sufficient to extract the wave propagation speeds at the shoreline (see Figure 4.34). These analytically determined speeds are imposed in an approximate Riemann solver when a wet/dry transition is detected.

Consider two control volumes $K$ and $L$ which share a common face. We must find the numerical flux $\Phi(\mathbf{w}_K, \mathbf{w}_L, \vec{n}_{KL})$ across this face. Let us summarize the key points of the method:

**Wet/wet interface:** If $H_L > 0$ and $H_R > 0$, we apply in the usual way an approximate Riemann solver which gives the numerical flux $\Phi$.

**Dry/dry interface:** If $H_L = H_R = 0$, we just return the zero flux $\Phi = 0$ since there is no flow between two dry cells.

**Wet/dry interface:** If $H_R = 0$ and $H_L > 0$, we have a situation corresponding to the left shoreline Riemann problem. Its solution yields the following choice of the wave speeds:

$$s_L := (\vec{u}_L \cdot \vec{n}_{KL}) - c_L, \qquad s_R := (\vec{u}_L \cdot \vec{n}_{KL}) + 2c_L.$$

Then we apply the HLL or the HLLC scheme with the above values of $s_L$ and $s_R$ (see Figure 4.34 for illustration).

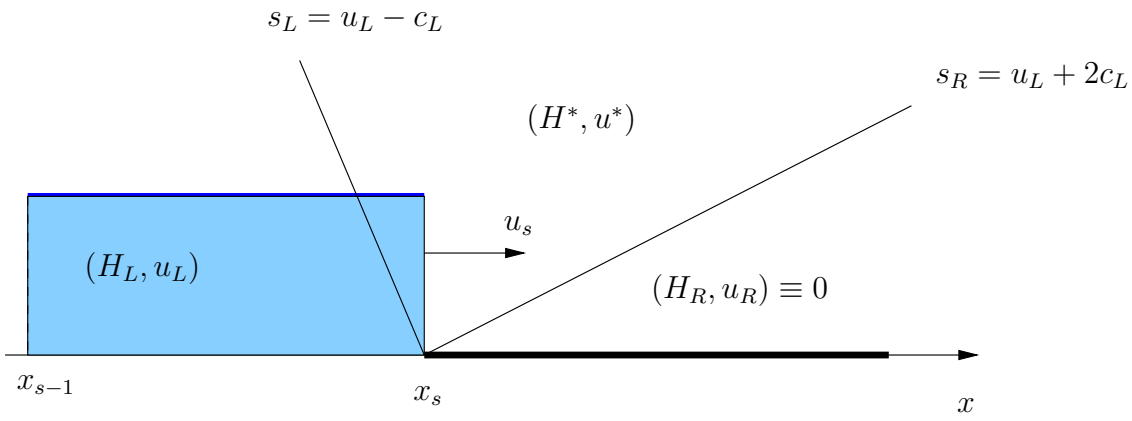


**Figure 4.34:** Shoreline Riemann problem (left) and wave propagation speeds.

**Dry/wet interface:** If $H_R > 0$ and $H_L = 0$, we have a situation symmetric to the previous case. One must solve the right shoreline Riemann problem. It provides the following speeds:

$$s_L := (\vec{u}_R \cdot \vec{n}_{KL}) - 2c_R, \qquad s_R := (\vec{u}_R \cdot \vec{n}_{KL}) + c_R.$$

Here again, the HLL or the HLLC scheme is applied.

We would like to underline the simplicity of this approach. In fact, there is no special treatment for the interface. This algorithm is run uniformly in the whole computational domain leading to an easy and robust implementation. We validate this method in sections 4.3.4.2 – 4.3.4.4.

#### 4.3.3.4 Source terms discretization

In this section we discuss some issues related to the source term discretization and we explain a technique to remedy them.

Source terms of the form $gH\nabla h$ arise in the horizontal momentum conservation equation (4.64). Obviously, this term is equal to zero when the bottom is even $h = const$. However, it is not the case in the real world applications. The magnitude of this term is proportional to the bed slope and may take large values when abrupt changes are present in the bathymetry.

Another profound property of NSWE is that the system (4.63), (4.64) admits non-trivial steady states. They can be determined from the following steady equations:

$$\begin{cases} \nabla \cdot (H\vec{u}) = 0, \\ \nabla \cdot \left(H\vec{u} \otimes \vec{u} + \frac{g}{2}H^2\right) = gH\nabla h \end{cases}$$

It is not so trivial to find analytical solutions to these equations. However, an ideal numerical scheme should preserve them. Recall that for 1D flows it is possible to describe the whole family of steady states and this information can be used to design efficient source term discretizations [LR98, VC99]. Since realistic applications require a 2D solver, we will address this problem directly in 2D.

As explained above, it seems to be extremely difficult to construct a scheme which preserves exactly all steady state solutions. Thus, we have to simplify the problem. We will focus our attention on a simple class of steady solutions which are called in the literature "lake at rest":

$$\vec{u} = 0, \qquad \eta := H - h = const. \tag{4.84}$$

The last relations can be expressed in discrete variables:

$$\vec{u}_K = \vec{u}_L = 0, \qquad H_K - h_K = H_L - h_L = const. \tag{4.85}$$

We briefly present the method chosen for our code and developed in [ABB+04, AB05]. It is mainly based on the idea of the interface hydrostatic reconstruction.

The well-balanced algorithm takes as input the vector of conservative variables $\{\mathbf{w}_K\}_{K\in\mathbf{T}}$, bathymetry data $\{h_K\}_{K\in\mathbf{T}}$ and is composed of the following steps:

- Assume that the control volumes $K$ and $L$ share a common face $f = K \cap L$. In this case, the interface bathymetry is defined as $h^*_{KL} := \min(h_K, h_L)$. This step is done only once at the initialization stage.

- The hydrostatic reconstructed interface water depth is given by

$$H^*_{KL} = (H_K - h_K + h^*_{KL})_+, \quad \text{where} \quad z_+ = \max(z, 0).$$

  From the dicrete interpretation (4.85) of the well-balanced condition (4.84), we define a new vector of the interface conservative variables:

$$\mathbf{w}^*_{KL} := \begin{pmatrix} H^*_{KL} \\ H^*_{KL}\vec{u}_K \end{pmatrix}. \tag{4.86}$$

- From the balance of hydrostatic forces $\nabla\left(\frac{g}{2}H^2\right) = gH\nabla h$, the adapted discretization of the source terms is introduced:

$$\mathbf{S}^*_K(\mathbf{w}_K, \mathbf{w}^*_{KL}, \vec{n}_{KL}) := \begin{pmatrix} 0 \\ \frac{g}{2}(H^{*2}_{KL} - H^2_K)\vec{n}_{KL} \end{pmatrix}$$

- The well-balanced scheme is obtained by replacing cell-centered values $\mathbf{w}_K$ by new interface values (4.86):

$$\frac{\mathbf{w}_K^{n+1} - \mathbf{w}_K^n}{\Delta t} + \sum_{L \in \mathcal{N}(K)} \frac{\text{area}(L \cap K)}{\text{vol}(K)} \Phi(\mathbf{w}_{KL}^{*,n}, \mathbf{w}_{LK}^{*,n}; \vec{n}_{KL}) = \mathbf{S}_K^*(\mathbf{w}_K^n, \mathbf{w}_{KL}^{*,n}, \vec{n}_{KL}), \quad \forall K \in \mathbf{T} .$$

It can be proven [AB05] that the hydrostatic reconstruction strategy preserves the "lake at rest" solutions and ensures the positivity property. We describe here only the first-order algorithm for the sake of simplicity. The extension to the second order can be found in the original papers and in [Aud04].

#### 4.3.3.5 Time discretization

In the previous sections we considered the spatial discretization procedure with a finite-volume scheme. It is a common practice in solving time-dependent PDEs to first discretize the spatial variables. This approach is called method of lines:

$$w_t + \partial_x f(w) = S(w) \overset{\text{FV}}{\Longrightarrow} w_t = \mathcal{L}(w) \tag{4.87}$$

In order to obtain a fully discrete scheme, we must discretize the time evolution operator. In the present work we chose the so-called Strong Stability-Preserving (SSP) time discretization methods described in [Shu88, GST01, SR02]. Historically these methods were initially called Total Variation Diminishing (TVD) time discretizations.

The main idea behind SSP methods is to assume that the first order forward Euler method is strongly stable (see the definition below) under a certain norm for the method of lines ODE (4.87). Then, we try to find a higher order scheme. Usually the relevant norm is the total variation[9] norm:

$$\text{TV}(w^n) := \sum_j \left| w_j^n - w_{j-1}^n \right|$$

and TVD discretizations have the property $\text{TV}(w^{n+1}) \leq \text{TV}(w^n)$.

**Remark 11.** *Special approaches are needed for hyperbolic PDEs since they contain discontinuous solutions and the usual linear stability analysis is inadequate. Thus a stronger measure of stability is usually required:*

**Definition 3.** *A sequence $\{w^n\}$ is said to be **strongly stable** in a given norm $||\cdot||$ provided that $||w^{n+1}|| \leq ||w^n||$ for all $n \geq 0$.*

[9] The notion of total variation is used essentially for 1D discrete solutions.

A general $m$-stage Runge-Kutta method for (4.87) can be written in the form

$$w^{(0)} = w^n, \tag{4.88}$$

$$w^{(i)} = \sum_{k=0}^{i-1}\Big(\alpha_{i,k}w^{(k)} + \Delta t\beta_{i,k}\mathcal{L}(w^{(k)})\Big), \quad \alpha_{i,k} \geq 0, \quad i = 1, \ldots, m, \tag{4.89}$$

$$w^{n+1} = w^{(m)}. \tag{4.90}$$

In [SO88] the following result is proved

**Theorem 1.** *If the forward Euler method is strongly stable under the CFL restriction* $\Delta t \leq \Delta t_{FE}$

$$||w^n + \Delta t\mathcal{L}(w^n)|| \leq ||w^n||,$$

*then the Runge-Kutta method (4.88) – (4.90) with* $\beta_{i,k} \geq 0$ *is SSP,* $||w^{n+1}|| \leq ||w^n||$, *provided the following CFL restriction is fulfilled:*

$$\Delta t \leq c\Delta t_{FE}, \quad c = \min_{i,k}\frac{\alpha_{i,k}}{\beta_{i,k}}.$$

Here we give a few examples of SSP schemes which are commonly used in applications:

- Optimal[10] second order two-stage SSP-RK(2,2) scheme with CFL = 1:

$$\begin{aligned} w^{(1)} &= w^{(n)} + \Delta t\mathcal{L}(w^{(n)}), \\ w^{(n+1)} &= \frac{1}{2}w^{(n)} + \frac{1}{2}w^{(1)} + \frac{1}{2}\Delta t\mathcal{L}(w^{(1)}); \end{aligned}$$

- Optimal third order three-stage SSP-RK(3,3) scheme with CFL = 1:

$$\begin{aligned} w^{(1)} &= w^{(n)} + \Delta t\mathcal{L}(w^{(n)}), \\ w^{(2)} &= \frac{3}{4}w^{(n)} + \frac{1}{4}w^{(1)} + \frac{1}{4}\Delta t\mathcal{L}(w^{(1)}), \\ W^{(n+1)} &= \frac{1}{3}w^{(n)} + \frac{2}{3}w^{(2)} + \frac{2}{3}\Delta t\mathcal{L}(w^{(2)}); \end{aligned}$$

- Third order four-stage SSP-RK(3,4) scheme with CFL = 2:

$$\begin{aligned} w^{(1)} &= w^{(n)} + \frac{1}{2}\Delta t\mathcal{L}(w^{(n)}), \\ w^{(2)} &= w^{(1)} + \frac{1}{2}\Delta t\mathcal{L}(w^{(1)}), \\ w^{(3)} &= \frac{2}{3}w^{(n)} + \frac{1}{3}w^{(2)} + \frac{1}{6}\Delta t\mathcal{L}(w^{(n)}), \\ w^{(n+1)} &= w^{(3)} + \frac{1}{2}\Delta t\mathcal{L}(w^{(3)}). \end{aligned}$$

[10] Optimality in the sense of CFL condition.

The linear absolute stability region for the RK and SSP-RK schemes is the same. However the nonlinear absolute stability regions are quite different [CP92].

We tested these different schemes in our numerical code and we decided to adopt SSP-RK(3,4) due to its accuracy and wide stability region. In our opinion this scheme represents a very good trade-off between precision and robustness.

#### 4.3.3.6 Second order extension

If we analyze the above scheme, we understand that in fact, we have only one degree of freedom per data storage location. Hence, it seems that we can expect to be first order accurate at most. In the numerical community first order schemes are generally considered to be too inaccurate for most quantitative calculations. Of course, we can always make the mesh spacing extremely small but it cannot be a solution since it makes the scheme inefficient. From the theoretical point of view the situation is even worse since an $\mathcal{O}(h^{\frac{1}{2}})$ $L_1$-norm error bound for the monotone and E-flux schemes [Osh84] is known to be sharp [Pet91], although an $\mathcal{O}(h)$ solution error is routinely observed in numerical experiments. On the other hand, Godunov has shown [God59] that all linear schemes that preserve solution monotonicity are at most first order accurate. This rather negative result suggests that a higher order accurate scheme has to be essentially nonlinear in order to attain simultaneously a monotone resolution of discontinuities and high order accuracy in continuous regions.

A significant breakthrough in the generalization of finite volume methods to higher order accuracy is due to N.E. Kolgan [Kol72, Kol75] and van Leer [vL79]. They proposed a kind of post-treatment procedure currently known as solution *reconstruction* or MUSCL[11] scheme. In the above papers the authors used linear reconstruction (it will be chosen in this study as well) but this method has already been extended to quadratic approximations in each cell [BF90].

**4.3.3.6.1 Historical remark** In general, when we read numerical articles which use the MUSCL scheme, the authors often cite the paper by van Leer [vL79]. It is commonly believed in the scientific community that B. van Leer was first to propose the gradient reconstruction and slope limiting ideas. Unfortunately, because of political reasons, the works of N.E. Kolgan [Kol72, Kol75] remained unknown for a long time. We would like to underline the fact that the first publication of Kolgan came out seven years before van Leer's paper. Van Leer seems to be aware of this situation since in his recent review paper [vL06] one can find "A historical injustice" section:

[11] MUSCL stands for Monotone Upstream-centered Scheme for Conservation Laws.

> "It has been pointed out to me by Dr. Vladimir Sabelnikov, formerly of TsAGI, the Central Aerodynamical National Laboratory near Moscow, that a scheme closely resembling MUSCL (including limiting) was developed in this laboratory by V. P. Kolgan (1972). Kolgan died young; his work apparently received little notice outside TsAGI."

**4.3.3.6.2 TVD and MUSCL schemes** There is a property of scalar nonlinear conservation laws, which was probably observed for the first time by Peter Lax [Lax73]:

> The total increasing and decreasing variations of a differentiable solution between any pair of characteristics are conserved.

In the presence of shock waves, information is lost and the total variation decreases. For compactly supported or periodic solutions, one can establish the following inequality

$$\int_{-\infty}^{+\infty} |dw(x,t_2)| \leq \int_{-\infty}^{+\infty} |dw(x,t_1)|\,, \quad t_2 \geq t_1. \tag{4.91}$$

This motivated Harten [Har83] to introduce the notion of discrete total variation of numerical solution $u_h := \{u_j\}$

$$TV(w_h) := \sum_j |w_{j+1} - w_j|\,,$$

and the discrete counterpart to (4.91)

$$TV(w_h^{n+1}) \leq TV(w_h^n).$$

If this property is fulfilled, then a finite volume scheme is said to be total variation diminishing (TVD). The following theorem was proved in [Har83]:

**Theorem 2. (i):** *Monotone schemes are TVD*

**(ii):** *TVD schemes are monotonicity preserving, i.e. the number of solution extrema is preserved in time.*

**Remark 12.** *From the mathematical point of view it would be more correct to say "the total variation non-increasing (TVNI) scheme" but the "wrong" term TVD is generally accepted in the scientific literature.*

In one space dimension the construction of TVD schemes is not a problem anymore. Let us recall that in this study we are rather interested in two space dimensions (or even three in future work). In these cases the situation is considerably more complicated. Even if we consider the simplest case of structured cartesian meshes and apply a 1D TVD scheme on a dimension-by-dimension basis, a result of Goodman and Leveque shows [GV85] that TVD schemes in two or more space dimensions are only first order accurate. Motivated by this negative result, weaker conditions yielding solution monotonicity preservation should be developed.

In this work we will describe the construction and practical implementation of a second-order nonlinear scheme on unstructured (possibly highly distorted) meshes. The main idea is to find our solution as a piecewise affine function on each cell. This kind of linear reconstruction operators on simplicial control volumes often exploit the fact that the cell average is also a pointwise value of any valid (conservative) linear reconstruction evaluated at the gravity center of a simplex. This reduces the reconstruction problem to that of gradient estimation given cell averaged data. In this case, we express the reconstruction in the form

$$\mathbf{w}_K(\mathbf{x}) = \bar{\mathbf{w}}_K + (\nabla \mathbf{w})_K \cdot (\mathbf{x} - \mathbf{x}_0), \quad K \in \mathbf{T}\ , \tag{4.92}$$

where $\bar{\mathbf{w}}_K$ is the cell averaged value given by the finite volume method, $(\nabla \mathbf{w})_K$ is the solution gradient estimate (to be determined) on the cell $K$, $\mathbf{x} \in K$ and the point $\mathbf{x}_0$ is chosen to be the gravity center for the simplex $K$.

It is very important to note that with this type of representation (4.92) we remain absolutely conservative, i.e.

$$\frac{1}{\mathrm{vol}(K)} \int_K \mathbf{w}_K(\mathbf{x})\ d\Omega \equiv \bar{\mathbf{w}}_K$$

due to the choice of the point $\mathbf{x}_0$. This point is crucial for finite volumes because of intrinsic conservative properties of this method.

In next sections we describe briefly two common techniques: Green-Gauss integration and least squares methods for solution gradient estimation on each cell. There are other available techniques. We can mention here an implicit gradient reconstruction method proposed in [MG96] and reused later in [AMS04], for example. We decided not to implement this approach in our research code since this procedure is computationally expensive[12].

[12]In order to reconstruct the solution gradient we have to solve a linear system of equations. Recall that the gradient is estimated at each time step on each control volume. This factor slows down considerably explicit time discretizations.

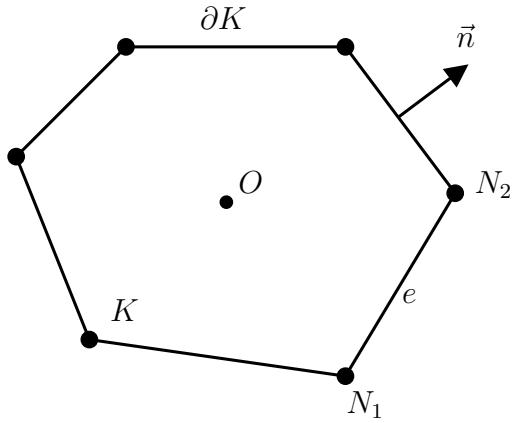


**Figure 4.35:** Illustration for Green-Gauss gradient reconstruction. Control volume $K$ with barycenter $O$ and exterior normal $\vec{n}$.

**4.3.3.6.3 Green-Gauss gradient reconstruction** This gradient reconstruction technique can be easily implemented on simplicial meshes. It is based on two very simple ideas: the mean value approximation and Green-Gauss-Ostrogradsky formula.

Consider a control volume $K$ with barycenter $O$. The exterior normal to an edge $e \in \partial K$ is denoted by $\vec{n}_e$. This configuration is depicted on Figure 4.35. In order to estimate the solution gradient on $K$ (or in other words, to estimate its value at gravity center $O$) we make the following mean value approximation

$$(\nabla \mathbf{w})_K = (\nabla \mathbf{w})|_O \cong \frac{1}{\mathrm{vol}(K)} \int_K \nabla \mathbf{w} \, d\Omega,$$

and apply Green-Gauss-Ostrogradsky formula

$$(\nabla \mathbf{w})_K \cong \frac{1}{\mathrm{vol}(K)} \int_{\partial K} \mathbf{w} \otimes \vec{n} \, d\sigma = \frac{1}{\mathrm{vol}(K)} \sum_{e \in \partial K} \int_e \mathbf{w} \otimes \vec{n}_e \, d\sigma \cong$$

$$\sum_{e \in \partial K} \frac{\mathrm{area}(e)}{\mathrm{vol}(K)} \mathbf{w}|_{e/2} \otimes \vec{n}_e,$$

where $\mathbf{w}|_{e/2}$ denote the solution value at the face (or edge in 2D) centroid. The face value needed to compute the reconstruction gradient can be obtained from a weighted average of the values at the vertices on the face [HC89]. In 2D it simply becomes

$$\mathbf{w}|_{e/2} = \frac{\mathbf{w}_{N_1} + \mathbf{w}_{N_2}}{2}.$$

This approximation yields the following formula for gradient estimation:

$$(\nabla \mathbf{w})_K \cong \sum_{e \in \partial K} \frac{\mathrm{area}(e)}{\mathrm{vol}(K)} \frac{(\mathbf{w}_{N_1} + \mathbf{w}_{N_2})}{2} \otimes \vec{n}_e.$$

The gradient calculation is exact whenever the numerical solution varies linearly over the support of the reconstruction.

This procedure requires the knowledge of the solution values at the mesh nodes $\{N_i\}$. Recall that a cell centered finite volume scheme provides us with data located at cell gravity centers. Thus, an interpolation technique is needed. The quality of Green-Gauss gradient reconstruction greatly depends on the chosen interpolation method. The method chosen here is explained in Section 4.3.3.6.6.

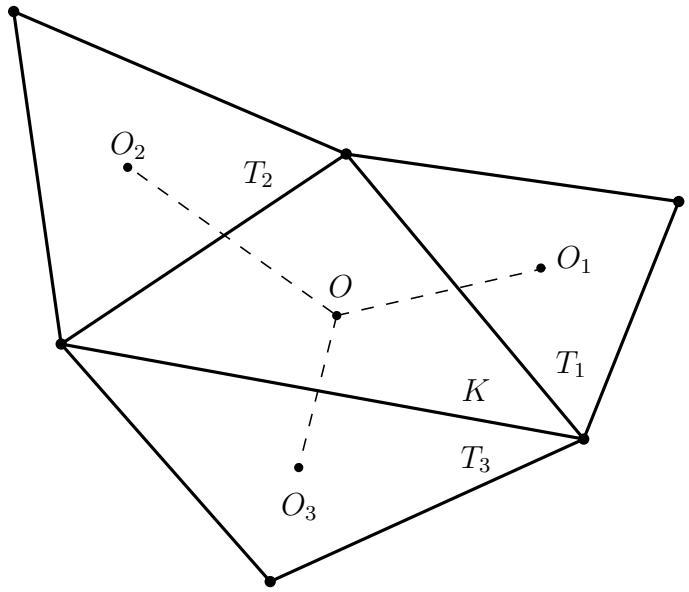


**Figure 4.36:** Illustration for least-squares gradient reconstruction. A triangle control volume with three adjacent neighbors is depicted.

**4.3.3.6.4 Least-squares gradient reconstruction method** In this section we consider a triangle[13] control volume $K$ with three adjacent neighbors $T_1$, $T_2$ and $T_3$. Their barycenters are denoted by $O(\mathbf{x}_0)$, $O_1(\mathbf{x}_1)$, $O_2(\mathbf{x}_2)$ and $O_3(\mathbf{x}_3)$ respectively. In the following we denote by $\mathbf{w}_i$ the solution value at gravity centers $O_i$:

$$\mathbf{w}_i := \mathbf{w}(\mathbf{x}_i), \quad \mathbf{w}_0 := \mathbf{w}(\mathbf{x}_0).$$

Our purpose here is to estimate $\nabla \mathbf{w} = (\partial_x \mathbf{w}, \partial_y \mathbf{w})$ on the cell $K$. Using Taylor formula, we can write down the three following relations:

$$\mathbf{w}_1 - \mathbf{w}_0 = (\nabla \mathbf{w})_K \cdot (\mathbf{x}_1 - \mathbf{x}_0) + \mathcal{O}(h^2), \tag{4.93}$$

$$\mathbf{w}_2 - \mathbf{w}_0 = (\nabla \mathbf{w})_K \cdot (\mathbf{x}_2 - \mathbf{x}_0) + \mathcal{O}(h^2), \tag{4.94}$$

$$\mathbf{w}_3 - \mathbf{w}_0 = (\nabla \mathbf{w})_K \cdot (\mathbf{x}_3 - \mathbf{x}_0) + \mathcal{O}(h^2). \tag{4.95}$$

[13] Generalization to other simplicial control volumes is straightforward.

If we drop higher order terms $\mathcal{O}(h^2)$, these relations can be viewed as a linear system of three equations for two unknowns[14] $(\partial_x \mathbf{w}, \partial_y \mathbf{w})$. This situation is due to the fact that the number of edges incident to a simplex mesh in $\mathbb{R}^d$ is greater or equal (in this case see Remark 13) to $d$ thereby producing linear constraint equations (4.93) – (4.95) which will be solved analytically here in a least squares sense.

First of all, each constraint (4.93) – (4.95) is multiplied by a weight $\omega_i \in (0,1)$ which will be chosen below to account for distorted meshes. In matrix form our non-square system becomes

$$\begin{pmatrix} \omega_1\Delta x_1 & \omega_1\Delta y_1 \\ \omega_2\Delta x_2 & \omega_2\Delta y_2 \\ \omega_3\Delta x_3 & \omega_3\Delta y_3 \end{pmatrix} (\nabla \mathbf{w})_K = \begin{pmatrix} \omega_1(\mathbf{w}_1 - \mathbf{w}_0) \\ \omega_2(\mathbf{w}_2 - \mathbf{w}_0) \\ \omega_3(\mathbf{w}_3 - \mathbf{w}_0) \end{pmatrix},$$

where $\Delta x_i = x_i - x_0$, $\Delta y_i = y_i - y_0$. For further developments it is convenient to rewrite our constraints in abstract form

$$[\vec{L_1},\ \vec{L_2}] \cdot (\nabla \mathbf{w})_K = \vec{f}. \tag{4.96}$$

We use a normal equation technique in order to solve symbolically this abstract form in a least squares sense. Multiplying on the left both sides of (4.96) by $[\vec{L_1}\vec{L_2}]^t$ yields

$$G(\nabla \mathbf{w})_K = \vec{b}, \quad G = (l_{ij})_{1\le i,j\le 2} = \begin{pmatrix} (\vec{L_1}\cdot\vec{L_1}) & (\vec{L_1}\cdot\vec{L_2}) \\ (\vec{L_2}\cdot\vec{L_1}) & (\vec{L_2}\cdot\vec{L_2}) \end{pmatrix} \tag{4.97}$$

where $G$ is the Gram matrix of vectors $\left\{\vec{L_1}, \vec{L_2}\right\}$ and $\vec{b} = \begin{pmatrix} (\vec{L_1}\cdot\vec{f}) \\ (\vec{L_2}\cdot\vec{f}) \end{pmatrix}$. The so-called normal equation (4.97) is easily solved by Cramer's rule to give the following result

$$(\nabla \mathbf{w})_K = \frac{1}{l_{11}l_{22} - l_{12}^2} \begin{pmatrix} l_{22}(\vec{L_1}\cdot\vec{f}) - l_{12}(\vec{L_2}\cdot\vec{f}) \\ l_{11}(\vec{L_2}\cdot\vec{f}) - l_{12}(\vec{L_1}\cdot\vec{f}) \end{pmatrix}.$$

The form of this solution suggests that the least squares linear reconstruction can be efficiently computed without the need for storing a non-square matrix.

Now we discuss the choice of weight coefficients $\{\omega_i\}_{i=1}^3$. The basic idea is to attribute bigger weights to cells barycenters closer to the node $N$ under consideration. One of the possible choices consists in taking a harmonic mean of respective distances $r_i = ||\mathbf{x}_i - \mathbf{x}_N||$. This purely metric argument takes the following mathematical form:

$$\omega_i = \frac{||\mathbf{x}_i - \mathbf{x}_N||^{-k}}{\sum_{j=1}^3 ||\mathbf{x}_j - \mathbf{x}_N||^{-k}},$$

where $k$ in practice is taken to be one or two (in our numerical code we choose $k = 1$).

[14]This simple estimation is done for the scalar case only $\mathbf{w} = (w)$. For more general vector problems the numbers of equations and unknowns must be changed depending on the dimension of vector $\mathbf{w}$.

**Remark 13.** *When a triangle shares an edge with the boundary $\partial\Omega$ (see Figure 4.38 for illustration), the gradient reconstruction procedure becomes even simpler, since the number of constraints is equal to d and the linear system (4.93) – (4.95) becomes completely determined:*

$$\begin{aligned} \mathbf{w}_1 - \mathbf{w}_0 &= (\nabla \mathbf{w})_K \cdot (\mathbf{x}_1 - \mathbf{x}_0) + \mathcal{O}(h^2), \\ \mathbf{w}_2 - \mathbf{w}_0 &= (\nabla \mathbf{w})_K \cdot (\mathbf{x}_2 - \mathbf{x}_0) + \mathcal{O}(h^2), \end{aligned}$$

*or in componentwise form it reads*

$$\begin{pmatrix} x_1 - x_0 & y_1 - y_0 \\ x_2 - x_0 & y_2 - y_0 \end{pmatrix} (\nabla \mathbf{w})_K = \begin{pmatrix} \mathbf{w}_1 - \mathbf{w}_0 \\ \mathbf{w}_2 - \mathbf{w}_0 \end{pmatrix}.$$

*The unique solution to this linear system is given again by Cramer's rule*

$$(\nabla \mathbf{w})_K = \frac{\begin{pmatrix} (y_2 - y_0)(\mathbf{w}_1 - \mathbf{w}_0) - (y_1 - y_0)(\mathbf{w}_2 - \mathbf{w}_0) \\ (x_1 - x_0)(\mathbf{w}_2 - \mathbf{w}_0) - (x_2 - x_0)(\mathbf{w}_1 - \mathbf{w}_0) \end{pmatrix}}{(x_1 - x_0)(y_2 - y_0) - (x_2 - x_0)(y_1 - y_0)}.$$

**4.3.3.6.5 Slope limiter** The idea of incorporating limiter functions to obtain non-oscillatory resolution of discontinuities and steep gradients dates back to Boris and Book [BB73]. When the limiter is identically equal to 1, we have the unlimited form of the linear interpolation. In the 1D case one can easily find in the literature about 15 different limiter functions such as CHARM, minmod, superbee, van Albada and many others. On unstructured meshes the situation is quite different. In the present study we decided to choose the Barth-Jespersen limiter proposed in [BJ89]. Here we do not discuss its construction and properties but just give the final formula. We need to introduce the following notation

$$\mathbf{w}_K^{min} := \min_{L \in \mathcal{N}(K)} \mathbf{w}_L, \quad \mathbf{w}_K^{max} := \max_{L \in \mathcal{N}(K)} \mathbf{w}_L \, .$$

The limited version of (4.92) is given by the following modified reconstruction operator

$$\mathbf{w}_K(\mathbf{x}) = \bar{\mathbf{w}}_K + \alpha_K (\nabla \mathbf{w})_K \cdot (\mathbf{x} - \mathbf{x}_0), \quad K \in \mathbf{T} \, ,$$

where it is assumed that $\alpha_K \in [0, 1]$. Obviously, the choice $\alpha_K = 0$ corresponds to the first order scheme while $\alpha_K = 1$ is the unlimited form. Barth and Jespersen [BJ89] propose the following choice of $\alpha_K$:

$$\alpha_K^{BJ} := \min_{\forall f \in \partial K} \begin{cases} \frac{\mathbf{w}_K^{max} - \bar{\mathbf{w}}_K}{\mathbf{w}_K(\mathbf{x}_f) - \bar{\mathbf{w}}_K} & \text{if } \mathbf{w}_K(\mathbf{x}_f) > \mathbf{w}_K^{max}, \\ \frac{\mathbf{w}_K^{min} - \bar{\mathbf{w}}_K}{\mathbf{w}_K(\mathbf{x}_f) - \bar{\mathbf{w}}_K} & \text{if } \mathbf{w}_K(\mathbf{x}_f) < \mathbf{w}_K^{min}, \\ 1 & \text{otherwise.} \end{cases}$$

where $\mathbf{x}_f$ denotes the face $f$ centroid.

Although this limiter function does not fulfill all the requirements of finite volume maximum principle on unstructured meshes [BO04], it can be shown that it yields finite volume schemes possessing a global extremum diminishing property. Also this limiter produces the least amount of slope reduction which can be advantageous for accuracy. Note that in practical implementation minor modifications are required to prevent near zero division for almost constant solution data.

**4.3.3.6.6 Solution interpolation to mesh nodes** We have seen above that several gradient reconstruction procedures (in particular gradient estimation on the faces) require the knowledge of the solution at mesh nodes (or vertices). This information is not directly given by the finite volume method since we chose the cell-centered approach.

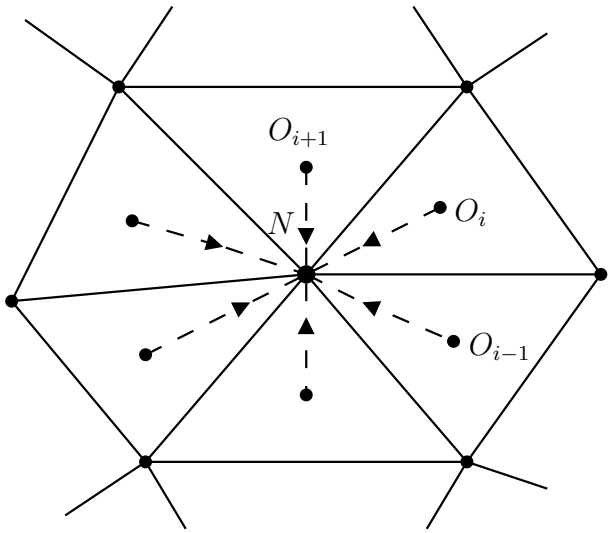


**Figure 4.37:** Triangles with their barycenters $O_i$ sharing the same vertex $N$.

Let us consider a node $N(x_n, y_n)$ of the tesselation $\mathbf{T}$ and a control volume $K_i$ with barycenter $O_i(x_i, y_i)$ having this node as a vertex (see Figure 4.37 for illustration). The MUSCL procedure provides a solution gradient on each cell. Thus, using the Taylor formula or, equivalently, the representation (4.92) we can estimate the solution value at the node $N$

$$\mathbf{w}_N = \bar{\mathbf{w}}_{K_i} + (\nabla \mathbf{w})_{K_i} \cdot (\mathbf{x}_N - \mathbf{x}_i). \tag{4.98}$$

The problem is that we will have $d(N)$ different values of the solution in the same point depending on the control volume under consideration. Here $d(N)$ is the degree of vertex $N$ in the sense of graph theory. One of the possible ways to overcome this contradiction is averaging. One interesting technique was proposed in [HC89] and further improved in

[KMC03]. In our turn, we slightly modified this method. The algorithm implemented in our code is briefly described here.

First of all, let us look for the vertex value $\bar{\mathbf{w}}_N$ as a weighted sum of the values $\mathbf{w}_{N_i}$ computed by formula (4.98) from each surrounding cell

$$\bar{\mathbf{w}}_N = \frac{\sum_{i=1}^{d(N)} \omega_i \mathbf{w}_{N_i}}{\sum_{i=1}^{d(N)} \omega_i} .$$

The weighting factors $\{\omega_i\}_{i=1}^{d(N)}$ are made to satisfy the condition of zero pseudo-Laplacian

$$L(x_n) \equiv \sum_{i=1}^{d(N)} \omega_i (x_i - x_n), \quad L(y_n) \equiv \sum_{i=1}^{d(N)} \omega_i (y_i - y_n) . \tag{4.99}$$

These conditions have a very simple interpretation. They are imposed so that the method be exact for affine data over the stencil.

As in the original formulation by Holmes and Connell [HC89], the weighting factor $\omega_i$ is written as

$$\omega_i = 1 + \Delta\omega_i .$$

The weights $\{\omega_i\}$ are determined by solving an optimization problem in which the cost-function to be minimized is defined as

$$\frac{1}{2} \sum_{i=1}^{d(N)} \left(r_i \Delta\omega_i\right)^2 \to \min \tag{4.100}$$

with two constraints given by (4.99). It should be noted that the cost function is slightly different from the original formulation. The difference lies in the factor of

$$r_i^2 \equiv ||\vec{ON} - \vec{OO_i}||^2$$

which was introduced in [KMC03]. This modification effectively allows larger values of weight $\Delta\omega_i$ for those cells closer to the node in question.

Employing the method of Lagrange multipliers, the original optimization problem, which was to minimize the cost function given by (4.100) with the constraints (4.99) is equivalent to minimizing the function $\mathcal{L}$ defined by

$$\mathcal{L} = \frac{1}{2} \sum_{i=1}^{d(N)} \left(r_i \Delta\omega_i\right)^2 - \lambda \sum_{i=1}^{d(N)} \omega_i (x_i - x_n) - \mu \sum_{i=1}^{d(N)} \omega_i (y_i - y_n) \to \min$$

which leads to

$$\Delta\omega_i = \frac{\lambda(x_i - x_n) + \mu(y_i - y_n)}{r_i^2} .$$

The two Lagrangian multipliers, $\lambda$ and $\mu$, are obtained from

$$\lambda = \frac{r_y I_{xy} - r_x I_{yy}}{I_{xx} I_{yy} - I_{xy}^2}, \quad \mu = \frac{r_x I_{xy} - r_y I_{xx}}{I_{xx} I_{yy} - I_{xy}^2},$$

where

$$r_x = \sum_{i=1}^{d(N)} (x_i - x_n), \quad r_y = \sum_{i=1}^{d(N)} (y_i - y_n).$$

$$I_{xx} = \sum_{i=1}^{d(N)} \frac{(x_i - x_n)^2}{r_i^2}, \quad I_{yy} = \sum_{i=1}^{d(N)} \frac{(y_i - y_n)^2}{r_i^2}, \quad I_{xy} = \sum_{i=1}^{d(N)} \frac{(x_i - x_n)(y_i - y_n)}{r_i^2}.$$

The last step consists in renormalizing the weights $\{\omega_i\}_{i=1}^{d(N)}$ to the range $[0, 1]$.

**Remark 14.** *The above algorithm is not computationally expensive since the weights $\{\omega_i\}_{i=1}^{d(N)}$ depend only on the tesselation $\mathbf{T}$ geometry. It means that they can be computed and stored before the main loop in time and reused during the computations later.*

**Remark 15.** *Even if we suggest to use the above method (since it gives slightly better results), we would like to give another idea (based on a purely metrics argument) of how to construct the weights $\{\omega_i\}_{i=1}^{d(N)}$. This approach is considerably simpler than solving an optimization problem and it was already used in the least squares gradient reconstruction method (see Section 4.3.3.6.4). In fact, in order to calculate $\omega_i$ one can simply take the harmonic mean of distances between the node $N$ under the question and respective cell barycenter $O_i$ (see Figure 4.37):*

$$\omega_i := \frac{||\mathbf{x}_N - \mathbf{x}_i||^{-k}}{\sum_{j=1}^{d(N)} ||\mathbf{x}_N - \mathbf{x}_i||^{-k}},$$

*where $k$ in practice is equal to 1 or 2.*

*This choice does not guarantee exact interpolation of globally linear functions.*

#### 4.3.3.7 Boundary conditions implementation

So far we have not discussed the implementation of boundary conditions. The flavor of boundary conditions treatment for hyperbolic systems is given here and we refer to [GP05] for a general discussion. This is a very important topic since they actually determine the solution. Let us consider the space discretization of the system (4.69) by a cell centered finite volume method. For instance for the time explicit discretization we have the scheme (4.83). Of course this formula is not valid when $K$ meets the boundary of $\Omega$ (see Figure4.38 for illustration). When this occurs, we have to find the numerical flux $\Phi(v_K^n, K, \partial\Omega)$. In

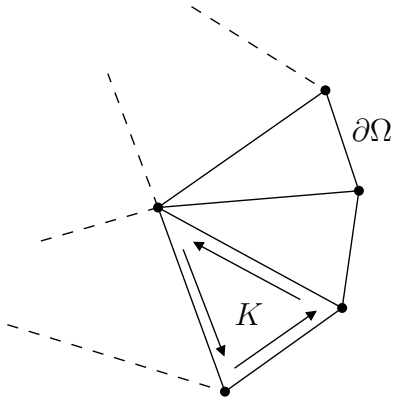


**Figure 4.38:** Control volume sharing a face with boundary $\partial\Omega$.

practice, this flux is not given by the physical boundary conditions and moreover, in general, (4.69) is an ill-posed problem if we try to impose either $v$ or $F(v)\cdot\vec{n}$ on $\partial\Omega$. This can be understood in a simple way by using the following linearization of this system:

$$\frac{\partial w}{\partial t} + \underline{A}_n \frac{\partial w}{\partial n} = 0\,, \tag{4.101}$$

where $\vec{n}$ represents the direction of the external normal on $K\cap\partial\Omega$, $\underline{A}_n$ is the advection matrix:

$$\underline{A}_n \equiv \frac{\left(\partial F(w)\cdot\vec{n}\right)}{\partial w}|_{w=\underline{w}}, \tag{4.102}$$

and $\underline{w}$ is the state around which the linearization is performed. When (4.69) is hyperbolic, the matrix $\underline{A}_n$ is diagonalizable on $\mathbb{R}$ and by a change of coordinates, this system becomes an uncoupled set of $m$ advection equations:

$$\frac{\partial \xi_k}{\partial t} + \lambda_k \frac{\partial \xi_k}{\partial n} = 0\,, \quad k = 1,\ldots,m\,. \tag{4.103}$$

Here the $\lambda_k$ are the eigenvalues of $\underline{A}_n$ and according to their sign, waves are going either into the domain $\Omega$ ($\lambda_k<0$) or out of the domain $\Omega$ ($\lambda_k>0$). Hence we expect that it is only possible to impose $p$ conditions on $K\cap\partial\Omega$ where $p\equiv\sharp\{k\in\{1,\ldots,m\}$ such that $\lambda_k<0\}$.

Let us consider now a control volume $K$ which meets the boundary $\partial\Omega$. We take $\underline{w}=w_K^n$ and write the previous linearization. We denote by $x$ the coordinate along the outer normal so that (4.101) reads:

$$\frac{\partial w}{\partial t} + \underline{A}_n \frac{\partial w}{\partial x} = 0\,, \tag{4.104}$$

which happens to be the linearization of the 1D (*i.e.* when $nd=1$) system. First we label the eigenvalues $\lambda_k(\underline{w})$ of $\underline{A}_n$ by increasing order:

$$\lambda_1(\underline{w}) \le \lambda_2(\underline{w}) \le \ldots \le \lambda_p(\underline{w}) < 0 \le \lambda_{p+1}(\underline{w}) \ldots \le \lambda_m(\underline{w})\,. \tag{4.105}$$

(i) The case $p = 0$. In this case information comes from inside $\Omega$ and therefore we take:

$$\Phi(w_K^n, K, \partial\Omega) = F(w_K^n) \cdot \vec{n}_K \,. \tag{4.106}$$

In the Computational Fluid Dynamics literature this is known as the "supersonic outflow" case.

(ii) The case $p = m$. In this case information comes from outside $\Omega$ and therefore we take:

$$\Phi(w_K^n, K, \partial\Omega) = \Phi_{given} \,, \tag{4.107}$$

where $\Phi_{given}$ are the given physical boundary conditions. In the Computational Fluid Dynamics literature this is known as the "supersonic inflow" case.

(iii) The case $1 \leq p \leq m-1$. As already discussed, we need $p$ scalar information coming from outside of $\Omega$. Hence we assume that we have on physical ground $p$ relations on the boundary:

$$g_l(w) = 0 \,, \quad l = 1, \ldots, p. \tag{4.108}$$

**Remark 16.** *The notation $g_l(w) = 0$ means that we have a relation between the components of $w$. However, in general, the function $g_l$ is not given explicitly in terms of $w$. For example $g_l(w)$ could be the pressure which is not, in general, one of the components of $w$.*

Since we have to determine the $m$ components of $\Phi(w_K^n, K, \partial\Omega)$, we need $m - p$ supplementary scalar conditions. Let us write them as

$$h_l(w) = 0 \,, \quad l = p+1, \ldots, m. \tag{4.109}$$

In general (4.108) are referred to as "physical boundary conditions" while (4.109) are referred to as "numerical boundary conditions".

Then we take:

$$\Phi(w_K^n, K, \partial\Omega) = F(w) \cdot \vec{n}_K \,, \tag{4.110}$$

where $w$ is solution to (4.108)-(4.109) (see however Remark 19 and (4.116)).

**Remark 17.** *The system (4.108)-(4.109) for the $m$ unknowns $w \in G$ is a $m \times m$ nonlinear system of equations. We are going to study its solvability, see Theorem 3.*

Let us first discuss the numerical boundary conditions (4.109). By analogy with what we did on an interface between two control volumes $K$ and $L$, we take (recall that $\underline{w} = w_K^n$):

$$\tilde{l}_k(\underline{w}) \cdot (F(w) \cdot \vec{n}_K) = \tilde{l}_k(\underline{w}) \cdot (F(w_K^n) \cdot \vec{n}_K) \,, \quad k = p+1, \ldots, m. \tag{4.111}$$

In other words, we set $h_k(w) \equiv \tilde{l}_k(w_K^n) \cdot (F(w) \cdot \vec{n}_K) - \tilde{l}_k(w_K^n) \cdot (F(w_K^n) \cdot \vec{n}_K)$. We have denoted by $(\tilde{l}_1(\underline{w}), \ldots, \tilde{l}_m(\underline{w}))$ a set of left eigenvectors of $\underline{\tilde{A}}_n$: ${}^t\underline{\tilde{A}}_n l_k(\underline{w}) = \lambda_k l_k(\underline{w})$ and by $(r_1(\underline{w}), \ldots, r_m(\underline{w}))$ a set of right eigenvectors of $\underline{\tilde{A}}_n$: $\underline{\tilde{A}}_n r_k(\underline{w}) = \lambda_k r_k(\underline{w})$. Moreover the following normalization is taken: $\tilde{l}_k(\underline{w}) \cdot \tilde{r}_p(\underline{w}) = \delta_{k,p}$.

According to [GP05] we have the following result on the solvability of (4.108)-(4.109).

**Theorem 3.** *In the case $1 \leq p \leq m-1$, assume that $\lambda_{p+1}(\underline{w}) > 0$, and*

$$\det_{1 \leq k,l \leq p} \left( \sum_{i=1}^{m} r_k^i(\underline{w}) \frac{\partial g_l}{\partial w_i}(\underline{w}) \right) \neq 0 \,. \tag{4.112}$$

*With the choice (4.111) the nonlinear system (4.108)-(4.109) has one and only one solution $v$, for $v - \underline{w}$ and $g_l(\underline{w})$ sufficiently small.*

**Remark 18.** *In this result we exclude the case where the boundary is characteristic i.e. the case where one of the $\lambda_k$ is equal to 0. This case cannot be dealt with at this level of generality. On the other hand, wall boundary conditions belong to this category. They can be discussed and handled directly on the physical system under consideration. In this section we will show how to do it for the NSWE equations (see Paragraph 4.3.3.7.1). Moreover, the treatment of wall boundaries of compressible Euler equations and some two-phase systems [DDG08c, DDG10, DDG08a, Dut07] can be done in a similar way.*

**Remark 19.** *In practice, (4.108)-(4.109) are written in a parametric way. We have a set of $m$ physical variables $w$ (e.g. pressure, densities, velocities,...) and we look for $w$ satisfying:*

$$g_l(w) = 0 \,, \quad l = 1, \ldots, p \,, \tag{4.113}$$

$$\tilde{l}_k(\underline{w}) \cdot \Phi = \tilde{l}_k(\underline{w}) \cdot (F(w_K^n) \cdot \vec{n}_K) \,, \tag{4.114}$$

$$\Phi = F(w) \cdot \vec{n}_K \,, \tag{4.115}$$

*and then we take:*

$$\Phi(w_K^n, K, \partial\Omega) = \Phi \,. \tag{4.116}$$

*The system (4.113)-(4.114)-(4.115) is then solved by Newton's method.*

#### 4.3.3.7.1 Impermeable boundary

Consider the case of a rigid wall boundary

$$\vec{u}(\mathbf{x}, t) \cdot \vec{n} = 0, \quad \mathbf{x} \in \partial\Omega, \tag{4.117}$$

and the hyperbolic system (4.63), (4.64). The flux $\Phi$ that we have to determine on the boundary $\partial\Omega$ has the following form if we take into account (4.117):

$$\Phi = \left( \mathcal{F} \cdot \vec{n} \right)\big|_{\partial\Omega} = \begin{pmatrix} 0 \\ \frac{g}{2} H^2 n_x \\ \frac{g}{2} H^2 n_y \end{pmatrix} . \tag{4.118}$$

Thus, we have to determine $\frac{g}{2}H^2$ on the boundary $\partial\Omega$. For this purpose we employ a complementary numerical boundary condition as it was explained above:

$$l_3(\mathbf{w}_K)\cdot\Phi = l_3(\mathbf{w}_K)\cdot\mathcal{F}_n(\mathbf{w}_K), \tag{4.119}$$

where $l_3$ is the left eigenvector corresponding to the positive eigenvalue $\lambda_3 = u_n + c = c > 0$. Solving equation (4.119) leads to the following value of the unknown component:

$$\frac{g}{2}H^2\Big|_{\partial\Omega} = \Big(cHu_n + \frac{g}{2}H^2\Big)\Big|_K,$$

which determines completely the boundary flux (4.118).

**4.3.3.7.2 Generating boundary** Now let us consider a boundary where the total water depth is prescribed:

$$H|_{\partial\Omega} = H_0(\mathbf{x}_s, t) > 0, \quad \mathbf{x}_s \in \partial\Omega.$$

Taking into account this information, the flux $\Phi$ to be determined has the following form:

$$\Phi = \big(\mathcal{F}\cdot\vec{n}\big)\big|_{\partial\Omega} = \begin{pmatrix} H_0u_n \\ H_0uu_n + \frac{g}{2}H_0^2n_x \\ H_0vu_n + \frac{g}{2}H_0^2n_y \end{pmatrix}. \tag{4.120}$$

Hence, we have to find $u$ and $v$ on the generating boundary $\partial\Omega$. The normal velocity will be immediately deduced from this information $u_n := un_x + vn_y$.

Throughout this section we will assume that the flow is "subsonic", i.e. $|\vec{u}\cdot\vec{n}| \le c$. We could also consider the "supersonic" case, but physically this situation is rather exotic. Henceforth, we have one negative eigenvalue $\lambda_1 = u_n - c$, one positive $\lambda_3 = u_n + c$ and $\lambda_2 = u_n$ can be in principle of any sign. Thus we have to consider two cases: $u_n < 0$ and $u_n \ge 0$. In the first case we need a supplementary physical condition (on the tangential velocity to the boundary), in the second one we use a supplementary numerical condition:

$$l_2(\mathbf{w}_K)\cdot\Phi = l_2(\mathbf{w}_K)\cdot\mathcal{F}_n(\mathbf{w}_K).$$

Both lead to the same conclusion: $u_\tau|_{\partial\Omega} = u_\tau|_K$, where $u_\tau := un_y - vn_x$ is the tangential velocity. Computations very similar to the previous section 4.3.3.7.1 lead to the following solution:

$$u_n|_{\partial\Omega} = \frac{Hcu_n + \frac{g}{2}(H^2 - H_0^2)}{H_0c}, \quad u|_{\partial\Omega} = u_n|_{\partial\Omega}\,n_x + u_\tau n_y, \quad v|_{\partial\Omega} = u_n|_{\partial\Omega}\,n_y - u_\tau n_x.$$

Substituting these expressions into (4.120) gives the boundary flux $\Phi$.

### 4.3.4 Numerical results

The numerical tests presented here are of two kinds. The first one is a comparison with analytical solutions (or approximate analytical solutions) : sections 4.3.4.1, 4.3.4.2, 4.3.4.4. This allows us to test the correctness and precision of the numerical scheme. The second one is a comparison with results from laboratory experiments : sections 4.3.4.3. This allows us to test the capacity of the code to reproduce actual events, and in particular assess the validity of the nonlinear shallow-water equations for tsunami modeling.

#### 4.3.4.1 Convergence test

We begin the presentation of numerical tests by the simplest one – convergence test. We would like to show the accuracy of the MUSCL scheme implementation. To do it, we solve numerically the following scalar linear advection equation

$$\frac{\partial w}{\partial t} + \vec{u}_0 \cdot \nabla w = 0, \quad \vec{u}_0 \in \mathbb{R}^2$$

with smooth[15] initial conditions. Moreover, it has almost compact support in order to reduce the influence of boundary conditions. It is obvious that this equation will just translate the initial form in the direction $\vec{u}_0$. So, we have an analytical solution which can be used to quantify the numerical method error. On the other hand, to measure the convergence rate, we constructed a sequence of refined meshes.

Figure 4.39 shows the error of the numerical method in $L_\infty$ norm as a function of the mesh characteristic size. The slope of these curves represents an approximation to the theoretical convergence rate. On this plot, the blue curve corresponds to the first order upwind scheme while the other two (red and black) correspond to the MUSCL scheme with least-squares (see Section 4.3.3.6.4) and Green-Gauss (see Section 4.3.3.6.3) gradient reconstruction procedures respectively. One can see that the blue curve slope is equal approximatively to 0.97 which means first order convergence. The other two curves have almost the same slope equal to 1.90 indicating a second order convergence rate for the MUSCL scheme. We remark that in our implementation of the second-order scheme the least-squares reconstruction seems to give slightly more accurate results than the Green-Gauss procedure.

The next figure represents the measured CPU time in seconds again as a function of the mesh size. Obviously, this kind of data is extremely computer dependent but the qualitative behaviour is the same on all systems. On Figure 4.40 one can see that the "fastest" curve is the blue one (first order upwind scheme). Then we have two almost

[15] We intentionally choose a smooth initial condition since the discontinuities can decrease the overall accuracy of the scheme.

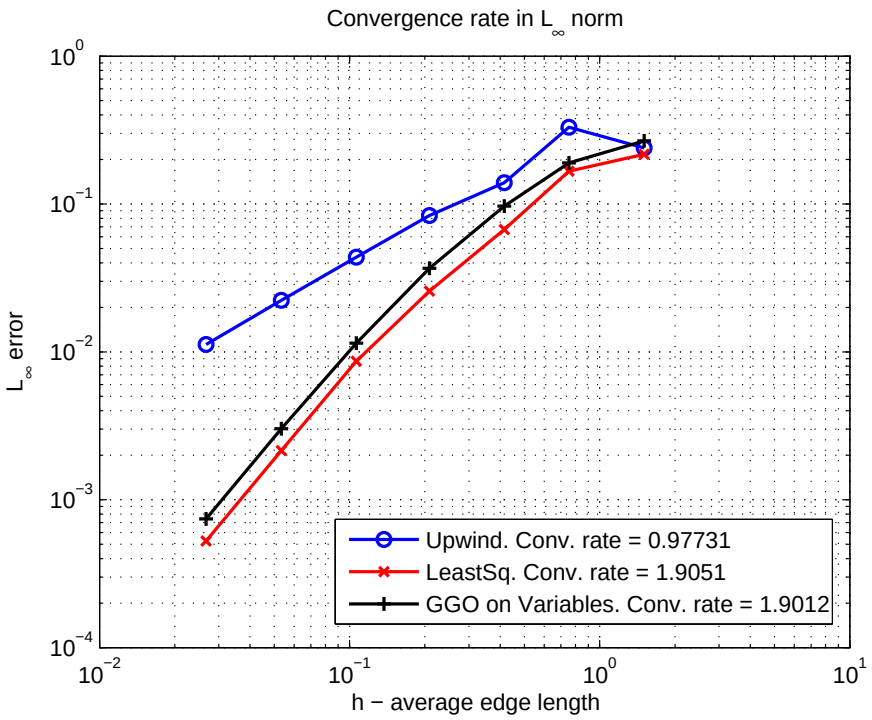


**Figure 4.39:** Numerical method error in $L_\infty$ norm.

superimposed (black and red) curves referring to the second-order gradient reconstruction on variables. Here again one can notice that the least-squares method is slightly faster than the Green-Gauss procedure. On this figure we represented one more curve (the highest one) which corresponds to Green-Gauss gradient reconstruction on fluxes (it seems to be very natural in the context of the FVCF scheme explained in Section 4.3.3.1.1). Our numerical tests show that this method is quite expensive from the computational point of view and we decided not to choose it.

The next three sections deal with the validation of VOLNA again a set of benchmarks for tsunami modelling proposed at the Catalina 2004 workshop on long waves ; they are among the 6 benchmarks currently recommended by the United States National Oceanic and Atmospheric Administration (NOAA) for the evaluation of operational tsunami forecasting models [SBT+07]. In order to help the reproductibility and comparison of numerical results, all the following test cases make use of publicly available data[16]. Although, for each benchmark, we present results for one mesh only, we have checked that the simulations converge as the mesh resolution increases.

[16] `http://www.cee.cornell.edu/longwave/index.cfm?page=benchmark`

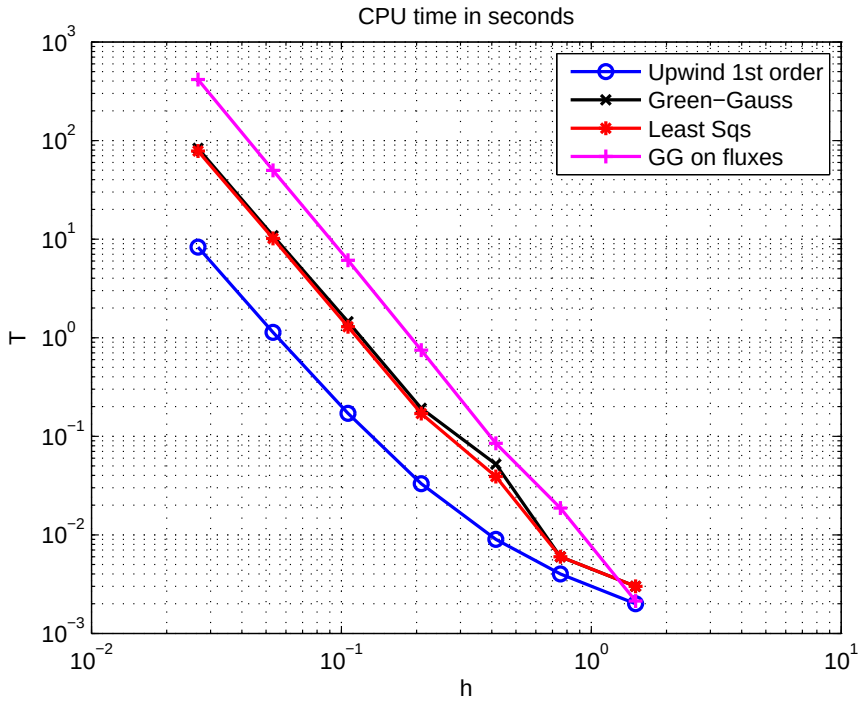


**Figure 4.40:** CPU time for different finite volume schemes.

#### 4.3.4.2 Tsunami run-up onto a plane beach

In this test case, we look at the runup of a tsunami wave over a plane sloping beach (of slope $\frac{1}{10}$). The initial depression wave propagates leftwards (see figure 4.50). The result of the simulation is compared to an analytical solution, obtained using the initial value problem technique of Carrier, Wu and Yeh [CWY03]. Note that the computational domain is approximately 50 km long, whereas the shoreline motion scale is 1 km ; hence, we choose to refine the mesh by a factor 10 near the initial shoreline. The results presented here correspond to a resolution of 8 meters in the direction of propagation. Moreover, the initial free surface amplitude is a few meters high. Thus, due to the difference of spatial scales between the bathymetry, the initial free surface and the computational domain dimensions, the source term $gH\nabla h$ is very steep (see figure 4.50), which renders the use of a well-balanced scheme mandatory. This test case is one-dimensional. Since our code is two-dimensional, we implement it using a two dimensional computational domain, with translation invariance in the transverse direction.

We can see on Figures 4.41 and 4.42 that the numerical results match pretty well the approximate analytical solution, especially near the shoreline location. This ensures the accuracy of the runup algorithm presented in section 4.3.3.3.

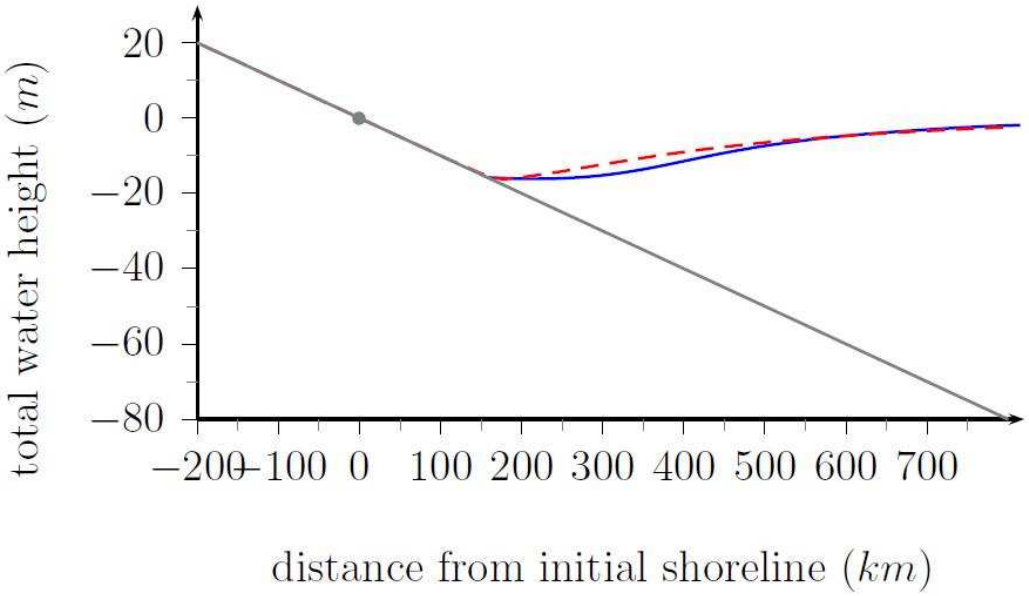


**Figure 4.41:** Catalina 1 benchmark — comparison between analytical (solid) and numerical (dashed) values for free surface at time 160 seconds. The gray line represents the beach, and the gray point the initial shoreline location.

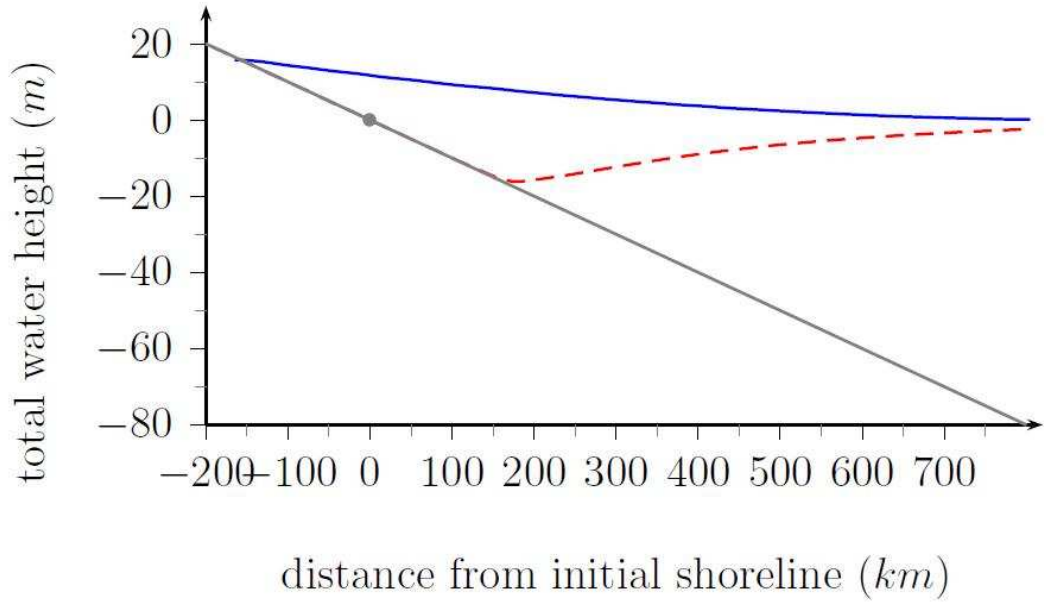


**Figure 4.42:** Catalina 1 benchmark — comparison between analytical (solid) and numerical (dashed) values for free surface at time 220 seconds. The gray line represents the beach, and the gray point the initial shoreline location.

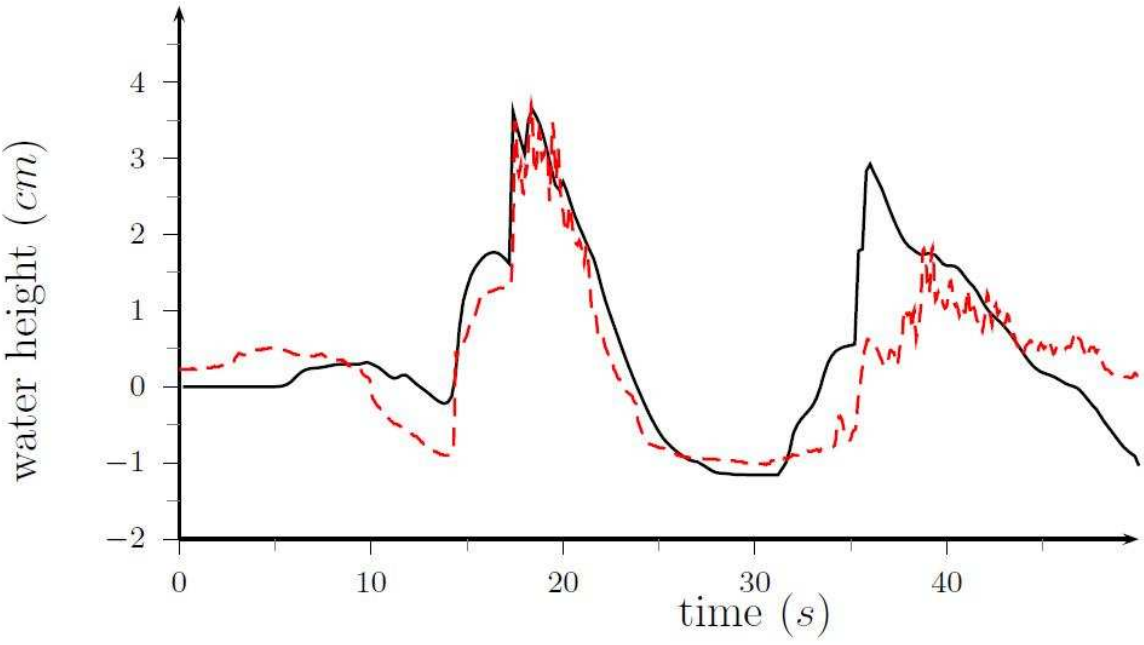


**Figure 4.43:** Catalina 2 benchmark — comparison between numerical results and experimental data at gage 5.

#### 4.3.4.3 Tsunami run-up onto a complex 3-dimensional beach

This experiment reproduces at $\frac{1}{400}$ scale the Monai valley tsunami, which struck the Island of Okushiri (Hokkaido, Japan) in 1993, in a 205 meters long wave tank. The computational domain reproduces the last 5 meters of the wave tank. The initial incident wave offshore is given by experimental data, and fed as a time dependent boundary condition.

We compare the numerical results with the recorded data at three of the wave gages installed in the wave tank : gages number 5, 7 and 9, of respective coordinates $(4.521, 1.196)$, $(4.521, 1.696)$ and $(4.521, 2.196)$. This can be seen in Figures 4.43 – 4.45. The main wave (between times 15 and 25 seconds) is very accurately described, at all gages considered. Moreover, the maximal runup is adequately captured by the code. This value is extremely high, and occured in Monai Valley (the corresponding canyon in the experimental setup, along with the free surface at the moment of maximum elevation are shown in figure 4.52). We obtain a maximal runup value of 8.05 centimeters, which corresponds to 32.2 meters put back at field scale. This is remarkably close to the measured value of 31.7 meters.

Hence the numerical model is able to reproduce the laboratory scenario accurately, even without bottom friction modelling (and thus without any free parameter). In this realistic test case, the ability to refine the mesh near the zones of interest is a very nice asset.

We performed another computation using the set-up described above. Namely, we

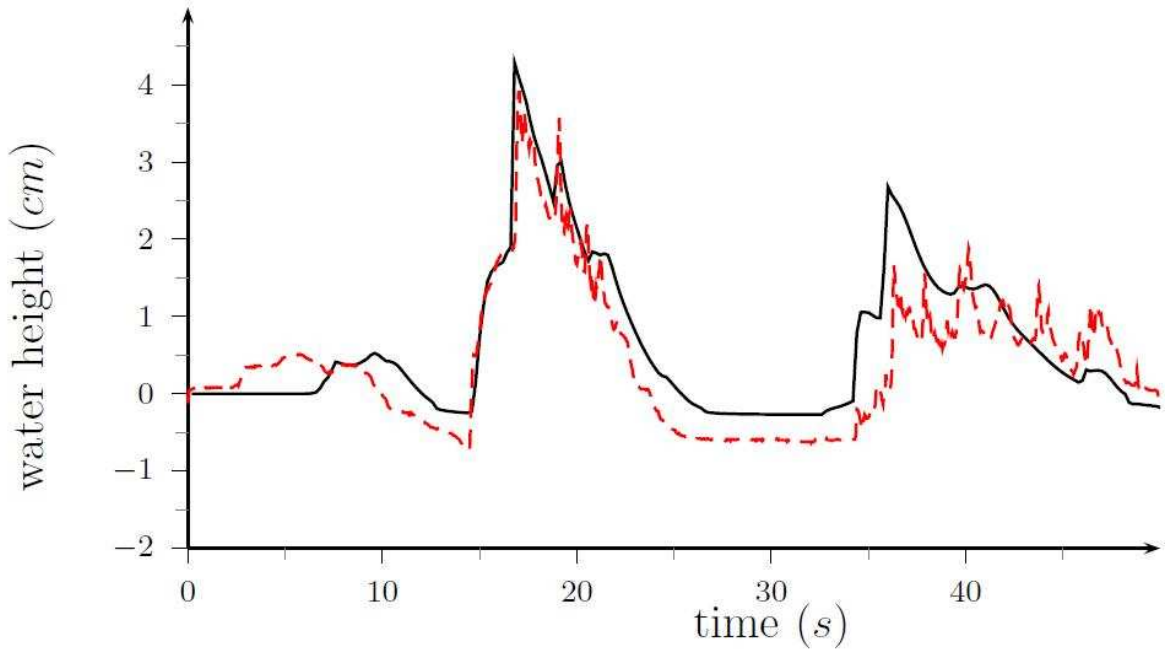


**Figure 4.44:** Catalina 2 benchmark — comparison between numerical results and experimental data at gage 7.

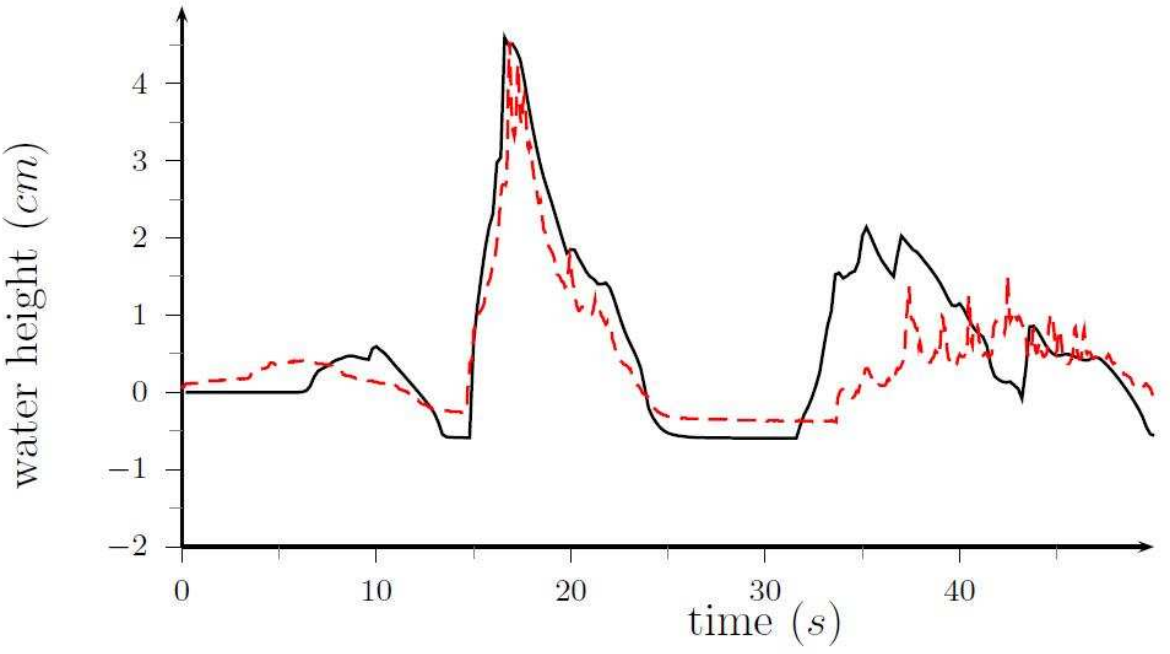


**Figure 4.45:** Catalina 2 benchmark — comparison between numerical results and experimental data at gage 9.

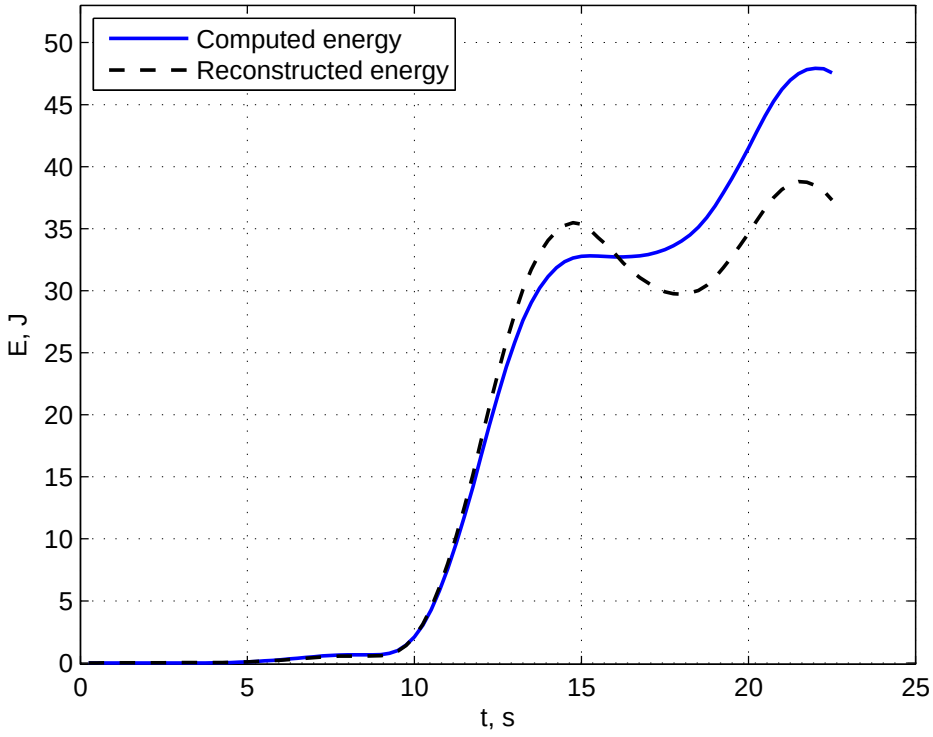


**Figure 4.46:** Computed and reconstructed wave energy profiles for Catalina 2 benchmark problem.

solved equations (4.63), (4.64) completed by a conservation law for the wave energy. This system was recently proposed by Dutykh & Dias and we refer to [DD09a] for technical details and discussions. The total energy evolution is depicted on Figure 4.46. We represented two curves. The blue solid line corresponds to the solution of the augmented system of equations. The black broken line refers to the total energy, estimated from conservative variables:

$$E \approx \frac{1}{2}\rho H|\vec{u}|^2 + \frac{1}{2}\rho g\eta^2,$$

where $\rho$ is the constant fluid density and $\eta = H - h$ is the free surface elevation with respect to the undisturbed water level. In complete accordance with results reported in [DD09a], the computed wave energy is not prone to numerical diffusion and has excellent monotonicity properties. Just at the end of the simulation one can notice a little decrease in both curves. In fact, it is induced by energy losses due to the wave run-up on the beach.

#### 4.3.4.4 Tsunami generation and runup due to a 2-dimensional landslide

In this test case, a translating Gaussian shaped mass, initially at the shoreline, translates rightwards and creates a wave (see figure 4.53). The seafloor can be described by the following equation :

$$h(x,t) = H(x) - h_0(x,t),$$

$$H(x) = x\tan(\beta), \quad \text{and} \quad h_0(x,t) = \delta \exp\left[-\left(2\sqrt{\frac{x\mu^2}{\delta\tan(\beta)}} - \sqrt{\frac{g}{\delta}}\mu t\right)\right],$$

$x$ being the direction of propagation. Here, $\delta$ represent the maximum thickness of the sliding mass, $\mu$ the ratio between $\delta$ and the horizontal length of the mass, and $\beta$ the beach slope. Notice that, at initial time, the submarine mass is partially underwater. Hence, this test case corresponds to a subaerial landslide. A sketch of this experiment can be seen in figure 4.53. This benchmark is one-dimensional, but is implemented using a two-dimensional computational domain, as in section 4.3.4.2. The numerical results we present are obtained as a one dimensional slice (which does not depend on the transverse variable).

The result of the numerical simulation is compared to an analytical solution, computed as an approximate solution of the linear shallow water equations with a forcing term [LLS03]. In Figure 4.47, we can see the comparison between the analytical and numerical wave surface profiles at times 16, 32 and 48 seconds, for $\beta = 5.7^o$, $\delta = 1$ m, and $\mu = 0.01$ (see Figure 4.47). These values ensure that we are in the linear regime of the shallow water equations (and thus that the analytical solution is a good approximation of the nonlinear equations solution). Hence, the comparison is meaningful. Good agreement is reached.

We also performed wave energy computation for this test-case. To our knowledge, the energy evolution has not been shown yet for a landslide generated wave. Computation results are presented on Figures 4.48 and 4.49 for two cases $\mu = 0.01$ and $\mu = 0.1$. In the latter case the linear shallow water equations (LSWE) are not valid even on small time scales. For more information, please refer to [LLS03].

Figure 4.48 shows the wave energy evolution with time. On Figure 4.49 we represented two trajectories in the energy phase-space $(E_k, E_p)$, where $E_k$ is the kinetic energy and $E_p$ is the potential one. We would like to point out the approximate energy repartition on the black curve ($\mu = 0.1$).

#### 4.3.4.5 Summary

Using different analytical benchmarks, we have validated all components of our code : accuracy and order of convergence of the numerical scheme (section 4.3.4.1), run up algo-

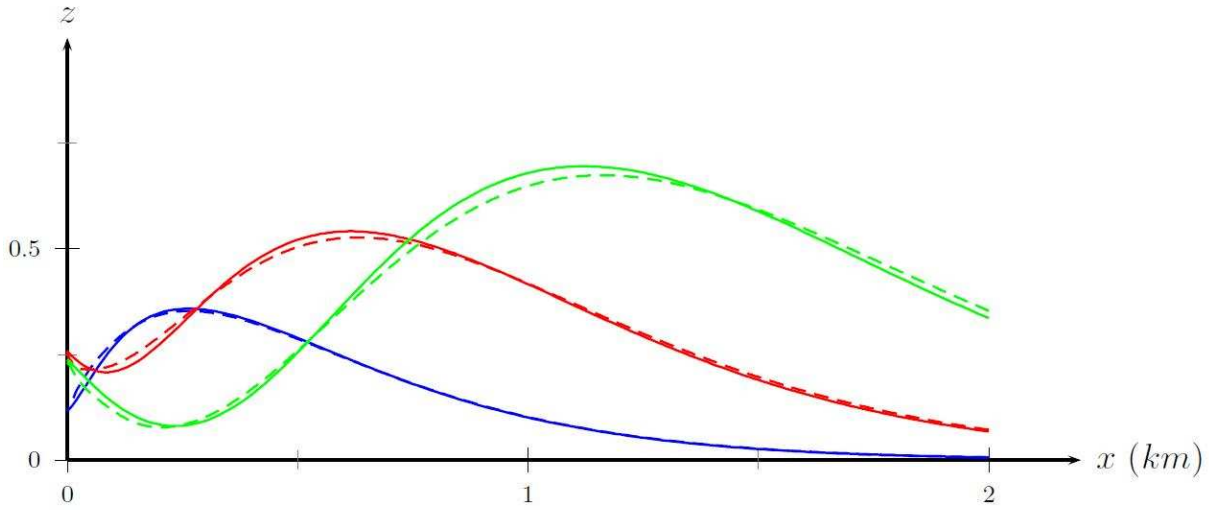


**Figure 4.47:** Catalina 3 benchmark — free surface profiles at three different times — comparison between numerical results (dashed) and analytical formulas (solid lines), at times 16 (blue), 32 (red) and 48 (green) seconds.

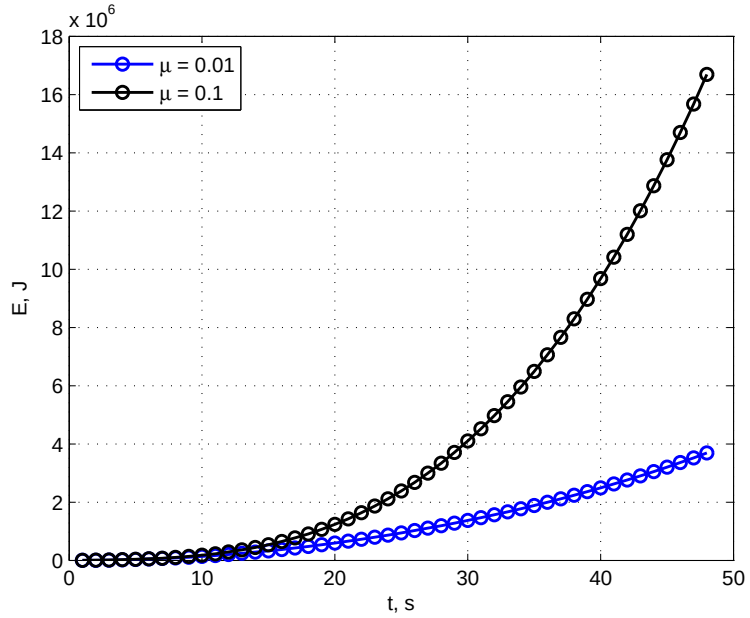


**Figure 4.48:** Energy evolution with time for the 2-dimensional landslide test-case.

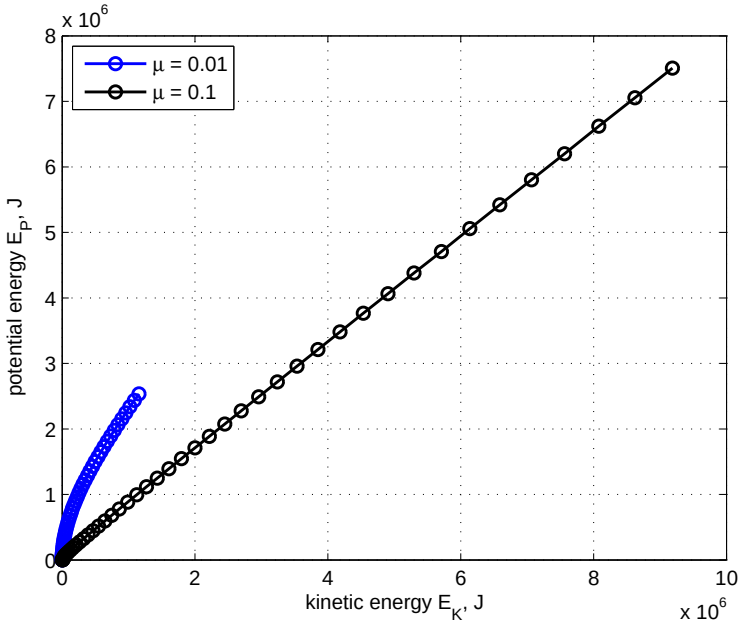


**Figure 4.49:** Trajectories in the energy phase-space $(E_k, E_p)$ for the 2-dimensional landslide test-case.

rithm and treatment of steep depth fields (section 4.3.4.2), and time varying bathymetry in a conservative shallow-water framework (section 4.3.4.4). Moreover, we have shown the capability of the code to model realistic events, using an experimental benchmark (section 4.3.4.3).

### 4.3.5 Conclusions and perspectives

In the present paper we provided a detailed description of the VOLNA code, designed for complete tsunami wave modelling. Namely, we are able to simulate the whole life-cycle of a tsunami from generation to inundation. Special attention was payed to the run-up algorithm described in Section 4.3.3.3. The overall performance test and validation were done in Section 4.3.4.

The VOLNA code is operational and is able to run in complex and rapidly varying conditions. The use of unstructured meshes allows for taking into account the geometry of real coasts. Owing to the implementation of various types of boundary conditions, the code VOLNA can be coupled to other solvers and treat exclusively the zones where the NSWE are physically relevant.

Some new results were presented concerning the energy of tsunami waves [DD09a]. In particular, we show the wave energy evolution for the Catalina 2 test case (run-up on a

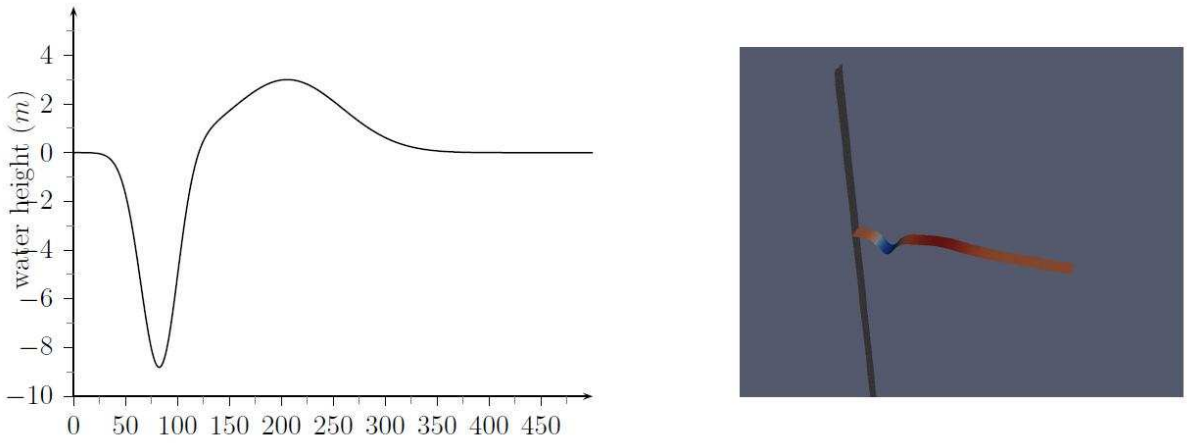


**Figure 4.50:** Catalina 1 benchmark — initial free surface profile (left) ; bathymetry and initial free surface, at the same vertical scale (right).

complex 3D beach) and a landslide generated tsunami (Catalina 3 benchmark problem).

In the future we would like to add more physics to the VOLNA code: dissipative effects [DD07c, Dut09b] (one could for example implement the dissipative terms from Bresch and Desjardins [BD03]) and dispersive effects.

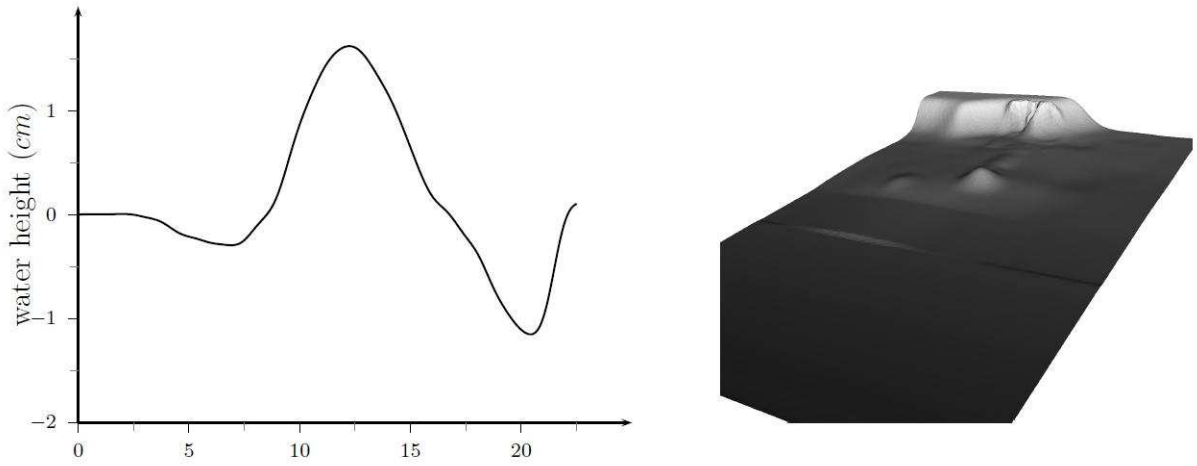


**Figure 4.51:** Catalina 2 benchmark : initial free surface profile (left) ; bathymetry (right).

## 4.4 On the use of finite fault solution for tsunami generation problem

*In physics, your solution should convince a reasonable person. In math, you have to convince a person who's trying to make trouble. Ultimately, in physics, you're hoping to convince Nature. And I've found Nature to be pretty reasonable.*

Frank Wilczek

ABSTRACT. The present study is devoted the tsunami wave generation problem. The main goal of this work is twofold. First of all, we propose a simple, computationally inexpensive model for the sea bed displacement during an underwater earthquake. The main ingredient consists in the finite fault solution for the slip distribution under some assumptions on the rupturing process dynamics. Once the bottom motion is reconstructed, then we study waves induced on the free surface of the ocean. For this purpose we consider three different models approximating the Euler equations of the water wave theory. Namely, we deal with linearized Euler equations (also known as Cauchy-Poisson problem), a Boussinesq system and a weakly nonlinear model. An intercomparison of these three approaches is performed. All developments in this study are illustrated on the real world example of the July 17, 2006 Java event.

### 4.4.1 Introduction

Tsunami waves have attracted a lot of attention of researchers. The scientific community interest has especially increased since the Tsunami Boxing day [SB06] in Decem-

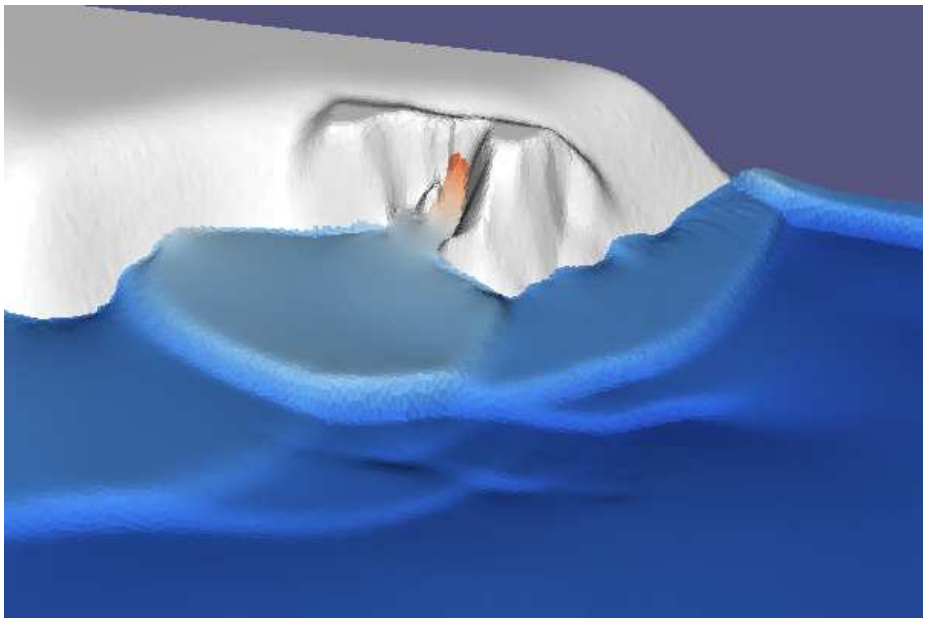

**Figure 4.52:** Maximal runup in Monai valley. The vertical scale is magnified by a factor 3.

ber 2004, killing nearly 230,000 people in fourteen countries. This event has also incited countries concerned with tsunami hazard to develop respective Tsunami Warning Systems (TWS) [Syn05, Bas06]. Perhaps, the most elaborated warning system have been settled in the Pacific Ocean by efforts of NOAA's specialists [TGB+05, GBM+05]. Similarly, the Indian Ocean TWS has been developed by joint collaborative efforts of indonesian and german specialists.

An operational tsunami wave modeling tool is an indispensable part of any warning system [TGB+05, TDS07]. Henceforth, mathematical and numerical models in use should be improved to produce more accurate results in less CPU time [Ima96, TG97, DPD10]. A numerical model of a tsunami wave propagation needs to be provided by an initial condition. The present study is an attempt to improve the initial tsunami waveform construction. The set of existing practices described in the literature constitutes the field of the so-called tsunami generation modeling [Ham73, TT01, DD07d, Dut07, DD09b, DD10].

The Tsunami generation modelling initiated in the early sixties by the prominent work of K. Kajiura [Kaj63], who proposed the use of the static sea bed displacement onto the free surface as an initial condition. Classically, the celebrated Okada [Oka85, Oka92] and sometimes Mansinha & Smylie[17] [MS67, MS71] solutions are used to compute the co-seismic sea bed displacements. This approach is still widely used by the tsunami wave modeling community. However, some progress has been recently made in this direction

[17]In fact, Mansinha & Smylie solution is a particular case of the more general Okada solution.

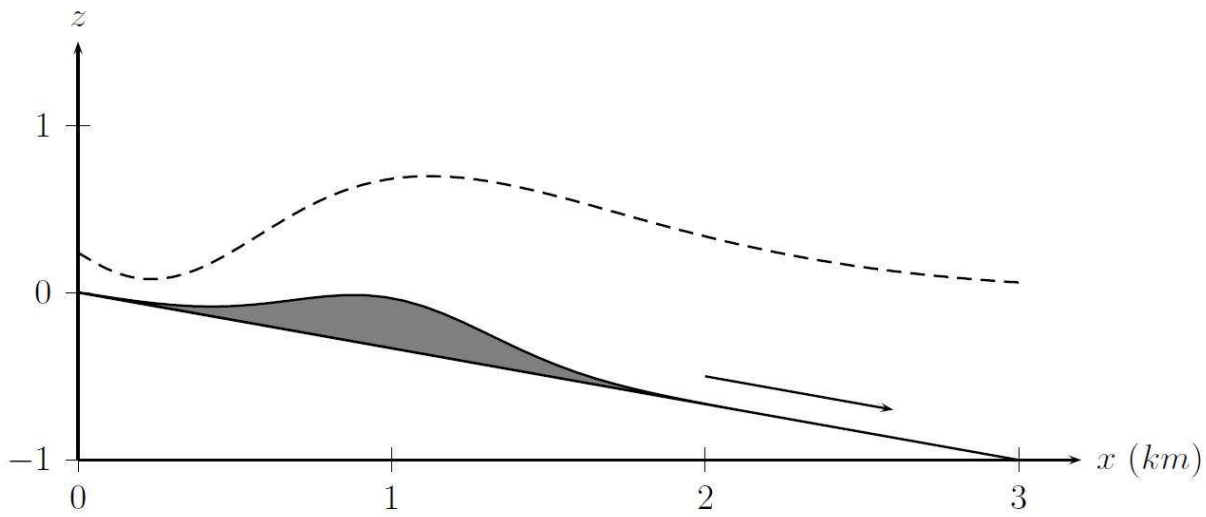


**Figure 4.53:** Sketch of the analytical landslide test case. The submarine mass displacement (in gray) and free surface (dashed line) have been magnified by a factor 1000.

[OTM01, DD07d, Dut07, DD09b, RLF+08, SF09, DPD10].

In the present study we propose to exploit some recent advances in the seismology to reconstruct better co-seismic displacements of a tsunamigenic earthquake. More precisely, we suggest the use of the so-called finite fault solution developed by C. Ji and his collaborators [BLM00, JWH02] and based on static and seismic data inversion. This solution provides us multiple fault segments with variable local slip, rake angle and several other parameters. By applying the Okada solution to each subfault, we reconstruct the sea bed displacement with higher resolution. To our knowledge, this technique was already employed to model Kuril islands tsunamis 15 November 2006 and 13 January 2007, cf. [RLF+08]. Since the Okada solution is constituted of relatively simple closed-form analytical expressions, all computations can be done efficiently enough to be used in a real-time TWS (cf. [WL08]). The obvious *sine qua non* condition is that the corresponding finite fault inversion is also performed in a reasonable time.

In our study we go further in reconstructing the dynamic sea bed displacement according to the rupture propagation speed and the rise time also provided by the finite fault solution. Constructed in this special way sea bed displacements are then coupled with several water wave models. Among them there is a novel weakly nonlinear solver based on a formulation ivolving the Dirichlet-to-Neumann operator which is approximatively computed using the Fourier transform. Two remaining models are the linearized free surface Euler equations and a Boussinesq type system. Developments presented in this study are then illustrated on the example of July 17, 2006 Java event [AKLV06]. However, we un-

| | |
|---|---|
| Fault length, $km$ | 80.9 |
| Fault width, $km$ | 40.0 |
| Focal depth, $km$ | 20.0 |
| Slip, $m$ | 2.5 |
| Dip angle | 10° |
| Slip angle | 95° |
| Strike angle (CW from N) | 289° |

**Table 4.5:** Seismic fault parameters for the Java 2006 event that are classically used for the construction of the initial tsunami waveform [Yal08]. (The corresponding seismic moment can be taken $M_0 = 2.52 \times 10^{27} N \cdot m$ ($M_w = 7.56$).)

derline that presented in this study methodology is quite general and can be applied to any other tsunamigenic earthquake for which a finite fault solution is available.

The study is organized as follows. In Section 4.4.2 we describe the static and the dynamic sea bed displacements, while in Section 4.4.3 we present a simple approximate water wave solver with moving bottom. In Section 4.4.4 we study numerically the generation process of a real-world event. An intercomparison of three mentioned above models is performed. A few important conclusions are drawn out in Section 4.4.5.

### 4.4.2 Co-seismic displacement construction

The problem of tsunami generation modeling is directly related to the problem of the bottom motion during an underwater earthquake. Traditionally, the so-called Okada solution [Oka85, Oka92] is used in cases of regimes characterized by an active fault of small or intermidiate size i.e. constituted by one or a few segments (e.g. the great Sumatra 2004 earthquake, [SB06, IAK+07]). In this case the resulting vertical displacement field is superposed at the free-surface. This approach is conventionally referred to as *passive tsunami generation* [DDK06], contrary to the *active generation* which explicitly involves the bottom motion dynamics [DD07d]. Since in this study we decided to illustrate our methods on the example of July 17, 2006 Java event, we show on Figure 4.54 a typical single-fault based initial condition used for the corresponding tsunami wave modeling [Yal08]. The seismic parameters used to produce this vertical displacement are given in Table 4.5.

**Remark 20.** *The celebrated Okada solution [Oka85, Oka92] is based on two main ingredients — the dislocation theory of Volterra [Vol07] and Mindlin's fundamental solution for an elastic half-space [Min36]. Particular cases of this solution were known before Okada's work, for example the well-known Mansinha & Smylie's solution [MS67, MS71]. Usually*

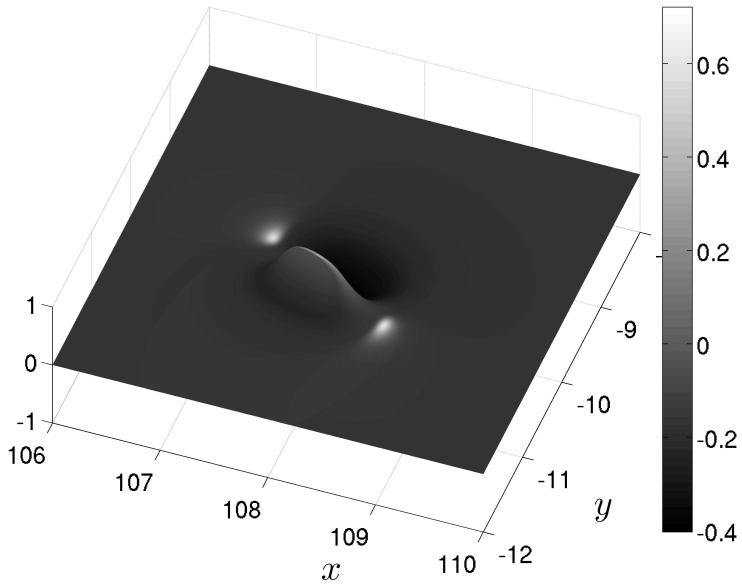


**Figure 4.54:** Static vertical displacement computed according to the single fault parameters of Table 4.5. This solution is typically used as an initial condition for the Java 2006 tsunami propagation simulations.

*all these particular cases differ by the choice of the dislocation and the Burger's vector orientation [Pre65]. We recall the basic assumptions behind this solution:*

- *Fault is immersed into the linear homogeneous and isotropic half-space*
- *Fault is a Volterra's type dislocation*
- *Dislocation has a rectangular shape*

*For more information on Okada's solution we refer to [DD07d, DD07a, Dut07].*

The finite fault solution is based on the multi-fault representation of the rupture [BLM00, JWH02]. The rupture complexity is reconstructed using a joint inversion of the static and seismic data. Fault's surface is parametrized by multiple segments with variable local slip, rake angle, rise time and rupture velocity. The inversion is performed in an appropriate wavelet transform space. The objective function is a weighted sum of $L_1$, $L_2$ norms and some correlative functions. With this approach seismologists are able to recover rupture slip details [BLM00, JWH02]. These available seismic information are exploited in this study to compute the sea bed displacements produced by an underwater earthquake with higher geophysical resolution.

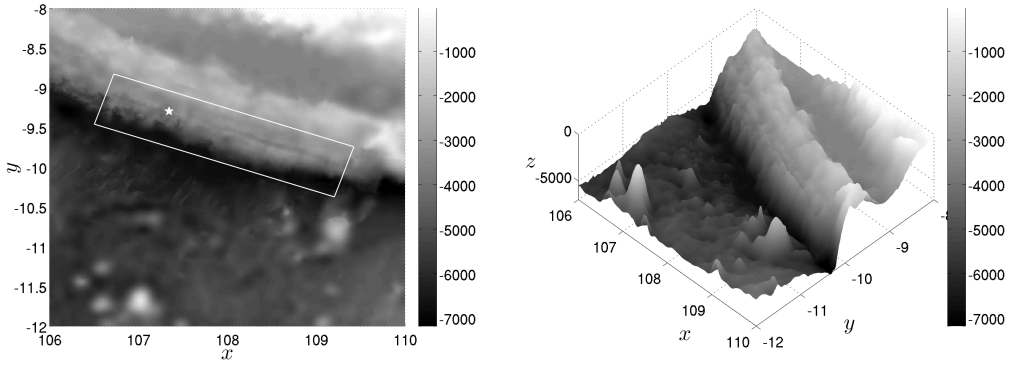


(a) Top view.

(b) Bathymetry side view.

**Figure 4.55:** Surface projection of the fault's plane and the ETOPO1 bathymetric map of the region we study. The symbol $\star$ indicates the hypocenter's location at $(107.345°, -9.295°)$. The local Cartesian coordinate system is centered at the point $(108°, -10°)$. This region is located between $(106°, -8°)$ and $(110°, -12°)$.

The proposed approach will be directly illustrated on the Java's 2006 event. The July 17, 2006 Java's earthquake involved thrust faulting in the Java's trench and generated a tsunami wave that inundated the southern coast of Java [AKLV06, FKM+07]. The estimates of the size of the earthquake (cf. [AKLV06]) indicate a seismic moment of $6.7 \times 10^{20}\ N \cdot m$, which corresponds to the magnitude $M_w = 7.8$. Later this estimation was refined [Ji06] to $M_w = 7.7$. Like other events in this region, Java's event had an unusually low rupture speed of 1.0 – 1.5 $km/s$, and occurred near the up-dip edge of the subduction zone thrust fault. According to C. Ammon *et al* [AKLV06], most aftershocks involved normal faulting. The rupture propagated approximatively 200 $km$ along the trench with an overall duration of approximatively 185 $s$. The fault's surface projection along with ocean ETOPO1 bathymetric map are shown in Figure 4.55. We note that Indian Ocean's bathymetry considered in this study varies between 7186 and 20 meters in the shallowest region.

**Remark 21.** *We have to mention that the finite fault inversion for this earthquake was also performed by the Caltech team [OK06]. They estimated the July 17, Southern Java earthquake magnitude was $M_w = 7.9$. In this study we do not present numerical simulations involving their data but it is straightforward to apply our algorithms to this case as well.*

#### 4.4.2.1 Static displacement

In order to illustrate the advantages of the proposed approach we will compute also the static co-seismic displacements using the finite fault solution [Ji06]. The fault is

| | |
|---|---|
| $P$-wave celerity $c_p$, $m/s$ | 6000 |
| $S$-wave celerity $c_s$, $m/s$ | 3400 |
| Crust density $\rho$, $kg/m^3$ | 2700 |
| Dip angle, $\delta$ | 10.35° |
| Slip angle (CW from N) | 288.94° |

**Table 4.6:** Geophysical parameters used to model elastic properties of the subduction zone in the region of Java.

considered to be the rectangle with vertices located at (109.20508° (Lon), −10.37387° (Lat), 6.24795 $km$ (Depth)), (106.50434°, −9.45925°, 6.24795 $km$), (106.72382°, −8.82807°, 19.79951 $km$), (109.42455°, −9.74269°, 19.79951 $km$) (see Figure 4.55 (a)). The fault's plane is conventionally divided into $N_x = 21$ subfaults along strike and $N_y = 7$ subfaults down the dip angle, leading to the total number of $N_x \times N_y = 147$ equal segments. Parameters such as subfault location $(x_c, y_c)$, depth $d_i$, slip $u$ and rake angle $\phi$ for each segment are given in Table 4.7 and can be also downloaded at [Ji06]. The common elastic constants to all subfaults parameters such as dip and slip angles are given in Table 4.6. (We note that the slip angle is measured traditionally in the counter-clockwise direction from the North. The relations between the elastic wave celerities $c_p$, $c_s$ and Lamé coefficients $\lambda$, $\mu$ used in Okada's solution are outlined in Section 4.4.8.)

We compute the Okada's solution at the sea bottom (substituting $z = 0$ in the geophysical coordinate system) and taking the vertical component of the displacement field $\mathcal{O}_i(\mathbf{x}; \delta, \lambda, \mu, \ldots)$, where $\delta$ is the dip angle, $\lambda$, $\mu$ are the Lamé coefficients (see Appendix 4.4.8) and dots denote the dependence of the function $\mathcal{O}(\mathbf{x})$ on other 8 parameters, cf. [DD07d]. The resulting co-seismic vertical bottom displacement $\zeta(\mathbf{x})$ can be computed as a simple superposition of subfault contributions:

$$\zeta(\mathbf{x}) = \sum_{i=1}^{N_x \times N_y} \mathcal{O}_i(\mathbf{x}; \delta, \lambda, \mu, \ldots)$$

The graph of $\zeta(\mathbf{x})$ is presented in Figure 4.56. The specific static displacement can be compared with the single fault classical approach depicted on Figure 4.54. It is worth to mention that more than one local extrema can be found in this solution due to a higher slip resolution.

Hereafter we will adopt the short-hand notation $\mathcal{O}_i(\mathbf{x})$ for the vertical displacement component of the Okada's solution for the $i^{\text{th}}$ segment having in mind its dependence on various parameters from Tables 4.6 and 4.7.

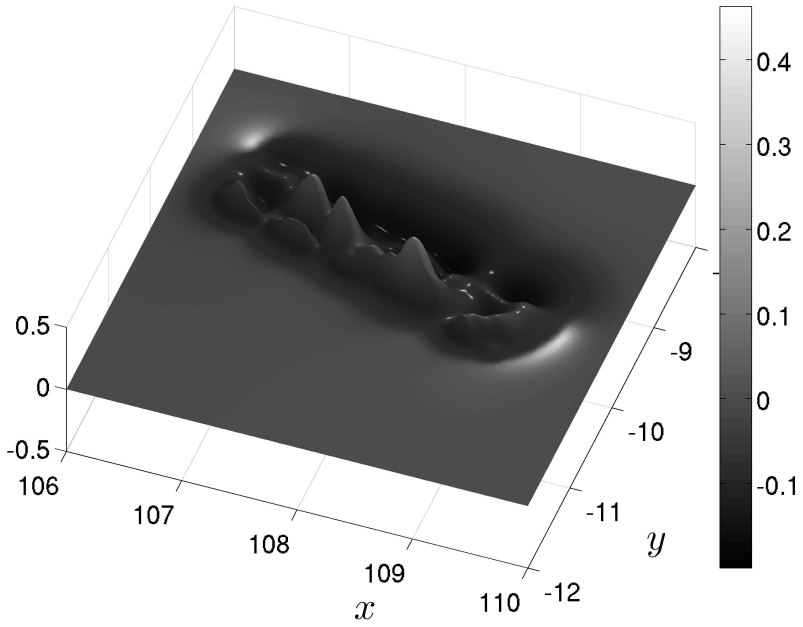


**Figure 4.56:** The vertical displacement of the finite fault solution, cf. [Ji06]. The corresponding seismic moment is $M_0 = 3.53 \times 10^{27}\ N \cdot m$ ($M_w = 7.65$).

#### 4.4.2.2 Dynamic co-seismic displacements

Here, we go even further in the reconstruction of the bottom motion. By making some assumptions on the time dependence of displacement fields, we can have an insight into the dynamics of the sea bed motion.

The finite fault solution provides two additional parameters concerning the rupture dynamics of the July 17, 2006 event — the rupture velocity $v_r = 1.1\ km/s$ and the rise time $t_r = 8\ s$. The epicenter is located at the point $\mathbf{x}_e = (107.345°, -9.295°)$ (cf. [Ji06]). Given the origin $\mathbf{x}_e$, the rupture velocity $v_r$ and $i^{\text{th}}$ subfault location $\mathbf{x}_i$ (the full list is provided in Table 4.7), we define the *subfault activation times* $t_i$ needed for the rupture to achieve the corresponding segment $i$ by the formulas:

$$t_i = \frac{||\mathbf{x}_e - \mathbf{x}_i||}{v_r}, \quad i = 1, \ldots, N_x \times N_y.$$

We will follow also the pioneering idea of J. Hammack [Ham72, Ham73] developed later in [TT01, THT02, DD07d, DDK06, KDD07] where the maximum bottom deformation is achieved during some finite time (known as the rise time) according to a specific (in *ad hoc* manner) dynamic scenario. Various scenarios on the time dependence (instanteneous, linear, trigonometric, exponential, etc) can be found in [Ham73, DDK06, DD07d]. In this

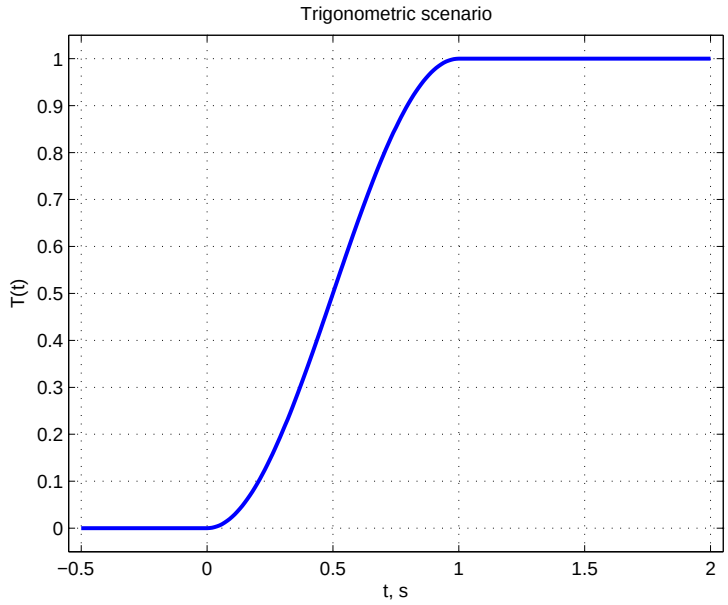


**Figure 4.57:** Trigonometric scenario with rise time $t_r = 1\ s$.

study we will adopt the trigonometric scenario which can be described by the formula:

$$T(t) = \mathcal{H}(t - t_r) + \frac{1}{2}\mathcal{H}(t)\mathcal{H}(t_r - t)\big(1 - \cos(\pi t/t_r)\big),$$

where $\mathcal{H}(t)$ is the Heaviside step function. For illustrative purposes this dynamic scenario is represented on Figure 4.57.

Finally, we put together all ingredients in order to construct the dynamic sea bed motion:

$$\zeta(\mathbf{x}, t) = \sum_{i=1}^{N_x \times N_y} \mathcal{H}(t - t_i)T(t - t_i)\mathcal{O}_i(\mathbf{x}). \tag{4.121}$$

In the following sections we will present several approaches to couple this dynamic deformation with the hydrodynamic problem to predict waves induced on the ocean's free surface.

### 4.4.3 Fluid layer solution

Once the sea bed deformation is determined, a water wave problem has to be solved in order to compute the free surface motion induced by the ocean bottom shaking. Traditionally this difficulty is circumvented by the simple translation of the static bottom deformation onto the free surface [Kaj63], known as the passive generation approach [DDK06, KDD07]. In this section we present three approximate models to the water

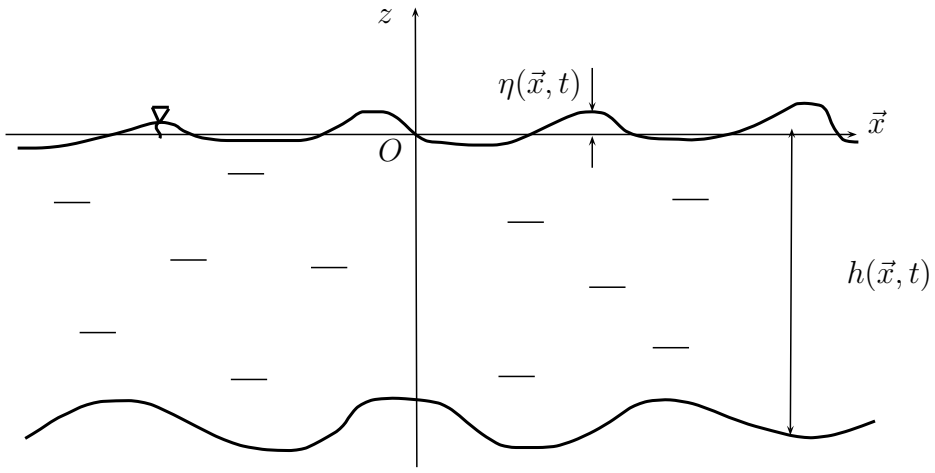


**Figure 4.58:** Sketch of the physical domain for the water wave problem.

wave problem with moving bottom that we will use in combination with the finite-fault solution to study the tsunami generation problem.

#### 4.4.3.1 Linearized Euler equations

In the sequel we will consider an ideal incompressible fluid of constant density $\rho$ in the domain $\Omega \subseteq \mathbb{R}^2$. The horizontal independent variables will be denoted by $\mathbf{x} = (x, y)$ and the vertical by $z$. The origin of the cartesian coordinate system is chosen such that the surface $z = 0$ corresponds to the still water level. The fluid is bounded below by the bottom $z = -h(\mathbf{x}, t)$ and above by the free surface $z = \eta(\mathbf{x}, t)$. Usually we assume that the total depth $H(\mathbf{x}, t) := h(\mathbf{x}, t) + \eta(\mathbf{x}, t)$ remains positive $H(\mathbf{x}, t) \geq h_0 > 0$ under the system dynamics $\forall t \in [0, T]$. The sketch of the physical domain is shown in Figure 4.58.

**Remark 22.** *Classically in water wave modeling, we make the assumption that the free surface is a graph $z = \eta(\mathbf{x}, t)$ of a single-valued function. It means in practice that we exclude some interesting phenomena, (e.g. wave breaking phenomena) which are out of scope of this modeling paradigm.*

The linearized water wave problem consists of the following set of equations [Ham72, Ham73, DD07d]:

$$\Delta\phi = \nabla^2\phi + \partial^2_{zz}\phi = 0, \qquad (\mathbf{x}, z) \in \Omega \times [-h, 0], \tag{4.122}$$

$$\partial_t\eta - \partial_z\phi = 0, \qquad z = \eta(\mathbf{x}, t), \tag{4.123}$$

$$\partial_t\phi + g\eta = 0, \qquad z = \eta(\mathbf{x}, t), \tag{4.124}$$

$$\partial_t h + \partial_z\phi = 0, \qquad z = -h(\mathbf{x}, t). \tag{4.125}$$

This set of equations is also often referred in the literature as the Cauchy-Poisson (CP) problem after the pioneering work of A.-L. Cauchy [Cau27].

In view of the specific applications' requirements on analytical techniques, we will assume first that the domain $\Omega = \mathbb{R}^2$, i.e. unbounded in the horizontal extent, and the bottom has a special form:

$$h(\mathbf{x}, t) = h_0 - \zeta(\mathbf{x}, t),$$

where $h_0$ is some uniform depth and $\zeta(\mathbf{x}, t)$ is the sea bed displacement due to an underwater earthquake. In Section 4.4.2.2 one possible construction of the bottom displacement is proposed. Using integral transform methods (cf. [Ham73, TT01, DD07d, KDD07]), one can derive the following expression for the free surface elevation $\eta(\mathbf{x}, t)$:

$$\eta(\mathbf{x}, t) = \frac{\gamma^2}{2}\mathcal{F}^{-1}\Big\{\sum_{i=1}^{n} \frac{\mathcal{H}(t - t_i)\hat{\zeta}_i(\mathbf{k})}{(\gamma^2 - \omega^2)\cosh(|\mathbf{k}|h_0)}\big(\cos(\omega(t - t_i)) - \cos(\gamma(t - t_i)) + \mathcal{H}(t - t_i - t_0)[\cos(\omega(t - t_i - t_0)) + \cos(\gamma(t - t_i))]\big)\Big\},$$

where $\gamma = \dfrac{\pi}{t_r}$ and $t_r$ is the rise time defined in Section 4.4.2.2. A similar expression can be also derived for the velocity potential $\phi(\mathbf{x}, z, t)$, however we do not directly need it in our study.

This semi-analytical solution will be used below in numerical simulations. It has a big advantage of being simple and, thus, computationally inexpensive. However, the flat bottom assumption ($h(\mathbf{x}) = h_0 = const$) prevents us from using this solution beyond some small evolution times. The validity of this approximation has already been addressed in the literature [KDD07, SF09] and will be discussed at some point below.

#### 4.4.3.2 The weakly-nonlinear model

A tsunami wave during its generation is well described even by the CP problem [DD07d, KDD07, SF09]. The main reason for this simplicity is the fact that a wave of a half meter amplitude represents only a tiny perturbation of a 4000 m water column. However, the real world bathymetry is generally complex and may contain simultaneously various scales. For example, the subduction zone bathymetry represented on Figure 4.55 ranges from 7000 to 20 m and thus, nonlinear effects may be locally important. In order to take into account all realistic bathymetry features and study at least the initial stages of a tsunami propagation we propose below a new numerical model.

Here we consider the physical setting and notation from Section 4.4.3.1. The governing equations of the classical water wave problem are the following [Lam32, Sto58, Mei94,

Whi99]:

$$\Delta\phi = \nabla^2\phi + \partial^2_{zz}\phi = 0, \qquad (\mathbf{x}, z) \in \Omega \times [-h, \eta], \tag{4.126}$$

$$\partial_t\eta + \nabla\phi \cdot \nabla\eta - \partial_z\phi = 0, \qquad z = \eta(\mathbf{x}, t), \tag{4.127}$$

$$\partial_t\phi + \tfrac{1}{2}|\nabla\phi|^2 + \tfrac{1}{2}(\partial_z\phi)^2 + g\eta = 0, \qquad z = \eta(\mathbf{x}, t), \tag{4.128}$$

$$\partial_t h + \nabla\phi \cdot \nabla h + \partial_z\phi = 0, \qquad z = -h(\mathbf{x}, t), \tag{4.129}$$

with $\phi$ the velocity potential, $g$ the acceleration due to gravity force and $\nabla = (\partial_x, \partial_y)$ denotes the gradient operator in horizontal Cartesian coordinates.

Fluid incompressibility and flow irrotationality assumptions lead to the Laplace equation (4.126) for the velocity potential $\phi(\mathbf{x}, z, t)$. The main difficulty of the water wave problem lies on the boundary conditions. Equations (4.127) and (4.129) express the free surface and bottom impermeability, while the Bernoulli condition (4.128) expresses the free surface isobarity respectively.

Function $h(\mathbf{x}, t)$ represents the ocean's bathymetry (depth below the still water level, see Figure 4.58) and is assumed to be known. The dependence on time is included in order to take into account the bottom motion during an underwater earthquake [DD07a, DD07d, DDK06, Dut07]. In this study the bathymetry is decomposed in the permanent part $h_0(\mathbf{x})$ (given e.g. by the ETOPO1 database, cf. Figure 4.55) and of the dynamic sea bed displacement $\zeta(\mathbf{x}, t)$ constructed above (4.121):

$$h(\mathbf{x}, t) = h_0(\mathbf{x}) - \zeta(\mathbf{x}, t). \tag{4.130}$$

**Remark 23.** *Surface tension effects can also be included in the water wave problem. In this case, the Bernoulli condition (4.128) has to be modified:*

$$\partial_t\phi + \tfrac{1}{2}|\nabla\phi|^2 + \tfrac{1}{2}(\partial_z\phi)^2 + g\eta = \frac{\sigma}{\rho}\nabla \cdot \left(\frac{\nabla\eta}{\sqrt{1 + |\nabla\eta|^2}}\right), \quad z = \eta(\mathbf{x}, t),$$

*where $\sigma$ is the surface tension coefficient. However, this effect is negligible for the applications considered in the present study and will be ignored.*

**Remark 24.** *Recently, some weak dissipative effects have also beed included into the classical water wave problem (4.126) – (4.129). For more details on the visco-potential formulation we refer to [DDZ08, DD07c, Dut07, Dut09b, Dut09a].*

For the exposition below we will need also to compute unitary exterior normals to the fluid domain. It is straightforward to obtain the following expressions for the normals at the free surface and bottom respectively:

$$\vec{n}_f = \frac{1}{\sqrt{1 + |\nabla\eta|^2}} \begin{vmatrix} -\nabla\eta \\ 1 \end{vmatrix}, \qquad \vec{n}_b = \frac{1}{\sqrt{1 + |\nabla h|^2}} \begin{vmatrix} -\nabla h \\ -1 \end{vmatrix}.$$

In 1968 V. Zakharov proposed a different formulation of the water wave problem based on the trace of the velocity potential at the free surface [Zak68]:

$$\varphi(\mathbf{x},t) := \phi(\mathbf{x},\eta(\mathbf{x},t),t).$$

This variable plays a role of the generalized momentum in the Hamiltonian description of water waves [Zak68, DB06]. The second canonical variable is the free surface elevation $\eta$.

Another important ingredient is the normal velocity at the free surface $v_n$ which is defined as:

$$v_n(\mathbf{x},t) := \sqrt{1+|\nabla\eta|^2}\,\frac{\partial\phi}{\partial\vec{n}_f}\bigg|_{z=\eta} = (\partial_z\phi - \nabla\phi\cdot\nabla\eta)|_{z=\eta}\,. \tag{4.131}$$

Dynamic boundary conditions (4.127) and (4.128) at the free surface can be rewritten in terms of $\varphi$, $v_n$ and $\eta$ [CSS92, CS93, FCKG05]:

$$\begin{aligned} \partial_t\eta - \mathbf{D}_\eta(\varphi) &= 0, \\ \partial_t\varphi + \tfrac{1}{2}|\nabla\varphi|^2 + g\eta - \tfrac{1}{2(1+|\nabla\eta|^2)}\big[\mathbf{D}_\eta(\varphi) + \nabla\varphi\cdot\nabla\eta\big]^2 &= 0. \end{aligned} \tag{4.132}$$

Here we introduced the so-called Dirichlet-to-Neumann operator (D2N) [CM85, CS93] which maps the velocity potential at the free surface $\varphi$ to the normal velocity $v_n$:

$$\mathbf{D}_\eta : \quad \varphi \mapsto v_n = \sqrt{1+|\nabla\eta|^2}\,\tfrac{\partial\phi}{\partial\vec{n}_f}\Big|_{z=\eta}$$

$$\left|\begin{aligned} \nabla^2\phi + \partial_{zz}^2\phi &= 0, \quad (\mathbf{x},z)\in\Omega\times[-h,\eta], \\ \phi &= \varphi, \quad z=\eta, \\ \sqrt{1+|\nabla h|^2}\frac{\partial\phi}{\partial\vec{n}_b} &= \partial_t h, \quad z=-h. \end{aligned}\right.$$

The name of this operator comes from the fact that it makes a correspondance between Dirichlet data $\varphi$ and Neumann data $\sqrt{1+|\nabla\eta|^2}\,\dfrac{\partial\phi}{\partial\vec{n}_f}\Big|_{z=\eta}$ at the free surface. For the sake of completeness we provide in Section 4.4.7 the complete derivation of the Zakharov's formulation formulation for the water wave problem.

#### 4.4.3.2.1 Numerical estimation of D2N operator

It was shown that the water wave problem can be reduced to a system of two PDEs governing the evolution of the canonical variables $\eta$ and $\varphi$. In order to solve this system of equations we have to be able to compute efficiently $\mathbf{D}_\eta(\varphi)$. In this section we present a simple approximate method for the computation of Dirichlet-to-Neumann (D2N) operator. This approach is based on the extensive use of the Fourier transform. On the discrete level this transformation can be efficiently implemented thanks to the Fast Fourier Transform (FFT) algorithm [CT65, FJ05].

The direct $\mathcal{F}$ and inverse $\mathcal{F}^{-1}$ Fourier transforms in 2D are defined as follows:

$$\mathcal{F}[f] = \hat{f}(\mathbf{k}) = \int_{\mathbb{R}^2} f(\mathbf{x}) e^{-i\mathbf{k}\cdot\mathbf{x}}\, d\mathbf{x}, \quad \mathcal{F}^{-1}[\hat{f}] = f(\mathbf{x}) = \frac{1}{(2\pi)^2} \int_{\mathbb{R}^2} \hat{f}(\mathbf{k}) e^{i\mathbf{k}\cdot\mathbf{x}}\, d\mathbf{k}.$$

In this study, the Fourier transform of a function $f$ will be denoted $\hat{f} = \mathcal{F}[f]$.

Let us recall the problem we have to solve:

$$\begin{aligned} \nabla^2\phi + \partial^2_{zz}\phi &= 0, \quad (\mathbf{x}, z) \in \Omega \times [-h, \eta], && (4.133)\\ \phi &= \varphi, \quad z = \eta, && (4.134)\\ \sqrt{1+|\nabla h|^2}\frac{\partial\phi}{\partial\vec{n}_b} &= \partial_t h, \quad z = -h. && (4.135) \end{aligned}$$

Once the function $\phi$ is determined, we have to compute its normal derivative at the free surface $\sqrt{1+|\nabla\eta|^2}\left.\dfrac{\partial\phi}{\partial\vec{n}_f}\right|_{z=\eta}$.

Since a tsunami wave induces a special flow regime in which the horizontal extent is much more important than variations in vertical direction, we can apply the Fourier transform to the Laplace equation (4.133) as if it were posed in a strip-like domain:

$$\frac{d^2\hat{\phi}}{dz^2} - |\mathbf{k}|^2\hat{\phi} = 0.$$

The general exact solution to this ODE can be easily computed:

$$\hat{\phi}(\mathbf{k}; z) = A(\mathbf{k})\cosh(|\mathbf{k}|z) + B(\mathbf{k})\sinh(|\mathbf{k}|z). \tag{4.136}$$

Two unknown functions $A(\mathbf{k})$ and $B(\mathbf{k})$ have to be determined from boundary conditions (4.134), (4.135). For our convenience we will rewrite the Neumann boundary condition at the bottom (4.135) in this form:

$$\left.\frac{\partial\phi}{\partial z}\right|_{z=-h} = -\partial_t h - \nabla\phi|_{z=-h}\cdot\nabla h \equiv f(\mathbf{x}, t). \tag{4.137}$$

The right-hand side will be denoted by $f(\mathbf{x}, t)$ that implicitly depends on the solution $\phi$.

The application of the boundary conditions leads to the following system of linear equations:

$$\begin{aligned} \cosh(|\mathbf{k}|\eta)A(\mathbf{k}) + \sinh(|\mathbf{k}|\eta)B(\mathbf{k}) &= \hat{\varphi}\\ -|\mathbf{k}|\sinh(|\mathbf{k}|h)A(\mathbf{k}) + |\mathbf{k}|\cosh(|\mathbf{k}|h)B(\mathbf{k}) &= \hat{f}, \end{aligned}$$

which can be easily solved:

$$A(\mathbf{k}) = \frac{\hat{\varphi}\cosh(|\mathbf{k}|h) - \hat{f}\dfrac{\sinh(|\mathbf{k}|\eta)}{|\mathbf{k}|}}{\cosh(|\mathbf{k}|H)}, \quad B(\mathbf{k}) = \frac{\hat{\varphi}\sinh(|\mathbf{k}|h) + \hat{f}\dfrac{\cosh(|\mathbf{k}|\eta)}{|\mathbf{k}|}}{\cosh(|\mathbf{k}|H)},$$

where $H = h + \eta$ is the total water depth. The knowledge of these functions leads the determination of the velocity potential in the whole domain thanks to general solution (4.136).

Finally, we compute the normal velocity at the free surface $\mathbf{D}_\eta(\varphi) = \partial_z\phi|_{z=\eta} - \nabla\phi|_{z=\eta} \cdot \nabla\eta$. If we compute this quantity in Fourier transform space, the answer will be given immediately by the inverse transformation $\mathcal{F}^{-1}$. The first term is readily given by the formula:

$$\partial_z\hat{\phi}\Big|_{z=\eta} = \hat{\varphi}|\mathbf{k}|\tanh(|\mathbf{k}|H) + \hat{f}\,sech(|\mathbf{k}|H).$$

To compute the second term we use the following approximate expression:

$$\widehat{\nabla\phi|_{z=\eta}} \cdot \nabla\eta = \mathcal{F}\Big[\mathcal{F}^{-1}\big[i\mathbf{k}\hat{\varphi}\big] \cdot \mathcal{F}^{-1}\big[i\mathbf{k}\hat{\eta}\big]\Big]. \tag{4.138}$$

**Remark 25.** *From equation (4.137) it follows that function $f(\mathbf{x}, t_n)$ depends implicitly on the unknown solution $\phi(\mathbf{x}, z, t_n)$. In order to resolve this apparent contradiction, we apply a fixed point-type iteration initialized with the value of $f(\mathbf{x}, t_{n-1})$ from the previous time step:*

$$\hat{f}^{k+1} = -\widehat{\partial_t h} - \mathcal{F}\Big[\nabla\phi|_{z=-h}(\hat{f}^k) \cdot \nabla h\Big], \quad \hat{f}^0 = \hat{f}(\mathbf{k}; t_{n-1}).$$

*The last product is computed in the physical space:*

$$\mathcal{F}\Big\{\nabla\phi|_{z=-h}(f^k) \cdot \nabla h\Big\} = \mathcal{F}\Big[\mathcal{F}^{-1}\big[\widehat{\nabla\phi}\Big|_{z=-h}(\hat{f}^k)\big] \cdot \nabla h\Big],$$

*where after simple computations one obtains:*

$$\widehat{\nabla\phi}\Big|_{z=-h}(f^k) = i\mathbf{k}\Big[\hat{\varphi}\,sech(|\mathbf{k}|H) - \hat{f}^k\frac{\tanh(|\mathbf{k}|H)}{|\mathbf{k}|}\Big].$$

*Our numerical experiments show that this iterative procedure is convergent and the tolerance $\varepsilon := ||f^{k+1} - f^k||_\infty \leq 10^{-5}$ is reached after four iterations in average.*

The resulting model is only weakly nonlinear since some information about the solution is lost when we solve the Laplace equation (4.133) in a strip-like domain. However, the WN model contrary to the CP model not only takes into account some nonlinear effects but can be also efficiently applied to cases with realistic bathymetry. We note that this model is analogous at some point to the first order approximation model proposed in [GN07].

#### 4.4.3.3 Time integration

The application of the previously derived Fourier type spectral method to equations (4.132) governing the evolution of canonical variables $\eta$ and $\tilde{\phi}$, leads to a system of ordinary differential equations, i.e.

$$\Phi_t = \mathbb{A}(t, \Phi), \qquad \Phi(t_0) = \Phi_0. \tag{4.139}$$

In order to integrate numerically this system of ODEs we apply an integrating multiplier method analogous to one used in [FCKG05, XG09]. This method appears to decrease the ODEs system stiffness and, therefore, allows for efficient application of explicit time integration schemes. We start by extracting the linear part of equations (4.139):

$$\Phi_t + \mathcal{L} \cdot \Phi = \mathcal{N}(\Phi), \tag{4.140}$$

where $\mathcal{L} = \begin{pmatrix} 0 & -\frac{\omega^2}{g} \\ g & 0 \end{pmatrix}$ and $\omega = \sqrt{g|\mathbf{k}| \tanh(|\mathbf{k}|h_0)}$ is the wave frequency corresponding to the wave number $|\mathbf{k}|$. For a general bathymetry we choose the constant $h_0$ to be the mean water depth. The term $\mathcal{N}(\Phi)$ incorporates remaining nonlinear terms:

$$\mathcal{N}(\Phi) = \begin{pmatrix} \mathcal{F}\{\mathbf{D}_\eta(\tilde{\phi})\} - \frac{\omega^2}{g}\hat{\tilde{\phi}} \\ \mathcal{F}\Big\{ \frac{1}{2(1+|\nabla\eta|^2)} \big[\mathbf{D}_\eta(\tilde{\phi}) + \nabla\tilde{\phi}\cdot\nabla\eta\big]^2 - \frac{1}{2}|\nabla\tilde{\phi}|^2 \Big\} \end{pmatrix}.$$

Linear terms can be integrated exactly by the following change of variables:

$$\Psi(t) := e^{\mathcal{L}(t-t_0)}\Phi(t), \qquad e^{\mathcal{L}(t-t_0)} = \begin{pmatrix} \cos(\omega(t-t_0)) & -\frac{\omega}{g}\sin(\omega(t-t_0)) \\ \frac{g}{\omega}\sin(\omega(t-t_0)) & \cos(\omega(t-t_0)) \end{pmatrix}.$$

Consequently, we solve in practice the following system of ODEs:

$$\Psi_t = e^{\mathcal{L}(t-t_0)}\mathcal{N}\big(e^{-\mathcal{L}(t-t_0)}\Psi\big) \equiv \mathbf{B}(t,\Psi), \qquad \Psi(t_0) = \Phi_0.$$

This simple modification allows us to take larger CFL number, thus, improving the overall time stepping performance.

Finally, the last system of ODEs is discretized with the standard fourth-order Runge-Kutta (RK4) scheme [HNW09]:

$$\begin{aligned} \Psi_{n+1} &= \Psi_n + \tfrac{1}{6}h(k_1 + 2k_2 + 2k_3 + k_4), \\ k_1 &= \mathbf{B}(t_n, \Psi_n), \\ k_2 &= \mathbf{B}(t_n + \tfrac{1}{2}h, \Psi_n + \tfrac{1}{2}hk_1), \\ k_3 &= \mathbf{B}(t_n + \tfrac{1}{2}h, \Psi_n + \tfrac{1}{2}hk_2), \\ k_4 &= \mathbf{B}(t_n + h, \Psi_n + hk_3), \end{aligned} \tag{4.141}$$

where the subscript refers to the discrete time instance $\Psi_n := \Psi(t_n)$ and $h$ is the discrete time step: $t_{n+1} = t_n + h$.

We have to mention that in computations presented below, we use a slightly more complex Runge-Kutta (4,5) scheme with an adaptive time step control (cf. [DP80]). However, fundamentally it is not so different from the classical RK4 scheme (4.141) described above.

#### 4.4.3.4 The BBM-BBM type system

When the so-called long wave approximation is applied to the water wave problem (4.126) – (4.129), one obtains the well-known nonlinear shallow water (or Saint-Venant) equations [dSV71, Sto58, Whi99] which have been extensively used for tsunami simulations [Ima96, TG97, TS98, DKK08, DPD10]. If we go further in asymptotic expansions, some dispersive effects can be included and generally the resulting system is referred to as Boussinesq equations [Bou72, MBS03, DD07b, DMS07, DMS09].

In this study we will also use a Boussinesq system of BBM-BBM type with variable bottom derived in [Mit09]. The system in dimensional variables can be written as:

$$\begin{aligned} \eta_t + \nabla\cdot((h_0+\eta)\vec{u}) + \nabla\cdot\{Ah_0^2[\nabla(\nabla h_0\cdot\vec{u}) + \nabla h_0\nabla\cdot\vec{u}] - bh_0^2\nabla\eta_t\} + \\ A\nabla\cdot(h_0^2\nabla\zeta_t) + \zeta_t &= 0, \\ \vec{u}_t + g\nabla\eta + \tfrac{1}{2}\nabla|\vec{u}|^2 + Bgh_0[\nabla(\nabla h\cdot\nabla\eta) + \nabla h_0\Delta\eta] - dh_0^2\Delta\vec{u}_t \\ -Bh_0\nabla\zeta_{tt} &= 0, \end{aligned} \tag{4.142}$$

where $A$, $B$, $b$ and $d$ are constants defined as:

$$A = \sqrt{\frac{2}{3}} - \frac{2}{3}, \quad B = 1 - \sqrt{\frac{2}{3}}, \quad b = d = \frac{1}{6}.$$

The variable $\vec{u}(\mathbf{x},t)$ denotes the horizontal velocity of the fluid at $z = -h + \sqrt{2/3}(\eta + h)$, and bathymetry variables $h(\mathbf{x},t)$, $h_0(\mathbf{x})$, $\zeta(\mathbf{x},t)$ defined in Senction 4.4.2.

We integrate numerically system (4.142) using the standard Galerkin/finite element method with $\mathbf{P}1$ elements for the spatial discretization coupled with the 2nd order explicit Runge-Kutta method for the temporal discretization [HNW09].

In order to obtain a well-posed problem, we impose homogeneous Dirichlet boundary conditions which absorb partially the wave while reflecting only small amplitude oscillatory waves. Moreover, the specific numerical method appears to converge with optimal rate in the $L^2$ and $L^\infty$ norms whether we consider structured or unstructured grids contrary to the respective initial boundary values problems with zero Dirichlet boundary conditions on $\vec{u}$ for Peregrine's system [Per67] where the analogous numerical method converges with suboptimal orders on structured and unstructured grids. For more information on the properties and the implementation of the numerical method for the BBM-BBM type system we refer to [DMS07, Mit09].

### 4.4.4 Numerical results

In this section we compare the propagation of a solitary wave when used as initial condition in both CP and WN models. More over we study the generation and the initial

stages of the propagation of the tsunami wave of July 17, 2006 event. We also present a comparison between the WN, CP and Boussinesq models.

#### 4.4.4.1 Solitary wave propagation

Before performing Java 2006 tsunami generation simulations, we study the propagation of a solitary wave solution to the full water wave problem using WN and CP models. The initial condition is provided by the well-known Tanaka's method [Tan86].

Consider the two-dimensional water wave problem in a channel of uniform depth $h_0 = const$. Since we look for travelling wave solutions, the flow field can be reduced to the steady state by choosing a frame of reference moving with the wave speed $c$.

After passing to dimensionless variables, there remains only one scaling parameter — the Froude number which is traditionally defined as $\mathrm{Fr} := \dfrac{c}{\sqrt{gh_0}}$. Hereafter governing equations are considered in dimensionless form.

The complex velocity potential is classically introduced as $w = \phi + i\psi$, where $\psi$ is the stream function. We choose $\phi = 0$ at the crest and $\psi = 0$ at the bottom. The fluid region is then mapped onto the strip $0 < \psi < 1$, $-\infty < \phi < \infty$ on the plane $w$ with $\psi = 1$ corresponding to the free surface.

We introduce the quantity $\Omega = \log \dfrac{dw}{dz} = \tau - i\theta$, where $\theta$ is the angle between the velocity vector and horizontal axis $Ox$. The real part $\tau$ is expressed in terms of the velocity magnitude $q$ as $\tau = \log q$.

Boundary conditions to be satisfied are the Bernoulli condition at the free surface and the bottom impermeability which are expressed as

$$\frac{dq^3}{d\phi} = -\frac{3}{\mathrm{Fr}^2}\sin\theta, \quad \text{on } \psi = 1 \qquad \text{and} \qquad \theta = 0, \quad \text{on } \psi = 0. \tag{4.143}$$

Consequently, the problem now is transformed to the determination of complex function $\Omega$, analytic with respect to $w$ within the region of the unit strip $0 < \psi < 1$, decays at infinity and satisfies two boundary conditions (4.143). By applying Cauchy's integral theorem, one can find the following integral equation on the free surface $\psi = 1$:

$$-\theta(\phi) - \frac{2}{\pi}\int_{-\infty}^{\infty} \frac{\theta(\phi)}{(\tilde{\phi}-\phi)^2+4}\,d\tilde{\phi} = -\frac{1}{\pi}\int_{-\infty}^{\infty} \frac{(\tilde{\phi}-\phi)\tau(\tilde{\phi})}{(\tilde{\phi}-\phi)^2+4}\,d\tilde{\phi} + \frac{1}{\pi}\mathrm{p.v.}\int_{-\infty}^{\infty} \frac{\tau(\tilde{\phi})}{\tilde{\phi}-\phi}\,d\tilde{\phi},$$

where $\tau(\phi)$ and $\theta(\phi)$ denote the traces of corresponding functions at the free surface $\psi = 1$.

The last integral equation is solved iteratively with a method analogous to the one proposed [Tan86]. The convergence is tested with respect to the Froude number. Several

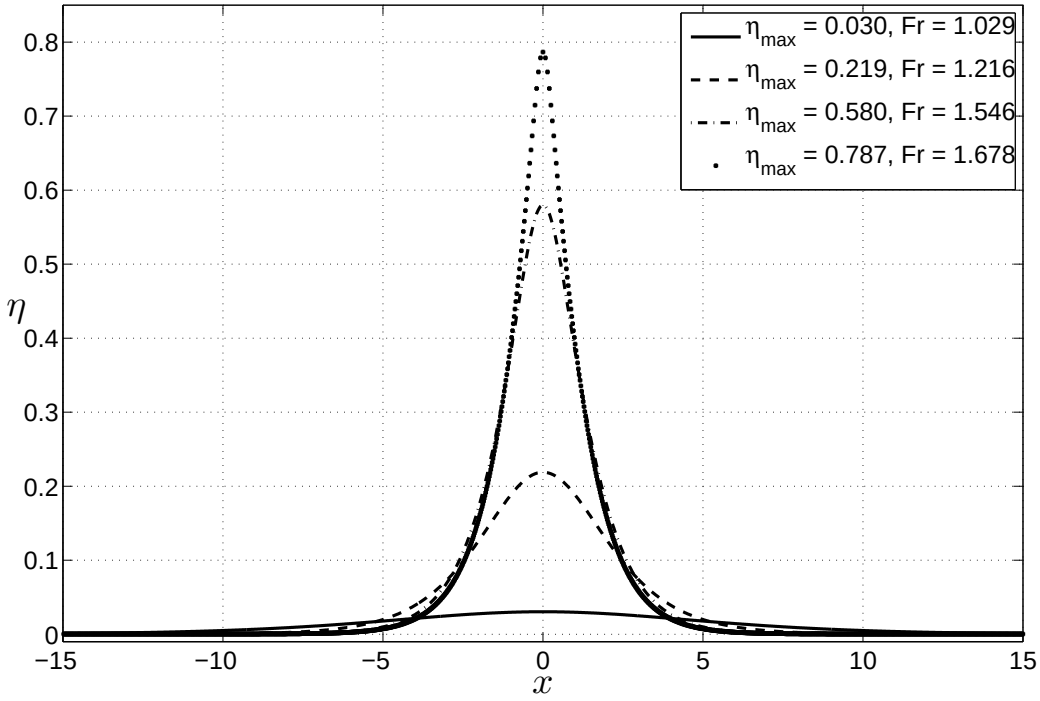


**Figure 4.59:** Solitary wave solutions of various amplitudes for the full water wave problem.

solitary wave solutions computed in this way are plotted on Figure 4.59 for illustrative purposes.

In order to illustrate the advantages of the proposed weakly-nonlinear model over the classical CP solution, we let a solitary wave with amplitude $A/h_0 = 0.1$ propagate up to $T = 80$.

We recall that the classical CP solution of (4.122)–(4.125) corresponding to the initial free surface height $\eta|_{t=0} = \eta_0(x)$ and the velocity potential distribution at the free surface $\varphi|_{t=0} = \varphi_0(x)$, takes the following form:

$$\eta(\mathbf{x},t) = \mathcal{F}^{-1}\Big\{\hat{\eta}_0(\mathbf{k})\cos(\omega t) + \frac{\omega}{g}\hat{\varphi}_0(\mathbf{k})\sin(\omega t)\Big\},$$

$$\phi(\mathbf{x},z,t) = \mathcal{F}^{-1}\Big\{\big(\hat{\varphi}_0(\mathbf{k})\cos(\omega t) - \frac{g}{\omega}\hat{\eta}_0(\mathbf{k})\sin(\omega t)\big) \big(\cosh(|\mathbf{k}|z) + \tanh(|\mathbf{k}|h)\sinh(|\mathbf{k}|z)\big)\Big\},$$

where $\hat{\eta}_0(\mathbf{k}) = \mathcal{F}\{\eta_0(\mathbf{x})\}$ and $\hat{\varphi}_0(\mathbf{k}) = \mathcal{F}\{\varphi_0(\mathbf{x})\}$ are Fourier transforms of initial conditions.

The solution profiles of both models are presented in Figures 4.60 (a)–(e). One can observe that the weakly-nonlinear method retains much better the solitary wave while shedding a small dispersive tail behind. The CP solution gradually transforms the initial

wave into the dispersive tail according to the linear nature of equations (4.122)–(4.125). In Figure 4.60 (f) we present the normalized amplitude error defined as:

$$\epsilon(t) := \frac{|\max_x\{\eta(x,t)\} - A/h_0|}{A/h_0},$$

where $\max_x\{\eta(x,t)\}$ denotes the discrete maximum of the numerical solution and $A/h_0 = 0.1$ is the exact solitary wave amplitude. In both computations a uniform grid with 512 nodes is used. Here again we notice better performance of the WN solver comparing to the CP solution. This specific experiment shows that the WN model includes necessary nonlinear effects to study a tsunami generation and propagation phenomena.

#### 4.4.4.2 The July 17, 2006 tsunami generation simulation

The main purpose of this study is to present a novel methodology for tsunami generation. This approach is illustrated on the example of 17 July 2006 Java tsunami since this event is not completely understood yet and there is an available finite fault solution for the respective underwater earthquake.

In this section we show some numerical results on water waves generated by moving bottom. Namely, we exploit the bottom motion (4.121) constructed in Section 4.4.2.2. The corresponding hydrodynamic problem is solved by three methods discussed above: the linearized water wave problem (CP), BBM-BBM system and the new WN model.

The solution given by the WN model and the exact solutions to linearized Euler equations (4.122) – (4.125) are computed on a uniform grid of $512 \times 512$ points. The time step $\Delta t$ is chosen adaptively according to the RK(4,5) method proposed in [DP80]. The BBM-BBM system is solved on a triangular unstructured grid with 86276 elements. For the time integration the classical RK2 scheme [HNW09] with the time step $\Delta t = 0.5\ s$ is employed.

Several snapshots of the free surface elevation computed by the WN model are shown in Figures 4.61 (a) – (f). The analogous contour plots of the solutions of the CP and the BBM-BBM models are almost identical and differences cannot be observed within the graphical accuracy and therefore are not presented here. The parameters of the bottom motion, bathymetry and computational domain geometry were explained in Section 4.4.2.

In this computation we can see a complex process of simultaneous wave evolution together with rupture propagation during approximatively 210 $s$. Namely, the free surface deformed by first subfaults starts to evolve while the rupture propagates along the fault. This kind of fluid / moving bottom interaction cannot be described in the passive generation framework.

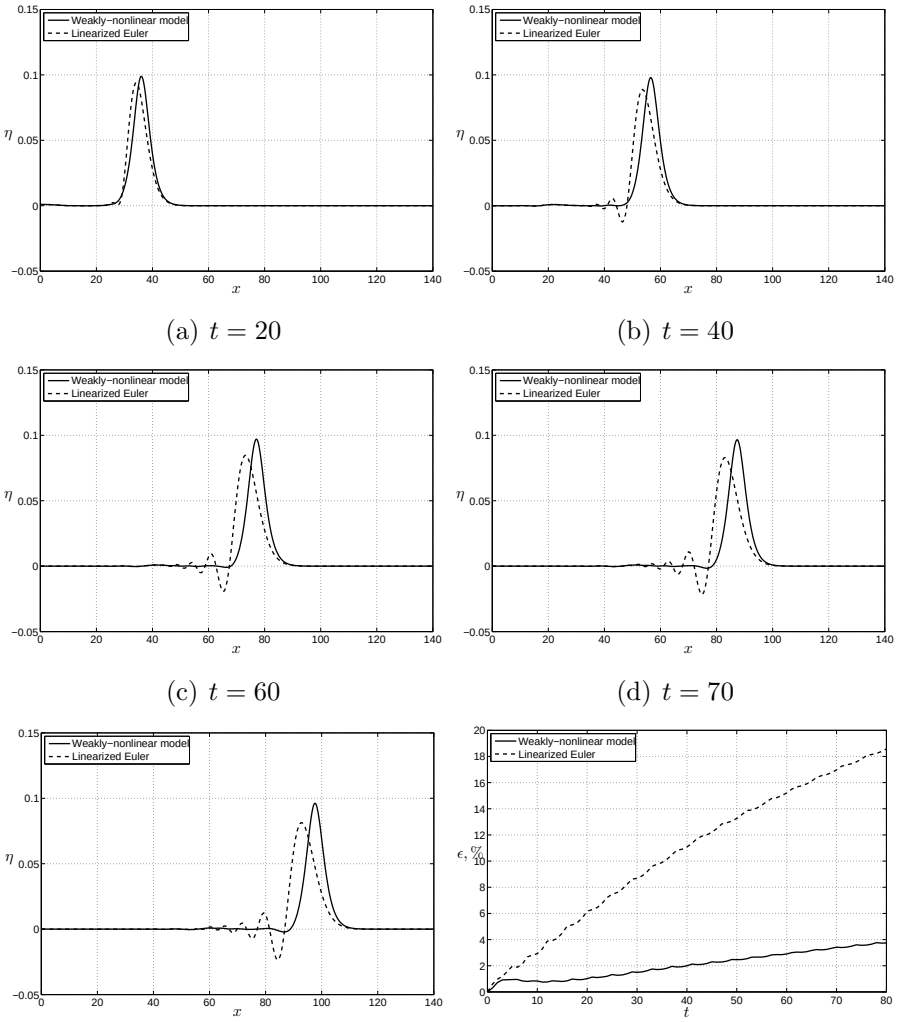


(a) $t = 20$ (b) $t = 40$

(c) $t = 60$ (d) $t = 70$

(e) $t = 80$ (f) Amplitude error

**Figure 4.60:** Tanaka's solution propagation with the weakly-nonlinear method (solid line) and Cauchy-Poisson (CP) solution (dashed line). Solitary wave amplitude is $A/h_0 = 0.1$.

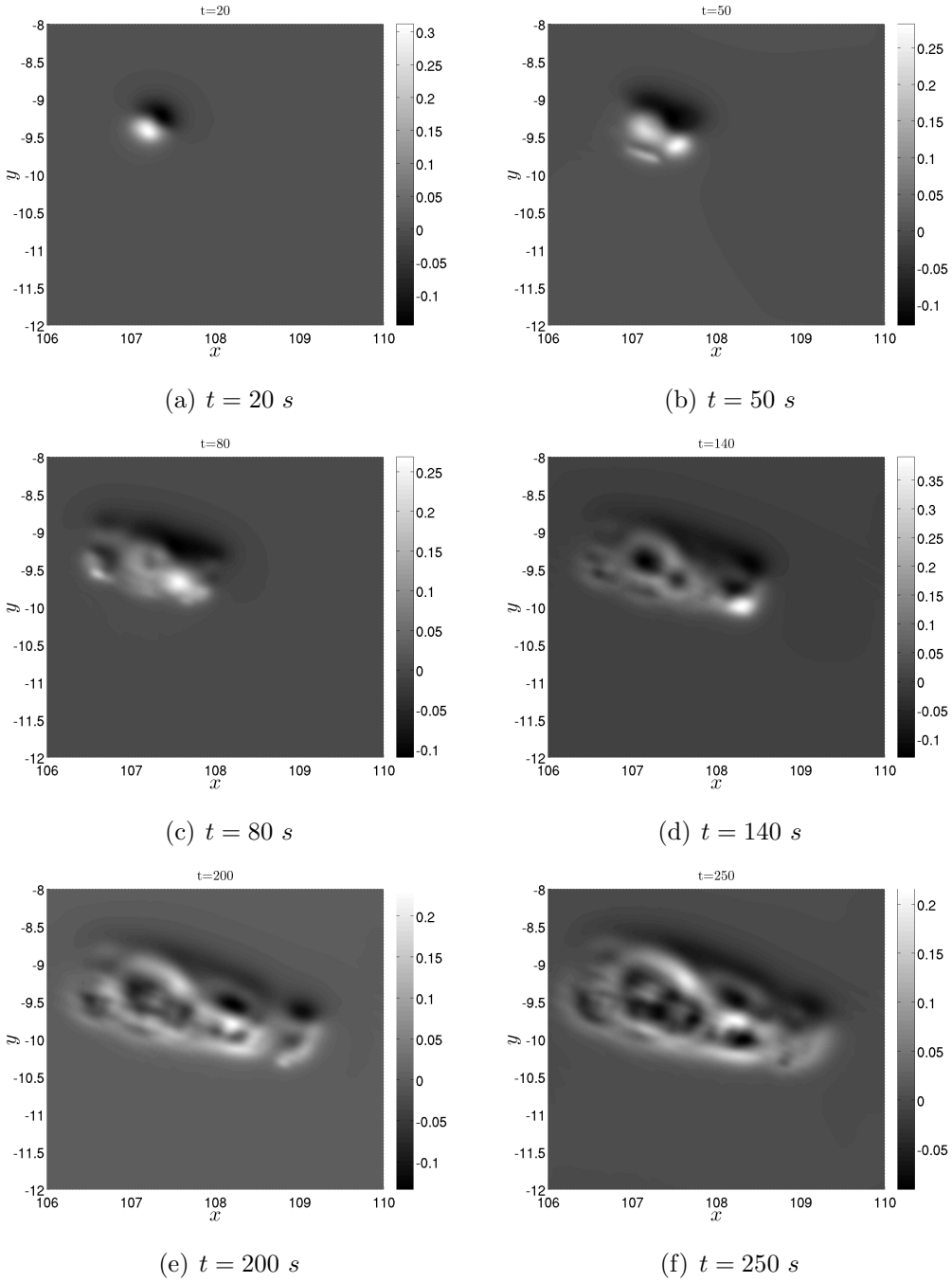


(a) $t = 20\ s$ (b) $t = 50\ s$

(c) $t = 80\ s$ (d) $t = 140\ s$

(e) $t = 200\ s$ (f) $t = 250\ s$

**Figure 4.61:** Snapshots of the free surface elevation computed with the Weakly Nonlinear (WN) method. Water waves are generated by dynamic co-seismic bottom displacements (4.121) reconstructed using the corresponding finite fault solution [Ji06].

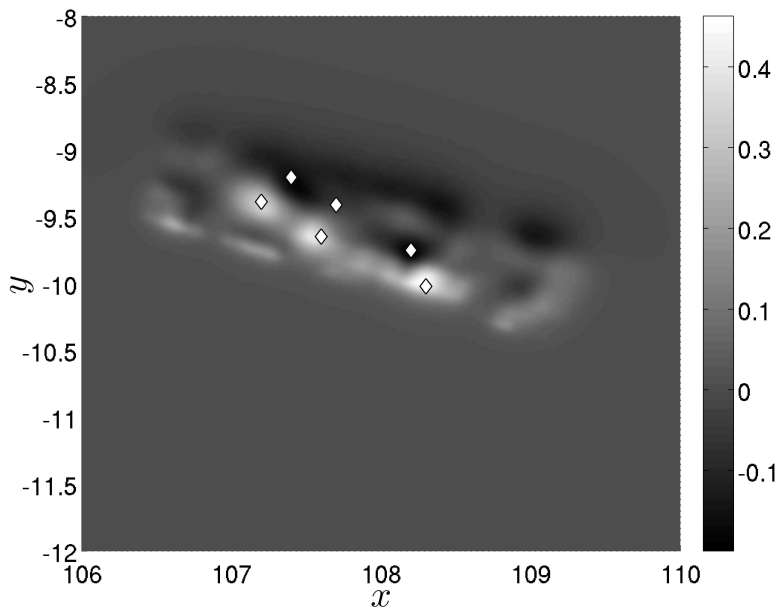


**Figure 4.62:** Location of the six numerical wave gauges (indicated by the symbol ⋄) superposed with the static co-seismic bottom displacement.

In order to perform the intercomparison among the three models described above we put six numerical wave gauges at the following locations: (a) (107.2°, −9.388°), (b) (107.4°, −9.205°), (c) (107.6°, −9.648°), (d) (107.7°, −9.411°), (e) (108.3°, −10.02°), (f) (108.2°, −9.75°). The locations of the wave gauges is represented by the symbol ⋄ on Figure 4.62 along with the static sea bed displacement. Wave gauges are intentionally put in places where the largest waves were expected.

The six wave gauge records are presented in Figures 4.63 (a) – (f). The first impression is that the overall agreement among all models is satisfactory. We underline that the CP solution is very close to other solutions despite the fact that bathymetric features are neglected. We also note that the specific BBM-BBM type system underestimates by a small amount the maximum wave amplitude compared to the WN model. Our further numerical tests showed some sensitivity of the BBM-BBM solution to the bottom motion scenario [DD07d]. Namely, we can report, for example, that the exponential scenario led to a slight overestimation of the wave amplitude comparing to other models.

### 4.4.5 Conclusions and perspectives

In the present work we considered an important problem of the tsunami generation modeling. Namely, a new method for dynamic co-seismic sea bed displacements construc-

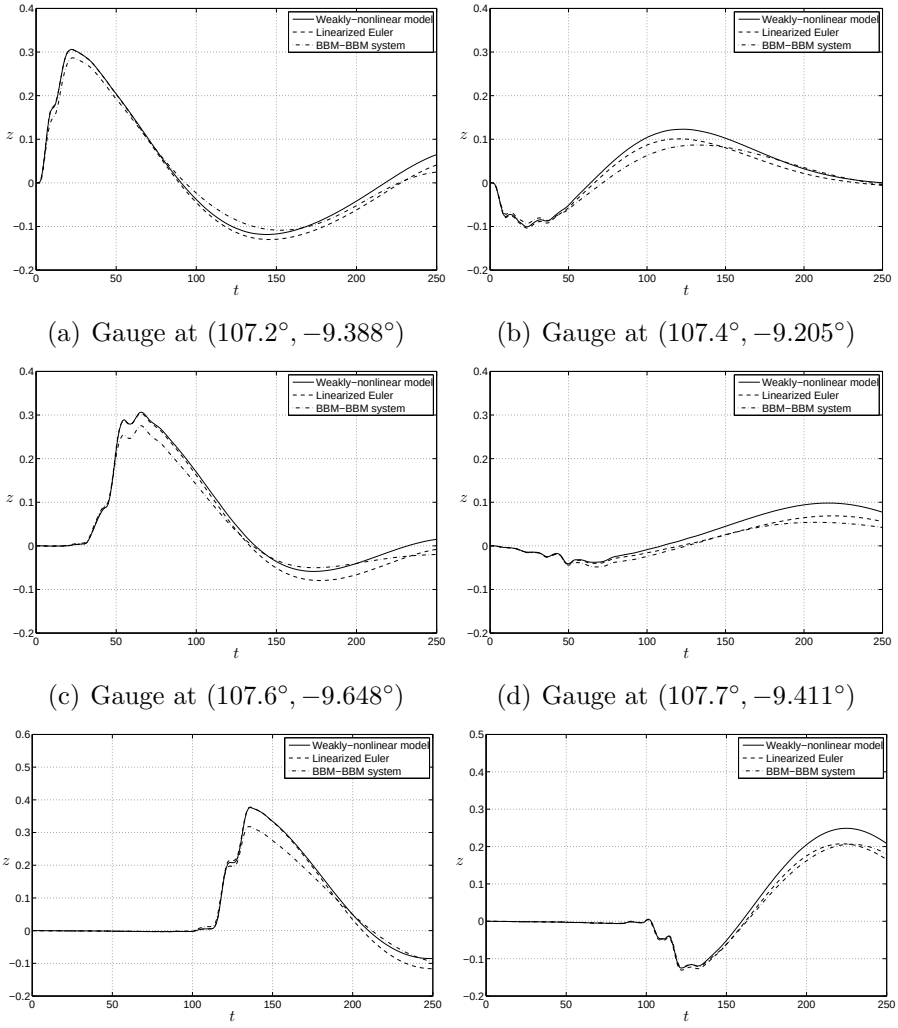


(a) Gauge at $(107.2°, -9.388°)$ (b) Gauge at $(107.4°, -9.205°)$

(c) Gauge at $(107.6°, -9.648°)$ (d) Gauge at $(107.7°, -9.411°)$

(e) Gauge at $(108.3°, -10.02°)$ (f) Gauge at $(108.2°, -9.75°)$

**Figure 4.63:** Free surface elevation computed numerically at six wave gauges located approximately at the local extrema of the static bottom displacement. The solid line — represents the numerical solution given by the weakly nonlinear solver, dashed line $- - -$ is the Cauchy-Poisson solution and, finally, the dash-dotted line $- \cdot - \cdot -$ refers to the BBM-BBM system solution. The vertical axis is represented in meters.

tion was proposed. This method basically relies on two main ingredients:

- the finite fault solution [BLM00, JWH02] giving us the slip distribution along the fault
- dynamic sea bed deformation scenarios [Ham73, DDK06, DD07d] allowing us to take into account available information of the rupture dynamics

To our knowledge this reconstruction of the bottom motion is new. All developments presented in this paper are illustrated on the example of the July, 17 2006 Java event.

Along with the bottom motion construction, we discussed three models to solve approximately the corresponding hydrodynamic problem and compute the induced free surface motions. The July 17, 2006 tsunami generation case was computed with three different models and a comparison was performed. We obtained a surprisingly good agreement between the CP solution and the solutions of the other two models. Recall that in the latter the bottom is assumed to be flat. Some discrepancies might appear later in time since the bathymetry plays a crucial role in the tsunami propagation.

Taking into account the simplicity and the relatively good accuracy of the new WN approximation to the full water wave problem with time dependent variable bottom, we suggest its use for the computation of the initial stages ($\approx 300\ s$) of tsunami's life. The propagation and runup can be computed afterwards by other sophisticated tools [TG97, IYO06, SBT+07, DPD10] some of them being already integrated into tsunami warning systems [TGB+05, WL08].

However we point out that extreme runup values measured after the July, 17 Java 2006 event [FKM+07] are still to be investigated in future studies.

### 4.4.6 Appendix I: Finite fault parameters

**Table 4.7:** Subfault parameters given by the finite fault inversion [Ji06].

| Lattitude, ° | Longitude, ° | Depth, $km$ | Slip, $cm$ | Rake, ° |
|---|---|---|---|---|
| -10.33298 | 109.17112 | 6.81260 | 5.01844 | 121.65860 |
| -10.28919 | 109.04183 | 6.81260 | 4.31652 | 80.93857 |
| -10.24541 | 108.91254 | 6.81260 | 48.94745 | 85.43047 |
| -10.20162 | 108.78325 | 6.81260 | 3.60585 | 101.68500 |
| -10.15784 | 108.65396 | 6.81260 | 0.86479 | 67.04596 |
| -10.11405 | 108.52467 | 6.81260 | 0.96921 | 99.45411 |
| -10.07027 | 108.39538 | 6.81260 | 0.62447 | 71.54340 |

Continued on the next page

| Lattitude, ° | Longitude, ° | Depth, *km* | Slip, *cm* | Rake, ° |
|---|---|---|---|---|
| -10.02648 | 108.26609 | 6.81260 | 0.02449 | 99.44887 |
| -9.98270 | 108.13680 | 6.81260 | 2.71502 | 119.63240 |
| -9.93891 | 108.00751 | 6.81260 | 0.57000 | 114.25760 |
| -9.89513 | 107.87822 | 6.81260 | 14.54725 | 112.71920 |
| -9.85134 | 107.74893 | 6.81260 | 31.66312 | 107.26750 |
| -9.80756 | 107.61964 | 6.81260 | 2.74176 | 85.79224 |
| -9.76377 | 107.49035 | 6.81260 | 3.35868 | 78.97166 |
| -9.71999 | 107.36105 | 6.81260 | 67.95367 | 64.89334 |
| -9.67620 | 107.23177 | 6.81260 | 62.33453 | 65.43832 |
| -9.63242 | 107.10248 | 6.81260 | 35.33318 | 66.90181 |
| -9.58863 | 106.97318 | 6.81260 | 1.75233 | 101.93900 |
| -9.54485 | 106.84389 | 6.81260 | 40.63542 | 81.77631 |
| -9.50106 | 106.71461 | 6.81260 | 84.20831 | 68.95723 |
| -9.45728 | 106.58531 | 6.81260 | 25.12981 | 66.62241 |
| -10.24093 | 109.20313 | 8.78887 | 0.68254 | 88.79068 |
| -10.19714 | 109.07384 | 8.78887 | 30.70282 | 97.90491 |
| -10.15336 | 108.94455 | 8.78887 | 76.07102 | 99.93182 |
| -10.10957 | 108.81525 | 8.78887 | 0.56201 | 79.59160 |
| -10.06579 | 108.68597 | 8.78887 | 0.95023 | 114.32920 |
| -10.02201 | 108.55668 | 8.78887 | 64.78191 | 121.81120 |
| -9.97822 | 108.42738 | 8.78887 | 81.31910 | 105.21240 |
| -9.93443 | 108.29810 | 8.78887 | 137.60680 | 121.72020 |
| -9.89065 | 108.16881 | 8.78887 | 85.81732 | 88.13734 |
| -9.84686 | 108.03951 | 8.78887 | 30.61069 | 80.38488 |
| -9.80308 | 107.91022 | 8.78887 | 60.08308 | 113.75000 |
| -9.75929 | 107.78094 | 8.78887 | 46.98381 | 96.25403 |
| -9.71551 | 107.65164 | 8.78887 | 21.69421 | 80.82516 |
| -9.67173 | 107.52235 | 8.78887 | 11.01957 | 112.63110 |
| -9.62794 | 107.39307 | 8.78887 | 27.85978 | 75.88463 |
| -9.58416 | 107.26377 | 8.78887 | 5.96505 | 77.66200 |
| -9.54037 | 107.13448 | 8.78887 | 3.85634 | 83.57522 |
| -9.49658 | 107.00520 | 8.78887 | 3.23158 | 113.73070 |
| -9.45280 | 106.87590 | 8.78887 | 29.89915 | 116.10890 |
| -9.40902 | 106.74661 | 8.78887 | 65.25044 | 72.60931 |
| -9.36523 | 106.61732 | 8.78887 | 19.62932 | 65.99193 |
| -10.14888 | 109.23514 | 10.76514 | 20.60663 | 124.43320 |
| -10.10510 | 109.10584 | 10.76514 | 69.91051 | 122.64720 |

Continued on the next page

| Lattitude, ° | Longitude, ° | Depth, *km* | Slip, *cm* | Rake, ° |
|---|---|---|---|---|
| -10.06131 | 108.97655 | 10.76514 | 63.10052 | 99.23547 |
| -10.01753 | 108.84727 | 10.76514 | 0.63700 | 74.09311 |
| -9.97374 | 108.71797 | 10.76514 | 1.02761 | 117.53560 |
| -9.92996 | 108.58868 | 10.76514 | 85.54328 | 123.64950 |
| -9.88617 | 108.45940 | 10.76514 | 167.18620 | 104.56840 |
| -9.84239 | 108.33010 | 10.76514 | 202.60880 | 122.12460 |
| -9.79860 | 108.20081 | 10.76514 | 144.76970 | 81.50333 |
| -9.75482 | 108.07152 | 10.76514 | 53.97212 | 72.84430 |
| -9.71103 | 107.94223 | 10.76514 | 79.21021 | 98.66053 |
| -9.66725 | 107.81294 | 10.76514 | 82.95619 | 80.81979 |
| -9.62346 | 107.68365 | 10.76514 | 119.13390 | 74.36982 |
| -9.57968 | 107.55436 | 10.76514 | 95.90159 | 116.24710 |
| -9.53589 | 107.42507 | 10.76514 | 36.94965 | 102.32060 |
| -9.49211 | 107.29578 | 10.76514 | 0.28681 | 81.49704 |
| -9.44832 | 107.16649 | 10.76514 | 8.06018 | 98.40840 |
| -9.40454 | 107.03720 | 10.76514 | 3.02927 | 116.89820 |
| -9.36075 | 106.90791 | 10.76514 | 10.73559 | 74.60908 |
| -9.31697 | 106.77862 | 10.76514 | 57.94233 | 75.39254 |
| -9.27318 | 106.64933 | 10.76514 | 60.97223 | 64.77096 |
| -10.05684 | 109.26714 | 12.74141 | 21.97392 | 121.10740 |
| -10.01305 | 109.13785 | 12.74141 | 74.47045 | 119.75060 |
| -9.96927 | 109.00856 | 12.74141 | 17.25334 | 124.09410 |
| -9.92548 | 108.87927 | 12.74141 | 14.38904 | 87.41515 |
| -9.88170 | 108.74998 | 12.74141 | 3.03040 | 106.36440 |
| -9.83791 | 108.62069 | 12.74141 | 8.97587 | 101.53580 |
| -9.79413 | 108.49140 | 12.74141 | 114.85160 | 115.94270 |
| -9.75034 | 108.36211 | 12.74141 | 91.90382 | 115.95240 |
| -9.70656 | 108.23282 | 12.74141 | 64.72478 | 100.08050 |
| -9.66277 | 108.10353 | 12.74141 | 17.30368 | 123.06770 |
| -9.61899 | 107.97424 | 12.74141 | 57.09099 | 68.20686 |
| -9.57520 | 107.84495 | 12.74141 | 64.81193 | 79.84035 |
| -9.53142 | 107.71566 | 12.74141 | 131.04410 | 76.45924 |
| -9.48763 | 107.58636 | 12.74141 | 112.11020 | 99.51801 |
| -9.44385 | 107.45708 | 12.74141 | 60.23628 | 97.77266 |
| -9.40006 | 107.32778 | 12.74141 | 126.96870 | 80.27277 |
| -9.35628 | 107.19849 | 12.74141 | 63.39000 | 65.00801 |
| -9.31249 | 107.06921 | 12.74141 | 0.52621 | 94.79313 |

Continued on the next page

| Lattitude, ° | Longitude, ° | Depth, *km* | Slip, *cm* | Rake, ° |
|---|---|---|---|---|
| -9.26871 | 106.93991 | 12.74141 | 1.52171 | 66.78681 |
| -9.22492 | 106.81062 | 12.74141 | 10.96743 | 81.94861 |
| -9.18114 | 106.68134 | 12.74141 | 2.38062 | 123.04830 |
| -9.96479 | 109.29915 | 14.71768 | 22.40949 | 123.90350 |
| -9.92100 | 109.16986 | 14.71768 | 48.62879 | 115.45630 |
| -9.87722 | 109.04057 | 14.71768 | 5.99559 | 83.81007 |
| -9.83343 | 108.91128 | 14.71768 | 7.22945 | 123.80940 |
| -9.78965 | 108.78199 | 14.71768 | 0.10031 | 93.40998 |
| -9.74586 | 108.65269 | 14.71768 | 0.36991 | 69.37087 |
| -9.70208 | 108.52341 | 14.71768 | 104.18760 | 123.83230 |
| -9.65829 | 108.39411 | 14.71768 | 46.12533 | 95.97049 |
| -9.61451 | 108.26482 | 14.71768 | 0.28679 | 89.56866 |
| -9.57072 | 108.13554 | 14.71768 | 2.06597 | 80.14312 |
| -9.52694 | 108.00624 | 14.71768 | 30.55070 | 66.23147 |
| -9.48315 | 107.87695 | 14.71768 | 73.72994 | 87.91253 |
| -9.43937 | 107.74767 | 14.71768 | 112.90700 | 92.28181 |
| -9.39558 | 107.61837 | 14.71768 | 74.73608 | 86.51558 |
| -9.35180 | 107.48908 | 14.71768 | 121.73820 | 64.68654 |
| -9.30801 | 107.35979 | 14.71768 | 231.20940 | 65.50779 |
| -9.26423 | 107.23050 | 14.71768 | 96.55727 | 87.01543 |
| -9.22044 | 107.10121 | 14.71768 | 28.29534 | 122.55670 |
| -9.17666 | 106.97192 | 14.71768 | 0.84110 | 70.21989 |
| -9.13287 | 106.84263 | 14.71768 | 7.99213 | 87.51706 |
| -9.08909 | 106.71334 | 14.71768 | 1.33281 | 96.33266 |
| -9.87274 | 109.33115 | 16.69394 | 43.31154 | 121.79150 |
| -9.82896 | 109.20187 | 16.69394 | 87.17052 | 124.49750 |
| -9.78517 | 109.07257 | 16.69394 | 61.47630 | 87.10537 |
| -9.74139 | 108.94328 | 16.69394 | 31.53286 | 70.58137 |
| -9.69760 | 108.81400 | 16.69394 | 0.70628 | 65.17896 |
| -9.65382 | 108.68470 | 16.69394 | 5.74160 | 87.70702 |
| -9.61003 | 108.55541 | 16.69394 | 93.47714 | 107.32000 |
| -9.56625 | 108.42612 | 16.69394 | 93.55753 | 85.39201 |
| -9.52246 | 108.29683 | 16.69394 | 47.25525 | 74.24297 |
| -9.47868 | 108.16754 | 16.69394 | 24.65230 | 124.20110 |
| -9.43489 | 108.03825 | 16.69394 | 35.63115 | 71.78733 |
| -9.39111 | 107.90896 | 16.69394 | 25.11757 | 75.27779 |
| -9.34732 | 107.77967 | 16.69394 | 68.15302 | 107.42980 |

Continued on the next page

| Lattitude, ° | Longitude, ° | Depth, *km* | Slip, *cm* | Rake, ° |
|---|---|---|---|---|
| -9.30354 | 107.65038 | 16.69394 | 24.66007 | 112.77880 |
| -9.25975 | 107.52109 | 16.69394 | 0.50688 | 79.86887 |
| -9.21597 | 107.39180 | 16.69394 | 119.92850 | 75.03103 |
| -9.17218 | 107.26250 | 16.69394 | 77.08335 | 110.83160 |
| -9.12840 | 107.13322 | 16.69394 | 31.65430 | 123.83060 |
| -9.08461 | 107.00393 | 16.69394 | 11.42768 | 66.47282 |
| -9.04083 | 106.87463 | 16.69394 | 33.80650 | 115.65650 |
| -8.99704 | 106.74535 | 16.69394 | 39.47481 | 65.15574 |
| -9.78069 | 109.36316 | 18.67021 | 35.42621 | 111.95830 |
| -9.73691 | 109.23387 | 18.67021 | 103.05030 | 124.62650 |
| -9.69312 | 109.10458 | 18.67021 | 101.38220 | 122.70620 |
| -9.64934 | 108.97529 | 18.67021 | 76.76701 | 68.20042 |
| -9.60556 | 108.84600 | 18.67021 | 10.71945 | 77.79713 |
| -9.56177 | 108.71671 | 18.67021 | 1.32449 | 100.72950 |
| -9.51799 | 108.58742 | 18.67021 | 37.46857 | 124.59330 |
| -9.47420 | 108.45813 | 18.67021 | 118.99580 | 100.38000 |
| -9.43042 | 108.32883 | 18.67021 | 79.62616 | 91.56905 |
| -9.38663 | 108.19955 | 18.67021 | 97.61735 | 109.86430 |
| -9.34285 | 108.07026 | 18.67021 | 87.67753 | 87.57239 |
| -9.29906 | 107.94096 | 18.67021 | 15.14859 | 64.75201 |
| -9.25528 | 107.81168 | 18.67021 | 82.60960 | 71.66805 |
| -9.21149 | 107.68239 | 18.67021 | 66.06397 | 98.55843 |
| -9.16771 | 107.55309 | 18.67021 | 0.43085 | 67.81042 |
| -9.12392 | 107.42381 | 18.67021 | 35.30429 | 124.04570 |
| -9.08014 | 107.29452 | 18.67021 | 59.17323 | 124.55130 |
| -9.03635 | 107.16522 | 18.67021 | 15.23214 | 66.82615 |
| -8.99257 | 107.03593 | 18.67021 | 28.10358 | 76.08198 |
| -8.94878 | 106.90664 | 18.67021 | 48.09923 | 124.24450 |
| -8.90500 | 106.77735 | 18.67021 | 42.38682 | 124.42850 |

### 4.4.7 Appendix II: Zakharov's formulation of the water wave problem

In the present section we are going to recast governing equations (4.126) – (4.129) of the water wave problem in more compact and mathematically more convenient form [Zak68, CS93].

Using the definition of the normal velocity (4.131), it is straightforward to rewrite the

kinematic free surface condition (4.127):

$$\partial_t \eta - \mathbf{D}_\eta(\tilde{\phi}) = 0.$$

The time derivative and the horizontal gradient of the velocity potential trace at the free surface can be computed:

$$\partial_t \tilde{\phi} = \partial_t \phi + \partial_t \eta \, \partial_z \phi|_{z=\eta} = \partial_t \phi + \mathbf{D}_\eta(\tilde{\phi}) \, \partial_z \phi|_{z=\eta}, \tag{4.144}$$

and similarly one can compute the horizontal gradient:

$$\nabla \tilde{\phi} = \nabla \phi|_{z=\eta} + \nabla \eta \, \partial_z \phi|_{z=\eta}, \tag{4.145}$$

In order to close the system, we have to express all derivatives of the potential $\phi$ computed at the free surface, in terms of $\tilde{\phi}$, $\eta$ and $\mathbf{D}_\eta(\tilde{\phi})$.

From the definition of the normal velocity (4.131) and the D2N operator one readily obtains:

$$\nabla \phi|_{z=\eta} \cdot \nabla \eta = \partial_z \phi|_{z=\eta} - \mathbf{D}_\eta(\tilde{\phi}). \tag{4.146}$$

Substituting the last identity into (4.145) multiplied by $\nabla \eta$, leads to the following expression:

$$\partial_z \phi|_{z=\eta} = \frac{\mathbf{D}_\eta(\tilde{\phi}) + \nabla \tilde{\phi} \cdot \nabla \eta}{1 + |\nabla \eta|^2}. \tag{4.147}$$

Now we have all elements to find the horizontal derivatives of the velocity potential:

$$\nabla \phi|_{z=\eta} = \nabla \tilde{\phi} - \nabla \eta \, \partial_z \phi|_{z=\eta} = \frac{(1 + |\nabla \eta|^2) \nabla \tilde{\phi} - \mathbf{D}_\eta(\tilde{\phi}) \nabla \eta - (\nabla \tilde{\phi} \cdot \nabla \eta) \nabla \eta}{1 + |\nabla \eta|^2}. \tag{4.148}$$

In order to rewrite Bernoulli condition (4.128) in new variables, we make the following observation (using (4.145) and (4.146)):

$$\begin{aligned} &\tfrac{1}{2}|\nabla \phi|^2 + \tfrac{1}{2}(\partial_z \phi)^2 = \tfrac{1}{2} \nabla \phi \cdot \nabla \phi + \tfrac{1}{2} \partial_z \phi \, \partial_z \phi = \\ &= \tfrac{1}{2} \nabla \phi \cdot (\nabla \tilde{\phi} - \partial_z \phi \nabla \eta) + \tfrac{1}{2} \partial_z \phi (\mathbf{D}_\eta(\tilde{\phi}) + \nabla \phi \cdot \nabla \eta) = \tfrac{1}{2} \nabla \phi \cdot \nabla \tilde{\phi} + \tfrac{1}{2} \mathbf{D}_\eta(\tilde{\phi}) \partial_z \phi, \quad z = \eta. \end{aligned}$$

Taking into account this observation and expression (4.144) for the time derivative of $\tilde{\phi}$, the Bernoulli condition takes this equivalent form:

$$\partial_t \tilde{\phi} + g\eta + \tfrac{1}{2} \nabla \phi \cdot \nabla \tilde{\phi} - \tfrac{1}{2} \mathbf{D}_\eta(\tilde{\phi}) \partial_z \phi = 0, \quad z = \eta.$$

After substituting expressions (4.147), (4.148) into the last equation and summarizing all the developments made above, we get the following set of dynamic equations equivalent to the complete water wave problem (4.126) – (4.129):

$$\begin{aligned} \partial_t \eta - \mathbf{D}_\eta(\tilde{\phi}) &= 0, \\ \partial_t \tilde{\phi} + \tfrac{1}{2} |\nabla \tilde{\phi}|^2 + g\eta - \tfrac{1}{2(1+|\nabla \eta|^2)} \left[ \mathbf{D}_\eta(\tilde{\phi}) + \nabla \tilde{\phi} \cdot \nabla \eta \right]^2 &= 0. \end{aligned}$$

### 4.4.8 Appendix III: Relations between elastic constants

In the classical elasticity theory, coefficients in Lamé equations (governing the displacements field in an elastic solid), can be expressed in terms of various sets of physical parameters [Lov44, SS46]. The purpose of this Appendix is to recall some relations between them.

Lamé coefficients $\lambda$ and $\mu$ can be defined in terms of the Young's modulus $E$ (having the dimension of the pressure $[Pa]$) and Poisson's ratio $\nu$ (dimensionless coefficient $0 < \nu < 1/2$):

$$\lambda = \frac{E\nu}{(1+\nu)(1-2\nu)}, \quad \mu = \frac{E}{2(1+\nu)},$$

and inversely:

$$E = \frac{(3\lambda+2\mu)\mu}{\lambda+\mu}, \quad \nu = \frac{\lambda}{2(\lambda+\mu)}.$$

The celerities of $P$ and $S$ waves have the following expressions in terms of Lamé coefficients:

$$c_p = \sqrt{\frac{\lambda+2\mu}{\rho}}, \quad c_s = \sqrt{\frac{\mu}{\rho}},$$

where $\rho$ is the density of elastic medium. It is straightforward to invert last relations:

$$\mu = \rho c_s^2, \quad \lambda = \rho c_p^2 - 2\mu.$$

# Chapter 5

# Simulation of inundation

*On two occasions I have been asked [by members of Parliament]: 'Pray, Mr. Babbage, if you put into the machine wrong figures, will the right answers come out?' I am not able rightly to apprehend the kind of confusion of ideas that could provoke such a question.*

Charles Babbage

*It is impossible to exaggerate the extent to which modern applied mathematics has been shaped and fueled by the general availability of fast computers with large memories. Their impact on mathematics, both applied and pure, is comparable to the role of the telescopes in astronomy and microscopes in biology.*

Peter Lax, Siam Rev. Vol. 31 No. 4

## Contents

# 5.1 Finite volume schemes for dispersive wave propagation and runup

*It is a capital mistake to theorize before one has data.*

Sir Arthur Conan Doyle

*It doesn't matter how beautiful your theory is, it doesn't matter how smart you are. If it doesn't agree with experiment, it's wrong.*

Richard Feynman

ABSTRACT. Finite volume schemes are commonly used to construct approximate solutions to conservation laws. In this study we extend the framework of the finite volume methods to dispersive water wave models, in particular to Boussinesq type systems. We focus mainly on the application of the method to bidirectional nonlinear, dispersive wave propagation in one space dimension. Special emphasis is given to important nonlinear phenomena such as solitary waves interactions, dispersive shock wave formation and the runup of breaking and non-breaking long waves.

## 5.1.1 Introduction

The simulation of water waves in realistic and complex environments is a very challenging problem. Most of the applications arise from the areas of coastal and naval engineering, but also from natural hazards assessment. These applications may require the computation of the wave generation [DD07d, KDD07], propagation [TG97], interaction with solid bodies, the computation of long wave runup [TS94, TS98] and even the extraction of the wave energy [Sim81]. Issues like wave breaking, robustness of the numerical algorithm in wet-dry processes along with the validity of the mathematical models in the near-shore zone are some basic problems in this direction [HP79]. During past years, the classical Nonlinear Shallow Water Equations (NSWE) have been employed to solve some of these problems [AC99, DPD10]:

$$\begin{aligned} &H_t + (Hu)_x = 0, \\ &(Hu)_t + \left(Hu^2 + \tfrac{g}{2}H^2\right)_x = gHD_x, \end{aligned} \tag{5.1}$$

where $H(x,t) := \eta(x,t) + D(x)$ is the total water depth, $D(x)$ describes the depth below the mean sea level while $\eta(x,t)$ is the free surface elevation, $u(x,t)$ denotes the depth-averaged fluid velocity and $g$ is the gravity acceleration constant. Mathematically, equations (5.1) represent a system of conservation laws describing the propagation of infinitely long waves with a hydrostatic pressure assumption. The wave breaking phenomenon is commonly

assimilated to the formation of shock waves (or hydraulic jumps) which is a common feature of hyperbolic PDEs. Consequently, the Finite Volumes (FV) method has become the method of choice for these problems due to its excellent intrinsic conservative and shock-capturing properties [AC99, DK03, DKK08, DPD10]. Furthermore, Nonlinear Shallow Water Equations (NSWE) have been proven in practice to predict accurately the maximum runup of long waves [HH70, Syn87, TS94, TS98, KS98].

On the other hand, various studies have shown that the inclusion of dispersive effects is beneficial for the description of long wave propagation and runup processes [Zel91, WKGS95, LR02]. Moreover, J.A. Zelt [Zel91] reported a divergence in the prediction of the rundown and in the prediction of the reflected wave-train after the wave climbing on the beach when a dispersionless model is employed. According to J.A. Zelt results [Zel91], his nonlinear dispersive model showed better performance. During the last fifty years numerous dispersive models have been proposed for the simulation of long waves [Ser53, Per67, BS76, Nwo93, KCKD00, MBS03, Mit09].

In this paper we will study numerically bidirectional water wave models. Specifically, we consider the following family of Boussinesq type systems of water wave theory, introduced in [BCS02], written in nondimensional, unscaled variables

$$\begin{aligned} &\eta_t + u_x + (\eta u)_x + a\, u_{xxx} - b\, \eta_{xxt} = 0, \\ &u_t + \eta_x + u u_x + c\, \eta_{xxx} - d\, u_{xxt} = 0, \end{aligned} \tag{5.2}$$

where $a$, $b$, $c$, $d \in \mathbb{R}$, $\eta = \eta(x,t)$, $u = u(x,t)$ are real functions defined for $x \in \mathbb{R}$ and $t \geq 0$.

For more realistic situations we introduce a modified Boussinesq type system with variable bottom topography based on Peregrine's system, [Per67]. The new system incorporates a very important property — the invariance under vertical translations, thus more appropriate for practical applications such as wave runup on non-uniform beaches. In dimensional variables the model reads

$$\begin{aligned} &H_t + Q_x = 0, \\ &Q_t + (Q^2/H + \tfrac{g}{2}H^2)_x \\ &- \left[\tfrac{H^2}{3}Q_{xxt} - (\tfrac{1}{3}H_x^2 - \tfrac{1}{6}HH_{xx})Q_t + \tfrac{1}{3}HH_xQ_{xt}\right] = gHD_x. \end{aligned} \tag{5.3}$$

where $H(x,t) = \eta(x,t) + D(x)$, $Q(x,t) = H(x,t)u(x,t)$.

There is a wide range of numerical methods in the literature for computing approximate solutions to these models. Finite difference schemes [KWC+98, JFBM06, HMK+09], finite element methods [BDM07, Mit09, DM08, AVSS09] and spectral methods [PD01, Ngu08] have been proposed. More contemporary Discontinuous Galerkin (DG) schemes have also been adapted with some success to dispersive wave equations [YS02, LSY04, ES06, ESB06] while the application of Finite Volumes (FV) or hybrid FV/FD methods remain most

infrequent for this type of problems. To our knowledge, only a few very recent works are in this direction [BB01, EIK05, BS08, TP09, SM09].

Finite volume method is well known for its accuracy, efficiency and robustness for approximating solutions to conservation laws and in particular to Nonlinear Shallow Water Equations (5.1). The aforementioned bidirectional models (5.2) and (5.3) are rewritten in a conservative form and discretization by the finite volume method follows. Three different numerical fluxes are employed

- a simple *average flux* (m-scheme),
- a *central flux*, (KT-scheme) [NT90, KT00], as a representative of central schemes,
- a *characteristic flux* (CF-scheme), as a representative of the linearized Riemann solvers, [GKC96].

along with *TVD*, *UNO* and *WENO* reconstruction techniques, [Swe84, HO87, LOC94]. Time discretization is based on Runge-Kutta (RK) methods which preserve the TVD property of the finite volume scheme, [SO88, GST01, SR02]. We use explicit RK methods since we work with BBM type systems (5.2) and not with KdV equation which is well known to be notoriously stiff. These methods have been studied thoroughly in the case of nonlinear conservation laws. The average flux although is known to be unstable for conservation laws is proved to be very accurate for nonlinear dispersive waves. On other hand finite volume methods based on the central flux as well as on characteristic flux work equally well for the numerical simulation of waves even in realistic environments.

The performance of the finite volume method applied to models (5.2) and to the new system (5.3) is studied in a systematic way through a series of numerical experiments. In particular, in this study we take up on the following points

- accuracy of the finite volume method in the propagation of solitary waves with very satisfactory results.
- conservation of various invariant quantities during the formation of dispersive shocks is studied numerically. The finite element as well as spectral methods break down for these experiments. The finite volume method provides very accurate results.
- Interactions of solitary waves are computed with high accuracy. It is shown numerically that Boussinesq type systems describe better overtaking collisions of solitary waves than unidirectional models like KdV-BBM. We compare our results, whenever possible, with experimental measurements with very good agreement

- Finite volume method allows to use appropriate techniques to treat this transition from wet to dry regions and vice versa. These techniques are applied successfully to systems with dispersive terms modeling runup of long waves. On the other hand, when the model fails due to wave breaking, the method allows to use locally the nonlinear shallow water system, thus enabling us to resolve a wide spectrum of hydrodynamic phenomena using a single computational framework.

- it is shown numerically the advantage of using dispersive models over standard nonlinear shallow water equations in computing the wave runup and, in particular, in capturing the reflected wave. We also illustrated on an example why it is important to have the system invariance under vertical translations.

The paper is organized as follows. In Section 5.1.2 Boussinesq type systems are presented along with some of their basic properties. A new system with uneven bottom and invariant under vertical translations is derived. In Section 5.1.3 the finite volume method is presented for a general framework incorporating all models.

Section 5.1.4 presents a series of numerical experiments for the Boussinesq systems (5.2). In this mathematical setting we validate the finite volume method and measure its accuracy. We study the propagation as well as the interaction of solitary waves: we consider in particular head-on and overtaking collisions, but also we present results concerning the small dispersion effect. Finally, in Section 5.1.5 the new system with variable bottom, (5.3) is studied. Numerical simulations of non-breaking and breaking long wave runup are presented and compared with experimental data.

## 5.1.2 Mathematical models

We present briefly the mathematical models being considered and some of their main properties.

### 5.1.2.1 Dispersive models with flat bottom

We consider the following family of Boussinesq type systems of water wave theory, introduced in [BCS02], which may be written in nondimensional, unscaled variables

$$\begin{aligned} &\eta_t + u_x + (\eta u)_x + a u_{xxx} - b\eta_{xxt} = 0, \\ &u_t + \eta_x + u u_x + c\eta_{xxx} - d u_{xxt} = 0, \end{aligned} \tag{5.4}$$

where $\eta = \eta(x,t)$, $u = u(x,t)$ are real functions defined for $x \in \mathbb{R}$ and $t \geq 0$. Coefficients $a$, $b$, $c$ and $d$ are defined as

$$\begin{aligned} a &= \tfrac{1}{2}(\theta^2 - \tfrac{1}{3})\nu, \quad & b &= \tfrac{1}{2}(\theta^2 - \tfrac{1}{3})(1-\nu), \\ c &= \tfrac{1}{2}(1-\theta^2)\mu, \quad & d &= \tfrac{1}{2}(1-\theta^2)(1-\mu), \end{aligned} \tag{5.5}$$

where $0 \leq \theta \leq 1$ and $\mu, \nu \in \mathbb{R}$. The variables in (5.4) are non-dimensional and unscaled: $x$ and $t$ are proportional to position along the channel and time, respectively, while $\eta(x,t)$ and $u(x,t)$ are proportional to the deviation of the free surface above an undisturbed level, and to the horizontal velocity of the fluid at a height $y = -1 + \theta(1 + \eta(x,t))$, respectively. In terms of these variables the channel bottom is located at $y = -1$, $(\theta = 0)$, while the free surface corresponds to $\theta = 1$. Boussinesq systems (5.4) with $b = d$ conserve the energy functional:

$$I_1(t) = \int_{\mathbb{R}} (\eta^2(x,t) + (1+\eta(x,t))u^2(x,t) - c\,\eta_x^2(x,t) - a\,u_x^2(x,t))\,dx, \tag{5.6}$$

i.e. $I_1(t) = I_1(0)$. The system (5.4) is derived under following assumptions:

$$\varepsilon := A/h_0 \ll 1\,, \quad \sigma := h_0/\lambda \ll 1 \quad S := \frac{A\lambda^2}{h_0^3} = O(1)\,,$$

where $S$ is the Stokes (or Ursell) number, $A$ is a typical wave amplitude and $\lambda$ is a characteristic wavelength. If one takes $S = 1$ and switches to scaled, dimensionless variables, one may derive from Euler equations a scaled version of (5.4) by appropriate asymptotic expansion in powers of $\varepsilon$, cf. [BCS04]:

$$\begin{aligned} &\eta_t + u_x + \varepsilon(\eta u)_x + \epsilon[a u_{xxx} - b\eta_{xxt}] = O(\varepsilon^2), \\ &u_t + \eta_x + \varepsilon u u_x + \epsilon[c\eta_{xxx} - d u_{xxt}] = O(\varepsilon^2), \end{aligned} \tag{5.7}$$

from which we obtain (5.4) by unscaling and neglecting higher order terms $O(\varepsilon^2)$.

We list several examples of particular Boussinesq systems of the form (5.4) that we will refer to in the sequel. The initial-value problem for all these systems has been shown to be at least nonlinearly well-posed locally in time, cf. [BCS04].

(i) The 'classical' Boussinesq system ($\mu = 0$, $\theta^2 = 1/3$, i.e. $a = b = c = 0$, $d = 1/3$ in (5.4)), whose initial-value problem is globally well-posed, [Ami84, Sch81],

$$\begin{aligned} &\eta_t + u_x + (\eta u)_x = 0, \\ &u_t + \eta_x + u u_x - \tfrac{1}{3} u_{xxt} = 0. \end{aligned} \tag{5.8}$$

(ii) The BBM-BBM system ($\nu = \mu = 0$, $\theta^2 = 2/3$, i.e. $a = c = 0$, $b = d = 1/6$ in (5.4)), whose initial-value problem is locally well-posed, [BC98]

$$\begin{aligned} &\eta_t + u_x + (\eta u)_x - \tfrac{1}{6}\eta_{xxt} = 0, \\ &u_t + \eta_x + uu_x - \tfrac{1}{6}u_{xxt} = 0. \end{aligned} \tag{5.9}$$

(iii) The Bona-Smith system ($\nu = 0$, $\mu = (4 - 6\theta^2)/3(1 - \theta^2)$, i.e. $a = 0$, $b = d = (3\theta^2 - 1)/6$, $c = (2 - 3\theta^2)/3$, $2/3 < \theta^2 < 1$ in (5.4)), whose initial-value problem is globally well-posed, cf. [BS76]. The limiting form of this system as $\theta \to 1$, corresponding to $a = 0$, $b = d = 1/3$, $c = -1/3$, is the system actually studied by Bona and Smith, [BS76]. These systems are given by

$$\begin{aligned} &\eta_t + u_x + (\eta u)_x - \tfrac{3\theta^2-1}{6}\eta_{xxt} = 0, \\ &u_t + \eta_x + uu_x + \tfrac{2-3\theta^2}{3}\eta_{xxx} - \tfrac{3\theta^2-1}{6}u_{xxt} = 0. \end{aligned} \tag{5.10}$$

The existence of solitary wave solutions to the above systems, in some cases the uniqueness also, has been proved in [Che00, Che98, DM04] and in the case of the Bona-Smith type systems (5.10) for each $\theta^2 \in (7/9, 1)$ there exists one solitary wave in the closed form [Che98]

$$\begin{aligned} \eta(\xi) &= \eta_0 \, sech^2(\lambda\xi), \\ u(\xi) &= B\,\eta(\xi), \end{aligned} \tag{5.11}$$

with

$$\begin{aligned} \eta_0 &= \tfrac{9}{2} \cdot \tfrac{\theta^2 - 7/9}{1-\theta^2}, & c_s &= \tfrac{4(\theta^2-2/3)}{\sqrt{2(1-\theta^2)(\theta^2-1/3)}}, \\ \lambda &= \tfrac{1}{2}\sqrt{\tfrac{3(\theta^2-7/9)}{(\theta^2-1/3)(\theta^2-2/3)}}, & B &= \sqrt{\tfrac{2(1-\theta^2)}{\theta^2-1/3}}. \end{aligned} \tag{5.12}$$

#### 5.1.2.2 Dispersive models with variable bottom

For more realistic applications one should consider Boussinesq systems with variable bottom. After the pioneering work of Peregrine, [Per67], who derived the following Boussinesq type system

$$\begin{aligned} &\eta_t + [(D + \eta)u]_x = 0, \\ &u_t + g\eta_x + uu_x - \tfrac{D}{2}(Du)_{xxt} - \tfrac{D^2}{6}u_{xxt} = 0, \end{aligned} \tag{5.13}$$

where $\eta(x,t)$ and $u(x,t)$ are defined as before, $D(x)$ describes the water depth below its rest position. Many other systems have been derived also, including systems with improved dispersion characteristics [Nwo93], high-order Boussinesq systems [MBS03] and other generalizations of (5.4), cf. [Mit09]. Most of these systems break Galilean invariance and the invariance under vertical translations. This is a restrictive property especially in the studies of realistic problems like the water wave runup on non-uniform beaches. We note also that the complete water wave problem possesses these symmetries [BO82].

To overcome this deficiency we develop a new system, analogous to the original Peregrine's system, [Per67], which is invariant under vertical translations. To derive the system we begin with (5.13) written in dimensionless scaled variables (in analogy with (5.7))

$$\begin{aligned} &\eta_t + [(D+\varepsilon\eta)u]_x = 0, \\ &u_t + \eta_x + \varepsilon u u_x - \sigma^2 \left[\tfrac{D}{2}(Du)_{xxt} - \tfrac{D^2}{6}u_{xxt}\right] = O(\varepsilon^2, \varepsilon\sigma^2). \end{aligned} \tag{5.14}$$

Then by setting $H = D + \varepsilon\eta$, we obtain

$$\begin{aligned} &H_t + (Hu)_x = 0, \\ &(Hu)_t + (\varepsilon H u^2 + \tfrac{1}{2\varepsilon}H^2)_x \\ &-\sigma^2 \left[\tfrac{HD}{2}(Du)_{xxt} - \tfrac{HD^2}{6}(\tfrac{Du}{D})_{xxt}\right] = \tfrac{1}{\varepsilon}HD_x + O(\varepsilon^2, \varepsilon\sigma^2). \end{aligned} \tag{5.15}$$

Observing that $\left(\frac{Du}{D}\right)_{xx} = [2\frac{D_x^2}{D^3} - \frac{D_{xx}}{D^2}](Du) - 2\frac{D_x}{D^2}(Du)_x + \frac{1}{D}(Du)_{xx}$ and that $H = D + O(\varepsilon)$ we have that

$$\begin{aligned} &H_t + (Hu)_x = 0, \\ &(Hu)_t + (\varepsilon H u^2 + \tfrac{1}{2\varepsilon}H^2)_x \\ &-\sigma^2 \left[\tfrac{D^2}{3}(Du)_{xxt} - (\tfrac{1}{3}D_x^2 - \tfrac{1}{6}DD_{xx})Du_t + \tfrac{1}{3}DD_x(Du)_{xt}\right] \\ &= \tfrac{1}{\varepsilon}HD_x + O(\varepsilon^2, \varepsilon\sigma^2). \end{aligned} \tag{5.16}$$

By setting $Q = Hu$, and using again the relation $H = D + O(\varepsilon)$ we have

$$\begin{aligned} &H_t + Q_x = 0, \\ &Q_t + (\varepsilon Q^2/H + \tfrac{1}{2\varepsilon}H^2)_x \\ &-\sigma^2 \left[\tfrac{H^2}{3}Q_{xxt} - (\tfrac{1}{3}H_x^2 - \tfrac{1}{6}HH_{xx})Q_t + \tfrac{1}{3}HH_xQ_{xt}\right] = \tfrac{1}{\varepsilon}HD_x + O(\varepsilon^2, \varepsilon\sigma^2). \end{aligned} \tag{5.17}$$

and in dimensional variables, neglecting the higher order terms at the right-hand side:

$$\begin{aligned} &H_t + Q_x = 0, \\ &Q_t + (Q^2/H + \tfrac{g}{2}H^2)_x - P(H,Q) = gHD_x. \\ &P(H,Q) = \tfrac{H^2}{3}Q_{xxt} - (\tfrac{1}{3}H_x^2 - \tfrac{1}{6}HH_{xx})Q_t + \tfrac{1}{3}HH_xQ_{xt} \end{aligned} \tag{5.18}$$

where $H(x,t) = \eta(x,t) + D(x)$, $Q(x,t) = H(x,t)u(x,t)$. We underline that system (5.18) is invariant under vertical translations and therefore more appropriate for the study of long wave runup. Moreover, the linearization of the system (5.18) coincides with the original Peregrine's system (5.14) and, therefore, inherits all its linear dispersive characteristics. System (5.18) cannot be regarded as a correct asymptotic model to the Euler equations since it contains terms of the order $O(\varepsilon\sigma^2)$ and higher. On the other hand, such terms considered in the correct (small amplitude and long wave) regime are negligible and, therefore,

their contribution will be negligible. Finally we note that ignoring the dispersive terms $P(H, Q)$ in (5.18) will lead Nonlinear Shallow Water equations (5.1).

We also note that even if Boussinesq systems are not valid in the near-shore region, in practice they appear to predict well the behavior of small amplitude waves from moderately deep to shallower waters, cf. [Zel91]. Of course, more accurate systems in the near-shore zone have been derived such as the Sérre equations (sometimes referred also as Green-Naghdi equations), cf. [Ser53, LB09, DM10]. These systems appeared in practice to model better the breaking phenomena in the near shore zone but recent numerical studies of the Sérre equations showed that unphysical oscillations might appear in analogy with the Boussinesq equations during the wave breaking and the runup process, [CBB06, CBB07].

#### 5.1.2.3 Source terms

Nonlinear shallow water model (5.1) and Boussinesq system (5.3) may be completed to take into account some dissipative or friction effects which are very beneficial in describing the wave breaking phenomena. Usually it is done by including appropriate source or dissipative terms into momentum conservation equations (5.1) or (5.3). One of the possible choices is the following :

$$\text{Friction:} \qquad F(u, H) = -c_m\, g\, \frac{u|u|}{H^{1/3}}, \tag{5.19}$$

$$\text{Viscosity:} \qquad V(u, H) = \mu \frac{\partial}{\partial x}\left(H \frac{\partial u}{\partial x}\right), \tag{5.20}$$

where $c_m$ is the Manning roughness coefficient and $\mu$ denotes the kinematic viscosity of the fluid. The particular form of the source terms is suggested by empirical laws, which are generally obtained for steady state flows. Similar models have been derived from Navier-Stokes system for incompressible flows with a free surface. More complex friction laws can be also formulated to model bottom rugosity effects, etc.

### 5.1.3 Numerical schemes

In the present section we generalize the finite volume method to systems (5.2) and (5.3) of dispersive PDEs. In our work we rely on corresponding schemes for conservation laws. Next we present briefly the finite volume framework for conservation laws. Based on this framework we introduce finite volume schemes for the dispersive models.

#### 5.1.3.1 Finite volume method for conservation laws

We present briefly the finite volume method for conservation laws. Consider the initial value problem

$$\begin{aligned} &w_t + \big(F(w)\big)_x = S(w),\ x \in \mathbb{R}, t > 0 \\ &w(x,0) = w_0(x), \end{aligned} \tag{5.21}$$

where $w(x,t)$ is the state variable, $F$ denotes the flux and $S$ is the source term. Let $\mathcal{T} = \{x_i\},\ i \in \mathbb{Z}$ denotes a partition of $\mathbb{R}$ into cells $C_i = (x_{i-\frac{1}{2}}, x_{i+\frac{1}{2}})$ where $x_i = (x_{i+\frac{1}{2}} + x_{i-\frac{1}{2}})/2$ denotes the midpoints of $C_i$. Let $\Delta x_i = x_{i+\frac{1}{2}} - x_{i-\frac{1}{2}}$ denotes the length of the cell $C_i$, $\Delta x_{i+\frac{1}{2}} = x_{i+1} - x_i$. Without loss of generality we assume a uniform partition $\mathcal{T}$ that is $\Delta x_i = \Delta x_{i+\frac{1}{2}} = \Delta x,\ i \in \mathbb{Z}$. Let $w_i$ denotes the cell average of $w$ on $C_i$ i.e $w_i(t) = \frac{1}{\Delta x}\int_{C_i} w(x,t)\,dx$. Then a simple integration of (5.21) over a cell $C_i$ yields

$$\frac{d}{dt}w_i(t) + \frac{1}{\Delta x}\Big(F(w(x_{i+\frac{1}{2}},t)) - F(w(x_{i-\frac{1}{2}},t))\Big) = \frac{1}{\Delta x}\int_{C_i} S(w(x,t))\,dx. \tag{5.22}$$

**5.1.3.1.1 Semidiscrete schemes** We now define the semidiscrete finite volume approximation of $w(x,t)$. Let $\chi_{C_i}$ denotes the characteristic function of the cell $C_i$, we seek a piecewise constant function $w_h(x,t) = \sum_{i\in\mathbb{Z}} W_i(t)\chi_{C_i}(x)$ with

$$\begin{aligned} &\tfrac{d}{dt}W_i(t) + \tfrac{1}{\Delta x}\Big(\mathcal{F}_{i+\frac{1}{2}} - \mathcal{F}_{i-\frac{1}{2}}\Big) = \mathcal{S}_i, \quad i \in \mathbb{Z}, \\ &W_i(0) = \tfrac{1}{\Delta x}\int_{C_i} w(x,0)\,dx, \quad i \in \mathbb{Z} \end{aligned} \tag{5.23}$$

where $\mathcal{F}_{i+\frac{1}{2}} = \mathcal{F}(W^L_{i+\frac{1}{2}}, W^R_{i+\frac{1}{2}})$ is an approximation to $F(w(x_{i+\frac{1}{2}},t))$ while $\mathcal{S}_i$ approximates the source term $\mathcal{S}_i = \mathcal{S}_i(W_i) \approx \frac{1}{\Delta x}\int_{C_i} S(w(x,t))\,dx$. The values $W^L_{i+\frac{1}{2}}, W^R_{i+\frac{1}{2}}$ are approximations to the point value $w(x_{i+\frac{1}{2}},t)$ from cells $C_i,\ C_{i+1}$ respectively and $\mathcal{F}$ is a numerical flux function which is monotone and conservative. The values $W^L_{i+\frac{1}{2}}, W^R_{i+\frac{1}{2}}$ are computed by a reconstruction process described below (see Section 5.1.3.1.3).

**5.1.3.1.2 The numerical fluxes** There are many possible choices for the numerical flux function $\mathcal{F}$. In the present study we choose to work with three following fluxes

$$\mathcal{F}^m(W,V) = F\left(\frac{W+V}{2}\right), \tag{5.24}$$

$$\mathcal{F}^{KT}(W,V) = \frac{1}{2}\left\{[F(V) + F(W)] - \mathcal{A}(W,V)\,[V - W]\right\} \tag{5.25}$$

$$\mathcal{F}^{CF}(W,V) = \frac{1}{2}\left\{[F(V) + F(W)] - \mathcal{A}(W,V)\,[F(V) - F(W)]\right\}. \tag{5.26}$$

The *average* flux (5.24) is the simplest one. It is well known that although this flux is unstable for nonlinear conservation laws, it is proven very stable and accurate for nonlinear dispersive models.

The *central* flux (5.25) is a Lax-Friedrichs type flux and is a representative of central schemes [KT00, NT90]. The operator $\mathcal{A}$ is related to the characteristic speeds of the flow and is defined as

$$\mathcal{A}(W,V) = \max\left[\rho\left(DF(W)\right), \rho\left(DF(V)\right)\right], \tag{5.27}$$

where $DF$ denotes the Jacobian matrix and $\rho(A)$ is the spectral radius of $A$.

The *characteristic* flux function (5.26), [GKC96, GKC01], is similar to the upwind flux and the operator $\mathcal{A}$ in this case is defined by

$$\mathcal{A}(W,V) = \text{sign}\left(DF\left(\frac{W+V}{2}\right)\right). \tag{5.28}$$

**5.1.3.1.3 The reconstruction process** The values $W^L_{i+\frac{1}{2}}, W^R_{i+\frac{1}{2}}$ are approximations to $w(x_{i+\frac{1}{2}}, t)$ from cells $C_i$ and $C_{i+1}$ correspondingly. The simplest possible choice is to take the piecewise constant approximation in each cell

$$W^L_{i+\frac{1}{2}} = W_i, \quad W^R_{i+\frac{1}{2}} = W_{i+1}. \tag{5.29}$$

The resulting semidiscrete finite volume scheme is formally first order accurate in space.

To construct a higher order scheme in space, the piecewise constant data is replaced by a piecewise polynomial representation. The main idea here is to construct higher order approximations to $w(x_{i+\frac{1}{2}}, t)$ using the computed cell averages $W_i$. For this purpose the classical MUSCL type (TVD2) linear reconstruction [Kol75, vL79] as well as UNO2, [HO87] or WENO type reconstructions, [LOC94], have been developed.

The classical TVD2 type linear reconstruction is given by following formulas:

$$W^L_{i+\frac{1}{2}} = W_i + \frac{1}{2}\phi(r_i)(W_{i+1} - W_i), \quad W^R_{i+\frac{1}{2}} = W_{i+1} + \frac{1}{2}\phi(r_{i+1})(W_{i+2} - W_{i+1}), \tag{5.30}$$

where $r_i = \frac{W_i - W_{i-1}}{W_{i+1} - W_i}$, and $\phi$ is an appropriate slope limiter, [Swe84]. There exist many options in choosing a limiter function. Some of the most popular choices are

- MinMod (MM) limiter: $\phi(\theta) = \max(0, \min(1, \theta))$,
- VanLeer (VL) limiter: $\phi(\theta) = \frac{\theta + |\theta|}{1 + |\theta|}$,
- Monotonized Central (MC) limiter: $\phi(\theta) = \max(0, \min((1+\theta)/2, 2, 2\theta))$,
- Van Albada (VA) limiter: $\phi(\theta) = \frac{\theta + \theta^2}{1 + \theta^2}$.

The last three limiters have been shown to exhibit sharper resolution of discontinuities since they do not reduce the slope as severely as (MM) near a discontinuity. The TVD2 reconstruction is second order accurate except at the local extrema where it reduces to the first order. A remedy is to consider the UNO2 type reconstruction.

The UNO2 reconstruction is a linear interpolation which is second order accurate even at local extrema, [HO87]. The values $W^L_{i+\frac{1}{2}}, W^R_{i+\frac{1}{2}}$ are defined as

$$W^L_{i+\frac{1}{2}} = W_i + \frac{1}{2}S_i, \quad W^R_{i+\frac{1}{2}} = W_{i+1} - \frac{1}{2}S_{i+1}, \tag{5.31}$$

where

$$\begin{aligned}
&S_i = m(S_i^+, S_i^-), \quad S_i^\pm = d_{i\pm\frac{1}{2}}W \mp \frac{1}{2}D_{i\pm\frac{1}{2}}W,\\
&d_{i+\frac{1}{2}}W = W_{i+1} - W_i, \quad D_{i+\frac{1}{2}}W = m(D_iW, D_{i+1}W),\\
&D_iW = W_{i+1} - 2W_i + W_{i-1}, \quad m(x,y) = \frac{1}{2}(\mathrm{sign}(x) + \mathrm{sign}(y))\min(|x|,|y|).
\end{aligned}$$

Using either (TVD2) or (UNO2) reconstructions the semidiscrete finite volume scheme (5.23) is formally second order accurate.

In order to achieve higher order accuracy we also employed WENO type reconstructions for the values $W^R_{i\pm\frac{1}{2}}$, $W^L_{i\pm\frac{1}{2}}$. We implemented 3rd and 5th order accurate WENO methods (also referred to as WENO3 and WENO5, respectively) as they are described in [LOC94]. For the sake of simplicity we only present the WENO3 case. In order to compute the approximations $W^L_{i+\frac{1}{2}}$ and $W^R_{i-\frac{1}{2}}$, we first compute the 3rd order reconstructed values

$$\begin{aligned}
W^{(0)}_{i+\frac{1}{2}} &= \frac{1}{2}(W_i + W_{i+1}), \qquad W^{(1)}_{i+\frac{1}{2}} = \frac{1}{2}(-W_{i-1} + 3W_i),\\
W^{(0)}_{i-\frac{1}{2}} &= \frac{1}{2}(3W_i - W_{i+1}), \qquad W^{(1)}_{i-\frac{1}{2}} = \frac{1}{2}(W_{i-1} + W_i).
\end{aligned}$$

We define the smoothness parameters

$$\beta_0 = (W_{i+1} - W_i)^2, \qquad \beta_1 = (W_i - W_{i-1})^2,$$

and the parameters $d_0 = \frac{2}{3}$, $d_1 = \frac{1}{3}$ and $\tilde{d}_0 = d_1$, $\tilde{d}_1 = d_0$, along with the weights

$$\begin{aligned}
\omega_0 &= \frac{\alpha_0}{\alpha_0 + \alpha_1}, \qquad \omega_1 = \frac{\alpha_0}{\alpha_0 + \alpha_1},\\
\tilde{\omega}_0 &= \frac{\tilde{\alpha}_0}{\tilde{\alpha}_0 + \tilde{\alpha}_1}, \qquad \tilde{\omega}_1 = \frac{\tilde{\alpha}_1}{\tilde{\alpha}_0 + \tilde{\alpha}_1},
\end{aligned}$$

where $\alpha_i = \frac{d_i}{\epsilon+\beta_i}$, $\tilde{\alpha}_i = \frac{\tilde{d}_i}{\epsilon+\beta_i}$ and $\epsilon$ to be a small, positive number (in our computations we set $\epsilon = 10^{-15}$). Then the reconstructed values are given by the following formulas

$$W^L_{i+\frac{1}{2}} = \sum_{r=0}^{1} \omega_r W^{(r)}_{i+\frac{1}{2}}, \qquad W^R_{i-\frac{1}{2}} = \sum_{r=0}^{1} \tilde{\omega}_r W^{(r)}_{i-\frac{1}{2}}. \tag{5.32}$$

**5.1.3.1.4 Discretization of source terms** The finite volume discretization of the source term $S(w)$ in (5.21) depends on the particular choice. On the other hand the resulting approximation should preserve the upwind nature and the overall scheme should be well balanced. One possible discretization of the source term $S(w)$ is given by:

$$\frac{1}{\Delta x}\int_{C_i} S(w)\,dx \approx \frac{\mathcal{S}_{i-\frac{1}{2}}+\mathcal{S}_{i+\frac{1}{2}}}{2}, \quad \mathcal{S}_{i+\frac{1}{2}} = S\left(\frac{W^L_{i+\frac{1}{2}}+W^R_{i+\frac{1}{2}}}{2}\right). \tag{5.33}$$

**5.1.3.1.5 Fully discrete schemes** Then we consider fully discrete schemes for (5.23). Equation (5.23) is an initial value problem and can be discretized by various methods. In our case we use a special class of Runge-Kutta methods which ensure the TVD property of the finite volume scheme, [SO88, GST01, SR02].

Let $\Delta t$ be the time step and let $t^{n+1} = t^n + \Delta t,\ n \geq 0$ be discrete time levels. Assuming that the approximation at $t^n,\ W_i^n,\ i \in \mathbb{Z}$ are known then $W_i^{n+1}$ are defined by

$$\begin{aligned} W_i^{n+1} &= W_i^n - \frac{\Delta t}{\Delta x}\sum_{j=1}^{s} b_j\left(\mathcal{F}^{n,j}_{i+\frac{1}{2}} - \mathcal{F}^{n,j}_{i-\frac{1}{2}}\right) + \Delta t\sum_{j=1}^{s} b_j\ \mathcal{S}_i^{n,j}, \\ W_i^{n,j} &= W_i^n - \frac{\Delta t}{\Delta x}\sum_{\ell=1}^{s} a_{j\ell}\left(\mathcal{F}^{n,\ell}_{i+\frac{1}{2}} - \mathcal{F}^{n,\ell}_{i-\frac{1}{2}}\right) + \Delta t\sum_{\ell=1}^{s} a_{j\ell}\,\mathcal{S}_i^{n,\ell}, \end{aligned} \tag{5.34}$$

where $\mathcal{F}^{n,j}_{i+\frac{1}{2}} = \mathcal{F}(W_i^{n,j}, W_{i+1}^{n,j})$, $\mathcal{S}_i^{n,j} = \mathcal{S}(W_i^{n,j})$. The set of constants $A = (a_{j\ell})$, $b = (b_1, \ldots, b_s)$ define an $s-$stage Runge-Kutta method. The following *tableau* are examples of explicit TVD RK-methods which are of 2nd and 3rd order respectively

$$\begin{array}{cc|c} 0 & 0 & 0 \\ 1 & 0 & 1 \\ \hline \frac{1}{2} & \frac{1}{2} & \end{array} \qquad \begin{array}{ccc|c} 0 & 0 & 0 & 0 \\ 1 & 0 & 0 & 1 \\ \frac{1}{4} & \frac{1}{4} & 0 & \frac{1}{2} \\ \hline \frac{1}{6} & \frac{1}{6} & \frac{2}{3} & \end{array} \tag{5.35}$$

In our computations we mainly use the three stage 3rd order method.

### 5.1.3.2 Finite volume schemes for dispersive models

To construct the finite volume schemes for the dispersive PDEs the main idea is to rewrite governing equations or systems in a conservative like form and discretize the resulting conservation laws using the aforementioned framework. One can use any of the numerical fluxes, $\mathcal{F}^m$, $\mathcal{F}^{KT}$, $\mathcal{F}^{CF}$ and reconstruction techniques TVD2, UNO2 or WENO. Temporal discretization is based on the TVD-Runge-Kutta methods, (5.35).

**5.1.3.2.1 Boussinesq systems with flat bottom** Boussinesq system (5.2) can be rewritten in a conservative like form as follows:

$$(I - \mathbf{D})\mathbf{v}_t + [\mathbf{F}(\mathbf{v})]_x + [\mathbf{G}(\mathbf{v})]_x = 0, \tag{5.36}$$

where $\mathbf{v} = (\eta, u)^T$, $\mathbf{F}(\mathbf{v}) = ((1+\eta)u, \eta + \frac{1}{2}u^2)^T$, $\mathbf{G}(\mathbf{v}) = (a\, u_{xx}, c\, \eta_{xx})$, and $\mathbf{D} = \mathrm{diag}\,(b\,\partial_x^2, d\,\partial_x^2)$. The simplest discretization is based on the average fluxes $\mathcal{F}^m$ for $\mathbf{F}$ and $\mathcal{G}^m$ for $\mathbf{G}$. For the other two choices of the numerical flux $\mathcal{F}$ the evaluation of Jacobian is needed. Let $A$ denotes the Jacobian of $\mathbf{F}$, then

$$A = \begin{pmatrix} u & 1+\eta \\ 1 & u \end{pmatrix},$$

with eigenvalues $\lambda_i = u \pm \sqrt{1+\eta}$, $i = 1, 2$. It is readily seen, since $\mathbf{F}$ is a hyperbolic flux, that $A$ can be decomposed as $A = L\Lambda R$ thus for the characteristic flux $\mathcal{F}^{CF}$ we have with $\mu = \frac{W+V}{2}$, $s_i = \mathrm{sign}(\lambda_i)$, $i = 1, 2$

$$\mathcal{A}(W, V) = \begin{pmatrix} \frac{1}{2}(s_1 + s_2) & \frac{1}{2}\sqrt{1+\mu_1}(s_1 - s_2) \\ \frac{s_1 - s_2}{2\sqrt{1+\mu_1}} & \frac{1}{2}(s_1 + s_2) \end{pmatrix}.$$

For evaluating the numerical fluxes $\mathcal{F}$, $\mathcal{G}$ simple cell averages or higher order approximations such as UNO2 (5.31) or WENO (5.32) can be used.

**Remark 26.** *The discretization of the elliptic operator* $\mathbf{D}$ *is based on the standard centered difference. This is a second order accurate approximation and it is compatible with the TVD2 and UNO2 reconstructions. For higher order interpolation we need to modify the elliptic and flux discretization to match the reconstruction's order of approximation. Indeed, the finite volume scheme is modified as*

$$\frac{d}{dt}\left[\frac{\mathbf{V}_{i-1} + 10\mathbf{V}_i + \mathbf{V}_{i+1}}{12} - (b, d)\frac{\mathbf{V}_{i+1} - 2\mathbf{V}_i + \mathbf{V}_{i-1}}{\Delta x^2}\right] + \frac{\mathcal{H}_{i-1} + 10\mathcal{H}_i + \mathcal{H}_{i+1}}{12} = 0$$

*where* $\mathcal{H}_i = \frac{1}{\Delta x}(\mathcal{F}_{i+\frac{1}{2}} - \mathcal{F}_{i-\frac{1}{2}}) + \frac{1}{\Delta x}(\mathcal{G}_{i+\frac{1}{2}} - \mathcal{G}_{i-\frac{1}{2}})$, *is a fourth order accurate approximation.*

**Remark 27.** *In the sequel for the discretization of the dispersive term* $\mathbf{G}$ *we use mainly the average numerical flux* $\mathcal{G}^m$ *defined as* $\mathcal{G}^m_{i+\frac{1}{2}} = (a, c)\frac{\mathbf{Y}_i + \mathbf{Y}_{i+1}}{2}$, *where* $\mathbf{Y}_i = \frac{\mathbf{V}_{i+1} - 2\mathbf{V}_i + \mathbf{V}_{i-1}}{\Delta x^2}$. *In case of higher order WENO reconstructions we use the average numerical flux based on the reconstructed values of* $\mathbf{Y}_i$ *i.e. the flux* $\mathcal{G}^{lm}_{i+\frac{1}{2}} = (a, c)\frac{\mathbf{Y}^L_{i+\frac{1}{2}} + \mathbf{Y}^R_{i+\frac{1}{2}}}{2}$, *where* $\mathbf{Y}^L_{i+\frac{1}{2}}$ *and* $\mathbf{Y}^R_{i+\frac{1}{2}}$ *are reconstructed values of* $\mathbf{Y}_i$ *on* $x_{i+\frac{1}{2}}$.

**5.1.3.2.2 Boussinesq system with variable bottom** We write system (5.18) in terms of dependent variables $\mathbf{v} := (H, Q)^T$ in the following conservative form

$$[\mathbf{D}(\mathbf{v})]_t + [\mathbf{F}(\mathbf{v})]_x = \mathbf{S}(\mathbf{v}), \tag{5.37}$$

where

$$\mathbf{D}(\mathbf{v}) = \begin{pmatrix} H \\ (1 + \frac{1}{3}H_x^2 - \frac{1}{6}HH_{xx})Q - \frac{1}{3}HH_xQ_x - \frac{H^2}{3}Q_{xx} \end{pmatrix} \tag{5.38}$$

and

$$\mathbf{F}(\mathbf{v}) = \begin{pmatrix} Q \\ \frac{Q^2}{H} + \frac{g}{2}H^2 \end{pmatrix}, \qquad \mathbf{S}(\mathbf{v}) = \begin{pmatrix} 0 \\ gHD_x \end{pmatrix}. \tag{5.39}$$

We consider a uniform mesh and we denote by $H_i$, $U_i$ and $D_i$ the respective cell averages. To discretize the dispersive terms in (5.38) we consider the following approximations:

$$\frac{1}{\Delta x}\int_{x_{i-\frac{1}{2}}}^{x_{i+\frac{1}{2}}} \left[1 + \frac{1}{3}(H_x)^2 - \frac{1}{6}HH_{xx}\right] Q\, dx \approx \left(1 + \frac{1}{3}\left(\frac{H_{i+1} - H_{i-1}}{2\Delta x}\right)^2 - \frac{1}{6}H_i\,\frac{H_{i+1} - 2H_i + H_{i-1}}{\Delta x^2}\right) Q_i,$$

$$\frac{1}{\Delta x}\int_{x_{i-\frac{1}{2}}}^{x_{i+\frac{1}{2}}} \frac{1}{3}HH_xQ_x\, dx \approx \frac{1}{3}H_i\,\frac{H_{i+1} - H_{i-1}}{2\Delta x}\frac{Q_{i+1} - Q_{i-1}}{2\Delta x} \tag{5.40}$$

$$\frac{1}{\Delta x}\int_{x_{i-\frac{1}{2}}}^{x_{i+\frac{1}{2}}} \frac{1}{3}H^2Q_{xx}\, dx \approx \frac{1}{3}H_i^2\,\frac{Q_{i+1} - 2Q_i + Q_{i-1}}{\Delta x^2}. \tag{5.41}$$

This discretization leads to a linear system with tridiagonal matrix denoted by $\mathbf{D}_i$ that can be inverted efficiently. For the time integration the explicit third-order TVD-RK method, (5.35) is used. In the numerical experiments we observed that the fully discrete scheme is stable and preserves the positivity of $H$ during the runup under mild restriction on the time step $\Delta t$.

Therefore, the semidiscrete problem of (5.38) — (5.39) is written as a system of ODEs in the form

$$\mathbf{D}_i\mathbf{v}_{it} + \frac{1}{\Delta x}(\mathcal{F}_{i+\frac{1}{2}} - \mathcal{F}_{i-\frac{1}{2}}) = \frac{1}{\Delta x}\mathbf{S_i}. \tag{5.42}$$

$\mathcal{F}_{i+\frac{1}{2}}$ can be chosen to be one of the numerical flux functions mentioned in the previous sections. In the sequel we will use the KT and the CF numerical fluxes. In this case the Jacobian of $\mathbf{F}$ is given by the matrix

$$A = \begin{pmatrix} 0 & 1 \\ gH - (Q/H)^2 & 2Q/H \end{pmatrix},$$

and the eigenvalues are $\lambda_{1,2} = Q/H \pm \sqrt{gH}$. Therefore, the CF numerical flux takes the form

$$\mathcal{F}_{i+\frac{1}{2}} = \frac{\mathbf{F}(\mathbf{v}^L_{i+\frac{1}{2}}) + \mathbf{F}(\mathbf{v}^R_{i+\frac{1}{2}})}{2} - \mathbf{U}(\boldsymbol{\mu})\frac{\mathbf{F}(\mathbf{v}^R_{i+\frac{1}{2}}) - \mathbf{F}(\mathbf{v}^L_{i+\frac{1}{2}})}{2} \tag{5.43}$$

where $\boldsymbol{\mu} = (\mu_1, \mu_2)^T$,

$$\mu_1 = \frac{H^L_{i+\frac{1}{2}} + H^R_{i+\frac{1}{2}}}{2}, \quad \mu_2 = \frac{\sqrt{H^L_{i+\frac{1}{2}}}U^L_{i+\frac{1}{2}} + \sqrt{H^R_{i+\frac{1}{2}}}U^R_{i+\frac{1}{2}}}{\sqrt{H^L_{i+\frac{1}{2}}} + \sqrt{H^R_{i+\frac{1}{2}}}}$$

and

$$\mathbf{U}(\boldsymbol{\mu}) = \begin{pmatrix} \frac{s_2(\mu_2+c)-s_1(\mu_2-c)}{2c} & \frac{s_1-s_2}{2c} \\ \frac{(s_2-s_1)(\mu_2^2-c^2)}{2c} & \frac{s_1(\mu_2+c)-s_2(\mu_2-c)}{2c} \end{pmatrix}, \; c = \sqrt{g\mu_1}, \; s_i = \text{sign}(\lambda_i). \tag{5.44}$$

In order to guarantee the positivity of the reconstructed values $H_{i+\frac{1}{2}}$ on the interfaces of the cells we employed the well balanced hydrostatic reconstruction algorithm, [ABB+04]. Here we briefly recall the great lines of this reconstruction algorithm.

In the cell $C_i$ we compute first the reconstructions $\mathbf{v}_{i,r}$ and $\mathbf{v}_{i,l}$ at $(i+\frac{1}{2})^-$ and $(i-\frac{1}{2})^+$, respectively using either TVD2 or UNO2 with MinMod limiter. Moreover, we compute in the same way the values $\eta_{i,l}$ and $\eta_{i,r}$ of the free surface elevation $\eta_i = H_i - D_i$. Now we can deduce the values $D_{i,l} = H_{i,l} - \eta_{i,l}$ and $D_{i,r} = H_{i,r} - \eta_{i,r}$. Letting $D_{i+\frac{1}{2}} = \min(D_{i,r}, D_{i,l})$ we compute

$$H^R_{i+\frac{1}{2}} = \max(0, H_{i,r} + D_{i,r} - D_{i+\frac{1}{2}}), \quad H^L_{i+\frac{1}{2}} = \max(0, H_{i+1,l} + D_{i+1,l} - D_{i+\frac{1}{2}}), \tag{5.45}$$

and we deduce conservative reconstructed variables

$$\mathbf{v}^L_{i+\frac{1}{2}} = \begin{pmatrix} H^L_{i+\frac{1}{2}} \\ H^L_{i+\frac{1}{2}}u_{i,r} \end{pmatrix}, \qquad \mathbf{v}^R_{i+\frac{1}{2}} = \begin{pmatrix} H^R_{i+\frac{1}{2}} \\ H^R_{i+\frac{1}{2}}u_{i+1,l} \end{pmatrix}. \tag{5.46}$$

Then the term $\mathbf{S}_i$ can be written as $\mathbf{S}_i = \mathbf{S}^L_{i+\frac{1}{2}} + \mathbf{S}^R_{i+\frac{1}{2}} + \mathbf{S}_{ci}$, where

$$\mathbf{S}^L_{i+\frac{1}{2}} = \begin{pmatrix} 0 \\ \frac{g}{2}\left[(H^L_{i+\frac{1}{2}})^2 - (H_{i,r})^2\right] \end{pmatrix}, \qquad \mathbf{S}^R_{i+\frac{1}{2}} = \begin{pmatrix} 0 \\ \frac{g}{2}\left[(H_{i,l})^2 - (H^R_{i+\frac{1}{2}})^2\right] \end{pmatrix}$$

and

$$\mathbf{S}_{ci} = \begin{pmatrix} 0 \\ g\frac{H_{i,l}+H_{i,r}}{2}(z_{i,l} - z_{i,r}) \end{pmatrix}.$$

Numerical experiments show that the resulting scheme is well-balanced even for Boussinesq system of equations.

**5.1.3.2.3 Boundary conditions** In the case of Bona-Smith type systems with flat bottom we consider herein only the initial-periodic boundary value problem which is known to be well-posed [ADM09].

In case of the modified Peregrine's system with an uneven bottom we use reflective boundary conditions. We note that for the classical Boussinesq system posed in a bounded domain $I = [b_1, b_2]$, one needs to impose boundary conditions only in one of the two dependent variables, cf. [FP05]. In the case of reflective boundary conditions it is sufficient to take $u(b_1, t) = u(b_2, t) = 0$ cf. [AD]. In [AD] it was also observed that during solitary waves reflection the derivatives $\eta_x(b_1, t) = \eta_x(b_2, t) \to 0$, while for other wave types these derivatives remained very small.

In our case we consider analogous reflective boundary conditions taking the cell averages of $u$ on the first and the last cell to be $u_0 = u_{N+1} = 0$. We don't impose explicitly boundary conditions on $H$. The reconstructed values on the first and the last cell are computed using neighboring ghost cells and taking odd and even extrapolation for $u$ and $H$ respectively. These specific boundary conditions appeared to reflect incident waves on the boundaries while conserving the mass.

## 5.1.4 Interactions of solitary waves

For the Boussinesq system (5.2) we present first results demonstrating the accuracy of the finite volume scheme. We study the propagation as well as the interaction of solitary waves. In particular we consider head-on and overtaking collisions.

### 5.1.4.1 Accuracy test, validation

We consider the initial value problem with periodic boundary conditions for the Bona-Smith systems (5.10) with known solitary wave solutions (5.11) — (5.12) to study the accuracy of the finite volume method. We fix $\theta^2 = 8/10$ in the system and an analytic solitary wave of amplitude $\eta_0 = 1/2$ is used as the exact solution in $[-50, 50]$ computed up to $T = 100$. The error is measured with respect to discrete $L^2$ and $L^\infty$ norms, namely we use:

$$E_h^2(k) = \|U^k\|_h / \|U^0\|_h, \quad \|U^k\|_h = \left( \sum_{i=1}^{N} \Delta x |U_i^k|^2 \right)^{1/2},$$
$$E_h^\infty(k) = \|U^k\|_{h,\infty} / \|U^0\|_{h,\infty}, \quad \|U^k\|_{h,\infty} = \max_{i=1,\dots,N} |U_i^k|,$$

where $U^k = \{U_i^k\}_{i=1}^N$ denotes the solution of the fully-discrete scheme at the time $t^k = k\,\Delta t$. The expected theoretical order of convergence was confirmed for all finite volume methods

(a) Average Flux

| $\Delta x$ | Rate($E_h^2$) | Rate($E_h^\infty$) |
|---|---|---|
| 0.5 | 1.910 | 1.978 |
| 0.25 | 1.910 | 1.954 |
| 0.125 | 1.923 | 1.937 |
| 0.0625 | 1.936 | 1.941 |
| 0.03125 | 1.946 | 1.948 |

(b) TVD2 MinMod

| $\Delta x$ | Rate($E_h^2$) | Rate($E_h^\infty$) |
|---|---|---|
| 0.5 | 2.042 | 2.032 |
| 0.25 | 2.033 | 2.029 |
| 0.125 | 2.026 | 2.023 |
| 0.0625 | 2.021 | 2.019 |
| 0.03125 | 2.017 | 2.016 |

**Table 5.1:** Rates of convergence.

we presented above. Two indicative cases are reported in Table 5.1 for the average flux and TVD2 implementation with MinMod limiter.

We also check the preservation of the invariant (5.6) by computing its discrete counterpart:

$$I_1^h = \sum_i \Delta x \left( \eta_i^2 + [(1+\eta_i)u_i]^2 - c\left[\frac{\eta_{i+1}-\eta_i}{\Delta x}\right]^2 - a\left[\frac{u_{i+1}-u_i}{\Delta x}\right]^2 \right), \tag{5.47}$$

as well as the discrete mass $I_0^h = \Delta x \sum_i \eta_i$. On Figure 5.1 we represent the amplitude and the invariant $I_1^h$ of the same solitary wave as above up to $T = 200$. The comparison of various methods is performed. We observe that the UNO2 reconstruction is more accurate while KT and the CF schemes show comparable performance. We note that the invariant $I_0^h = 1.932183566158$ conserved the digits shown for all numerical schemes. In this experiment we took $\Delta x = 0.1,\ \Delta t = \Delta x/2$.

#### 5.1.4.2 Head-on collisions

The head-on collision of two counter-propagating solitary waves is characterized by the change of the shape along with a small phase-shift of the waves as a consequence of the nonlinearity and the dispersion. These effects have been studied extensively before by numerical means using high order numerical methods such as finite differences, [BC98], spectral and finite element methods [ADM10, DDLMM07, PD01], Boundary Integral Equation Method [CKT09] and recently experimentally in [CGH+06]. In Figure 5.2 we present the numerical solutions of the BBM-BBM system (5.9) and the Bona-Smith system (5.10) with $\theta^2 = 9/11$ (in dimensional and unscaled variables) along with the experimental data from [CGH+06]. The spatial variable is expressed in centimeters while the time in seconds. The solutions were obtained using the CF-scheme with UNO2 and WENO3 reconstruction using $\Delta x = 0.05$ cm and $\Delta t = 0.01$ s. For this experiment we constructed solitary waves for

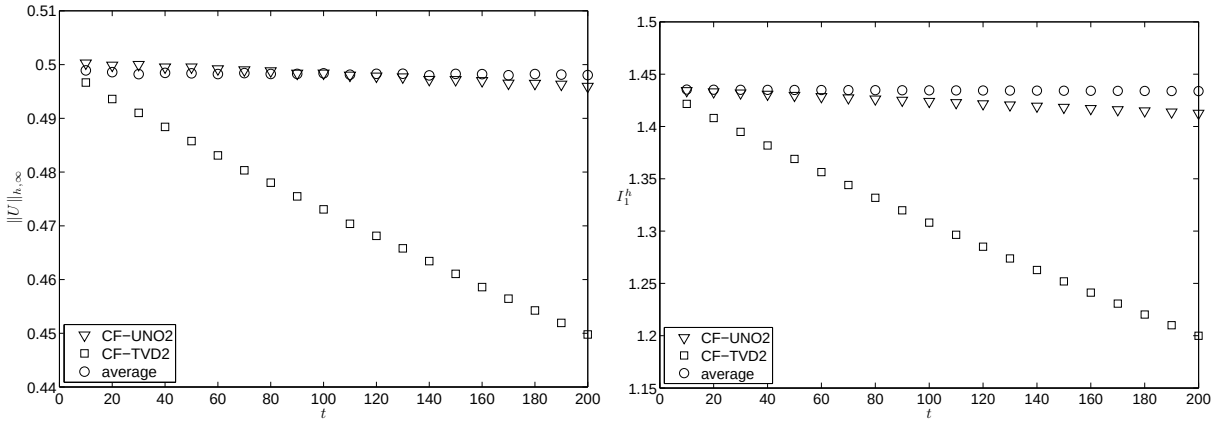


(a) Evolution of $\eta$ amplitude

(b) Evolution of $I_1^h$

**Figure 5.1:** Conservation of the solitary wave amplitude and of the invariant $I_1^h$: $G^m$ flux with Minmod limiter

Boussinesq systems by solving the respective ODEs system in the spirit of [BDM07] such that they fit to experimentally generated solitary waves before the collision. The speeds of the right and left-traveling solitary waves are $c_{r,s} = 0.854$ m/s and $c_{l,s} = 0.752$ m/s respectively.

We observe that Boussinesq models converge to the same numerical solution with all numerical schemes we tested. Generally a very good agreement with the experimental data was obtained. The maximum height predicted by the numerical solution during the collision process is slightly higher in the case of the BBM-BBM system but the difference is negligible within the specific experimental scale. Furthermore, we observe similar underestimation of the maximum amplitude of colliding waves compared to the experimental data, [CGH+06]. This discrepancy might be explained by a possible "splash" phenomenon during the collision reported also earlier by T. Maxworthy, [Max76]. After the collision we observe that the phase shift of the solitary waves is the same in both numerical and experimental data, while the shape of the experimental solitary waves were not stabilized due to interactions with other small amplitude dispersive waves. We note that after the head-on collision of the waves small amplitude dispersive tails were developed, [BC98, ADM10, DDLMM07].

The discrete mass for the Bona-Smith system is $I_0^h = 0.0059904310418$ and for the BBM-BMM system is $I_0^h = 0.0059199389479$ for all fluxes and reconstructions used. The variances in $I_1^h$ are mainly due to different types of reconstruction and not to the choice of numerical fluxes. In Table 5.2 these values are reported.

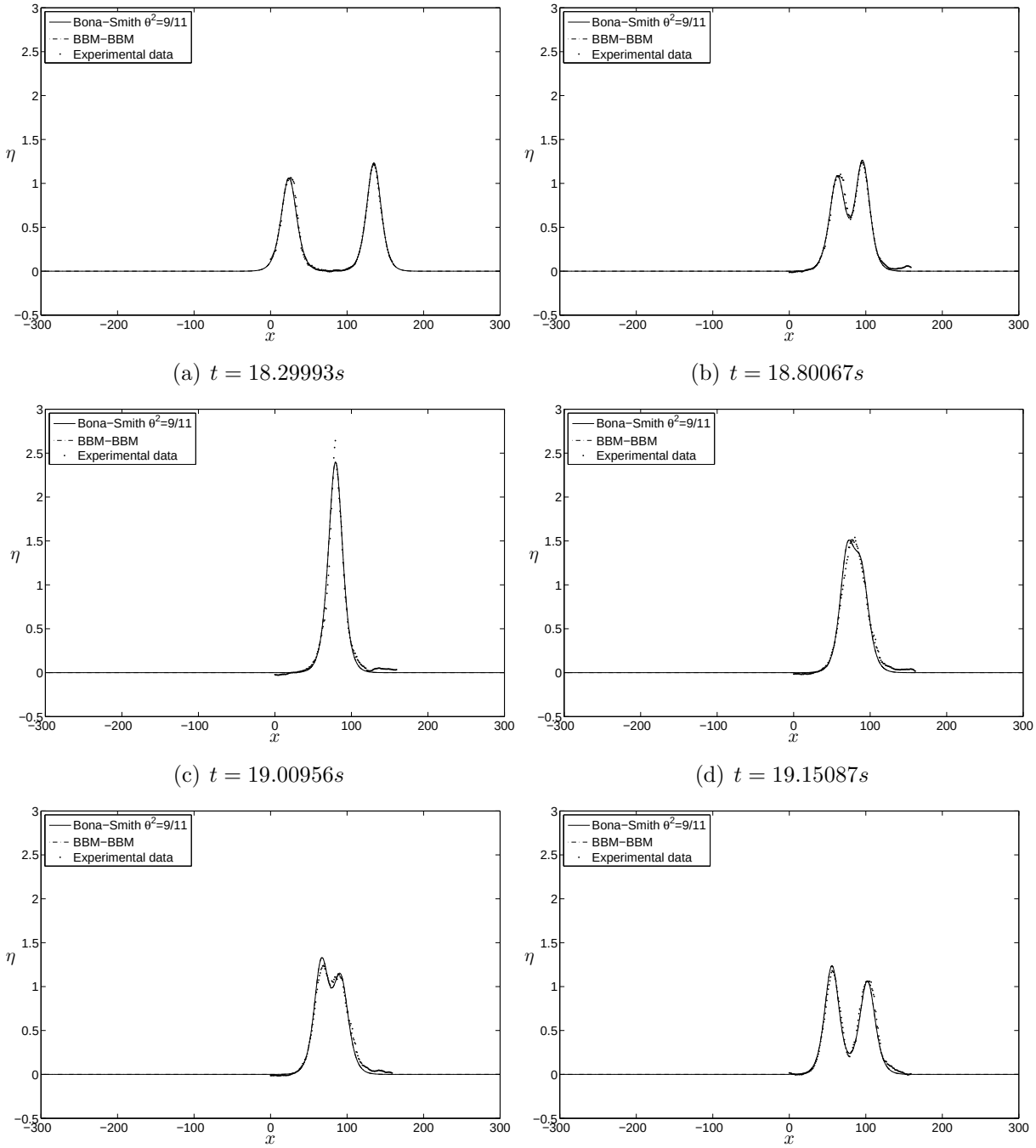


(a) $t = 18.29993s$ (b) $t = 18.80067s$

(c) $t = 19.00956s$ (d) $t = 19.15087s$

(e) $t = 19.19388s$ (f) $t = 19.32904s$

**Figure 5.2:** Head-on collision of two solitary waves: —: BBM-BBM, −−: Bona-Smith ($\theta^2 = 9/11$), •: experimental data of [CGH+06]

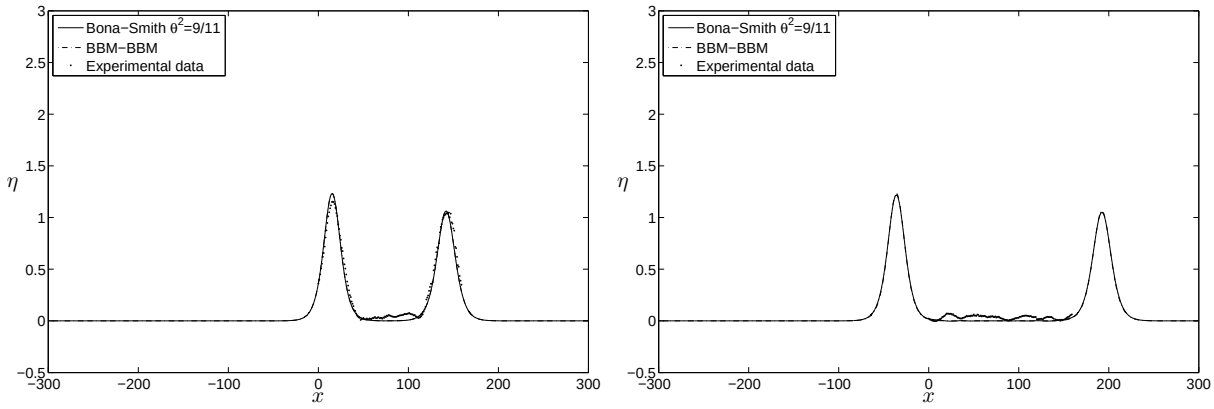


(a) $t = 19.84514s$ (b) $t = 20.49949s$

**Figure 5.2:** (Cont'd) Head-on collision of two solitary waves. —: BBM-BBM, −−: Bona-Smith ($\theta^2 = 9/11$), •: experimental data of [CGH+06]

(a) Bona-Smith

| | $I_1^h$ |
|---|---|
| m-flux | 0.000944236 |
| UNO2 | 0.00094423 |
| TVD2 | 0.00094 |
| WENO3 | 0.00094423 |

(b) BBM-BBM

| | $I_1^h$ |
|---|---|
| m-flux | 0.00092793 |
| UNO2 | 0.00092793 |
| TVD2 | 0.00092 |
| WENO3 | 0.00092793 |

**Table 5.2:** Preservation of the invariant $I_1^h$.

#### 5.1.4.3 Overtaking collisions

The overtaking collision of two solitary waves similarly to the head-on collision incorporates nonlinear and dispersive effects. Overtaking collision has been studied recently in the case of bidirectional models in [ADM10]. The interaction is similar to that of the unidirectional models but it was found that a new N-shape wavelet is generated during the interaction. This wavelet is of small amplitude and travels in the opposite direction to solitary waves and its shape depends on the Boussinesq system in use. Furthermore, as it was observed numerically and experimentally in [CGH+06], the interaction of two solitary waves during an overtaking collision is characterized by a mass exchange and not by a simple superposition of the solitary pulses. These pulses remain separate retaining two different maxima contrary to unidirectional models where they merge into a single pulse momentarily.

To study this interaction we solve numerically the Bona-Smith system (5.10) with $\theta^2 = 9/11$. Following the same process as before two solitary waves were generated numerically with speeds $c_{1,s} = 1.2$ and $c_{2,s} = 1.4$. We solved the system using all fluxes, UNO2 and WENO3 reconstructions with discretization parameters $\Delta x = 0.01$, $\Delta t = 0.005$ up to $T = 600$. During simulations we were able to observe the generation and propagation of a small N-shape wavelet. In all computations the invariants were $I_0^h = 4.6098804880$, $I_1^h = 5.116$ conserving the digits shown for all methods.

In Figure 5.3 we present the interaction of two solitary waves. Figure 5.4 shows a magnification on the generation of a small wavelet along with the generation of dispersive tails as an effect of the inelastic interaction of two waves. In Figure 5.5 we observe that the overtaking collision is accompanied by an exchange of mass between pulses while both peaks are permanently present. The situation is different for unidirectional models where two pulses merge during a few time-steps to travel as a single pulse. Up to the graphic resolution we could not see any difference in numerical solutions between UNO2 and WENO3 reconstructions.

#### 5.1.4.4 Small dispersion effect

In this section we study the small dispersion effects on solitary waves of the classical Boussinesq system. The motivation for this study is the lack of theory supporting the breaking phenomena in Boussinesq systems contrary to the KdV equation. For this reason we employed the Boussinesq system with $a = b = c = 0$, $d = 10^{-5}$ and we take the solitary wave of the Boussinesq systems (5.8) as an initial condition. In Figure 5.6 we present numerical results obtained with CF-UNO2 and CF-WENO3 schemes. In these experiments we take $\Delta x = 0.001$ and $\Delta t = \Delta x/2$. The invariant $I_0^h$ is 1.629096452537

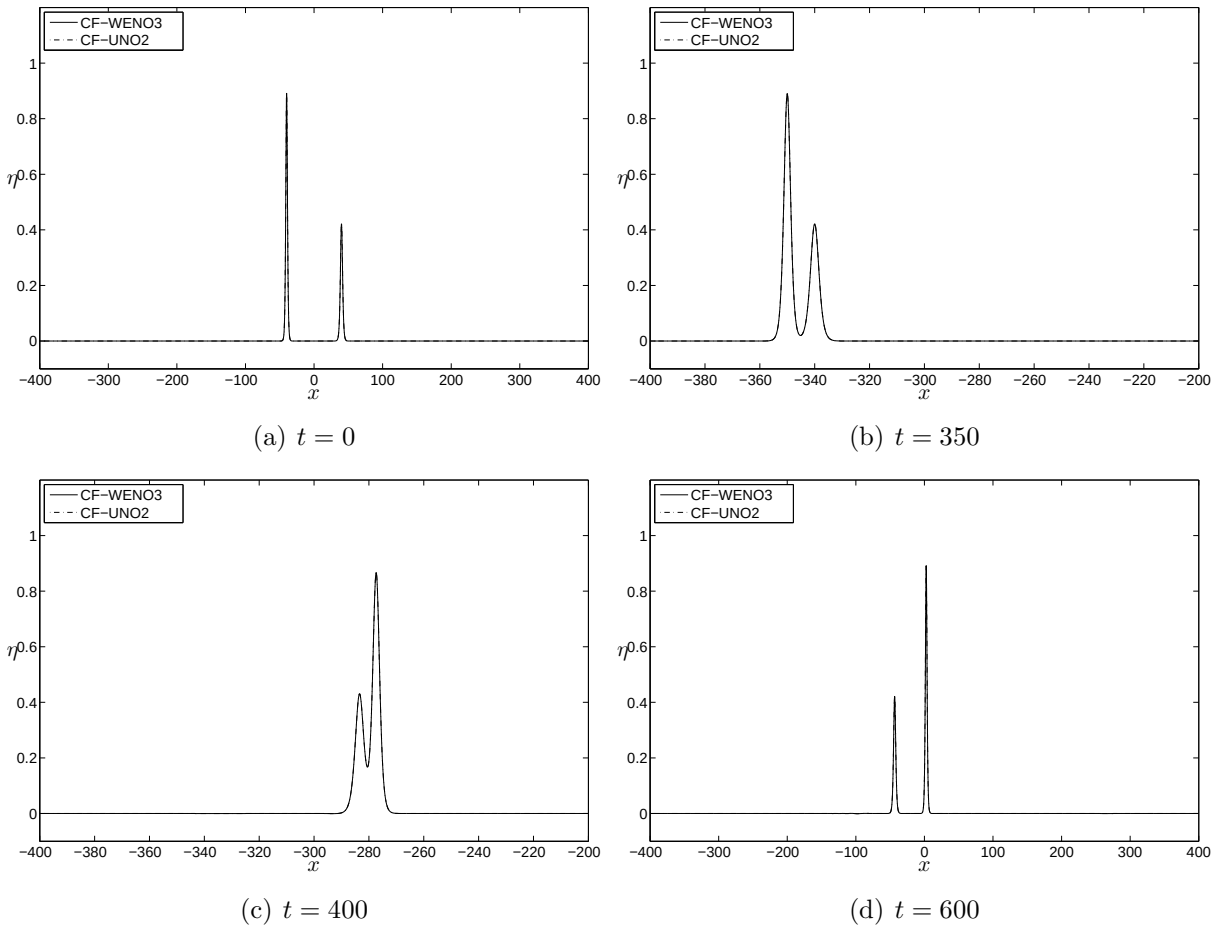


(a) $t = 0$ (b) $t = 350$

(c) $t = 400$ (d) $t = 600$

**Figure 5.3:** Overtaking collision of two solitary waves of the Bona-Smith system with $\theta^2 = 9/11$.

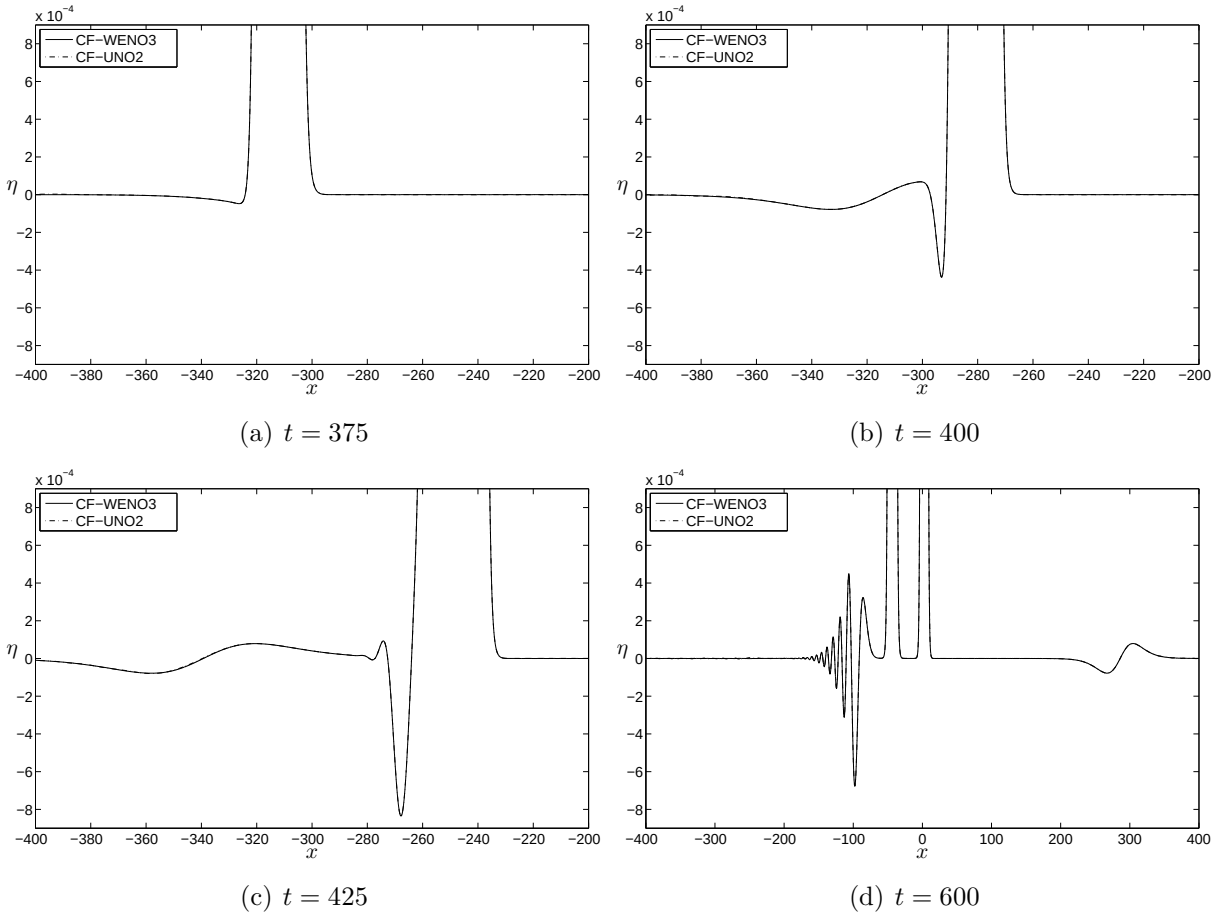


(a) $t = 375$ (b) $t = 400$

(c) $t = 425$ (d) $t = 600$

**Figure 5.4:** Generation of a wavelet during the overtaking collision of two solitary waves of the Bona-Smith system with $\theta^2 = 9/11$.

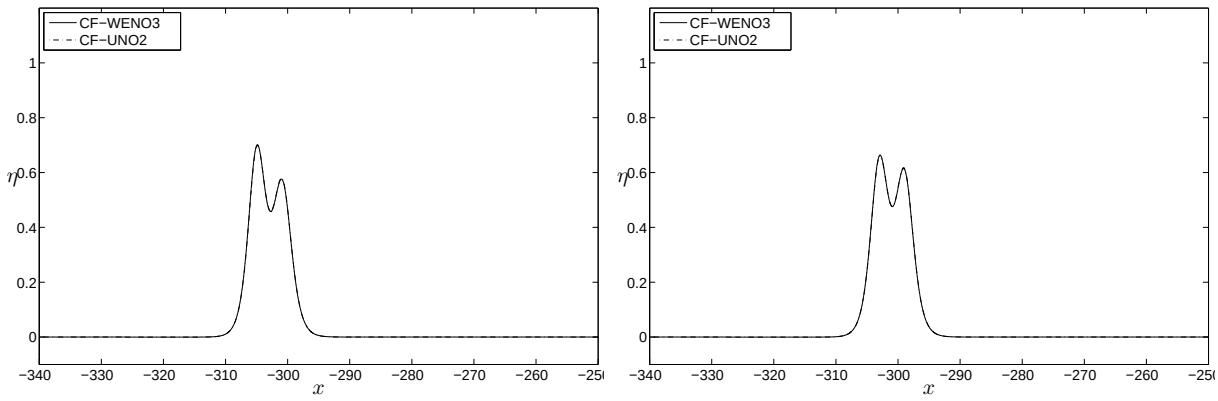


(a) $t = 382.5$ (b) $t = 384$

(c) $t = 385$ (d) $t = 386$

**Figure 5.5:** Overtaking collision of two solitary waves of the Bona-Smith system with $\theta^2 = 9/11$: mass exchange process.

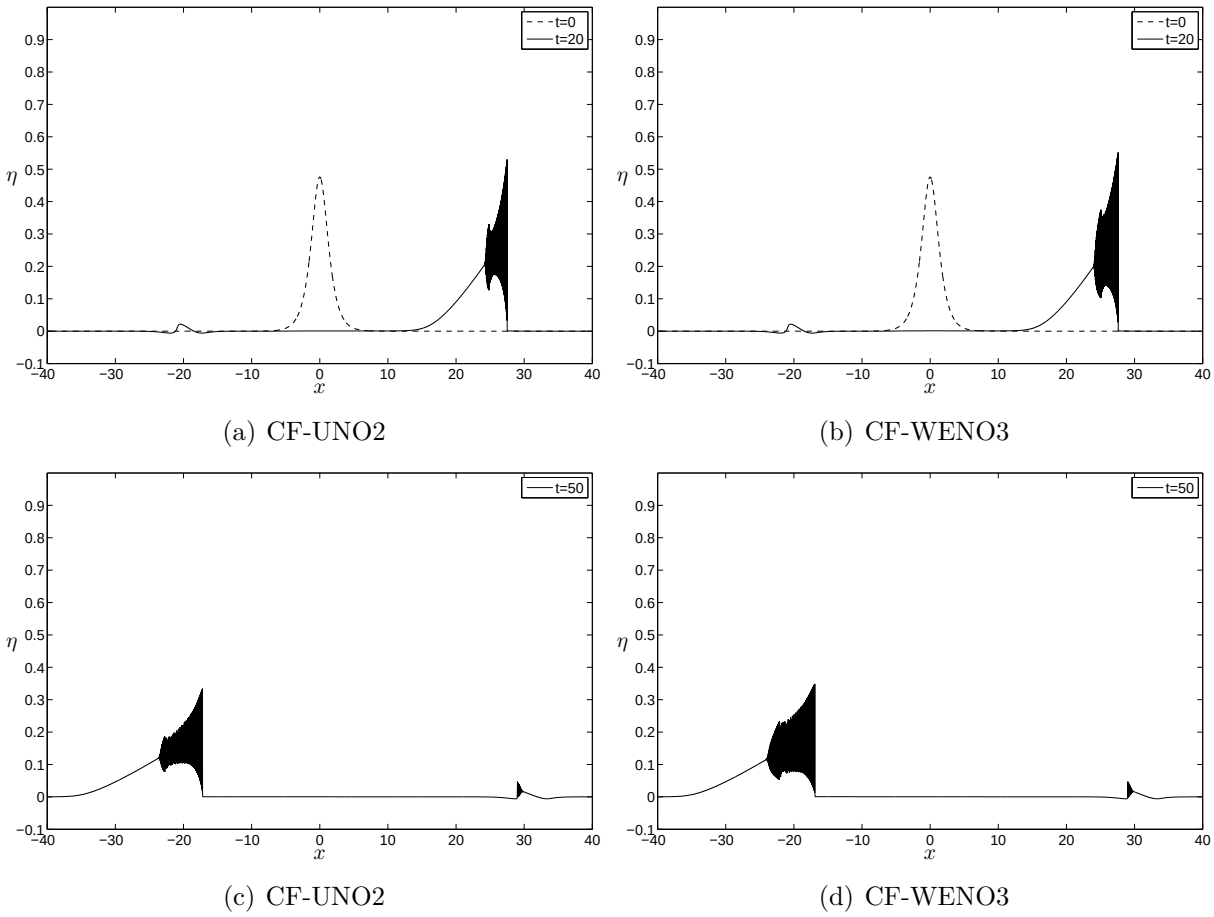


(a) CF-UNO2 (b) CF-WENO3

(c) CF-UNO2 (d) CF-WENO3

**Figure 5.6:** Small dispersion effect onto classical Boussinesq equations solutions.

preserving the digits shown during all simulations. The invariant $I_1^h$ is not preserved by this model since the coefficient $b$ is not equal to $d$. The oscillations generated in the case of the WENO3 reconstruction were larger compared to those generated by the UNO2 reconstruction. Moreover, a new W-shaped wavelet is generated traveling to the left. This small wavelet finishes by producing a secondary breaking very similar to that of the initial solitary wave.

### 5.1.5 Boussinesq system with variable bottom: runup of long waves

Nonlinear Shallow Water Equations are routinely used to predict a tsunami wave runup and, subsequently, constitute inundation maps for tsunami hazard areas. One of the main questions we address in this study is whether the inclusion of dispersive effects is beneficial for the description of the wave/beach interaction. In this section we perform a comparison of numerical solutions to Boussinesq equations (5.18), Nonlinear Shallow Water Equations

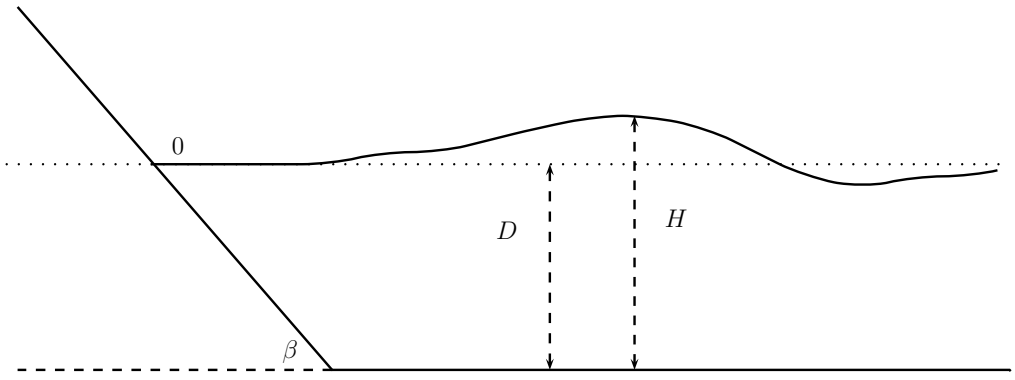


**Figure 5.7:** Sketch of the problem setup.

(NSWE) (5.1) (solved by the same numerical method) and experimental measurements made by C.E. Synolakis [Syn87] and J.A. Zelt [Zel91]. In these experiments we consider a bottom of the form

$$-D(x) = \begin{cases} -x \tan\beta, & x \le \cot\beta, \\ -1, & x > \cot\beta, \end{cases}$$

schematically depicted in Figure 5.7.

In all experiments over a flat bottom, $D(x) = D_0$, we use an approximate solitary wave solution of the following form:

$$\eta_0(x) = A_s sech^2\left(\lambda(x - X_0)\right), \quad \lambda = \sqrt{\frac{3A_s}{4(1+A_s)}},$$
$$u_0(x) = -c_s \frac{\eta_0(x)}{D_0 + \eta_0(x)}, \quad c_s = g\frac{\sqrt{6}(1+A_s)}{\sqrt{3+2A_s}} \cdot \frac{(1+A_s)\log(1+A_s) - A_s}{A_s},$$

where $A_s$ denotes the amplitude, $c_s$ is the correct speed of the solitary wave propagation for classical Boussinesq equations and $\lambda$ is the wavelength of the KdV soliton.

The first three experiments we tested are described in [Syn87] and deal with the runup of solitary waves on a beach with a mild slope of $1 : 19.85$. The first is a non-breaking solitary wave with dimensionless and scaled amplitude $A_s/D_0 = 0.0185$, the second one is a nearly breaking solitary wave with $A_s/D_0 = 0.04$, while the third experimental setup is a breaking solitary wave with $A_s/D_0 = 0.28$.

System (5.18) has some advantages over other asymptotically equivalent models with variable bottom. Namely, coupled with our robust discretization procedure, it shows excellent stability properties even for nearly breaking waves on the shore. However, for the simulation of strong breaking events, it is beneficial to include some friction or dissipative terms taking into account turbulence generation.

We also considered two experiments from [Zel91] concerning the runup of solitary waves on a beach with steep slope $1 : 2.74$. These experiments shed some light on the differences between dispersive and non-dispersive models.

Finally we consider a non-uniform sloping beach that contains a small lake demonstrating the capability of the modified Peregrine's system to handle simultaneously and correctly dispersive effects in two basins with different mean sea levels.

In the sequel $t$ denotes the dimensionless time scaled by the quantity $\sqrt{g/D_0}$. Furthermore, we denote by $R$ the height of the last dry cell at a specific time instance. In our computations a cell is considered as dry if the total water depth $H_i$ inside is less than $5 \cdot 10^{-14}$. The quantity $R$ will also be referred to as *runup*. The maximum runup will be denoted by $R_\infty$. In all experiments the discretization parameters were taken to be equal $\Delta x = 0.05$, $\Delta t = \Delta x/10$, unless otherwise mentioned. Further, we compute in all cases the discrete mass $I_0^h$ and show the preserved digits. We use the KT and CF schemes combined with the TVD2 and UNO2 reconstructions. The CF-scheme appeared to be less dissipative and we emphasize the results of this method.

#### 5.1.5.1 Runup of a solitary wave on a gradual slope $\beta = 2.88°$ with $A_s/D_0 = 0.0185$

We consider first the simplest case — the runup of a non-breaking solitary wave. In this experiment we take an initial solitary wave with the amplitude $A_s = 0.0185$, $D_0 = 1$ and $X_0 = 19.85$ in $I = [-10, 70]$ and a mildly sloping beach $1 : 19.85$. This specific solitary wave does not break [Syn87] and the solution remains smooth during the runup and the rundown processes. In Figure 5.8 we show several profiles of numerical solutions to Boussinesq and Nonlinear Shallow Water Equations along with the experimental data of [Syn87]. We observe that both models converge to the same solution. The runup as well as the rundown in this experiment is predicted very well. The runup value $R$ for both models is almost the same. The maximum runup is $R_\infty \approx 0.085$ for the Boussinesq system, while for NSWE is $R_\infty \approx 0.088$. The experimental value reported in [Syn87] is equal to $R_\infty \approx 0.078$. In Figure 5.9 the runup $R$ as a function of time is represented. The discrete mass is preserved $I_0^h = 60.3667671231$ conserving the digits shown for both models.

#### 5.1.5.2 Runup of a solitary wave on a gradual slope $\beta = 2.88°$ with $A_s/D_0 = 0.04$

We consider the same sloping beach as before. We study the runup of a solitary wave with amplitude $A_s = 0.04$, placed initially at $X_0 = 19.85$ in $I = [-10, 70]$. The solitary wave does not break during the runup phase. Breaking occurs during the rundown process as in experimental observations [Syn87]. Results of the numerical simulations are presented in Figure 5.10. In Figure 5.11 the evolution of the runup value is shown. The maximum

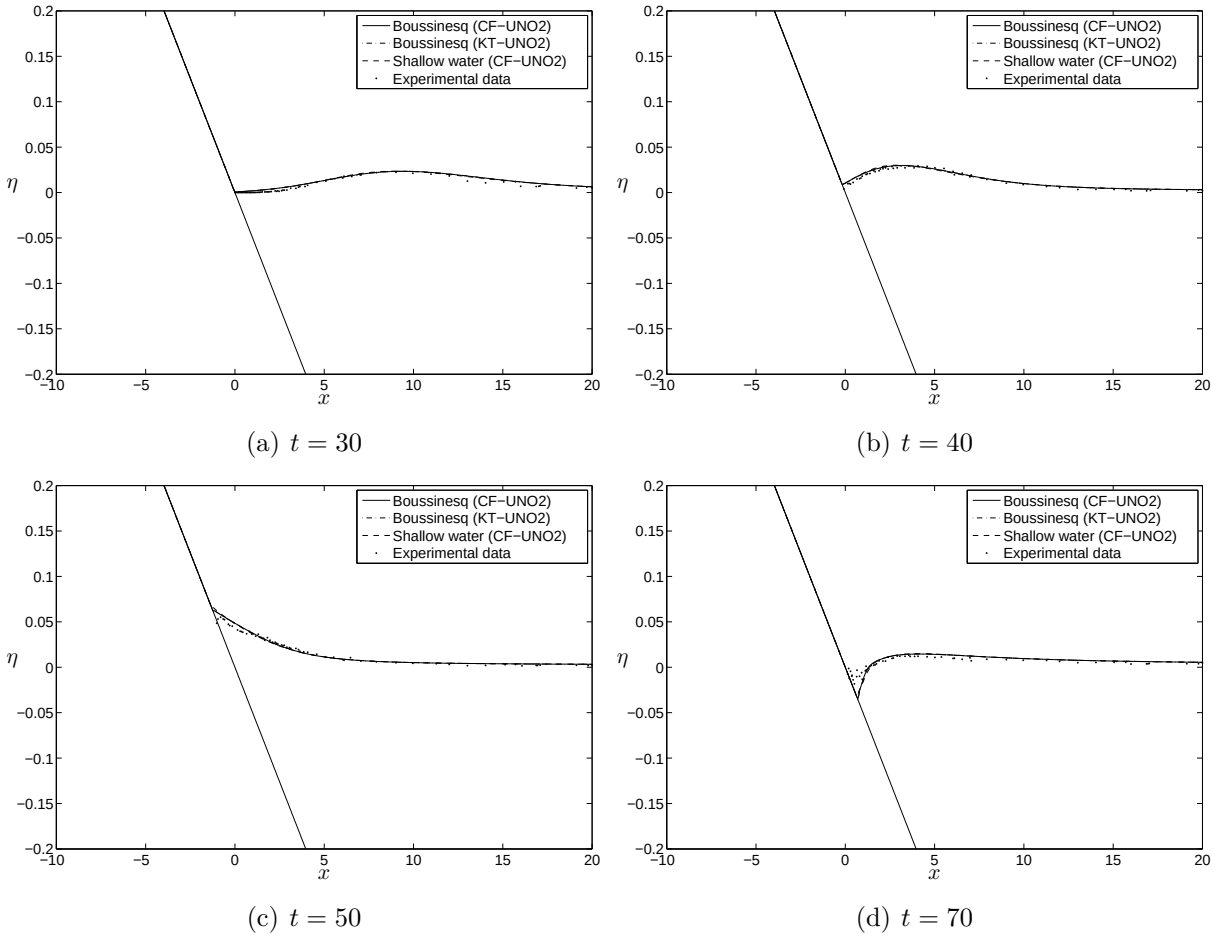


(a) $t = 30$ (b) $t = 40$

(c) $t = 50$ (d) $t = 70$

**Figure 5.8:** Solitary wave runup on a sloping beach: $A_s = 0.0185$ case.

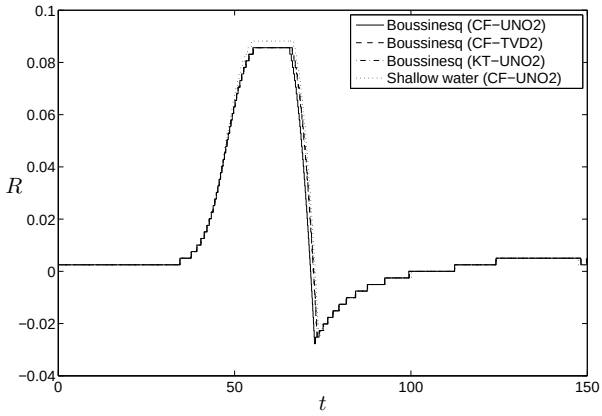


**Figure 5.9:** Runup value $R$ as a function of time: $A_s = 0.0185$ case.

runup for the Boussinesq system is $R_\infty \approx 0.20$ and $R_\infty \approx 0.21$ for NSWE. The experimental value reported in [Syn87] is $R_\infty \approx 0.156$.

In Figure 5.12 we perform a comparison with tide gauge data (free surface elevation measured in [Syn87]) collected at 32.1 m from the still shoreline position. We observe again a good agreement between the dispersive and nondispersive models. The discrete mass is preserved, $I_0^h = 60.5210181987$ conserving the digits shown.

#### 5.1.5.3 Runup of a solitary wave on a gradual slope $\beta = 2.88°$ with $A_s/D_0 = 0.28$

Finally we present the stiffest case of a solitary wave with amplitude $A_s = 0.28$, placed initially at $X_0 = 19.85$ in $I = [-10, 60]$. This specific initial condition is characterized by the wave breaking phenomenon before even reaching the shoreline. Strictly speaking, in this case Boussinesq model is not valid unless a wave breaking mechanism is considered, cf. [Zel91].

In order to ensure the stability of the simulation and to study the runup, instead of smoothing, filtering or adding extra dissipative terms, we simply excluded the contribution of the term $Q_{xxt}$ in the vicinity of the shoreline (where $D_i < 0.3$). Wave transition between these two regions appeared to be smooth as one may witness on Figure 5.13. After this slight modification, the algorithm became more robust for large amplitude breaking waves without creating any unphysical oscillations.

In this experiment the friction appeared to play a significant role during the runup process, contrary to previous cases. The maximum runup computed without taking into account the friction of the bottom was far away from the experimentally measured values. For this reason, and only in this specific test case we included the empirical friction term (5.19) into the momentum conservation equation (5.18), with coefficient $c_m = 2 \cdot 10^{-4}$. The friction term is discretized according to formula (5.33). This discretization preserves the positivity of all numerical schemes we tested. Mass conservation in this experiment was perfect $I_0^h = 51.7504637472$ preserving the digits shown.

In Figure 5.13 we show the propagation of a breaking wave including its runup and rundown. We observe a significant difference between NSWE and the dispersive model during the wave propagation. Discrepancies are present in the amplitude and in the phase speed simultaneously. However the dispersive model solution approximates better the measurements of J.A. Zelt [Zel91]. Nevertheless, we have to underline that the runup and rundown are fairly well described by both models. The maximum runup value according to the dispersive and nondispersive models is $R_\infty \approx 0.47$ which is in the range of $[0.42, 0.53]$ of the theoretical prediction of C.E. Synolakis, [Syn87]. There is no single experimental value reported for the maximum runup in [Syn87] due to practical difficulties in generating a solitary wave of so big amplitude. Finally, we mention that the specific technique

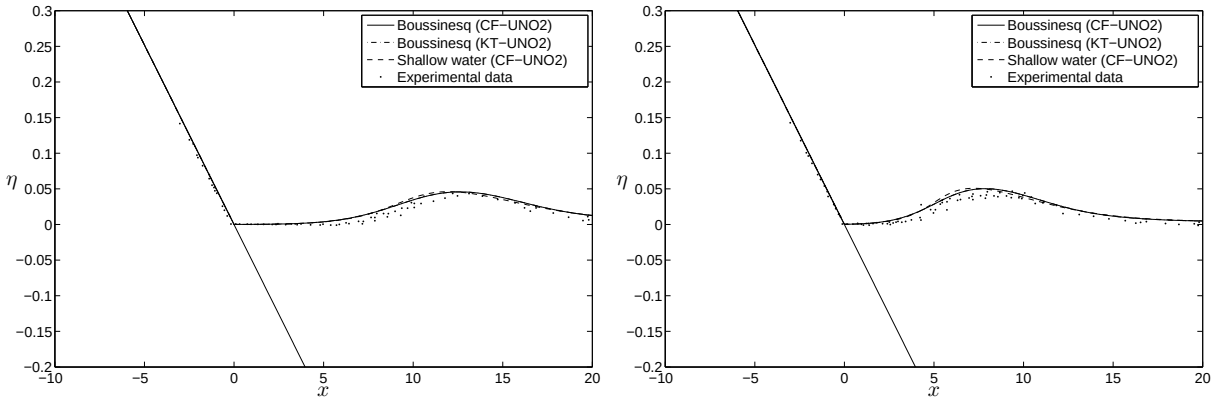


(a) $t = 20$ (b) $t = 26$

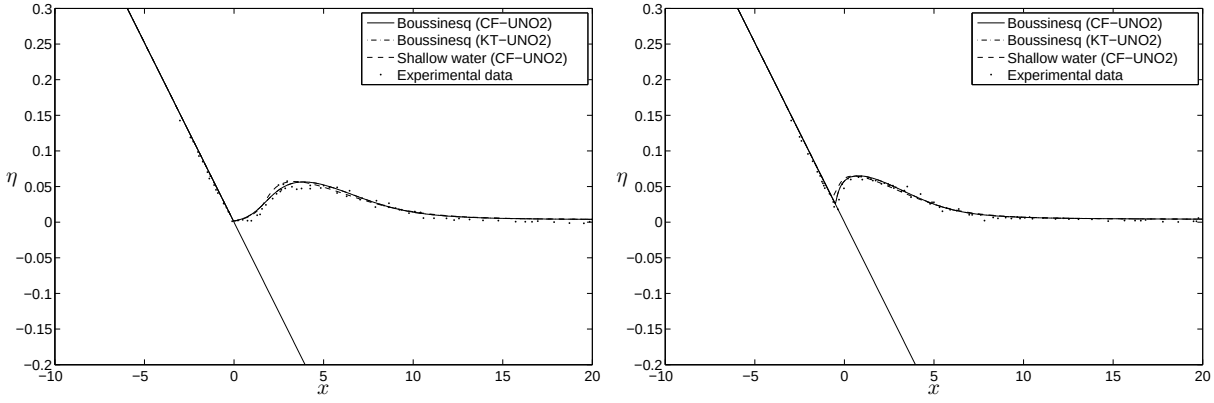


(c) $t = 32$ (d) $t = 38$

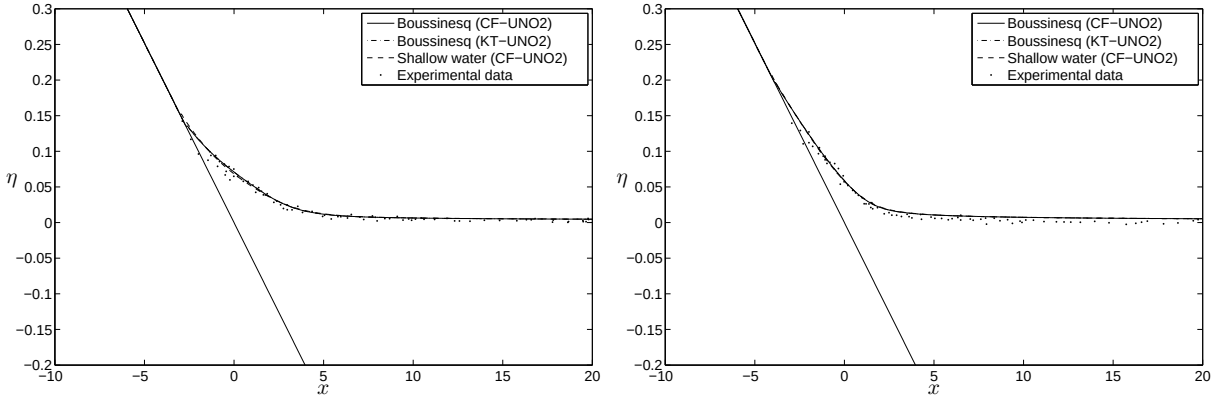


(e) $t = 44$ (f) $t = 50$

**Figure 5.10:** Solitary wave runup on a sloping beach: $A_s = 0.04$ case.

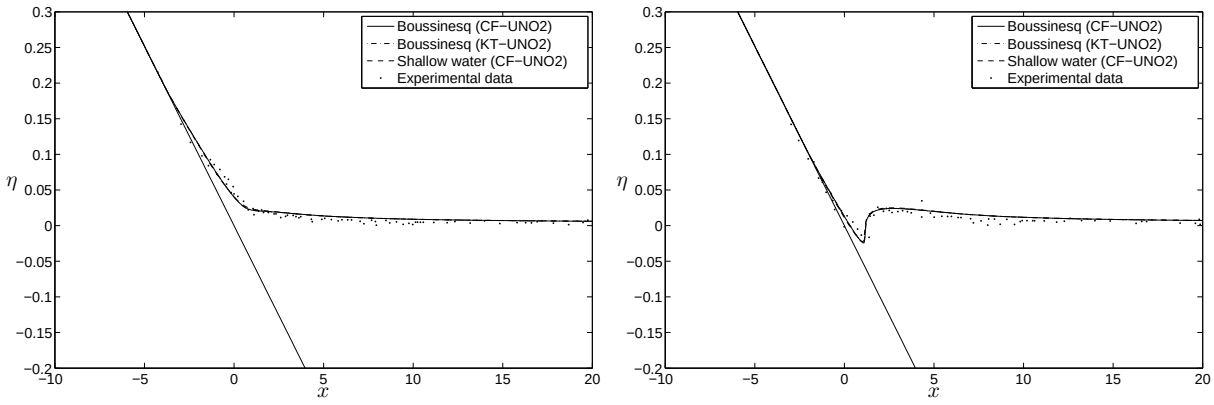


(a) $t = 56$ (b) $t = 62$

**Figure 5.10:** (Cont'd) Solitary wave runup on a sloping beach: $A_s = 0.04$ case.

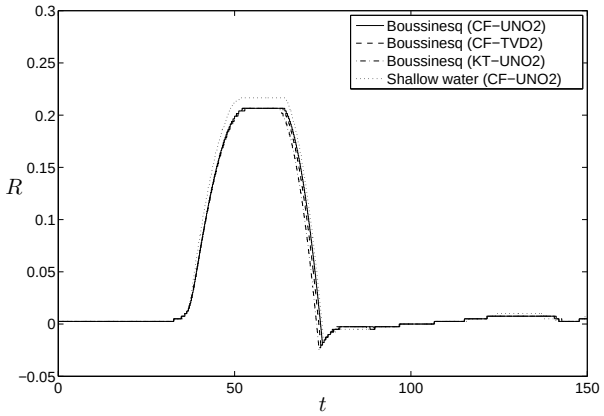


**Figure 5.11:** Runup value $R$ as a function of time: $A_s = 0.04$ case.

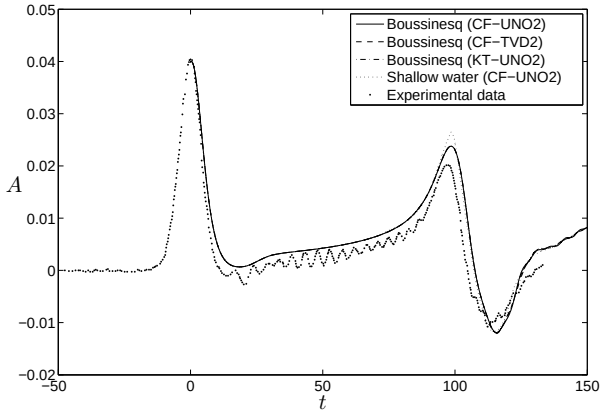


**Figure 5.12:** Free surface elevation measured at $x = 32.1$ m.

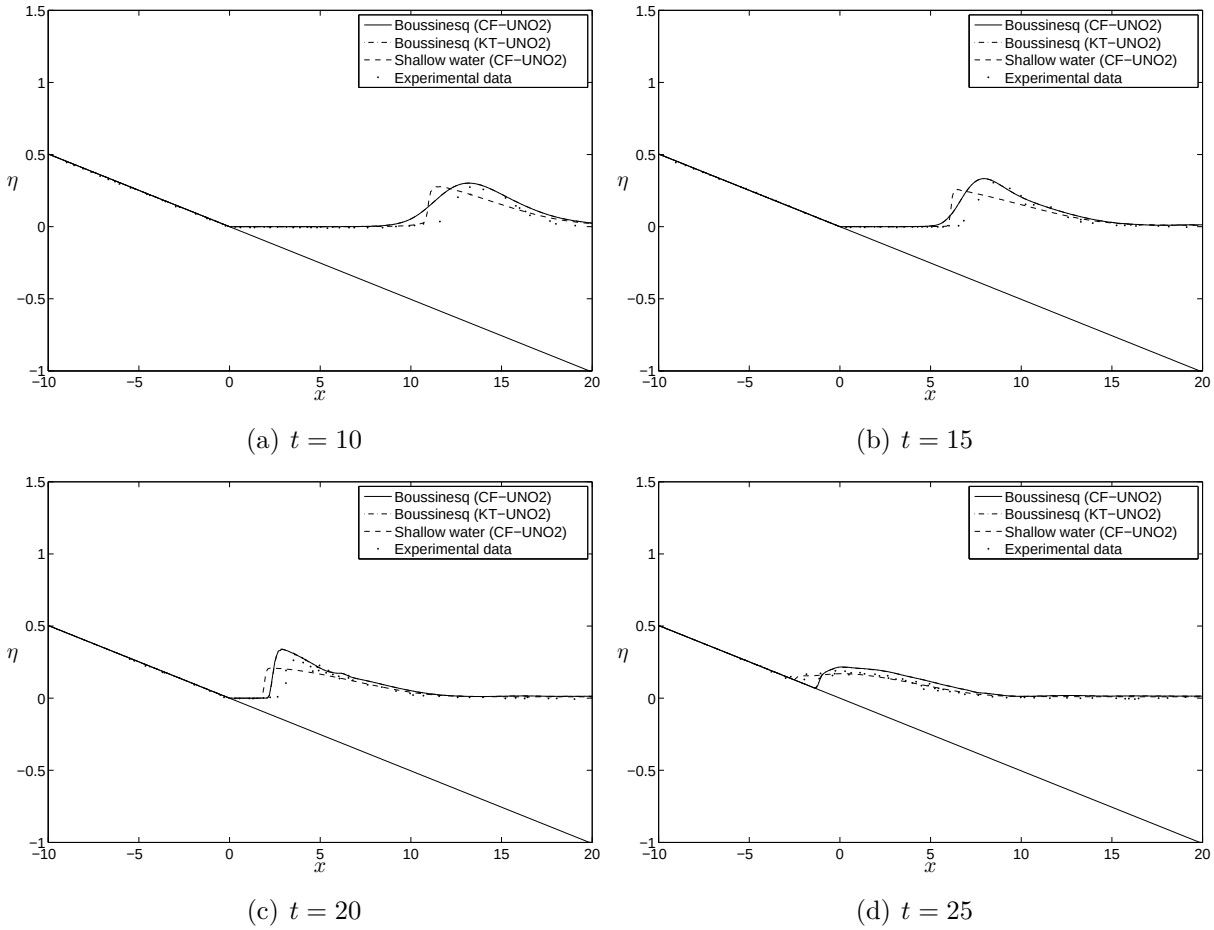


(a) $t = 10$ (b) $t = 15$

(c) $t = 20$ (d) $t = 25$

**Figure 5.13:** Solitary wave runup on a sloping beach: $A_s = 0.28$ case.

of C.E. Synolakis for handling the breaking wave leads to more accurate results for the rundown process than one presented in [Zel91].

#### 5.1.5.4 Solitary wave runup on a steep slope $\beta = 20°$

Now we present two experiments pointing out some further differences in solutions to dispersive and nondispersive models. These experiments were performed by J.A. Zelt, [Zel91] and consist also in the runup on a steep slope of a solitary wave with an average amplitude. We will consider here two waves with amplitudes $A_s = 0.12$ and $A_s = 0.2$ initially located at $X_0 = 8.85$ and $X_0 = 10.62$ respectively, in the total computational domain $I = [-10, 30]$. These waves propagate onto a steep sloping beach $1 : 2.74$. A very fine grid of $\Delta x = 0.01,\ \Delta t = \Delta x/100$ is used to guarantee the accuracy and stability of simulations.

As it was observed in [Zel91] both waves do not break during the runup but the second

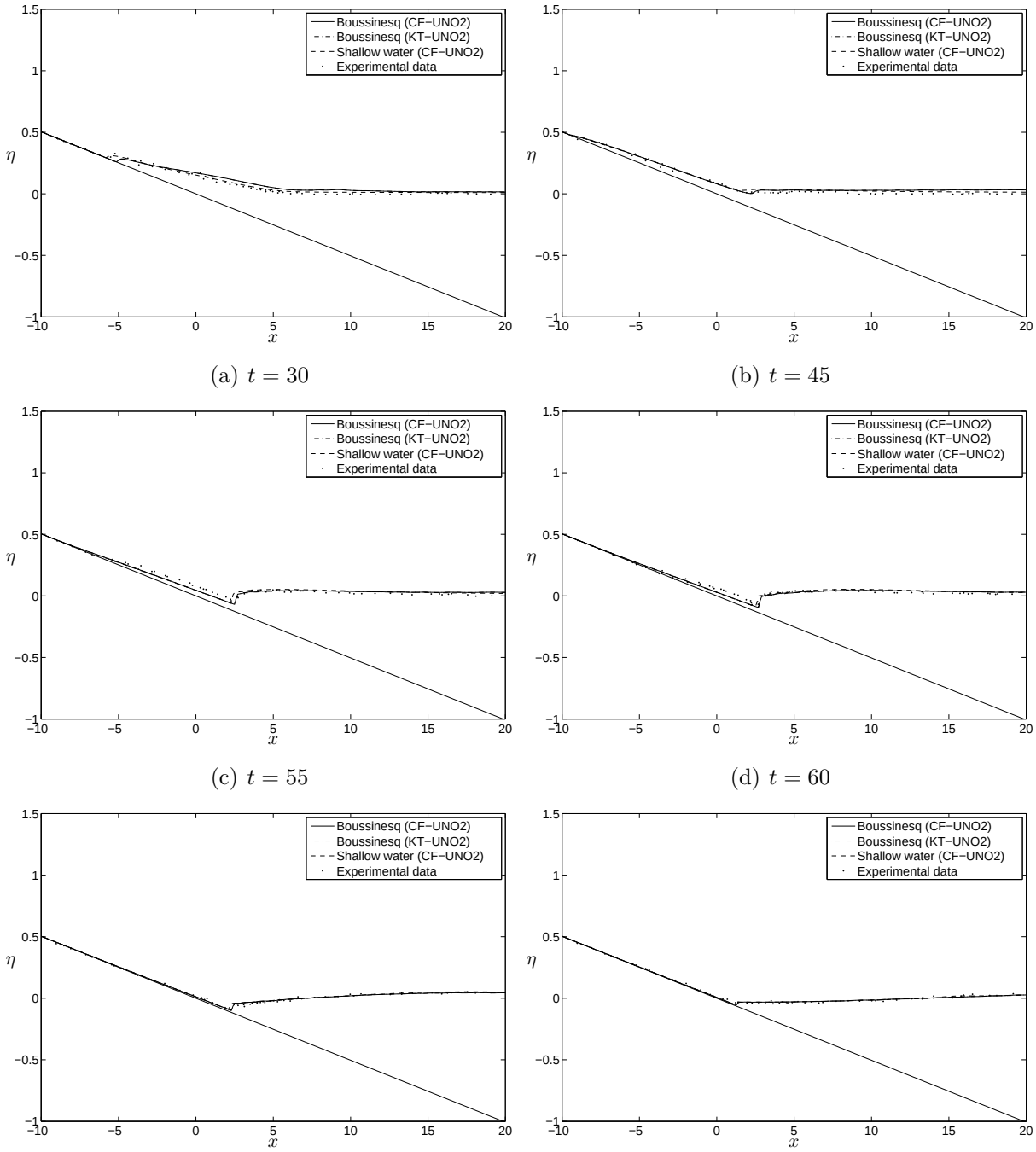


(a) $t = 30$ (b) $t = 45$

(c) $t = 55$ (d) $t = 60$

(e) $t = 70$ (f) $t = 80$

**Figure 5.13:** (Cont'd) Solitary wave runup on a sloping beach: $A_s = 0.28$ case.

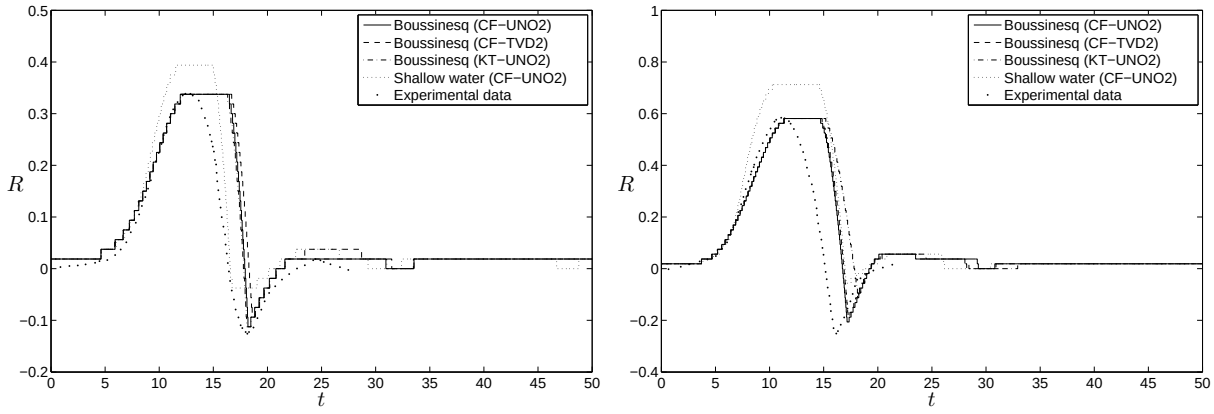


(a) $A_s = 0.12$ (b) $A_s = 0.2$

**Figure 5.14:** Runup value $R$ as a function of time.

one generates a strong breaking event during the rundown. The friction effects do not play any important role in these experiments. Consequently, no friction term is included into the models.

Figure 5.14 shows the runup value $R$ as a function of time. We observe that for both models there is a phase lag compared to the experimental data. We believe that this discrepancy can be removed by changing the definition of the last dry cell. We also observe that NSWE over-predict the maximum runup and the minimum rundown while the Boussinesq model predicts correctly the extrema in both cases.

Figure 5.15 shows the rundown of the solitary wave of amplitude $A_s = 0.2$ during the breaking event. One may observe that the experimental data consist of two curves due to the difficulty in measuring the surface elevation of the breaking wave due to 3D effects which become important. On Figure 5.16 the free surface elevation tide gauge data is presented. The gauge is located 8.85 meters away from the still shoreline position. The reflected wave appears in both cases to be highly dispersive thus, the Boussinesq model provides a much better approximation. In the case $A_s = 0.2$, the mass remained equal to $I_0^h = 29.770808175$, while in the case case $A_s = 0.12$ then $I_0^h = 29.4861671693$ conserving the digits shown.

#### 5.1.5.5 Solitary wave runup on a gradual slope $\beta = 2.88°$ with a pond

We repeat the experiment of Section 5.1.5.2 in $I = [-10, 50]$ with solitary wave amplitude equal to $A_s = 0.04$. However, we modify the bottom by adding a small pond over the shoreline described by the exponential function $0.1\, e^{-(x+4)^2}$. The Boussinesq system preserves the correct dispersion characteristics for the waves reaching the pond. In Figure

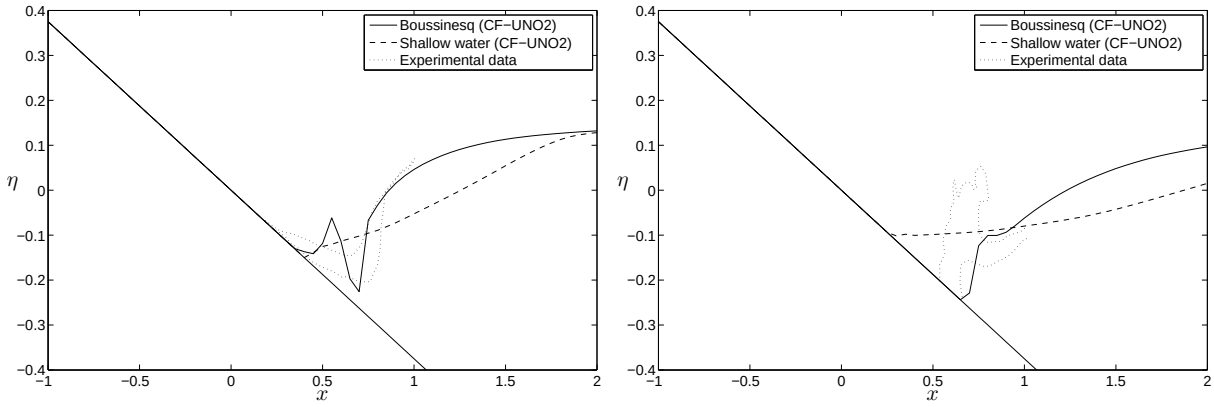


(a) $t = 15.71$ (b) $t = 16.62$

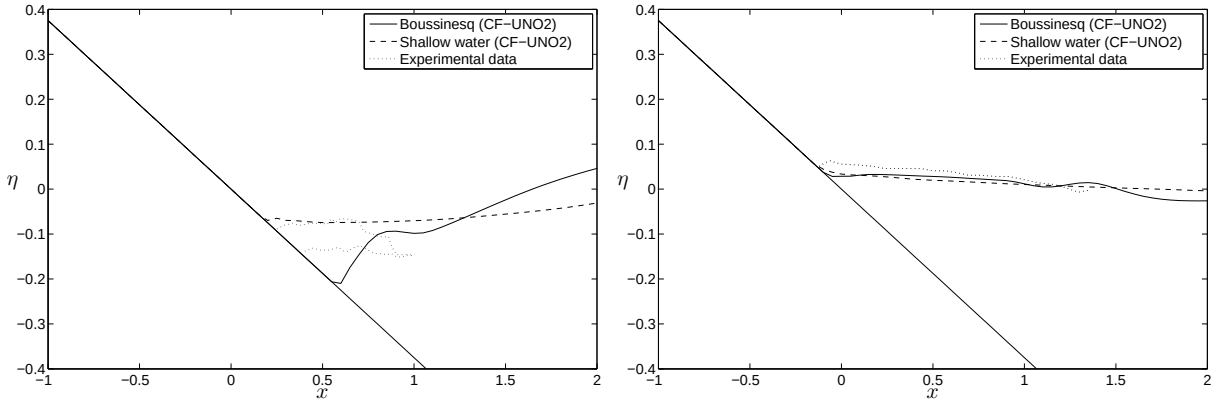


(c) $t = 17.32$ (d) $t = 22.29$

**Figure 5.15:** Rundown of the wave with amplitude $A_s = 0.2$.

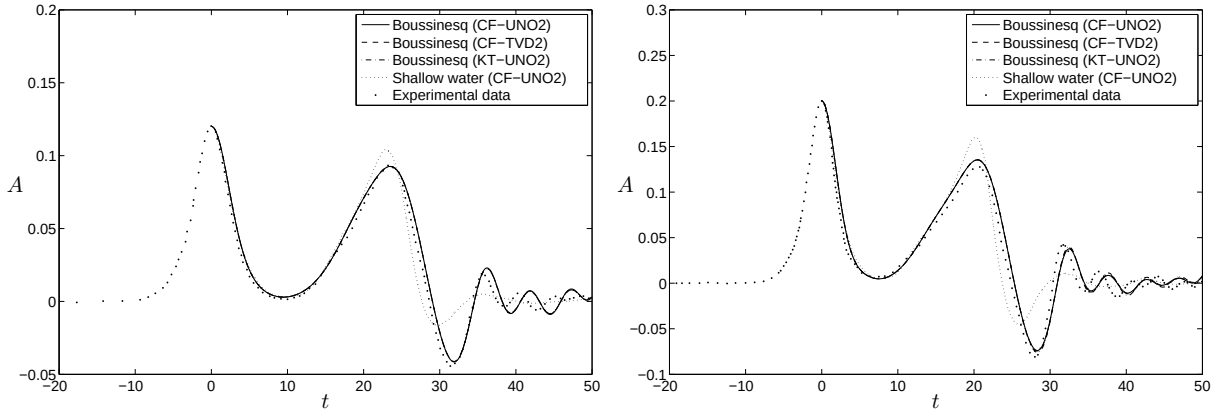


(a) $A_s = 0.12$ (b) $A_s = 0.2$

**Figure 5.16:** The amplitude at the wave gauge $A$.

5.17 we present the overall process. It is worth noting that after the pond was filed a breaking wave was reflected back. As the wave slides down, a small hydraulic jump appears. In the case of NSWE this jump propagates as a shock wave due to hyperbolic character of equations. On the other hand, the Boussinesq system develops it into an Airy type wave according to its dispersive characteristics. In Figure 5.18 we show the solution at two wave gauges located at $x = -3.4$ and $x = 8$ for both the dispersive and nondispersive models. The mass during the simulations is constantly equal to $I_0^h = 40.5198087147$.

### 5.1.6 Conclusions

Initially, the finite volume method was proposed by S. Godunov [God99] to find approximate solutions to hyperbolic conservation laws. In the present study we made a further attempt to generalize this method to the framework of dispersive PDEs. This type of equations arises naturally in many physical problems. In the water wave theory dispersive equations have been well known since pioneering works of J. Boussinesq [Bou71a] and Korteweg-de Vries [KdV95]. Currently, the so-called Boussinesq-type models become more and more popular as an operational model for coastal hydrodynamics and other fields of engineering.

Most often Boussinesq equations are solved with some finite difference schemes. Meanwhile, the finite volume method has conquered the "hyperbolic" community. Currently, Nonlinear Shallow Water Equations (NSWE) are routinely discretized with robust, efficient, higher order, shock-capturing schemes [DK03, DKK08, DPD10]. Since Boussinesq equations can be viewed mathematically as a dispersive perturbation to NSWE, it is tempting to apply the finite volume method to discretize them.

We tested several choices of numerical fluxes (average, Kurganov-Tadmor, characteristic fluxes), various reconstruction methods ranging from classical (TVD2, UNO2) to modern approaches (WENO3, WENO5). Various choices of limiters have been also tested out. Advantages of specific methods are discussed and some recommendations are outlined.

For operational modeling of the wave runup we derived a modification of Peregrine's system [Per67] which has some advantages over its classical counterpart. The new system together with proposed novel discretization procedure are validated by extensive comparisons with experimental data of C.E. Synolakis [Syn87] and J.A. Zelt [Zel91].

We paid a special attention to the comparison of dispersive (Boussinesq) and nondispersive (NSWE) models. Nowadays NSWE have become the model of choice for operational tsunami modeling including the inundation zone estimation [TG97, SBT+08]. The question of dispersive effects importance arises recurrently in the tsunami wave modeling community [KML05, DT07]. Our results show that NSWE are sufficient to predict maximum runup

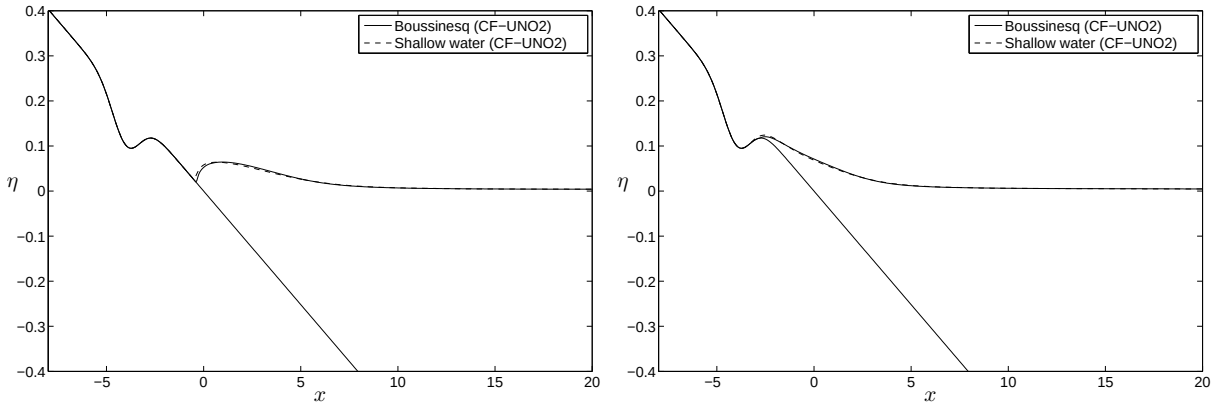


(a) $t = 37.58$




(b) $t = 48.31$

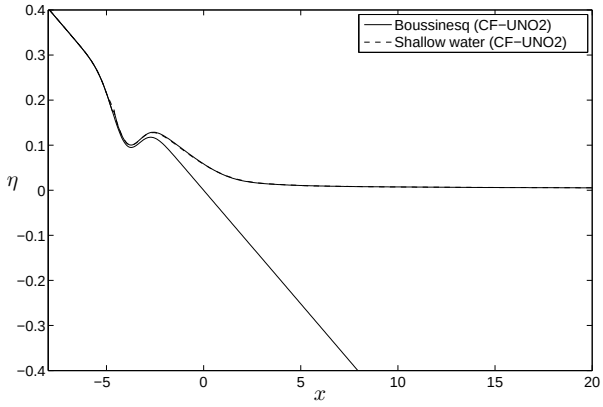


(c) $t = 55.22$

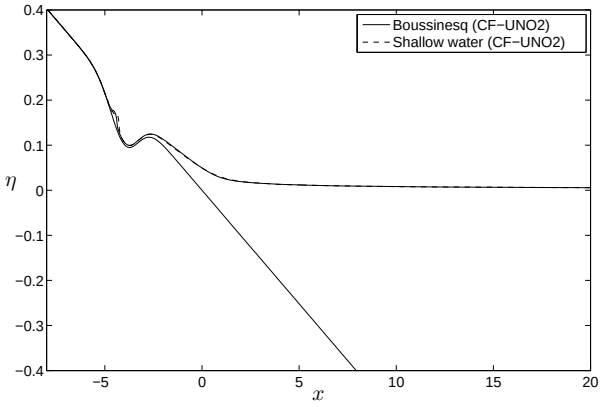


(d) $t = 58.67$

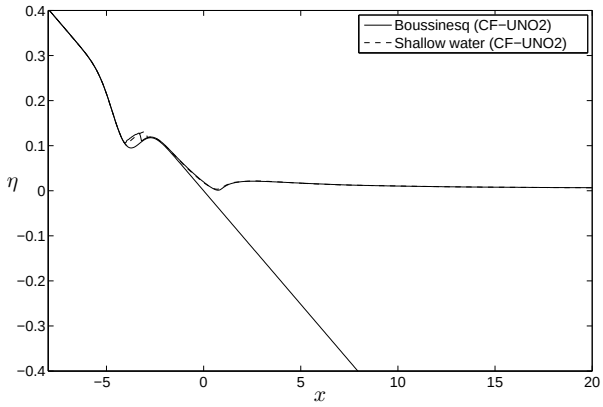


(e) $t = 65.57$

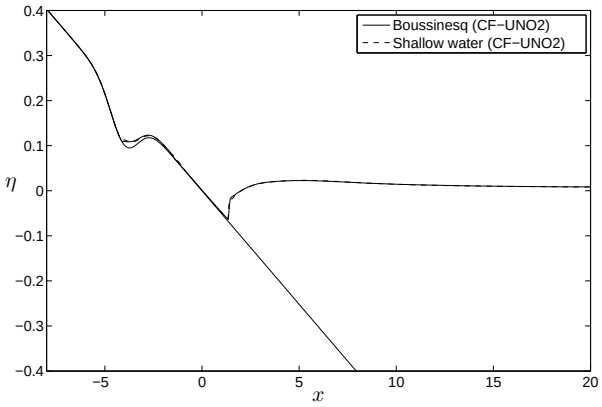


(f) $t = 72.47$

**Figure 5.17:** Long wave runup on a beach with a pond.

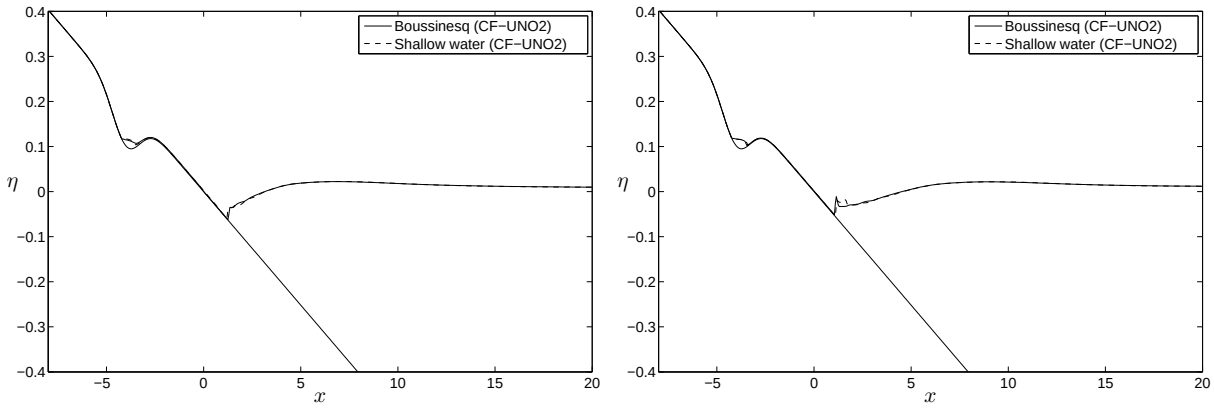


(a) $t = 75.93$ (b) $t = 79.38$

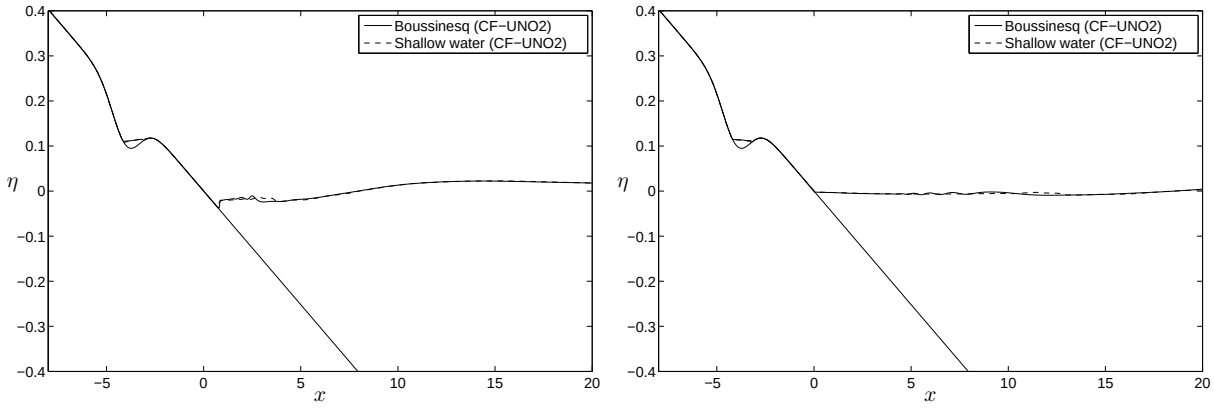


(c) $t = 86.28$ (d) $t = 103.54$

**Figure 5.17:** (Cont'd): Long wave runup on a beach with a pond.

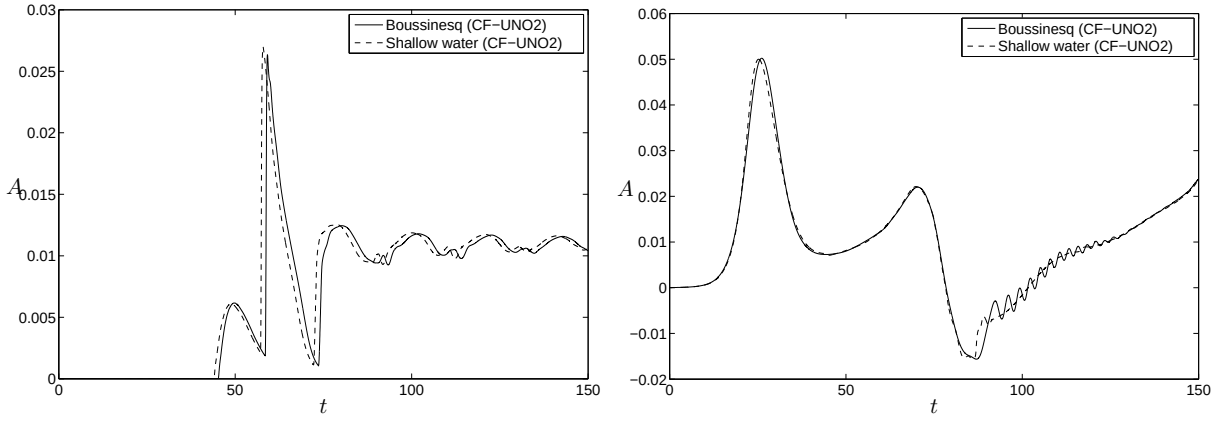


(a) Wave gauge at $x = -3.4$ (b) Wave gauge at $x = 8$

**Figure 5.18:** Evolution of the free surface elevation at two wave gauges.

values. However, the dispersive effects can be beneficial for more accurate description of long wave propagation, runup and rundown.

## 5.2 On the relevance of the dam break problem in the context of nonlinear shallow water equations

*In mathematics you don't understand things. You just get used to them.*

Johann von Neumann

*If builders built buildings the way programmers wrote programs, then the first woodpecker that came along would destroy civilization.*

Gerald Weinberg

ABSTRACT. The classical dam break problem has become the *de facto* standard in validating the nonlinear shallow water equations solvers. Moreover, the NSWE are widely used for flooding simulations. While applied mathematics community is essentially focused on developing new numerical schemes, we tried to examine the validity of the mathematical model under consideration. The main purpose of this study is to check the pertinence of the NSWE for flooding processes. From the mathematical point of view, the answer is not obvious since all derivation procedures assumes the total water depth positivity. We performed a comparison between the two-fluid Navier-Stokes simulations and the NSWE solved analytically and numerically. Several conclusions are drawn out and perspectives for future research are outlined.

### 5.2.1 Introduction

During the last century there were more than 200 failures of dams greater than 15 m high [Sin96, ZR00]. They have caused a loss of more than 8000 lives and millions of dollars worth of damage. Consequently, dam break flows have become an important practical problem in civil engineering. Numerical models have become essential as a predictive tool in evaluating the risks associated with the failure of the hydraulic structures. That is why, the number of numerical studies has drastically increased during past decades.

To our knowledge, the dam break problem was studied analytically for the first time in the PhD thesis of Pohle (1950), [Poh50], who used a lagrangian description to solve this problem. The classical analytical solution for the dam break problem in the context of the NSWE can be found in the book of Stoker (1957), [Sto57]. Later, this solution was generalized to the constant slope case by Mangeney *et al.* (2000), [MHR00]. Note, that Hunt (1982), [Hun82], also considered the sloping channel case and he obtained a closed-form solution using a kinematic wave approximation. Among classical works on this topic, we have to mention the prominent paper by Benjamin (1968), [Ben68]. Recently, Korobkin & Yilmaz (2008), [KO08], studied the initial stages of the dam break flow in the framework of potential free surface flows.

It is interesting, however, to recall some other known analytical solutions to NSWE even if they are not directly related to the dam break problem. Wave run-up on a sloping beach was investigated by Carrier & Greenspan (1958), [CG58, CWY03], using a hodograph transformation[1]. This solution is extensively used in the tsunami waves community to validate the run-up algorithm of various NSWE solvers [Ima96, TG97, TS98, SBT+07, SB06, IYO06, DPD10]. The transform of Carrier & Greenspan was employed later by Synolakis and his collaborators to study analytically tsunami run up on a sloping beach, cf. e.g. [Syn87, TS94, TS96, KS06]. There is also an analytical solution by Liu *et al.* (2003), [LLS03] to linearized shallow water equations on a sloping beach. They used a forcing term to model an underwater landslide. This solution is also currently used to test numerical codes [DPD10].

On the other hand, the dam break problem and various lock exchange flows were extensively studied experimentally, cf. e.g. [MM52, Woo70, KC91, HLD96, SCB98, BDP00, Bel04, SDL04]. In this study, we do not directly appeal to them, since our main concern is to study the validity of NSWE as an approximation to more complex mathematical models in some extreme situations.

Numerical studies are also countless. We can divide them conventionally in two big groups. In the first group, authors solved this problem in the framework of the NSWE, cf. e.g. [Wub88, AC99, Tse99, ZR00, Her00, CIM+00, ZCIM02, GV04, Bok05, XS05, BQ06, BX07, PD08] and in the second one more advanced models were used, cf. e.g. [HW65, NH71, HN81, HMN00, SL03, OFDI04, BMM05, Ooi06, OFDI06, BDF+07, OIF+07, CLLL08]. Obviously, this list does not pretend to be exhaustive.

The authors decided to perform this study because there is an apparent contradiction between the mathematical origins of the NSWE and some applications of this model. When we look carefully at any derivation procedure of NSWE, we will see that an implicit assumption of water depth positivity is adopted. Moreover, these equations are designed to model infinitely long waves. That is why, strictly speaking, these equations can be valid only in fluid regions. However, using various numerical techniques (sometimes ad-hoc, semiempirical) this model is routinely used for wetting/drying (run-up/run-down) simulations, cf. e.g. [TG97, TS98]. This process is considerably more complex and the validity of the NSWE is not obvious *a priori*. Recall, that the shoreline can be considered as a triple point: water, air and solid (soil) meet their. Of course, this situation is simplified for mathematical modelling.

We choose a Direct Numerical Simulation (DNS) by the two-fluid Navier-Stokes equa-

[1] In this case, the hodograph transformation means that Riemann invariants were chosen as independent variables. After this change of variables, governing equations become linear and they are further solved by Hankel transform.

tions [SZ99, PZ99] as the reference solution. This system contains all the necessary physical effects ranging from viscosity to the surface tension. Moreover, the ambient fluid (air) is resolved. In the absence of experimental data, these simulations can be assimilated to an idealized experiment. Up to graphical resolution, our numerical results are very similar to the experiments of J. Martin and W. Moyce [MM52] and we remain clearly in the laminar régime. Remind that we take also a realistic density ratio 1:1000 as for the air/water interface (see Table 5.3). The results of the DNS are compared with several solutions to the NSWE. Namely, the analytical solution by Stoker (see Section 5.2.3.3) was used in our comparison. Numerical solutions to the NSWE were obtained using the VOLNA code, cf. [Dut07, PD08, DPD10].

The present study is organized as follows. In Section 5.2.2 we present two mathematical models which are used in this study. In the same section we also discuss several mathematical properties and extensions of the NSWE. In Section 5.2.3 we review some known analytical solutions to the NSWE of the dam break problem. After discussing briefly the numerical techniques, (Section 5.2.4), we present and discuss our numerical results in Section 5.2.5. Conclusions are outlined in Section 5.2.6.

## 5.2.2 Mathematical models

In this section we briefly present two mathematical models which are used in the sequel. The first model is the well-known Nonlinear Shallow Water Equations (NSWE) which were derived for the first time by Saint-Venant (1871), cf. [dSV71]. The second model is the two-fluid Navier-Stokes equations written under the assumption of fluids immiscibility. These equations are much more complete from physical and mathematical points of view. That is why, the two-fluid model is supposed to provide us reliable results.

### 5.2.2.1 Nonlinear Shallow Water Equations

The Nonlinear Shallow Water Equations can be written in the following conservative form (2DH):

$$H_t + \nabla \cdot (H\vec{u}) = 0, \tag{5.48}$$

$$(H\vec{u})_t + \nabla \cdot \left( H\vec{u} \otimes \vec{u} + \frac{g}{2} H^2 \underline{\underline{I}} \right) = gH\nabla h, \tag{5.49}$$

where $H(\mathbf{x}, t)$ is the total water depth and $\vec{u}(\mathbf{x}, t) : \mathbb{R}^2 \times \mathbb{R}^+ \mapsto \mathbb{R}^2$ is the depth-averaged horizontal velocity. Traditionally, $g$ denotes the acceleration due to the gravity, $h(\mathbf{x}, t)$ is the bathymetry function and $\underline{\underline{I}}$ is the identity tensor.

We do not provide here the derivation of these equations since it is more than classical and can be found in various sources [Sto57, Mei94].

**Remark 28.** *The bathymetry function $h(\mathbf{x},t)$ can be time-dependent. It is especially important for tsunami generation problem by submarine earthquakes, landslides, etc. The coupling with seismology is usually done through this function. Namely, various earthquake models, cf. e.g. [DD07d, DD09b, DD10, KDD07] give us the seabed displacements which are then transmitted to the ocean layer. Obviously, in this study we consider the fluid propagation over the flat bottom in view of applying analytical techniques.*

Governing equations (5.48), (5.49) form the system of balance laws (conservation laws, if the bottom is even $h = \text{const}$). Moreover, this system is strictly hyperbolic provided that $H > 0$. This property is extensively used in the construction of various numerical schemes and, in particular, in the Characteristic Flux approach, cf. [GKC96, Ghi98, Ghi01, GKC01, DPD10], which is also implemented in the code VOLNA .

Let us discuss the eigensystem of the advective flux. First, we introduce the so-called conservative variables and rewrite the governing equations as a system of conservation laws:

$$\frac{\partial \vec{w}}{\partial t} + \nabla \cdot \mathcal{F}(\vec{w}) = \mathcal{S}(\vec{w}), \tag{5.50}$$

where we introduced the following notations:

$$\vec{w}(\mathbf{x},t) : \mathbb{R}^2 \times \mathbb{R}^+ \mapsto \mathbb{R}^3, \qquad \vec{w} = (w_1, w_2, w_3) = (H, Hu, Hv),$$

$$\mathcal{F}(\vec{w}) = \begin{pmatrix} Hu & Hv \\ Hu^2 + \frac{g}{2}H^2 & Huv \\ Huv & Hv^2 + \frac{g}{2}H^2 \end{pmatrix} = \begin{pmatrix} w_2 & w_3 \\ \frac{w_2^2}{w_1} + \frac{g}{2}w_1^2 & \frac{w_2 w_3}{w_1} \\ \frac{w_2 w_3}{w_1} & \frac{w_3^2}{w_1} + \frac{g}{2}w_1^2 \end{pmatrix}.$$

After projecting the flux $\mathcal{F}(\vec{w})$ on a unit normal direction $\vec{n} = (n_x, n_y)$, $|\vec{n}| = 1$, one can compute the Jacobian matrix $\mathbb{A}_n$. Its expression in the physical variables has the following form:

$$\mathbb{A}_n = \frac{\partial\big(\mathcal{F}(\vec{w}) \cdot \vec{n}\big)}{\partial \vec{w}} = \begin{pmatrix} 0 & n_x & n_y \\ -uu_n + gHn_x & u_n + un_x & un_y \\ -vu_n + gHn_y & vn_x & u_n + vn_y \end{pmatrix},$$

where $u_n = \vec{u} \cdot \vec{n}$ is the velocity vector projected on $\vec{n}$. The Jacobian matrix $\mathbb{A}_n$ has three distinct eigenvalues:

$$\lambda_1 = u_n - c, \quad \lambda_2 = u_n, \quad \lambda_3 = u_n + c, \tag{5.51}$$

where $c = \sqrt{gH}$ is the gravity wave speed in infinite wavelength limit. This quantity plays the same rôle as the speed of sound in compressible fluid mechanics. The hyperbolicity condition for the system (5.48), (5.49) follows immediately from (5.51) and the definition of $c$. The eigenstructure of the Jacobian matrix $\mathbb{A}_n$ is fundamental for constructing numerical flux function, cf. [DPD10], and thus, upwinding the discrete solution.

**5.2.2.1.1 Properties** Nonlinear Shallow Water Equations have many other interesting properties. Some of them will be briefly recalled here. To reveal these properties, we shall take the water wave theory point of view.

Let us recast equations (5.48), (5.49) in the following nonconservative form in one space dimension:

$$\partial_t \eta + \partial_x\big((h+\eta)u\big) = 0, \tag{5.52}$$

$$\partial_t u + \frac{1}{2}\partial_x |u|^2 + g\partial_x \eta = 0. \tag{5.53}$$

These equations possess a (non-canonical) Hamiltonian structure [Sal88, ZK97, Rad99]:

$$\partial_t \begin{pmatrix} \eta \\ u \end{pmatrix} + \begin{pmatrix} 0 & \partial_x \\ \partial_x & 0 \end{pmatrix} \begin{pmatrix} \frac{\delta \mathcal{H}}{\delta \eta} \\ \frac{\delta \mathcal{H}}{\delta u} \end{pmatrix} = 0,$$

where the Hamiltonian $\mathcal{H}$ is defined as

$$\mathcal{H} := \frac{1}{2}\int\limits_{-\infty}^{+\infty} g\eta^2 \, dx + \frac{1}{2}\int\limits_{-\infty}^{+\infty} (h+\eta)u^2 \, dx.$$

Moreover, the pair of equations (5.52), (5.53) possesses an infinity of conservation laws [Ben74, Miu74].

Equations (5.52), (5.53) can be also derived from Luke's Lagrangian variational principle [Luk67] if we introduce the velocity potential function $\phi(\mathbf{x}, t)$ such that $\vec{u} = \nabla\phi$. In this case, the Lagrangian reads

$$\mathcal{L} = \int\limits_{t_1}^{t_2} \int\limits_{\mathbf{x}_1}^{\mathbf{x}_2} \Big\{ (\eta + h)\big(\phi_t + \frac{1}{2}|\nabla\phi|^2\big) + \frac{1}{2} g\eta^2 \Big\} \, d\mathbf{x} \, dt.$$

Governing equations (5.52), (5.53) are obtained by varying $\mathcal{L}$ with respect to $\eta$ and $\phi$. Recently, a generalized variational principle was proposed by Clamond & Dutykh, cf. [CD10]. Their approach allows for more flexibility and can be used to derive various generalized shallow and deep water approximations.

**5.2.2.1.2 Extensions** The Nonlinear Shallow Water Equations (5.48), (5.49) arise after a series of approximations applied to complete set of equations. Strictly speaking, they model the propagation and transformation of infinitely long water waves. That is why, their validity for run-up and flooding simulations is not so obvious *a priori*.

The validity region of these equations can be extended by adding some new physical effects. The inclusion of the dispersion is beneficial for description of shorter wavelengths.

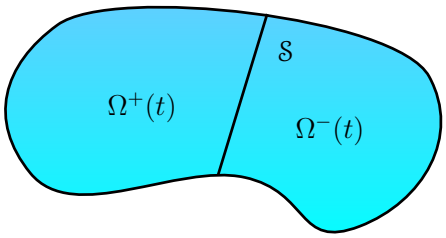


**Figure 5.19:** Two immiscible fuids separated by an interface.

As a result, one can derive Boussinesq equations, [Bou71b, Bou72, MBS03, BCS02, BCS04, BCL05, BDM07], Serre equations, [Ser53, Bar04], Green-Naghdi model, [GLN74, GN76, KBEW01, Li02], and several others.

Another physical effect is the dissipation. Situations where dissipation becomes important for water waves are discussed in [ZG71, BPS81, Wu81, DD07c, Dut09b, Dut09a]. If one neglects the bottom boundary layer effects [DD07c, Dut09b], dissipative equations (5.52), (5.53) take the following form, cf. [DDZ08, DD07c, Dut09b]:

$$\partial_t \eta + \nabla \cdot \big((h+\eta)\vec{u}\big) = \nu \nabla^2 \eta,$$
$$\partial_t \vec{u} + \frac{1}{2}\nabla|\vec{u}|^2 + g\nabla\eta = \nu\nabla^2\vec{u},$$

where $\nu$ is the kinematic viscosity. Corresponding dissipative Boussinesq equations can be found in [Kha97, LO04, LSVO06, DD07c, Dut09b].

When equations are recast in the conservative form (5.48), (5.49), there is also an alternative approach to include the dissipation initiated by Gerbeau & Perthame and followed by other authors, cf. e.g. [GP01, BD03, BD06, Mar07].

#### 5.2.2.2 Two-fluid Navier-Stokes equations

Let us consider two immiscible and incompressible[2] fluids (water and air, for example) occupying domain $\Omega = \Omega^+ \cup \Omega^-$, where they are separated by an interface $\mathcal{S}$. This situation is schematically depicted in Figure 5.19. We note that we do not make any assumption on the interface complexity and topology. In what follows we will denote by superscripts $\pm$ all quantities related to the heavy and light fluids respectively.

[2]The case of the two compressible and miscible fluids was recently studied by Dias, Dutykh and Ghidaglia, cf. [Dut07, DDG10, DDG08c, DDG08a].

In each fluid we can write mass and momentum balance equations:

$$\nabla \cdot \vec{u} = 0, \tag{5.54}$$

$$\rho^{\pm}(\partial_t \vec{u} + \vec{u} \cdot \nabla \vec{u}) + \nabla p = \nabla \cdot (2\mu^{\pm}\mathbf{D}) + \sigma\kappa\delta_{\mathcal{S}}\vec{n} + \rho^{\pm}\vec{g}. \tag{5.55}$$

The latter may be written in conservative form:

$$\partial_t(\rho^{\pm}\vec{u}) + \nabla \cdot (\rho^{\pm}\vec{u} \otimes \vec{u} + p\underline{\underline{I}}) = \nabla \cdot (2\mu^{\pm}\mathbf{D}) + \sigma\kappa\delta_{\mathcal{S}}\vec{n} + \rho^{\pm}\vec{g},$$

where $\vec{u}$ is the fluid velocity, $\rho^{\pm}$ are the fluids densities, $\mu^{\pm}$ are the fluids dynamic viscosities, $\mathbf{D} = \frac{1}{2}(\partial_i u_j + \partial_j u_i)$ is the rate of deformation tensor. The surface tension term is a force concentrated at the interface, $\sigma$ is the surface tension coefficient, $\kappa$ is the curvature of the interface, $\vec{n}$ is the unit normal to the interface and $\delta_{\mathcal{S}}$ is the distribution (Dirac mass function) concentrated on the interface $\mathcal{S}$.

Governing equations (5.54), (5.55) have to be completed by the following jump conditions across the interface:

- Velocity continuity

$$[\vec{u}]_{\mathcal{S}} = 0 \tag{5.56}$$

- Tangential stress condition

$$[\mu\vec{t} \cdot \mathbf{D} \cdot \vec{n}]_{\mathcal{S}} = 0, \tag{5.57}$$

- Normal stress condition

$$[\vec{n} \cdot (-p\underline{\underline{I}} + 2\mu\mathbf{D}) \cdot \vec{n}]_{\mathcal{S}} = \sigma\kappa, \tag{5.58}$$

where $\vec{t}$ is a tangent vector ($\vec{t} \cdot \vec{n} = 0$) to the interface and notation $[\cdot]_{\mathcal{S}}$ represents the jump of a quantity across the surface $\mathcal{S}$.

However, for numerical computations it is advantageous to introduce a characteristic function $\phi$, (cf. [Ish75, TK96, GKC01, DDG10, DDG08c, DDG08a]) defined as:

$$\phi = \begin{cases} 1, & \mathbf{x} \in \Omega^{+}(t), \\ 0, & \mathbf{x} \in \Omega^{-}(t). \end{cases}$$

Thus, $\phi$ and $\vec{n}$ are related by the formula $\nabla\phi = \vec{n}\delta_{\mathcal{S}}$. In the absence of phase change, $\phi$ is simply advected by the fluid motion:

$$\partial_t\phi + \nabla \cdot (\phi\vec{u}) = 0. \tag{5.59}$$

In order to write a unique formulation for the entire domain, we express the density and the viscosity as functions of $\phi$:

$$\rho = \phi\rho^+ + (1-\phi)\rho^-, \quad \mu = \phi\mu^+ + (1-\phi)\mu^-.$$

Thus, we have the following momentum balance equation:

$$\rho(\partial_t\vec{u} + \vec{u}\cdot\nabla\vec{u}) + \nabla p = \nabla\cdot(2\mu\mathbf{D}) + \sigma\kappa\delta_{\mathcal{S}}\vec{n} + \rho\vec{g}. \tag{5.60}$$

Along with the mass conservation equation (5.54) and the volume fraction advection equation (5.59), it forms the two-fluid Navier-Stokes equations with an interface, which are solved numerically below.

**Remark 29.** *We can recover jump conditions (5.56) – (5.58) if we investigate the governing equations (5.54), (5.59), (5.60) in the neighborhood of the surface $\mathcal{S}$ and making use of the formula $\nabla\phi = \vec{n}\delta_{\mathcal{S}}$.*

## 5.2.3 Analytical solutions

In this section we review known analytical solutions related to the dam break problem that we use in the comparison with the numerical results.

### 5.2.3.1 Linear solution

The simplest analytical solution for the dam break problem can be derived when we consider Linear Shallow Water Equations (LSWE). The latter can be obtained in a straightforward manner from (5.52), (5.53):

$$\begin{aligned}\partial_t\eta + \partial_x(h_0 u) &= 0,\\ \partial_t u + g\partial_x\eta &= 0.\end{aligned}$$

In some situations, it is advantageous to eliminate the velocity variable $u$ to obtain

$$\frac{\partial^2\eta}{\partial t^2} - \frac{\partial}{\partial x}\Big(c_0^2\frac{\partial\eta}{\partial x}\Big) = 0, \quad c_0 := \sqrt{gh_0}. \tag{5.61}$$

The Initial Value Problem (IVP) for (5.61) corresponding to the dam break takes the following form:

$$\eta(x,0) = h_0\mathcal{H}(x), \quad \partial_t\eta(x,0) = 0,$$

where $\mathcal{H}(x)$ is the Heaviside function. This IVP can be easily solved using the Fourier transform:

$$\eta(x,t) = h_0\Big(\frac{1}{2} + \frac{1}{\pi}\int_0^{+\infty}\frac{\sin(kx)}{k}\cos(c_0kt)\,dk\Big).$$

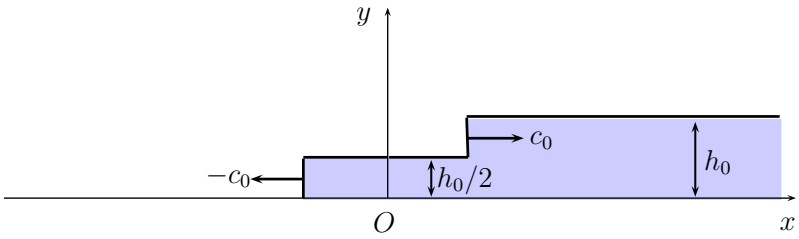


**Figure 5.20:** Sketch of the solution to the LSWE.

The sketch of this solution is presented in Figure 5.20. Namely, it consists of two waves propagating in opposite directions with velocities $\pm c_0$. Hence, the front speed is equal to $-c_0$. Of course, this result is nonphysical as it will be shown below.

Similar solutions can be constructed considering the linearized Euler equations for either one or two fluids separated by an interface.

#### 5.2.3.2 Small time asymptotics

Several small time asymptotics were proposed to solve the dam break problem. One of the first solutions was derived by Pohle (1950), [Poh50]. Such methods generally require the use of lagrangian description. The prominent book by Stoker, [Sto57], also contains such a solution:

$$X(a,b,t) = a - \frac{g}{2\pi}t^2 \log\left(\frac{\cos^2\frac{\pi b}{4h_0} + \sinh^2\frac{\pi a}{4h_0}}{\sin^2\frac{\pi b}{4h_0} + \sinh^2\frac{\pi a}{4h_0}}\right) + o(t^2), \tag{5.62}$$

$$Y(a,b,t) = b - \frac{g}{\pi}t^2 \arctan\left(\frac{\sin\frac{\pi b}{2h_0}}{\sinh\frac{\pi a}{2h_0}}\right) + o(t^2), \tag{5.63}$$

where $(X, Y)$ are new coordinates of the particle $(a, b)$ at time $t$. Recently this solution was generalized by Korobkin & Oguz (2008) [KO08]. We tried to compare the solution (5.62), (5.63) to our numerical results and found that its validity time is too short for any practical use. That is why this solution is not plotted bellow.

Note, that expressions (5.62) and (5.63) are singular at the shoreline $(a, b) = (0, 0)$. Thus, some special care is needed to get an asymptotic expansion valid in the vicinity of this point, cf. [KO08].

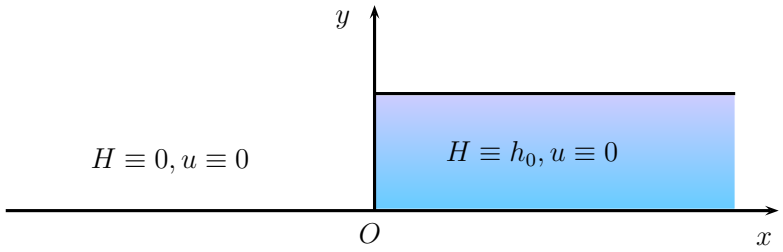


**Figure 5.21:** Sketch of the initial condition for the shallow water computations.

#### 5.2.3.3 Nonlinear solution

The classical book by J.J. Stoker, [Sto57], contains an analytical solution for the dam break problem. Consider the classical initial condition:

$$H(x,0) = \begin{cases} h_0, & x \geq 0, \\ 0, & x < 0. \end{cases} \qquad u(x,0) \equiv 0, \ \forall x \in \mathbb{R}.$$

Schematically it is depicted on Figure 5.21.

Then, by considering the Riemann invariants and using the method of characteristics, [Lax73, GR90, GR96, CG09], one can derive the following solution:

$$H(x,t) = \begin{cases} 0, & x < -2c_0 t, \\ \frac{1}{9g}\left(\frac{x}{t} + 2c_0\right)^2, & -2c_0 t \leq x \leq c_0 t, \\ h_0, & x > c_0 t, \end{cases} \tag{5.64}$$

$$u(x,t) = \begin{cases} 0, & x < -2c_0 t, \\ \frac{2}{3}\left(\frac{x}{t} - c_0\right), & -2c_0 t \leq x \leq c_0 t, \\ 0, & x > c_0 t, \end{cases} \tag{5.65}$$

where $c_0 := \sqrt{g h_0}$ is the gravity wave speed in the undisturbed region. The front position is given by the characteristic outgoing from the fluid region:

$$x_f(t) = -2c_0 t.$$

Recall that recently this solution was generalized to the constant slope case by Mangeney *et al.* (2000), [MHR00].

**Remark 30.** *The run-up algorithm used in our numerical code VOLNA is based on this analytical result. Namely, we impose just obtained front speed when the wet/dry transition is detected. This simple approach was validated and shown to be very robust. For more details we refer to Dutykh et al. (2009), [DPD10].*

### 5.2.4 Numerical methods

The main purpose of this study is to draw out some conclusions on the validity of NSWE for wetting (flooding) process simulations. That is why, we do not provide here any details about numerical methods used to compute solutions. The interested reader can consult references given below to get technical details.

In order to solve numerically the two-fluid Navier-Stokes equations (5.54), (5.60) and (5.59), we applied the finite volumes method, cf. e.g. [Jas96, Rus02, Ope07]. Namely, a freely available solver `interDyMFoam` of the OpenFOAM CFD Toolbox [Ope07] was used. The interface between two fluids is reconstructed from the volume fraction $\phi$ distribution using the VOF method, cf. [HN81, SZ99, PZ99]. Let us underline that all two-fluid computations presented in this study are 3D with only one cell in $z$-direction. Everywhere we impose the classical no-slip boundary condition.

Nonlinear Shallow Water Equations are solved with our operational numerical code VOLNA , cf. [Dut07, DPD10]. This code was developed in close collaboration with R. Poncet and F. Dias when the first author was at CMLA, ENS de Cachan. The VOLNA code uses unstructured triangular meshes and is able to run in arbitrary complex coastal regions. The numerical method is a second-order finite volumes MUSCL-TVD scheme along with the SSP-RK3(4) method for the discretization in time, cf. [SR02]. Details on adopted discretization procedure can be found in [Dut07, PD08, DPD10]. All the computations we performed are in 2D and only one-dimensional cross sections are presented below. On the lateral boundaries we impose the wall boundary condition $\vec{u} \cdot \vec{n} = 0$. This choice is consistent with two-fluid computation and allows us to have an insight into the impact process.

### 5.2.5 Results comparison and discussion

In this section we perform a comparison between a two-fluid simulation (DNS), the analytical solution by Stoker (1957) and numerical solutions to the NSWE by the VOLNA code. The initial set-up for the VOLNA code is shown in Figure 5.21. Sketch of the initial condition for the DNS is depicted on Figure 5.22. The simulation time and propagation distance is chosen so that the right boundary do not influence obtained results. All parameters used in computations are given in Table 5.3. These parameters are chosen suitable to simulate the air/water interaction.

The snapshots of our simulations are given on Figures 5.23 – 5.29. On the left image (a) we represent the volume fraction $\phi$ distribution provided by the DNS. On the right image (b) we plot together the analytical solution (5.64) (red dotted line) and simulation results by the VOLNA code (black solid line) for the free surface elevation $\eta$. The analytical

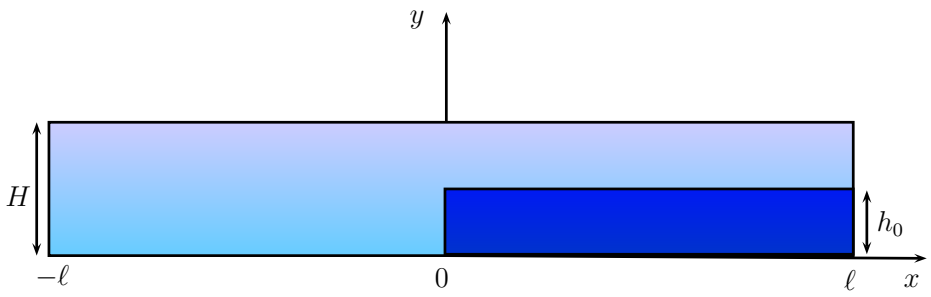


**Figure 5.22:** Sketch of the initial condition for two-fluid numerical simulation (DNS).

| *parameter* | *value* |
|---|---|
| gravity acceleration, $g$, $m/s^2$ | 1.0 |
| fluid column height, $h_0$, $m$ | 0.25 |
| fluid column length, $\ell$, $m$ | 1.0 |
| total domain height, $H$, $m$ | 0.5 |
| fluid density, $\rho^+$, $kg/m^3$ | 1000.0 |
| fluid viscosity, $\nu^+$, $m^2/s$ | $10^{-6}$ |
| air density, $\rho^-$, $kg/m^3$ | 1.0 |
| air viscosity, $\nu^-$, $kg/m^3$ | $10^{-6}$ |
| surface tension, $\sigma$, $kg$ | 0.07 |

**Table 5.3:** Parameters used in numerical simulations.

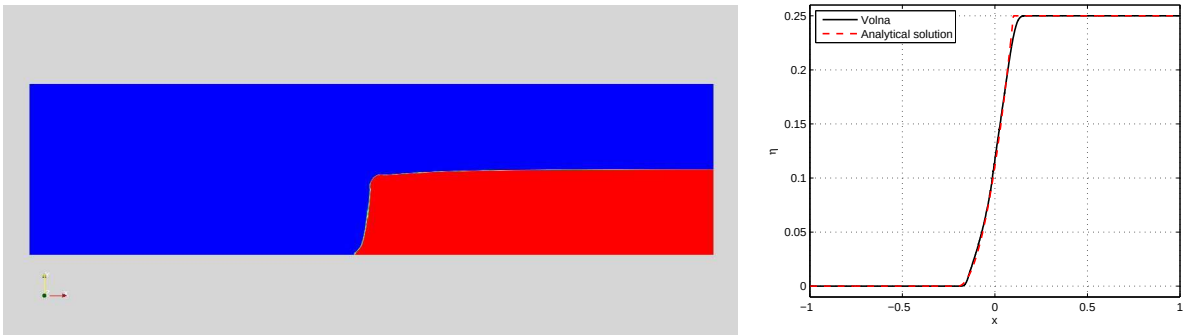


(a) Two-fluid simulation

(b) NSWE

**Figure 5.23:** Initial deformation of the water column under the gravity force ($t = 0.2$ s).

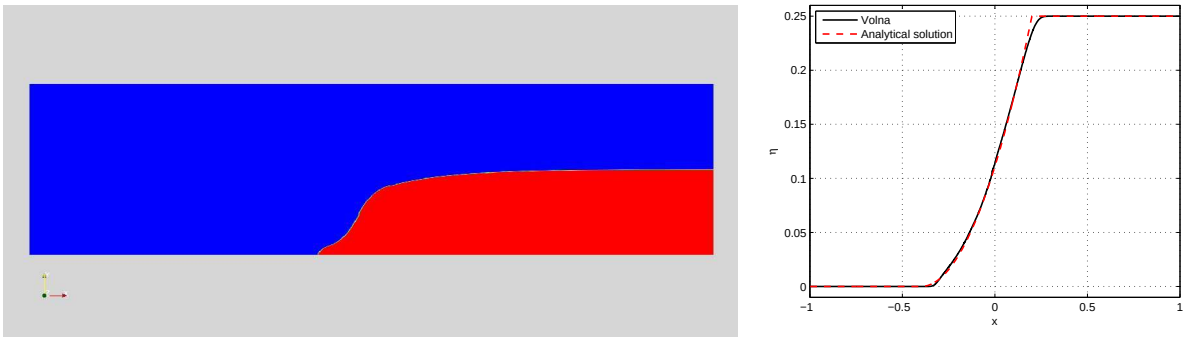


(a) Two-fluid simulation (b) NSWE

**Figure 5.24:** Transition to the propagation regime ($t = 0.4$ s).

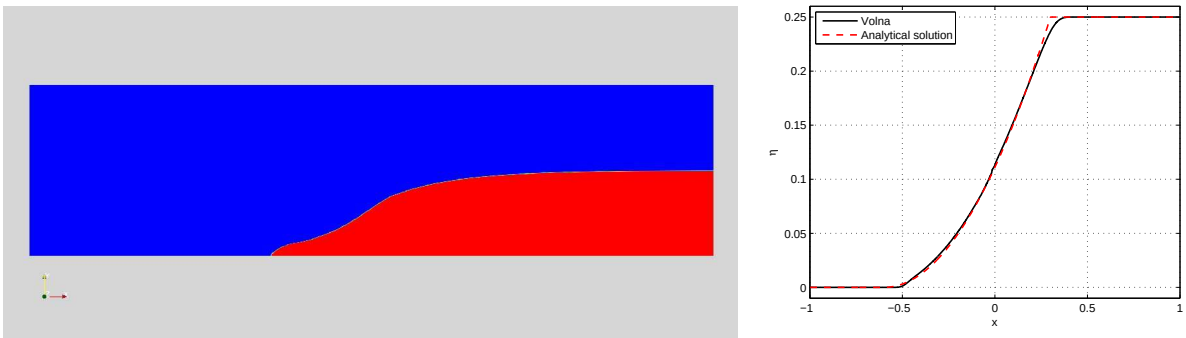


(a) Two-fluid simulation (b) NSWE

**Figure 5.25:** Heavy fluid entering into the propagation regime ($t = 0.6$ s).

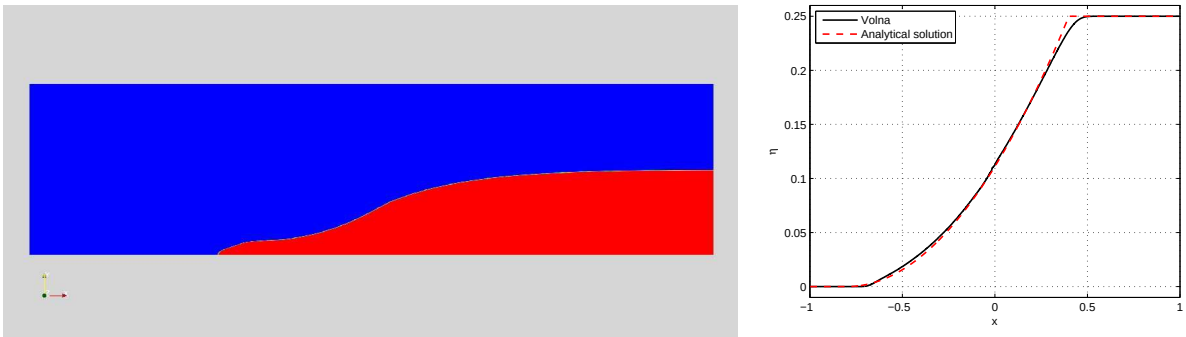


(a) Two-fluid simulation (b) NSWE

**Figure 5.26:** Heavy fluid in the propagation regime ($t = 0.8$ s).

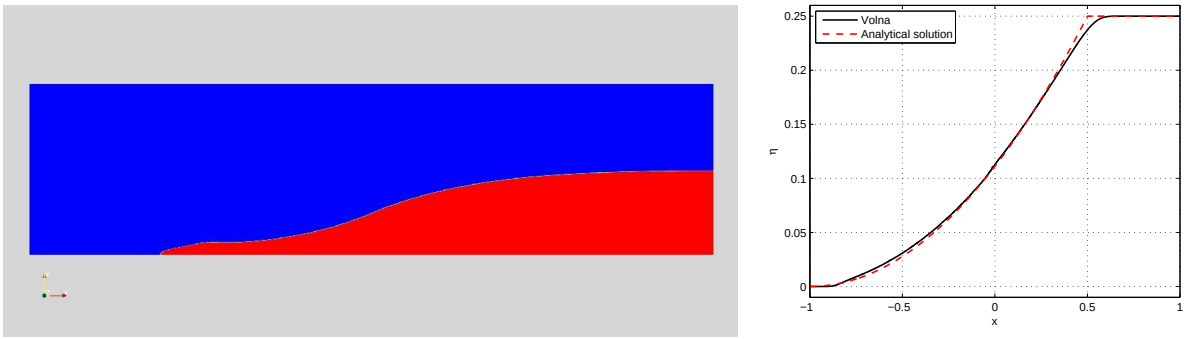


(a) Two-fluid simulation (b) NSWE

**Figure 5.27:** Heavy fluid in the propagation regime ($t = 1$ s).

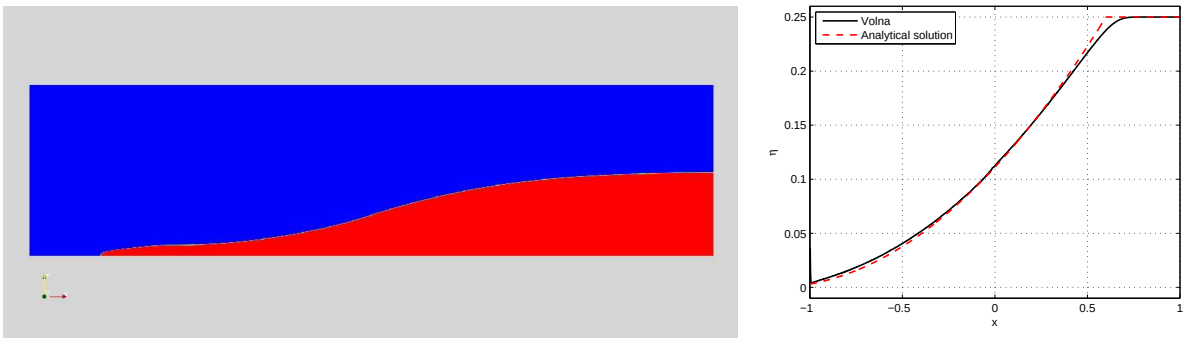


(a) Two-fluid simulation (b) NSWE

**Figure 5.28:** Heavy fluid front before the interaction with the left wall ($t = 1.2$ s).

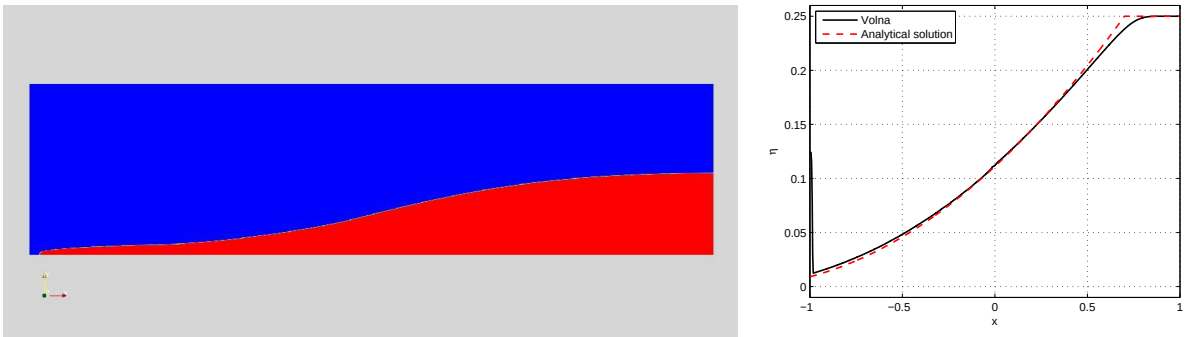


(a) Two-fluid simulation (b) NSWE

**Figure 5.29:** Heavy fluid front before the interaction with the left wall ($t = 1.4$ s).

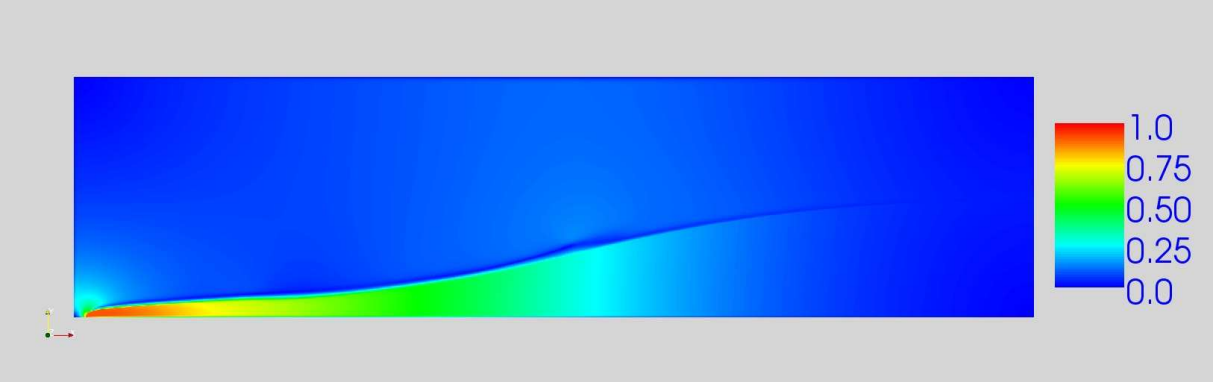


**Figure 5.30:** Velocity field magnitude at $t = 1.4$ s.

solution is almost superposed with our numerical simulation as it is expected. This result can be considered as one more validation test of the wetting/drying algorithm used in the VOLNA code.

In the beginning of the simulation, the water column is slightly deformed due to the gravity force (Figure 5.23). Only a small time interval is needed for the heavy fluid to acquire the kinetic energy and to enter into the propagation régime depicted on Figures 5.24 – 5.29. Analytical solution (5.64) prescribes a parabolic form of the interface. However, the DNS shows somehow different shape. Lower fluid layers undergo stronger acceleration than in NSWE and thus propagate faster. Nonuniform distribution of the velocity field along the heavy fluid is illustrated on Figure 5.30. This creates a strong distortion of the interface which is elongated near the bottom (it can be easily seen in Figures 5.28 – 5.29). This effect is not present in NSWE simulations since, the vertical flow structure is not resolved by this approximate model. Consequently, in NSWE we obtain a piecewise linear distribution of the velocity field as it follows from analytical solution (5.65).

Let us notice another one fact. In Figure 5.29 one can observe that the NSWE solution has already achieved the left vertical wall. From this moment, the analytical solution is not valid anymore. However, the two-fluid simulation has not yet reached the left boundary. This discrepancy comes from the time lag due to initial acceleration stage, on one hand, and slightly different front propagation speeds, on the other hand. Bottom boundary layer may have some effect onto the propagation speed of the heavy fluid front [Dut07, Dut09b].

From these simulations, we extracted the wave front position, shown in Figure 5.31 as a function of time for two different initial heights: $h_0 = 0.25$ m (as in simulations presented above) and $h_0 = 0.125$ m. Qualitatively these two results are similar. We can underline again a very good agreement between numerical and analytical NSWE results. On the other hand, there is a slightly increasing difference in the front position with the two-fluid DNS. It can be attributed to the initial acceleration stage ($t \leq 0.25$ s) which is

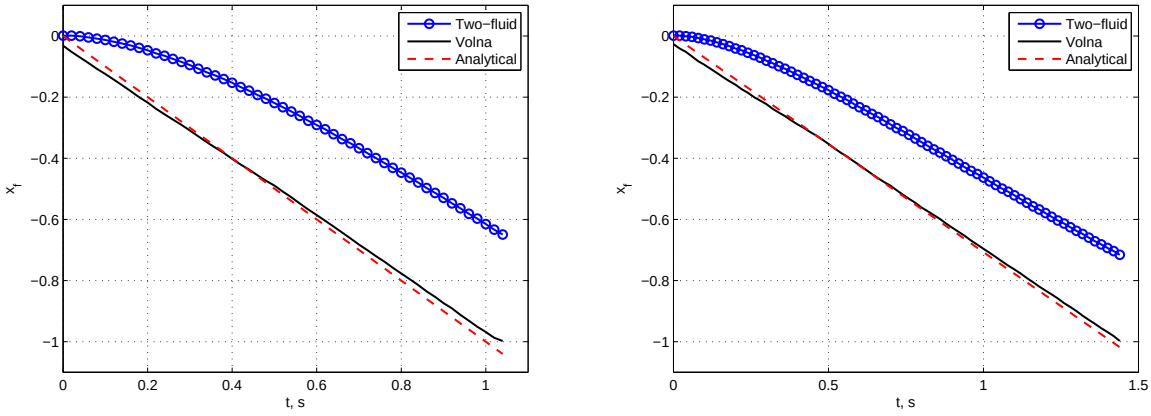


(a) $h_0 = 0.25$ m (b) $h_0 = 0.125$ m

**Figure 5.31:** Comparison of the front position according to three different models: blue line with circles corresponds to the DNS, black line shows the front position predicted by VOLNA solver (NSWE) and the red dotted line is the analytical solution (5.64).

| | $h_0 = 0.25$ m | $h_0 = 0.125$ m |
|---|---|---|
| *Two-fluid (DNS)* | $-0.81$ | $-0.58$ |
| *VOLNA (NSWE)* | $-0.96$ | $-0.68$ |
| *Analytical (NSWE)* | $-1.0$ | $-0.71$ |
| *Analytical (LSWE)* | $-0.5$ | $-0.35$ |

**Table 5.4:** Front speed predicted by four different approaches.

present in the two-fluid model. Another explanation consists in the front velocity which can be determined by measuring the slope to the curve $t \to x_f(t)$. Determined in this way front speeds (in permanent régime, $t \geq 0.25$ s) are given in Table 5.4. The LSWE give completely wrong results showing again that the nonlinearity plays the crucial rôle in this process. It is also worth to note that the numerical front speed by the VOLNA code is closer to the DNS. This positive fact can be attributed to the effect of the numerical diffusion on unstructured meshes.

#### 5.2.5.1 Impact process

In the previous section we presented results concerning the initial and propagation stages of the dam break problem. However, we continued computations until the interaction with the left wall and even slightly beyond. The goal is to test again the validity of

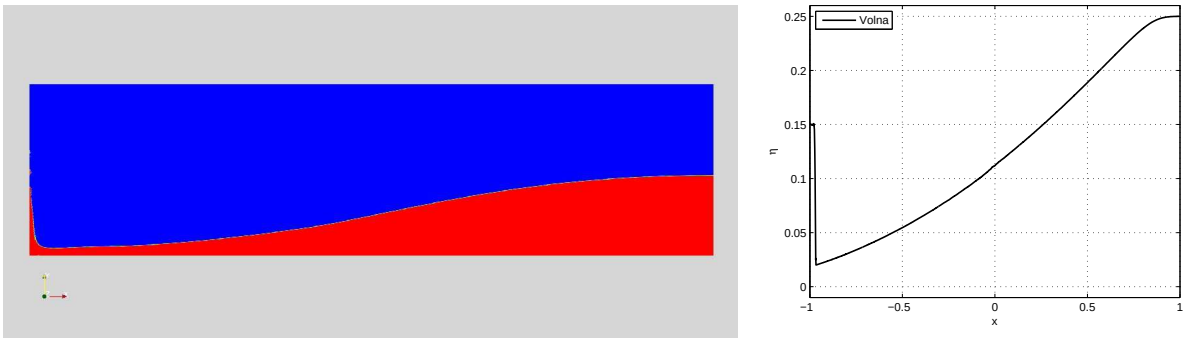


(a) Two-fluid simulation (b) NSWE with VOLNA solver

**Figure 5.32:** Interaction with the left vertical wall at $t = 1.6$ s.

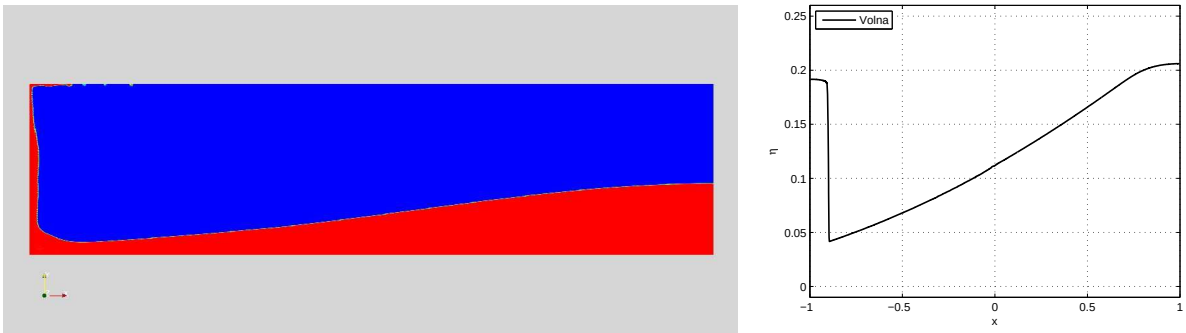


(a) Two-fluid simulation (b) NSWE with VOLNA solver

**Figure 5.33:** Interaction with the left vertical wall at $t = 2.2$ s.

the NSWE in such extreme conditions. For this kind of situations we do not know any analytical solution. Thus, we compare only DNS and VOLNA code results. In two-fluid simulation we use the same no-slip condition as on all solid boundaries. Wall boundary condition implementation in VOLNA solver is detailed in [DPD10]. Here we can say that it is based on consideration of incoming characteristics. The general methodology is presented in works of J.-M. Ghidaglia and F. Pascal [GP02b, GP02a, GP05].

The comparison results are presented on Figures 5.32 and 5.33. For instance, the wave amplitude on Figure 5.33 (a) reaches the upper boundary (its height is 0.5 m), while NSWE numerical solution amplitude does not exceed 0.2 m.

From these results it is obvious that the wave impact process is not correctly modelled by NSWE. It is possible to foresee this conclusion if one recalls two main constutive assumptions behind NSWE:

- The pressure is hydrostatic

- Vertical velocity and acceleration are neglected

Notice, that for infinitely long waves, these two hypotheses are equivalent. Since, the dynamic pressure dominates in the impact process, we get qualitatively wrong results (it is especially clear from Figure 5.33).

### 5.2.6 Conclusions and perspectives

In the present study we tried to examine the validity of the NSWE for wetting (flooding) process modelling. As a test-case we chose the classical dam break problem which is the *de facto* standard in this field. This problem was solved in the context of two completely different models in terms of physical precision and, by consequence, of different complexity. The two-fluid DNS was chosen as the reference solution since all necessary physical effects are included in it.

Comparison results presented above show good overall performance of the NSWE. In order to appreciate more these results, one should take into account also the computational cost of the DNS and relatively inexpensive shallow water simulations.

However, we revealed several drawbacks of the depth-integrated model. Namely, the free surface shape differs from the parabolic profile predicted by NSWE. This discrepancy is attributed to the non-piecewise linear distribution of the velocity field inside the water column. To compare, see Figure 5.30 for the DNS result and formula (5.65) for the analytical prediction by NSWE. The experimental and theoretical study of P.K. Stansby *et al* (1998) [SCB98] also revealed some differences during the initial stages. However, their objection concerned essentially some new jet-like phenomena just after release. For later times, they found relatively close agreement with NSWE.

We went beyond the initial purpose of this study and continued our simulations until the impact process with the left wall. It was shown that the NSWE strongly underestimate the wave height. This discrepancy has its origins in the hydrostatic pressure assumption. Actually, the dynamic pressure becomes dominant during the impact process. Its excess is responsible of spectacular splashes that we may have a chance to observe in nature.

Concerning the front propagation speed, we obtained slightly different values between the DNS and the NSWE solutions. We have to note that in a physical experiment this quantity strongly depends on the soil conditions. The standard no-slip boundary condition is clearly insufficient to describe all kinds of soils. We believe that future research activities will focus on developing wall function laws and realistic boundary conditions for Navier-Stokes equations (two-fluid or with free surface). On the other hand, NSWE are also improvable. To produce physically correct results, these equations should be completed by friction laws (Chézy, Manning, Darcy-Weisbach and other laws) with properly adjusted

coefficients. Recently, bottom boundary layer effects on long waves were studied [Dut09b]. Another direction consists in extending NSWE to account for bed material transport as it was recently proposed by Fraccarollo & Capart (2002) [FC02].

# Part III

# Multi-fluid flows

# Chapter 6

# Two-phase flows

*We live in a Newtonian world of Einsteinian physics ruled by Frankenstein logic.*

David Russell

## Contents

## 6.1 Velocity and energy relaxation in two-phase flows

*The second law of thermodynamics holds, I think, the supreme position among the laws of nature. If someone points out to you that your pet theory of the Universe is in disagreement with Maxwell's equations - then so much the worse for Maxwell's equations. If it is found to be contradicted by observation - well, those experimentalists do bungle things up sometimes. but if your theory is found to be against the second law of thermodynamics I can give you no hope; there is nothing to do but to collapse in deepest humiliation.*

Arthur S. Eddington

ABSTRACT. In the present study we investigate analytically the process of velocity and energy relaxation in two-phase flows. We begin our exposition by considering the so-called six equations two-phase model [Ish75, Rov06]. This model assumes each phase to possess its own velocity and energy variables. Despite recent advances, the six equations model remains computationally expensive for many practical applications. Moreover, its advection operator may be non-hyperbolic which poses additional theoretical difficulties to construct robust numerical schemes [GKC01]. In order to simplify this system, we complete momentum and energy conservation equations by relaxation terms. When relaxation characteristic time tends to zero, velocities and energies are constrained to tend to common values for both phases. As a result, we obtain a simple two-phase model which was recently proposed for simulation of violent aerated flows [DDG10]. The preservation of invariant regions and incompressible limit of the simplified model are also discussed. Finally, several numerical results are presented.

### 6.1.1 Introduction

Currently, single phase flows modeling is essentially understood besides the problem of turbulence. In two-phase flows the situation is completely different. Nowadays there is no general consensus on the two-phase flow modeling. Turbulence modeling in two-phase flows is even more tricky [Llo05]. The two-phase models are based on space and time (ensemble) averaging of the local governing equations of each phase. Consequently, these models can only provide information on the average flow behaviour. The derivation of the *proper* model is far from being achieved [Ish75, DL79, DCL79, BD82, SW84, DW94, IH06]. One of the main difficulties lies in the determining the mass, momentum and energy transfers in the presence of steep gradients across the interfaces. Very often more or less accurate empirical correlations are used to describe such interface processes. In the same time, two-phase flows are very frequent in industry and in nature. Typical examples include water

waves (especially during the wave breaking), petroleum and gas flow in pipes, nuclear reactors [SFW+05], etc.

The most important industrial application of two-phase flows is the simulation of a wide spectrum of accident scenarios in Pressurized (or Boiling) Water Reactors (PWR, BWR). Extensive experimental programmes for the PWRs are extremely expensive. Currently, new reactor design requires more and more numerical simulations of basic reactor features [SFW+05]. The goal is to reduce experimental programmes to a minimum. On the other hand, industrial codes (such as CATHARE [Bes90], RELAP5 [Ran85], THYC [ACOR95] or Neptune_CFD [BG05, GCMM09, GBBea07], for example) need to be supplemented by a large number of empirical closures which prevents reliable code application outside of their validity domain. Also these codes use robust but higly diffusive numerical schemes which make it difficult the computation of strong variable gradients proper to many accident conditions.

Two-phase models play also an important role in simulation of interfaces between two immiscible compressible fluids. This problem is very challenging from numerical point of view. All existing methods to address this problem can be conventionally divided into four big groups:

- Volume of fluid (VOF) [HN81, SZ99]
- Level set method [OS88, OS94]
- Lagrangian interface tracking [GGLT00]
- Diffuse interface method [Lar90, AMW98, Shy98]

In the last approach we do not compute precisely the interface position. Due to numerical diffusion, the volume fraction takes intermediate values between 0 and 1 even if it is initialized by values in $\{0, 1\}$. The resulting mixture of two fluids has to be properly modelled in the transition region. Two-phase models that we will discuss below provide a sound physical description of mixing zones. The diffuse interface approach is less accurate than mentioned above methods (unless some special sharpening techniques are employed) but it is much simpler to implement and can naturally handle arbitrary topological changes in the flow.

Recently, a single velocity/single energy two-phase model was proposed [Dut07, DDG08b, DDG08c, DDG10] in ad-hoc way as a model for violent aerated flows. By analogy with the six equations model, this system was called the four equations model since in one space dimension it consists of two equations of the mass conservation, one equation of the momentum and one of the energy conservation. Two-phase models where both fluids share the same velocity were previously considered in [ACK02, Del05], for example.

The main goal of the present paper is to show the connection between the six equations model [GKC01, GP05, Rov06, IH06] (two equations of mass, momentum and energy conservation) and recently proposed four equations model [Dut07, DDG08b, DDG08c, DDG10] with single velocity and single energy. Physically it is done by introducing relaxation terms into momentum and energy relaxation equations. These relaxation terms constrain velocities and energies to tend to a common value. Then, after taking the singular limit when the characteristic relaxation time goes to zero, one obtains a simplified model. Mathematically, it is achieved by employing a Chapman-Enskog type expansion [CC95]. This technique has been already successfully applied to the so-called Baer-Nunziato model [BGN86, BN86] in [MG05]. The present study is greatly inspired by their work. This type of reduction from the barotropic six equations model were recently done in [MDG09].

The present manuscript is organized as follows. We start our exposition by presenting the so-called six equations model in Section 6.1.2. Then, we complete this model by relaxation terms and derive in Section 6.1.3 a single velocity, single energy model. Preservation of invariant regions and incompressible limit of the resulting four equations model are studied in Sections 6.1.4 and 6.1.5 correspondingly. Then we present some numerical results in Section 6.1.6. Finally, this paper is ended by drawing out main conclusions of this study and some perspectives for future research (Section 6.1.7).

### 6.1.2 Mathematical model

Consider a fluid domain $\Omega \subseteq \mathbb{R}^3$ which is filled by two miscible fluids. All physical quantities related to the heavy and light fluids will be denoted by the superscripts $+$ and $-$ correspondingly. For example, if we consider a plunging breaker with important mixing processes, then water velocity, density, viscosity, etc. will be denoted with the superscript $+$, while variables related to the air will have the superscript $-$. When the interfaces are so multiple that it is impossible any more to follow them, the classical modelling procedure consists in applying a volume average operator [Ish75, Rov06]. At this level of description, two additional variables naturally appear. The so-called volume fractions $\alpha^{\pm}(\mathbf{x}, t)$, $\mathbf{x} \in \Omega$ are defined as

$$\alpha^{\pm}(\mathbf{x}, t) := \lim_{\substack{|d\Omega| \to 0 \\ \mathbf{x} \in d\Omega}} \frac{|d\Omega^{\pm}|}{|d\Omega|}, \tag{6.1}$$

the heavy fluid occupies volume $d\Omega^{+} \subseteq d\Omega$ and the light one the volume $d\Omega^{-} \subseteq d\Omega$ (see Figure 6.2) such that

$$|d\Omega| = |d\Omega^{+}| + |d\Omega^{-}|. \tag{6.2}$$

After taking the limit in relation (6.2), one readily finds

$$\alpha^{+}(\mathbf{x}, t) + \alpha^{-}(\mathbf{x}, t) \equiv 1, \quad \forall (\mathbf{x}, t) \in \Omega \times [0, T]. \tag{6.3}$$

**Figure 6.1:** A quasi uniform air/water mixture after the wave breaking has occured.

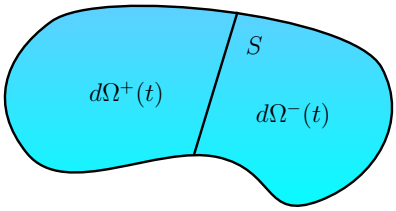


**Figure 6.2:** An elementary fluid volume $d\Omega$ occupied by two phases.

The volume fractions $\alpha^\pm$ characterize the volume occupied by the corresponding phase per unit volume of the mixture.

After applying the averaging procedure, we obtain the so-called six equations model [Ish75, SW84, GKC01, Rov06]:

$$\partial_t(\alpha^\pm\rho^\pm) + \nabla\cdot(\alpha^\pm\rho^\pm\vec{u}^\pm) = 0, \tag{6.4}$$

$$\partial_t(\alpha^\pm\rho^\pm\vec{u}^\pm) + \nabla\cdot(\alpha^\pm\rho^\pm\vec{u}^\pm\otimes\vec{u}^\pm) + \alpha^\pm\nabla p = \nabla\cdot(\alpha^\pm\boldsymbol{\tau}^\pm) + \alpha^\pm\rho^\pm\vec{g}, \tag{6.5}$$

$$\partial_t(\alpha^\pm\rho^\pm E^\pm) + \nabla\cdot(\alpha^\pm\rho^\pm H^\pm\vec{u}^\pm) + p\,\partial_t\alpha^\pm = \nabla\cdot(\alpha^\pm\boldsymbol{\tau}^\pm\vec{u}^\pm) - \nabla\cdot(\alpha^\pm\vec{q}^\pm) + \alpha^\pm\rho^\pm\vec{g}\cdot\vec{u}^\pm, \tag{6.6}$$

where $\rho^{\pm}(\mathbf{x},t)$, $\vec{u}^{\pm}(\mathbf{x},t)$, $E^{\pm}(\mathbf{x},t)$ are densities, velocities and energies of each fluid respectively. The total energy $E^{\pm}$ is the sum of the internal and kinetic energies $E^{\pm} := e^{\pm}+\frac{1}{2}|\vec{u}^{\pm}|^2$. The specific total enthalpy $H^{\pm}$ is defined as $H^{\pm} := h^{\pm} + \frac{1}{2}|\vec{u}^{\pm}|^2 = E^{\pm} + \dfrac{p}{\rho^{\pm}}$, where $h^{\pm}$ is just the specific enthalpy. Finally, $\vec{g}$ stands for the vector of the gravity acceleration.

The symbol $\boldsymbol{\tau}^{\pm}$ denotes the viscous stress tensor of each phase. If we assume both fluids to be Newtonian, the viscous stress tensor $\boldsymbol{\tau}^{\pm}$ can be written as

$$\boldsymbol{\tau}^{\pm} = \lambda^{\pm}\,\mathrm{tr}\,\mathbf{D}(\vec{u}^{\pm})\mathrm{Id} + 2\mu^{\pm}\mathbf{D}(\vec{u}^{\pm}), \quad \mathrm{tr}\,\mathbf{D}(\vec{u}^{\pm}) = \nabla\cdot\vec{u}^{\pm}, \tag{6.7}$$

where $\mathrm{Id} := (\delta_{ij})_{1\le i,j\le 3}$ is the identity tensor, $\mathbf{D}(\vec{u}) := \frac{1}{2}\Big(\nabla\vec{u} + {}^t(\nabla\vec{u})\Big)$ is the deformation rate and $\lambda^{\pm}$, $\mu^{\pm}$ are viscosity coefficients. For ideal gases, for example, these coefficients are related by Stokes relation $\lambda^{\pm}+\frac{2}{3}\mu^{\pm} = 0$. Recall that the derivation procedure presented in the next section does not require any particular form of the tensor $\boldsymbol{\tau}^{\pm}$.

Finally, the heat flux in each fluid is denoted by $\vec{q}^{\pm}$ (see Equation (6.6)). As with viscous stress tensor, we do not assume any particular form of the heat flux. However, in most cases the Fourier's law [Fou22] is adopted:

$$\vec{q}^{\pm} := -K^{\pm}\nabla T^{\pm},$$

where $K^{\pm}$ is the thermal conductivity coefficient and $T^{\pm}$ is the thermodynamic temperature.

**Remark 31.** *When a material demonstrates flagrant anisotropic properties, it is advised to use the generalized Fourier's law [IH06]:*

$$\vec{q}^{\pm} := -\mathbb{K}^{\pm}\cdot\nabla T^{\pm},$$

*where $\mathbb{K}^{\pm}$ is the conductivity tensor. The same remark applies to the viscous stress tensor $\boldsymbol{\tau}^{\pm}$ as well.*

In order to close the system (6.4) – (6.6), we have to provide two equations of state which relate the pressure $p$ to other thermodynamic variables $p = p^{\pm}(\rho^{\pm}, e^{\pm})$. We assume the equations of state to satisfy some general thermodynamic assumptions:

$$p^{\pm}(\rho^{\pm}, e^{\pm}) > 0, \quad \left.\frac{\partial p^{\pm}(\rho^{\pm}, e^{\pm})}{\partial \rho^{\pm}}\right|_{s^{\pm}} > 0, \quad \text{for} \quad \rho^{\pm} > 0. \tag{6.8}$$

The symbol $\left.\frac{\partial p^{\pm}(\rho^{\pm},e^{\pm})}{\partial\rho^{\pm}}\right|_{s^{\pm}}$ denotes the partial differentiation with respect to the density $\rho^{\pm}$ while the entropy $s^{\pm}$ is kept constant. Physically this quantity corresponds to the squared velocity of pressure waves in each fluid (see Lemma 2).

**Remark 32.** *We reiterate that the model (6.4) – (6.6) is a one pressure model, i.e. two phases share the same pressure. Models with two pressures can also be derived [SW84, BN86, BGN86, RH88, MG05]. In this situation, an extra closure (algebraic or differential) must be added. In many cases this additional closure represents a relaxation process which will tend to equilibrate the pressures.*

**Remark 33.** *The momentum balance Equation (6.5) can be rewritten differently:*

$$\partial_t(\alpha^\pm\rho^\pm\vec{u}^\pm) + \nabla\cdot\left(\alpha^\pm\rho^\pm\vec{u}^\pm\otimes\vec{u}^\pm + \alpha^\pm p\mathrm{Id}\right) - p\nabla\alpha^\pm = \nabla\cdot(\alpha^\pm\boldsymbol{\tau}^\pm) + \alpha^\pm\rho^\pm\vec{g}. \tag{6.9}$$

*These two forms are obviously equivalent for smooth solutions. However, it is not the case for discontinuous ones. We believe that this form is more relevant from physical point of view, since the flux of momentum involves the pressure. In our analytical investigations we consider smooth solutions, however for numerics we advise using the last form (6.9).*

**Remark 34.** *While considering two-phase flows, it is useful to introduce several additional quantities which play an important rôle in the description of such flows. The mixture density $\rho$ and mass fractions $m^\pm$ are naturally defined as*

$$\rho(\mathbf{x},t) := \alpha^+\rho^+ + \alpha^-\rho^- > 0, \quad \forall(\mathbf{x},t)\in\Omega\times[0,T], \tag{6.10}$$

$$m^\pm := \frac{\alpha^\pm\rho^\pm}{\rho}, \quad \textit{consequently} \quad m^+ + m^- = 1.$$

*The total density $\rho$ is assumed to be strictly positive everywhere in the domain $\Omega$. Hence, the void creation is forbidden in our modeling paradigm. Important quantities $\rho$, $m^\pm$ will appear several times below.*

The six-equations two-phase model presented in this section contains some other simplifications. Namely, we neglect capillarity effects which could be taken into account in the form of the Korteweg term [Kor01, BDGG09]. Moreover, terms modeling mass, momentum and energy exchange between the phases are neglected as well. In general, their form depends strongly on the flow regime under consideration and is a subject of current debates.

**Remark 35.** *Even if the Jacobian matrix of the advection operator in (6.4) – (6.6) is not diagonalizable over $\mathbb{R}$, the existence of global weak solutions was recently proven at least in barotropic case [BDGG09] if we supplement the model by viscous and surface tension effects [Kor01]. Previously, it was already shown that viscosity and thermal diffusivity are indeed sufficient for the evolution problem well-posedness in the linearized or in the nonlinear sense for small data [Ara80, Ram00].*

Despite recent advances in numerical methods [GKC96, GKC01, Rov06] and several simplifications made above, the system (6.4) – (6.6) is still very complex to solve numerically for industrial scale problems. One of the main difficulties lies in the advection operator which is known to be generally non-hyperbolic. In the next section we will derive a simplified two-phase model which has fewer variables and possesses the requested hyperbolic structure for quite general equations of state.

### 6.1.3 Relaxation process

In this section we will supplement momentum and energy conservation Equations (6.5), (6.6) by relaxation terms. Physically, they represent the friction or drag force between two phases. When time evolves, this mechanism will ensure the convergence of two velocities $\vec{u}^{\pm}$ and energies $E^{\pm}$ to common for both phases values $\vec{u}$ and $E$. Augmented Equations (6.5), (6.6) take the following form:

$$\partial_t(\alpha^{\pm}\rho^{\pm}\vec{u}^{\pm}) + \nabla\cdot(\alpha^{\pm}\rho^{\pm}\vec{u}^{\pm}\otimes\vec{u}^{\pm}) + \alpha^{\pm}\nabla p = \nabla\cdot(\alpha^{\pm}\boldsymbol{\tau}^{\pm}) + \alpha^{\pm}\rho^{\pm}\vec{g} \pm \vec{F}_d, \tag{6.11}$$

$$\partial_t(\alpha^{\pm}\rho^{\pm}E^{\pm}) + \nabla\cdot(\alpha^{\pm}\rho^{\pm}H^{\pm}\vec{u}^{\pm}) + p\,\partial_t\alpha^{\pm} = \nabla\cdot(\alpha^{\pm}\boldsymbol{\tau}^{\pm}\vec{u}^{\pm}) - \nabla\cdot(\alpha^{\pm}\vec{q}^{\pm}) + \alpha^{\pm}\rho^{\pm}\vec{g}\cdot\vec{u}^{\pm} \pm E_d. \tag{6.12}$$

In the present study we choose friction terms $\vec{F}_d$ and $E_d$ in this form:

$$\vec{F}_d := \frac{\kappa}{\varepsilon}\frac{\alpha^-\rho^-\alpha^+\rho^+}{\alpha^+\rho^+ + \alpha^-\rho^-}(\vec{u}^+ - \vec{u}^-), \quad E_d := \frac{\kappa}{\varepsilon}\frac{\alpha^-\rho^-\alpha^+\rho^+}{\alpha^+\rho^+ + \alpha^-\rho^-}\vec{u}\cdot(\vec{u}^+ - \vec{u}^-),$$

where $\vec{u} := m^+\vec{u}^+ + m^-\vec{u}^-$ is the barycentric velocity, $\kappa = \mathcal{O}(1)$ is a dimensionless constant and $\varepsilon$ is a small parameter which controls the magnitude of the relaxation term. Physically it represents the characteristic relaxation time. In the following we are going to take the singular limit as the relaxation parameter $\varepsilon \to 0$. This goal is achieved with a Chapman-Enskog type expansion [CC95].

This kind of computations has already been successfully carried out for the Baer-Nunziato model [BN86]. In this section we follow in great lines the work of Guillard & Murrone [MG05]. However, the computation details are substantially different.

The first step consists in rewriting the governing Equations (6.4), (6.11), (6.12) in quasilinear form. To shorten the notation, we will also use the material derivative which is classically defined for any smooth scalar function $\phi(\mathbf{x}, t)$ as

$$\frac{d^{\pm}\phi}{dt} := \frac{\partial\phi}{\partial t} + \vec{u}^{\pm}\cdot\nabla\phi.$$

In computations below, we will need the following technical lemma:

**Lemma 2.** *Consider two compressible fluids with general equations of state $p = p^{\pm}(\rho^{\pm}, e^{\pm})$. Then, partial derivatives of pressure $p$ are given by:*

$$\left.\frac{\partial p}{\partial s^{\pm}}\right|_{\rho^{\pm}} = \frac{T^{\pm}}{\theta^{\pm}}, \qquad \left.\frac{\partial p}{\partial \rho^{\pm}}\right|_{s^{\pm}} \equiv (c_s^{\pm})^2 = \frac{1}{\theta^{\pm}}\Big(\frac{p}{(\rho^{\pm})^2} - \chi^{\pm}\Big),$$

*where $s^{\pm}$, $c_s^{\pm}$ are the entropy and the sound velocity in the phase $\pm$ respectively. We also denote by $\chi^{\pm} := \left.\frac{\partial e^{\pm}}{\partial \rho^{\pm}}\right|_p$ and by $\theta^{\pm} := \left.\frac{\partial e^{\pm}}{\partial p}\right|_{\rho^{\pm}}$.*

*Proof.* Obviously, one can write:

$$dp = \left.\frac{\partial p}{\partial \rho^{\pm}}\right|_{s^{\pm}} d\rho^{\pm} + \left.\frac{\partial p}{\partial s^{\pm}}\right|_{\rho^{\pm}} ds^{\pm}. \tag{6.13}$$

Similarly, if one takes into account the definitions of $\chi^{\pm}$ and $\theta^{\pm}$:

$$de^{\pm} = \chi^{\pm} d\rho^{\pm} + \theta^{\pm} dp. \tag{6.14}$$

Now we will use the Gibbs relation [Ish75, Cal85, IH06]:

$$de^{\pm} = T^{\pm} ds^{\pm} + \frac{p}{(\rho^{\pm})^2} d\rho^{\pm}. \tag{6.15}$$

After expanding $de^{\pm}$ and $dp$ according to (6.14), (6.13) correspondingly, we get the following differential inequality:

$$\Big(\frac{p}{(\rho^{\pm})^2} - \chi^{\pm} - \theta^{\pm} \left.\frac{\partial p}{\partial \rho^{\pm}}\right|_{s^{\pm}}\Big) d\rho^{\pm} + \Big(T^{\pm} - \theta^{\pm} \left.\frac{\partial p}{\partial s^{\pm}}\right|_{\rho^{\pm}}\Big) ds^{\pm} = 0.$$

Since this equality must be true for arbitrary $de^{\pm}$ and $dp$, we conclude the proof by requiring the coefficients to be equal to zero. □

**Theorem 4.** *Smooth solutions to Equations (6.4), (6.11), (6.12) satisfy the following system:*

$$\alpha^{\pm}\rho^{\pm}T^{\pm}\frac{d^{\pm}s^{\pm}}{dt} = \alpha^{\pm}\boldsymbol{\tau}^{\pm} : \nabla\vec{u}^{\pm} - \nabla\cdot(\alpha^{\pm}\vec{q}^{\pm}) \pm (E_d - \vec{F}_d\cdot\vec{u}^{\pm}), \tag{6.16}$$

$$\alpha^{\pm}\rho^{\pm}\frac{d^{\pm}\vec{u}^{\pm}}{dt} + \alpha^{\pm}\nabla p = \nabla\cdot(\alpha^{\pm}\boldsymbol{\tau}^{\pm}) + \alpha^{\pm}\rho^{\pm}\vec{g} \pm \vec{F}_d, \tag{6.17}$$

$$\alpha^{\pm}\rho^{\pm}\theta^{\pm}\frac{d^{\pm}p}{dt} \pm (\rho^{\pm})^2(c_s^{\pm})^2\theta^{\pm}(\partial_t\alpha^{+} \pm \nabla\cdot(\alpha^{\pm}\vec{u}^{\pm})) = \alpha^{\pm}\boldsymbol{\tau}^{\pm} : \nabla\vec{u}^{\pm} - \nabla\cdot(\alpha^{\pm}\vec{q}^{\pm}) \pm (E_d - \vec{F}_d\cdot\vec{u}^{\pm}), \tag{6.18}$$

*where $s^{\pm}$ is the entropy, $(c_s^{\pm})^2$ and $\theta^{\pm}$ are defined in Lemma 2.*

*Proof.* The mass conservation Equation (6.4) is straightforwardly rewritten using the material derivative:

$$\frac{d^{\pm}(\alpha^{\pm}\rho^{\pm})}{dt} + \alpha^{\pm}\rho^{\pm}\nabla\cdot\vec{u}^{\pm} = 0. \tag{6.19}$$

If we multiply the latter by $\vec{u}^{\pm}$ and subtract the result from (6.11), we will obtain announced above Equation (6.17). Similarly, multiplying Equation (6.19) by $E^{\pm}$ and subtracting it from (6.12) leads to the total energy equation in quasilinear form:

$$\alpha^{\pm}\rho^{\pm}\frac{d^{\pm}E^{\pm}}{dt} + \nabla\cdot(\alpha^{\pm}p\vec{u}^{\pm}) + p\alpha_t^{\pm} = \nabla\cdot(\alpha^{\pm}\boldsymbol{\tau}^{\pm}\vec{u}^{\pm}) - \nabla\cdot(\alpha^{\pm}\vec{q}^{\pm}) + \alpha^{\pm}\rho^{\pm}\vec{g}\cdot\vec{u}^{\pm} \pm E_d. \tag{6.20}$$

The kinetic energy evolution equation is straightforwardly obtained after taking the scalar product of (6.17) with $\vec{u}^{\pm}$:

$$\alpha^{\pm}\rho^{\pm}\frac{d^{\pm}(\frac{1}{2}|\vec{u}^{\pm}|^2)}{dt} + \alpha^{\pm}\vec{u}^{\pm}\cdot\nabla p = \vec{u}^{\pm}\cdot\nabla\cdot(\alpha^{\pm}\boldsymbol{\tau}^{\pm}) + \alpha^{\pm}\rho^{\pm}\vec{g}\cdot\vec{u}^{\pm} \pm \vec{F}_d\cdot\vec{u}^{\pm}. \tag{6.21}$$

Recall that the total energy $E^{\pm}$ is constituted of internal and kinetic energies: $E^{\pm} = e^{\pm} + \frac{1}{2}|\vec{u}^{\pm}|^2$. Consequently, the internal energy evolution equation is derived by subtracting (6.21) from (6.20):

$$\alpha^{\pm}\rho^{\pm}\frac{d^{\pm}e^{\pm}}{dt} + p\nabla\cdot(\alpha^{\pm}\vec{u}^{\pm}) + p\alpha_t^{\pm} = \alpha^{\pm}\boldsymbol{\tau}^{\pm} : \nabla\vec{u}^{\pm} - \nabla\cdot(\alpha^{\pm}\vec{q}^{\pm}) \pm (E_d - \vec{F}_d\cdot\vec{u}^{\pm}). \tag{6.22}$$

In order to introduce the entropy variable $s^{\pm}$ into our considerations, we will make use of the Gibbs relation. After multiplying (6.15) by $\alpha^{\pm}\rho^{\pm}$ and passing to the material derivative, one gets:

$$\alpha^{\pm}\rho^{\pm}T^{\pm}\frac{d^{\pm}s^{\pm}}{dt} = \alpha^{\pm}\rho^{\pm}\frac{d^{\pm}e^{\pm}}{dt} - \frac{\alpha^{\pm}p}{\rho^{\pm}}\frac{d^{\pm}\rho^{\pm}}{dt}.$$

Substituting (6.22) into the last relation and taking into account (6.19), leads to the requested entropy Equation (6.16).

From lemma 2 we directly obtain the following equality:

$$\alpha^{\pm}\rho^{\pm}\theta^{\pm}\frac{d^{\pm}p}{dt} = \alpha^{\pm}\rho^{\pm}\Big(\frac{p}{(\rho^{\pm})^2} - \chi^{\pm}\Big)\frac{d^{\pm}\rho^{\pm}}{dt} + \alpha^{\pm}\rho^{\pm}T^{\pm}\frac{d^{\pm}s^{\pm}}{dt}.$$

After substituting (6.16) and replacing $\big(\frac{p}{(\rho^{\pm})^2} - \chi^{\pm}\big)$ by $\theta^{\pm}(c_s^{\pm})^2$, we obtain (6.18) and the proof is completed. □

Computations that we will perform below will be clearer if the governing Equations (6.16) – (6.18) are recast in the vectorial form:

$$\mathbf{A}(V_\varepsilon)\frac{\partial V_\varepsilon}{\partial t} + \mathbf{B}(V_\varepsilon)\nabla V_\varepsilon = \nabla\cdot\mathbf{T}(V_\varepsilon) + \mathbf{S}(V_\varepsilon) + \frac{\mathbf{R}(V_\varepsilon)}{\epsilon}, \tag{6.23}$$

where we introduced several notations. The vector $V_\varepsilon$ represents six unknown physical variables $V_\varepsilon := {}^t(s^+, s^-, \vec{u}^+, \vec{u}^-, p, \alpha^+)$ and $\frac{\partial V_\varepsilon}{\partial t}$ is the componentwise partial time derivative. Symbol $\nabla V_\varepsilon$ denotes this vector:

$$\nabla V_\varepsilon := {}^t\big(\nabla s^+, \nabla s^-, (\cdot\nabla)\vec{u}^+, (\cdot\nabla)\vec{u}^-, \nabla p, \nabla\alpha^+\big).$$

Matrices $\mathbf{A}(V_\varepsilon)$ and $\mathbf{B}(V_\varepsilon)$ are defined as

$$\mathbf{A}(V_\varepsilon) := \begin{pmatrix} a_T^+ & 0 & 0 & 0 & 0 & 0 \\ 0 & a_T^- & 0 & 0 & 0 & 0 \\ 0 & 0 & \alpha^+\rho^+\mathrm{Id} & 0 & 0 & 0 \\ 0 & 0 & 0 & \alpha^-\rho^-\mathrm{Id} & 0 & 0 \\ 0 & 0 & 0 & 0 & a_\theta^+ & p_\theta^+ \\ 0 & 0 & 0 & 0 & a_\theta^- & -p_\theta^- \end{pmatrix}$$

$$\mathbf{B}(V_\varepsilon) := \begin{pmatrix} a_T^+\vec{u}^+ & 0 & 0 & 0 & 0 & 0 \\ 0 & a_T^-\vec{u}^- & 0 & 0 & 0 & 0 \\ 0 & 0 & \alpha^+\rho^+\vec{u}^+ & 0 & \alpha^+\mathrm{Id} & 0 \\ 0 & 0 & 0 & \alpha^-\rho^-\vec{u}^- & \alpha^-\mathrm{Id} & 0 \\ 0 & 0 & \alpha^+p_\theta^+\mathrm{Id} & 0 & a_\theta^+\vec{u}^+ & p_\theta^+\vec{u}^+ \\ 0 & 0 & 0 & \alpha^-p_\theta^-\mathrm{Id} & a_\theta^-\vec{u}^- & -p_\theta^-\vec{u}^- \end{pmatrix},$$

where several symbols were introduced to shorten the notation:

$$p_\theta^\pm := (\rho^\pm)^2(c_s^\pm)^2\theta^\pm, \quad a_T^\pm := \alpha^\pm\rho^\pm T^\pm, \quad a_\theta^\pm := \alpha^\pm\rho^\pm\theta^\pm.$$

In these matrix notations the size of zero entries must be chosen to make the multiplication operation possible.

On the right hand side of (6.23), the work of viscous forces is denoted by symbol $\nabla\cdot\mathbf{T}(V_\varepsilon)$ which is defined as

$$\begin{aligned}\nabla\cdot\mathbf{T}(V_\varepsilon) := {}^t(&\alpha^+\boldsymbol{\tau}^+ : \nabla\vec{u}^+ - \nabla\cdot(\alpha^+\vec{q}^+), \alpha^-\boldsymbol{\tau}^- : \nabla\vec{u}^- - \nabla\cdot(\alpha^-\vec{q}^-),\\ &\nabla\cdot(\alpha^+\boldsymbol{\tau}^+), \nabla\cdot(\alpha^-\boldsymbol{\tau}^-), \alpha^+\boldsymbol{\tau}^+ : \nabla\vec{u}^+ - \nabla\cdot(\alpha^+\vec{q}^+), \alpha^-\boldsymbol{\tau}^- : \nabla\vec{u}^- - \nabla\cdot(\alpha^-\vec{q}^-)).\end{aligned}$$

The source term $\mathbf{S}(V_\varepsilon) := {}^t(0, 0, \alpha^+\rho^+\vec{g}, \alpha^-\rho^-\vec{g}, 0, 0)$ incorporates the gravity force and $\mathbf{R}(V_\varepsilon)$ contains the relaxation terms:

$$\begin{aligned}\mathbf{R}(V_\varepsilon) := \kappa\frac{\alpha^+\rho^+\alpha^-\rho^-}{\alpha^+\rho^+ + \alpha^-\rho^-}\,{}^t\Big(&\vec{u} - \vec{u}^+, -(\vec{u} - \vec{u}^-),\\ &1, -1, \vec{u} - \vec{u}^+, -(\vec{u} - \vec{u}^-)\Big) \times (\vec{u}^+ - \vec{u}^-).\end{aligned}$$

Since we expect the limit $V_\varepsilon \to V$ to be finite as $\varepsilon \to 0$, necessary the limiting vector $V$ lies in the hypersurface $\mathbf{R}(V) = 0$. In terms of physical variables, it implies $\vec{u} = \vec{u}^+ = \vec{u}^-$. Consequently, we find our solution in the form of the following Chapman-Enskog type expansion [CC95]:

$$V_\varepsilon = V + \varepsilon W + \mathcal{O}(\varepsilon^2).$$

After substituting this expansion into (6.23) and taking into account the fact that $\mathbf{R}(V) \equiv 0$, at the leading order in $\epsilon$ one obtains:

$$\mathbf{A}(V)\frac{\partial V}{\partial t} + \mathbf{B}(V)\nabla V = \nabla \cdot \mathbf{T}(V) + \mathbf{S}(V) + \mathbf{R}'(V)W, \tag{6.24}$$

where

$$\mathbf{R}'(V) := \kappa \frac{\alpha^+\rho^+\alpha^-\rho^-}{\alpha^+\rho^+ + \alpha^-\rho^-} \begin{pmatrix} 0 & 0 & 0 & 0 & 0 & 0 \\ 0 & 0 & 0 & 0 & 0 & 0 \\ 0 & 0 & \mathrm{Id} & -\mathrm{Id} & 0 & 0 \\ 0 & 0 & -\mathrm{Id} & \mathrm{Id} & 0 & 0 \\ 0 & 0 & 0 & 0 & 0 & 0 \\ 0 & 0 & 0 & 0 & 0 & 0 \end{pmatrix}$$

Henceforth, we make a technical assumption of the presence of both phases in any point $\mathbf{x} \in \Omega$ of the flow domain. Mathematically it means that $0 < \alpha^+ < 1$. Since $\alpha^+ + \alpha^- = 1$, obviously the same inequality holds for $\alpha^-$. Otherwise, the relaxation process physically does not make sense and we will have some mathematical technical difficulties.

Under the aforementioned assumption, the matrix $\mathbf{A}(V)$ is invertible. Hence, we can multiply on the left both sides of (6.24) by $\mathbf{P}\mathbf{A}^{-1}(V)$ where the projection matrix $\mathbf{P}$ is to be specified below:

$$\mathbf{P}\frac{\partial V}{\partial t} + \mathbf{P}\mathbf{A}^{-1}(V)\mathbf{B}(V)\nabla V = \mathbf{P}\mathbf{A}^{-1}(V)\nabla \cdot \mathbf{T}(V) + \mathbf{P}\tilde{\mathbf{R}}'(V)W + \mathbf{P}\mathbf{A}^{-1}(V)\mathbf{S}(V), \tag{6.25}$$

where $\tilde{\mathbf{R}}'(V) := \mathbf{A}^{-1}(V)\mathbf{R}'(V)$ and has the following components

$$\tilde{\mathbf{R}}'(V) = \kappa \frac{\alpha^+\rho^+\alpha^-\rho^-}{\alpha^+\rho^+ + \alpha^-\rho^-} \begin{pmatrix} 0 & 0 & 0 & 0 & 0 & 0 \\ 0 & 0 & 0 & 0 & 0 & 0 \\ 0 & 0 & \dfrac{1}{\alpha^+\rho^+}\mathrm{Id} & -\dfrac{1}{\alpha^+\rho^+}\mathrm{Id} & 0 & 0 \\ 0 & 0 & -\dfrac{1}{\alpha^-\rho^-}\mathrm{Id} & \dfrac{1}{\alpha^-\rho^-}\mathrm{Id} & 0 & 0 \\ 0 & 0 & 0 & 0 & 0 & 0 \\ 0 & 0 & 0 & 0 & 0 & 0 \end{pmatrix}$$

The vector of physical variables $V$ has six components (in 1D):

$$V = {}^t(s^+, s^-, \vec{u}, \vec{u}, p, \alpha^+)$$

and only five are different. In order to remove the redundant information, we will introduce the new vector $U$ defined as $U := {}^t(s^+, s^-, \vec{u}, p, \alpha^+)$. The Jacobian matrix of this transformation can be easily computed:

$$\mathbf{J} := \frac{\partial V}{\partial U} = \begin{pmatrix} 1 & 0 & 0 & 0 & 0 \\ 0 & 1 & 0 & 0 & 0 \\ 0 & 0 & \mathrm{Id} & 0 & 0 \\ 0 & 0 & \mathrm{Id} & 0 & 0 \\ 0 & 0 & 0 & 1 & 0 \\ 0 & 0 & 0 & 0 & 1 \end{pmatrix}.$$

In new variables Equation (6.25) becomes:

$$\mathbf{P}\mathbf{J}\frac{\partial U}{\partial t} + \mathbf{P}\mathbf{A}^{-1}(U)\mathbf{B}(U)\mathbf{J}\nabla U = \mathbf{P}\mathbf{A}^{-1}(U)\nabla\cdot\mathbf{T}(U) + \mathbf{P}\tilde{\mathbf{R}}'(U)W + \mathbf{P}\mathbf{A}^{-1}(U)\mathbf{S}(U). \quad (6.26)$$

Now we can formulate two conditions to construct the matrix $\mathbf{P}$. First of all, the vector $W$ is unknown and we need to remove it from Equation (6.26). Hence, we require $\mathbf{P}\tilde{\mathbf{R}}'(V) = 0$. Then, we would like the governing equations to be explicitly resolved with respect to time derivatives. It gives us the second condition $\mathbf{P}\mathbf{J} = \mathrm{Id}$. The existence and effective construction of the matrix $\mathbf{P}$ satisfying two aforementioned conditions

$$\mathbf{P}\tilde{\mathbf{R}}'(V) = 0, \quad \mathbf{P}\mathbf{J} = \mathrm{Id},$$

are discussed below. Presented in this section results follow in great lines [MG05].

We will consider a slightly more general setting. Let be vector $V \in \mathbb{R}^n$ and its reduced counterpart $U \in \mathbb{R}^{n-k}$, $k < n$. In such geometry, $\tilde{\mathbf{R}}'(V) \in \mathrm{Mat}_{n,n}(\mathbb{R})$, $\mathbf{J} \in \mathrm{Mat}_{n,n-k}(\mathbb{R})$ and, consequently, $\mathbf{P} \in \mathrm{Mat}_{n-k,n}(\mathbb{R})$. Here, the notation $\mathrm{Mat}_{m,n}(\mathbb{R})$ denotes the set of $m \times n$ matrices with coefficients in $\mathbb{R}$. We have to say also that from algebraic point of view, matrices $\tilde{\mathbf{R}}'(V)$ and $\mathbf{R}'(V)$ are completely equivalent. Thus, for the sake of simplicity, the following propositions will be formulated in terms of the matrix $\mathbf{R}'(V)$.

**Lemma 3.** *The columns of the Jacobian matrix* $\mathbf{J}$ *form a basis of* $\ker\big(\mathbf{R}'(V)\big)$.

*Proof.* If we differentiate the relation $\mathbf{R}(V) = 0$ with respect to $U$, we will get the identity $\mathbf{R}'(V)\mathbf{J} = 0$. It implies that $\mathrm{range}\big(\mathbf{J}\big) \subseteq \ker\big(\mathbf{R}'(V)\big)$. By direct computation one verifies that $\dim \mathrm{range}\big(\mathbf{R}'(V)\big) = k$. From the well-known identity $\mathrm{range}\big(\mathbf{R}'(V)\big) \oplus \ker\big(\mathbf{R}'(V)\big) = \mathbb{R}^n$, one concludes that $\dim\ker\big(\mathbf{R}'(V)\big) = n - k$. But in the same time, the rank of $\mathbf{J}$ is equal to $n - k$ as well. It proves the result. □

**Theorem 5.** *We suppose that for all* $V$, $\mathrm{range}\big(\mathbf{R}'(V)\big) \cap \ker\big(\mathbf{R}'(V)\big) = \{0\}$ *then there exists a matrix* $\mathbf{P} \in \mathrm{Mat}_{n-k,n}(\mathbb{R})$ *such that* $\mathbf{P}\mathbf{R}'(V) = 0$ *and* $\mathbf{P}\mathbf{J} = \mathrm{Id}_{n-k}$.

*Proof.* Assumption $\mathrm{range}\big(\mathbf{R}'(V)\big) \cap \ker\big(\mathbf{R}'(V)\big) = \{0\}$ implies that

$$\mathrm{range}\big(\mathbf{R}'(V)\big) \oplus \ker\big(\mathbf{R}'(V)\big) = \mathbb{R}^n.$$

From Lemma 3 it follows that $\mathrm{range}\big(\mathbf{J}\big) = \ker\big(\mathbf{R}'(V)\big)$. Thus, the space $\mathbb{R}^n$ can be also represented as a direct sum $\mathrm{range}\big(\mathbf{R}'(V)\big) \oplus \mathrm{range}\big(\mathbf{J}\big)$. We will define $\mathbf{P}$ to be the projection on $\ker\big(\mathbf{R}'(V)\big) \equiv \mathrm{range}\big(\mathbf{J}\big)$. Since obviously $\mathbf{R}'(V) \in \mathrm{range}\big(\mathbf{R}'(V)\big)$ and $\mathbf{J} \in \mathrm{range}\big(\mathbf{J}\big)$, we have two required identities: $\mathbf{PJ} = \mathrm{Id}_{n-k}$ and $\mathbf{PR}'(V) = 0$. □

Now, in order to compute effectively the projection matrix $\mathbf{P}$, we will construct an auxiliary matrix $\mathbf{D}(V) = [J^1, \ldots, J^{n-k}, I^1, \ldots, I^k]$, where $J^i$ is the column $i$ of the matrix $\mathbf{J}$ and $\{I^1, \ldots, I^k\}$ are vectors which form a basis of $\mathrm{range}\big(\mathbf{R}'(V)\big)$. We remark that $\mathbf{PD}(V) = [\mathrm{Id}_{n-k}, 0]$. Lemma 3 implies that the matrix $\mathbf{D}(V)$ is invertible. Thus, the projection $\mathbf{P}$ can be computed by inverting $\mathbf{D}(V)$:

$$\mathbf{P} = [\mathrm{Id}_{n-k}, 0] \cdot \mathbf{D}^{-1}(V). \tag{6.27}$$

Let us apply this general framework to our model (6.25), where $n = 6$ and $k = 1$. The matrix $\mathbf{D}(V)$ and its inverse $\mathbf{D}^{-1}(V)$ take this form:

$$\mathbf{D}(V) = \begin{pmatrix} 1 & 0 & 0 & 0 & 0 & 0 \\ 0 & 1 & 0 & 0 & 0 & 0 \\ 0 & 0 & \mathrm{Id} & 0 & 0 & m^-\mathrm{Id} \\ 0 & 0 & \mathrm{Id} & 0 & 0 & -m^+\mathrm{Id} \\ 0 & 0 & 0 & 1 & 0 & 0 \\ 0 & 0 & 0 & 0 & 1 & 0 \end{pmatrix}, \quad \mathbf{D}^{-1}(V) = \begin{pmatrix} 1 & 0 & 0 & 0 & 0 & 0 \\ 0 & 1 & 0 & 0 & 0 & 0 \\ 0 & 0 & m^+\mathrm{Id} & m^-\mathrm{Id} & 0 & 0 \\ 0 & 0 & 0 & 0 & 1 & 0 \\ 0 & 0 & 0 & 0 & 0 & 1 \\ 0 & 0 & \mathrm{Id} & -\mathrm{Id} & 0 & 0 \end{pmatrix},$$

where $m^\pm$ are mass fractions defined in Remark 34.

Now, the projection matrix $\mathbf{P}$ can be immediately computed by (6.27):

$$\mathbf{P} = \begin{pmatrix} 1 & 0 & 0 & 0 & 0 & 0 \\ 0 & 1 & 0 & 0 & 0 & 0 \\ 0 & 0 & m^+\mathrm{Id} & m^-\mathrm{Id} & 0 & 0 \\ 0 & 0 & 0 & 0 & 1 & 0 \\ 0 & 0 & 0 & 0 & 0 & 1 \end{pmatrix}.$$

Finally, after computing all matrix products $\mathbf{P}\mathbb{A}^{-1}(U)\mathbf{B}(U)\mathbf{J}$, $\mathbf{P}\mathbb{A}^{-1}(U)\nabla\cdot\mathbf{T}(U)$, $\mathbf{P}\mathbb{A}^{-1}(U)\mathbf{S}(U)$ present in Equation (6.26), we obtain the following model:

$$\alpha^\pm\rho^\pm T^\pm \frac{ds^\pm}{dt} = \alpha^\pm \boldsymbol{\tau}^\pm : \nabla\vec{u}^\pm - \nabla\cdot(\alpha^\pm\vec{q}^\pm), \tag{6.28}$$

$$\rho\frac{d\vec{u}}{dt} + \nabla p = \rho\vec{g} + \nabla\cdot\boldsymbol{\tau}, \tag{6.29}$$

$$\Pi\Big(\frac{dp}{dt}+\rho c_s^2\nabla\cdot\vec{u}\Big)=\frac{\rho^-(c_s^-)^2}{\theta^+\rho^+}\big(\alpha^+\boldsymbol{\tau}^+:\nabla\vec{u}-\nabla\cdot(\alpha^+\vec{q}^+)\big)$$
$$+\frac{\rho^+(c_s^+)^2}{\theta^-\rho^-}\big(\alpha^-\boldsymbol{\tau}^-:\nabla\vec{u}-\nabla\cdot(\alpha^-\vec{q}^-)\big),\quad(6.30)$$

$$\Pi\Big(\frac{d\alpha^+}{dt}+\alpha^+\alpha^-\delta\nabla\cdot\vec{u}\Big)=\frac{\alpha^-}{\theta^+\rho^+}\big(\alpha^+\boldsymbol{\tau}^+:\nabla\vec{u}-\nabla\cdot(\alpha^+\vec{q}^+)\big)$$
$$-\frac{\alpha^+}{\theta^-\rho^-}\big(\alpha^-\boldsymbol{\tau}^-:\nabla\vec{u}-\nabla\cdot(\alpha^-\vec{q}^-)\big),\quad(6.31)$$

where $\rho=\alpha^+\rho^++\alpha^-\rho^-$ is the mixture density (6.10), $c_s^2$ physically is the sound velocity in the mixture:

$$\Pi\rho c_s^2:=\rho^+(c_s^+)^2\rho^-(c_s^-)^2.\quad(6.32)$$

To shorten the notation, we also introduced a quantity $\delta$ defined by

$$\Pi\delta:=\rho^+(c_s^+)^2-\rho^-(c_s^-)^2\quad(6.33)$$

and $\Pi:=\alpha^-\rho^+(c_s^+)^2+\alpha^+\rho^-(c_s^-)^2$.

The viscous stress tensor of the mixture is defined as $\boldsymbol{\tau}:=\alpha^+\boldsymbol{\tau}^++\alpha^-\boldsymbol{\tau}^-$. If both fluids are assumed to be Newtonian (6.7), we can express it in closed form:

$$\boldsymbol{\tau}:=\lambda\operatorname{tr}\mathbf{D}(\vec{u})\mathrm{Id}+2\mu\mathbf{D}(\vec{u}),\quad\lambda:=\alpha^+\lambda^++\alpha^-\lambda^-,\quad\mu:=\alpha^+\mu^++\alpha^-\mu^-.$$

Similarly, the thermal flux $\vec{q}$ in the mixture is given by this formula:

$$\vec{q}:=\alpha^+\vec{q}^++\alpha^-\vec{q}^-.$$

For practical computations it is better to rewrite Equations (6.28) – (6.31) in conservative form [Lax73, GR96] which is valid for discontinuous solutions as well. After repeating in inverse sense computations from Theorem (4) one obtains the following system:

$$\partial_t(\alpha^\pm\rho^\pm)+\nabla\cdot(\alpha^\pm\rho^\pm\vec{u})=0,\quad(6.34)$$
$$\partial_t(\rho\vec{u})+\nabla\cdot(\rho\vec{u}\otimes\vec{u}+p\mathrm{Id})=\rho\vec{g}+\nabla\cdot\boldsymbol{\tau},\quad(6.35)$$
$$\partial_t(\rho E)+\nabla\cdot(\rho H\vec{u})=\rho\vec{u}\cdot\vec{g}+\nabla\cdot(\boldsymbol{\tau}\vec{u})-\nabla\cdot\vec{q}.\quad(6.36)$$

If we neglect viscous stress $\boldsymbol{\tau}$ and thermal flux $\vec{q}$, we will obtain the so-called four equations model recently proposed by F. Dias, D. Dutykh and J.-M. Ghidaglia [Dut07, DDG08c, DDG10, DDG08b] for simulation of violent aerated flows. Formal computations presented in this study can be considered as a step towards justification of the four equations model. It can be also shown [DDG10], that the advection operator of Equations (6.34) – (6.36) is hyperbolic for quite general equations of state (6.8). Hence, derived here four equations model is very attractive from modeling and computational point of view.

### 6.1.4 Invariant regions

Consider only the hyperbolic part of the system (6.34) – (6.36) together with source terms due to gravity:

$$\partial_t(\alpha^\pm\rho^\pm) + \nabla\cdot(\alpha^\pm\rho^\pm\vec{u}) = 0, \tag{6.37}$$

$$\partial_t(\rho\vec{u}) + \nabla\cdot(\rho\vec{u}\otimes\vec{u} + p\mathrm{Id}) = \rho\vec{g}, \tag{6.38}$$

$$\partial_t(\rho E) + \nabla\cdot(\rho H\vec{u}) = \rho\vec{u}\cdot\vec{g}. \tag{6.39}$$

In this section we would like to study the preservation of invariant regions under the dynamics of the system (6.37) – (6.39). This property is very important in practice for stability of computations. Namely, from physical sense and from definition (6.1) of volume fractions $\alpha^\pm$ it follows that $0 \le \alpha^\pm \le 1$, $\forall(\mathbf{x},t) \in \Omega\times[0,T]$. The question we address here is whether the region $0 \le \alpha^\pm \le 1$ remains invariant under the system (6.37) – (6.39) dynamics. This property can be checked only for $\alpha^+$, for example, since $\alpha^+ + \alpha^- = 1$. If the answer is negative, the model can be hardly applied to any practical situation. Positive result was already proved for a barotropic model with two velocities in [BDGG09]. In the same work of Bresch et al. (2009) it was also shown that two-phase mixtures of compressible/incompressible fluids do not preserve the invariant regions.

The notion of invariant regions is due to Chueh, Conley and Smoller [CCS77]. Independently it was also introduced by Weinberger [Wei75] for scalar parabolic equations.

In order to handle this problem, it is more convenient to rewrite Equations (6.37) – (6.39) in terms of the so-called physical variables $W =^t (\vec{u}, p, \alpha^+, s)$. The derivation of the equation for the velocity $\vec{u}$ evolution is straightforward. Equations for thermodynamical variables $p$, $\alpha^+$ and $s$ are trickier to obtain. However, it was already done in [DDG08b, DDG10] and partially above (see Equations (6.28) – (6.31)):

**Lemma 4.** *Smooth solutions to Equations (6.37) – (6.39) satisfy the following quasilinear system:*

$$\partial_t\vec{u} + \vec{u}\cdot\nabla\vec{u} + \frac{\nabla p}{\rho} = \vec{g}, \tag{6.40}$$

$$\partial_t p + \vec{u}\cdot\nabla p + \rho c_s^2\nabla\cdot\vec{u} = 0, \tag{6.41}$$

$$\partial_t\alpha^+ + \vec{u}\cdot\nabla\alpha^+ + \alpha^+\alpha^-\delta\nabla\cdot\vec{u} = 0, \tag{6.42}$$

$$\partial_t s + \vec{u}\cdot\nabla s = 0, \tag{6.43}$$

*where $\rho c_s^2$ and $\delta$ are defined in (6.32) and (6.33) respectively.*

*Proof.* For the proof see, for example, Dias et al. (2009) [DDG10] where the authors worked with an auxiliary variable $\alpha := \alpha^+ - \alpha^-$. Taking into account the relation $\alpha^+ + \alpha^- = 1$,

one can express the volume fractions in terms of $\alpha$: $\alpha^{\pm} = \dfrac{1 \pm \alpha}{2}$. Consequently, $\alpha^{+}\alpha^{-} = \dfrac{1-\alpha^2}{4}$. □

**Corollary 1.** *System (6.40) – (6.43) which governs the evolution of physical variables can be recast under the following matricial form:*

$$\frac{\partial W}{\partial t} + \mathbb{M}(W)\frac{\partial W}{\partial x} = \mathbf{S}(W), \tag{6.44}$$

*where* $W = (\vec{u}, p, \alpha^{+}, s)$, *source terms* $\mathbf{S}(W) = {}^{t}(\vec{g}, 0, 0, 0)$ *and if* $\vec{n} = (n_1, n_2, n_3)$ *is a normal direction,* $u_n = \vec{u}\cdot\vec{n}$ *is a normal velocity, then*

$$\mathbb{M}(W)\vec{n} = \sum_{i=1}^{3} M_i(W)n_i = \begin{pmatrix} u_n & 0 & 0 & \frac{1}{\rho}n_1 & 0 & 0 \\ 0 & u_n & 0 & \frac{1}{\rho}n_2 & 0 & 0 \\ 0 & 0 & u_n & \frac{1}{\rho}n_3 & 0 & 0 \\ \rho c_s^2 n_1 & \rho c_s^2 n_2 & \rho c_s^2 n_3 & u_n & 0 & 0 \\ \alpha^{+}\alpha^{-}\delta n_1 & \alpha^{+}\alpha^{-}\delta n_2 & \alpha^{+}\alpha^{-}\delta n_3 & 0 & u_n & 0 \\ 0 & 0 & 0 & 0 & 0 & u_n \end{pmatrix}.$$

Now we can state the main result:

**Theorem 6.** *For smooth solutions to Equations (6.37) – (6.39), the region* $0 \leq \alpha^{\pm} \leq 1$ *remains invariant under the system dynamics.*

*Proof.* The proof is based on the theory of J. Smoller [Smo94]. We know that the value $\alpha^{-} = 0$ corresponds to $W_5 = \alpha^{+} = 1$. Obviously, the case $\alpha^{+} = 0$ can be treated similarly with the same conclusions. The matrices $M_i(W)$ are smooth functions of $W$ in the neighborhood of $W$ which satisfies $W_5 \in [0, 1]$. We would like to check whether the boundary $W_5 = 1$ is invariant under the dynamics of (6.44). According to the theory of invariant regions by Chueh, Conway and Smoller ([CCS77]), this will be the case if and only if $d(W_5 - 1) = dW_5 = (0, 0, 0, 0, 1, 0)$ is a left eigenvector of matrices $M_i(\vec{u}, p, 1, s)$ for all admissible values of $\vec{u}$, $p$ and $s$. By straightforward computation one can easily check that

$$(0, 0, 0, 0, 1, 0)\cdot M_i(\vec{u}, p, 1, s) = \vec{u}_i(0, 0, 0, 0, 1, 0).$$

The theorem is shown now. □

**Remark 36.** *The present result shows also that if negative values of volume fractions* $\alpha^{\pm}$ *are reported in simulations, they are due to some numerical instabilities and have nothing to do with mathematical properties of the four equations model (6.37) – (6.39).*

### 6.1.5 Incompressible limit

In practice, there are many situations when governing equations can be further simplified by filtering out acoustic effects. For various combustion models it was done by A. Majda and his collaborators [Maj82, KM82, MS85]. More recently these techniques were applied to some two-phase models [KPTV00, Del05, Del07].

In the present section we derive the incompressible limit of the four equations model (6.34) – (6.36). For the sake of simplicity we will neglect thermal fluxes which are not important for the exposition below and do not directly affect acoustic waves propagation. Hence, in this section we consider the following set of equations in nonconservative form for convenience:

$$\partial_t(\alpha^\pm\rho^\pm) + \nabla\cdot(\alpha^\pm\rho^\pm\vec{u}) = 0, \tag{6.45}$$

$$\rho\partial_t\vec{u} + \rho(\vec{u}\cdot\nabla)\vec{u} + \nabla p = \rho\vec{g} + \nabla\cdot\boldsymbol{\tau}, \tag{6.46}$$

$$\rho\partial_t e + \rho\vec{u}\cdot\nabla e + p\nabla\cdot\vec{u} = \boldsymbol{\tau} : \nabla\vec{u}, \tag{6.47}$$

where we expressed the energy balance in terms of the internal energy $e$.

In order to estimate the relative importance of various terms, we introduce dimensionless variables. In this section we use the special low Mach number scaling which reveals acoustic effects magnitude. The characteristic length, time, and velocity scales are denoted by $\ell$, $t_0$ and $U_0$ respectively. For example, $\ell$ can be chosen as a linear dimension of the fluid domain $\Omega$. The density, viscosity and sound velocity scales are chosen to be those of the heavy fluid, i.e. $\rho_0^+$, $\nu_0^+$ and $c_{0s}^+$ correspondingly. Since we are interested in acoustic effects, the natural pressure scale is given by $\rho_0^+(c_{0s}^+)^2$. If we summarize these remarks, dependent and independent dimensionless variables (denoted with primes) are defined as:

$$\mathbf{x}' := \frac{\mathbf{x}}{\ell}, \quad t' := \frac{t}{t_0}, \quad (\rho^\pm)' := \frac{\rho^\pm}{\rho_0^+}, \quad (\mu^\pm)' := \frac{\mu^\pm}{\rho_0^+\nu_0^+},$$

$$\vec{u}' := \frac{\vec{u}}{U_0}, \quad p' := \frac{p}{\rho_0^+(c_{0s}^+)^2}, \quad e' := \frac{e}{U_0^2}.$$

Since the volume fraction is dimensionless by definition (6.1) we keep this variable unchanged.

After dropping the tildes, nondimensional system (6.45) – (6.47) of equation becomes:

$$\mathrm{St}\,\partial_t(\alpha^\pm\rho^\pm) + \nabla\cdot(\alpha^\pm\rho^\pm\vec{u}) = 0, \tag{6.48}$$

$$\mathrm{St}\,\rho\partial_t\vec{u} + \rho(\vec{u}\cdot\nabla)\vec{u} + \frac{1}{\mathrm{Ma}^2}\nabla p = \frac{1}{\mathrm{Fr}^2}\rho\vec{g} + \frac{1}{\mathrm{Re}}\nabla\cdot\boldsymbol{\tau}, \tag{6.49}$$

$$\mathrm{St}\,\rho\partial_t e + \rho\vec{u}\cdot\nabla e + \frac{1}{\mathrm{Ma}^2}p\nabla\cdot\vec{u} = \frac{1}{\mathrm{Re}}\boldsymbol{\tau} : \nabla\vec{u}, \tag{6.50}$$

where several scaling parameters appear:

- **Strouhal number** $\mathrm{St} := \dfrac{\ell}{U_0 t_0}$. In this study we will assume the Strouhal number to be equal to one $\mathrm{St} \equiv 1$, i.e. $t_0 = \dfrac{\ell}{U_0}$.
- **Mach number** $\mathrm{Ma} := \dfrac{U_0}{c_{0s}^+}$ which measures the relative importance of the flow speed and the sound speed in the medium.
- **Froude number** $\mathrm{Fr} := \dfrac{U_0}{\sqrt{g\ell}}$ compares inertia and gravity forces.
- **Reynolds number** $\mathrm{Re} := \dfrac{U_0 \ell}{\nu_0^+}$ gives the measure of the ratio of inertial to viscous forces.

In this section we will consider the asymptotic limit as $\mathrm{Ma} \to 0$. Consequently, all physical variables $\alpha^\pm$, $\rho^\pm$, $p$, $\vec{u}$ and $e$ are expanded in formal series in powers of the Mach number:

$$\phi = \phi_0 + \mathrm{Ma}\,\phi_1 + \mathrm{Ma}^2 \phi_2 + \ldots, \qquad \phi \in \{\alpha^\pm, \rho^\pm, p, \vec{u}, e\}. \tag{6.51}$$

Formal expansion (6.51) is then substituted into the system (6.48) – (6.50). Our goal is to derive a system which governs the evolution of physical variables at the lowest order in the Mach number (e.g. $\vec{u}_0$, $\alpha_0^\pm$, etc.). Equation (6.49) at orders $\mathrm{Ma}^{-2}$ and $\mathrm{Ma}^{-1}$ leads:

$$\nabla p_0 = \nabla p_1 = 0.$$

In other words, $p_0 = p_0(t)$ and $p_1 = p_1(t)$ are only functions of time. Internal energy balance equation (6.50) gives us the incompressibility constraint $\nabla \cdot \vec{u}_0 = 0$ at the leading order $\mathrm{Ma}^{-2}$ and, correspondingly, $\nabla \cdot \vec{u}_1 = 0$ at the order $\mathrm{Ma}^{-1}$.

Relation (6.3) after asymptotic expansion (6.51) becomes

$$\alpha_k^+(\mathbf{x}, t) + \alpha_k^-(\mathbf{x}, t) = \delta_{0k},$$

where $\delta_{0k}$ is the Kronecker delta symbol equal to 1 if $k = 0$ and 0 otherwise. Thus, at the leading order in Mach number we keep usual relations:

$$\alpha_0^+ + \alpha_0^- = 1, \qquad \rho_0 = \alpha_0^+ \rho_0^+ + \alpha_0^- \rho_0^-.$$

Equations (6.48), (6.49) at the order $\mathrm{Ma}^0$ become:

$$\partial_t(\alpha_0^\pm \rho_0^\pm) + \nabla \cdot (\alpha_0^\pm \rho_0^\pm \vec{u}_0) = 0, \tag{6.52}$$

$$\rho_0 \partial_t \vec{u}_0 + \rho_0 (\vec{u}_0 \cdot \nabla)\vec{u}_0 + \nabla \pi = \frac{1}{\mathrm{Fr}^2} \rho_0 \vec{g} + \frac{1}{\mathrm{Re}} \nabla \cdot \boldsymbol{\tau}_0, \tag{6.53}$$

where by $\pi$ we denote the pressure oscillations $p_2$ at the order $\mathrm{Ma}^2$.

Finally, some information on the behaviour of $\rho_0^\pm$ can be deduced from the Gibbs relation (6.15) which takes the following dimensionless form:

$$T^\pm ds^\pm = de^\pm - \frac{p}{\mathrm{Ma}^2(\rho^\pm)^2} d\rho^\pm.$$

After dividing by $dt$ and expanding the Gibbs relation as in (6.51) we get these results:

$$\frac{d\rho_0^\pm}{dt} = 0, \qquad \frac{d\rho_1^\pm}{dt} = 0. \tag{6.54}$$

In particular, it means that if in each phase the density $\rho_{0,1}^\pm$ was initially constant[1], it remains so under the system dynamics. Moreover, taking into account the first relation in (6.54) and the flow incompressibility constraint $\nabla \cdot \vec{u}_0 = 0$, one can easily deduce from the mass conservation Equations (6.52) that volume fractions $\alpha_0^\pm$ are also simply transported by the flow:

$$\partial_t \alpha_0^\pm + \vec{u}_0 \cdot \nabla \alpha_0^\pm = 0.$$

If we summarize all the developments made above and turn back to physical variables, we will get the following system of equations which governs an incompressible two-phase flow:

$$\partial_t \alpha^\pm + \vec{u} \cdot \nabla \alpha^\pm = 0, \tag{6.55}$$

$$\nabla \cdot \vec{u} = 0, \tag{6.56}$$

$$\rho \partial_t \vec{u} + \rho(\vec{u} \cdot \nabla)\vec{u} + \nabla \pi = \rho \vec{g} + \nabla \cdot \boldsymbol{\tau}, \tag{6.57}$$

where we dropped the index 0 to simplify the notation. The mixture density $\rho$ and the viscous stress tensor $\boldsymbol{\tau}$ are defined as above. This system should be completed by appropriate boundary and initial conditions.

**Remark 37.** *Two-fluid incompressible models, such as the system just derived above (6.55) – (6.57), are often used in many practical situations such as wave breaking [CKZL99] and others [SZ99]. For powder-snow avalanches applications, the volume fraction Equation (6.55) is completed by a diffusive term according to the Fick's law:*

$$\partial_t \alpha^\pm + \vec{u} \cdot \nabla \alpha^\pm = \nabla \cdot (\nu_f \nabla \alpha^\pm).$$

*This extra term allows to take into account the mixing between two fluids due to turbulence effects, for example. For more details on this extension we refer to [JR93, ESH04, DARB10].*

[1]This assumption is often made in applications. For example, pure water and pure air are assumed to have constant densities under normal conditions. However, the mixture density can undergo strong variations (e.g. after the wave breaking).

### 6.1.6 Numerical results

In the present section we will consider only the advective part of the system (6.34) – (6.36), i.e. we neglect viscous and thermal fluxes:

$$\partial_t(\alpha^\pm\rho^\pm) + \nabla\cdot(\alpha^\pm\rho^\pm\vec{u}) = 0, \tag{6.58}$$

$$\partial_t(\rho\vec{u}) + \nabla\cdot(\rho\vec{u}\otimes\vec{u} + p\mathrm{Id}) = \rho\vec{g}, \tag{6.59}$$

$$\partial_t(\rho E) + \nabla\cdot(\rho H\vec{u}) = \rho\vec{u}\cdot\vec{g}. \tag{6.60}$$

Actually, the system we consider here is stiffer than the original Equations (6.34) – (6.36) since it does not contain any diffusive effects. The resulting equations have been shown to be hyperbolic for any reasonable equation of state [DDG10, DDG08b]. For illustrative purposes we assume here that both fluids are governed by stiffened gas type laws:

$$p^\pm + \pi^\pm = (\gamma^\pm - 1)\rho^\pm e^\pm, \quad e^\pm = c_v^\pm T^\pm + \frac{\pi^\pm}{\gamma^\pm\rho^\pm},$$

where $\gamma^\pm$, $\pi^\pm$ and $c_v^\pm$ are some constants determined by physical properties of pure fluids under consideration. Also we assume that two fluids are in the thermodynamic equilibrium:

$$p \equiv p^+ = p^-, \quad T \equiv T^+ = T^-.$$

We refer to [Dut07, DDG10, DDG08b] for more details on the construction of this equation of state and the discussion of some properties of such two-phase mixtures.

#### 6.1.6.1 Numerical schemes

For the numerical study we choose the finite volumes method [Kro97, BO04] since it is the method of choice for the systems of conservation laws due to its excellent local conservative properties. More precisely, we use the cell-centered approach [BJ89, Bar94] which is more natural in our opinion. For simplicity we assume that the system of equations is solved in $\mathbb{R}^2$. However the extension to 3D for cartesian meshes is straightforward. We briefly describe below the discretization procedure adopted in this study. References are also provided if more details of the discretization method are needed.

**6.1.6.1.1 Space discretization** System (6.58) – (6.60) can be written as

$$\frac{\partial\vec{w}}{\partial t} + \nabla\cdot\mathcal{F}(\vec{w}) = \mathbf{S}(\vec{w}), \tag{6.61}$$

where

$$\vec{w} = (w_i)_{i=1}^5 := (\alpha^+\rho^+,\ \alpha^-\rho^-,\ \rho u_1,\ \rho u_2,\ \rho E),$$

and, for every $\vec{n} = (n_1, n_2) \in \mathbb{R}^2$,

$$\mathcal{F}(\vec{w}) \cdot \vec{n} = (\alpha^+\rho^+\vec{u}\cdot\vec{n},\ \ \alpha^-\rho^-\vec{u}\cdot\vec{n},\ \ \rho\vec{u}\cdot\vec{n}u_1 + pn_1,\ \rho\vec{u}\cdot\vec{n}u_2 + pn_2,\ \ \rho H\vec{u}\cdot\vec{n})\,, \quad (6.62)$$

$$\mathbf{S}(\vec{w}) = (0,\ \ 0,\ \ \rho g_1,\ \ \rho g_2,\ \ \rho\vec{g}\cdot\vec{u})\,.$$

Then, the Jacobian matrix $\mathbb{A}(\vec{w})\cdot\vec{n}$ is defined by

$$\mathbf{A}_n(\vec{w}) := \mathbf{A}(\vec{w})\cdot\vec{n} = \frac{\partial(\mathcal{F}(\vec{w})\cdot\vec{n})}{\partial\vec{w}}\,. \quad (6.63)$$

In order to compute $\mathbb{A}(\vec{w})\cdot\vec{n}$, one writes Equation (6.62) for $\mathcal{F}(\vec{w})\cdot\vec{n}$ in terms of $\vec{w}$ and $p$:

$$\mathcal{F}(\vec{w})\cdot\vec{n} = \Big(w_1\frac{w_3n_1+w_4n_2}{w_1+w_2},\ \ w_2\frac{w_3n_1+w_4n_2}{w_1+w_2},\ \ w_3\frac{w_3n_1+w_4n_2}{w_1+w_2}+pn_1,\ w_4\frac{w_3n_1+w_4n_2}{w_1+w_2}+pn_2,\ \ (w_5+p)\frac{w_3n_1+w_4n_2}{w_1+w_2}\Big)\,.$$

The Jacobian matrix (6.63) then has the following expression:

$$\mathbf{A}(\vec{w})\cdot\vec{n} \ = \ \begin{pmatrix} u_n\frac{\alpha^-\rho^-}{\rho} & -u_n\frac{\alpha^+\rho^+}{\rho} & \frac{\alpha^+\rho^+}{\rho}n_1 & \frac{\alpha^+\rho^+}{\rho}n_2 & 0 \\ -u_n\frac{\alpha^-\rho^-}{\rho} & u_n\frac{\alpha^+\rho^+}{\rho} & \frac{\alpha^-\rho^-}{\rho}n_1 & \frac{\alpha^-\rho^-}{\rho}n_2 & 0 \\ -u_1u_n+\frac{\partial p}{\partial w_1}n_1 & -u_1u_n+\frac{\partial p}{\partial w_2}n_1 & u_n+u_1n_1+\frac{\partial p}{\partial w_3}n_1 & u_1n_2+\frac{\partial p}{\partial w_4}n_1 & \frac{\partial p}{\partial w_5}n_1 \\ -u_2u_n+\frac{\partial p}{\partial w_1}n_2 & -u_2u_n+\frac{\partial p}{\partial w_2}n_2 & u_2n_1+\frac{\partial p}{\partial w_3}n_2 & u_n+u_2n_2+\frac{\partial p}{\partial w_4}n_2 & \frac{\partial p}{\partial w_5}n_2 \\ u_n\big(\frac{\partial p}{\partial w_1}-H\big) & u_n\big(\frac{\partial p}{\partial w_2}-H\big) & u_n\frac{\partial p}{\partial w_3}+Hn_1 & u_n\frac{\partial p}{\partial w_4}+Hn_2 & u_n\big(1+\frac{\partial p}{\partial w_5}\big) \end{pmatrix},$$

where $u_n = \vec{u}\cdot\vec{n}$.

The computational domain $\Omega \subset \mathbb{R}^2$ is decomposed into a set of control volumes $\mathcal{T}$ such that $\Omega = \cup_{K\in\mathcal{T}}K$. We integrate Equation (6.61) on $K$:

$$\frac{d}{dt}\int_K \vec{w}\,d\Omega + \sum_{L\in\mathcal{N}(K)}\int_{K\cap L}\mathcal{F}(\vec{w})\cdot\vec{n}_{KL}\,d\sigma = \int_K \mathbf{S}(\vec{w})\,d\Omega\,, \quad (6.64)$$

where $\vec{n}_{KL}$ denotes the unit normal vector on $K\cap L$ pointing into $L$ and $\mathcal{N}(K) = \{L \in \mathcal{T} : \text{area}(K\cap L) \neq$
Then, setting

$$\vec{w}_K(t) := \frac{1}{\text{vol}(K)}\int_K \vec{w}(\mathbf{x},t)\,d\Omega\,,$$

we approximate (6.64) by

$$\frac{d\vec{w}_K}{dt} + \sum_{L\in\mathcal{N}(K)}\frac{\text{area}(L\cap K)}{\text{vol}(K)}\Phi(\vec{w}_K,\vec{w}_L;\vec{n}_{KL}) = \mathbf{S}_K\,,$$

where the numerical flux

$$\Phi(\vec{w}_K, \vec{w}_L; \vec{n}_{KL}) \approx \frac{1}{\text{area}(L \cap K)} \int_{K \cap L} \mathcal{F}(\vec{w}) \cdot \vec{n}_{KL} \, d\sigma$$

is explicitly computed by the FVCF formula of Ghidaglia *et al.* [GKC01]:

$$\Phi(\vec{w}_K, \vec{w}_L; \vec{n}) = \frac{\mathcal{F}(\vec{w}_K) \cdot \vec{n} + \mathcal{F}(\vec{w}_L) \cdot \vec{n}}{2} - \text{sign}(\mathbb{A}_n(\mu(\vec{w}_K, \vec{w}_L))) \frac{\mathcal{F}(\vec{w}_K) \cdot \vec{n} - \mathcal{F}(\vec{w}_L) \cdot \vec{n}}{2}. \quad (6.65)$$

Here the Jacobian matrix $\mathbb{A}_n(\mu)$ is defined in (6.63), $\mu(\vec{w}_K, \vec{w}_L)$ is an arbitrary mean between $\vec{w}_K$ and $\vec{w}_L$ and $\text{sign}(M)$ is the matrix whose eigenvectors are those of $M$ but whose eigenvalues are the signs of that of $M$. In this section we did not deal with boundary conditions. We refer to [GP05] for more details.

**6.1.6.1.2 Higher order extension** In the previous section we described the first order scheme which might be too diffusive for most practical applications. That is why we present here a higher-order extension which is a variant of MUSCL[2] limiting technique [Kol75, Kol72, vL79, vL06]. This numerical method ensures stability and non-oscillatory behaviour of numerical solutions. To describe this scheme we switch to Cartesian notation since a bigger stencil is needed for the gradient reconstruction procedure. In this notation $\vec{w}_i$ denotes the average of conservative variables in the cell $i$ and $\vec{w}^{L,R}_{i+\frac{1}{2}}$ denotes respectively reconstructed left and right states at cell faces. According to the method adopted in the current study [Bar94, BO04, TMD07], cell faces values are computed as:

$$\vec{w}^{L}_{i+\frac{1}{2}} = \vec{w}_i + \frac{1}{4}\Big((1-\kappa)\phi(r^L_i)(\vec{w}_i - \vec{w}_{i-1}) + (1+\kappa)\phi\big(\frac{1}{r^L_i}\big)(\vec{w}_{i+1} - \vec{w}_i)\Big), \quad (6.66)$$

$$\vec{w}^{R}_{i+\frac{1}{2}} = \vec{w}_{i+1} - \frac{1}{4}\Big((1-\kappa)\phi(r^R_i)(\vec{w}_{i+2} - \vec{w}_{i+1}) + (1+\kappa)\phi\big(\frac{1}{r^R_i}\big)(\vec{w}_{i+1} - \vec{w}_i)\Big), \quad (6.67)$$

where $\kappa \in [-1, 1)$ is a free parameter and

$$r^L_i := \frac{\vec{w}_{i+1} - \vec{w}_i}{\vec{w}_i - \vec{w}_{i-1}}, \quad r^R_i := \frac{\vec{w}_{i+1} - \vec{w}_i}{\vec{w}_{i+2} - \vec{w}_{i-1}}.$$

Then, reconstructed values $\vec{w}^{L,R}_{i+\frac{1}{2}}$ are used to compute the numerical flux (6.65) of the FVCF scheme.

The function $\phi(r)$ is called the limiter function and is incorporated to obtain non-oscillatory resolution of discontinuities and steep gradients [BB73, Swe84]. We tested in practice two following limiter functions:

[2]Acronym MUSCL stands for Monotone Upstream-centered Scheme for Conservation Laws [vL79]

- M3 limiter proposed in [ZD98, TMD07]:

$$\phi_{M3}(r) = 1 - \Big(1 + \frac{2Nr}{1+r^2}\Big)\Big(1 - \frac{2r}{1+r^2}\Big)^N, \quad N = 2, \tag{6.68}$$

- MinMod limiter with compression parameter [Bar94, BO04]:

$$\phi_{MM}(r) = \max\{0, \min\{r, \beta\}\}, \quad \beta \in \big(1, \frac{3-\kappa}{1-\kappa}\big]. \tag{6.69}$$

In the smooth unlimited form ($\phi(r) \equiv 1$), the truncation error $\varepsilon$ for a scalar conservation law with the smooth flux $f(u)$ is given by [Bar94, BO04]:

$$\varepsilon = -\frac{\big(\kappa - \frac{1}{3}\big)}{4}\Delta x^2 \frac{\partial^3 f(u)}{\partial x^3}.$$

Consequently, for $\kappa = \frac{1}{3}$, the scheme provides theoretically in *smooth regions* an overall spatial discretization with $\mathcal{O}(\Delta x^3)$ error. In computations presented below, we use the optimal choice of this parameter together with M3 limiter (6.68).

**Remark 38.** *If the limiter function is symmetric, i.e.*

$$\frac{\phi(r)}{r} \equiv \phi\big(\frac{1}{r}\big),$$

*the reconstruction formulas (6.66), (6.67) are independent of the parameter $\kappa$ and degenerate to the classical MUSCL2 scheme. It is straightforward to show that limiter functions (6.68) and (6.69) are not symmetric.*

**6.1.6.1.3 Time discretization** In the previous section we briefly described the spatial discretization procedure with some finite-volume scheme. It is a common practice in solving time-dependent PDEs to first discretize the spatial variables. This approach is called a method of lines:

$$\frac{\partial \vec{w}}{\partial t} + \nabla \cdot \mathcal{F}(\vec{w}) = \mathbf{S}(\vec{w}) \overset{\text{FV}}{\Longrightarrow} \vec{w}_t = \mathcal{L}(\vec{w}),$$

where $\mathcal{L}(\vec{w})$ is a space discretization operator. In order to obtain a fully discrete scheme, we have to discretize the time evolution operator. In the present work we decided to retain the so-called Strong Stability-Preserving (SSP) time discretization methods described in [Shu88, GST01, SR02]. Historically these methods were initially called Total Variation Diminishing (TVD) time discretizations. However, this term is not completely correct. In computations presented below we use the following third order four-stage SSP-RK(3,4)

| | Velocity, $u$ | Density, $\rho^{\pm}$ | Volume fraction, $\alpha^{+}$ | Pressure, $p$ |
|---|---|---|---|---|
| Heavy fluid, $+$ | 0.0 | 1.0 | 0.98 | 1.0 |
| Light fluid, $-$ | 0.0 | 0.125 | 0.02 | 0.1 |

**Table 6.1:** Initial condition parameters for the two-fluid Sod shock tube problem.

scheme with CFL $= 2$:

$$\begin{aligned}
\vec{w}^{(1)} &= \vec{w}^{(n)} + \frac{1}{2}\Delta t \mathcal{L}(\vec{w}^{(n)}),\\
\vec{w}^{(2)} &= \vec{w}^{(1)} + \frac{1}{2}\Delta t \mathcal{L}(\vec{w}^{(1)}),\\
\vec{w}^{(3)} &= \frac{2}{3}\vec{w}^{(n)} + \frac{1}{3}\vec{w}^{(2)} + \frac{1}{6}\Delta t \mathcal{L}(\vec{w}^{(n)}),\\
\vec{w}^{(n+1)} &= \vec{w}^{(3)} + \frac{1}{2}\Delta t \mathcal{L}(\vec{w}^{(3)}),
\end{aligned}$$

where $\vec{w}^{(n)} = \vec{w}(\cdot, t_n)$ and $\vec{w}^{(n+1)} = \vec{w}(\cdot, t_{n+1})$.

The time step is chosen adaptively to satisfy the following stability condition [CFL67]:

$$\Delta t \leq \frac{\mathrm{CFL} \cdot \Delta x_{min}}{\max\{|u + c_s|_{max}, |u - c_s|_{max}\}},$$

where $\Delta x_{min}$ is the minimal mesh spacing, $u$ is the velocity and $c_s$ is the sound speed in the mixture (6.32).

**Remark 39.** *Presented above time step restriction is used together with the first order finite volumes scheme. The application of the MUSCL3 scheme requires the following modification of the CFL condition:*

$$\Delta t \leq \frac{1-\kappa}{2-\kappa} \cdot \frac{\mathrm{CFL} \cdot \Delta x_{min}}{\max\{|u + c_s|_{max}, |u - c_s|_{max}\}}.$$

#### 6.1.6.2 Two-fluid Sod shock tube problem

We present here a two-fluid generalization of the classical Sod shock tube problem [Sod78]. The sketch of the initial condition is given on Figure 6.3. The gravity force is not taken into account in this test case, i.e. $\vec{g} = \vec{0}$. Values of all parameters used in this computation are given in Tables 6.1 and 6.2.

The simulation was stopped at time $T = 0.4$ s and the computation results are presented on Figures 6.4 and 6.5. On all Figures we show the total density $\rho$ plots and perform a comparison between FVCF and MUSCL3 schemes. Figure 6.4 shows the behaviour of the

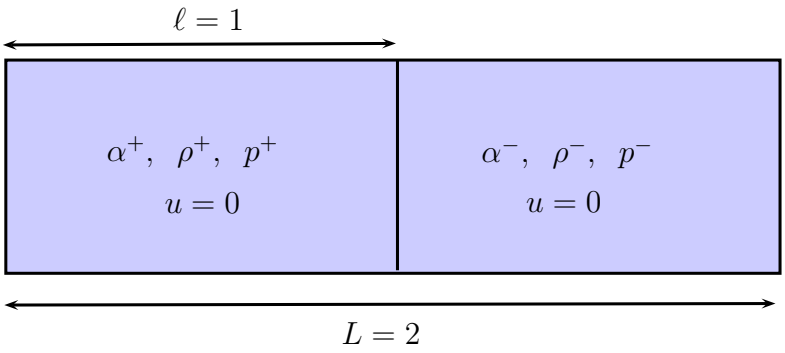


**Figure 6.3:** Sketch of the initial condition for the Sod shock tube test case.

| | $\gamma^{\pm}$ | $\pi^{\pm}$, Pa | $c_v^{\pm}$, $\frac{J}{kg \cdot K}$ |
|---|---|---|---|
| Heavy fluid, + | 2.6 | 0.0 | 661.0 |
| Light fluid, − | 1.4 | 0.0 | 661.0 |

**Table 6.2:** Equation of state parameters for the two-fluid Sod shock tube problem.

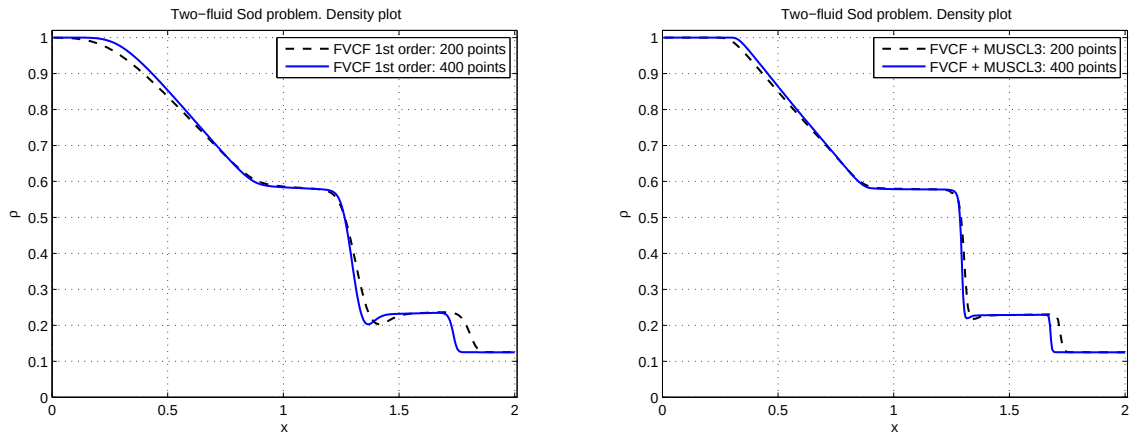


(a) FVCF 1st order

(b) MUSCL 3

**Figure 6.4:** Convergence of the solution with $h$-refinement.

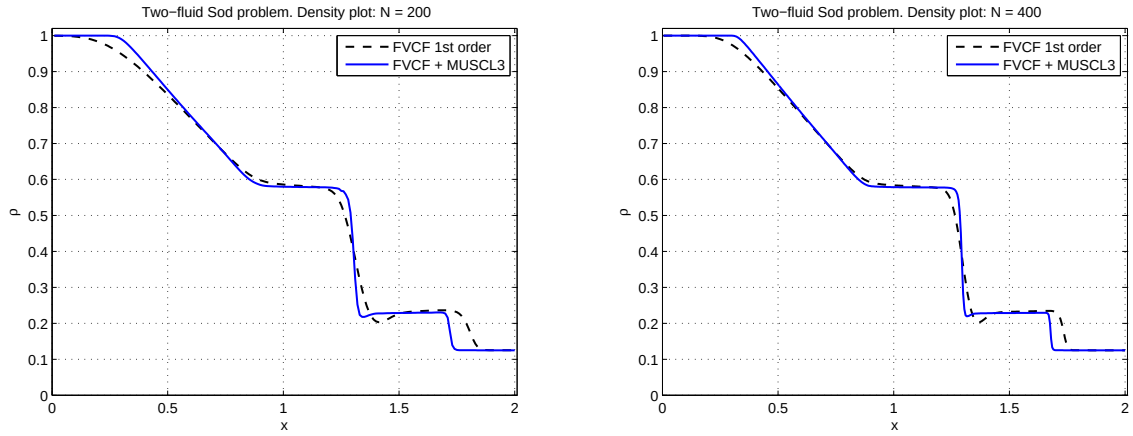


(a) $N = 200$ (b) $N = 400$

**Figure 6.5:** Convergence of the solution with $p$-refinement.

solution when the mesh is refined. Left image shows the results of the first order FVCF scheme, while the right one refers to the MUSCL3 extension. The improvement of the solution is obvious in both cases. In particular, we would like to underline the excellent shock resolution by the higher order scheme (Figure 6.4 (b)).

We perform also the comparison between two schemes (see Figure 6.5) for the same mesh size. As it was expected, higher order scheme greatly improves the sharp resolution of discontinuities for nearly comparable CPU time. Thus, there is an obvious interest in using MUSCL type schemes for practical applications.

This test case clearly shows the convergence of the numerical solution when the mesh is refined ($h$-convergence), but also with respect to the scheme order ($p$-convergence). Consequently, it validates our numerical code. In all subsequent computations we use the MUSCL3 scheme with the optimal choice of the parameter $\kappa = \frac{1}{3}$.

#### 6.1.6.3 Water drop test case

The sketch of this numerical experiment is given on Figure 6.6. The values of parameters are given in Table 6.3. Initially the velocity field is taken to be zero and the pressure field is uniform in all domain $p_0 = 10$ Pa. The gravity force is taken to be $g = 10$ m/s$^2$ and the computational domain is discretized with a uniform grid of $100 \times 100$ control volumes. Results of this simulation are presented in Figures 6.7 – 6.10. A similar test case has already been considered in [Dut07, DDG10, DDG08b] and results are in good qualitative agreement.

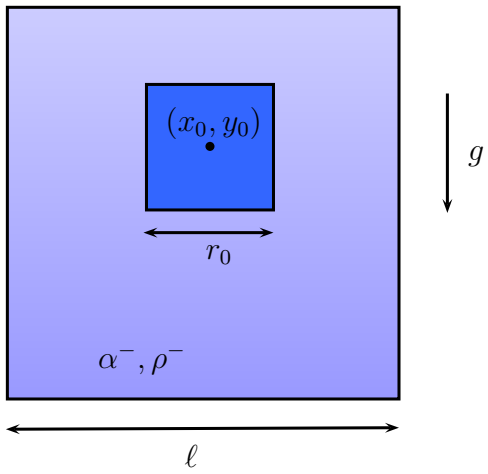


**Figure 6.6:** Sketch of the initial condition and computational domain geometry for the water drop test case. In our simulation we took the following values of geometrical parameters: $\ell = 1.0$ (the domain is square), $r_0 = 0.15$, $x_0 = 0.5$ and $y_0 = 0.7$. The gravity acceleration is taken to be $g = 10$ m/s$^2$.

| | $\gamma^{\pm}$ | $\pi^{\pm}$, Pa | $c_v^{\pm}$, $\frac{J}{kg \cdot K}$ | $\rho^{\pm}$, $\frac{kg}{m^3}$ | $\alpha^+$ |
|---|---|---|---|---|---|
| Heavy fluid, + | 1.6 | 0.0 | 1.0 | 5.0 | 0.99 |
| Light fluid, − | 1.4 | 0.0 | 1.0 | 1.0 | 0.01 |

**Table 6.3:** Equation of state parameters for the water drop test case.

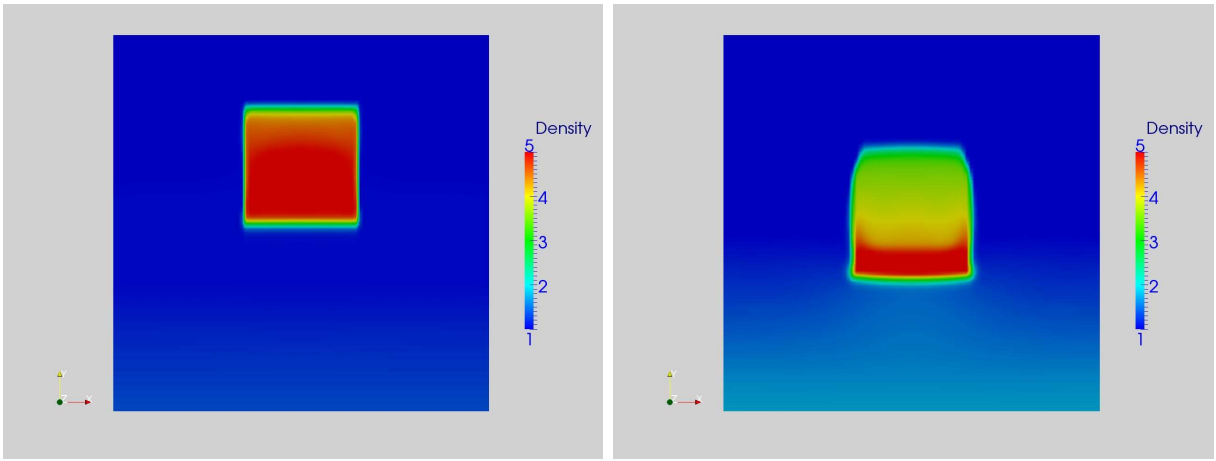


(a) $t = 0.1$ s (b) $t = 0.2$ s

**Figure 6.7:** Water drop test case: initial acceleration and deformation stage.

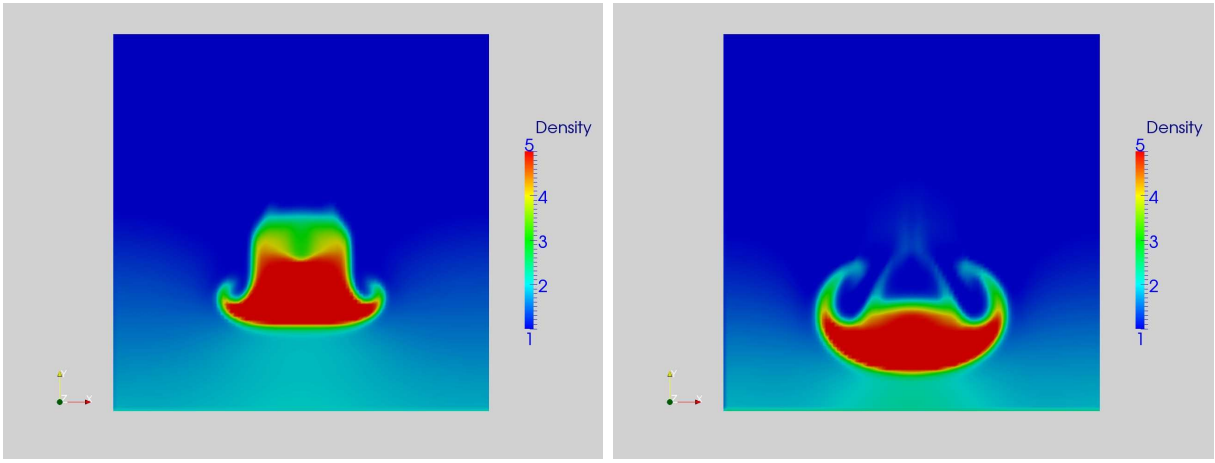


(a) $t = 0.3$ s (b) $t = 0.4$ s

**Figure 6.8:** Water drop test case: falling and further deformation of the drop.

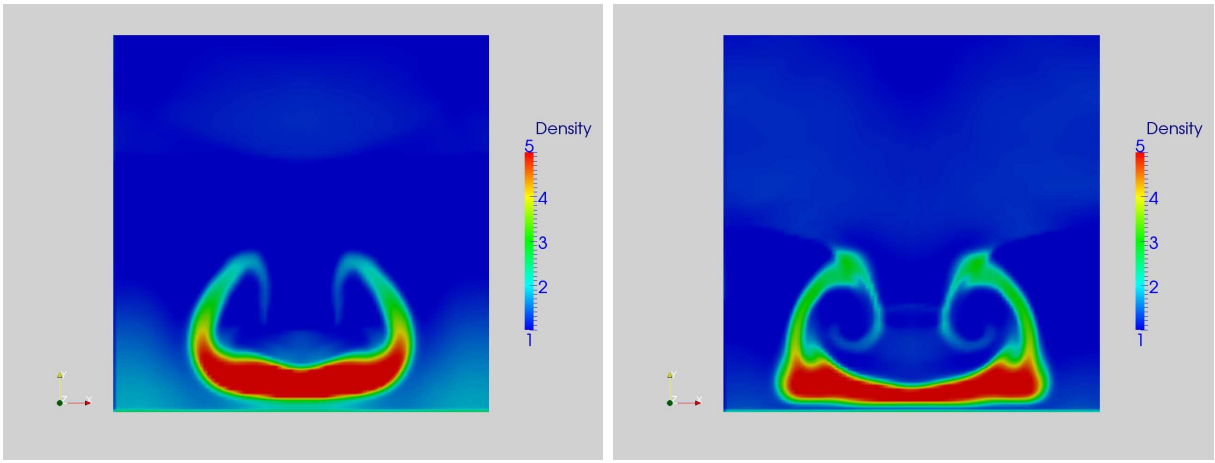


(a) $t = 0.5$ s (b) $t = 0.6$ s

**Figure 6.9:** Water drop hitting the tank bottom.

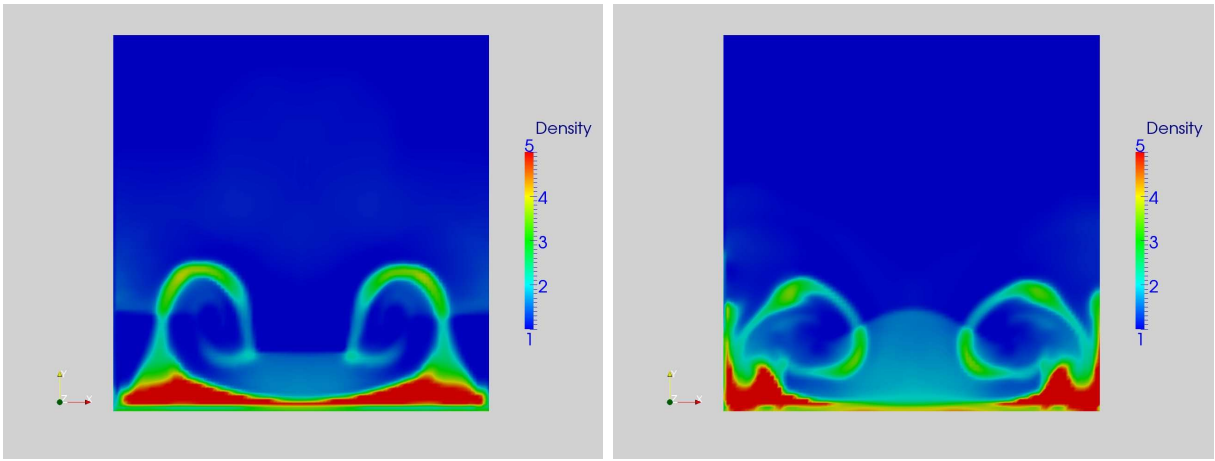


(a) $t = 0.7$ s (b) $t = 0.8$ s

**Figure 6.10:** Water drop flow on the bottom.

### 6.1.7 Perspectives and conclusions

In this study we considered several two-fluid models. We began the exposition by the so-called six equations model (6.4) – (6.6). Despite recent progress [ACOR95, GKC96, TKP99, GKC01, BG05, SFW+05, BQ06, Rov06, NKDVLG08, GCMM09], this system still represents some major difficulties for the numerical solution. Namely, the advection operator may be non-hyperbolic and contains non-conservative terms to be defined in some sense for discontinuous solutions. That is why, the six equations model was simplified through the velocity and energy relaxation process (see Section 6.1.3). In this way, we formally derived the so-called four equations model (6.34) – (6.36) recently proposed as a model for violent aerated flows [Dut07, DDG08c, DDG10, DDG08b]. Thus, the present work can be considered as an attempt towards further comprehension and at least formal justification of single velocity, single energy two-phase models. The resulting system (6.34) – (6.36) is hyperbolic for any reasonable equation of state [DDG10] and possesses several nice properties. In particular, in Section 6.1.4 we show that invariant regions $\alpha^{\pm} \in [0, 1]$ are preserved under the system dynamics. This property is necessary for the well-posedness of the system. In Section 6.1.5 we also formally derived the incompressible limit as the Mach number tends to zero. As a result, we recover usual two-fluid incompressible Navier-Stokes equations [PZ99, SZ99, CKZL99] if both fluids are assumed to be Newtonian. Finally, several numerical results are presented in Section 7.1.3.

# Chapter 7

# Two-fluid flows

*Mechanics is the paradise of the mathematical sciences, because by means of it one comes to the fruits of mathematics.*

Leonardo da Vinci

*The Book of Nature is written in mathematical characters, without whose help it is impossible to comprehend a single word, without which one wanders in vain through a dark labyrinth.*

Galileo Galilei

## Contents

## 7.1 Mathematical modeling of powder-snow avalanche flows

*No snowflake in an avalanche ever feels responsible.*

Voltaire

*There is no branch of mathematics, however abstract, which may not some day be applied to phenomena of the real world.*

Nikolai Lobatchevsky

ABSTRACT. Powder-snow avalanches are violent natural disasters which represent a major risk for infrastructures and populations in mountain regions. In this study we present a novel model for the simulation of avalanches in the aerosol regime. The second scope of this study is to get more insight into the interaction process between an avalanche and a rigid obstacle. An incompressible model of two miscible fluids can be successfully employed in this type of problems. We allow for mass diffusion between two phases according to the Fick's law. The governing equations are discretized with a contemporary fully implicit finite volume scheme. The solver is able to deal with arbitrary density ratios. Encouraging numerical results are presented. Volume fraction, velocity and pressure fields are presented and discussed. Finally we point out how this methodology can be used for practical problems.

### 7.1.1 Introduction

Snow avalanches are commonly defined as abrupt and rapid gravity-driven flows of snow down a mountainside, often mixed with air, water and sometimes debris (see Figure 7.1). Avalanches are physical phenomena of great interest, mainly because they represent a big risk for those who live or visit areas where this natural disaster can occur. During last several decades, the risk has increased due to important recreational and construction activities in high altitude areas. We remember recent events at Val d'Isère in 1970 and in Nothern Alps in 1999 [Anc01].

The avalanches arise from an instability in a pile of granular material like sand or snow [TM08]. The destabilization phase of an avalanche life is still a challenging problem. There are many factors which influence the release process. One can recall snowpack structure, liquid contain, shape and curvature of starting zone and many others [Anc01]. In this study we focus especially on sliding and stopping phases.

The serious research work on this natural phenomenon was preceded by the creation of scientific nivology at the end of the XIXth century. Among the pioneers we can mention Johann Coaz (swiss engineer) [Coa81] and P. Mougin (french forest engineer, author of the first avalanche model using an analogy with a sliding block) [Mou22, Mou31]. The work of

**Figure 7.1:** Two illustrations of powder-snow avalanche flows.

P. Mougin was ignored until the 1950s when A. Voellmy developed a similar model [Voe55]. Its somehow improved versions are still used by engineers nowadays.

We would like to point out here important contributions of the Soviet school by S.S. Grigorian, M.E. Eglit, A.G. Kulikovskiy, Y.L. Yakimov and many others [GEY67, KE73, BE73, BKK+75, KS77b, Egl83, Egl91, BL98, Egl98, BEN02]. They were at the origin of all modern avalanche models used nowadays in the engineering practice and, sometimes, in scientific research. Their works were mainly devoted to the derivation and comprehension of mathematical models while occidental scientists essentially looked for quantitative results.

Conventionally we can divide all avalanches in two idealized types of motion: flowing and powder-snow avalanches. A flowing avalanche is characterized by a high-density core ranging from 100 to 500 $kg/m^3$ and consists of various types of snow: pasty, granular, slush, etc. The flow depth is typically about a few meters which is much smaller than the horizontal extent. This argument is often used to justify numerous depth-integrated models of the Savage-Hutter type[1] [SH89, SH91]. These avalanches can cause extensive damage because of the important snow masses involved in the flow in spite of their low speed.

On the other hand, powder-snow avalanches are large-scale turbidity currents descending slopes at high velocities [RH04]. They seriously differ from flowing avalanches. These

[1] In hydrodynamics and hydraulics this type of modeling is also known as shallow water or Saint-Venant equations [dSV71].

**Figure 7.2:** Protecting wall in armed concrete at Taconnaz (Haute-Savoie, France) destroyed by the powder-snow avalanche of the 11 February 1999. The height is 7 m and the thickness is 1.5 m (Photo by C. Ancey).

clouds can reach 100 m in height and very high front velocities of the order of 100 m/s. They grow continously and the average density is fairly low (from 4 to 25 $kg/m^3$). These spectacular avalanches (see Figure 7.1) occur only under certain conditions (after abundant fresh snowfalls, cold, dry and weakly cohesive snow on strong slopes) and they produce a devastating pressure wave which breaks the trees, buildings, tears off the roofs, etc. During the propagation stage, they are able to cross the valleys and even to climb up on the opposite slope. Hence, measurements by intrusive probes are almost impossible. Avalanches in aerosol are not very frequent events in Alps but in the same time we cannot say they are very seldom. In the technical literature there is an opinion that an avalanche in aerosol is less destructive than a flowing one since the transported mass is much smaller. Nevertheless, recent events of the winter 1999 in Switzerland, Austria and France revealed the important destructive potential of the powder-snow avalanches (see Figure 7.2).

Recently several systematic measurements campaigns *in situ* were conducted in Norway, Switzerland and Japan [MS84, NTK90, NMKI93, NSKL95, DGBA00]. Researchers shed some light on the internal structure of big avalanches. More precisely, they show that there exists a dense part of the avalanche which remains permanently in contact with the bed. This dense core is covered by the aerosol suspension of snow particles in the air. From these results it follows that mentioned above two types of avalanches may coexist in nature and proposed above classification is rather conventional. Perhaps, future studies will perform a coupling between the dense core and powder-snow envelope in the spirit of SAMOS code [SZ04].

Let us review various existing approaches to the mathematical modeling of snow avalanches.

Generally, we have two big classes of mathematical models: probabilistic and deterministic. In the present study we deal with a deterministic model and we refer to the works of K. Lied and D.M. McClung [LB80, ML87, McC00, McC01] for more information on statistical approaches to avalanche modeling. Deterministic models can be further divided into continuous and discrete ones depending whether the material under consideration can be approximated as a continuum medium or not. For the review and some recent results on dense granular flows we refer to following works [NKMN98, MN01, Raj02b, Raj02a, Raj05] and the references therein. Some promising results were obtained with discrete models based on cellular automata [DGRS$^+$99, ADGM$^+$00, DSI06].

The first contemporary avalanche models appeared in 1970 by soviet scientists Kulikovskiy and Sveshnikova [KS77b, BL98]. Later, their idea was exploited by Beghin [Beg79, BB83, BO91] and others [HTD77, FP90, AU99, Anc04, RH04]. We call this type of modeling 0D-models since the avalanche is assimilated to semi-elliptic cloud with variable in time volume $V(t)$, momentum $(\rho U)(t)$, etc. All quantities of interest are assimilated to the center of mass and their dynamics is governed by conservation laws expressed as Ordinary Differential Equations (ODE).

On the next complexity level we have various depth-integrated models. The governing equations are of Shallow Water (or Saint-Venant [dSV71]) type. In general, they are derived by depth averaging process or some asymptotic expansion procedure from complete set of equations. Thus, a physical 3D (or 2D) problem results in a 2D model (1D correspondingly). From computational point of view these models are very affordable even for desktop computers. On the other hand, they provide us very approximative flow structure, especially in the vertical direction.

In France, G. Brugnot and R. Pochat were among the pioneers [BP81] while in Soviet Union this direction was explored in the beginning of 1970 by N.S. Bakhvalov et M.E. Eglit [BE73, BKK$^+$75]. Currently, each country concerned with the avalanche hazard, has its own code based on this type of equations. Probably the most representative model is that developed by S. Savage and K. Hutter [SH89]. Nowadays this set of equations is generally referred as the Savage-Hutter model. We refer to [Hop83, Hut96] as general good reviews of existing theoretical models and laboratory experiments.

This approach was further developed by incorporating more complex rheologies and friction laws [GWH98, Hut91, HG93, MCVB$^+$03, HWP05, FNBB$^+$08]. To conclude on this part of our review, we have to say that this modeling is more relevant to the flowing avalanche regime which is characterized by the small ratio of the flow depth $h$ to the horizontal extent $\ell$ (i.e. $\frac{h}{\ell} \ll 1$).

Finally, we come to the so-called *two-fluid* (or *two-phase*) models. In this paradigm both phases are resolved and, a priori, no assumption is made on the shallowness of the

flow under consideration. Another advantage consists in fact that efforts exerted by the ambient air on the sliding mass are naturally taken into account. From computational point of view, these models are the most expensive [NG98, ESH04, Eti04, EHS05]. In the same time, they offer quite complete information on the flow structure.

As it follows from the title, in this study we are mainly concerned with powder-snow avalanches. We would like to underline that our modeling paradigm allows for taking into account the dense core at the first approximation order. The density is completely determined by the snow volume fraction distribution. This parameter can be used to introduce a stratification in the initial condition, for example. Otherwise, it will happen automatically due to mixing and sedimentation processes in the flow, provided we follow its evolution for sufficiently long time.

We retained a simple incompressible two-fluid model which is described in detail in Section 7.1.2. Two phases are allowed to interpenetrate, forming a mixing zone in the vicinity of the interface. We make no Boussinesq-type hypothesis [Anc04] about the density ratio. Moreover, our solver is robust and is able to deal with high density ratios (we tested up to 3000). In nature, the flow under consideration is obviously highly turbulent but at the present stage we do not incorporate any explicit turbulence modeling beyond resolved scales. In the present study we focus mainly on the physically sound description of incompressible highly inhomogeneous two-phase flows.

Good understanding of these natural phenomena can improve the risk assessment of such natural hazards. Large scale experiments are not feasible[2]. Field measurements during the event are very hazardous and the events are rare. Laboratory experiments on powder-snow avalanches are essentially limited to Boussinesq clouds[3] [Kel95, NBNBH02, Pri03, NB03, PNBNF04] while it is not the case in nature. Thus, we do not really know how these results apply to real-world events. Fortunately, some progress has been made recently to remedy this situation [TM08].

Numerical simulations of avalanches provide useful information on the dynamics of these flows. Computer experiments may become in term the main tool in testing various situations. Experiments *in silico* should be complementary to those *in situ* or in laboratory. Direct Numerical Simulations (DNS) provide complete information about all flow quantities of interest such as the local density, the velocity field variations, the dynamic pressure and the energy. Recall that this information is not easily accessible by means of measurements.

[2]However, we would like to notice that there are two experimental sites: one in Switzerland (Sion Valley) and another one in France (Col d'Ornon). Unfortunately, field measurements provide very limited information on the flow structure [DGA01], even if some a posteriori analysis may be beneficial [TM07].

[3]The Boussinesq regime corresponds to the situation when $\frac{\rho^+ - \rho^-}{\rho^+} \ll 1$ where $\rho^\pm$ are densities of the heavy and light fluids respectively. This asymptotics allows to introduce the so-called Boussinesq approximation.

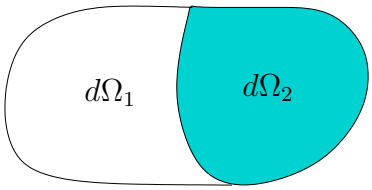


**Figure 7.3:** An elementary fluid volume $d\Omega$ occupied by two phases.

The present paper is organized as follows. In Section 7.1.2 we present the governing equations and some constitutive relations. Special attention is payed to the presence of strong density gradients in the flow and to the kinetic energy balance of the resulting system. The next Section 7.1.3 contains a brief description of the numerical methods and numerous computation results are presented. Finally, this paper is ended by outlining main conclusions and a few perspectives for future studies (see Section 7.1.4).

### 7.1.2 Mathematical model

In the present study we assume that an avalanche is a two-fluid flow formed by air and snow particles in suspension. The whole system moves under the force of gravity. For simplicity we assume that the mixture is a Newtonian fluid. The last assumption is not so restrictive as it can appear. The flow under consideration is such that the Reynolds number is very high ($\mathrm{Re} \sim 10^9$). Therefore, the transient behaviour is essentially governed by the convective terms and not by the fluid rheology. On the contrary, the rheology is very important in the flowing regime.

In two-fluid flows it is natural to operate with the so-called volume fractions [Ish75, TK96, TKP99, GKC01]. Consider an elementary fluid volume $d\Omega$ surrounding an interior point $P \in d\Omega$. Let us assume that the first fluid occupies volume $d\Omega_1 \subseteq d\Omega$ and the second the volume $d\Omega_2 \subseteq d\Omega$ (see Figure 7.3) such that

$$|d\Omega| \equiv |d\Omega_1| + |d\Omega_2|. \tag{7.1}$$

The volume fraction of the fluid $i = 1, 2$ in the point $P$ is defined as

$$\phi_i(P) := \lim_{\substack{|d\Omega| \to 0 \\ P \in d\Omega}} \frac{|d\Omega_i|}{|d\Omega|}.$$

From relation (7.1) it is obvious that $\phi_1(P) + \phi_2(P) \equiv 1$, for any point $P$ in the fluid domain. Henceforth, it is sufficient to retain only the heavy fluid volume fraction $\phi_1$, for example, which will be denoted just by $\phi$, for the sake of simplicity.

If we assume that constant densities and kinematic viscosities of the heavy and light fluids are respectively $\rho^{\pm}$ and $\nu^{\pm}$, the mixture density $\rho$ and the dynamic viscosity $\mu$ are

defined as follows:

$$\rho = \phi\rho^+ + (1-\phi)\rho^-, \quad \mu = \phi\rho^+\nu^+ + (1-\phi)\rho^-\nu^-. \tag{7.2}$$

In the following we assume that $\rho^+ \neq \rho^-$, otherwise the two-fluid modeling does not make much sense.

After some simple algebraic computations, the mixture dynamic viscosity $\mu$ can be expressed in terms of the mixture density $\rho$ as:

$$\mu = \mu_0 + \check{\nu}\rho, \tag{7.3}$$

where $\mu_0$ has the dimension of the dynamic viscosity $[kg/(m\cdot s)]$ and $\check{\nu}$ scales with the kinematic one $[m^2/s]$. These coefficients are related to the densities and kinematic viscosities of constitutive fluids in this way:

$$\mu_0 := \frac{\nu^-\rho^-\rho^+ - \nu^+\rho^+\rho^-}{\rho^+ - \rho^-}, \quad \check{\nu} := \frac{\nu^+\rho^+ - \nu^-\rho^-}{\rho^+ - \rho^-}.$$

Compressible Navier-Stokes equations with viscosities of the form (7.3) were studied mathematically in [Sy05].

**Remark 40.** *In view of our applications, the snow kinematic viscosity $\nu^+$ can be parameterized as a function of temperature $T$ and snow density $\rho^+$ according to [DAH+07]:*

$$\nu^+ = \frac{\mu_0}{\rho^+} e^{-\alpha T} e^{\beta\rho^+},$$

*where $\mu_0 = 3.6\times 10^6\ N\cdot s\cdot m^{-2}$, $\alpha = 0.08\ K^{-1}$, $\beta = 0.021\ m^3/kg$.*

Now we can state the governing equations of our physical problem. In this study we assume that both phases are constrained to have the same velocity variable $\vec{u}$. This assumption is not very restrictive. The formal justification of single-velocity two-phase models can be found in [MG05, MDG09, MDG10]. Also, this type models have already been successfully applied to a number of practical problems [Dut07, DDG08c, BPB09, DDG10, DDG08a].

The flow is assumed to be isentropic. The mass and momentum conservation equations have the classical form:

$$\partial_t\rho + \nabla\cdot(\rho\vec{u}) = 0, \tag{7.4}$$

$$\partial_t(\rho\vec{u}) + \nabla\cdot(\rho\vec{u}\otimes\vec{u}) + \nabla p = \nabla\cdot\big(2\mu\mathbf{D}(\vec{u})\big) + \rho\vec{g}, \tag{7.5}$$

where $\vec{g}$ is the acceleration due to gravity, $p$ is the hydrodynamic pressure and $\mathbf{D}(\vec{u}) = \frac{1}{2}\big(\nabla\vec{u} + (\nabla\vec{u})^t\big)$ is the strain rate tensor.

The fluid mixing is taken into account by Fick's type law [Fic55a, Fic55b] resulting in the following quasi-compressible equation:

$$\nabla \cdot \vec{u} = -\nabla \cdot (\kappa \nabla \log \rho), \tag{7.6}$$

where the coefficient $\kappa$ has the dimension of kinematic viscosity and will be defined below. For the moment, we assume $\kappa$ to be constant, consequently, the right-hand side of equation (7.6) can be equivalently rewritten as $-\kappa \Delta \log \rho$.

**Remark 41.** *Examples of closures similar to* (7.6) *of the form*

$$\nabla \cdot \vec{u} = \pm \nabla \cdot (\nabla \phi(\rho))$$

*may be found in [Gra55, KS77a, BadV83, Maj84, AKM90, FS01] (the sign* $\pm$ *depends on monotonicity properties of the function* $\phi(\rho)$*). It may lead to models of low Mach number combustion [Maj84] with* $\phi(\rho) = \dfrac{1}{\rho}$*, salt or pollutant motion in a shallow layer [FS01] and other practical situations involving highly inhomogeneous fluids [BadVSV82, BadV83, BES07].*

**Remark 42.** *Since we model an avalanche propagation along a sloping solid boundary, we take the gravity acceleration in the following form:*

$$\vec{g} = (g \sin \theta, -g \cos \theta),$$

*where* $\theta$ *is the slope of the hill and usually* $g := |\vec{g}| = 9.81\ m/s^2$.

#### 7.1.2.1 Model based on fluid volume velocity

In this section we transform governing equations (7.4), (7.5) and (7.6) to operate with more representative physical variables giving also a more convenient mathematical form.

Namely, we introduce the new velocity variable defined as

$$\vec{v} := \vec{u} + \kappa \nabla \log \rho, \tag{7.7}$$

which is sometimes referred in the literature as *the mean volume velocity* (cf. [FS01]) or *the fluid volume velocity* (cf. [Bre05a]). In this study we will retain the last term. It has been pointed out recently [Bre05b, Bre06] that the fluid volume velocity $\vec{v}$ is more pertinent for flows involving high density gradients. Now, let us rewrite the system (7.4), (7.5) and (7.6) in terms of new variable $\vec{v}$.

First of all, from Fick's law (7.6) it follows immediately that the flow is incompressible within the fluid volume velocity $\vec{v}$:

$$\nabla \cdot \vec{v} = 0.$$

The mass conservation equation (7.4) takes the following simple form:

$$\partial_t \rho + \nabla \cdot (\rho \vec{v}) = \nabla \cdot (\kappa \rho \nabla \log \rho).$$

By taking into account the fact that $\kappa$ is constant and the field $\vec{v}$ is divergence-free ($\nabla \cdot (\rho\vec{v}) = \vec{v} \cdot \nabla\rho$), we can rewrite the last equation as:

$$\partial_t \rho + \vec{v} \cdot \nabla \rho = \kappa \Delta \rho. \tag{7.8}$$

The latter equation is of parabolic type. The diffusive term comes from the Fick's law governing the mixing process between two fluids. In the case when $\kappa = 0$, the initial sharp interface between two phases would be simply advected by the velocity field $\vec{v}$ (coinciding with $\vec{u}$, when $\kappa \equiv 0$), thus, preventing any mixing. Henceforth, we consider the case $\kappa > 0$.

**Remark 43.** *The mass conservation equation (7.8) can be equivalently rewritten in terms of the volume fraction $\phi$ using the mixture density representation (7.2):*

$$\partial_t \phi + \vec{v} \cdot \nabla \phi = \kappa \Delta \phi. \tag{7.9}$$

Finally, we have to transform the momentum conservation equation (7.5) according to the change of the velocity variable (7.7). This operation will require several computations briefly presented below. For convenience, we work with equation (7.5) recasted in non-conservative form using the mass conservation (7.4):

$$\rho \partial_t \vec{u} + \rho(\vec{u} \cdot \nabla)\vec{u} + \nabla p = \rho \vec{g} + \nabla \cdot (2\mu \mathbf{D}(\vec{u})). \tag{7.10}$$

The three terms $\rho\partial_t\vec{u}$, $\rho(\vec{u} \cdot \nabla)\vec{u}$ and $\nabla \cdot (2\mu\mathbf{D}(\vec{u}))$ involving $\vec{u}$ have to be rewritten:

$$\begin{aligned}
\rho \partial_t \vec{u} &\equiv \rho \partial_t \vec{v} - \kappa \rho \partial_t \Big(\frac{\nabla \rho}{\rho}\Big), && (7.11)\\
\rho(\vec{u} \cdot \nabla)\vec{u} &\equiv \rho(\vec{v} \cdot \nabla)\vec{v} - \kappa\rho(\nabla \log \rho \cdot \nabla)\vec{v} - \kappa\rho(\vec{v} \cdot \nabla)\nabla \log \rho && (7.12)\\
&\quad + \kappa^2 \rho(\nabla \log \rho \cdot \nabla)\nabla \log \rho, && (7.13)\\
\nabla \cdot (2\mu \mathbf{D}(\vec{u})) &\equiv \nabla \cdot (2\mu \mathbf{D}(\vec{v})) - \kappa \nabla \cdot (2\mu \nabla\nabla \log \rho). && (7.14)
\end{aligned}$$

In order to obtain the evolution equation for the quantity $\dfrac{\nabla\rho}{\rho}$ arising in (7.11), we use the mass conservation equation (7.8):

$$\rho \partial_t \Big(\frac{\nabla \rho}{\rho}\Big) + \nabla\big(\vec{v} \cdot \nabla \rho\big) - (\vec{v} \cdot \nabla \rho)\frac{\nabla \rho}{\rho} = \kappa \Delta \nabla \rho - \kappa \Delta \rho \frac{\nabla \rho}{\rho}.$$

Consequently, relation (7.11) can be rewritten using the last result:

$$\rho \partial_t \vec{u} \equiv \rho \partial_t \vec{v} + \kappa \nabla(\vec{v} \cdot \nabla \rho) - \kappa(\vec{v} \cdot \nabla \rho)\frac{\nabla \rho}{\rho} + \kappa^2 \frac{\nabla \rho}{\rho}\Delta \rho - \kappa^2 \Delta \nabla \rho.$$

After all these developments, the momentum conservation equation (7.10) becomes:

$$\rho\partial_t\vec{v} + \rho(\vec{v}\cdot\nabla)\vec{v} + \nabla p + \underbrace{\kappa\nabla(\vec{v}\cdot\nabla\rho) - \kappa(\vec{v}\cdot\nabla\rho)\frac{\nabla\rho}{\rho}}_{(I)} + \underbrace{\kappa^2\frac{\nabla\rho}{\rho}\Delta\rho}_{(II)} - \kappa^2\Delta\nabla\rho$$
$$- \kappa\rho(\nabla\log\rho\cdot\nabla)\vec{v} - \underbrace{\kappa\rho(\vec{v}\cdot\nabla)\nabla\log\rho}_{(I)} + \underbrace{\kappa^2\rho(\nabla\log\rho\cdot\nabla)\nabla\log\rho}_{(II)} =$$
$$\rho\vec{g} + \nabla\cdot(2\mu\mathbf{D}(\vec{v})) - \kappa\nabla\cdot(2\mu\nabla\nabla\log\rho).$$

One can remark that terms in groups (I) and (II) can be simplified to give $\kappa^t\nabla\vec{v}\,\nabla\rho$ and $\kappa^2\nabla\cdot\left(\frac{\nabla\rho}{\rho}\otimes\rho\right)$ correspondingly:

$$\rho\partial_t\vec{v} + \rho(\vec{v}\cdot\nabla)\vec{v} + \nabla p + \kappa^t\nabla\vec{v}\,\nabla\rho - \kappa\nabla\rho\nabla\vec{v} - \underbrace{\kappa^2\Delta\nabla\rho + \kappa^2\nabla\cdot\left(\frac{\nabla\rho}{\rho}\otimes\rho\right)}_{(*)} =$$
$$\rho\vec{g} + \nabla\cdot(2\mu\mathbf{D}(\vec{v})) - \underbrace{2\check{\nu}\kappa\nabla\cdot(\rho\nabla\nabla\log\rho)}_{(*)} - \underbrace{2\kappa\mu_0\nabla\cdot(\nabla\nabla\log\rho)}_{(**)}. \quad (7.15)$$

In order to obtain last two terms on the right-hand side of (7.15), expression (7.3) for the mixture dynamic viscosity $\mu$ was used.

However, equation (7.15) can be further simplified if we make a special choice for the constant $\kappa$ arising in the Fick's law (7.6). More specifically, we take $\kappa \equiv 2\check{\nu}$, where $\check{\nu}$ is the mixture kinematic viscosity defined in equation (7.3). For this choice of Fick's diffusion coefficient $\kappa$, the terms marked with $(*)$ in (7.15) disappear, since it is straightforward to check the following differential identity:

$$\nabla\cdot(\rho\nabla\nabla\log\rho) \equiv \Delta\nabla\rho - \nabla\cdot\left(\frac{\nabla\rho}{\rho}\otimes\rho\right).$$

Finally, the term $(**)$ in equation (7.15) can be written as a gradient:

$$\nabla\cdot(\nabla\nabla\log\rho) \equiv \nabla\Delta\log\rho.$$

Consequently, it can be incorporated in the definition of the pressure:

$$\pi(\mathbf{x},t) := p(\mathbf{x},t) + 4\check{\nu}\mu_0\Delta\log\rho. \quad (7.16)$$

If we summarize developments made above, we can state the governing equations of the proposed model:

$$\nabla\cdot\vec{v} = 0, \quad (7.17)$$
$$\partial_t\rho + \vec{v}\cdot\nabla\rho = 2\check{\nu}\Delta\rho, \quad (7.18)$$
$$\rho\partial_t\vec{v} + \rho(\vec{v}\cdot\nabla)\vec{v} + \nabla\pi + 2\check{\nu}^t\nabla\vec{v}\,\nabla\rho - 2\check{\nu}\nabla\rho\nabla\vec{v} = \rho\vec{g} + \nabla\cdot(2\mu\mathbf{D}(\vec{v})) \quad (7.19)$$

Equations (7.17), (7.18) and (7.19) have to be completed by appropriate initial and boundary conditions to form a well-posed problem.

Initially, the velocity, pressure and density (or equivalently, volume fraction) fields have to be imposed. Concerning boundary conditions, the usual no-slip condition $\vec{v} = \vec{0}$ can be imposed. Another possibility is to impose the following partial slip condition:

$$\vec{v} \cdot \vec{n} = 0, \quad \big((1-\alpha)\vec{v} + \alpha(\mathbf{D}(\vec{v}) \cdot \vec{n})\big) \cdot \boldsymbol{\tau} = 0, \tag{7.20}$$

where $\boldsymbol{\tau}$ is the tangent vector to the boundary and $\alpha \in [0,1]$ is the friction parameter. We have to say that the latter is known to be physically more relevant [Eti04].

If it is required by a computational algorithm as in our case, for example, governing equations can be recast in the conservative form. Using the incompressibility condition (7.17), the mass conservation equation (7.18) becomes:

$$\partial_t \rho + \nabla \cdot (\rho \vec{v}) = \nabla \cdot (2\check{\nu} \nabla \rho).$$

If we sum up equation (7.19) with mass conservation (7.18) multiplied by $\vec{v}$, we will obtain the following equation with advective terms written in the conservative form:

$$\partial_t(\rho\vec{v}) + \nabla \cdot (\rho\vec{v} \otimes \vec{v}) + \nabla\pi + 2\check{\nu}^t \nabla\vec{v}\,\nabla\rho - 2\check{\nu}\nabla\rho\nabla\vec{v} = \rho\vec{g} + 2\check{\nu}\vec{v}\,\Delta\rho + \nabla \cdot (2\mu\mathbf{D}(\vec{v})). \tag{7.21}$$

The dimensionless form and discretization of these equations will be discussed briefly below in Sections 7.1.2.3 and 7.1.3 correspondingly.

#### 7.1.2.2 Kinetic energy evolution

In this section we would like to derive an integral identity which describes the kinetic energy evolution associated to the system (7.17) – (7.19). Throughout all developments in this section we assume the no-slip condition $\vec{v} = 0$ on the fluid domain $\Omega$ boundary $\partial\Omega$. The same result will hold if we assume periodic boundaries or appropriate decay conditions at the infinity.

First, we multiply the mass conservation equation (7.18) by $\dfrac{|\vec{v}|^2}{2}$, momentum conservation (7.19) by $\vec{v}$, sum them up and integrate over the fluid domain $\Omega$. After a few integrations by part, using the incompressibility (7.17) and boundary conditions, we obtain

the following identity:

$$\partial_t \int\limits_\Omega \rho\frac{|\vec{v}|^2}{2}\,d\mathbf{x} = \int\limits_\Omega \rho\vec{g}\cdot\vec{v}\,d\mathbf{x} + \underbrace{\int\limits_\Omega 2\check{\nu}\Delta\rho\frac{|\vec{v}|^2}{2}\,d\mathbf{x} + \int\limits_\Omega 2\check{\nu}(\nabla\rho\nabla\vec{v})\vec{v}\,d\mathbf{x}}_{(I)} +$$

$$\underbrace{\int\limits_\Omega \nabla\cdot(2\check{\nu}\rho\mathbf{D}(\vec{v}))\vec{v}\,d\mathbf{x} - \int\limits_\Omega 2\check{\nu}({}^t\nabla\vec{v}\nabla\rho)\vec{v}\,d\mathbf{x}}_{(II)} + \underbrace{\int\limits_\Omega \nabla\cdot(2\mu_0\mathbf{D}(\vec{v}))\vec{v}\,d\mathbf{x}}_{(III)}$$

Two terms from the group (I) cancel each other after one integration by parts:

$$\int\limits_\Omega 2\check{\nu}\Delta\rho\frac{|\vec{v}|^2}{2}\,d\mathbf{x} = -\int\limits_\Omega 2\check{\nu}\nabla\rho\cdot\nabla\Big(\frac{|\vec{v}|^2}{2}\Big)\,d\mathbf{x} = -\int\limits_\Omega 2\check{\nu}(\nabla\rho\nabla\vec{v})\vec{v}\,d\mathbf{x}.$$

The group (II) terms can be also transformed to give:

$$-\int\limits_\Omega 2\check{\nu}\rho|\mathbf{D}(\vec{v})|^2\,d\mathbf{x} + \int\limits_\Omega 2\check{\nu}\rho^t\nabla\vec{v} : \nabla\vec{v}\,d\mathbf{x} \equiv -\int\limits_\Omega 2\check{\nu}\rho|\mathbb{A}(\vec{v})|^2\,d\mathbf{x},$$

where $\mathbb{A}(\vec{v}) := \frac{1}{2}\big(\nabla\vec{v} - {}^t\nabla\vec{v}\big)$ is the antisymmetric part of the velocity gradient $\nabla\vec{v}$ and $A : B = a_{ij}b_{ij}$ is the usual contracted product of two square matrices $A = (a_{ij})_{1\le i,j\le n}$, $B = (b_{ij})_{1\le i,j\le n}$.

Finally, the term (III) similarly can be transformed as:

$$\int\limits_\Omega \nabla\cdot(2\mu_0\mathbf{D}(\vec{v}))\vec{v}\,d\mathbf{x} \equiv -\int\limits_\Omega 2\mu_0|\mathbf{D}(\vec{v})|^2\,d\mathbf{x}$$

Thus, we come to the following integral identity governing the kinetic energy evolution associated to the system (7.17) – (7.19) (in closed conditions):

$$\partial_t \int\limits_\Omega \rho\frac{|\vec{v}|^2}{2}\,d\mathbf{x} = \int\limits_\Omega \rho\vec{g}\cdot\vec{v}\,d\mathbf{x} - \underbrace{\int\limits_\Omega 2\mu_0|\mathbf{D}(\vec{v})|^2\,d\mathbf{x}}_{(a)} - \underbrace{\int\limits_\Omega 2\check{\nu}\rho|\mathbb{A}(\vec{v})|^2\,d\mathbf{x}}_{(b)}. \tag{7.22}$$

In this integral equality each term has a specific physical sense. The term on the left-hand side represents the rate of kinetic energy change per a unit of time. On the right-hand side the first term is the work done by the gravity force, thus, describing the energy input into the system. Two last terms represent various dissipative processes. The first term (a) can be seemingly ascribed to the dissipation due to viscous forces, while the second one (b) comes from mixing processes between two phases.

Despite the fact that governing equations (7.17) – (7.19) are more complicated than classical Navier-Stokes equations, due to the judicious choice of Fick's constant $\kappa$ we were able to get a kinetic energy balance in simple and physically sound form (7.22).

#### 7.1.2.3 Dimensional analysis

In this section we perform a dimensional analysis of the governing equations (7.17) – (7.19) in order to reveal important scaling parameters. Henceforth, starred variables denote dimensional quantities throughout this section.

The initial avalanche height $h_0$ and the heavy fluid density $\rho^+$ are chosen to be the characteristic length and density scales correspondingly. The velocity field is adimensionalized by a typical flow speed $u_0$. Finally, from characteristic length and velocity, it is straightforward to deduce the time scale. Consequently, the scaling for the independent variables is

$$\mathbf{x}^* = h_0\mathbf{x}, \quad t^* = \frac{h_0}{u_0}t,$$

and dimensionless dependent variables $\rho, \vec{u}, p$ are introduced in this way:

$$\rho^* = \rho^+\rho, \quad \vec{u}^* = u_0\,\vec{u}, \quad \pi^* = \rho^+u_0^2\,\pi, \quad \mu^* = \rho^+\check{\nu}\mu$$

The governing equations (7.17) – (7.19) in dimensionless form become:

$$\begin{aligned} \nabla\cdot\vec{v} &= 0, \\ \partial_t\rho + \vec{v}\cdot\nabla\rho &= \frac{1}{\mathrm{Re}}\Delta\rho, \\ \rho\partial_t\vec{v} + \rho(\vec{v}\cdot\nabla)\vec{v} + \nabla\pi + \frac{1}{\mathrm{Re}}{}^t\nabla\vec{v}\nabla\rho - \frac{1}{\mathrm{Re}}\nabla\rho\nabla\vec{v} &= \frac{1}{\mathrm{Fr}^2}\rho\vec{g} + \frac{1}{\mathrm{Re}}\nabla\cdot(\mu\mathbf{D}(\vec{v})) \end{aligned}$$

This procedure reveals two important scaling parameters – the Reynolds number Re [Rey83] and the Froude number Fr [Bź28] which are defined as

$$\mathrm{Re} := \frac{h_0u_0}{2\check{\nu}}, \qquad \mathrm{Fr} := \frac{u_0}{\sqrt{gh_0}}.$$

Recall that the Reynolds number Re gives a measure of the ratio of inertial forces to viscous forces. In practice this number characterizes different flow regimes, such as laminar or turbulent flow. The Froude number is a ratio of inertia and gravitational forces. It is a hydrodynamic equivalent of the Mach number. For free-surface flows it specifies the nature of the flow (subcritical or supercritical) [DVB02].

**Remark 44.** *We would like to discuss the difference between the physical pressure field $p(\mathbf{x},t)$ and the modified pressure $\pi(\mathbf{x},t)$. If we turn to dimensionless variables in equation (7.16), we will obtain the following relation:*

$$\pi(\mathbf{x},t) = p(\mathbf{x},t) + \frac{\mu}{\mathrm{Re}^2}\Delta\log\rho.$$

*Taking into account the typical values of the Reynolds number in our applications, we can conclude that this difference is completely negligible, at least from the practical point of view, since* $\mathrm{Re}^{-2} \ll 1$.

In fact, there are two additional scaling parameters $\delta$ and $\lambda$ hidden in definitions of the density $\rho$ and dynamic viscosity of the mixture:

$$\rho := \frac{\rho^*}{\rho^+} = \phi + (1-\phi)\delta, \qquad \delta := \frac{\rho^-}{\rho^+},$$

$$\mu := \frac{\mu^*}{\rho^+\check{\nu}} = (1-\delta)\phi + \frac{\delta\lambda(1-\delta)}{1-\delta\lambda}, \qquad \lambda := \frac{\nu^-}{\nu^+},$$

where we substituted the following representation of the Fick's coefficient:

$$\check{\nu} = \nu^+ \frac{1-\delta\lambda}{1-\delta}. \tag{7.23}$$

Actually, the densities ratio $\delta$ can be related to the well-known Atwood number At (cf. [GGL+01, LJ05]):

$$\mathrm{At} := \frac{\rho^+ - \rho^-}{\rho^+ + \rho^-} = \frac{1-\delta}{1+\delta}\,.$$

The powder-snow avalanche regime is characterized by very high values of Reynolds number Re and low density ratios $\delta$ [MS93, Anc03]:

$$\mathrm{Re} \sim 10^6, \qquad 0.05 \le \delta \le 0.25.$$

Thus, the flow is clearly turbulent. Nevertheless, in the present study we do not consider any turbulence modeling beyond the scales resolved by the numerical method.

There is much less available information on the snow viscosity and snow rheology, in general [DAH+07]. The viscosity ratio parameter $\lambda$ can be related (using equation (7.23)) to the so-called Schmidt number Sc which represents the ratio of the fluid viscosity to mass diffusivity:

$$\mathrm{Sc} := \frac{\nu^+}{2\check{\nu}} = \frac{1-\delta}{2(1-\delta\lambda)}$$

This number was named after the German engineer Ernst Heinrich Wilhelm Schmidt (1892 – 1975) and it is used to characterize fluid flows with simultaneous momentum and mass diffusion processes [YXS02, SS03]. For powder-snow avalanches, M. Clément-Rastello reported [CR01] the following values of the Schmidt number:

$$0.5 \le \mathrm{Sc} \le 1.$$

When the Reynolds number is sufficiently high (inertial regime), two scaling parameters to be respected are the density ratio $\delta = \frac{\rho^-}{\rho^+}$ and the Froude number $\mathrm{Fr} := \frac{u_0}{\sqrt{gh_0}}$. Recall that in the Boussinesq regime ($\delta \to 0$), only the Froude number has to be respected. We quote [PNBNF04] reporting on this important issue:

> ... Satisfying the Froude number and density ratio similarities in the laboratory means that a very high velocity is necessary, which calls for a very large channel. It is not possible to satisfy the density ratio similarity, because dimensionless number differs by several orders of magnitude between the processes that unfold in nature and those reproduced in the laboratory...

As a result, the interpretation of laboratory results is quite ambiguous. At this point, numerical simulation should be considered as a complementary tool to physical modeling.

### 7.1.3 Numerical methods and simulation results

In this study we perform Direct Numerical Simulations (DNS) of a snow cloud moving down a steep slope. Our solver is based on a freely available CFD toolbox OpenFOAM . All computations performed in this study are 3D with only one cell in $z$ direction for the sake of efficiency. In principle, the extension to truly 3D configurations is possible with this code.

In order to implement model (7.17) – (7.19) we modified the standard solver twoLiquidMixingFoam which discretizes incompressible two-fluid Navier-Stokes equations with Fick's diffusion term in the volume fraction transport equation (7.9). The main modification concerns the momentum balance equation. Namely, we had to incorporate two nonconservative terms $2\check{\nu}^t\nabla\vec{v}\,\nabla\rho$ and $2\check{\nu}\nabla\rho\nabla\vec{v}$. For information, we provide here a piece of the code written in the internal OpenFOAM language which corresponds to the discretization of equation (7.21):

```
fvVectorMatrix UEqn
(
  fvm::ddt(rho, U) +
  fvm::div(rhoPhi, U) -
  fvm::laplacian(muf, U) -
  U*fvc::div(DabRho*(mesh.Sf()&fvc::interpolate(fvc::grad(rho))))+
  DabRho*(fvc::grad(U)().T() & fvc::grad(rho)) -
  DabRho*(fvc::grad(U)() & fvc::grad(rho)) -
  fvc::div(muf*(mesh.Sf() & fvc::interpolate(fvc::grad(U)().T())))
);
```

Time derivatives were discretized with the classical implicit Euler scheme. An upwind second order finite volume method was employed in space. For more details on the retained discretization scheme we refer to [Jas96, Rus02, Ope07]. The choice of the finite volume method is justified by its excellent stability and local conservation properties (especially in comparison to FEM [ESH04, Eti04, EHS05]).

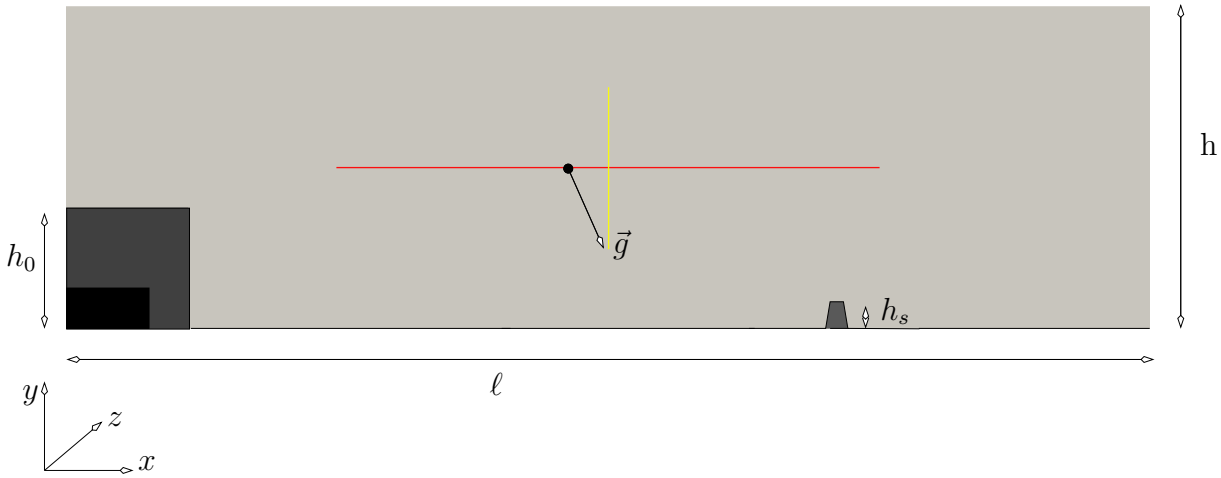


**Figure 7.4:** Sketch of the computational domain and initial condition description.

| *parameter* | *value* |
|---|---|
| gravity acceleration $g$, $m/s^2$ | 9.8 |
| slope, $\theta$ | 32° |
| friction parameter, $\alpha$ | 0.3 |
| heavy fluid density, $\rho^+$, $kg/m^3$ | 20 |
| light fluid density, $\rho^-$, $kg/m^3$ | 1 |
| heavy fluid kinematic viscosity, $\nu^+$, $m/s^2$ | $4.8\times10^{-4}$ |
| light fluid kinematic viscosity, $\nu^-$, $m/s^2$ | $1.0\times10^{-4}$ |

**Table 7.1:** Values of various parameters used for numerical simulations. The friction parameter is used in the partial slip boundary condition (7.20).

#### 7.1.3.1 Description of numerical computations

In this study we try to reproduce *in silico* a classical lock-exhange type flow with an obstacle placed in the computational domain. The sketch of the fluid domain and the initial condition description are given on Figure 7.4. Experiment consists in releasing a heavy fluid which flows under the gravity force along an inclined channel. The values of all physical parameters are provided in Table 7.1, while computational domain and discretization parameter are given in Table 7.2.

The objective of this study is twofold. Besides presenting numerical results on a gravity-driven two-fluid flow, we also would like to shed some light onto the interaction process between an avalanche and an obstacle. At the present stage we assume the obstacle to be absolutely rigid but this assumption can be relaxed in future investigations. Results

| *parameter* | *value* |
|---|---|
| domain height, $h$, m | 0.8 |
| total length, $\ell$, m | 2.7 |
| mesh height, $\Delta y$, m | 0.0026 |
| mesh length, $\Delta x$, m | 0.0033 |
| initial avalanche height, $h_0$, m | 0.3 |
| obstacle height, $h_s$, m | $0.2h_0$ |
| obstacle thickness, m | 0.04 |

**Table 7.2:** Computational domain dimensions and discretization parameters.

presented here are obtained for the obstacle height $h_s = 0.2h_0$, where $h_0$ is the initial mass height. We would like to underline also the presence of the stratification in our initial condition. We assume that there is a dense core of the height $h_0/3$ composed of the pure heavy fluid ($\phi = 1$, consequently $\rho = \rho^+$), which is surrounded by a lighter snow layer with the volume fraction $\phi = 0.4$. All results presented below are computed for simplicity with the usual no-slip boundary condition $\vec{v} = \vec{0}$. However, we performed several tests with the partial slip condition (7.20) leading generally to better results with respect to the snow entrainment at the bottom. Moreover, the friction coefficient $\alpha$ allows for some *tuning* depending on local soil conditions.

#### 7.1.3.2 Simulation results

Snapshots of the volume fraction evolution are presented on Figures 7.5 – 7.7. At the beginning, the initial rectangular mass gradually transforms under the force of gravity into more classical elliptic form (see Figure 7.5). Then, this mass enters into the sliding regime (see Figure 7.6) until the interaction with the obstacle (see Figure 7.7).

Our simulations clearly show that a Kelvin-Helmholtz type instability [Hel68, Kel71, Cha81, DR04] develops locally during the propagation stage. Previous simulations involving Adaptive Mesh Refinement (AMR) techniques confirmed this observation [Eti04, EHS05]. On the other hand, the interaction process with the obstacle creates a jet directed upward. This jet has a mushroom-like shape typical for Rayleigh-Taylor instability [Ray83, Tay50, DR04].

Several authors pointed out an intriguing feature of the avalanche type flows [DGA01, RH04]. Namely, it was shown by radar measurements that the maximum velocity inside the avalanche exceeds the front velocity by 30% – 40%. For this purpose we visualize the velocity field magnitude during the propagation stage (see Figures 7.8 and 7.9). Qualita-


**Figure 7.5:** Avalanche at $t = 10\ s$. The color scale ranges from 0 to the maximum value 1.0.


**Figure 7.6:** Avalanche at $t = 25\ s$. The color scale ranges from 0 to the maximum value 0.984.

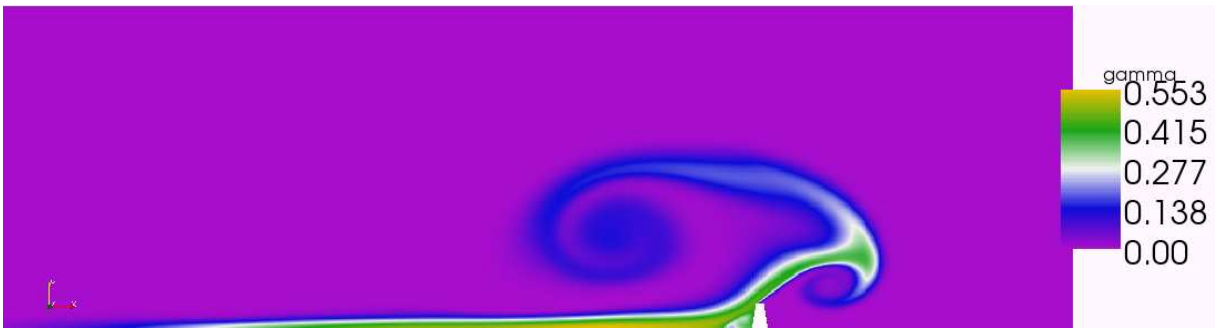


**Figure 7.7:** Avalanche at $t = 60\ s$. The color scale ranges from 0 to the maximum value 0.553.


**Figure 7.8:** Velocity field magnitude at $t = 25\ s$. The color scale ranges from 0 $m/s$ to the maximum value 3.07 $m/s$.

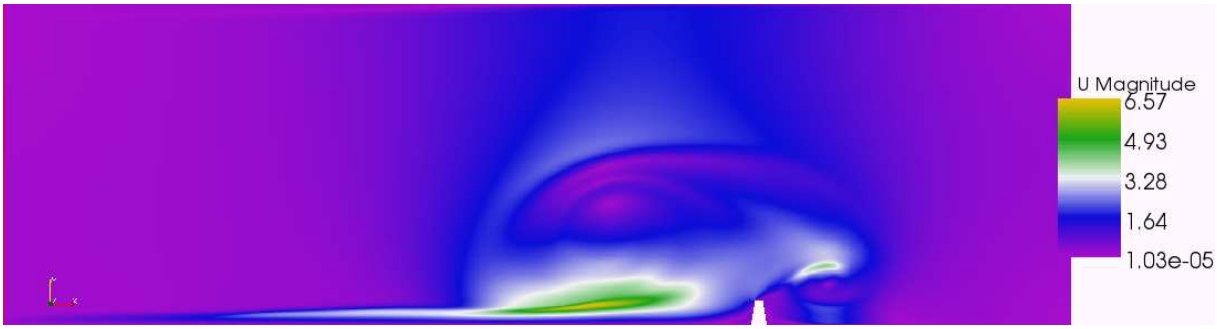


**Figure 7.9:** Velocity field magnitude at $t = 60\ s$. The color scale ranges from 0 $m/s$ to the maximum value 6.57 $m/s$.

tively, our computations are in conformity with these experimental results.

The same simulation was also performed with the so-called (in this study) standard model used in [ESH04] and implemented also in OpenFOAM as the twoLiquidMixingFoam solver:

$$\begin{aligned} \nabla \cdot \vec{v} &= 0, \\ \partial_t \rho + \vec{v} \cdot \nabla \rho &= 2\check{\nu} \Delta \rho, \\ \rho \partial_t \vec{v} + \rho(\vec{v} \cdot \nabla)\vec{v} + \nabla p &= \rho \vec{g} + \nabla \cdot (2\mu \mathbf{D}(\vec{v})) \end{aligned}$$

The standard model differs from governing equations (7.17) – (7.19) essentially by two non-conservative terms in the momentum balance equation along with small differences in the pressure definition.

The magnitude of the difference between velocity fields obtained with the standard and novel models is represented on Figure 7.10. One can see that differences are not negligible and attain its maximum value of 2.91 $m/s$ near the lower boundary. Corresponding difference field of two volume fraction distributions are shown on Figure 7.11. Here the maximum value of the difference 0.344 is attained in the avalanche front.

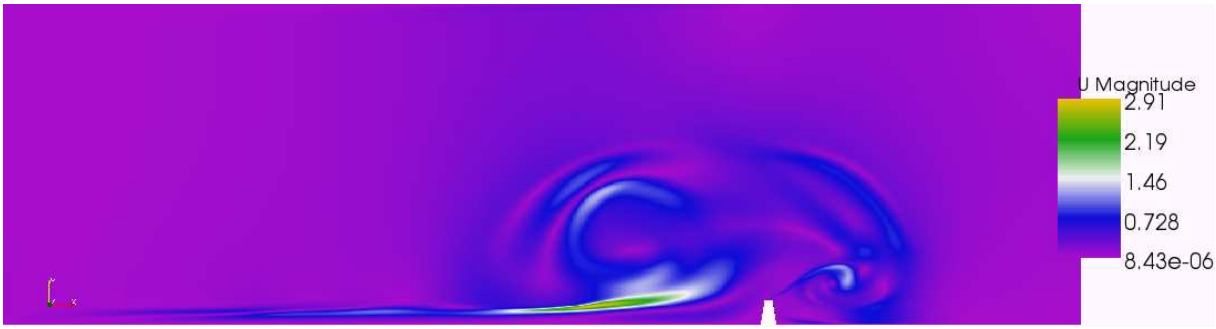


**Figure 7.10:** Magnitude of two velocity fields difference computed according to the standard and new models at $t = 60\ s$. The color scale ranges from 0 $m/s$ to the maximum value 2.91 $m/s$.

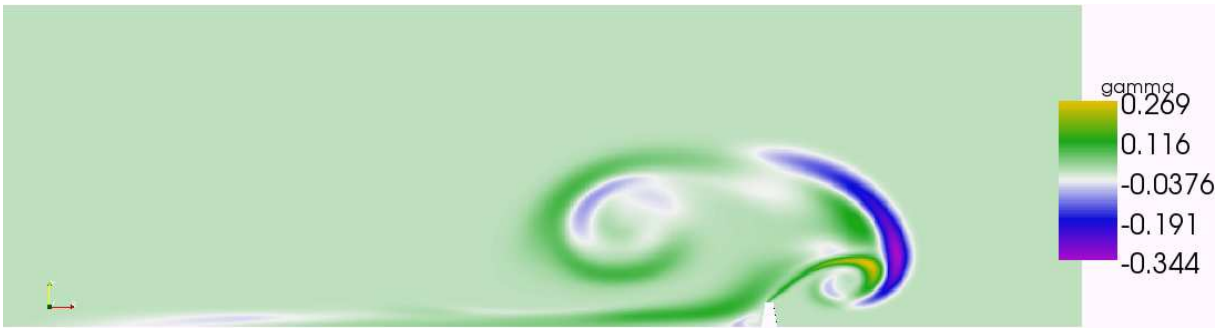


**Figure 7.11:** Difference of the volume fraction distributions computed according to the standard and new models at $t = 60\ s$. The color scale ranges from $-0.344$ to the maximum value 0.269.

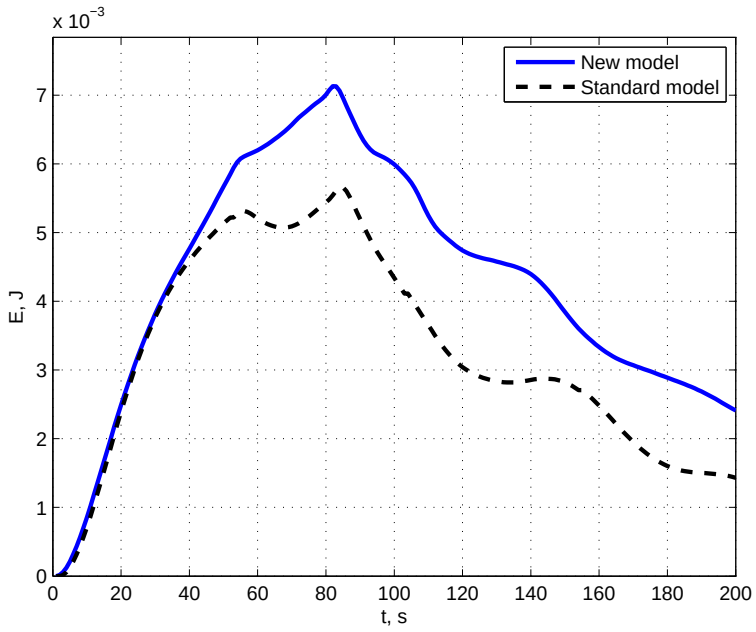


**Figure 7.12:** Kinetic energy evolution during the simulation. The continuous blue line corresponds to computations performed with equations (7.17) – (7.19), while the dashed black line is produced using the standard model.

During the simulation we also computed the kinetic energy evolution. The comparison result is presented on Figure 7.12. The energy grows almost linearly in time during the propagation stage for both models. The differences start to appear just before the interaction process with the obstacle. These results indicate that proposed above model (7.17) – (7.19) allows for higher energy levels under equal numerical conditions.

**Remark 45.** *The idea to use the kinetic energy loss to estimate the efficiency of a dike was already proposed by Beghin and Closet in 1990 [BC90]. However, they had very limited information on the flow structure (especially velocity and density profiles). That is why they decided to approximate this quantity by the ratio* $|U^2 - U'^2| / U^2$. *Here* $U'$ *is the front velocity at certain distance below the dike and* $U$ *is the front velocity of the reference avalanche measured at the same point.*

#### 7.1.3.3 Impact pressures

For many practical applications we have to estimate the loading exerted on a structure by an avalanche impact. Incidentally, the avalanche hazard level is attributed depending on the estimated impact pressure values [Lié06]. Moreover, this information is crucial for the design of buildings and other structures exposed to this natural hazard.

In engineering practice, it is common to determine the impact pressures according to the following formula [MS93]:

$$P_d = K p_{\text{ref}} = K \bar{\rho} U_f^2 \tag{7.24}$$

where $K$ is a parameter depending on the obstacle configuration, $\bar{\rho}$ is the average avalanche density and $U_f$ is the front velocity. For small obstacles it is advised to take $K = 1$ and for big ones $K = 2 \sin \alpha$, where $\alpha$ is the incidence angle. However, as it is pointed out in [BO91], it is difficult to estimate the maximum pressure exerted by an avalanche since we have only very limited information on the vertical structure of the flow.

**Remark 46.** *The given above formula (7.24) is applicable to avalanches in inertial regime. When we deal with a gravity flow regime (in Fluid Mechanics we call it the Stokes flow [HB83]), the situation is more complicated since the flow is governed by the rheology which is essentially unknown [AM04]. In this case, engineers use another expression [ABB+06]:*

$$P_d = 2\bar{\rho} g (h - z).$$

For aerosol avalanches, Beghin and Closet [BC90] proposed the following empirical law to estimate the impact pressure:

$$P_d = \frac{K}{2} K_a(z) \bar{\rho} U_f^2,$$

where $K_a(z)$ is a dimensionless factor taking into account for the velocity variations in the upward direction. They also suggested an idealized form of the factor $K_a(z)$:

$$K_a(z) = \begin{cases} 10, & z < 0.1h, \\ 19 - 90z, & 0.1h \le z \le 0.2h, \\ 1, & z > 0.2h, \end{cases} \tag{7.25}$$

where $h$ is the impacting avalanche height. It was shown later [NB03] that this approximation underestimates the dynamic pressure in all parts of the flow.

The big advantage of the presented here approach is that we have the complete information on the mass but also the pressure distribution in the whole domain. On Figure 7.13 one can see the distribution of the dynamic pressure at $t = 60$ s during the impact process. It is important to note that an "aspiration" zone is revealed near the obstacle base along with a high pressure field at the top. In civil engineering this shear-type loading is known to be particularly dangerous for structures.

The methodology presented in this study allows to determine the impact pressures with required accuracy. The pressure profiles along the impacted wall can be easily extracted from numerical computations, thus, replacing empirical formulas such as (7.25). Our numerical experiments show also that the form of the vertical pressure distribution does not

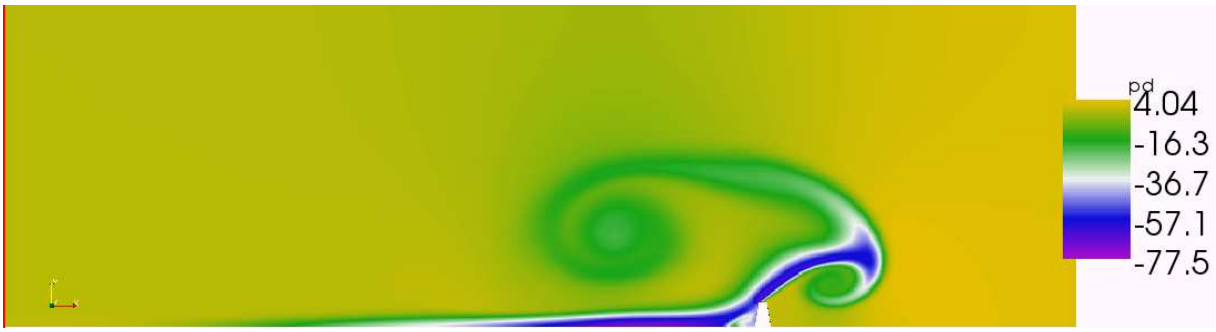


**Figure 7.13:** Dynamic pressure distribution in the computational domain at $t = 60\ s$. The color scale ranges from $-77.5\ Pa$ to the maximum value $4.04\ Pa$.

change drastically when we vary the obstacle height in some reasonable limits. It means that precomputed pressure profiles may be scaled and reused for different obstacles within engineering accuracy [BC90, MS93].

### 7.1.4 Conclusions and perspectives

In the present paper we derive a novel model for the flow of two miscible inhomogeneous fluids. The mixing between two fluids is assumed to be modeled by the Fick's law (7.6). Then, we reformulate the model in terms of the so-called volume-based velocity [Bre05a, Bre05b] in which the flow is exactly incompressible. It is also shown that the novel model allows for a physically sound evolution of the kinetic energy.

We show some preliminary results on the numerical modeling of powder-snow avalanches. We compute the evolution of an avalanche from the beginning until hitting against a trapezoidal obstacle. Impact pressures extracted from these computations can be used for the design of protecting structures.

For the moment the obstacle is assumed to be absolutely rigid. In future studies this assumption can be relaxed and efforts exerted on the obstacle could be coupled with a solid mechanics part [KB01]. This research axis seems to be still underexplored. However, there is already interesting experimental material on the avalanche interaction with solid obstacles [LSBH95, Pri03, PNBNF04, NB03, BR04].

There is also an important question of boundary conditions. All computational results presented above were obtained with the usual no-slip condition. The development of other types of physically sound boundary conditions which lead to well-posed mathematical problems is highly needed.

Recall that a powder-snow avalanche front can reach the speed up to 100 m/s. Conse-

quently, the Mach number Ma attains relatively high values:

$$\mathrm{Ma} := \frac{u_f}{c_s} \approx 0.3,$$

where $c_s$ is the sound speed in the air. It means that compressible effects may be important during the propagation stage. In general, impact events are followed by strong compressions. Hence, in future works we are planning to take into account the compressibility in some weak and strong senses [DDG08c, DDG10, DDG08a, Dut07] and to perform the comparisons with the present results. Obviously, at this point a validation against experimental data is highly recommended.

The rheology of avalanches should be further investigated [AM04] and future models will take this information into account. At this stage, close collaboration between physicists and mathematicians is needed to bring the answers on challenging questions.

# Appendix A

# Barotropic two-phase models

*What it means really to understand an equation – that is, in more than in a strictly mathematical sense – was described by Dirac. He said: "I understand what an equation means if I have a way of figuring out the characteristics of its solution without actually solving it." So if we have a way of knowing what should happen in given circumstances without actually solving the equations, then we "understand" the equations, as applied to those circumstances. A physical understanding is a completely unmathematical, imprecise, and inexact thing, but absolutely necessary for a physicist.*

Richard Feynman

## Contents

# A.1 Two-fluid barotropic models for powder-snow avalanche flows

Abstract. In the present study we discuss several modeling issues of powder-snow avalanche flows. We take a two-fluid modeling paradigm. For the sake of simplicity, we will restrict our attention to barotropic equations. We begin the exposition by a compressible model with two velocities for each fluid. However, this model may become non-hyperbolic and thus, represents serious challenges for numerical methods. To overcome these issues, we derive a single velocity model as a result of a relaxation process. This model can be easily shown to be hyperbolic for any reasonable equation of state. Finally, an incompressible limit of this model is derived.

## A.1.1 Introduction

Snow avalanches represent a serious problem for society in mountain regions. The avalanche winter of 1999 attracted a lot of attention to this hazardous natural phenomenon [ABB+06, Lie06]. Further development of mountain regions requires an adequate level of avalanche safety. Therefore, avalanche protective measures (deflecting and catching dams) become increasingly important [JGIL09]. During the same winter, several avalanches overran avalanche dams, underlining the need for further research in this field. Proper design of protecting structures necessitates profound understanding of the snow avalanches flow and of the interaction process with dams and other obstacles [DARB10, NBNBH02].

Natural snow avalanches are believed to consist of three different layers: a dense core, a fluidised layer and a suspension cloud. Sometimes the surrounding powder cloud is absent and we speak about an avalanche in the flowing régime. Obviously, transition boundaries between these layers are not sharp and this classification is rather conventional.

The dense core consists of snow particles in persistent frictional contact [Iss03]. The density is of the order of 300 kg/m$^3$ and the depth of this layer does not exceed 3 m. The fluidised régime is characterized by particle's mean-free-paths up to several particle's diameters. This dynamics at microscopic level explains more fluid-like behaviour at large scales. The density of this layer is in the range of 50 - 100 kg/m$^3$ and the height is about 3 - 5 m. To model successfully this kind of flows it is crucial to know the complex fluid rheology. Finally, these two interior layers can be covered by the powder cloud which is a turbulent suspension of snow particles in the air. The density ranges from 4 to 20 kg/m$^3$ and an avalanche in aerosol régime can reach the height of 100 m or more [RH04]. This flow is driven essentially by turbulent advection and particles collisions are unimportant.

In the present study we are concerned with some questions of powder-snow avalanche modelling. Since the interface cannot be defined for this type of flows, we choose the

modelling paradigm of two-phase flows. In this approach the governing equations of each phase are spatially averaged to come up with the description of the fluid mixture [Ish75, Rov06].

It is known [RH04] that the front of such an avalanche can develop the speed[1] $u_f \approx$ 100 m/s. For comparison, the speed of sound $c_0$ in the air is about 300 m/s. It means that the local Mach number Ma can reach the value of

$$\mathrm{Ma} := \frac{u_f}{c_0} \approx 0.33.$$

Hence, compressible effects may become important. That is why, we begin our exposition with a compressible model. Then, we gradually simplify it to come up with an incompressible one at the end of the present text. The goal is achieved by taking the limit as the Mach number tends to zero.

The present text is organized as follows. In Section A.1.2 we present a barotropic compressible two-phase model with two velocities. Then, this model is simplified in Section A.1.3 using a velocity relaxation process. The incompressible limit of resulting system is derived in Section A.1.4. Finally, several conclusions and perspectives are drawn out in Section A.1.5.

## A.1.2 Two-phase flow modelling

Let us consider a domain $\Omega \subseteq \mathbb{R}^3$ where a simultaneous flow of two barotropic fluids occurs. All quantities related to the heavy and light fluids will be denoted by $+$ and $-$ correspondingly. In view of application to snow avalanches, one can consider the heavy fluid of being constituted of snow particles and the light fluid is the air. When the mixing process is extremely complicated and it is impossible to follow the interface between two fluids, the classical modelling procedure consists in applying a volume average operator [Ish75, Rov06]. Thereby, we make appear two additional variables $\alpha^{\pm}(\mathbf{x}, t)$, $\mathbf{x} \in \Omega$ which are called the volume fractions and defined as:

$$\alpha^{\pm}(\mathbf{x}, t) := \lim_{\substack{|d\Omega| \to 0 \\ \mathbf{x} \in d\Omega}} \frac{|d\Omega^{\pm}|}{|d\Omega|},$$

the heavy fluid occupies volume $d\Omega^{+} \subseteq d\Omega$ and the light one the volume $d\Omega^{-} \subseteq d\Omega$ (see Figure A.1) such that

$$|d\Omega| \equiv |d\Omega^{+}| + |d\Omega^{-}|. \tag{A.1}$$

From the relation (A.1) it is obvious that $\alpha^{+}(\mathbf{x}, t) + \alpha^{-}(\mathbf{x}, t) \equiv 1$, $\forall \mathbf{x} \in \Omega$.

[1] When we estimate the Mach number magnitude, the particle characteristic velocity should be taken. However, this information is not easily accessible and we took the maximum front velocity. It can lead to some overestimation of the Mach number.

After performing the averaging process, one obtains two equations of mass and momentum conservation:

$$\partial_t(\alpha^\pm\rho^\pm) + \nabla\cdot(\alpha^\pm\rho^\pm\vec{u}^\pm) = 0, \tag{A.2}$$

$$\partial_t(\alpha^\pm\rho^\pm\vec{u}^\pm) + \nabla\cdot(\alpha^\pm\rho^\pm\vec{u}^\pm\otimes\vec{u}^\pm) + \alpha^\pm\nabla p = \nabla\cdot(\alpha^\pm\boldsymbol{\tau}^\pm) + \alpha^\pm\rho^\pm\vec{g}, \tag{A.3}$$

where $\rho^\pm(\mathbf{x},t), \vec{u}^\pm(\mathbf{x},t), \boldsymbol{\tau}^\pm(\mathbf{x},t)$ are densities, velocities and viscous stress tensors of each fluid respectively. Traditionally, the vector $\vec{g}$ denotes the gravity acceleration. We assume that both fluids share the same pressure[2] $p = p^\pm(\rho^\pm)$ and equations of state of each phase fulfill minimal thermodynamical requirements:

$$p^\pm(\rho^\pm) > 0, \quad \frac{\partial p^\pm(\rho^\pm)}{\partial\rho^\pm} > 0, \quad \text{for} \quad \rho^\pm > 0. \tag{A.4}$$

In order to obtain a well-posed problem, governing equations (A.2), (A.3) should be completed by appropriate initial and boundary conditions.

If we assume both fluids to be Newtonian, the viscous stress tensor $\boldsymbol{\tau}^\pm$ takes the following classical form:

$$\boldsymbol{\tau}^\pm = \lambda^\pm \operatorname{tr}\mathbf{D}(\vec{u}^\pm)\mathrm{Id} + 2\mu^\pm\mathbf{D}(\vec{u}^\pm), \quad \operatorname{tr}\mathbf{D}(\vec{u}^\pm) = \nabla\cdot\vec{u}^\pm, \tag{A.5}$$

where $\mathrm{Id} := (\delta_{ij})_{1\le i,j\le 3}$ is the identity tensor, $\mathbf{D}(\vec{u}) := \frac{1}{2}\Big(\nabla\vec{u}^\pm + {}^t(\nabla\vec{u}^\pm)\Big)$ is the deformation rate and $\lambda^\pm$, $\mu^\pm$ are viscosity coefficients. For ideal gases, for example, these coefficients are related by Stokes relation $\lambda^\pm + \frac{2}{3}\mu^\pm = 0$. In application to powder-snow avalanches, viscosity coefficients $\lambda^\pm$, $\mu^\pm$ should be understood in the sense of eddy viscosity.

**Remark 47.** *From physical point of view, presented here model (A.2), (A.3) is far from being complete. For example, one could supplement it by capillarity effects in the Korteweg form. Also we omited all the terms which model mass, momentum and energy exchange*

[2] In general, this kind of assumptions is reasonable, since relaxation processes will tend to equilibrate the system when time evolves.

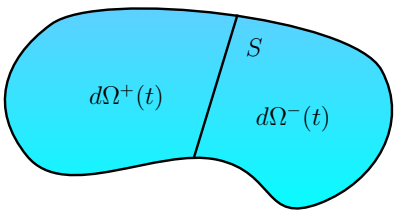


**Figure A.1:** An elementary fluid volume $d\Omega$ occupied by two phases.

*between two phases. Generally, their form is strongly dependent on the physical situation under consideration.*

**Remark 48.** *While considering two-phase flows, it is useful to introduce several additional quantities which play an important rôle in the description of such flows. The mixture density $\rho$ and mass fractions $m^{\pm}$ are naturally defined as:*

$$\rho(\mathbf{x},t) := \alpha^{+}\rho^{+} + \alpha^{-}\rho^{-} > 0, \quad \forall (\mathbf{x},t) \in \Omega \times [0,T],$$

$$m^{\pm} := \frac{\alpha^{\pm}\rho^{\pm}}{\rho}, \quad m^{+} + m^{-} = 1.$$

*The total density $\rho$ is assumed to be strictly positive everywhere in the domain $\Omega$. Hence, the void creation is forbidden in our modeling.*

*Important quantities $\rho$, $m^{\pm}$ will appear several times below.*

In principle, one could use equations (A.2), (A.3) to model various two-phase flows. However, this system remains quite expensive for large scale simulations required by real-life applications. The major difficulty comes from the advection operator associated to model (A.2), (A.3) which can be non-hyperbolic [BDGG09, Rov06]. In the next section we will derive a simplified two-fluid model which is proposed as a candidate for powder-snow avalanche compressible simulations.

### A.1.3 Velocity relaxation

We would like to reduce the number of variables in the system (A.2), (A.3). The main idea is to introduce the common velocity field for both phases. For this purpose, we will introduce a relaxation term to the momentum conservation equation (A.3):

$$\partial_t(\alpha^{\pm}\rho^{\pm}\vec{u}^{\pm}) + \nabla\cdot(\alpha^{\pm}\rho^{\pm}\vec{u}^{\pm}\otimes\vec{u}^{\pm}) + \alpha^{\pm}\nabla p = \nabla\cdot(\alpha^{\pm}\boldsymbol{\tau}^{\pm}) + \alpha^{\pm}\rho^{\pm}\vec{g} \pm \frac{\kappa}{\epsilon}(\vec{u}^{+} - \vec{u}^{-}), \quad \text{(A.6)}$$

where $\kappa = \mathcal{O}(1)$ is a constant and $\epsilon$ is a small parameter which controls the magnitude of the relaxation term. Physically this additional term represents the friction between two phases. In the following, we are going to take the singular limit as the relaxation parameter $\epsilon \to 0$. This is achieved with Chapman-Enskog type expansion. In this way, we constrain velocities $\vec{u}^{\pm}(\mathbf{x},t)$ to tend to the common value $\vec{u}(\mathbf{x},t)$. This technique has been already successfully applied to the Baer-Nunziato model [BN86] in [MG05].

The first step consists in rewriting the governing equations (A.2), (A.6) in the quasi-linear form. To shorten notations, we will also use the material time derivative which is classically defined for any smooth scalar function $\phi(\mathbf{x},t)$ as

$$\frac{d^{\pm}\phi}{dt} := \frac{\partial\phi}{\partial t} + \vec{u}^{\pm}\cdot\nabla\phi.$$

**Lemma 5.** *Smooth solutions to equations (A.2), (A.6) satisfy the following system:*

$$\alpha^{\pm}\frac{d^{\pm}p}{dt} + \rho^{\pm}(c_s^{\pm})^2\frac{d^{\pm}\alpha^{\pm}}{dt} + \alpha^{\pm}\rho^{\pm}(c_s^{\pm})^2\nabla\cdot\vec{u}^{\pm} = 0, \tag{A.7}$$

$$\alpha^{\pm}\rho^{\pm}\frac{d^{\pm}\vec{u}^{\pm}}{dt} + \alpha^{\pm}\nabla p = \nabla\cdot(\alpha^{\pm}\boldsymbol{\tau}^{\pm}) + \alpha^{\pm}\rho^{\pm}\vec{g} \pm \frac{\kappa}{\epsilon}(\vec{u}^{+} - \vec{u}^{-}), \tag{A.8}$$

*where* $(c_s^{\pm})^2 := \left.\frac{\partial p^{\pm}}{\partial \rho^{\pm}}\right|_{s^{\pm}}$ *represents the sound speed in each phase* $\pm$.

*Proof.* This result follows from direct calculations. First of all, we remark that the mass conservation equation (A.2) can be rewritten using the material derivative as follows:

$$\frac{d^{\pm}(\alpha^{\pm}\rho^{\pm})}{dt} + \alpha^{\pm}\rho^{\pm}\nabla\cdot\vec{u}^{\pm} = 0. \tag{A.9}$$

Using equations of state $p = p^{\pm}(\rho^{\pm})$, we can express the density material derivative in terms of the pressure and the sound speed:

$$\frac{d^{\pm}\rho^{\pm}}{dt} = \frac{1}{(c_s^{\pm})^2}\frac{d^{\pm}p}{dt}.$$

Now, it is straightforward to derive equation (A.7) from (A.9).

Finally, if we multiply equation (A.9) by $\vec{u}^{\pm}$ and subtract it from the momentum conservation equation (A.6), we will get desired result (A.8). □

Equations (A.7), (A.8) can be also recast in the matrix form which is particularly useful for further developments:

$$\mathbb{A}(V_\varepsilon)\frac{\partial V_\varepsilon}{\partial t} + \mathbf{B}(V_\varepsilon)\nabla V_\varepsilon = \nabla\cdot\mathbf{T}(V_\varepsilon) + \mathbf{S}(V_\varepsilon) + \frac{\mathbf{R}(V_\varepsilon)}{\epsilon}, \tag{A.10}$$

where we introduced several notations. The vector $V_\varepsilon$ represents four unknown physical variables $V_\varepsilon := {}^t(p, \alpha^{+}, \vec{u}^{+}, \vec{u}^{-})$ with respective time and space derivatives:

$$\frac{\partial V_\varepsilon}{\partial t} := {}^t(\partial_t p, \partial_t\alpha^{+}, \partial_t\vec{u}^{+}, \partial_t\vec{u}^{-}), \quad \nabla V_\varepsilon := {}^t\big(\nabla p, \nabla\alpha^{+}, (\cdot\nabla)\vec{u}^{+}, (\cdot\nabla)\vec{u}^{-}\big).$$

Matrices $\mathbb{A}(V_\varepsilon)$ and $\mathbf{B}(V_\varepsilon)$ are defined as

$$\mathbb{A}(V_\varepsilon) := \begin{pmatrix} \alpha^{+} & \rho^{+}(c_s^{+})^2 & 0 & 0 \\ \alpha^{-} & -\rho^{-}(c_s^{-})^2 & 0 & 0 \\ 0 & 0 & \alpha^{+}\rho^{+}\mathrm{Id} & 0 \\ 0 & 0 & 0 & \alpha^{-}\rho^{-}\mathrm{Id} \end{pmatrix},$$

$$\mathbf{B}(V_\varepsilon) := \begin{pmatrix} \alpha^{+}\vec{u}^{+} & \rho^{+}(c_s^{+})^2\vec{u}^{+} & \alpha^{+}\rho^{+}(c_s^{+})^2\mathrm{Id} & 0 \\ \alpha^{-}\vec{u}^{-} & -\rho^{-}(c_s^{-})^2\vec{u}^{-} & 0 & \alpha^{-}\rho^{-}(c_s^{-})^2\mathrm{Id} \\ \alpha^{+}\mathrm{Id} & 0 & \alpha^{+}\rho^{+}\vec{u}^{+} & 0 \\ 0 & \alpha^{-}\mathrm{Id} & 0 & \alpha^{-}\rho^{-}\vec{u}^{-} \end{pmatrix}.$$

In these matrix notations the size of zero entries must be chosen to make the multiplication operation possible.

On the right hand side of (A.10), the work of viscous forces is denoted by symbol $\nabla \cdot \mathbf{T}(V_\varepsilon) := {}^t(0, 0, \nabla\cdot\boldsymbol{\tau}^+, \nabla\cdot\boldsymbol{\tau}^-)$. The source term $\mathbf{S}(V_\varepsilon) := {}^t(0, 0, \alpha^+\rho^+\vec{g}, \alpha^-\rho^-\vec{g})$ incorporates the gravity force and $\mathbf{R}(V_\varepsilon) := {}^t(0, 0, \kappa(\vec{u}^+ - \vec{u}^-), -\kappa(\vec{u}^+ - \vec{u}^-))$ contains the relaxation terms.

Since we expect the limit $V_\varepsilon \to V$ to be finite as $\epsilon \to 0$, necessary the limiting vector $V$ lies in the hypersurface $\mathbf{R}(V) = 0$. In terms of physical variables, it implies $\vec{u}^+ \equiv \vec{u}^-$. Consequently, we find our solution in the form of the following Chapman-Enskog type expansion:

$$V_\varepsilon = V + \epsilon W + \mathcal{O}(\epsilon^2).$$

After substituting this expansion into (A.10) and taking into account that $\mathbf{R}(V) \equiv 0$, at the leading order in $\epsilon$ one obtains:

$$\mathbb{A}(V)\frac{\partial V}{\partial t} + \mathbf{B}(V)\nabla V = \nabla \cdot \mathbf{T}(V) + \mathbf{S}(V) + \mathbf{R}'(V)W, \tag{A.11}$$

where

$$\mathbf{R}'(V) := \begin{pmatrix} 0 & 0 & 0 & 0 \\ 0 & 0 & 0 & 0 \\ 0 & 0 & \kappa\mathrm{Id} & -\kappa\mathrm{Id} \\ 0 & 0 & -\kappa\mathrm{Id} & \kappa\mathrm{Id} \end{pmatrix}$$

Henceforth, we make a technical assumption of the presence of both phases in any point $\mathbf{x} \in \Omega$ of the flow domain. Mathematically it means that $0 < \alpha^+ < 1$. Since $\alpha^+ + \alpha^- = 1$, the same inequality holds for $\alpha^-$. Otherwise, the relaxation process physically does not make sense and we will have some mathematical technical difficulties.

Under the aforementioned assumption, the matrix $\mathbb{A}(V)$ is invertible. Hence, we can multiply on the left both sides of (A.11) by $\mathbf{P}\mathbb{A}^{-1}(V)$ where the projection matrix $\mathbf{P}$ is to be specified below:

$$\mathbf{P}\frac{\partial V}{\partial t} + \mathbf{P}\mathbb{A}^{-1}(V)\mathbf{B}(V)\nabla V = \mathbf{P}\mathbb{A}^{-1}(V)\nabla \cdot \mathbf{T}(V) + \mathbf{P}\tilde{\mathbf{R}}'(V)W + \mathbf{P}\mathbb{A}^{-1}(V)\mathbf{S}(V), \tag{A.12}$$

where $\tilde{\mathbf{R}}'(V) := \mathbb{A}^{-1}(V)\mathbf{R}'(V)$ and has the following components

$$\tilde{\mathbf{R}}'(V) = \begin{pmatrix} 0 & 0 & 0 & 0 \\ 0 & 0 & 0 & 0 \\ 0 & 0 & \dfrac{\kappa}{\alpha^+\rho^+}\mathrm{Id} & -\dfrac{\kappa}{\alpha^+\rho^+}\mathrm{Id} \\ 0 & 0 & -\dfrac{\kappa}{\alpha^-\rho^-}\mathrm{Id} & \dfrac{\kappa}{\alpha^-\rho^-}\mathrm{Id} \end{pmatrix}.$$

The vector of physical variables $V$ has four (in 1D) components ${}^t(p, \alpha^+, \vec{u}, \vec{u})$ and only three are different. In order to remove the redundant information, we will introduce the new vector $U$ defined as $U := {}^t(p, \alpha^+, \vec{u})$. The Jacobian matrix of this transformation can be easily computed:

$$\mathbf{J} := \frac{\partial V}{\partial U} = \begin{pmatrix} 1 & 0 & 0 \\ 0 & 1 & 0 \\ 0 & 0 & \mathrm{Id} \\ 0 & 0 & \mathrm{Id} \end{pmatrix}.$$

In new variables equation (A.12) becomes:

$$\mathbf{P}\mathbf{J}\frac{\partial U}{\partial t} + \mathbf{P}\mathbb{A}^{-1}(U)\mathbf{B}(U)\mathbf{J}\nabla U = \mathbf{P}\mathbb{A}^{-1}(U)\nabla\cdot\mathbf{T}(U) + \mathbf{P}\tilde{\mathbf{R}}'(U)W + \mathbf{P}\mathbb{A}^{-1}(U)\mathbf{S}(U). \quad \text{(A.13)}$$

Now we can formulate two conditions to construct the matrix $\mathbf{P}$. First of all, the vector $W$ is unknown and we need to remove it from equation (A.13). Hence, we require $\mathbf{P}\tilde{\mathbf{R}}'(V) = 0$. Then, we would like the governing equations to be explicitly resolved with respect to time derivatives. It gives us the second condition $\mathbf{P}\mathbf{J} = \mathrm{Id}$. The existence and effective construction of the matrix $\mathbf{P}$ satisfying two aforementioned conditions

$$\mathbf{P}\tilde{\mathbf{R}}'(V) = 0, \quad \mathbf{P}\mathbf{J} = \mathrm{Id},$$

are discussed below. Presented in this section results follow in great lines [MG05].

We will consider a slightly more general setting. Let be vector $V \in \mathbb{R}^n$ and its reduced counterpart $U \in \mathbb{R}^{n-k}$, $k < n$. In such geometry, $\tilde{\mathbf{R}}'(V) \in \mathrm{Mat}_{n,n}(\mathbb{R})$, $\mathbf{J} \in \mathrm{Mat}_{n,n-k}(\mathbb{R})$ and, consequently, $\mathbf{P} \in \mathrm{Mat}_{n-k,n}(\mathbb{R})$. Here, the notation $\mathrm{Mat}_{m,n}(\mathbb{R})$ denotes the set of $m \times n$ matrices with coefficients in $\mathbb{R}$. We have to say also that from algebraic point of view, matrices $\tilde{\mathbf{R}}'(V)$ and $\mathbf{R}'(V)$ are completely equivalent. Thus, for simplicity, in the following propositions we will reason in terms of $\mathbf{R}'(V)$.

**Lemma 6.** *The columns of the Jacobian matrix* $\mathbf{J}$ *form a basis of* $\ker\big(\mathbf{R}'(V)\big)$.

*Proof.* If we differentiate the relation $\mathbf{R}(V) = 0$ with respect to $U$, we will get the identity $\mathbf{R}'(V)\mathbf{J} = 0$. It implies that $\mathrm{range}\big(\mathbf{J}\big) \subseteq \ker\big(\mathbf{R}'(V)\big)$. By direct computation one verifies that $\dim \mathrm{range}\big(\mathbf{R}'(V)\big) = k$. From the well-known identity $\mathrm{range}\big(\mathbf{R}'(V)\big) \oplus \ker\big(\mathbf{R}'(V)\big) = \mathbb{R}^n$, one concludes that $\dim\ker\big(\mathbf{R}'(V)\big) = n - k$. But in the same time, the rank of $\mathbf{J}$ is equal to $n - k$ as well. It proves the result. □

**Theorem 7.** *We suppose that for all* $V$, $\mathrm{range}\big(\mathbf{R}'(V)\big) \cap \ker\big(\mathbf{R}'(V)\big) = \{0\}$ *then there exists a matrix* $\mathbf{P} \in \mathrm{Mat}_{n-k,n}(\mathbb{R})$ *such that* $\mathbf{P}\mathbf{R}'(V) = 0$ *and* $\mathbf{P}\mathbf{J} = \mathrm{Id}_{n-k}$.

*Proof.* Hypothesis $\text{range}\big(\mathbf{R}'(V)\big)\cap\ker\big(\mathbf{R}'(V)\big) = \{0\}$ implies that $\text{range}\big(\mathbf{R}'(V)\big)\oplus\ker\big(\mathbf{R}'(V)\big) = \mathbb{R}^n$. From Lemma 6 it follows that $\text{range}\big(\mathbf{J}\big) = \ker\big(\mathbf{R}'(V)\big)$. Thus, the space $\mathbb{R}^n$ can be also represented as a direct sum $\text{range}\big(\mathbf{R}'(V)\big)\oplus\text{range}\big(\mathbf{J}\big)$. We will define $\mathbf{P}$ to be the projection on $\ker\big(\mathbf{R}'(V)\big) \equiv \text{range}\big(\mathbf{J}\big)$. Since obviously $\mathbf{R}'(V) \in \text{range}\big(\mathbf{R}'(V)\big)$ and $\mathbf{J} \in \text{range}\big(\mathbf{J}\big)$, we have two required identities: $\mathbf{PJ} = \text{Id}_{n-k}$ and $\mathbf{PR}'(V) = 0$. □

Now, in order to compute effectively the projection matrix $\mathbf{P}$, we will construct an auxiliary matrix $\mathbf{D}(V) = [J^1, \dots, J^{n-k}, I^1, \dots, I^k]$, where $J^i$ is the column $i$ of the matrix $\mathbf{J}$ and $\{I^1, \dots, I^k\}$ are vectors which form a basis of $\text{range}\big(\mathbf{R}'(V)\big)$. We remark that $\mathbf{PD}(V) = [\text{Id}_{n-k}, 0]$. Lemma 6 implies that the matrix $\mathbf{D}(V)$ is invertible. Thus, the projection $\mathbf{P}$ can be computed by inverting $\mathbf{D}(V)$:

$$\mathbf{P} = [\text{Id}_{n-k}, 0] \cdot \mathbf{D}^{-1}(V).$$

Let us apply this general framework to our model (A.12), where $n = 4$ and $k = 1$. The matrix $\mathbf{D}(V)$ and its inverse $\mathbf{D}^{-1}(V)$ take this form:

$$\mathbf{D}(V) = \begin{pmatrix} 1 & 0 & 0 & 0 \\ 0 & 1 & 0 & 0 \\ 0 & 0 & \text{Id} & \dfrac{\kappa}{\alpha^+\rho^+}\text{Id} \\ 0 & 0 & \text{Id} & -\dfrac{\kappa}{\alpha^-\rho^-}\text{Id} \end{pmatrix}, \quad \mathbf{D}^{-1}(V) = \begin{pmatrix} 1 & 0 & 0 & 0 \\ 0 & 1 & 0 & 0 \\ 0 & 0 & m^+\text{Id} & m^-\text{Id} \\ 0 & 0 & \dfrac{m^+m^-\rho}{\kappa}\text{Id} & -\dfrac{m^+m^-\rho}{\kappa}\text{Id} \end{pmatrix},$$

where $m^\pm$ are mass fractions defined in Remark 48.

Now, the projection matrix $\mathbf{P}$ can be immediately computed:

$$\mathbf{P} = \begin{pmatrix} 1 & 0 & 0 & 0 \\ 0 & 1 & 0 & 0 \\ 0 & 0 & m^+\text{Id} & m^-\text{Id} \end{pmatrix}.$$

Finally, after computing all matrix products $\mathbf{P}\mathbb{A}^{-1}(U)\mathbf{B}(U)\mathbf{J}$, $\mathbf{P}\mathbb{A}^{-1}(U)\nabla\cdot\mathbf{T}(U)$, $\mathbf{P}\mathbb{A}^{-1}(U)\mathbf{S}(U)$ present in equation (A.13), we obtain the desired single velocity model:

$$\frac{\partial p}{\partial t} + \vec{u}\cdot\nabla p + \rho c_s^2 \nabla\cdot\vec{u} = 0, \tag{A.14}$$

$$\frac{\partial \alpha^+}{\partial t} + \vec{u}\cdot\nabla\alpha^+ + \alpha^+\alpha^-\delta\nabla\cdot\vec{u} = 0, \tag{A.15}$$

$$\rho\frac{\partial \vec{u}}{\partial t} + \rho(\vec{u}\cdot\nabla)\vec{u} = \rho\vec{g} + \nabla\cdot\boldsymbol{\tau}, \tag{A.16}$$

where $\rho = \alpha^+\rho^+ + \alpha^-\rho^-$ is the mixture density and $c_s^2$ is the sound velocity in the mixture which is determined by this formula:

$$\rho c_s^2 := \frac{\rho^+\rho^-(c_s^+)^2(c_s^-)^2}{\alpha^-\rho^+(c_s^+)^2 + \alpha^+\rho^-(c_s^-)^2},$$

and $\delta$ is given by

$$\delta := \frac{\rho^+(c_s^+)^2 - \rho^-(c_s^-)^2}{\alpha^-\rho^+(c_s^+)^2 + \alpha^+\rho^-(c_s^-)^2}.$$

Finally, $\boldsymbol{\tau} := \lambda \operatorname{tr} \mathbf{D}(\vec{u})\mathrm{Id} + 2\mu\mathbf{D}(\vec{u})$ is the viscous stress tensor of the mixture. Viscosity coefficients $\lambda$, $\mu$ are naturally defined as

$$\lambda := \alpha^+\lambda^+ + \alpha^-\lambda^-, \quad \mu := \alpha^+\mu^+ + \alpha^-\mu^-.$$

Equations (A.14) – (A.16) can be recast in the conservative form which is more convenient for numerical computations and theoretical analysis. To achieve this purpose, we replace the pressure $p$ in (A.14) by $\rho^\pm$ using the equation of state:

$$\frac{\partial \rho^\pm}{\partial t} + \vec{u}\cdot\nabla\rho^\pm + \frac{\rho c_s^2}{(c_s^\pm)^2}\nabla\cdot\vec{u} = 0.$$

The last equation is multiplied by $\alpha^\pm$, the second equation (A.15) is multiplied by $\rho^\pm$ and we sum them to come up with two mass conservation equations. Transformation of the momentum conservation equation (A.16) is straightforward. The resulting conservative system takes this form:

$$\partial_t(\alpha^\pm\rho^\pm) + \nabla\cdot(\alpha^\pm\rho^\pm\vec{u}) = 0, \tag{A.17}$$

$$\partial_t(\rho\vec{u}) + \nabla\cdot(\rho\vec{u}\otimes\vec{u}) + \nabla p = \nabla\cdot\boldsymbol{\tau} + \rho\vec{g}. \tag{A.18}$$

These equations represent a barotropic version of the four-equations model proposed in [DDG10, Dut07].

It can be shown that the advection operator of the model (A.17), (A.18) is hyperbolic for any reasonable equation of state (A.4). Moreover, this system contains fewer variables which allow more efficient computations required in practice.

### A.1.4 Incompressible limit

The main scope of this paper is certainly around compressible two-fluid models. However, we decided to derive an incompressible limit of the single velocity model (A.17), (A.18) for the case when acoustic effects should be filtered out. The presence of acoustic waves represent, for example, a major restriction for the time step, if an explicit scheme is used.

For the sake of simplicity, we will neglect dissipative effects which do not affect the acoustic wave propagation. Thus, in this section we consider the following system of

equations:

$$\partial_t(\alpha^\pm\rho^\pm) + \nabla\cdot(\alpha^\pm\rho^\pm\vec{u}) = 0, \tag{A.19}$$

$$\rho\partial_t\vec{u} + \rho(\vec{u}\cdot\nabla)\vec{u} + \nabla p = \rho\vec{g}. \tag{A.20}$$

$$\tag{A.21}$$

For convenience, we rewrite equation (A.18) in nonconservative form.

In order to estimate the relative importance of various terms, we introduce dimensionless variables. The characteristic length, time, and velocity scales are denoted by $\ell$, $t_0$ and $U_0$ respectively. For example, $\ell$ may be chosen as the diameter of the fluid domain $\Omega$, $t_0$ is the biggest vortex turnover time and $U_0$ is the typical flow velocity. The density and the sound velocity scales are chosen to be those of the heavy fluid, i.e. $\rho_0^+$ and $c_{0s}^+$ correspondingly. Since we are interested in acoustic effects, the natural pressure scale is given by $\rho_0^+(c_{0s}^+)^2$. If we summarize these remarks, dependent and independent dimensionless variables (denoted with primes) are defined as:

$$\mathbf{x}' := \frac{\mathbf{x}}{\ell}, \quad t' := \frac{t}{t_0}, \quad \vec{u}' := \frac{\vec{u}}{U_0}, \quad (\rho^\pm)' := \frac{\rho^\pm}{\rho_0^+}, \quad p' := \frac{p}{\rho_0^+(c_{0s}^+)^2}.$$

**Remark 49.** *There is nothing to do for the volume fractions $\alpha^\pm$, since this quantity is dimensionless by definition.*

After dropping the tildes, nondimensional system of equation becomes:

$$\mathrm{St}\,\partial_t(\alpha^\pm\rho^\pm) + \nabla\cdot(\alpha^\pm\rho^\pm\vec{u}) = 0, \tag{A.22}$$

$$\mathrm{St}\,\rho\partial_t\vec{u} + \rho(\vec{u}\cdot\nabla)\vec{u} + \frac{1}{\mathrm{Ma}^2}\nabla p = \frac{1}{\mathrm{Fr}^2}\rho\vec{g}, \tag{A.23}$$

where several scaling parameters have appeared:

- Strouhal number $\mathrm{St} := \dfrac{\ell}{U_0 t_0}$. In this study we will assume the Strouhal number to be equal to one, i.e. $t_0 = \dfrac{\ell}{U_0}$.
- Mach number $\mathrm{Ma} := \dfrac{U_0}{c_{0s}^+}$ which measures the relative importance of the flow speed and the sound speed in the medium.
- Froude number $\mathrm{Fr} := \dfrac{U_0}{\sqrt{g\ell}}$ compares inertia and gravitational force. This parameter will not play an important rôle in the present study.

All physical variables $\alpha^\pm$, $\rho^\pm$, $p$ and $\vec{u}$ are expanded in formal series in powers of the Mach number:

$$\phi = \phi_0 + \mathrm{Ma}\phi_1 + \mathrm{Ma}^2\phi_2 + \dots, \qquad \phi \in \{\alpha^\pm, \rho^\pm, p, \vec{u}\}. \tag{A.24}$$

Formal expansion (A.24) is then substituted into the system (A.22), (A.23). At the orders $\mathrm{Ma}^{-2}$ and $\mathrm{Ma}^{-1}$, we obtain

$$\nabla p_0 = \nabla p_1 = 0.$$

In other words, $p_0 = p_0(t)$ and $p_1 = p_1(t)$ are only functions of time. At the order $\mathrm{Ma}^0$ we get the following system of equations:

$$\partial_t(\alpha_0^\pm \rho_0^\pm) + \nabla \cdot (\alpha_0^\pm \rho_0^\pm \vec{u}_0) = 0, \tag{A.25}$$

$$\rho_0 \partial_t \vec{u}_0 + \rho_0(\vec{u}_0 \cdot \nabla)\vec{u}_0 + \nabla\pi = \frac{1}{\mathrm{Fr}^2}\rho_0 \vec{g}, \tag{A.26}$$

$$\tag{A.27}$$

where by $\pi$ we denote $p_2$.

Using the same asymptotic expansion (A.24), one can show that at the leading order we keep usual relations between densities and volume fractions:

$$\alpha_0^+ + \alpha_0^- = 1, \quad \rho_0 = \alpha_0^+ \rho_0^+ + \alpha_0^- \rho_0^-. \tag{A.28}$$

In order to investigate the behaviour of $\rho_0^\pm$, we will invert the equation of state[3] $\rho^\pm = \rho^\pm(p) = (p^\pm)^{-1}(p)$ and expand it in powers of Ma:

$$\rho^\pm(p) = \rho^\pm(p_0) + \mathrm{Ma}\left.\frac{\partial \rho^\pm}{\partial p}\right|_{p_0} p_1 + \mathrm{Ma}^2\left(\left.\frac{\partial \rho^\pm}{\partial p}\right|_{p_0} p_2 + \left.\frac{\partial^2 \rho^\pm}{\partial p^2}\right|_{p_0} p_1^2\right) + \mathcal{O}(\mathrm{Ma}^3)$$

On the other hand, from (A.24) we know that

$$\rho^\pm = \rho_0^\pm + \mathrm{Ma}\rho_1^\pm + \mathrm{Ma}^2\rho_2^\pm + \dots$$

Matching these expansions at two lowest orders shows that $\rho_{0,1}^\pm$ are functions only of the time variable:

$$\rho_0^\pm = \rho^\pm(p_0(t)) =: r_0^\pm(t), \quad \rho_1^\pm = \left.\frac{\partial \rho^\pm}{\partial p}\right|_{p_0(t)} p_1(t) =: r_1^\pm(t).$$

It is possible to show that $\rho_{0,1}^\pm$ are just constants. Consider the Gibbs relation which reads

$$T^\pm ds^\pm = de^\pm - \frac{p}{(\rho^\pm)^2} d\rho^\pm.$$

[3]The function $p = p^\pm(\rho^\pm)$ is invertible since it is a strictly increasing function $\dfrac{\partial p}{\partial \rho^\pm} > 0$.

Since we consider isentropic flows, $ds^{\pm} \equiv 0$ and, consequently, the Gibbs relation takes a much simpler form:

$$de^{\pm} = \frac{p}{(\rho^{\pm})^2} d\rho^{\pm}. \tag{A.29}$$

It can be shown by considering the total energy conservation equation [MDG10], that the internal energy $e^{\pm}$ naturally scales with $U_0^2$. After dividing (A.29) by $dt$ and switching to dimensionless variables, equation (A.29) takes the following form (after droping the primes):

$$\frac{de^{\pm}}{dt} = \frac{p}{\mathrm{Ma}^2(\rho^{\pm})^2} \frac{d\rho^{\pm}}{dt}.$$

Expanding $e^{\pm}$ in the series (A.24) and looking at two leading terms, leads to the desired result:

$$\frac{d\rho^{\pm}_{0,1}}{dt} = 0 \quad \Rightarrow \quad \rho^{\pm}_{0,1} = \text{const}.$$

The incompressibility condition $\nabla \cdot \vec{u}_0 = 0$ is obtained by summing up mass conservation equations (A.25) and taking into account relation (A.28).

If we summarize all developments made above and switch back to dimensional variables, the resulting incompressible system will become:

$$\partial_t \alpha^{\pm} + \nabla \alpha^{\pm} \cdot \vec{u} = 0, \tag{A.30}$$

$$\nabla \cdot \vec{u} = 0, \tag{A.31}$$

$$\rho \partial_t \vec{u} + \rho(\vec{u} \cdot \nabla)\vec{u} + \nabla \pi = \rho \vec{g} + \nabla \cdot \boldsymbol{\tau}, \tag{A.32}$$

where we dropped the index 0 and added again dissipative effects. Viscous stress tensor $\boldsymbol{\tau}$ is still defined by expression (A.5), as in compressible case. In this case, we can speak about two-fluid Navier-Stokes equations. This system of equations (A.30) – (A.32) is much easier to solve numerically than its compressible analogue (A.17), (A.18). In particular, this simplification is due to removed stiffness of acoustic waves.

## A.1.5 Conclusions and perspectives

In this study we presented several barotropic two-fluid models which can be used for numerical simulation of powder-snow avalanche flows. One of the main objectives of this paper was to reveal the connection between barotropic models with single and two velocities. The extension to more general fluids is in progress [MDG10].

Our exposition began with compressible two-phase model (A.2), (A.3) possessing two velocity variables. Then, using a relaxation process, we constrained the system to have a common velocity for both phases. Mathematically it was achieved with a Chapman-Enskog type expansion. Resulting model (A.17), (A.18) is hyperbolic for any reasonable equation

of state (A.4). Finally, two-fluid Navier-Stokes equations (A.30) – (A.32) were derived as an incompressible limit of the single velocity model (A.17), (A.18).

Hence, we presented three different two-fluid models which are related by formal derivation procedures. Simplifications made above, represent a good trade-off between accuracy and computational complexity. The final choice should be made after determining the flow régime and main goals of the simulation.

We did not incorporate yet any turbulence modeling. In this study we were focused essentially on the advection operators. However, it is obvious that the physical flow under consideration is fully turbulent in its aerosol part [RH04]. As the first physical approximation, turbulence effects can be taken into account by adding eddy viscosity terms and, thus, by modifying the viscous stress tensor $\boldsymbol{\tau}$. It will be done in future studies.

# Perspectives

*You have your way. I have my way. As for the right way, the correct way, and the only way, it does not exist.*

Friedrich Nietzsche

Scientific works presented in this manuscript are devoted to Fluid Mechanics in the large sense. More specifically, my primary scientific interests lie essentially in the fields of water waves and two-phase flows. The need of extensive numerical simulations of mathematical models arising in these domains yields my deep interest in numerical methods for PDEs. My future research activities will certainly deal with these branches of applied mathematics. Among various projects for the future, I can briefly describe a few ones which are the most crystallized in my mind.

Concerning tsunami waves, in collaboration with Dimitrios Mitsotakis and Leonid Chubarov we are going to prepare a sequel to our study with Frédéric Dias on tsunami wave energy, published in Proceedings of Royal Society in 2009. With Dimitrios we have also some ideas which could be used to develop a pseudo-spectral solver for the full water wave problem in non-periodic domains. It is an important direction to be explored. In collaboration with Theodoros Katsaounis we develop IMEX finite volume schemes for stiff dispersive KdV-BBM type equations.

In the topic of two-phase flows we would like to investigate the numerical simulation of quasi-incompressible flows with the four equations model. Godunov-type schemes are known to fail in this regime and we would like to develop an all-Mach version of the Finite Volumes Characteristic Flux (FVCF) approach. It would be a natural sequel to our works initiated with Frédéric Dias and Jean-Michel Ghidaglia and continued later in LAMA in collaboration with Marguerite Gisclon and Yannick Meyapin.

Since some time I feel an intellectual attraction to probabilities and stochastic processes. The cultural differences with continuous mechanics are enormous but I hope to overtake them during next several years. The inclusion of stochastic effects or random exterior conditions into mechanical models seems to me very exciting.

# Bibliography


[AB05] E. Audusse and M.-O. Bristeau. A well-balanced positivity preserving "second-order" scheme for shallow water flows on unstructured meshes. *J. Comput. Phys*, 206:311–333, 2005. 138, 139

[ABB+04] E. Audusse, F. Bouchut, O.M. Bristeau, R. Klein, and B. Perthame. A fast and stable well-balanced scheme with hydrostatic reconstruction for shallow water flows. *SIAM J. of Sc. Comp.*, 25:2050–2065, 2004. 121, 138, 213

[ABB+06] C. Ancey, V. Bain, E. Bardou, G. Borrel, R. Burnet, F. Jarry, O. Kolbl, and M. Meunier. *Dynamique des avalanches*. Presses polytechniques et universitaires romandes (Lausanne, Suisse), 2006. 311, 316

[AC99] K. Anastasiou and C. T. Chan. Solution of the 2d shallow water equations using the finite volume method on unstructured triangular meshes. *International Journal for Numerical Methods in Fluids*, 24:1225–1245, 1999. 121, 199, 200, 239

[ACK02] G. Allaire, S. Clerc, and S. Kokh. A five-equation model for the simulation of interfaces between compressible fluids. *J. Comput. Phys.*, 181:577–616, 2002. 261

[ACOR95] S. Aubry, C. Caremoli, J. Olive, and P. Rascle. The THYC three-dimensional thermal-hydraulic code for rod bundles : recent developments and validation tests. *Nuclear technology*, 112(3):331–345, 1995. 261, 288

[AD] D. C. Antonopoulos and V. D. Dougalis. Numerical solution of the 'classical' boussinesq system. *to apeer*. 214

[ADGM+00] M.V. Avolio, S. Di Gregorio, F. Mantovani, A. Pasuto, R. Rongo, S. Silvano, and W. Spataro. Simulation of the 1992 Tessina landslide by a cellular automata model and future hazard scenarios. *International Journal of Applied Earth Observation and Geoinformation*, 2:41–50, 2000. 293

[ADM09] D. C. Antonopoulos, V. A. Dougalis, and D. E. Mitsotakis. Initial-boundary-value problems for the Bona-Smith family of Boussinesq systems. *Advances in Differential Equations*, 14:27–53, 2009. 214

[ADM10] D. C. Antonopoulos, V. A. Dougalis, and D. E. Mitsotakis. Numerical solution of Boussinesq systems of the Bona-Smith family. *Appl. Numer. Math.*, 30:314–336, 2010. 215, 216, 219

[AGN05] F. Alcrudo and P. Garcia-Navarro. A high-resolution Godunov-type scheme in finite volumes for the 2d shallow-water equations. *Int. J. Numer. Methods Fluids*, 16:489–505, 2005. 121

[AKLV06] C. J. Ammon, H. Kanamori, T. Lay, and A. A. Velasco. The 17 July 2006 Java tsunami earthquake. *Geophysical Research Letters*, 33:L24308, 2006. 168, 171

[AKM90] S.N. Antonsev, A.V. Kazhikov, and V.N. Monakov. *Boundary Value Problems in Mechanics of Nonhomogeneous Fluids*. North-Holland, 1990. 297

[AM04] C. Ancey and M. Meunier. Estimating bulk rheological properties of flowing snow avalanches from field data. *J. Geophys. Res.*, 109:F01004, 2004. 311, 313

[Ami84] C. J. Amick. Regularity and uniqueness of solutions to the Boussinesq system of equations. *J. Diff. Eqns.*, 54:231–247, 1984. 203

[AMS04] F. Archambeau, N. Mehitoua, and M. Sakiz. Code Saturne: A finite volume code for the computation of turbulent incompressible flows - industrial applications. *International Journal On Finite Volumes*, 1:1–62, 2004. 143

[AMW98] D.M. Anderson, G.B. McFadden, and A.A. Wheeler. Diffuse-interface methods in fluid mechanics. *Ann. Rev. Fluid Mech.*, 30:139–165, 1998. 261

[Anc01] C. Ancey. *Geomorphological Fluid Mechanics*, volume 582, chapter Snow Avalanches, pages 319–338. Springer, 2001. 290

[Anc03] C. Ancey. Influence of particle entrainment from bed on the powder-snow avalanche dynamics. Technical report, Ecole Polytechnique Fédérale de Lausanne, Environmental Hydraulics Laboratory, 2003. 303

[Anc04] C. Ancey. Powder snow avalanches: Approximation as non-Boussinesq clouds with a Richardson number-dependent entrainment function. *J. Geophys. Res.*, 109:F01005, 2004. 293, 294

[AR02] K. Aki and P.G. Richards. *Quantitative Seismology*. University Science Books, 2002. 106

[Ara80] M. Arai. Characteristic and stability analyses for two-phase flow equation system with viscous terms. *Nucl. Sci. Eng.*, 74:74–77, 1980. 265

[AS65] M. Abramowitz and I. A. Stegun. *Handbook of Mathematical Functions*. Dover, 1965. 65

[AU99] J. Akiyama and M. Ura. Motion of 2d buoyant clouds downslope. *Journal of Hydraulic Engineering*, 125:474–480, 1999. 293

[Aud04] E. Audusse. *Modélisation hyperbolique et analyse numérique pour les écoulements en eaux peu profondes*. PhD thesis, Université Paris VI, 2004. 139

[AVSS09] P. Avilez-Valente and F.J. Seabra-Santos. A high-order Petrov-Galerkin finite element method for the classical Boussinesq wave model. *Int. J. Numer. Meth. Fluids*, 59:969–1010, 2009. 200

[BÉ28] J.-B. Bélanger. Essai sur la solution numérique de quelques problèmes relatifs au mouvement permanent des eaux courantes. *Carilian-Goeury, Paris, France*, page 38, 1828. 302

[BadV83] H. Beirão da Veiga. Diffusion on viscous fluids, existence ans asymptotic properties of solutions. *Ann. Scuola Norm Pisa*, 10:341–351, 1983. 297

[BadVSV82] H. Beirão da Veiga, H. Separioni, and A. Valli. On the motion of nonhomogeneous fluids in the presence of diffusion. *J. Math. Anal. Appl.*, 85:179–191, 1982. 297

[Bal96] A.M. Balk. A Lagragian for water waves. *Phys. Fluids*, 8:416–419, 1996. 47

[Bar94] T.J. Barth. Aspects of unstructured grids and finite-volume solvers for the Euler and Navier-Stokes equations. *Lecture series - van Karman Institute for Fluid Dynamics*, 5:1–140, 1994. 279, 281, 282

[Bar04] E. Barthélémy. Nonlinear shallow water theories for coastal waves. *Surveys in Geophysics*, 25:315–337, 2004. 243

[Bas06] R. Basher. Global early warning systems for natural hazards: Systematic and people-centred. *Philosophical Transactions: Mathematical, Physical and Engineering Sciences*, 364(1845):2167–2182, 2006. 167

[BB73] J.P. Boris and D.L. Book. Flux corrected transport: Shasta, a fluid transport algorithm that works. *J. Comp. Phys.*, 11:38–69, 1973. 147, 281

[BB83] P. Beghin and G. Brugnot. Contribution of theoretical and experimental results to powder-snow avalanche dynamics. *Cold Review Science and Technology*, 8:63–73, 1983. 293

[BB01] G. Bellotti and M. Brocchini. On the shoreline boundary conditions for Boussinesq-type models. *Int. J. Num. Meth. in Fluids*, 37(4):479–500, 2001. 201

[BBM72] T.B. Benjamin, J.L. Bona, and J.J. Mahony. Model equations for long waves in nonlinear dispersive systems. *Philos. Trans. Royal Soc. London Ser. A*, 272:47–78, 1972. 46

[BBMA01] M. Brocchini, R. Bernetti, A. Mancinelli, and G. Albertini. An efficient solver for nearshore flows based on the WAF method. *Coastal Engineering*, 43:105–129, 2001. 136

[BC90] P. Beghin and J.-F. Closet. Effet d'une digue sur l'écoulement d'une avalanche poudreuse. Technical report, Cemagref, 1990. 310, 311, 312

[BC98] J. L. Bona and M. Chen. A Boussinesq system for two-way propagation of nonlinear dispersive waves. *Physica D*, 116:191–224, 1998. 204, 215, 216

[BCCC97] P. Batten, N. Clarke, Lambert C., and D.M. Causon. On the choice of wavespeeds for the HLLC Riemann solver. *SIAM J. Sci. Comput.*, 18(6):1553–1570, 1997. 133

[BCL05] J.L. Bona, T. Colin, and D. Lannes. Long wave approximations for water waves. *Arch. Rational Mech. Anal.*, 178:373–410, 2005. 46, 243

[BCS02] J.L. Bona, M. Chen, and J.-C. Saut. Boussinesq equations and other systems for small-amplitude long waves in nonlinear dispersive media. I: Derivation and linear theory. *Journal of Nonlinear Science*, 12:283–318, 2002. 46, 51, 200, 202, 243

[BCS04] J.L. Bona, M. Chen, and J.-C. Saut. Boussinesq equations and other systems for small-amplitude long waves in nonlinear dispersive media: II. the nonlinear theory. *Nonlinearity*, 17:925–952, 2004. 46, 51, 203, 243

[BD82] J.A. Boure and J.-M. Delhaye. *Handbook of Multiphase Systems*, chapter General equations and two-phase flow modeling. Hemisphere, 1982. 260

[BD03] D. Bresch and B. Desjardins. Existence of global weak solutions for a 2d viscous shallow water equations and convergence to the quasi-geostrophic model. *Communications in Mathematical Physics*, 238:211–223, 2003. 165, 243

[BD06] D. Bresch and B. Desjardins. On the construction of approximate solutions for the 2D viscous shallow water model and for compressible Navier-Stokes models. *Journal de Mathématiques Pures et Appliqués*, 86(4):362–368, 2006. 243

[BD07] T.J. Bridges and F. Dias. Enhancement of the Benjamin-Feir instability with dissipation. *Phys. Fluids*, 19:104104, 2007. 79

[BDDV98] A. Bermudez, A. Dervieux, J.-A. Desideri, and M. E. Vazqueza. Upwind schemes for the two-dimensional shallow water equations with variable depth using unstructured meshes. *Computer Methods in Applied Mechanics and Engineering*, 155:49–72, 1998. 121

[BDF+07] V.P. Boñgolan-Walsh, J. Duan, P. Fischer, T. Özgökmen, and T. Iliescu. Impact of boundary conditions on entrainment and transport in gravity currents. *Applied Mathematical Modelling*, 31:1338–1350, 2007. 239

[BDGG09] D. Bresch, B. Desjardins, J.-M. Ghidaglia, and E. Grenier. On global weak solutions to a generic two-fluid model. *To appear in Archive for Rational Mechanics and Analysis*, 2009. 265, 274, 319

[BDM07] J.L. Bona, V.A. Dougalis, and D.E. Mitsotakis. Numerical solution of KdV-KdV systems of Boussinesq equations: I. The numerical scheme and generalized solitary waves. *Mat. Comp. Simul.*, 74:214–228, 2007. 200, 216, 243

[BDP00] N. Blaise, K. Debiane, and J.-M. Piau. Bed slope effect on the dam break problem. *J. Hydr. Res.*, 38(6), 2000. 239

[BE73] N.S. Bakhvalov and M.E. Eglit. Investigation of the one-dimensional motion of a snow avalanche along a flat slope. *Fluid Dynamics*, 8:683–689, 1973. 291, 293

[Beg79] P. Beghin. *Etude des bouffées bidimensionnelles de densité en écoulement sur pente avec application aux avalanches de neige poudreuse*. PhD thesis, Institut National Polytechnique de Grenoble, 1979. 293

[Bel04] C.V. Bellos. Experimental measurements of flood wave created by a dam break. *European Water*, 7/8:3–15, 2004. 239

[Ben67] T.B. Benjamin. Instability of periodic wavetrains in nonlinear dispersive systems. *Proc. R. Soc. London, Ser. A*, 299(59), 1967. 79

[Ben68] T.B. Benjamin. Gravity currents and related phenomenon. *J. Fluid Mech.*, 31:209–248, 1968. 238

[Ben74] D.J. Benney. *Nonlinear wave motion*, chapter Nonlinear waves. Amer. Math. Soc., Providence, RI, 1974. 242

[BEN02] V. Blagovechshenskiy, M. Eglit, and M. Naaim. The calibration of an avalanche mathematical model using field data. *Nat. Hazards Earth Syst. Sci.*, 2:217–220, 2002. 291

[Ber07] M.V. Berry. Focused tsunami waves. *Proc. R. Soc. A*, 463:3055–3071, 2007. 100

[Bes90] D. Bestion. The physical closure laws in the CATHARE code. *Nuclear Engineering and Design*, 124:229 – 245, 1990. 261

[BES07] D. Bresch, E. Essoufi, and M. Sy. Effect of density dependent viscosities on multiphasic incompressible fluid models. *J. Math. Fluid Mech.*, 9:377–397, 2007. 297

[BF67] T.B. Benjamin and J.E. Feir. The disintegration of wavetrains in deep water. part 1. *J. Fluid Mech.*, 27(417), 1967. 79

[BF90] T.J. Barth and P.O. Frederickson. Higher order solution of the Euler equations on unstructured grids using quadratic reconstruction. *AIAA*, 90-0013, 1990. 141

[BG05] D. Bestion and A. Guelfi. Status and perspective of two-phase flow modelling in the NEPTUNE multi-scale thermal-hydraulic platform for nuclear reactor simulation. *Nuclear Engineering and Technology*, 37(6):511–524, 2005. 261, 288

[BGN86] M.R. Baer, R.J. Gross, and J.W. Nunziato. An experimental and theoretical study of deflagration-to-detonation transition (DDT) in the granular explosive. *Combust. Flame*, 65(1):15–30, 1986. 262, 265

[BJ89] T.J. Barth and D.C. Jespersen. The design and application of upwind schemes on unstructured meshes. *AIAA*, 0366, 1989. 126, 147, 279

[BKK+75] N.S. Bakhvalov, A.G. Kulikovskiy, V.N. Kurkin, Y.I. Sveshnikova, and M.E. Eglit. Movement of snow avalanches. *Soviet Hydrology: Selected Papers, Rocky Mountain Station*, 4, 1975. 291, 293

[BL98] N. Bozhinskiy and K.S. Losev. The fundamentals of avalanche science. Technical report, EISFL, Davos, 1998. 291, 293

[BLM00] C. Bassin, G. Laske, and G. Masters. The current limits of resolution for surface wave tomography in North America. *EOS Trans AGU*, 81:F897, 2000. 168, 170, 190

[BMM05] V.K. Birman, J.E. Martin, and E. Meiburg. The non-Boussinesq lock-exchange problem. Part 2. High-resolution simulations. *J. Fluid Mech.*, 537:125–144, 2005. 239

[BMR72] A. Ben-Menahem and M. Rosenman. Amplitude patterns of tsunami waves from submarine earthquakes. *J. Geophys. Res.*, 77:3097–3128, 1972. 93, 104

[BN86] M.R. Baer and J.W. Nunziato. A two-phase mixture theory for the deflagration-to-detonation transition (DDT) in reactive granular materials. *International journal of multiphase flow*, 12(6):861–889, 1986. 262, 265, 266, 319

[BO82] T.B. Benjamin and P. Olver. Hamiltonian structure, symmetries and conservation laws for water waves. *J. Fluid Mech*, 125:137–185, 1982. 204

[BO91] P. Beghin and X. Olagne. Experimental and theoretical study of the dynamics of powder snow avalanches. *Cold Regions Science and Technology*, 19:317–326, 1991. 293, 311

[BO04] T.J. Barth and M. Ohlberger. *Encyclopedia of Computational Mechanics, Volume 1, Fundamentals*, chapter Finite Volume Methods: Foundation and Analysis. John Wiley and Sons, Ltd, 2004. 121, 126, 148, 279, 281, 282

[Bok05] O. Bokhove. Flooding and drying in discontinuous Galerkin finite-element discretizations of Shallow-Water equations. part 1: One dimension. *Journal of Scientific Computing*, 22–23:47–82, 2005. 239

[Bou71a] J. Boussinesq. Théorie de l'intumescence liquide appelée onde solitaire ou de translation se propageant dans un canal rectangulaire. *C.R. Acad. Sci. Paris Sér. A-B*, 72:755–759, 1871. 46, 234

[Bou71b] J. V. Boussinesq. Théorie générale des mouvements qui sont propagés dans un canal rectangulaire horizontal. *C. R. Acad. Sc. Paris*, 73:256–260, 1871. 243

[Bou72] J. Boussinesq. Théorie des ondes et des remous qui se propagent le long d'un canal rectangulaire horizontal, en communiquant au liquide contenu dans ce canal des vitesses sensiblement pareilles de la surface au fond. *J. Math. Pures Appl.*, 17:55–108, 1872. 182, 243

[BP81] G. Brugnot and R. Pochat. Numerical simulation study of avalanches. *Journal of Glaciology*, 27:77–88, 1981. 293

[BPB09] H. Bredmose, D.H. Peregrine, and G.N. Bullock. Violent breaking wave impacts. Part 2: modelling the effect of air. *J. Fluid Mech*, 641:389–430, 2009. 296

[BPS81] J.L. Bona, W.G. Pritchard, and L.R. Scott. An evaluation of a model equation for water waves. *Phil. Trans. R. Soc. Lond. A*, 302:457–510, 1981. 71, 243

[BQ06] F. Benkhaldoun and L. Quivy. A non homogeneous Riemann solver for shallow water and two phase flows. *Flow, Turbulence and Combustion*, 76:391–402, 2006. 121, 239, 288

[BR04] Ph. Berthet-Rambaud. *Structures rigides soumises aux avalanches et chutes de blocs: modélisation du comportement mécanique et caractérisation de l'interaction "phénomène-ouvrage"*. PhD thesis, Université Joseph Fourier, 2004. 312

[Bre05a] H. Brenner. Kinematics of volume transport. *Physica A*, 349:11–59, 2005. 297, 312

[Bre05b] H. Brenner. Navier-Stokes revisited. *Physica A*, 349:60–132, 2005. 297, 312

[Bre06] H. Brenner. Fluid mechanics revisited. *Physica A*, 370:190–224, 2006. 297

[Bri96] T.J. Bridges. Periodic patterns, linear instability, symplectic structure and mean-flow dynamics for three-dimensional surface waves. *Phil. Trans. Royal Soc. London A*, 354:533–574, 1996. 47

[BS76] J. L. Bona and R. Smith. A model for the two-way propagation of water waves in a channel. *Math. Proc. Camb. Phil. Soc.*, 79:167–182, 1976. 200, 204

[BS08] F. Benkhaldoun and M. Seaid. New finite-volume relaxation methods for the third-order differential equations. *Commun. Comput. Phys.*, 4:820–837, 2008. 201

[BX07] Y.-C. Bai and D. Xu. Numerical simulation of two-dimensional dam-break flows in curved channels. *Journal of Hydrodynamics, Ser. B*, 19(6):726–735, 2007. 239

[Cal85] H.B. Callen. *Thermodynamics and an Introduction to Thermostatistics*. Wiley, 1985. 267

[Cas90] V. Casulli. Semi-implicit finite difference methods for the two-dimensional shallow water equation. *Journal of Computational Physics*, 86:56–74, 1990. 121

[Cau27] A.-L. Cauchy. Mémoire sur la théorie de la propagation des ondes à la surface d'un fluide pesant d'une profondeur indéfinie. *Mém. Présentés Divers Savans Acad. R. Sci. Inst. France*, 1:3–312, 1827. 176

[CBB06] R. Cienfuegos, E. Barthelemy, and P. Bonneton. A fourth-order compact finite volume scheme for fully nonlinear and weakly dispersive Boussinesq-type equations. Part I: Model development and analysis. *Int. J. Numer. Meth. Fluids*, 51:1217–1253, 2006. 206

[CBB07] R. Cienfuegos, E. Barthelemy, and P. Bonneton. A fourth-order compact finite volume scheme for fully nonlinear and weakly dispersive Boussinesq-type equations. Part II: Boundary conditions and model validation. *Int. J. Numer. Meth. Fluids*, 53:1423–1455, 2007. 206

[CC95] S. Chapman and T.G. Cowling. *The Mathematical Theory of Non-Uniform Gases*. Cambridge University Press, Cambridge, England, 1995. 262, 266, 270

[CCS77] K. Chueh, C. Conley, and J. Smoller. Positively invariant regions for systems of nonlinear equations. *Ind. U. Math. J.*, 26:373–392, 1977. 274, 275

[CD10] D. Clamond and D. Dutykh. Practical use of variational principles for modeling water waves. *Submitted*, http://arxiv.org/abs/1002.3019/, 2010. 18, 242

[CFGR+05] M.J. Castro, A.M. Ferreiro, J.A. Garcia-Rodriguez, J.M. Gonzalez-Vida, J. Macias, C. Pares, and M.E. Vazquez-Cendon. The numerical treatment of wet/dry fronts in shallow flows: Application to one-layer and two-layer systems. *Mathematical and Computer Modelling*, 42:419–439, 2005. 121

[CFL67] R. Courant, K. Friedrichs, and H. Lewy. On the partial difference equations of mathematical physics. English translation of the 1928 German original. *IBM Journal*, pages 215–234, 1967. 283

[CG58] G. F. Carrier and H. P. Greenspan. Water waves of finite amplitude on a sloping beach. *J. Fluid Mech.*, 2:97–109, 1958. 239

[CG94] W. Craig and M.D. Groves. Hamiltonian long-wave approximations to the water-wave problem. *Wave Motion*, 19:367–389, 1994. 54

[CG00] J. Cortes and J.-M. Ghidaglia. Upwinding at low cost for complex models and flux schemes. In *Trends in Numerical and Physical Modeling for Industrial Multiphase Flows*, 2000. 131

[CG09] G.A. Chechkin and A. Yu. Goritsky. *Analytical and Numerical Aspects of Partial Differential Equations*, chapter S.N. Kruzhkov's lectures on first-order quasilinear PDEs. 2009. 247

[CGH+06] W. Craig, P. Guyenne, J. Hammack, D. Henderson, and C. Sulem. Solitary water wave interactions. *Phys. Fluids*, 18:57–106, 2006. 215, 216, 217, 218, 219

[CH93] R. Camassa and D. Holm. An integrable shallow water equation with peaked solitons. *Phys. Rev. Lett.*, 71(11):1661–1664, 1993. 46, 67

[Cha81] S. Chandrasekhar. *Hydrodynamic and Hydromagnetic Stability*. Dover Publications, 1981. 306

[Che98] M. Chen. Exact traveling-wave solutions to bidirectional wave equations. *International Journal of Theoretical Physics*, 37:1547–1567, 1998. 204

[Che00] M. Chen. Solitary-wave and multi pulsed traveling-wave solutions of Boussinesq systems. *Applic. Analysis.*, 75:213–240, 2000. 204

[CIM+00] D.M. Causon, D.M. Ingram, C.G. Mingham, G. Yang, and R.V. Pearson. Calculation of shallow water flows using a cartesian cut cell approach. *Advances in Water Resources*, 23:545–562, 2000. 121, 133, 239

[CKT09] J. Chambarel, C Kharif, and J. Touboul. Head-on collision of two solitary waves and residual falling jet formation. *Nonlin. Processes Geophys.*, 16:111–122, 2009. 215

[CKZL99] G. Chen, C. Kharif, S. Zaleski, and J. Li. Two-dimensional Navier-Stokes simulation of breaking waves. *Physics of Fluids*, 11(1):121–133, 1999. 278, 288

[CLLL08] W.-Y. Chang, L.-C. Lee, H.-C. Lien, and J.-S. Lai. Simulations of dam-break flows using free surface capturing method. *Journal of Mechanics*, 24(4):391–403, 2008. 239

[CLS04] B. Cockburn, F. Li, and C.-W. Shu. Locally divergence-free discontinuous Galerkin methods for the Maxwell equations. *Journal of Computational Physics*, 194:588–610, 2004. 124

[CM85] R.R. Coifman and Y. Meyer. Nonlinear harmonic analysis and analytic dependence. *Proc, symp. Pure Math*, 43:71–78, 1985. 178

[Coa81] J.W. Coaz. *Die Lawinen der Schweizer Alpen.* Schmid-Franke, Bern, 1881. 290

[CP92] J. H. E. Cartwright and O. Piro. The dynamics of Runge–Kutta methods. *Int. J. Bifurcation and Chaos*, 2:427–449, 1992. 141

[CR01] M. Clément-Rastello. A study on the size of snow particles in powder-snow avalanches. *Annals of Glaciology*, 32:259–262, 2001. 303

[Cra04] A.D.D. Craik. The origins of water wave theory. *Ann. Rev. Fluid Mech.*, 36:1–28, 2004. 46, 51

[CS93] W. Craig and C. Sulem. Numerical simulation of gravity waves. *J. Comput. Phys.*, 108:73–83, 1993. 47, 60, 69, 178, 194

[CSS92] W. Craig, C. Sulem, and P.-L. Sulem. Nonlinear modulation of gravity waves: a rigorous approach. *Nonlinearity*, 5(2):497–522, 1992. 178

[CSS06] A. Constantin, D. H. Sattinger, and W. Strauss. Variational formulations for steady water waves with vorticity. *J. Fluid Mech.*, 548:151–163, 2006. 68

[CT65] J.W. Cooley and J.W. Tukey. An algorithm for the machine calculation of complex Fourier series. *Math. Comput*, 19:297–301, 1965. 178

[CWY03] G. F. Carrier, T. T. Wu, and H. Yeh. Tsunami run-up and draw-down on a plane beach. *J. Fluid Mech.*, 475:79–99, 2003. 157, 239

[DAH+07] F. Domine, M. Albert, T. Huthwelker, H.-W. Jacobi, A. A. Kokhanovsky, M. Lehning, G. Picard, and W. R. Simpson. Snow physics as relevant to snow photochemistry. *Atmos. Chem. Phys. Discuss.*, 7:5941–6036, 2007. 296, 303

[DARB10] D. Dutykh, C. Acary-Robert, and D. Bresch. Mathematical modeling of powder-snow avalanche flows. *Submitted*, 2010. 21, 278, 316

[Dav88] S.F. Davis. Simplified second-order Godunov-type methods. *SIAM J. Sci. Statist. Comput.*, 9:445–473, 1988. 132

[DB06] F. Dias and T.J. Bridges. The numerical computation of freely propagating time-dependent irrotational water waves. *Fluid Dynamics Research*, 38:803–830, 2006. 68, 178

[DCL79] D. Drew, I. Cheng, and R.T. Lahey. The analysis of virtual mass effects in two-phase flow. *Int. J. Multiphase Flow*, 5(4):233 – 242, 1979. 260

[DD07a] F. Dias and D. Dutykh. *Extreme Man-Made and Natural Hazards in Dynamics of Structures*, chapter Dynamics of tsunami waves, pages 35–60. Springer, 2007. 170, 177

[DD07b] D. Dutykh and F. Dias. Dissipative Boussinesq equations. *C. R. Mecanique*, 335:559–583, 2007. 18, 72, 123, 182

[DD07c] D. Dutykh and F. Dias. Viscous potential free-surface flows in a fluid layer of finite depth. *C. R. Acad. Sci. Paris, Ser. I*, 345:113–118, 2007. 18, 72, 73, 165, 177, 243

[DD07d] D. Dutykh and F. Dias. Water waves generated by a moving bottom. In Anjan Kundu, editor, *Tsunami and Nonlinear waves*. Springer Verlag (Geo Sc.), 2007. 92, 97, 105, 121, 123, 167, 168, 169, 170, 172, 173, 175, 176, 177, 188, 190, 199, 241

[DD09a] D. Dutykh and F. Dias. Energy of tsunami waves generated by bottom motion. *Proc. R. Soc. A*, 465:725–744, 2009. 18, 161, 164

[DD09b] D. Dutykh and F. Dias. Tsunami generation by dynamic displacement of sea bed due to dip-slip faulting. *Mathematics and Computers in Simulation*, 80(4):837–848, 2009. 18, 104, 105, 106, 111, 121, 123, 167, 168, 241

[DD10] D. Dutykh and F. Dias. Influence of sedimentary layering on tsunami generation. *Computer Methods in Applied Mechanics and Engineering*, 199(21-22):1268–1275, 2010. 18, 121, 123, 167, 241

[DDG08a] F. Dias, D. Dutykh, and J.-M. Ghiadaglia. A compressible two-fluid model for the finite volume simulation of violent aerated flows. Analytical properties and numerical results. Research report, CMLA, ENS de Cachan, 2008. 153, 243, 244, 296, 313

[DDG08b] F. Dias, D. Dutykh, and J.-M. Ghidaglia. A compressible two-fluid model for the finite volume simulation of violent aerated flows. Analytical properties and numerical results. *http://hal.archives-ouvertes.fr/hal-00279671/*, pages 1–38, 2008. 21, 261, 262, 273, 274, 279, 285, 288

[DDG08c] F. Dias, D. Dutykh, and J.-M. Ghidaglia. Simulation of free surface compressible flows via a two fluid model. In *Proceedings of OMAE2008 27th International Conference on Offshore Mechanics and Arctic Engineering, June 15-20, 2008, Estoril, Portugal*, 2008. 21, 153, 243, 244, 261, 262, 273, 288, 296, 313

[DDG10] F. Dias, D. Dutykh, and J.-M. Ghidaglia. A two-fluid model for violent aerated flows. *Comput. & Fluids*, 39(2):283–293, 2010. 21, 153, 243, 244, 260, 261, 262, 273, 274, 279, 285, 288, 296, 313, 324

[DDK06] D. Dutykh, F. Dias, and Y. Kervella. Linear theory of wave generation by a moving bottom. *C. R. Acad. Sci. Paris, Ser. I*, 343:499–504, 2006. 91, 96, 97, 98, 105, 121, 169, 173, 174, 177, 190

[DDLMM07] V. Dougalis, A. Duran, M. A. Lopez-Marcos, and D. E. Mitsotakis. A numerical study of the stability of solitary waves of Bona-Smith family of Boussinesq systems. *J. Nonlinear Sci.*, 17:595–607, 2007. 215, 216

[DDZ08] F. Dias, A.I. Dyachenko, and V.E. Zakharov. Theory of weakly damped free-surface flows: a new formulation based on potential flow solutions. *Physics Letters A*, 372:1297–1302, 2008. 72, 74, 177, 243

[Del05] S. Dellacherie. On a diphasic low Mach number system. *ESAIM: M2AN*, 39:487–514, 2005. 261, 276

[Del07] S. Dellacherie. Numerical resolution of a potential diphasic low Mach number system. *J. Comput. Phys.*, 223:151–187, 2007. 276

[DGA01] F. Dufour, U. Gruber, and W. Ammann. Avalanches: études effectuées dans la Vallée de la Sionne en 1999. *Les Alpes*, 2:9–15, 2001. 294, 306

[DGBA00] F. Dufour, U. Gruber, P. Bartelt, and W.J. Ammann. Overview of the 1999 measurements at the SLF test site Vallée de la Sionne. In *Proceedings International Snow Science Workshop, Blue Sky MT, USA, October 1st-6th*, pages 527–534, 2000. 292

[DGRS+99] S. Di Gregorio, R. Rongo, C. Siciliano, M. Sorriso-Valvo, and W. Spataro. Mount Ontake landslide simulation by the cellular automata model SCIDDICA-3. *Physics and Chemistry of the Earth*, 24:97–100, 1999. 293

[DK97] S.F. Dotsenko and T.Yu. Korobkova. The effect of frequency dispersion on plane waves generated as a result of bed motions. *Phys. Oceanogr.*, 8(3):143–154, 1997. 85

[DK03] A. I. Delis and Th. Katsaounis. Relaxation schemes for the shallow water equations. *Int. J. Numer. Meth. Fluids*, 41:695–719, 2003. 200, 234

[DKK08] A. I. Delis, M. Kazolea, and N. A. Kampanis. A robust high-resolution finite volume scheme for the simulation of long waves over complex domains. *Int. J. Numer. Meth. Fluids*, 56:419–452, 2008. 121, 182, 200, 234

[DKM10] D. Dutykh, Th. Katsaounis, and D. Mitsotakis. Finite volume schemes for dispersive wave propagation and runup. *Submitted*, ( http://hal.archives-ouvertes.fr/hal-00472431/ ), 2010. 18

[DL79] D.A. Drew and R.T. Lahey. Application of general constitutive principles to the derivation of multidimensional two-phase flow equations. *Int. J. Multiphase Flow*, 5:243–264, 1979. 260

[DM04] V.A. Dougalis and D.E. Mitsotakis. *Advances in scattering theory and biomedical engineering*, chapter Solitary waves of the Bona-Smith system, pages 286–294. World Scientific, New Jersey, 2004. 204

[DM08] V. A. Dougalis and D. E. Mitsotakis. Theory and numerical analysis of Boussinesq systems: A review. In N. A. Kampanis, V. A. Dougalis, and J. A. Ekaterinaris, editors, *Effective Computational Methods in Wave Propagation*, pages 63–110. CRC Press, 2008. 51, 200

[DM10] F. Dias and P. Milewski. On the fully-nonlinear shallow-water generalized Serre equations. *Physics Letters A*, 374(8):1049–1053, 2010. 123, 206

[DMG10] D. Dutykh, D. Mitsotakis, and X. Gardeil. On the use of finite fault solution for tsunami generation problem. *Submitted (http://arxiv.org/abs/1008.2742)*, 2010. 18

[DMS07] V. A. Dougalis, D. E. Mitsotakis, and J.-C. Saut. On some boussinesq systems in two space dimensions: Theory and numerical analysis. *Math. Model. Num. Anal.*, 41(5):825–254, 2007. 182

[DMS09] V. A. Dougalis, D. E. Mitsotakis, and J.-C. Saut. On initial-boundary value problems for a boussinesq system of bbm-bbm type in a plane domain. *Discrete Contin. Dyn. Syst.*, 23(4):1191–1204, 2009. 182

[DP80] J. R. Dormand and P.J. Prince. A family of embedded Runge-Kutta formulae. *J. Comp. Appl. Math.*, 6:19–26, 1980. 181, 185

[DP99] A. Degasperis and M. Procesi. *Symmetry and Perturbation Theory*, chapter Asymptotic integrability, pages 23–37. World Scientific, 1999. 46, 67

[DPD10] D. Dutykh, R. Poncet, and F. Dias. Complete numerical modelling of tsunami waves: generation, propagation and inundation. *Submitted*, ( http://arxiv.org/abs/1002.4553 ), 2010. 18, 85, 91, 167, 168, 182, 190, 199, 200, 234, 239, 240, 241, 247, 248, 254

[DR04] P.G. Drazin and W.H. Reid. *Hydrodynamic Stability*. Cambridge University Press, 2004. 306

[DSI06] D. D'Ambrosio, W. Spataro, and G. Iovine. Parallel genetic algorithms for optimising cellular automata models of natural complex phenomena: an application to debris-flows. *Computers & Geosciences*, 32:861–875, 2006. 293

[dSV71] A.J.C. de Saint-Venant. Théorie du mouvement non-permanent des eaux, avec application aux crues des rivières et à l'introduction des marées dans leur lit. *C. R. Acad. Sc. Paris*, 73:147–154, 1871. 182, 240, 291, 293

[DT07] M.H. Dao and P. Tkalich. Tsunami propagation modelling - a sensitivity study. *Nat. Hazards Earth Syst. Sci.*, 7:741–754, 2007. 84, 234

[Dut07] D. Dutykh. *Mathematical modelling of tsunami waves*. PhD thesis, École Normale Supérieure de Cachan, 2007. 72, 73, 106, 121, 153, 167, 168, 170, 177, 240, 243, 248, 252, 261, 262, 273, 279, 285, 288, 296, 313, 324

[Dut09a] D. Dutykh. Group and phase velocities in the free-surface visco-potential flow: new kind of boundary layer induced instability. *Physics Letters A*, 373:3212–3216, 2009. 177, 243

[Dut09b] D. Dutykh. Visco-potential free-surface flows and long wave modelling. *Eur. J. Mech. B/Fluids*, 28:430–443, 2009. 18, 71, 72, 73, 76, 79, 165, 177, 243, 252, 256

[DVB02] F. Dias and J.-M. Vanden-Broeck. Steady two-layer flows over an obstacle. *Phil. Trans. R. Soc. Lond. A*, 360(1799):2137–2154, 2002. 302

[DW94] D.A. Drew and G.B. Wallis. *Multiphase Science and Technology*, chapter Fundamentals of two-phase flow modeling. Begell House, Inc., New York, 1994. 260

[Dys79] K.B. Dysthe. Note on a modification to the nonlinear Schrodinger equation for application to deep water. *Proc. R. Soc. Lond. A*, 369:105–114, 1979. 46, 67

[Eck60] C. Eckart. Variation principles of hydrodynamics. *Phys. Fluids*, 3:421–427, 1960. 68

[Egl83] E. M. Eglit. *Advances in the Mechanics and the Flow of Granular Materials*, chapter Some mathematical models of snow avalanches, pages 577–588. Trans Tech Publications, Clausthal-Zellerfeld, 1983. 291

[Egl91] M. Eglit. The dynamics of snow avalanches. In *Proceedings of the Steklov Institute of Mathematics*, volume 186, pages 187–193, 1991. 291

[Egl98] M. Eglit. Mathematical and physical modeling of powder-snow avalanches in Russia. *Annals of Glaciology*, 26:281–284, 1998. 291

[EHS05] J. Etienne, E.J. Hopfinger, and P. Saramito. Numerical simulations of high density ratio lock-exchange flows. *Phys. Fluids*, 17:036601, 2005. 294, 304, 306

[EIK05] K. S. Erduran, S. Ilic, and V. Kutija. Hybrid finite-volume finite-difference scheme for the solution of Boussinesq equations. *Int. J. Numer. Meth. Fluids*, 49:1213–1232, 2005. 201

[EMRS91] B. Einfeldt, C.D. Munz, P.L. Roe, and B. Sjogreen. On Godunov-type methods near low densities. *J. Comput. Phys.*, 92:273–295, 1991. 132

[EOS+05] M. Ergun, S. Okay, C. Sari, E.Z. Oral, M. Ash, J. Hall, and H. Miller. Gravity anomalies of the Cyprus Arc and their tectonic implications. *Marine Geology*, 221:349–358, 2005. 106

[ES05] C. Eskilsson and S.J. Sherwin. Discontinuous Galerkin spectral/hp element modelling of dispersive shallow water systems. *Journal of Scientific Computing*, 22:269–288, 2005. 90

[ES06] C. Eskilsson and S.J. Sherwin. Spectral/hp discontinuous Galerkin methods for modelling 2D Boussinesq equations. *J. Comput. Phys*, 212(2):566–589, 2006. 200

[ESB06] C. Eskilsson, S.J. Sherwin, and L. Bergdahl. An unstructured spectral/hp element model for enhanced Boussinesq-type equations. *Coastal Engineering*, 53(11):947–963, 2006. 200

[ESH04] J. Etienne, P. Saramito, and E.J. Hopfinger. Numerical simulations of dense clouds on steep slopes: application to powder-snow avalanches. *Annals of Glaciology*, 38:379–383(5), 2004. 278, 294, 304, 308

[Eti04] J. Etienne. *Numerical simulation of high density ratio gravity currents. Application to the avalanches.* PhD thesis, Institut National Polytechnique de Grenoble, 2004. 294, 300, 304, 306

[FB76] L. B. Freund and D. M. Barnett. A two-dimensional analysis of surface deformation due to dip-slip faulting. *Bull. Seism. Soc. Am.*, 66:667–675, 1976. 111

[FC02] L. Fraccarollo and H. Capart. Riemann wave description of erosional dam-break flows. *J. Fluid Mech.*, 461:183–228, 2002. 256

[FCKG05] D. Fructus, D. Clamond, O. Kristiansen, and J. Grue. An efficient model for threedimensional surface wave simulations. Part i: Free space problems. *J. Comput. Phys.*, 205:665–685, 2005. 60, 178, 181

[Fen99] J. D. Fenton. Numerical methods for nonlinear waves. *Adv. Coastal Ocean Engng*, 5:241–324, 1999. 68

[Fic55a] A. Fick. *Phil. Mag.*, 10:30, 1855. 297

[Fic55b] A. Fick. *Poggendorff's Annel. Physik*, 94:59, 1855. 297

[FJ02] T. Funada and D.D. Joseph. Viscous potential flow analysis of capillary instability. *International Journal of Multiphase Flow*, 28(9):1459–1478, 2002. 72

[FJ05] Matteo Frigo and Steven G. Johnson. The design and implementation of FFTW3. *Proceedings of the IEEE*, 93(2):216–231, 2005. special issue on "Program Generation, Optimization, and Platform Adaptation". 178

[FKM+07] H. M. Fritz, W. Kongko, A. Moore, B. McAdoo, J. Goff, C. Harbitz, B. Uslu, N. Kalligeris, D. Suteja, K. Kalsum, V. V. Titov, A. Gusman, H. Latief, E. Santoso, S. Sujoko, D. Djulkarnaen, H. Sunendar, and C. Synolakis. Extreme runup from the 17 July 2006 Java tsunami. *Geophys. Res. Lett.*, 34:L12602, 2007. 171, 190

[FNBB+08] E.D. Fernández-Nieto, F. Bouchut, D. Bresch, M.J. Castro-Díaz, and A. Mangeney. A new Savage-Hutter type models for submarine avalanches and generated tsunami. *J. Comput. Phys.*, 227:7720–7754, 2008. 293

[Fou22] J. Fourier. *Théorie analytique de la chaleur*. Didot, Paris, 1822. 264

[FP90] Y. Fukushima and G. Parker. Numerical simulation of powder-snow avalanches. *Journal of Glaciology*, 36:229–237, 1990. 293

[FP05] A. S. Fokas and B. Pelloni. Boundary value problems for Boussinesq type systems. *Math. Phys. Anal. Geom.*, 8:59–96, 2005. 214

[FS01] F. Franchi and B. Straughan. A comparison of the Graffi and Kazhikhov-Smagulov models for heavy pollution instability. *Adv. in Water Ressources*, 24:585–594, 2001. 297

[FT95] L. Fraccarollo and E.F. Toro. Experimental and numerical assessment of the shallow water model for two-dimensional dam break type problems. *Journal of Hydraulic Research*, 33:843–864, 1995. 133

[Fuk79] Y. Fukao. Tsunami earthquakes and subduction processes near deep-sea trenches. *J. Geophys. Res.*, 84:2303–2314, 1979. 105, 119

[FWB06] C.W. Fuller, S.D. Willett, and M.T. Brandon. Formation of forearc basins and their influence on subduction zone earthquakes. *Geology*, 34:65–68, 2006. 105

[GBBea07] A. Guelfi, D. Bestion, M. Boucker, and et al. NEPTUNE: a new software platform for advanced nuclear thermal hydraulics. *Nuclear Science and Engineering*, 156(3):281–324, 2007. 261

[GBM+05] F.I. González, E.N. Bernard, C. Meinig, M.C. Eble, H.O. Mofjeld, and S. Stalin. The NTHMP tsunameter network. *Natural Hazards*, 35:25–39, 2005. 167

[GCHJ03] J. Grue, D. Clamond, M. Huseby, and A. Jensen. Kinematics of extreme waves in deep water. *Applied Ocean Research*, 25:355–366, 2003. 57

[GCMM09] M.C. Galassi, P. Coste, Ch. More, and F. Moretti. Two-phase flow simulations for PTS investigation by means of Neptune_CFD code. *Science and Technology of Nuclear Installations*, 2009:12, 2009. 261, 288

[Gen03] F. Geniet. Large amplitude surface waves in infinite depth, a variational approach. Technical report, Preprint LPMT 2003 PM/03-25., 2003. 61, 63

[Geo06] D.L. George. *Finite Volume Methods and Adaptive Refinement for Tsunami Propagation and Inundation*. PhD thesis, Department of Applied Mathematics, University of Washington, Seattle, 2006. 121

[Geo08] D.L. George. Augmented Riemann solvers for the shallow water equations over variable topography with steady states and inundation. *J. Comput. Phys.*, 227:3089–3113, 2008. 121

[GEY67] S.S. Grigorian, M.E. Eglit, and Y.L. Yakimov. A new formulation and solution of the problem of a snow avalanche motion. *Trudy Vysokogornogo Geofizicheskogo Instituta*, 12:104–113, 1967. (in Russian). 291

[GGL+01] J. Glimm, J. W. Grove, X.-L. Li, W. Oh, and D. H. Sharp. A critical analysis of Rayleigh-Taylor growth rates. *J. Comput. Phys.*, 169:652–677, 2001. 303

[GGLT00] J. Glimm, J. Grove, X. Li, and D. Tan. Robust computational algorithms for dynamic interface tracking in three dimensions. *SIAM J. Sci. Comput.*, 21(6):2240, 2000. 261

[Ghi95] J.-M. Ghidaglia. Une approche volumes finis pour la résolution des systèmes hyperboliques de lois de conservation, note. Technical report, Département Transferts Thermiques et Aérodynamique, Direction des Etudes et Recherches, Electricité de France, HT-30/95/015/A, 1995. 128

[Ghi98] J.-M. Ghidaglia. Flux schemes for solving nonlinear systems of conservation laws. In J.J. Chattot and M. Hafez, editors, *Proceedings of the meeting in honor of P.L. Roe*, Arcachon, July 1998. 130, 241

[Ghi01] J.-M. Ghidaglia. *Innovative Methods for Numerical Solution of Partial Differential Equations*, chapter Flux schemes for solving nonlinear systems of conservation laws. World Scientific, Singapore, 2001. 241

[GHS03] T. Gallouet, J.-M. Hérard, and N. Seguin. Some approximate Godunov schemes to compute shallow-water equations with topography. *Computers & Fluids*, 32:479–513, 2003. 121

[Gis08] G.R. Gisler. Tsunami simulations. *Annu. Rev. Fluid Mech.*, 40:71–90, 2008. 86

[GKC96] J.-M. Ghidaglia, A. Kumbaro, and G. Le Coq. Une méthode volumes-finis à flux caractéristiques pour la résolution numérique des systèmes hyperboliques de lois de conservation. *C. R. Acad. Sci. I*, 322:981–988, 1996. 128, 201, 208, 241, 266, 288

[GKC01] J.-M. Ghidaglia, A. Kumbaro, and G. Le Coq. On the numerical solution to two fluid models via cell centered finite volume method. *Eur. J. Mech. B/Fluids*, 20:841–867, 2001. 128, 208, 241, 244, 260, 262, 263, 266, 281, 288, 295

[GL06] D.L. George and R.J. Leveque. Finite volume methods and adaptive refinement for global tsunami propagation and local inundation. *Sci. Tsunami Hazards*, 24(5):319, 2006. 121

[Gla88] P. Glaister. Approximate Riemann solutions of the shallow water equations. *Journal of Hydraulic Research*, 26:293–300, 1988. 121

[GLN74] A. E. Green, N. Laws, and P. M. Naghdi. On the theory of water waves. *Proc. R. Soc. Lond. A*, 338:43–55, 1974. 53, 243

[GN76] A.E. Green and P. M. Naghdi. A derivation of equations for wave propagation in water of variable depth. *J. Fluid Mech.*, 78:237–246, 1976. 46, 54, 243

[GN07] P. Guyenne and D.P. Nicholls. A high-order spectral method for nonlinear water waves over moving bottom topography. *SIAM J. Sci. Comput.*, 30(1):81–101, 2007. 180

[GNVC00] P. Garcia-Navarro and M. E. Vazquez-Cendon. On numerical treatment of the source terms in the shallow water equations. *Computers & Fluids*, 29:951–979, 2000. 121

[God59] S.K. Godunov. A finite difference method for the numerical computation of discontinuous solutions of the equations of fluid dynamics. *Mat. Sb.*, 47:271–290, 1959. 127, 141

[God99] S.K. Godunov. Reminiscences about difference schemes. *J. Comput. Phys.*, 153:6–25, 1999. 234

[GOSI97] C. Goto, Y. Ogawa, N. Shuto, and F. Imamura. Numerical method of tsunami simulation with the leap-frog scheme. Technical report, UNESCO, 1997. 121

[GP01] F. Gerbeau and B. Perthame. Derivation of viscous Saint-Venant system for laminar shallow water. *Discrete Contin. Dynam. Syst. Ser. B*, 1(1):89–102, 2001. 243

[GP02a] J.-M. Ghidaglia and F. Pascal. Flux boundary conditions for hyperbolic systems of conservations laws in the finite volume framework. In R. Herbin and D. Kröner, editors, *Finite volumes for complex applications III. Problems and perspectives*, pages 809–816, 2002. 254

[GP02b] J.-M. Ghidaglia and F. Pascal. On boundary conditions for multidimensional hyperbolic systems of conservation laws in the finite volume framework. Technical report, CMLA, ENS de Cachan, 2002. 254

[GP05] J.-M. Ghidaglia and F. Pascal. The normal flux method at the boundary for multidimensional finite volume approximations in cfd. *European Journal of Mechanics B/Fluids*, 24:1–17, 2005. 150, 153, 254, 262, 281

[GR90] E. Godlewski and P.-A. Raviart. *Hyperbolic systems of conservation laws*. Ellipses, 1990. 247

[GR96] E. Godlewski and P.-A. Raviart. *Numerical approximation of hyperbolic systems of conservation laws*, volume 118. Springer, New York, 1996. 247, 273

[Gra55] D. Graffi. Il teorema di unicitá per i fluidi incompressibili, perferri, eterogenei. *Rev. Unione Mar Argentina*, 17:73–77, 1955. 297

[GRP] http://www.lama.univ-savoie.fr/~dutykh/animations/groupvel.avi. 76, 79

[GST01] S. Gottlieb, C.-W. Shu, and E. Tadmor. Strong stability-preserving high-order time discretization methods. *SIAM Review*, 43:89–112, 2001. 139, 201, 210, 282

[Gus78] V.K. Gusiakov. *Ill-posed problems of mathematical physics and interpretation of geophysical data*, chapter Static displacement on the surface of an elastic space (in Russian), pages 23–51. VC SOAN SSSR, 1978. 111

[GV85] J.D. Goodman and R.J. Le Veque. On the accuracy of stable schemes for 2D conservation laws. *Math. Comp.*, 45(171):15–21, 1985. 143

[GV04] G. Gottardi and M. Venutelli. Central scheme for two-dimensional dam-break flow simulation. *Advances in Water Resources*, 27:259–268, 2004. 239

[GWH98] J.M.N.T. Gray, M. Wieland, and K. Hutter. Gravity-driven free surface flow of granular avalanches over complex basal topography. *Proc. R. Soc. Lond. A*, 455:1841–1874, 1998. 293

[Ham72] J.L. Hammack. *Tsunamis – A Model of Their Generation and Propagation*. PhD thesis, California Institute of Technology, 1972. 173, 175

[Ham73] J. Hammack. A note on tsunamis: their generation and propagation in an ocean of uniform depth. *J. Fluid Mech.*, 60:769–799, 1973. W. M. Keck Laboratory of Hydraulics and Water Resources, California Institute of Technology, Pasadena. 91, 167, 173, 175, 176, 190

[Har83] A. Harten. High resolution schemes for hyperbolic conservation laws. *J. Comp. Phys.*, 49:357–393, 1983. 142

[HB83] J. Happel and H. Brenner. *Low Reynolds number hydrodynamics*. D. Reidel Publishing Co., Hingham, MA, 1983. 311

[HC89] D.G. Holmes and S.D. Connel. Solution of the 2d Navier-Stokes equations on unstructured adaptive grids. In *AIAA 9th Computational Fluid Dynamics Conference*, volume 89-1932-CP, June 1989. 144, 148, 149

[Hel68] H. Helmholtz. On the discontinuous movements of fluids. *Monthly Reports of the Royal Prussian Academy of Philosophy in Berlin*, 23:215, 1868. 306

[Her00] J.-M. Hervouet. A high resolution 2-d dam-break model using parallelization. *Hydrol. Process.*, 14:2211–2230, 2000. 239

[HG93] K. Hutter and R. Greve. Two-dimensional similarity solutions for finite-mass granular avalanches with Coulomb and viscous-type frictional resistance. *Journal of Glaciology*, 39:357–372, 1993. 293

[HH70] K.L. Heitner and G.W. Housner. Numerical model for tsunami runup. *J. Waterway, Port, Coastal and Ocean Engineering*, 96:701–719, 1970. 200

[HLD96] J. Hacker, P.F. Linden, and S.B. Dalziel. Mixing in lock-release gravity currents. *Dynamics of Atmospheres and Oceans*, 24:183–195, 1996. 239

[HLvL83] A. Harten, P.D. Lax, and B. van Leer. On upstream differencing and Godunov-type schemes for hyperbolic conservation laws. *SIAM Review*, 25:35–61, 1983. 131, 132

[HMK+09] M. Hamidou, B. Molin, M. Kadri, O. Kimmoun, and A. Tahakourt. A coupling method between extended Boussinesq equations and the integral equation method with application to a two-dimensional numerical wave-tank. *Ocean Engineering*, 36:1377–1385, 2009. 200

[HMN00] C.J. Härtel, E. Meiburg, and F. Necker. Analysis and direct numerical simulation of the flow at a gravity-current head. Part 1. Flow topology and front speed for slip and no-slip boundaries. *J. Fluid Mech.*, 418(9):189–212, 2000. 239

[HN81] C.W. Hirt and B.D. Nichols. Volume of fluid (VOF) method for the dynamics of free boundaries. *J. Comput. Phys.*, 39:201–225, 1981. 239, 248, 261

[HNW09] E. Hairer, S.P. Nørsett, and G. Wanner. *Solving ordinary differential equations: Nonstiff problems*. Springer, 2009. 181, 182, 185

[HO87] A. Harten and S. Osher. Uniformly high-order accurate nonscillatory schemes, I. *SIAM J. Numer. Anal.*, 24:279–309, 1987. 201, 208, 209

[Hop83] E.J. Hopfinger. Snow avalanche motion and related phenomena. *Ann. Rev. Fluid Mech.*, 15:47–76, 1983. 293

[HP79] S. Hibberd and D.H. Peregrine. Surf and run-up on a beach: a uniform bore. *J. Fluid Mech.*, 95:323–345, 1979. 135, 199

[HPHO] F. Hecht, O. Pironneau, A. Le Hyaric, and K. Ohtsuka. *FreeFem++*. Laboratoire JL Lions, University of Paris VI, France. 109, 110

[HRR+04] B.A.A. Hoogakker, R.G. Rothwell, E.J. Rohling, M. Paterne, D.A.V. Stow, J.O. Herrle, and T. Clayton. Variations in terrigenous dilution in western Mediterranean Sea pelagic sediments in response to climate change during the last glacial cycle. *Marine Geology*, 211:21–43, 2004. 106

[HTD77] E.J. Hopfinger and J.-C. Tochon-Danguy. A model study of powder-snow avalanches. *Journal of Glaciology*, 81:343–356, 1977. 293

[Hun82] B. Hunt. Asymptotic solution for dam break problem. *J. Hydraul. Div. ASCE*, 108:115–126, 1982. 238

[Hut91] K. Hutter. Two- and three dimensional evolution of granular avalanche flow – theory and experiments revisited. *Acta Mechanica*, 1:167–181, 1991. 293

[Hut96] K. Hutter. *Hydrology of disasters*, chapter Avalanche dynamics, pages 317–394. Kluwer Academic Publishers, 1996. 293

[HW65] F.H. Harlow and J.E. Welch. Numerical calculation of time-dependent viscous incompressible flow of fluid with free surface. *Phys. Fluids*, 8:2182, 1965. 71, 239

[HWP05] K. Hutter, Y. Wang, and S.P. Pudasaini. The Savage-Hutter avalanche model. How far can it be pushed? *Phil. Trans. R. Soc. Lond. A*, 363:1507–1528, 2005. 293

[IAK+07] M. Ioualalen, J. Asavanant, N. Kaewbanjak, S.T. Grilli, J.T. Kirby, and P. Watts. Modeling the 26 december 2004 Indian Ocean tsunami: Case study of impact in Thailand. *Journal of Geophysical Research*, 112:C07024, 2007. 119, 169

[IH06] M. Ishii and T. Hibiki. *Thermo-fluid dynamics of two-phase flow*. Birkhäuser, 2006. 20, 260, 262, 264, 267

[Ima96] F. Imamura. *Long-wave runup models*, chapter Simulation of wave-packet propagation along sloping beach by TUNAMI-code, pages 231–241. World Scientific, 1996. 121, 167, 182, 239

[Ish75] M. Ishii. *Thermo-Fluid Dynamic Theory of Two-Phase Flow*. Eyrolles, Paris, 1975. 20, 244, 260, 262, 263, 267, 295, 317

[Iss03] D. Issler. Experimental information on the dynamics of dry-snow avalanches. In K. Hutter and N. Kirchner, editors, *Dynamic Response of Granular and Porous Materials Under Large and Catastrophic Deformations*, volume 11. Springer, Berlin, 2003. 316

[IYO06] F. Imamura, A.C. Yalciner, and G. Ozyurt. *Tsunami modelling manual*, April 2006. 190, 239

[Jas96] H. Jasak. *Error analysis and estimation for the finite volume method with applications to fluid flows*. PhD thesis, University of London and Imperial College, 1996. 248, 304

[JCHG07] A. Jensen, D. Clamond, M. Huseby, and J. Grue. On local and convective accelerations in steep wave events. *Ocean Engin*, 34:426–435, 2007. 57

[JFBM06] E. Jamois, D.R. Fuhrman, H.B. Bingham, and B. Molin. A numerical study of nonlinear wave run-up on a vertical plate. *Coastal Engineering*, 53:929–945, 2006. 200

[JGIL09] T. Johannesson, P. Gauer, P. Issler, and K. Lied. The design of avalanche protection dams. Technical report, European Commission, 2009. 316

[Ji06] C. Ji. Preliminary result of the 2006 July 17 magnitude 7.7 - south of Java, Indonesia earthquake. Technical report, `http://neic.usgs.gov/neis/eq_depot/2006/eq_060717_qgaf/neic_qgaf_ff.html`, 2006. 171, 172, 173, 187, 190

[JL94] D.D. Joseph and T.Y. Liao. Potential flows of viscous and viscoelastic fluids. *J. Fluid Mech.*, 265:1–23, 1994. 72

[Joh77] R.S. Johnson. On the modulation of water waves in the neighbourhood of $kh \approx 1.363$. *Proc. R. Soc. Lond. A*, 357:131–141, 1977. 79

[Joh97] R. S. Johnson. *A modern introduction to the mathematical theory of water waves*. Cambridge University Press, Cambridge, 1997. 85

[Jos06] D.D. Joseph. Potential flow of viscous fluids: Historical notes. *Int. J. Multiphase Flow*, 32:285–310, 2006. 72

[JR93] D. D. Joseph and Y. Y. Renardy. *Fundamentals of two-fluid dynamics*. Interdisciplinary Applied Mathematics. Springer Verlag, New-York, 1993. 278

[JW04] D.D. Joseph and J. Wang. The dissipation approximation and viscous potential flow. *J. Fluid Mech.*, 505:365–377, 2004. 72

[JWH02] C. Ji, D. J. Wald, and D. V. Helmberger. Source description of the 1999 Hector Mine, California earthquake; Part I: Wavelet domain inversion theory and resolution analysis. *Bull. Seism. Soc. Am.*, 92(4):1192–1207, 2002. 168, 170, 190

[Kaj63] K. Kajiura. The leading wave of tsunami. *Bull. Earthquake Res. Inst., Tokyo Univ.*, 41:535–571, 1963. 167, 174

[Kaj70] K. Kajiura. Tsunami source, energy and the directivity of wave radiation. *Bull. Earthquake Research Institute*, 48:835–869, 1970. 85, 93

[Kau75] D.J. Kaup. Higher-order water-wave equation and method for solving it. *Prog. Theor. Phys.*, 54:396–408, 1975. 54

[KB01] C.J. Keylock and M. Barbolini. Snow avalanche impact pressure - vulnerability relations for use in risk assessment. *Can. Geotech. J.*, 38(2):227–238, 2001. 312

[KBEW01] J.W. Kim, K.J. Bai, R.C. Ertekin, and W.C. Webster. A derivation of the Green-Naghdi equations for irrotational flows. *Journal of Engineering Mathematics*, 40(1):17–42, 2001. 47, 50, 54, 243

[KC91] J.J. Keller and Y.-P. Chyou. On the hydrodynamic lock-exchange problem. *Journal of Applied Mathematics and Physics*, 42, 1991. 239

[KCKD00] A.B. Kennedy, Q. Chen, J.T. Kirby, and R.A. Dalrymple. Boussinesq modelling of wave transformation, breaking, and runup. *J. Waterway, Port, Coastal and Ocean Engineering*, 126:39–47, 2000. 200

[KCY07] D.-H. Kim, Y.-S. Cho, and Y.-K. Yi. Propagation and run-up of nearshore tsunamis with HLLC approximate Riemann solver. *Ocean Engineering*, 34:1164–1173, 2007. 121, 133

[KDD07] Y. Kervella, D. Dutykh, and F. Dias. Comparison between three-dimensional linear and nonlinear tsunami generation models. *Theor. Comput. Fluid Dyn.*, 21:245–269, 2007. 91, 121, 123, 173, 174, 176, 199, 241

[KDID07] C. Kassiotis, F. Dias, A. Ibrahimbegovic, and D. Dutykh. A partitioned approach to model tsunami impact on coastal protections. In A. Ibrahimbegovic, F. Dias, H. Matthies, and P. Wriggers, editors, *ECCOMAS Thematic Conference on Multi-scale Computational Methods for Solids and Fluids*, pages 134–139, 2007. 106

[KdV95] D.J. Korteweg and G. de Vries. On the change of form of long waves advancing in a rectangular canal, and on a new type of long stationary waves. *Phil. Mag.*, 39(5):422–443, 1895. 46, 67, 234

[KE73] A.G. Kulikovskiy and M.E. Eglit. Two-dimensional problem of the motion of a snow avalanche along a slope with smoothly changing properties. *Journal of Applied Mathematics and Mechanics*, 37:792–803, 1973. 291

[Kel71] Lord Kelvin. Hydrokinetic solutions and observations. *Philosophical Magazine*, 42:362–377, 1871. 306

[Kel95] S. Keller. Measurements of powder snow avalanches: Laboratory. *Surveys in Geophysics*, 16:661–670, 1995. 294

[Keu48] G.H. Keulegan. Gradual damping of solitary waves. *J. Res. Nat. Bureau Standards*, 40(6):487–498, 1948. 72

[Kha87] G.A. Khabakhpashev. Effect of bottom friction on the dynamics of gravity perturbations. *Fluid Dynamics*, 22(3):430–437, 1987. 72

[Kha97] G. A. Khabakhpashev. Nonlinear evolution equation for sufficiently long two-dimensional waves on the free surface of a viscous liquid. *Computational Technologies*, 2:94–101, 1997. 72, 243

[Kir97] J.T. Kirby. *Gravity Waves in Water of Finite Depth*, volume 10, chapter Nonlinear, dispersive long waves in water of variable depth, pages 55–125. Computational Mechanics Publications, 1997. 51

[KKLW07] Z. Kowalik, W. Knight, T. Logan, and P. Whitmore. The tsunami of 26 December, 2004: Numerical modeling and energy considerations. *Pure and Applied Geophysics*, 164:379–393, 2007. 84, 85

[KKS05] M. Kameyama, A. Kageyama, and T. Sato. Multigrid iterative algorithm using pseudo-compressibility for three-dimensional mantle convection with strongly variable viscosity. *J. Comput. Phys*, 206:162–181, 2005. 47

[KLM05] R. A. Kraenkel, J. Leon, and M. A. Manna. Theory of small aspect ratio waves in deep water. *Physica D*, 211:377–390, 2005. 46, 58, 67

[KM75] T. Kakutani and K. Matsuuchi. Effect of viscosity on long gravity waves. *J. Phys. Soc. Japan*, 39:237–246, 1975. 72

[KM82] S. Klainerman and A. Majda. Compressible and incompressible fluids. *Comm. Pure Appl. Math.*, 35:629, 1982. 276

[KMC03] S.-E. Kim, B. Makarov, and D. Caraeni. A multi-dimensional linear reconstruction scheme for arbitrary unstructured grids. Technical report, Fluent Inc., 2003. 149

[KML05] E.A. Kulikov, P.P. Medvedev, and S.S. Lappo. Satellite recording of the Indian Ocean tsunami on December 26, 2004. *Doklady Earth Sciences A*, 401:444–448, 2005. 83, 234

[KO08] A. Korobkin and Y. Oguz. The initial stage of dam-break flow. *J. Eng. Math.*, 2008. 238, 246

[Kol72] N.E. Kolgan. Application of the minimum-derivative principle in the construction of finite-difference schemes for numerical analysis of discontinuous solutions in gas dynamics. *Uchenye Zapiski TsaGI [Sci. Notes Central Inst. Aerodyn]*, 3(6):68–77, 1972. 141, 281

[Kol75] N.E. Kolgan. Finite-difference schemes for computation of three dimensional solutions of gas dynamics and calculation of a flow over a body under an angle of attack. *Uchenye Zapiski TsaGI [Sci. Notes Central Inst. Aerodyn]*, 6(2):1–6, 1975. 141, 208, 281

[Kor01] D.J. Korteweg. Sur la forme que prennent les équations du mouvement des fluides si l'on tient compte des forces capillaires causées par des variations de densité considérables mais continues et sur la théorie de la capillarité dans

l'hypothèse d'une variation continue de la densité. *Archives Néerlandaises des Sciences Exactes et Naturelles*, 6:1, 1901. 265

[KPTV00] A. Kumbaro, H. Paillère, I. Toumi, and C. Viozat. Comparison of low Mach number models for natural convection problems. *Heat Mass Transfer*, 36:567–573, 2000. 276

[Kro97] D. Kroner. *Numerical Schemes for Conservation Laws*. Wiley, Stuttgart, 1997. 121, 279

[KRTB96] E.A. Kulikov, A.B. Rabinovich, R.E. Thomson, and B.D. Bornhold. The landslide tsunami of November 3, 1994, Skagway Harbor, Alaska. *J. Geophys. Res.*, 101(C3):6609–6615, 1996. 84

[KS77a] A. Kazhikov and Sh. Smagulov. The correctness of boundary value problems in a diffusion problem of an homogeneous fluid. *Sov. Phys. Dokl.*, 22:249–252, 1977. 297

[KS77b] A.G. Kulikovskiy and E.I. Sveshnikova. A model for computing a powder snow avalanche motion. *Glaciological Studies*, 31:74–80, 1977. (in Russian). 291, 293

[KS98] U. Kanoglu and C.E. Synolakis. Long wave runup on piecewise linear topographies. *J. Fluid Mech.*, 374:1–28, 1998. 200

[KS06] U. Kanoglu and C. Synolakis. Initial value problem solution of nonlinear shallow water-wave equations. *Phys. Rev. Lett.*, 97:148501, 2006. 84, 239

[KT00] A Kurganov and E Tadmor. New high-resolution central schemes for nonlinear conservation laws and convection-diffusion equations. *J. Comput. Phys.*, 160(1):241–282, 2000. 201, 208

[Kup85] B.A. Kupershmidt. Mathematics of dispersive water waves. *Commun. Math. Phys.*, 99:51–73, 1985. 54

[KWC+98] J. T. Kirby, G. Wei, Q. Chen, A. B. Kennedy, and R. A. Dalrymple. Funwave 1.0, fully nonlinear boussinesq wave model documentation and user's manual. Research Report No. CACR-98-06, 1998. 200

[Lag81] J.-L. Lagrange. Mémoire sur la théorie du mouvement des fluides. *Nouv. Mém. Acad. Berlin*, 196, 1781. 51

[Lam32] H. Lamb. *Hydrodynamics*. Cambridge University Press, 1932. 176

[Lar90] B. Larrouturou. How to preserve the mass fraction positivity when computing compressible multi-component flows. *J. Comput. Phys.*, 95:59–84, 1990. 261

[Lax73] P.D. Lax. *Hyperbolic Systems of Conservation Laws and the Mathematical Theory of Shock Waves*. SIAM, Philadelphia, Penn., 1973. 142, 247, 273

[LB80] K. Lied and S. Bakkehøi. Empirical calculations of snow avalanche run-out distances based on topographic parameters. *Journal of Glaciology*, 26:165–177, 1980. 293

[LB09] D. Lannes and P. Bonneton. Derivation of asymptotic two-dimensional time-dependent equations for surface water wave propagation. *Phys. Fluids*, 21:016601, 2009. 206

[Li02] Y.A. Li. Hamiltonian structure and linear stability of solitary waves of the Green-Naghdi equations. *J. Nonlin. Math. Phys.*, 9, 1:99–105, 2002. 53, 243

[Lie06] K. Lied. Satsie: Avalanche studies and model validation in europe. Technical report, European Commission, 2006. 316

[Lié06] J. Liévois. *Guide méthodologique des plans de prévention des risques d'avalanches*. La Documentation Française, Paris, 2006. 310

[LJ05] O.A. Likhachev and J.W. Jacobs. A vortex model for Richtmyer-Meshkov instability accounting for finite Atwood number. *Phys. Fluids*, 17:031704, 2005. 303

[LKA+05] T. Lay, H. Kanamori, C. J. Ammon, M. Nettles, S. N. Ward, R. C. Aster, S. L. Beck, S. L. Bilek, M. R. Brudzinski, R. Butler, H. R. DeShon, G. Ekstrom, K. Satake, and S. Sipkin. The great Sumatra-Andaman earthquake of 26 December 2004. *Science*, 308:1127–1133, 2005. 118

[Llo05] A. Llor. *Statistical hydrodynamic models for developed mixing instability flows : analytical "0D" evaluation criteria, and comparison of single- and two-phase flow approaches*. Springer Verlag, 2005. 260

[LLS03] P.L.-F. Liu, P. Lynett, and C.E. Synolakis. Analytical solutions for forced long waves on a sloping beach. *J. Fluid Mech.*, 478:101–109, 2003. 162, 239

[LMMR86] D. Lewis, J. Marsden, R. Montgomery, and T. Ratiu. The Hamiltonian structure for dynamic free boundary problems. *Physica D*, 18:391–404, 1986. 68

[LO04] P.L.-F. Liu and A. Orfila. Viscous effects on transient long-wave propagation. *J. Fluid Mech.*, 520:83–92, 2004. 72, 73, 243

[LOC94] X.-D. Liu, S. Osher, and T. Chan. Weighted essentially non-oscillatory schemes. *J. Comp. Phys.*, 115:200–212, 1994. 201, 208, 209

[Lov44] A. E. H. Love. *A treatise on the mathematical theory of elasticity*. Dover Publications, New York, 1944. 196

[LR98] A.-Y. Le Roux. Riemann solvers for some hyperbolic problems with a source term. *ESAIM: Proceedings*, 6:75–90, 1998. 138

[LR02] Y. Li and F. Raichlen. Non-breaking and breaking solitary wave run-up. *J. Fluid Mech.*, 456:295–318, 2002. 200

[LSBH95] G.F. Lane-Serff, L.M. Beal, and T.D. Hadfield. Gravity current flow over obstacles. *J. Fluid Mech.*, 292:39–53, 1995. 312

[LSVO06] P.L.-F. Liu, G. Simarro, J. Vandever, and A. Orfila. Experimental and numerical investigation of viscous effects on solitary wave propagation in a wave tank. *Coastal Engineering*, 53:181–190, 2006. 72, 243

[LSY04] D. Levy, C.-W. Shu, and J. Yan. Local discontinuous Galerkin methods for nonlinear dispersive equations. *J. Comput. Phys.*, 196(2):751–772, 2004. 200

[Luk67] J.C. Luke. A variational principle for a fluid with a free surface. *J. Fluid Mech.*, 27:375–397, 1967. 47, 48, 68, 69, 242

[Lun89] T.S. Lundgren. *Mathematical aspects of vortex dynamics*, chapter A free surface vortex method with weak viscous effects, pages 68–79. SIAM, 1989. 72

[LWC98] P.L.-F. Liu, S.-B. Woo, and Y.-K. Cho. Computer programs for tsunami propagation and inundation. Technical report, School of Civil and Environmental Engineering, Cornell University, 1998. 121

[Ma10] Q. Ma. Advances in numerical simulation of nonlinear water waves. In *Adv. Coastal Ocean Engng*. World Scientific, 2010. 68

[Maj82] A. Majda. Equations of low Mach number combustion. Technical Report 112, Center for Pure and Applied Mathematics, University of California, Berkeley, 1982. 276

[Maj84] A. Majda. Compressible fluid flow and systems of conservation laws in several space dimensions. *Appl. Math. Sci.*, 53, 1984. 297

[Mar07] F. Marche. Derivation of a new two-dimensional viscous shallow water model with varying topography, bottom friction and capillary effects. *European Journal of Mechanics - B/Fluids*, 26(1):49–63, 2007. 243

[Mat76] K. Matsuuchi. Numerical investigations on long gravity waves under the influence of viscosity. *J. Phys. Soc. Japan*, 41(2):681–686, August 1976. 72

[Max76] T. Maxworthy. Experiments on collisions between solitary waves. *J Fluid Mech*, 76:177–185, 1976. 216

[MBS03] P. A. Madsen, H. B. Bingham, and H. A. Schaffer. Boussinesq-type formulations for fully nonlinear and extremely dispersive water waves: derivation and analysis. *Proc. R. Soc. Lond. A*, 459:1075–1104, 2003. 67, 123, 182, 200, 204, 243

[McC00] D.M. McClung. Extreme avalanche runout in space and time. *Can. Geotech. J.*, 37:161–170, 2000. 293

[McC01] D.M. McClung. Extreme avalanche runout: a comparison of empirical models. *Can. Geotech. J.*, 38:1254–1265, 2001. 293

[MCVB+03] A. Mangeney-Castelnau, J.-P. Vilotte, M.O. Bristeau, B. Perthame, F. Bouchut, C. Simeoni, and S. Yerneni. Numerical modeling of avalanches based on Saint-Venant equations using a kinetic scheme. *J. Geophys. Res.*, 108:2527, 2003. 293

[MDG09] Y. Meyapin, D. Dutykh, and M. Gisclon. Two-fluid barotropic models for powder-snow avalanche flows. In *The Fourth Russian-German Advanced Research Workshop on Computational Science and High Performance Computing*, Springer series "Notes on Numerical Fluid Mechanics and Multidisciplinary Design", 2009. 21, 262, 296

[MDG10] Y. Meyapin, D. Dutykh, and M. Gisclon. Velocity and energy relaxation in two-phase flows. *Stud. Appl. Maths.*, 125(2):179–212, 2010. 21, 296, 327

[Mei89] C. C. Mei. *The applied dynamics of water waves.* World Scientific, 1989. 46

[Mei94] C.C. Mei. *The applied dynamics of ocean surface waves.* World Scientific, 1994. 111, 176, 240

[MG96] S. Musaferija and D. Gosman. Finite-volume CFD procedure and adaptive error control strategy for grids of arbitrary topology. *J. Comp. Phys.*, 138:766–787, 1996. 143

[MG05] A. Murrone and H. Guillard. A five equation reduced model for compressible two phase flow problems. *J. Comput. Phys.*, 202:664–698, 2005. 262, 265, 266, 271, 296, 319, 322

[MHR00] A. Mangeney, Ph. Heinrich, and R. Roche. Analytical solution for testing debris avalanche numerical models. *Pure Appl. Geophys.*, 157:1081–1096, 2000. 238, 247

[Mil76] J.W. Miles. Korteweg-de Vries equation modified by viscosity. *Phys. Fluids*, 19(7), 1976. 72

[Mil77] J.W. Miles. On Hamilton's principle for water waves. *J. Fluid Mech.*, 83:153–158, 1977. 50

[Min36] R. D. Mindlin. Force at a point in the interior of a semi-infinite medium. *Physics*, 7:195–202, 1936. 169

[Mit09] D.E. Mitsotakis. Boussinesq systems in two space dimensions over a variable bottom for the generation and propagation of tsunami waves. *Math. Comp. Simul.*, 80:860–873, 2009. 182, 200, 204

[Miu74] R.M. Miura. Conservation laws for the fully nonlinear long wave equations. *Stud. Appl. Maths.*, 53:45–56, 1974. 242

[ML87] D.M. McClung and K. Lied. Statistical and geometrical definition of snow avalanche runout. *Cold Regions Science and Technology*, 13:107–119, 1987. 293

[MM52] J.C. Martin and W.J. Moyce. Part IV. An experimental study of the collapse of liquid columns on a rigid horizontal plane. *Phil. Trans. R. Soc. London. Series A.*, 244(882):312–324, 1952. 239, 240

[MN01] J.N. McElwaine and K. Nishimura. *Particulate Gravity Currents*, chapter Ping-pong ball avalanche experiments, pages 135–148. Blackwell Science, 2001. 293

[Mor98] P. J. Morrison. Hamiltonian description of the ideal fluid. *Rev. Mod. Phys.*, 70(2):467–521, 1998. 68

[Mou22] P. Mougin. *Les avalanches en Savoie IV*. Ministère de l'Agriculture, Direction Générale des Eaux et Forêts, Service des Grandes Forces Hydrauliques, Paris, 1922. 290

[Mou31] P. Mougin. *Restauration des montagnes*. Imprimerie Nationale, Paris, 1931. 290

[MS67] L. Mansinha and D. E. Smylie. Effect of earthquakes on the Chandler wobble and the secular polar shift. *J. Geophys. Res.*, 72:4731–4743, 1967. 167, 169

[MS71] L. Mansinha and D. E. Smylie. The displacement fields of inclined faults. *Bull. Seism. Soc. Am.*, 61:1433–1440, 1971. 111, 167, 169

[MS84] D. McClung and P.A. Schaerer. Determination of avalanche dynamics, friction coefficients from measured speeds. *J. Glaciology*, 20:109–120, 1984. 292

[MS85] A. Majda and J. Sethian. The derivation and numerical solution of the equations for zero Mach number combustion. *Combust. Sci. and Tech.*, 42:185–205, 1985. 276

[MS93] D.M. McClung and P.A. Schaerer. *The Avalanche Handbook*. The Mountaineers, Seattle, 1993. 303, 311, 312

[MS99] P.A. Madsen and H.A. Schaffer. A review of Boussinesq-type equations for surface gravity waves. *Adv. Coastal & Ocean Engin.*, 5:1–94, 1999. 51

[MSS97] P.A. Madsen, H.A. Sorensen, and H.A. Schaffer. Surf zone dynamics simulated by a Boussinesq-type model. Part I. Model description and cross-shore motion of regular waves. *Coastal Engineering*, 32:255–287, 1997. 135

[NB03] F. Naaim-Bouvet. *Approche macro-structurelle des écoulements biphasiques turbulents de neige et de leur interaction avec des obstacles*. Habilitation à diriger les recherches, Cemagref, 2003. 294, 311, 312

[NBNBH02] F. Naaim-Bouvet, M. Naaim, M. Bacher, and L. Heiligenstein. Physical modelling of the interaction between powder avalanches and defence structures. *Nat. Hazards Earth Syst. Sci.*, 2:193–202, 2002. 294, 316

[NG98] M. Naaim and I. Gurer. Two-phase numerical model of powder avalanche. Theory and application. *Natural Hazards*, 117:129–145, 1998. 294

[Ngu08] H.Y. Nguyen. *Modèles pour les ondes interfaciales et leur intégration numérique*. PhD thesis, Ecole Normale Supérieure de Cachan, 2008. 200

[NH71] B.D. Nichols and C.W. Hirt. Improved free surface conditions for numerical incompressible flow computations. *J. Comput. Phys.*, 8:434–448, 1971. 239

[NKDVLG08] M. Ndjinga, A. Kumbaro, F. De Vuyst, and P. Laurent-Gengoux. Numerical simulation of hyperbolic two-phase flow models using a Roe-type solver. *Nuclear Engineering and Design*, 238:2075–2083, 2008. 288

[NKMN98] K. Nishimura, S. Keller, J. McElwaine, and Y. Nohguchi. Ping-pong ball avalanche at a ski jump. *Granular matter*, 1:51–56, 1998. 293

[NMKI93] K. Nishimura, N. Maneo, K. Kawada, and K. Izumi. Structures of snow cloud in dry-snow avalanches. *Annals of Glaciology*, 18:173–178, 1993. 292

[NPPN06] S. Noelle, N. Pankratz, G. Puppo, and J.R. Natvig. Well-balanced finite volume schemes of arbitrary order of accuracy for shallow water flows. *J. Comput. Phys.*, 213:474–499, 2006. 121

[NSKL95] K. Nishimura, F. Sandersen, K. Kristensen, and K. Lied. Measurements of powder snow avalanche – Nature. *Surveys in Geophysics*, 16:649–660, 1995. 292

[NSS+05] S. Neetu, I. Suresh, R. Shankar, D. Shankar, S.S.C. Shenoi, S.R. Shetye, D. Sundar, and B. Nagarajan. Comment on "The Great Sumatra-Andaman Earthquake of 26 December 2004". *Science*, 310:1431a–1431b, 2005. 118

[NT90] H. Nessyahu and E. Tadmor. Nonoscillatory central differencing for hyperbolic conservation laws. *J. Computational Physics*, 87(2):408–463, 1990. 201, 208

[NTK90] H. Norem, K. Tronstad, and K. Kristensen. The Ryggfonn project: Avalanche data from the 1983 – 1989 winters. Technical report, Norwegian Geotechnical Institute, 1990. 292

[Nwo93] O. Nwogu. Alternative form of Boussinesq equations for nearshore wave propagation. *J. Waterway, Port, Coastal and Ocean Engineering*, 119:618–638, 1993. 67, 101, 200, 204

[OFDI04] T. Özgökmen, P.J. Fischer, J. Duan, and T. Iliescu. Entrainment in bottom gravity currents over complex topography from three-dimensional nonhydrostatic simulations. *Geophys. Res. Lett.*, 31:L13212, 2004. 239

[OFDI06] T. Özgökmen, P.F. Fischer, J. Duan, and T. Iliescu. Three-dimensional turbulent bottom density currents from a high-order nonhydrostatic spectral element method. *J. Phys. Ocean.*, 34:2006–2026, 2006. 239

[OHK97] H.T. Ozkan-Haller and J.T. Kirby. A Fourier-Chebyshev collocation method for the shallow water equations including shoreline runup. *Applied Ocean Research*, 19:21–34, 1997. 135

[OIF+07] T. Özgökmen, T. Iliescu, P.F. Fischer, A. Srinivasan, and J. Duan. Large eddy simulation of stratified mixing in two-dimensional dam-break problem in a rectangular enclosed domain. *Ocean Modelling*, 16:106–140, 2007. 239

[OK06] A. Ozgun Konca. Preliminary result 06/07/17 (Mw 7.9) , Southern Java earthquake. Technical report, http://www.tectonics.caltech.edu/slip_history/2006_s_java/s_java.html, 2006. 171

[Oka85] Y. Okada. Surface deformation due to shear and tensile faults in a half-space. *Bull. Seism. Soc. Am.*, 75:1135–1154, 1985. 91, 111, 167, 169

[Oka88] E. Okal. Seismic parameters controlling far-field tsunami amplitudes: A review. *Natural Hazards*, 1:67–96, 1988. 105, 109, 111, 119

[Oka92] Y. Okada. Internal deformation due to shear and tensile faults in a half-space. *Bull. Seism. Soc. Am.*, 82:1018–1040, 1992. 167, 169

[Oka03] E.A. Okal. Normal mode energetics for far-field tsunamis generated by dislocations and landslides. *Pure Appl. Geophys.*, 160:2189–2221, 2003. 83, 100

[Olv84] P. J. Olver. Hamiltonian perturbation theory and water waves. *Contemp. Math.*, 28:231–249, 1984. 67

[Olv88] P.J. Olver. Unidirectionalization of hamiltonian waves. *Physics Letters A*, 126:501–506, 1988. 67

[Ooi06] S.K. Ooi. *High resolution numerical simulations of lock-exchange gravity-driven flows*. PhD thesis, University of Iowa, 2006. 239

[Ope07] OpenCFD. *OpenFOAM. The Open Source CFD Toolbox. User Guide*, August 2007. 248, 304

[OS70] E. Ott and R.N. Sudan. Damping of solitary waves. *Phys. Fluids*, 13:1432–1434, 1970. 72

[OS88] S. Osher and J. Sethian. Front propagating with curvature dependent speed: algorithms based on Hamilton-Jacobi formulations. *J. Comput. Phys.*, 78:12–49, 1988. 261

[OS94] S. Osher and P. Smereka. A level set approach for computing solutions to incompressible two-phase flow. *J. Comput. Phys.*, 114:146–159, 1994. 261

[OS03] E.A. Okal and C.E. Synolakis. A theoretical comparison of tsunamis from dislocations and landslides. *Pure and Applied Geophysics*, 160:2177–2188, 2003. 98, 100, 104

[OS04] E.A. Okal and C.E. Synolakis. Source discriminants for near-field tsunamis. *Geophys. J. Int.*, 158:899–912, 2004. 100

[Osh84] S. Osher. Riemann solvers, the entropy condition, and difference approximations. *SIAM J. Numer. Anal.*, 21(2):217–235, 1984. 141

[OTM01] T. Ohmachi, H. Tsukiyama, and H. Matsumoto. Simulation of tsunami induced by dynamic displacement of seabed due to seismic faulting. *Bull. Seism. Soc. Am.*, 91:1898–1909, 2001. 168

[OTR07] E. A. Okal, J. Talandier, and D. Reymond. Quantification of hydrophone records of the 2004 Sumatra tsunami. *Pure Appl. Geophys.*, 164:309–323, 2007. 83

[PD01] B. Pelloni and V. Dougalis. Numerical modelling of two-way propagation of nonlinear dispersive waves. *Mat. Comp. Simul.*, 55:595–606, 2001. 200, 215

[PD08] R. Poncet and F. Dias. On the inclusion of arbitrary topography and bathymetry in the nonlinear shallow-water equations. In *XXII ICTAM, 25 - 29 August 2008, Adelaide, Australia*, 2008. 239, 240, 248

[Per67] D. H. Peregrine. Long waves on a beach. *J. Fluid Mech.*, 27:815–827, 1967. 102, 123, 182, 200, 204, 205, 234

[Pet91] T. Peterson. A note on the convergence of the discontinuous Galerkin method for a scalar hyperbolic equation. *SIAM J. Numer. Anal.*, 28(1):133–140, 1991. 141

[PNBNF04] M. Primus, F. Naaim-Bouvet, M. Naaim, and T. Faug. Physical modeling of the interaction between mounds or deflecting dams and powder snow avalanches. *Cold Regions Science and Technology*, 39:257–267, 2004. 294, 303, 312

[Poh50] F.V. Pohle. *The Lagragian equations of hydrodynamics: solutions which are analytic functions of time.* PhD thesis, New York University, USA, 1950. 238, 246

[Pre65] F. Press. Displacements, strains and tilts at tele-seismic distances. *J. Geophys. Res.*, 70:2395–2412, 1965. 170

[Pri03] M. Primus. *Modélisation physique des interactions entre avalanches de neige poudreuse et dispositifs de protection.* Mémoire du stage de dea mmge, Cemagref, 2003. 294, 312

[PZ99] S. Popinet and S. Zaleski. A front-tracking algorithm for accurate representation of surface tension. *Int. J. Numer. Meth. Fluids*, 30:775–793, 1999. 240, 248, 288

[Rad99] A.C. Radder. Hamiltonian dynamics of water waves. *Adv. Coast. Ocean Engng.*, 4:21–59, 1999. 47, 242

[Raj02a] J. Rajchenbach. Development of grain avalanches. *Phys. Rev. Lett.*, 89:074301, 2002. 293

[Raj02b] J. Rajchenbach. Dynamics of grain avalanches. *Phys. Rev. Lett.*, 88:014301, 2002. 293

[Raj05] J. Rajchenbach. Rheology of dense granular materials: steady, uniform flow and the avalanche regime. *J. Phys.: Condens. Matter*, 17:S2731–S2742, 2005. 293

[Ram00] D. Ramos. *Quelques résultats mathématiques et simulations numériques d'écoulements régis par des modèles bifluides*. PhD thesis, CMLA, Ecole Normale Supérieure de Cachan, 2000. 265

[Ran85] V.H. Ransom. RELAP5/MOD2 code manual. Technical Report NUREG/CR-4312, EGG-23986, Idaho Engineering Laboratory, 1985. 261

[Ray83] L. Rayleigh. Investigation of the character of the equilibrium of an incompressible heavy fluid of variable density. *Proceedings of the London Mathematical Society*, 14:170–177, 1883. 306

[Rey83] O. Reynolds. An experimental investigation of the circumstances which determine whether the motion of water shall be direct or sinuous, and of the law of resistance in parallel channels. *Phil. Trans. Roy. Soc.*, 174:935–982, 1883. 302

[RH88] V.H. Ransom and D.L. Hicks. Hyperbolic two-pressure models for two-phase flows revisited. *J. Comput. Phys.*, 75:498–504, 1988. 265

[RH04] M. Rastello and E.J. Hopfinger. Sediment-entraining suspension clouds: a model of powder-snow avalanches. *J. Fluid. Mech.*, 509:181–206, 2004. 291, 293, 306, 316, 317, 328

[RLF+08] A. B. Rabinovich, L. I. Lobkovsky, I. V. Fine, R.E. Thomson, T. N. Ivelskaya, and E. A. Kulikov. Near-source observations and modeling of the Kuril Islands tsunamis of 15 November 2006 and 13 January 2007. *Adv. Geosci.*, 14:105–116, 2008. 168

[Roe81] P. L. Roe. Approximate Riemann solvers, parameter vectors and difference schemes. *J. Comput. Phys.*, 43:357–372, 1981. 130

[Rov06] J.-M. Rovarch. *Solveurs tridimensionnels pour les écoulements diphasiques avec transferts d'énergie*. PhD thesis, Ecole Normale Supérieure de Cachan, 2006. 260, 262, 263, 266, 288, 317, 319

[Rus02] H. Rusche. *Computational Fluid Dynamics of Dispersed Two-Phase Flows at High Phase Fractions*. PhD thesis, University of London and Imperial College, 2002. 248, 304

[RWG95] J. Ritsema, S. N. Ward, and F. I. González. Inversion of deep-ocean tsunami records for 1987 to 1988 Gulf of Alaska earthquake parameters. *Bulletin of the Seismological Society of America*, 85:747–754, 1995. 83

[Sal88] R. Salmon. Hamiltonian fluid mechanics. *Ann. Rev. Fluid Mech.*, 20:225–256, 1988. 47, 68, 242

[SB06] C.E. Synolakis and E.N. Bernard. Tsunami science before and beyond Boxing Day 2004. *Phil. Trans. R. Soc. A*, 364:2231–2265, 2006. 18, 68, 83, 105, 119, 120, 166, 169, 239

[SBG04] B. Sapoval, A. Baldassarri, and A. Gabrielli. Self-stabilized fractality of seacoasts through damped erosion. *Phys. Rev. Lett.*, 93:098501 [4 pages], 2004. 120, 121

[SBT+07] C.E. Synolakis, E.N. Bernard, V.V. Titov, U. Kanoglu, and F.I. Gonzalez. Standards, criteria, and procedures for NOAA evaluation of tsunami numerical models. Technical report, NOAA/Pacific Marine Environmental Laboratory, 2007. 156, 190, 239

[SBT+08] C.E. Synolakis, E.N. Bernard, V.V. Titov, U. Kânoglu, and F.I. González. Validation and verification of tsunami numerical models. *Pure Appl. Geophys.*, 165:2197–2228, 2008. 234

[SCB98] P.K. Stansby, A. Chegini, and T.C.D. Barnes. The initial stages of dambreak flow. *J. Fluid Mech.*, 374:407–424, 1998. 239, 255

[Sch81] M. E. Schonbek. Existence of solutions for the Boussinesq system of equations. *J. Diff. Eqns.*, 42:325–352, 1981. 203

[SDL04] J.O. Shin, S.B. Dalziel, and P.F. Linden. Gravity currents produced by lock exchange. *J. Fluid Mech.*, 521:1–34, 2004. 239

[Ser53] F. Serre. Contribution à l'étude des écoulements permanents et variables dans les canaux. *La Houille blanche*, 8:374–388 & 830–872, 1953. 46, 53, 123, 200, 206, 243

[SF09] T. Saito and T. Furumura. Three-dimensional tsunami generation simulation due to sea-bottom deformation and its interpretation based on the linear theory. *Geophys. J. Int.*, 178:877–888, 2009. 168, 176

[SFW+05] H. Staedtke, G. Franchello, B. Worth, U. Graf, P. Romstedt, A. Kumbaro, J. García-Cascales, H. Paillère, H. Deconinck, M. Ricchiuto, B. Smith, F. De Cachard, E.F. Toro, E. Romesnki, and S. Mimouni. Advanced three-dimensional two-phase flow simulation tools for application to reactor safety (ASTAR). *Nuclear Engineering and Design*, 235:379–400, 2005. 261, 288

[SG69] C.H. Su and C.S. Gardner. Korteweg-de Vries equation and generalizations. III. Derivation of the Korteweg-de Vries equation and Burgers equation. *J. Math. Phys.*, 10:536–539, 1969. 53

[SH89] S.B. Savage and K. Hutter. The motion of a finite mass of granular material down a rough incline. *J. Fluid Mech.*, 199:177–215, 1989. 291, 293

[SH91] S.B. Savage and K. Hutter. The dynamics of avalanches of granular materials from initiation to runout, I: Analysis. *Acta Mechanica*, 86:201–233, 1991. 291

[SHC+05] H. Segur, D. Henderson, J. Carter, J. Hammack, C. Li, D. Pheiff, and K. Socha. Stabilizing the Benjamin-Feir instability. *J. Fluid Mech.*, 539:229–271, 2005. 79

[Shu88] C.-W. Shu. Total-variation-diminishing time discretizations. *SIAM J. Sci. Statist. Comput.*, 9:1073–1084, 1988. 139, 282

[Shy98] K.M. Shyue. An efficient shock-capturing algorithm for compressible multicomponent problems. *J. Comput. Phys.*, 142:208–242, 1998. 261

[Sim81] M.J. Simon. Wave-energy extraction by a submerged cylindrical resonant duct. *Journal of Fluid Mechanics*, 104:159–187, 1981. 199

[Sin96] V.P. Singh. *Dam Breach Modelling Technology.* Kluwer Academic Publishers, Dordrecht, 1996. 238

[SK06] C.E. Synolakis and L. Kong. Runup measurements of the December 2004 Indian ocean tsunami. *Earthquake Spectra*, 22:S67–S91, 2006. 118

[SKP96] C. Skandrani, C. Kharif, and J. Poitevin. Nonlinear evolution of water surface waves: the frequency down-shift phenomenon. *Contemp. Math.*, 200:157–171, 1996. 72

[SL03] S. Shao and E.Y.M. Lo. Incompressible SPH method for simulating Newtonian and non-Newtonian flows with a free surface. *Advances in Water Resources*, 26:787–800, 2003. 239

[SLCY97] C. Synolakis, P.L.-F. Liu, G. F. Carrier, and H. Yeh. Tsunamigenic seafloor deformations. *Science*, 278:598–600, 1997. 105

[SM09] J. B. Shiach and C. G. Mingham. A temporally second-order accurate Godunov-type scheme for solving the extended Boussinesq equations. *Coastal Engineering*, 56:32–45, 2009. 201

[Smo94] J. Smoller. *Shock waves and Reaction-Diffusion Equations*. Springer, Berlin, 2nd edition, 1994. 275

[SO88] C.-W. Shu and S. Osher. Efficient implementation of essentially non-oscillatory shock-capturing schemes. *J. Comput. Phys.*, 77:439–471, 1988. 140, 201, 210

[Sod78] G. A. Sod. A survey of several finite difference methods for systems of nonlinear hyperbolic conservation laws. *J. Comput. Phys.*, 43:1–31, 1978. 283

[SR02] R. J. Spiteri and S. J. Ruuth. A new class of optimal high-order strong-stability-preserving time discretization methods. *SIAM Journal on Numerical Analysis*, 40:469–491, 2002. 139, 201, 210, 248, 282

[SS46] I. S. Sokolnikoff and R. D. Specht. *Mathematical theory of elasticity*. McGraw-Hill, New York, 1946. 196

[SS03] J. Schumacher and K.R. Sreenivasan. Geometric features of the mixing of passive scalars at high schmidt numbers. *Phys. Rev. Lett.*, 91:174501, 2003. 303

[Sto57] J.J. Stoker. *Water Waves: The mathematical theory with applications*. Interscience, New York, 1957. 52, 73, 136, 238, 240, 246, 247

[Sto58] J.J. Stoker. *Water waves, the mathematical theory with applications*. Wiley, 1958. 85, 176, 182

[Sug91] N. Sugimoto. Burgers equation with a fractional derivative; hereditary effects on nonlinear acoustic waves. *J. Fluid Mech.*, 225:631–653, 1991. 72

[SW84] H.B. Stewart and B. Wendroff. Two-phase flows: models and methods. *J. Comput. Phys*, 56:363–409, 1984. 260, 263, 265

[Swe84] P.K. Sweby. High resolution schemes using flux limiters for hyperbolic conservation laws. *SIAM J. Numer. Anal.*, 21(5):995–1011, 1984. 201, 208, 281

[Sy05] M. Sy. A remark on the Kazhikhov-Smagulov type model: the vanishing initial density. *Applied Mathematics Letters*, 18:1351–1358, 2005. 296

[Syn87] C. Synolakis. The runup of solitary waves. *J. Fluid Mech.*, 185:523–545, 1987. 20, 52, 200, 224, 225, 227, 234, 239

[Syn05] C. Synolakis. India must cooperate on tsunami warning system. *Nature*, 434:17–18, 2005. 120, 167

[SZ99] R. Scardovelli and S. Zaleski. Direct numerical simulation of free-surface and interfacial flow. *Annu. Rev. Fluid Mech.*, 31:567–603, 1999. 71, 240, 248, 261, 278, 288

[SZ04] P. Sampl and T. Zwinger. Avalanche simulation with SAMOS. *Annals of Glaciology*, 38(1):393–398, 2004. 292

[Tan86] M. Tanaka. The stability of solitary waves. *Phys. Fluids*, 29(3):650–655, 1986. 183

[Tat97] H. Tatehata. *Perspectives on Tsunami Hazard Reduction: Observations, Theory and Planning*, chapter The New Tsunami Warning System of the Japan Meteorological Agency, pages 175–188. Springer, 1997. 120

[Tay50] G. Taylor. The instability of liquid surfaces when accelerated in a direction perpendicular to their planes. *Proceedings of the Royal Society of London. Series A*, 201:192–196, 1950. 306

[TB00] S. Tinti and E. Bortolucci. Energy of water waves induced by submarine landslides. *Pure Appl. Geophys.*, 157:281–318, 2000. 85

[TC88] M.D. Thomas and A.D.D. Craik. Three-wave resonance for free-surface flows over flexible boundaries. *J. Fluids Structures*, 2:323–338, 1988. 49

[TDS07] P. Tkalich, M.H. Dao, and C.E. Soon. Tsunami propagation modeling and forecasting for early warning system. *Journal of Earthquake and Tsunami*, 1(1):87–98, 2007. 167

[TG97] V.V. Titov and F.I. González. Implementation and testing of the method of splitting tsunami (MOST) model. Technical Report ERL PMEL-112, Pacific Marine Environmental Laboratory, NOAA, 1997. 121, 167, 182, 190, 199, 234, 239

[TGB+05] V.V. Titov, F.I. Gonzalez, E. N. Bernard, M.C. Eble, H.O. Mofjeld, J.C. Newman, and A.J. Venturato. Real-time tsunami forecasting: Challenges and solutions. *Natural Hazards*, 35:41–58, 2005. 120, 167, 190

[THT02] M.I. Todorovska, A. Hayir, and M.D. Trifunac. A note on tsunami amplitudes above submarine slides and slumps. *Soil Dynamics and Earthquake Engineering*, 22:129–141, 2002. 173

[TK96] I. Toumi and A. Kumbaro. An approximate linearized Riemann solver for a two-fluid model. *J. Comput. Physics*, 124:286–300, 1996. 244, 295

[TKDV00] K. Trulsen, I. Kliakhandler, K. B. Dysthe, and M. G. Velarde. On weakly nonlinear modulation of waves on deep water. *Phys. Fluids*, 12:2432–2437, 2000. 46

[TKP99] I. Toumi, A. Kumbaro, and H. Paillère. Approximate Riemann solvers and flux vector splitting schemes for two-phase flow. Technical report, CEA Saclay, 1999. 288, 295

[TM07] B. Turnbull and J.N. McElwaine. A comparison of powder-snow avalanches at Vallée de la Sionne, Switzerland, with plume theories. *Journal of Glaciology*, 53(180):30–40, 2007. 294

[TM08] B. Turnbull and J.N. McElwaine. Experiments on the non-Boussinesq flow of self-igniting suspension currents on a steep open slope. *J. Geophys. Res.*, 113:F01003, 2008. 290, 294

[TMD07] B. Thornber, A. Mosedale, and D. Drikakis. On the implicit large eddy simulations of homogeneous decaying turbulence. *J. Comput. Phys.*, 226:1902–1929, 2007. 281, 282

[Tor92] E.F. Toro. Riemann problems and the WAF method for solving the two-dimensional shallow water equations. *Philosophical Transactions: Physical Sciences and Engineering*, 338:43–68, 1992. 121

[TP09] M. Tonelli and M. Petti. Hybrid finite-volume finite-difference scheme for 2DH improved Boussinesq equations. *Coastal Engineering*, 56:609–620, 2009. 201

[TRM+05] V.V. Titov, A.B. Rabinovich, H.O. Mofjeld, R.E. Thomson, and F.I. González. The global reach of the 26 December 2004 Sumatra tsunami. *Science*, 309:2045–2048, 2005. 84

[TS94] S. Tadepalli and C. E. Synolakis. The run-up of N-waves on sloping beaches. *Proc. R. Soc. Lond. A*, 445:99–112, 1994. 199, 200, 239

[TS96] S. Tadepalli and C.E. Synolakis. Model for the leading waves of tsunamis. *Phys. Rev. Lett.*, 77:2141–2144, 1996. 239

[TS98] V. V. Titov and C. E. Synolakis. Numerical modeling of tidal wave runup. *J. Waterway, Port, Coastal, and Ocean Engineering*, 124:157–171, 1998. 182, 199, 200, 239

[Tse99] M.-H. Tseng. Explicit finite volume non-oscillatory schemes for 2D transient free-surface flows. *Int. J. Num. Meth. Fluids*, 30:831–843, 1999. 239

[TSS94] E.F. Toro, M. Spruce, and W. Speares. Restoration of the contact surface in the HLL Riemann solver. *Shock Waves*, 4:25–34, 1994. 133

[TT01] M. I. Todorovska and M. D. Trifunac. Generation of tsunamis by a slowly spreading uplift of the seafloor. *Soil Dynamics and Earthquake Engineering*, 21:151–167, 2001. 167, 173, 176

[Urs53] F. Ursell. The long-wave paradox in the theory of gravity waves. *Proc. Camb. Phil. Soc.*, 49:685–694, 1953. 102

[VC99] M.E. Vazquez-Cendon. Improved treatment of source terms in upwind schemes for the shallow water equations in channels with irregular geometry. *Journal of Computational Physics*, 148:497–526, 1999. 121, 138

[VDP02] A.S. Velichko, S.F. Dotsenko, and É.N. Potetyunko. Amplitude-energy characteristics of tsunami waves for various types of seismic sources generating them. *Phys. Oceanogr.*, 12(6):308–322, 2002. 85

[vL79] B. van Leer. Towards the ultimate conservative difference scheme V: a second order sequel to Godunov' method. *J. Comput. Phys.*, 32:101–136, 1979. 141, 208, 281

[vL06] B. van Leer. Upwind and high-resolution methods for compressible flow: From donor cell to residual-distribution schemes. *Communications in Computational Physics*, 1:192–206, 2006. 141, 281

[Voe55] A. Voellmy. Über die zerstörungskraft von lawinen. *Schweizerische Bauzeitung*, 73:159–162, 212–217, 246–249, 280–285, 1955. 291

[Vol07] V. Volterra. Sur l'équilibre des corps élastiques multiplement connexes. *Annales Scientifiques de l'Ecole Normale Supérieure*, 24(3):401–517, 1907. 169

[VS93] M. Villeneuve and S.B. Savage. Nonlinear, dispersive, shallow-water waves developed by a moving bed. *J. Hydraulic Res.*, 31:249–266, 1993. 101

[War80] S.N. Ward. Relationship of tsunami generation and an earthquake source. *J. Phys. Earth*, 28:441–474, 1980. 83

[Wei75] H. Weinberger. Invariant sets for weakly coupled parabolic and elliptic systems. *Rend. Mat. Univ. Roma*, 8:295–310, 1975. 274

[WETG01] G.X. Wu, R. Eatock Taylor, and D.M. Greaves. The effect of viscosity on the transient free-surface waves in a two-dimensional tank. *Journal of Engineering Mathematics*, 40:77–90, 2001. 79

[Whi65] G. B. Whitham. A general approach to linear and non-linear dispersive waves using a Lagrangian. *J. Fluid Mech.*, 22:273–283, 1965. 48

[Whi99] G.B. Whitham. *Linear and nonlinear waves*. John Wiley & Sons Inc., New York, 1999. 73, 177, 182

[WKGS95] G. Wei, J. T. Kirby, S. T. Grilli, and R. Subramanya. A fully nonlinear Boussinesq model for surface waves. Part 1. Highly nonlinear unsteady waves. *J. Fluid Mech.*, 294:71–92, 1995. 200

[WL60] J. V. Wehausen and E. V. Laitone. Surface waves. *Handbuch der Physik*, 9:446–778, 1960. 52

[WL08] S.A. Weinstein and P.R. Lundgren. Finite fault modeling in a tsunami warning center context. *Pure Appl. Geophys.*, 165:451–474, 2008. 168, 190

[WLY06] G. Wu, Y. Liu, and D. Yue. A note on stabilizing the Benjamin-Feir instability. *J. Fluid Mech.*, 556:45–54, 2006. 79, 80

[WMC06] Y. Wei, X.-Z. Mao, and K.F. Cheung. Well-balanced finite-volume model for long-wave runup. *Journal of Waterwave, Port, Coastal and Ocean Engineering*, 132:114–124, 2006. 121

[Woo70] I.R. Wood. A lock exchange flow. *J. Fluid Mech.*, 42(4):671–687, 1970. 239

[Wu81] T.Y. Wu. Long waves in ocean and coastal waters. *Journal of Engineering Mechanics*, 107:501–522, 1981. 71, 243

[Wu01] T.Y. Wu. A unified theory for modeling water waves. *Adv. App. Mech.*, 37:1–88, 2001. 51, 53

[Wub88] F. W. Wubs. *Numerical Solution of the Shallow-Water Equations*. Stichting Mathematisch Centrum, Amsterdam, 1988. 239

[WY07] C.H. Wu and H. Yuan. Efficient non-hydrostatic modelling of surface waves interacting with structures. *Applied Mathematical Modelling*, 31:687–699, 2007. 71

[XG09] L. Xu and P. Guyenne. Numerical simulation of three-dimensional nonlinear water waves. *J. Comput. Phys.*, 228(22):8446–8466, 2009. 181

[XS05] Y. Xing and C.-W. Shu. High order finite difference weno schemes with the exact conservation property for the shallow water equations. *J. Comput. Phys.*, 208:206–227, 2005. 239

[Yal08] A.C. Yalciner. July 17, 2006 Indonesia Java tsunami. Technical report, `http://yalciner.ce.metu.edu.tr/java/`, 2008. 169

[YL89] S.B. Yoon and P.L.-F. Liu. Interactions of currents and weakly nonlinear water waves in shallow water. *J. Fluid Mech.*, 205:397–419, 1989. 101

[YLB08] A. Yahalom and D. Lynden-Bell. Simplified variational principles for barotropic magnetohydrodynamics. *J. Fluid Mech*, 607:235–265, 2008. 47

[YS02] J. Yan and C.-W. Shu. A local discontinuous Galerkin method for KdV type equations. *SIAM J. Num. Anal.*, 40:769–791, 2002. 200

[YXS02] P.K. Yeung, S. Xu, and K.R. Sreenivasan. Schmidt number effects on turbulent transport with uniform mean scalar gradient. *Phys. Fluids*, 14:4178–4191, 2002. 303

[Zak68] V.E. Zakharov. Stability of periodic waves of finite amplitude on the surface of a deep fluid. *J. Appl. Mech. Tech. Phys.*, 9:1990–1994, 1968. 47, 48, 69, 178, 194

[ZCIM02] J.G. Zhou, D.M. Causon, D.M. Ingram, and C.G. Mingham. Numerical solutions of the shallow water equations with discontinuous bed topography. *Int. J. Numer. Meth. Fluids*, 38:769–788, 2002. 52, 121, 133, 239

[ZD98] J. Zoltak and D. Drikakis. Hybrid upwind methods for the simulation of unsteady shock-wave diffraction over a cylinder. *Comput. Method. Appl. M*, 162:165–185, 1998. 282

[Zel91] J.A. Zelt. The run-up of nonbreaking and breaking solitary waves. *Coastal Engineering*, 15:205–246, 1991. 200, 206, 224, 225, 227, 230, 234

[ZG71] N.J. Zabusky and C.C.J. Galvin. Shallow water waves, the Korteweg-de Vries equation and solitons. *J. Fluid Mech.*, 47:811–824, 1971. 71, 243

[ZK97] V.E. Zakharov and E.A. Kuznetsov. Hamiltonian formalism for nonlinear waves. *Usp. Fiz. Nauk*, 167:1137–1168, 1997. 47, 242

[ZLF92] V.E. Zakharov, V.S. Lvov, and G. Falkovich. *Kolmogorov Spectra of Turbulence I*. Springer-Verlag, Berlin, 1992. 79

[ZR00] C. Zoppou and S. Roberts. Numerical solution of the two-dimensional unsteady dam break. *Applied Mathematical Modelling*, 24:457–475, 2000. 238, 239